

WOLFGANG DREYBRODT
FRANCI GABROVŠEK
DOUCHKO ROMANOV

PROCESSES OF SPELEOGENESIS: A MODELING APPROACH



WITH GUEST CHAPTERS

BY SEBASTIAN BAUER, STEFFEN BIRK, RUDOLF LIEDL, MARTIN SAUTER
AND BY GEORG KAUFMANN

FOREWORD BY DEREK C. FORD

C A R S O L O G I C A



C A R S O L O G I C A

WOLFGANG DREYBRODT, FRANCI GABROVŠEK, DOUCHKO ROMANOV • PROCESSES OF SPELEOGENESIS:
A MODELING APPROACH





Carsologica 4

Urednik zbirke / Series Editor
Franci Gabrovšek

Wolfgang Dreybrodt, Franci Gabrovšek, Douchko Romanov
Processes of Speleogenesis: A Modeling Approach

© 2005, Založba ZRC, Inštitut za raziskovanje krasa ZRC SAZU
ZRC Publishing, Karst Research Institute at ZRC SAZU

Recenzenta / Reviewed by
Derek C. Ford *in/and* Arthur N. Palmer
Oblikovanje / Graphic art and design
Milojka Žalik Huzjan

Izdala in založila / Published by
Inštitut za raziskovanje krasa ZRC SAZU, Založba ZRC
Karst Research Institute at ZRC SAZU, ZRC Publishing
Zanj / Represented by
Tadej Slabe, Oto Luthar
Glavni urednik / Editor-in-Chief
Vojislav Likar

Tisk / Printed by
Collegium graphicum d. o. o., Ljubljana

Izdajo je finančno podprla / The publication was financially supported by
Agencija za raziskovalno dejavnost Republike Slovenije
Slovenian Research Agency

Fotografija na naslovnici / Front cover photo: Markov spodmol
Foto / Photo by Arne Hodalič

Digitalna verzija (pdf) je pod pogoji licence <https://creativecommons.org/licenses/by-nc-nd/4.0/>
prosto dostopna: <https://doi.org/10.3986/9789610503125>.

CIP - Kataložni zapis o publikaciji
Narodna in Univerzitetna knjižnica, Ljubljana

551.442

DREYBRODT, Wolfgang

Processes of speleogenesis : a modeling approach / Wolfgang Dreybrodt, Franci Gabrovšek, Douchko Romanov ; with guest chapters by Sebastian Bauer ... [et al.].
- Postojna : Inštitut za raziskovanje krasa ZRC SAZU = Karst Research Institute at ZRC SAZU ; Ljubljana : Založba ZRC = ZRC Publishing, 2005. - (Carsologica ; 4)

ISBN 961-6500-91-0 (Založba ZRC)

1. Gabrovšek, Franci, 1968- 2. Romanov, Douchko
220478208





PROCESSES OF SPELEOGENESIS: A MODELING APPROACH

**Wolfgang Dreybrodt,
Franci Gabrovšek,
Douchko Romanov**

With guest contributions by:
Sebastian Bauer, Steffen Birk, Rudolf Liedl, Martin Sauter
and by
Georg Kaufmann

**POSTOJNA - LJUBLJANA
2005**





CONTENTS

FOREWORD (Derek Ford)	11
PREFACE	13
1. INTRODUCTION	15
1.1 Karst: understanding it and the aim of this work	15
1.2 A karst aquifer and its properties	16
1.3 Conceptual models of cave development in karst aquifers	17
1.4 Models derived from basic principles of physics and chemistry	18
1.5 The concept of this work and the philosophy behind it	19
2. EQUILIBRIUM CHEMISTRY AND DISSOLUTION KINETICS OF LIMESTONE IN H_2O-CO_2 SOLUTIONS	23
2.1 Equilibrium chemistry of $H_2O-CO_2-CaCO_3$ system	23
2.1.1 Boundary conditions for achieving equilibrium	24
2.1.2 Mixing of saturated solutions in the closed system	26
2.2 Chemical kinetics of the of $H_2O-CO_2-CaCO_3$ system.....	27
2.2.1 Processes and rate equations	27
2.2.2 Dissolution in turbulent flow	30
3. THE EVOLUTION OF A SINGLE FRACTURE	32
3.1 Evolution under constant head conditions: The feedback mechanism and breakthrough	32
3.1.1 Basic concepts and results	33
The range of the parameters relevant for natural karstification.....	35
Discretisation of x and t.....	36
Numerical results for “standard” fracture.....	36
3.1.2 An analytical approximation for the breakthrough time.....	39
An important conclusion: The bottleneck principle.....	44
3.1.3 Solutions with high initial saturation ratios. “Switch off” of the feedback mechanism.....	44
3.1.4 Evolution of a single fracture under linear dissolution kinetics	45
3.1.5 The difference between the evolution of wide fractures and tubes.....	49
3.1.6 Some general conclusions on the evolution of a single fracture.....	50



3.1.7	Time variation of the hydraulic head	50
3.2	The influence of fracture roughness on karstification times	52
3.3	Evolution of a single fracture with varying lithology	55
3.3.1	Numerical results	56
3.3.2	The case $n_2 > n_1$	58
3.3.3	The case $n_2 < n_1$	59
3.3.4	Multiple boundaries and boundaries with insoluble rock	60
3.4	The influence of subterranean CO ₂ sources on the initial karstification of a single fracture	61
3.4.1	Point sources of CO ₂	62
	Numerical results	63
	Analytical estimation of T _B	66
3.4.2	Extended sources of CO ₂	67
	Numerical results	68
	Analytical approximations	69
3.4.3	The reverse case: extended input in the second half of the fracture	72
3.4.3	Conclusion	74
3.5	The role of mixing corrosion in early karst evolution	74
3.5.1	Background and model structure	74
	A brief history of mixing corrosion: when and why?	74
	Model structure	75
3.5.2	Numerical results and discussion	77
	Model parameters	77
	Linear kinetics with MC vs. nonlinear kinetics without MC	77
	Nonlinear kinetics with MC	78
	Chemical evolution of the solution in fractures	79
3.5.3	The reduction of the breakthrough time due to the MC	81
3.5.4	Asymmetric confluence	83
3.5.5	Conclusion	84
3.6	Evolution of a single fracture with constant recharge	85
3.6.1	The model structure and numerical results	85
3.6.2	Analytical approximations	87
3.6.3	Fracture with a constant recharge and varying geochemical parameters	88
3.6.4	Conclusion	90

4. MODELING KARST EVOLUTION ON TWO-DIMENSIONAL NETWORKS:	
CONSTANT HEAD BOUNDARY CONDITIONS	91
4.1 Modeling domain	92
Code box: An assistance to read the figures: bar codes and color codes	92
4.2 Percolation networks	94
4.2.1 Calculation of network evolution	96
4.2.2 Results for the standard percolation network	97





4.3	Evolution of 2-D percolation networks and breakthrough.....	103
4.3.1	Mixing at fracture intersections	107
4.3.2	Validity of constant head boundary conditions	108
4.4	Statistical 2D-networks	109
	The high-dip model	109
4.4.1	Applications of 2-D network simulations	112
	The low dip model	112
	High-dip model with varying lithology.....	114
	High dip model containing a region of insoluble rock	116
4.5	One step closer to reality. The dual-fracture system	117
4.5.1	Single prominent fracture embedded in the net: Enhancement of karst evolution	119
4.5.2	Retardation of karstification by flow into prominent fractures	125
4.5.3	A loop of prominent fractures: An example with inflow and outflow	126
	Profiles of dissolution rates	130
4.5.4	The dual-fracture aquifer: A percolation-net of prominent fractures embedded into a statistical net of fine fractures.....	133
4.5.5	Results and discussion	134
4.6	Geochemical boundary conditions.....	139
4.6.1	Influence of the input concentration	139
	Percolation networks	140
	Statistical networks	141
4.6.2	Mixing corrosion in 2-D nets: The chemical pathways	143
4.6.3	Mixing corrosion in a 2-D statistical network: Two modes of evolution ...	144
	Two extreme cases	145
	The intermediate cases.....	149
4.6.4	Mixing corrosion in percolation nets	153
4.7	Mixing corrosion in dual-fracture aquifers	159
4.7.1	Pure mixing corrosion: One prominent fracture in a statistical network....	160
4.7.2	Pure mixing corrosion. Two prominent fractures in a uniform network	163
4.7.3	Pure mixing corrosion: Two fractures in a statistical net.....	165
4.7.4	Pure mixing corrosion: A more complex case by adding isolated fractures and dead ends.....	167
4.8	Mixing corrosion and breakthrough.....	170
4.8.1	One prominent fracture in a statistical network.....	170
4.8.2	Two prominent fractures in a 2D-network.....	176
4.8.3	The more complex case by adding isolated fractures and dead ends	179
4.8.4	The dual-fracture system.....	182
4.9	Dual-fracture aquifer: Mixing corrosion from differently vegetated areas.....	186
4.10	Dual-fracture aquifer: Subterranean input of CO ₂	190
4.11	Evolution of dual-fracture aquifers after breakthrough: Integration of conduits ...	194
4.12	Concluding remarks	199





5. UNCONFINED AQUIFERS UNDER VARIOUS BOUNDARY CONDITIONS	201
5.1 Calculation of the water table and the evolution of an unconfined aquifer	204
5.2 Scenario A: The evolution of unconfined aquifers under conditions of constant recharge.....	205
5.2.1 Statistical network.....	205
5.2.2 Dual-fracture network.....	207
5.3 Scenario B: A combination of constant recharge and constant head boundary conditions in a dual-fracture aquifer	209
5.4 Scenario C: Two valleys of different altitude at the margins of the plateau.	215
5.5 Mixing corrosion in unconfined aquifers.....	222
5.5.1 Unconfined aquifers under conditions of constant recharge including mixing corrosion (Scenario A).....	222
5.5.2 Mixing corrosion in a combination of constant recharge and constant head boundary conditions (Scenario B).....	227
5.5.3 Mixing corrosion for an aquifer bordered by two valleys (Scenario C).....	234
5.6 Evolution of unconfined aquifers under unevenly distributed recharge	236
5.7 Unconfined aquifers under miscellaneous boundary conditions	239
5.7.1 The influence of input concentrations on the simple scenario A	239
5.7.2 Influence of the depth of the limestone aquifer	240
5.7.3 Adding master joints and bedding planes	243
5.7.4 Down-cutting and up-filling of a valley.....	246
5.7.5 Subterranean sources of CO ₂ in Scenario A.....	248
5.7.6 The influence of lithology on the evolution of unconfined karst aquifers....	251
5.7.7 The evolution of karst aquifers at the contact of limestone to insoluble rocks	253
5.8 Conclusion and summary.....	256
6. KARSTIFICATION BELOW DAM SITES	258
6.1 Basic settings and modeling domain.....	259
6.2 Numerical results for scenarios with uniform nets	262
6.2.1 Standard scenario A.....	263
6.2.2 Standard scenario B	267
6.3 Numerical results for scenarios with statistical nets	268
6.3.1 Standard scenario A.....	268
6.3.2 Standard scenario B	270
6.3.4 Evolution of flow rates for statistical scenarios A and B.....	271
6.4 Influence of basic hydrological and geochemical parameters on breakthrough time	272
6.5 Examples of more complex geological settings.....	275
6.6 Conclusion.....	278





7. CONCLUSION AND FUTURE PERSPECTIVES	279
8. BIBLIOGRAPHY	281

GUEST CHAPTER by Sebastian Bauer, Steffen Birk, Rudolf Liedl and Martin Sauter

SIMULATION OF KARST AQUIFER GENESIS USING A DOUBLE PERMEABILITY APPROACH – INVESTIGATION FOR CONFINED AND UNCONFINED SETTINGS	287
1. Introduction.....	287
2. Model formulation	290
3. Influence of exchange flow on early karstification.....	294
4. Karst development in confined settings.....	298
4.1 Single conduit development	300
4.2 Conduit network	302
5. Karst development in unconfined settings.....	304
6. Karst development under man made conditions.....	311
7. Conclusions.....	316
Acknowledgements.....	317
References.....	317

GUEST CHAPTER by Georg Kaufmann

STRUCTURE AND EVOLUTION OF KARST AQUIFERS: A FINITE-ELEMENT NUMERICAL MODELLING APPROACH	323
1. Introduction.....	323
1.1 Aquifer geometry	324
1.2 Aquifer response	325
2. Theory	327
2.1 Dissolution kinetics of CaCO ₃ -CO ₂ -H ₂ O system.....	327
2.2 Flow and evolution of single fracture	332
2.3 Aquifer network	336
3. Results for flat-lying strata.....	338
3.1 Long-term evolution.....	339
3.1.1 Distributed recharge.....	339
3.1.2 Recharge through sinks.....	348
3.1.3 Recharge through sinks including mixing corrosion	355
3.1.4 Summary of long-term evolution models	361
3.2 Short-term spring response	362
3.2.1 Homogeneous karst aquifer	362
3.2.2 Heterogeneous karst aquifer	364
3.2.3 Summary of short-term spring response models	369
Acknowledgements.....	370
References.....	371







FOREWORD

Human beings have explored limestone caves throughout time. Prehistoric people not merely used their entrances as dwellings but walked or crawled long distances inside. In Europe, interior chambers preserve the earliest sculptures and polychrome paintings. In the Americas, effluorescences of Epsom salts and others compounds on cave walls were scavenged as much as three km underground for medicinal purposes. Early folklore had highly imaginative ideas about the nature of caves; karst areas are full of tales of ducks and such being swept underground by floods, to emerge days later at cave springs with their feathers scorched by their passage through the Infernal regions. Scientific speculation on the origin and development of the caves came later. European writings from the 14th Century onwards at first stressed catastrophic openings during earthquakes or violent volcanic eruptions. In the 17th and 18th Centuries the role of flowing water began to be recognized, with early attribution to the scouring impacts of Noah's Flood. In the 19th Century it was recognized that carbonate dissolution was of major importance and it was appreciated that the solubility of the rocks in pure water might be enhanced by carbonic acid from atmospheric and soil sources. Despite this, the solubility of carbonate rocks is low and, in the middle of the 20th Century, scientists continued to wonder how initial fractures, much less than one mm in aperture came to be enlarged into man-sized conduits km in length when evidence suggested that the solvent capacity of the water must be exhausted within a metre or two of the input point. This is the problem of solution kinetics that attracted the attention of practical researchers such as the oil geologist, Peter Weyl, in turn stimulating others such as the geomorphologist, Alfred Bögli, to propose solvent enhancement by mixing of different waters, or the introduction of exotic acids.

Turning to the three-dimensional problem of how cave passage patterns might develop between the groundwater sink points and the springs in a massif, the early focus was upon the dimensions of length and depth and the relationship between the cave and the water table. By the 1950s there were propositions that caves must develop chiefly above the water table, or chiefly beneath it, or chiefly along it! In 1965 and after I put forward a conceptual model based on field studies in caves of the Mendip Hills, England, that showed that all three types might occur; it depends upon differing combinations of initial penetrable fissure frequency and geometry, and the hydrogeologic setting. At the same time, hardware modeling of the evolution of cave plan patterns was beginning. Some used the flow of electricity through grids as analogues. Ralph Ewers at the University of Cincinnati investigated the dissolution of salt along an artificial fracture then, in 1972–5, joined me at McMaster University, Canada, for PhD studies of this question. He used plaster of Paris slabs to simulate solvent penetration of bedding planes. We systematically explored conduit evolution for the case of one point input of water, for multiple inputs in one rank, and for multiple ranks. We also attempted to build a 100×100 grid computer model to calculate dissolution and discharge at each node but, at a time of limited access to slow main frame computers, failed to complete it satisfactorily. Our plaster dissolution caves gave us considerable insight into the manner in which cave patterns might develop, however, but they were only 30 cm or so in length and tiny in diameter. Independent testing and expansion of the conclusions was needed.

Wolfgang Dreybrodt blazed onto the scene later in the 1970s. He was a specialist in Raman spectroscopy, a subject remote from limestone caves, but like me was also a passionate



explorer and observer of them. He took up the challenges of cave science wholeheartedly. It was the dawn of the personal computer era and so it was natural that computer modeling of speleogenesis, the focus of this book, should become central to his research. Readers must appreciate, however, that he is also a hands-on experimentalist who has made important contributions to solution kinetics through hardware laboratory studies of the dissolution of calcite and dolomite, and gypsum under controlled conditions. He has truly broad interests in speleology that include models for rate controls of calcite deposition on stalagmites, and mechanisms of condensation corrosion that (we now recognize) can effect substantial dissolution caves after they are drained of their formative groundwater. He has attracted a number of very good PhD students to work with him. He is an excellent collaborator, a quality that is not true of all scientists. Two students of outstanding ability, Franci Gabrovšek and Douchko Romanov, are his co-authors in this book.

The treatment of limestone cave genesis in this volume is very systematic. Following a brief introduction, Chapter 2 gives a careful outline of the chemistry and kinetics of the $\text{CaCO}_3 + \text{H}_2\text{O} + \text{CO}_2$ system. It utilizes many of Wolfgang's original contributions. Chapter 3 then considers the fundamental case of the genesis of a conduit from a single input point in a single fracture; its discussion of the possible roles of mixing corrosion and deep source CO_2 makes it the most complete treatment that is to be found in the literature. Chapter 4 and 5 then enlarge upon more complex, multi-input modeling of plan patterns and length-depth evolution respectively. These chapters are the heart of the volume, an explosion of explanation that uses no less than 142 colour computer plots and graphs in what must be described as a "tour de force". I am very impressed by the rational sequencing of multi-input and -rank models, with most imaginative development of mixing corrosion situations, of varying lithological and structural geologic controls, and hydrologic and soil CO_2 controls. These chapters conclude by tying the models clearly to larger scale regional developments such as valley entrenchment or aggradation, and the concomitant karst aquifer evolution. The work is pertinent at all scales from the local epikarst to terrains that are hundreds of km^2 in area.

Every nation with substantial water resources in limestone or dolomite highlands has experienced failures due to leakage when attempting to store water and regulate its flow behind dams. This has been an interest of the authors. In Chapter 6 they conclude the modeling with careful analyses of a number of sub-dam leakage scenarios. Chapter 7 offers a brief look into the future, which is considered to be 3-D modeling, the next big step forward.

The Dreybrodt team's modeling has always focused upon the genesis of caves. In contrast, most hydrogeologists are concerned with understanding the distribution and behaviour of the groundwater resources within a given basin, whether it has caves or not. Computer modeling has been a leading part of their work since the 1970s, but chiefly with rather simple assumptions that the bedrock or alluvium, etc. of the aquifer functions as an homogeneous porous medium. The problem of coping with the occurrence of massive heterogeneities such as dissolutional conduits whose size, organization and distribution within an aquifer is simply unknown, has been generally ignored or at best approached by assigning different values of bulk porosity to different volumes of the rock. The consequences have been that modeling forecasts of the instantaneous discharge and (very important) the rapidity of transport of pollutants in karst aquifers has often been grossly in error. In the 1970s and 1980s, some groups in Europe sought to address these difficulties by introducing more sophisticated assumptions of dual porosity everywhere within the aquifer. The group based at the University of Tübingen has been at the forefront of this work. Its modeling explorations have inevitably led it to at-





tempt to evolve the dissolutional conduits rather than merely fit guessed patterns of them into the aquifer as static entities. The Tübingen CAVE model is one of the products of this work. It is carefully explained and illustrated by its authors in the first of two guest chapters. Readers will be struck by the contrast with the approaches adopted by the Dreybrodt team, but also impressed by the convergence of findings that occurs and that upholds the validity of both.

Georg Kaufmann, University of Göttingen, is a geophysicist whose enthusiasm for cave exploration has brought him into cave science. He has broad interests within it, publishing stimulating and independent model studies on the evolution of karst canyon landscapes, or the morphogenesis of calcite stalagmites under changing climatic conditions. In his contribution he utilizes finite element modeling to produce patterns of dissolutional cave networks in a variety of hydrogeologic settings. The behaviour of their spring hydrographs as these aquifers evolve to full conduit control of their discharge during timespans up to 100,000 years is well developed. It is a distinct and striking contribution with which to complete the volume.

“Processes of Speleogenesis: a Modeling Approach” is an exciting book that brings together and displays the products of the first and second generations of karst cave and aquifer computer modeling in a succinct fashion, with excellent illustrations and stimulating contrasts of approach. It is a ‘benchmark’ publication that all who are interested in speleogenesis should read. It will be a very useful volume for teaching, not only in karst and hydrogeology, but for others who use computer modeling in the physical and spatial sciences.

May 2005

Derek Ford,
Lake Couchiching, Ontario

PREFACE

Karst is a fascinating phenomenon. It inspires our emotions for beauty and adventure when we walk through its exciting sceneries on the surface or in caves underground. However, it also rouses our curiosity to understand how these landscapes emerged. The simple answer was, of course, for a long time: through the dissolution of limestone by water containing carbon dioxide. But this simple statement raises many further questions. One has to know how fast limestone can be dissolved and to what extent. After these questions had been answered by numerous laboratory experiments, the next logical step was to model karst aquifers by combining dissolution chemistry with the hydrodynamics of flow in fractures of the rock. In a first step we modeled one-dimensional conduits in the group in Bremen, which Franci Gabrovšek joined in 1997. His thesis, which was published by the publisher of this book, already contained many of the ideas on which this work is based. When Douchko Romanov joined us later in 2000, we dived into a world of models. We developed the concept of karst evolution in dual-fracture aquifers and improved programs and concepts.

When we all met in Postojna at the Symposium: “Evolution of Karst: From Prekarst to Cessation” in 2002, we realized that Franci Gabrovšek’s book had been sold out, so we had the idea of working on an improved and extended 2nd edition. However, during this work we had so many new results which we wanted to include, that the 2nd edition became a new book.





The first part, mainly chapters 1–3, are a revised version of Franci's text on one-dimensional conduits. The second part, chapters 4 to 6, is new and was written within the immediate context of the modeling work, such that the modeling results influenced the text, and, conversely, the writing process led to the introduction of new modeling scenarios. As a result, this book contains many results which have not been published previously.

*We know that the subject of this book is complex. In view of this fact and the short time between the production of the results and their publication, it may not be easy to read. We hope, however, that the illustrations and the animations on the CD will help the reader to understand the variety of processes active in karst evolution, particularly those not so familiar with karst modeling. We were encouraged in the venture of writing this book when we realized that our review article about the basic processes in karst evolution, published in the *Proceedings of the Postojna Symposium* and republished by the on-line journal www.speleogenesis.info, found so much interest. This book would never have been written without the interest and the open mindedness shown by the scientific karst community, in supporting the ideas of a few physicists, coming from outside the scene, but introducing some new ideas from their field. Especially Wolfgang Dreybrodt, as the oldest of us, wishes to express his thanks to A. N. Palmer, W. B. White, J. Thrailkill, J. F. Quinlan and R. O. Ewers as representatives of all the people, who introduced him to karst and the karst community on his first visit to the United States in 1986. As a consequence of the first step into the community, later support has also been given by Derek Ford, Alexander Klimchouk, John Gunn and many others. The list of all the names would be too long. They all share merits to the outcome of our work. We express our thanks to Derek Ford for writing a foreword for this book. This symbolizes the support given to us by him and also by the community of karst researchers.*

Since the summer of 2000 an informal workshop has been held annually in Tübingen to discuss concepts in karst modeling, which we, Georg Kaufmann, and the group of Martin Sauter and Rudolf Liedl have attended regularly. Laszlo Kiraly and Pierre-Yves Jeannin also participated. This was a fruitful exchange of ideas, sometimes also controversial. A book on karst modeling should contain the results of alternative approaches such as those of the group of R. Liedl and the work of Georg Kaufmann. Since we wanted to publish our ideas and concepts in this book, rather than writing a review of karst modeling approaches, we invited the Tübingen group and Georg Kaufmann to publish a review of their ideas as guest contributions in this book. These articles are in the responsibility of their authors and have not been edited by us. Thus this book offers an almost complete overview of karst modeling approaches in Europe.

We thank Annegret Ebert and Katrin Vosbeck for their work on the manuscript. D. Romanov expresses his thanks for a one-year postdoctoral grant of the University of Bremen, dedicated to work on this book. Parts of this book were written during two stays of W. Dreybrodt at the Karst Institute in Postojna, who is grateful to the colleagues and to Tadej Slabe for their support and hospitality. F. Gabrovšek thanks to the University of Bremen and the Scientific Research Center SAZU for enabling his stays in Bremen. We highly appreciate the financial support of the Slovenian Research Agency.

Finally we all thank our wives for patiently enduring our frequent absences, physical or mental, during our work on the book.

Bremen, Postojna, April 2005

*Wolfgang Dreybrodt
Franci Gabrovšek
Douchko Romanov*





1. INTRODUCTION

1.1 KARST: UNDERSTANDING IT AND THE AIM OF THIS WORK

Karst is a typical landscape on soluble rocks with a distinctive hydrology, unique landforms and fantastic underground features, which attract people to observe and study it. The longest cave systems reach beyond 500 km, the deepest beyond a vertical distance of 2 km (2080 m at the time of writing) between their highest and lowest points. A mature karst landscape is characterized by the absence of surface flow. Karst covers about 10 %–20 % of the Earth's land ice-free area (Ford and Williams, 1989).

To study karst is not only important for its unique features. It has also practical significance. About 25 % of the world population drinks water from karst aquifers. One should not forget that the fresh water supply is expected to be one of our mayor problems in this century.

The facts quoted above should be sufficient to justify this work, which deals with the early evolution of karst.

The main process rendering karst unique is the dissolution of bedrock by water. The most common types of karst rocks are sedimentary carbonates, limestone and dolomite. Gypsum, anhydrite, salt and quartzite karst areas are also known around the world. Karst rocks attain a considerable secondary porosity during its evolution.

Many karst features on the surface owe their origin to the subsurface drainage of water in karst aquifers. The question how do karst aquifers evolve in time and consequently how do caves develop, has puzzled scientists and observers for a long time. And it still does.

To understand karst and its evolution one has to study and understand the basic processes behind it. Basically there are two approaches to this:

- From large to small scales, an empirical approach, which describes the basic processes mainly from field observations.
- From small to large scales, an analytical approach, which builds complex systems with simple elements based on the basic principles of physics and chemistry.

Neither is good alone. The empirical approach may lead to wrong conclusions because the general picture is too complex. The analytical approach uses extremely simplified models of reality and neglects many parameters, which can be important.



One or the other concept remains just a concept or a hypothesis if the two do not meet. Once both ways match a good theory might appear.

The idea of this work is to contribute a few building blocks to the bridge between the empirical and analytical concepts from the side of the analytical approach.

1.2 A KARST AQUIFER AND ITS PROPERTIES

Before we give a review on speleogenetic ideas, we define “our playground”: a karst aquifer. Figure 1.1 presents a simple example of it.

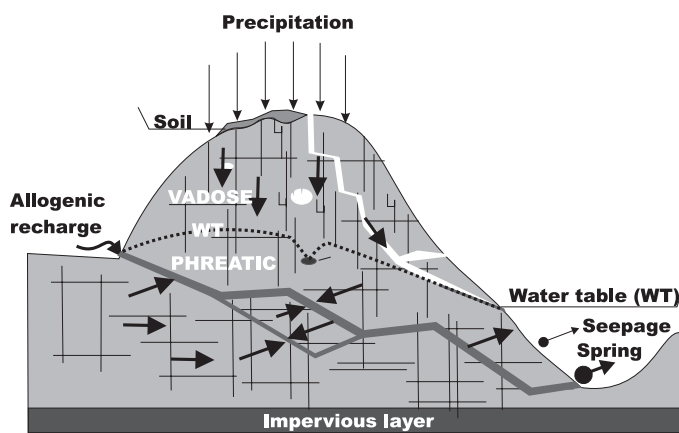


Figure 1.1: Conceptual model of a karst hydrological system with its elements and flow systems.

The term aquifer defines a rock body sufficiently permeable to transmit groundwater (Bear and Verruijt, 1987). What makes karst aquifers specific is that their transmissivity and storage are increasing in time by dissolution of bedrock. Typical karst aquifers exhibit a small primary porosity, but attain high secondary porosity due to the circulation of water, which dissolves bedrock. In the initial state of a karst aquifer flow of water is limited to fractures and bedding planes. Our study will deal with flow systems, which owe their origin to meteoric water circulating within the massif of limestone or other soluble rocks. This way the so-called “common caves” (Ford and Williams, 1989) are formed. In most of the following discussion, we assume aquifers originating from fractured limestone.

Pure water cannot dissolve much limestone. Already in the 18th century it was well accepted that water-containing CO_2 is the aggressive agent in karst. Only atmospheric CO_2 was considered at that time. This way the CO_2 - H_2O solutions cannot dissolve much limestone, since the CO_2 represents only about 0.03 % of the atmosphere. Later Swinnerton (1932) stressed the importance of soil CO_2 . The CO_2 content in the soil “atmosphere” is often above 5 % (Ford and Williams, 1989).

Mature karst aquifers exhibit an extreme heterogeneity of hydraulic conductivities. They range from 10^{-10} m/s up to 10^{-1} m/s (Halihan *et al.*, 1999; Worthington, 1999). The lowest conductivity is due to the intergranular porosity of the rock matrix, the highest

is from large cave conduits. Therefore flow in karst aquifers can be of any type: from laminar flow in narrow fissures to turbulent flow in filled or open channels.

The key question of speleogenesis is how does this secondary porosity evolve? How does a relatively homogeneous aquifer characterized by the rock matrix, fractures and bedding planes with aperture widths less than about 0.01 cm evolve to such a complex structures like extensive cave systems?

1.3 CONCEPTUAL MODELS OF CAVE DEVELOPMENT IN KARST AQUIFERS

In the 18th and 19th (Ford and Williams, 1989) century big steps were taken once the importance of chemical dissolution was known and basic equations on fluid flow in porous and fractured rock aquifers were given.

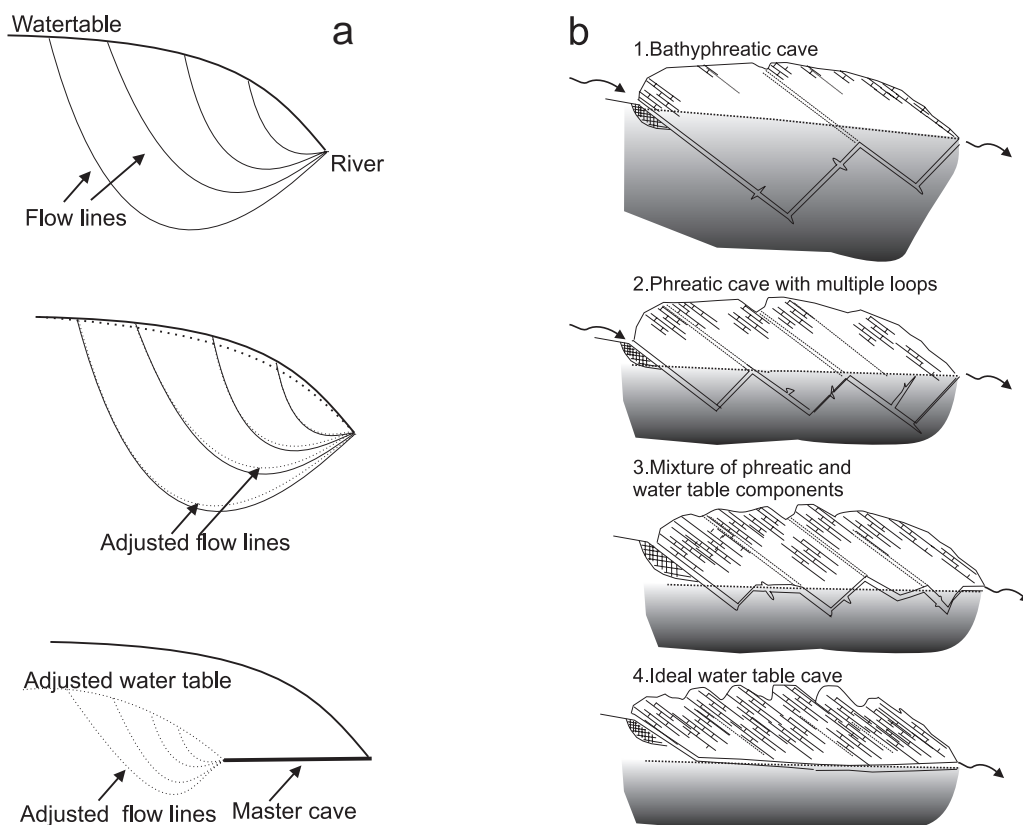


Figure 1.2: a) The water table cave hypothesis proposed by Rhoades and Sinacori. b) Ford and Ewers's four-state model. Depending on the fissure frequency various types of caves evolve: When fissure frequency is low, bathypneatic caves (state 1) originate. With increasing fissure frequency the number of phreatic loops increases (states 2 and 3). High fissure frequency results in the evolution of water-table caves. Extremely low or extremely high fissure frequency does not allow evolution of caves (states 0 and 5, not shown here). Both figures are taken from Ford (1999).

Most of the modern concepts of speleogenesis were put forward between 1900 and 1950. The theories were rather conflicting, since each of them was based on a specific location. Three hypotheses were accepted at that time (Ford and Williams, 1989):

- The vadose hypothesis implies that open channel cave streams in the vadose zone excavate caves.
- The deep phreatic hypothesis assumes that caves develop deep below the water table in the phreatic zone.
- The water-table hypothesis (Rhoades and Sinacori, 1941; Swinnerton, 1932) is based on the fact that most of the water movement is along the water table at the top of the phreatic zone. Therefore, the caves develop there. See Figure 1.2a.

Each of these hypotheses was at least partially right. Evidences all around the globe supported them, but none was generally valid. Ford and Ewers (1978) linked these hypotheses into one genetic theory. They proposed a four-state model in which deep phreatic and water table caves are the end members. In their model the fissure frequency determines what kind of cave develops. See Figure 1.2b.

1.4 MODELS DERIVED FROM BASIC PRINCIPLES OF PHYSICS AND CHEMISTRY

The basic knowledge of the properties of karst aquifers and of dissolution kinetics of limestone, as well as access to computational power, enabled another approach towards understanding the evolution of karst aquifers.

Starting from the basic principles of groundwater chemistry and hydrology and applying parameters and boundary conditions typical for karst, the first numerical models were presented in the late 1980 and beginning of 90 by Dreybrodt (1990; 1996) and Palmer (1991). They presented the evolution of a basic building block of karst aquifers: a single fracture.

Later Lauritzen *et al.* and Petersen (1992) and Groves and Howard (1994b; 1995) and Howard and Groves (1995) presented a model of speleogenesis on two-dimensional networks. A further step was taken by Siemers and Dreybrodt (1998) and Dreybrodt and Siemers (2000) who presented the evolution of 2D percolation networks and implied various lithological and hydraulic conditions. They also presented the evolution of 2D networks in the vicinity of hydraulic structures. This is a case where the potential of numerical models is of great practical importance.

Recently Liedl *et al.* (2003) used a double porosity model to couple the conduit flow with the flow in the surrounding continuum and to calculate the evolution of conduits under constant recharge conditions. The further progress of this concept is summarized in a guest article by Bauer *et al.* in this book. There, also citations of their original publications are given.

A similar approach was made by Kaufmann and Brown (1999; 2000) who simulated



the double porosity by incorporating the prominent fractures directly into continuum. In a second guest article in this book Kaufmann reports on the further progress of his work.

Much of the knowledge accumulated in the last century has been reviewed in “Speleogenesis. The evolution of karst aquifers” (Klimchouk *et al.*, 2000). This book gives an excellent overview on speleogenetic field observations, on the dissolution kinetics of limestone and gypsum, on concepts of numerical models, and on the history of speleogenetic ideas. It is highly recommended to the reader.

In 2002 a symposium on “Evolution of Karst” was held in Postojna, Slovenia. The contributions given during this symposium have been edited by Gabrovšek (2002) in “Evolution of Karst. From Prekarst to Cessation.”

A recent online journal “Speleogenesis and Evolution of Karst Aquifers” (<http://www.speleogenesis.info>) is freely available. Besides original contributions it also contains many articles republished from conference proceedings, which are not easily available. There the reader can also find a review article by Dreybrodt and Gabrovšek on the basic processes and mechanisms governing the evolution of karst.

1.5 THE CONCEPT OF THIS WORK AND THE PHILOSOPHY BEHIND IT

There are several ways to build up numerical models of karst aquifer evolution. The first type, let us name them “application oriented”, can be a three-dimensional model of an aquifer with multiple porosity and complex boundary conditions applied to it. Such models can be developed nowadays but their interpretation can be as hard as the interpretation of observations in nature. Of course in the model one can envisage many different scenarios and play with the parameters much easier than nature does. Anyway the traps are similar to those in the empirical approach.

What we want to understand are the basic processes and mechanisms. Therefore we employ the process modeling and start with the simplest elements of karst aquifers. Then we build more complex models gradually, not adding new parameters before the effects of all the old ones are investigated. This approach is of course time consuming, since the addition of any parameter demands the analyses of its impact on the scenarios with all the parameters used before. According to our experience, one can easily misinterpret the results of more complex models without a deep understanding of simpler ones.

The path of this work starts with simple models and takes us towards more complex ones. It resembles the historical development of the models presented so far. Especially in the simple systems our approach will be partially analytical, i.e. we will try to make analytical approximations to elucidate the obtained numerical results. By this way we gain a deeper understanding of the models and their more general results.

The book is organized in the following way. In chapter 2 we discuss the geochemical principles of the system $CaCO_3-H_2O-CO_2$ and present its dissolution kinetics as a basic keystone for the models.



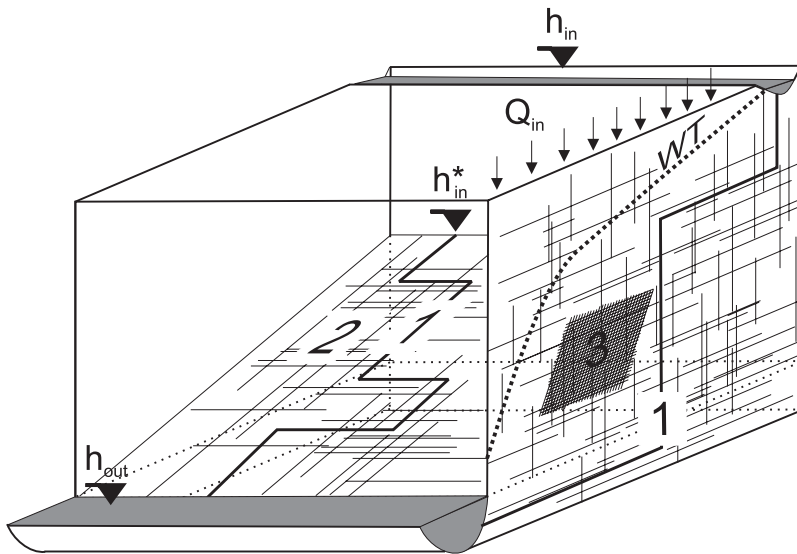


Figure 1.3: The elements of a karst aquifer discussed in this work. 1: A single fracture under constant head conditions. 2: 2D fracture network under constant head conditions. 3: A vertical section of an unconfined aquifer with a constant recharge and constant head conditions applied to it. As shown, a dense network of fine fractures and a coarse network of prominent fractures are superimposed to simulate the multiple porosity character of karst aquifers. The thick dashed line WT represents the position of the water table. The hydraulic heads at the inputs and outputs are denoted as h_{in} , h_{in}^* and h_{out} .

Figure 1.3 schematically illustrates the approach, which is taken in the following chapters 3–5. In chapter 3 we discuss the evolution of a single isolated one-dimensional fracture fracture as shown by **1** in Figure 1.3, where a constant head drop drives a flow of CO_2 -containing water through it. In this case a positive feedback loop is active and although widening of the fracture is initially slow, later on the fracture aperture width increases dramatically causing a breakthrough of flow.

For such simple systems approaches of numerical modelling can be complemented by analytical approaches, which give a deeper insight. After discussing the evolution of a single conduit, we study the influence of varying lithology, expressed by the constants of the rate laws describing the dissolution kinetics on its evolution. Then we turn to the action of subterranean CO_2 -sources to speleogenesis of a single conduit. Finally we look for the role of mixing corrosion. This chapter provides the basic blocks needed later on. The mathematics used for the analytical approximation consists mostly of basic calculus and should not deter the reader. The results can be understood without following the derivations in detail. In the following chapters numerical models will replace analytical approaches.

In chapter 4 we first extend the models to simple two-dimensional percolation networks, which represent limestone terrains with only a few fractures widely spaced and extending along large distances, as shown by **2** in Figure 1.3. We again consider boundary conditions of constant head and explore the evolution of fracture widths and flow. It turns out that the behaviour is similar to that of single channels.



1. INTRODUCTION

As another extreme a 2-D-net of fissures, closely spaced, with a statistical distribution of aperture width is constructed. This scenario simulates terrains with highly fractured rock.

The breakthrough behaviour of such aquifers is modeled under various boundary conditions, such as Ford and Ewers's high-dip and low-dip models (Ewers, 1982; Ford and Williams, 1989). We also investigate the influence of varying lithologies.

If both extremes of fracturing are combined in a dual-fracture aquifer as illustrated in Figure 1.3 by nesting a percolation net of prominent fractures with wide spacing and large aperture widths into a dense net of fine fissures, exchange of flow between these two networks adds new complexity. The influence of exchange flow in such dual-fracture aquifers is modeled in several scenarios in dependence of the intensity of the coupling expressed by the ratio of the aperture widths in the dense net to that of those in the wide percolation net. The patterns of conduit evolution are dominated by the structure of the percolation net when the strength of coupling is small. At increasing strength conduits evolve along shortcuts through the fine net.

Different chemical compositions of the inflowing waters can be caused by vegetation on karst plateaus, e.g., high soil p_{CO_2} in grassland and low p_{CO_2} at regions of bare rocks. Depending on the content of carbonates in the soil also the calcium concentration of the solutions entering into the fractures can vary considerably. As a consequence mixing corrosion becomes active deep inside the aquifer, where waters from areas with different p_{CO_2} mix. On the other hand when the calcium input concentrations are low breakthrough behaviour may be dominant. Therefore chapter 4 also deals with the influence of these chemical boundary conditions to confined dual-fracture aquifers.

We describe two modes of karstification. When all differing input concentrations are saturated with respect to calcite mixing corrosion inside the aquifer causes dissolutional widening and karstification proceeds on time scales of about 1 million years, whereby flow rates are increasing steadily. When the input concentrations are below about 90 % of saturation breakthrough is dominant in comparably short times. Between these two extremes with input concentrations close to saturation, both slow widening of fractures from the unsaturated input solutions and mixing corrosion are active. We present a series of examples for various hydrochemical boundary conditions.

In chapter 5 we turn our attention to unconfined aquifers in the dimensions of length and depth, which are recharged by meteoric precipitation and can also exhibit input regions of constant head. This is illustrated by 3 in Figure 1.3. We explore three basic scenarios.

In the first scenario A recharge to the aquifer is delivered solely by infiltration of meteoric water. A water table is established and dissolutional widening is focused close to it. The increasing permeability causes the water table to drop until it reaches base level and a water table cave migrates upstream into the aquifer. We study the impact of mixing corrosion, caused by different vegetation zones on top of the limestone massive, which give rise to different CO_2 -concentrations of the infiltrating water. As a result isolated water table caves are created, which have connections to the output only via narrow conduits.





1. INTRODUCTION

Similar results are obtained when the recharge to the aquifer is unevenly distributed at the top of the plateau. Finally we explore the influence of different lithology, and discuss contact karst at borders between limestone and insoluble but permeable rock.

In the second scenario B a river or lake on top of the plateau additionally supplies water at constant head conditions. In this case the water table cannot drop as long as the constant head supply delivers a sufficient amount of water. In dual-fracture aquifers caves can develop along pathways of prominent fractures, but also along the water table, where dissolutional widening by infiltrating meteoric recharge increases permeability. At low hydraulic coupling breakthrough occurs through percolating pathways of prominent fractures. But with increasing aperture widths of the fine fractures breakthrough cuts through along the water table, employing the system of fine fractures. If the water from the river has a different CO_2 -concentration than that of the meteoric recharge, mixing corrosion becomes active. A few examples are presented.

The last scenario C deals with a limestone plateau recharged by meteoric water at its top and two valleys, with a river in the upper one, at its borders. This supplies a constant head recharge from the upper valley through the limestone massive to base level at the lower valley. The evolution of karst is similar to that in scenario B, and exhibits breakthrough behavior along pathways of prominent fractures and/or through the net along the water table.

Finally in chapter 6 we apply the concepts of chapter 3 to dam sites constructed in limestone and show that under unfavorable conditions dam sites can be endangered by karstification of the limestone below them.





2. EQUILIBRIUM CHEMISTRY AND DISSOLUTION KINETICS OF LIMESTONE IN H_2O-CO_2 SOLUTIONS

Chemical processes are a key for understanding early karst evolution. To model speleogenesis we need to know the dissolution rates of limestone in karst environments. These are a function of undersaturation of the solution, and therefore knowledge of its chemistry is required. The first part of this chapter focuses on the equilibrium chemistry of the $H_2O-CO_2-CaCO_3$ system. In the second part we discuss the chemical kinetics of the dissolution rates. One has to be aware that the knowledge of equilibrium chemistry alone is not enough to model and understand early karstification. The knowledge how fast limestone is dissolved is an indispensable ingredient of conduit evolution. As mentioned in the introduction we only regard the action of H_2O-CO_2 solutions. Note that karstification of limestone might also be caused by other aggressive solutions, such as sulphuric acid in the case of hypogenic karst (Ford and Williams, 1989). These processes will not be discussed in this work.

2.1 EQUILIBRIUM CHEMISTRY OF $H_2O - CO_2 - CaCO_3$ SYSTEM

The most common aggressive agent in karst is CO_2 rich water, which percolates through the limestone massif. The equilibrium chemistry of the $H_2O-CO_2-CaCO_3$ system is well known and discussed in the literature. See (Appelo and Postma, 1993; Dreybrodt, 1988; Dreybrodt, 2000; Morse and Mackenzie, 1990) for more details.

We first focus on pure H_2O-CO_2 solutions. Carbon dioxide dissolves in water. The p_{CO_2} of the surrounding atmosphere and the activity of dissolved CO_2 are related by Henry's law

$$(CO_2^{aq}) = K_H p_{CO_2}. \quad 2.1$$

K_H is the Henry's constant, which is temperature dependent; at 10 °C, $\log(K_H)$ is about -1.27.

CO_2 reacts with water to form H_2CO_3 . This dissociates in steps to $H^+ + HCO_3^-$ and further to $H^+ + CO_3^{2-}$. Mass action laws with the temperature dependent mass action constants K_1 and K_2 govern these dissociation steps.

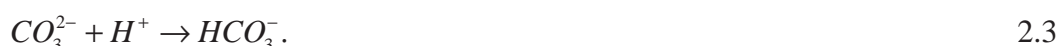
The saturation state of the solution with respect to $CaCO_3$ is defined by K_c



$$\Omega = \frac{(Ca^{2+})(CO_3^{2-})}{K_c}, \text{ where } K_c = (Ca^{2+})_{eq} (CO_3^{2-})_{eq} \quad 2.2$$

The subscript *eq* denotes the state of equilibrium and K_c is the equilibrium constant. Round brackets denote the activity of ionic species. At 10 °C the logarithm of K_c is -8.41 .

Protons produced by dissociation of H_2CO_3 react with carbonate ions released from the mineral:



This reaction keeps the ion activity product $(Ca^{2+})(CO_3^{2-})$ sufficiently low and enables the dissolution of calcite.

The reaction mechanisms at the calcite surface in the presence of carbonic acid were first described by Plummer *et al.* (1978). They proposed three surface reactions which can be summarized by the following overall reaction:



From Eq. 2.4 an important conclusion follows. For each Ca^{2+} ion that enters the solution one molecule of CO_2 is consumed and converted into HCO_3^- .

Further derivation of equilibrium equations will be omitted here and only results important for the following chapters will be presented. For details the reader is referred to (Dreybrodt, 1988; Dreybrodt, 2000).

The basic result of the equilibrium chemistry is the equation describing the equilibrium concentration of Ca^{2+} as a function of p_{CO_2} :

$$[Ca^{2+}]_{eq} = \left(p_{CO_2} \cdot \frac{K_1 K_2 K_H}{4K_c \gamma_{Ca} \gamma_{HCO_3}} \right)^{1/3} \approx 10.75(1 - 0.0139T) \sqrt[3]{p_{CO_2}} \left[\frac{\mu mol}{cm^3} \right] \quad 2.5$$

γ_{Ca} and γ_{HCO_3} are the activity coefficients of Ca^{2+} and HCO_3^- at equilibrium. K_1 and K_2 are the mass action constants for the both dissociation steps, K_c is the solubility constant. T is the temperature in °C. This relation is valid for $p_{CO_2} > 3 \cdot 10^{-4}$ atm.

2.1.1 Boundary conditions for achieving equilibrium

Dissolution of calcite by CO_2 containing water proceeds under various boundary conditions:

- **Open system conditions:** the solution is in contact with limestone and a gas phase containing CO_2 . The flux of CO_2 between the liquid-gas interface replaces the CO_2 consumed by dissolution of calcite.

- **Closed system conditions:** there is no interface between an atmosphere and the solution. CO_2 consumed by dissolution of calcite is not replaced, therefore its concentration decreases with increasing Ca^{2+} concentration.

For the open system the equilibrium concentration is given by Eq. 2.5. In the phreatic zone of karst aquifers, which is the domain of our models, dissolution proceeds under closed system conditions. In this case one has to consider that p_{CO_2} in the solution decreases as dissolution proceeds. Therefore, Eq. 2.5 cannot be directly applied. If $p_{CO_2}^i$ is the partial pressure of CO_2 prior to any dissolution of calcite, than the p_{CO_2} at the closed system equilibrium is given by:

$$p_{CO_2} \approx p_{CO_2}^i - \frac{[Ca^{2+}]_{eq}}{K_H}, \quad 2.6$$

which is valid for $p_{CO_2}^i > 7 \cdot 10^{-4}$ atm. Inserting this into Eq. 2.5 a cubic equation for $[Ca^{2+}]_{eq}$ is obtained. Its solution gives the $[Ca^{2+}]_{eq}$ for the closed system.

The intermediate cases where the solution is in contact with a limited amount of CO_2 rich gas are discussed by Dreybrodt (1988; 2000).

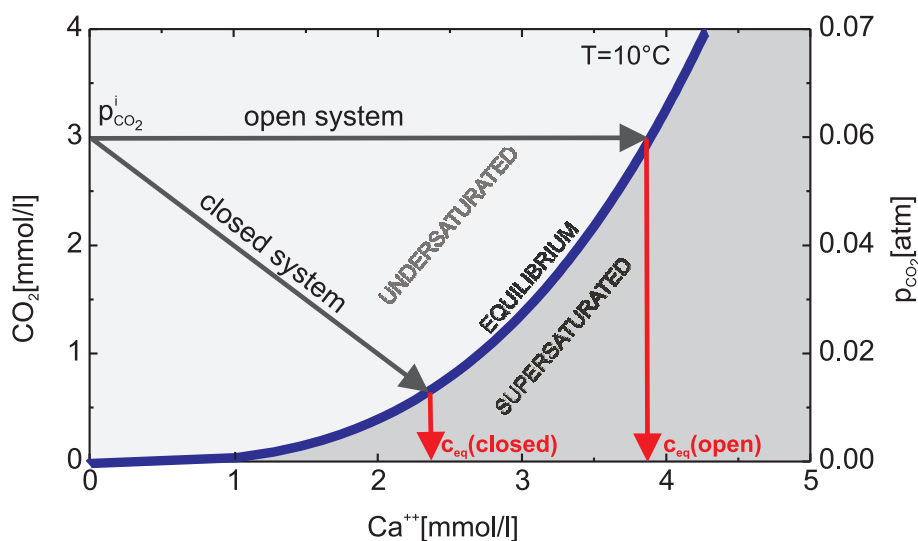


Figure 2.1: Chemical pathways of the solutions in the open and closed system. The thick line represents the CO_2 - Ca^{2+} equilibrium curve as given in Eq. 2.5. Black arrows represent the pathway of solutions in the open and closed system. In a closed system the CO_2 -concentration of the solution drops, because each Ca^{2+} ion released consumes one CO_2 molecule. For an open system this molecule is replaced from the atmosphere and, therefore the CO_2 -concentration stays constant. From the intersection between the pathways and equilibrium curves the equilibrium concentrations can be read. The red arrows point them.

Figure 2.1 shows the pathways of the solution during dissolution of calcite under open and closed system conditions. The thick solid line represents the equilibrium curve as given by Eq. 2.5. The black arrows show the pathways of the solutions in an open and

closed system as denoted. The intersections between the black arrows and the equilibrium curve are the equilibrium points. The red arrows point to the equilibrium concentrations of Ca^{2+} for the open and closed system, respectively.

2.1.2 Mixing of saturated solutions in the closed system

The non-linearity of the CO_2-Ca^{2+} equilibrium curve has an important consequence shown in Figure 2.2. The equilibrium curve divides the regions of undersaturated and supersaturated solutions. If the $([CO_2], [Ca^{2+}])$ composition of the solution is above the equilibrium curve the solution is undersaturated, if it is below, it is supersaturated. For convenience, to avoid too many brackets, we will write (CO_2, Ca^{2+}) instead of $([CO_2], [Ca^{2+}])$.

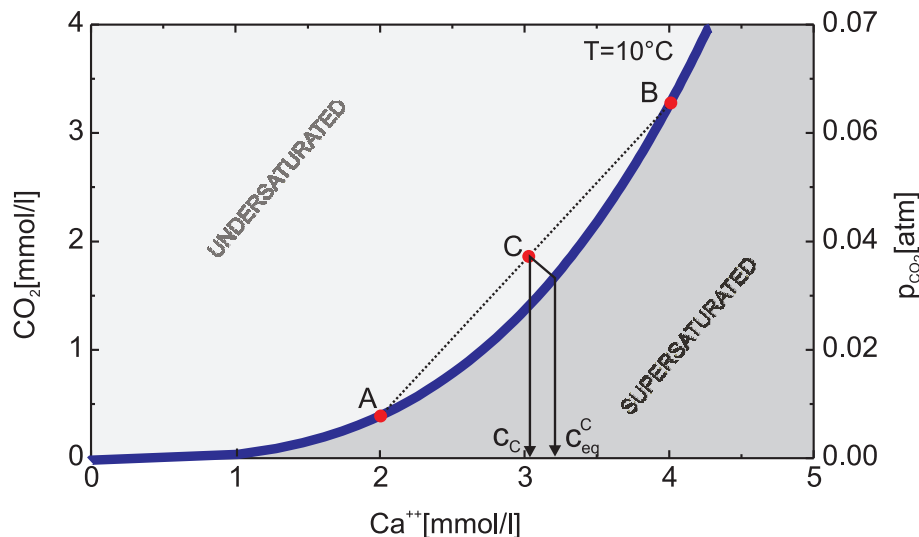


Figure 2.2: Equilibrium curve and the regions of supersaturated and undersaturated solutions. Mixing of saturated solutions A and B, produces an undersaturated solution C. The arrows point to the calcium concentration of solution C and its equilibrium calcium concentration. See text for details.

Figure 2.2 shows the mixing of two solutions A and B, saturated with respect to calcite. The (CO_2, Ca^{2+}) pair of the resulting solution C is on the line connecting A and B. Due to the non-linearity of the equilibrium curve this point presents an undersaturated solution. The arrows point to the Ca^{2+} concentration c_c of the mixed solution C and its equilibrium concentration c_{eq} . In consequence, when two saturated solutions mix the mixed solution becomes aggressive. The importance of this phenomenon to the karst evolution was stressed by Bögli (1964). “Mischungkorrosion” is not a crucial cave forming mechanism, although it enhances early karst evolution as presented recently by Gabrovšek and Dreybrodt (2000) and Romanov *et al.* (2003b). This is discussed in detail latter in Section 3.5 and in Chapters 4 and 5.



2.2 CHEMICAL KINETICS OF THE OF H_2O - CO_2 - $CaCO_3$ SYSTEM

2.2.1 Processes and rate equations

So far we have discussed the chemical pathways of karst waters with respect to Ca^{2+} and CO_2 . The question remains, how fast do the solutions “move” along these pathways in karst environments.

The knowledge of the chemical kinetics of limestone is crucial to the models presented in the following sections. Dissolution of limestone in undersaturated water is controlled by three coupled mechanisms.

- 1. The surface reaction.** The detachment rate at the surface of the mineral is dependent on the composition of the solution and on the concentration of impurities in the mineral. For karst waters Plummer *et al.* (1978) experimentally found that the following rate equation is valid far from equilibrium:

$$F_s = k_3 - k_4 (Ca^{2+})_s (HCO_3^-)_s \quad 2.7$$

where k_3 is a constant dependent only on temperature, and k_4 depends also on the CO_2 -concentration in the solution. The term k_3 represents dissolution, the term k_4 the back reaction, which depends on the activities of $(Ca^{2+})_s$ and $(HCO_3^-)_s$ at the surface of the mineral.

Close to equilibrium natural limestone exhibits much lower rates than predicted by the PWP equation. Based on the experimental data of Plummer *et al.*, Palmer (1991) showed that the surface rates can be described by an empirical rate law given by:

$$F_s(c) = \begin{cases} k_{n_1} (1 - c/c_{eq})^{n_1} & c \leq c_s \\ k_{n_2} (1 - c/c_{eq})^{n_2} & c > c_s \end{cases} \quad 2.8$$

where n_1 is in the range between 1.5 and 2.2, $n_2 \approx 4$ and a the switch concentration $c_s \approx 0.8c_{eq}$. This rate law was experimentally verified for natural calcite by Svensson and Dreybrodt (1992) for the open system and later by Eisenlohr *et al.* (1999) for the closed system. They report values of n_2 between 4 and 11. They also showed that the drop of the rates with respect to PWP is due to impurities in natural limestone which accumulate on the surface and inhibit dissolution.

- 2. The transport.** Ions released from the surface of a mineral must be transported away into the bulk of the solution, otherwise if they would accumulate there, dissolution would stop. This transport is affected by molecular diffusion. As a consequence concentration gradients build up and the concentrations at the surface are different from those in the bulk.



3. **The CO_2 conversion.** Each CO_3^- detached from the mineral requires one molecule of CO_2 to be reacted to HCO_3^- . Mass conservation requires that the flux of Ca^{2+} from the surface must be equal to flux of Ca^{2+} transported into the bulk and equal to flux of CO_2 towards the mineral surface. If the surface dissolution rates are high, CO_2 conversion or mass transport may be rate limiting. CO_2 conversion is a slow process. For pH between 6 and 8 it takes times up to one minute until CO_2 has come to equilibrium with HCO_3^- . If water of volume V dissolves limestone with dissolution rate F from a surface area A mass conservation requires

$$V \cdot \frac{d[CO_2]}{dt} = A \cdot F \quad 2.9$$

If the ratio V/A becomes sufficiently small, the rates will be limited by CO_2 because F does not depend on A and V . Note that for water flowing in a fracture with aperture width 2δ the ratio $V/A = \delta$. On the other hand if the aperture widths 2δ becomes sufficiently large the diffusional resistance can also limit rates.

Generally, all three mechanisms have to be considered. On the other hand the specific settings can favor one or two mechanisms such that these exhibit much higher rates than the rest. In this case the fast mechanisms can be excluded and the rates can be calculated by considering only the slow processes. When only one mechanism is slow we say that the rates are surface, transport, or CO_2 controlled.

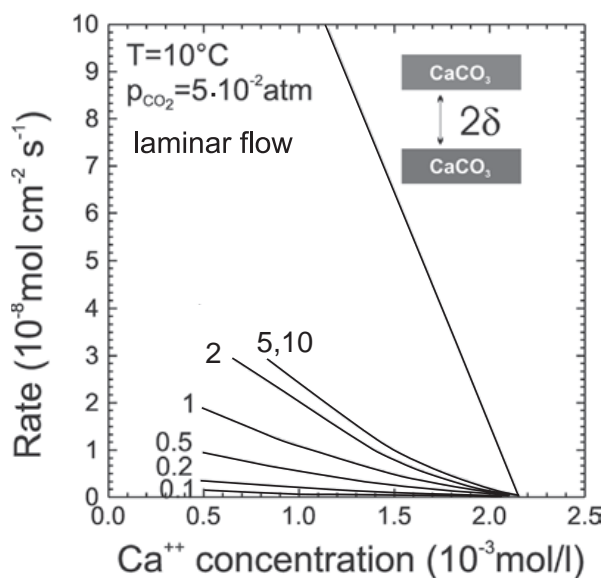


Figure 2.3: Dissolution rates from the theoretical model for a free drift run under the conditions of a system closed to CO_2 . The numbers on the curves denote the values of δ , i.e. half the distance between the parallel calcite surfaces in 10^{-3} cm. For $\delta = 5 \cdot 10^{-3}$ cm and $\delta = 10^{-2}$ cm the curves are identical. The uppermost curve gives the rates for fully turbulent motion and $\delta = 1$ cm. The insert in the upper right depicts the geometry of the fracture.

Figure 2.3 shows dissolution rates for laminar flow in an aperture with limestone walls under closed system conditions. The numbers on the curve give the value of δ in 10^{-3} cm. The dissolution rates are shown as a function of Ca , as they develop in free drift, when the solution approaches equilibrium. For small $\delta = V/A$, e.g. 10^{-4} cm the rates are very low. This is the region where CO_2 conversion is rate limiting. When δ increases

they first increase linearly with δ provided the Ca-concentration is kept constant. With increasing δ the rates approach a limit d_{lim} , where they become almost independent of δ in the region of $5 \cdot 10^{-3}$ cm to 10^{-1} cm. This is of high relevance since this region covers the dimension of initial fracture aperture widths in the early evolution of karst.

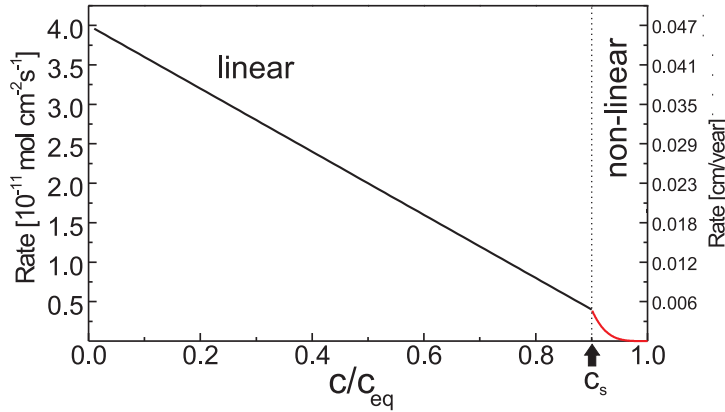


Figure 2.4: Dependence of dissolution rates on saturation ratio c/c_{eq} .

All the curves in Figure 2.4 can be reasonably well approximated by

$$F[\text{mol cm}^{-2}\text{s}^{-1}] = \alpha (c_{eq} - c) \quad 2.10$$

The kinetic constant $\alpha[\text{cm s}^{-1}]$ is in the order of $10^{-5} \text{ cm s}^{-1}$ and is listed by (see (Buhmann and Dreybrodt, 1985a, b; Dreybrodt, 1988; Dreybrodt *et al.*, 1996)). If $\delta > 1$ cm mass transport becomes rate limiting and the rates are given by

$$F = \frac{\alpha_{lim}}{1 + 3 \frac{\alpha_{lim} \cdot \delta}{D}} (c_{eq} - c) = \alpha_D (c_{eq} - c) \quad 2.11$$

where α_{lim} is the kinetic constant at the limit and D is the constant of diffusion for Ca^{2+} ($\approx 10^{-5} \text{ cm}^2\text{s}^{-1}$). With $\alpha_{lim} \approx 3 \cdot 10^{-5} \text{ cm s}^{-1}$ the rates are reduced by a factor of 2 for $\delta \approx 0.3$ cm.

In the early state of karstification flow is laminar, and as we will see later, after short distances from the entrance the solution comes very close to equilibrium. Close to equilibrium as has been shown experimentally by Eisenlohr *et al.* (1999) natural calcite carbonates exhibit inhibition of dissolution rates due to impurities in the limestone (e.g. phosphate or silicates). Then the dissolution rates drop by orders of magnitude to a non-linear rate law.

The dissolution rates for limestone are therefore given

$$F = \begin{cases} k_1(1 - c/c_{eq}) ; c \leq c_s ; k_1 = \alpha c_{eq} \\ k_n(1 - c/c_{eq})^n ; c > c_s \end{cases} \quad 2.12$$



n varies between 3 and 11, and c_s between $0.7c_{eq}$ and $0.9c_{eq}$. Eqn. 2.12 is presented by Figure 2.4. It should be noted here that gypsum rocks follow a similar rate law (Jeschke *et al.*, 2001) and that gypsum karst therefore can be modeled the same way as karst in limestone. In the following for limestone we use as representative numbers, $k_l = 4 \cdot 10^{-11}$ mol $cm^{-2}s^{-1}$, $n = 4$, $c_s = 0.9c_{eq}$, and $k_n = 4 \cdot 10^{-8}$ mol $cm^{-2}s^{-1}$ for limestone. It must be stressed here that the values of $k_l = \alpha c_{eq}$ are constant only for aperture widths from about 0.01 cm to 0.1 cm. According to Eq. 2.11 they drop for $\delta > 10^{-1}$ cm, as long flow stays laminar. The rate constants k_n are properties of the mineral's surface, solely. Due to inhibition the non-linear surface rates close to equilibrium are so low that they become rate limiting. Figure 2.4 represents Eq. 2.12. The vertical line separates the region of linear kinetics ($n = 1$) from that of the non linear kinetics ($n=4$). The dotted line extends the rates of linear kinetics into the non-linear region. This visualises the steep drop of inhibited non-linear rates in comparison to linear kinetics.

2.2.2 Dissolution in turbulent flow

When the flow becomes turbulent the bulk of the solution is mixed by eddies, such that concentration gradients are leveled out. The completely mixed bulk is separated from the surface of the limestone by a diffusion boundary layer (DBL) of thickness ε . Mass transport from the mineral's surface into the bulk and vice versa is affected by molecular diffusion through this layer. The thickness of this DBL depends on the hydrodynamic conditions of flow and is given by

$$\varepsilon = a / Sh \quad 2.13$$

where a is the aperture width of the conduit and Sh is the dimensionless Sherwood number given by (Incropera and DeWitt, 2002),

$$Sh = \frac{(f/8)(Re-1000)Sc}{1+12.7\sqrt{f/8}(Sc^{2/3}-1)} \quad 2.14$$

Re is Reynolds number, f is the friction factor and Sc is the Schmidt number $Sc = \eta / (\rho D)$. For water $Sc \approx 1000$. The resistance to mass transport through the boundary layer is determined also by conversion of CO_2 . When the diffusion length of CO_3^{2-} -ions (i.e. the distance a CO_3^{2-} -ion travels from the mineral's surface until it is converted to HCO_3^-) is small compared to ε then diffusion is rate limiting and the effective rate constant k drops with increasing ε . If $\varepsilon \geq \lambda$ than CO_2 conversion becomes rate limiting because it is affected mainly in the boundary layer. Detailed numbers are given by Liu and Dreybrodt (1997). The thickness of the boundary layer (Eq. 2.13) in our calculations was in the order of several tenth of a mm.



Dissolution rates used in our models			
Laminar flow	$c < c_s$	$F = \frac{k_1}{(1 + k_1 a / 3 D c_{eq})} \left(1 - \frac{c}{c_{eq}}\right)$	$k_1 = 4 \cdot 10^{-11} \text{ mol cm}^{-2} \text{ s}^{-1}$ $D = 10^{-5} \text{ cm}^2/\text{s}$ $n = 4$ $k_n = 4 \cdot 10^{-8} \text{ mol cm}^{-2} \text{ s}^{-1}$ See Eqs. 2.13 and 2.14 for the calculation of ε .
	$c \geq c_s$	$F = \min(F_D, F_S)$ $F_D = 2D(c_{eq} - c)/\alpha$ $F_S = k_n(1 - c/c_{eq})^n$	
Turbulent flow	$c < c_s$	$F = \min(F_D, F_S)$ $F_D = D(c_{eq} - c)/\varepsilon$ $F_S = k_1(1 - c/c_{eq})$	
	$c \geq c_s$	$F = \min(F_D, F_S)$ $F_D = D(c_{eq} - c)/\varepsilon$ $F_S = k_n(1 - c/c_{eq})^n$	

Table 2.1: An overview of the rate equations used throughout the book.

3. THE EVOLUTION OF A SINGLE FRACTURE

3.1 EVOLUTION UNDER CONSTANT HEAD CONDITIONS: THE FEEDBACK MECHANISM AND BREAKTHROUGH

The evolution of a basic element of a karst aquifer – a single fracture – is of utmost importance for understanding the evolution of more complex structures like fracture networks. The term “single fracture” in our case does not only imply straight fractures like that in Figure 3.1: A sequence of fractures forming a pathway between input and output can also be discussed in this context (see elements “1” in Figure 1.3).

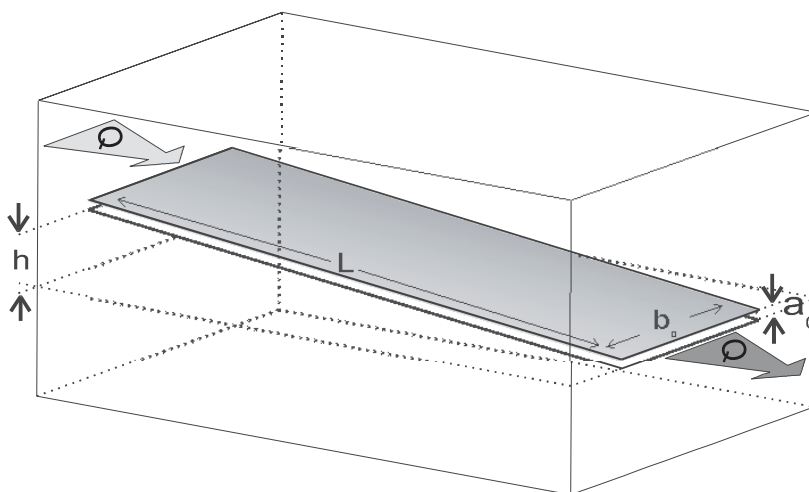


Figure 3.1: Uniform fracture with aperture width a_0 , width b_0 , and length L . Calcite aggressive water is driven through it by time-independent hydraulic head h .

This chapter presents the evolution of a single fracture in various settings, which are defined by the physical and chemical parameters used in the presented models. Reaction-transport mechanisms in tubes and fractures are well known and discussed also in the other fields of science (Beek and Mutzall, 1999; Bird *et al.*, 2002). Weyl (1958) was the first who applied them to the fractures and tubes in calcite. His experiments and those of Erga and Terjesen (1956) revealed a linear rate law for calcite dissolution in $CO_2-H_2O-CaCO_3$ solutions. These results caused some trouble to researchers as discussed by White and Longyear (White and Longyear, 1962), since large conduits in the

natural hydrogeochemical conditions do not evolve in geologically relevant time scales if only linear kinetics is operative. Non-linear rate laws as pointed out by White (1977) and Palmer (1984) were first introduced into the model of single fracture evolution by Dreybrodt (1990) and Palmer (1991). A detailed mathematical analysis of the problem was later done by Dreybrodt (1996) and Dreybrodt and Gabrovšek (2000).

3.1.1 Basic concepts and results

This section presents the basic mechanisms acting when water driven by a time-independent hydraulic head h flows through an initially uniform fracture in soluble rock. The setting is shown in Figure 3.1.

The flow rate Q [cm^3/s] depends on the flow resistance R and on the hydraulic head h . The resistance is a function of the fracture aperture width a , the fracture width b , the fracture length L , and the kinematic viscosity of the water η/ρ (η is viscosity in $\text{g}/\text{cm}\cdot\text{s}$ and ρ is the density in g/cm^3). For laminar flow, the flow rate through the fracture is given by the Hagen-Poiseuille equation (Beek *et al.*, 1999),

$$Q = h/R = iL/R, \quad 3.1$$

where i is hydraulic gradient defined as h/L and

$$R = \frac{12\eta}{\rho g} \int_0^L \frac{dx}{a^3(x,t)b(x,t)M(x,t)}. \quad 3.2$$

M is geometrical factor and depends on the ratio a/b :

$$M = 0.6 - 0.3a/b \quad \text{for elipsoidal shape}, \quad 3.3$$

$$M = 1 - 0.6a/b \quad \text{for the rectangular shape}. \quad 3.4$$

When flow rates exceed a threshold of discharge Q flow becomes turbulent. In this case the motion of each water particle shows large fluctuations from its average flow path and also eddies will occur. As we will see later this has a significant impact on dissolution rates. The threshold when flow becomes turbulent is given by the Reynold's number $Re = av/\eta$, where v is the flow velocity in the conduit.

For smooth fractures and tubes flow becomes turbulent for $Re > 2000$. Then the relation between head and flow rate is no longer linear and the Darcy-Weissbach equation has to be applied (Dreybrodt, 1988). It reads

$$Q = \sqrt{\frac{2gA^2d}{f}} \cdot \sqrt{\frac{h}{L}} \cdot \frac{h}{|h|}, \quad 3.5$$

where A is the cross-sectional area and d is the hydraulic diameter of the conduit. f is a friction factor given by:



3. THE EVOLUTION OF A SINGLE FRACTURE

$$\frac{1}{\sqrt{f}} = -2 \log_{10} \left(\frac{r}{3.71d} + \frac{2.51\eta}{\rho \sqrt{2gd^3h/L}} \right) \quad 3.6$$

r is the roughness of the wall. It is important to note that change to turbulent flow, especially in non-uniform tubes and in nets of tubes alters the distribution of heads and this puts the evolution of karst to a new stage.

This would be the end of the story if the system was non-reactive. The CO_2 containing water is aggressive with respect to the karst rocks, therefore it widens the fracture by dissolving limestone from the walls.

The widening rate at any point in the fracture is proportional to the dissolution rate there, which is given by Eq. 2.12 (see also Table 2.1) and depends on the undersaturation of the solution. Therefore we need to know the concentration of calcium ions along the fracture in order to calculate its widening. The mass conservation law requires that the amount of calcite dissolved from the walls within any part of the fracture (e.g. between x and $x+dx$) is equal to the difference between the amount of calcium leaving and the amount of calcium entering the selected part (c.f. Figure 3.2). From this one obtains:

$$F(c(x))P(x)dx = v(x)A(x)dc = Qdc, \quad 3.7$$

$v(x)$ is the velocity of the solution at position x and $A(x)$ the cross-section of the fracture there.

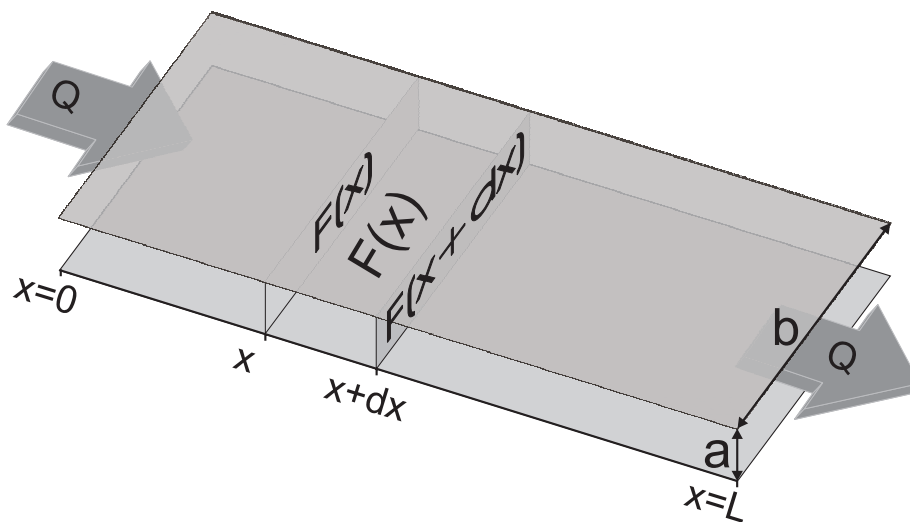


Figure 3.2: Mass conservation in the part of the fracture located between x and $x+dx$.

Note that $Q = v(x)A(x)$ is the flow rate through the fracture. In the integral form, taking $c(x=0) = c_0$, we get:



$$Q \int_{c_0}^{c(x)} \frac{dc}{F(c)} = \int_0^x P(x) dx. \quad 3.8$$

To obtain the dissolution rates along the fracture we have to solve Eq. 3.7 or Eq. 3.8. The aperture width $a(x, T)$ at some position x at time T is given by the time integral of the dissolution rate:

$$a(x, T) = 2\gamma \int_0^T F(x, t) dt + a_0. \quad 3.9$$

$F(x, T)$ is obtained from Eq. 3.8. The factor γ (value of γ for the limestone is $1.7 \cdot 10^9$) converts the dissolution rates from $\text{mol cm}^{-2}\text{s}^{-1}$ to the retreat of the wall in cm/year .

We cannot obtain a general analytical solution of Eqs. 3.7 to 3.9. To solve the problem numerically, we discretize time and spatial variables t and x into suitable increments Δt and Δx and perform the following procedure (Dreybrodt, 1996):

0. Define some criteria to end the run
1. Calculate $Q(t)$ from using Eqs. 3.1 to 3.6.
2. Calculate $F(x)$ from Eq. 2.12 and 3.7
3. Calculate the new profile assuming a constant rate in the time interval Δt according to

$$\begin{aligned} a(x, t + \Delta t) &= a(x, t) + 2\gamma F(c(x), t) \Delta t \\ b(x, t + \Delta t) &= b(x, t) + 2\gamma F(c(x), t) \Delta t. \end{aligned} \quad 3.10$$

4. If the criteria given in step 0 is met exit, if not return to step 1.

The range of the parameters relevant for natural karstification

There are two types of parameters defining the evolution of a fracture: physical parameters and chemical parameters. Chemical parameters were discussed in Chapter 2. Once we define the geochemical settings at the site of karstification, the values of the chemical parameters can be calculated from thermodynamical data (c_{eq}) or measured in the laboratory (rate law and its constants).

Physical parameters depend on the particular hydrogeological setting in which karstification proceeds. Typical aperture widths of fractures in nature are in the order of several tenths of a millimeter (Motyka and Wilk, 1984). In natural systems hydraulic gradients are usually smaller than 0.1. Typical lengths of pathways connecting inputs and outputs are in the order of several hundred meters to several kilometers. In man-made hydraulic conditions, such as at dam sites, hydraulic gradients can be greater than 1 and the lengths of pathways less than 1 km.

Models of karstification in man-made conditions can be of great practical importance (Dreybrodt, 1992, 1996; Kaufmann, 2003a; Romanov, 2003; Romanov *et al.*, 2003). These will be discussed in chapter 6. In this Chapter we focus on the natural karstification. Typical values of parameters for natural settings are given in Table 3.1. This set of parameters will be used throughout this work and referred as a **standard fracture**.

3. THE EVOLUTION OF A SINGLE FRACTURE

Description	Name	Unit	Initial or Standard value
Aperture width	a_0	cm	0.02
Fracture length	L	cm	10^5
Fracture width	b_0	cm	100
Hydraulic gradient	i		0.05
Order of non linear kinetics	n		4
Linear kinetics constant	k_l	mol cm ² s ⁻¹	4×10^{-11}
Non linear kinetics constant	k_n	mol cm ² s ⁻¹	4×10^{-8}
Concentration of calcium	c	mol/cm ³	
Switch concentration	c_s	mol/cm ³	1.8×10^{-6}
Equilibrium concentration	c_{eq}	mol/cm ³	2×10^{-6}
Viscosity of the solution	η	g/cms	1.2×10^{-2}
Density of the solution	ρ	g/cm ³	1

Table 3.1: Parameters used for the model of the evolution of a single fracture (standard)

Discretisation of x and t

As pointed out by Dreybrodt (1996), discretisation of the spatial variable x has to be done with care. The change of concentration Δc within the interval Δx (see Eq. 3.7) is given by:

$$\Delta c(x,t) = \frac{F(x,t)P(x,t)}{Q(t)} \Delta x. \quad 3.11$$

When taking constant Δx increments, Δc increments are large at the entrance and then decrease rapidly when dissolution rates become small. At the entrance of the “standard” fracture (see Table 3.1) $\Delta c(x=0)[\mu\text{mol}/\text{cm}^3] \approx 0.003 \cdot \Delta x [\text{cm}]$. In this case the solution would already attain equilibrium within the first Δx if $\Delta x > 60$ cm. To avoid such a numerical saturation one has to use sufficiently small Δx increments. It is more convenient to use fixed Δc increments and calculate suitable Δx . We will use $\Delta c = c_s/i_1$ for $c < c_s$ and $\Delta c = (c_{eq} - c_s)/i_2$ for $c > c_s$. Parameters i_1 and i_2 are in the order of 100–1000. Note that in this case Δx varies in time which has to be considered in a numerical algorithm. See also (Dreybrodt, 1996) for more details.

Time discretisation is chosen that a further decrease of Δt increments does not considerably affect the time scale of the evolution. Time increments can be either fixed or they can be calculated for each time step such that the maximal widening rate does not exceed some prescribed value.

Numerical results for “standard” fracture

Figure 3.3 shows the numerical results for the evolution of the standard fracture (Table 3.1). Figure 3.3a in a logarithmic plot depicts as a function of time the flow rate

3. THE EVOLUTION OF A SINGLE FRACTURE

through an initially plane parallel fracture with initial parameters as given in Table 3.1. The flow rate exhibits a slow increase that is enhanced in time until it is drastically accelerated to such an extent that it exceeds the water available at the surface. At this breakthrough time T_b the hydraulic head breaks down, and the initial phase of laminar flow through the fracture is terminated.

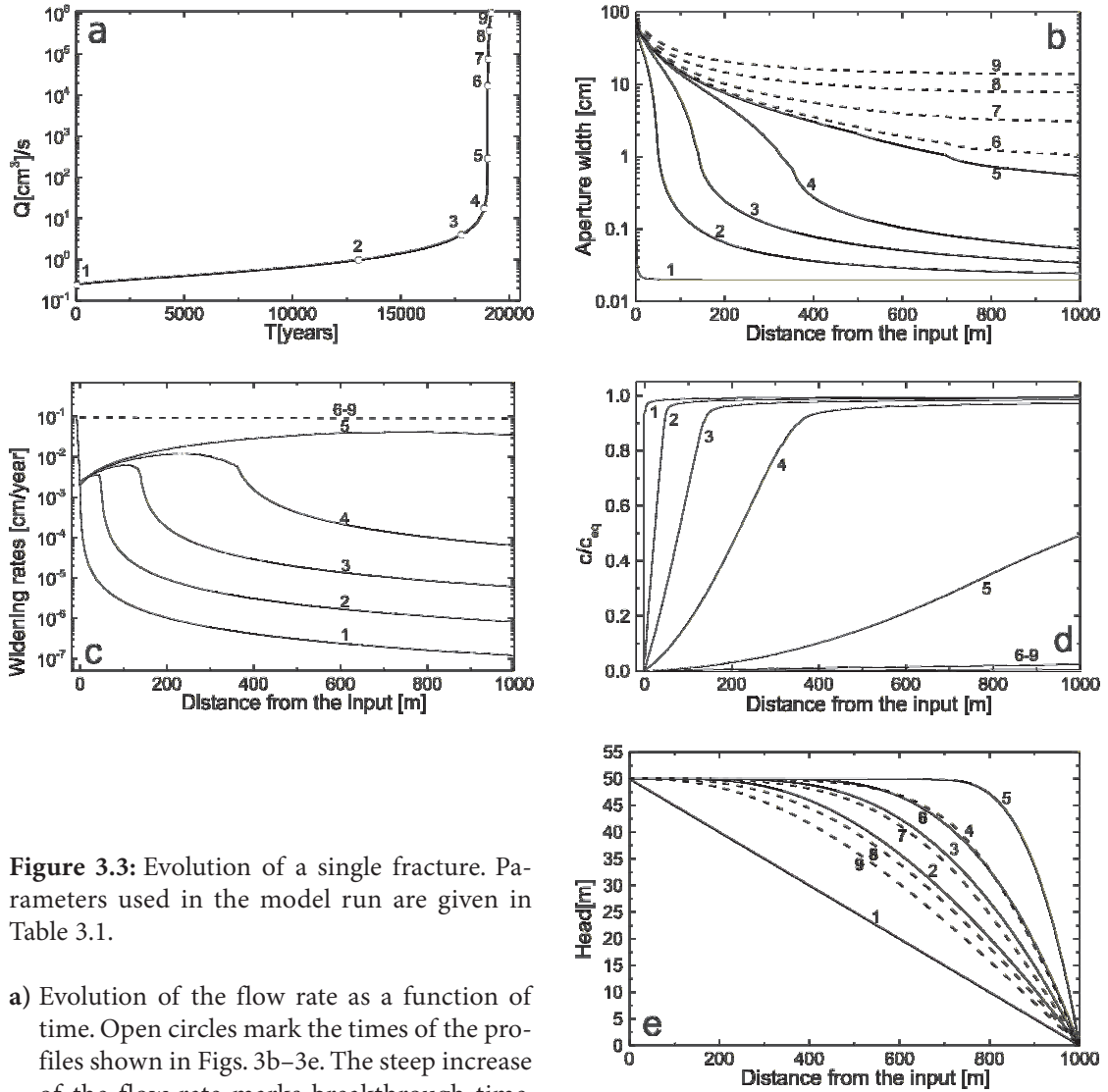


Figure 3.3: Evolution of a single fracture. Parameters used in the model run are given in Table 3.1.

- a) Evolution of the flow rate as a function of time. Open circles mark the times of the profiles shown in Figs. 3b–3e. The steep increase of the flow rate marks breakthrough time. Note the logarithmic scale on $Q(t)$.
- b) Profiles of the aperture widths $a(x)$ recorded at various times: 0, 13.1 ky, 17.8 ky, 18.85 ky, 19.01 ky, 19.014 ky, 19.032 ky, 19.082 ky, 19.152 ky, labeled from 1–9 respectively. Full lines indicate laminar flow and dashed lines turbulent flow.
- c) Dissolution rates along the fracture at times given above.
- d) Concentration profiles.
- e) Distribution of hydraulic heads along the fractures.

Figure 3.3b represents the evolution of the aperture widths along the fracture for various times depicted by points 1 to 9 in Figure 3.3a. The widening rates ($2\gamma F$) in cm/y are shown by Figure 3.3c. In the beginning when the aperture widths at the entrance (2–4) are below 1 mm the rates are given by Eq. 2.11. They are maximal at $c = 0$. Later when the entrance widens, molecular diffusion becomes rate limiting (cf. Chapter 2, Table 2.1) and the rates close to the entrance drop. But they rise downstream as the aperture widths decrease. Finally when 4th order non linear kinetics becomes active, rates are determined by Eq. 2.12 and drop again. After breakthrough when flow is turbulent (dashed lines) the rates become high and even along the conduit. Details of this dynamic behaviour are given in the literature. Figure 3.3d shows the saturation ratio c/c_{eq} along the fracture. At the beginning the ratio rises steeply until $c = c_s$. Then the higher kinetics order become active causing a further slow increase towards equilibrium. With increasing flow rate the region of first order kinetics ($c < c_s$) penetrates downstream until at breakthrough the concentration drops drastically.

To elucidate the mechanisms of the feedback loop Figure 3.3e depicts the head distribution along the fracture. In the beginning when the profile is even $a(x) = a_0$ there is a linear decline from h to zero. The funnel shaped profile at later times distorts this decline. In the widened parts the head becomes close to the boundary value h , and at the bottleneck the head declines from this value to zero at the output. Thus the hydraulic gradient upstream increases as this bottleneck becomes shorter. Consequently flow velocity increases and dissolution rates at the exit are enhanced. After breakthrough flow becomes turbulent. Therefore the heads are redistributed (dashed curves) and the decline along the fracture becomes more even. This is also important for 2 or 3-dimensional nets, because after breakthrough this new distribution of heads determines the further evolution of the aquifer.

The **breakthrough time** is an important parameter which will be in the center of our attention whenever constant head conditions will be present. It can be defined in several ways:

- When the linear kinetics reaches the exit of the fracture.
- At the onset of turbulent flow, according to the Reynolds number.
- At the time when the ratio $Q(t)/Q(t = 0)$ reaches some value; e.g. 10^3 .

All these criteria give similar results for most cases of interest. The breakthrough event terminates the initial state of speleogenesis and can thus be taken as a measure for the intensity of a subsurface karstification.

By sensitivity analysis one finds that the dependence of breakthrough time on the basic parameters can be expressed in the form of a power law:

$$T_B = \tau (L/i)^{n/(n-1)} a_0^{-(2n+1)/(n-1)} k_n^{1/(n-1)} c_{eq}^{-n/(n-1)}. \quad 3.12$$

The value of τ is $9 \cdot 10^{-14} \pm 10^{-14}$ for square and circular cross-sections, and about one order of magnitude smaller for wide fractures, i.e. $b_0 \gg a_0$ (Dreybrodt, 1996). The error is less than 15 % for $T_B > 10^4$ years.



3.1.2 An analytical approximation for the breakthrough time

Figure 3.3 shows that during 90 % of the evolution time, high dissolution rates are restricted only close to the entrance. The rest of the fracture is widened almost uniformly by low dissolution rates, not much higher than that at the exit. This suggests the assumption, that the dissolution rates along the fracture are almost constant and equal to that at the exit. Explicitly this approximation yields:

$$\begin{aligned} a(x,t) &= a(L,t), \\ F(x,t) &= F(L,t). \end{aligned} \quad 3.13$$

Figure 3.4: The funnel shaped fracture is approximated by a plane parallel fracture of uniform aperture width widened evenly by the dissolution rates at its end. This enables one to give analytical treatment of its evolution.

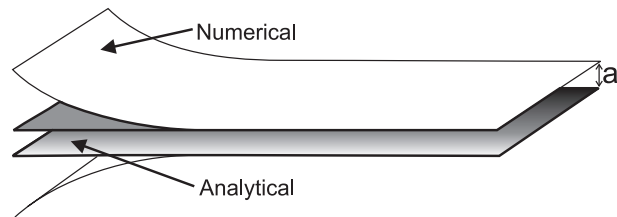


Figure 3.4 illustrates this. The evolving funnel shape of the fracture is neglected and the fracture is kept parallel during the evolution. For the uniform fracture Eq. 3.8 can be solved analytically. The solution will give an overestimation of the breakthrough time, because the flow rates will always be lower than in the numerical solution, when the wider profile of the fracture is taken into an account.

To obtain the concentrations $c(x)$ and rates $F(x)$ for the uniform fracture, we insert the expressions for the dissolution rate (Eq. 2.12) into Eq. 3.8 and obtain:

$$\frac{1}{k_1} \int_{c_0}^{c_s} \frac{dc}{1 - c(x)/c_{eq}} = \int_0^x \frac{P}{Q} dx, \quad x \leq x_s, \quad 3.14$$

$$\frac{1}{k_n} \int_{c_s}^{c(x)} \frac{dc}{(1 - c(x)/c_{eq})^n} = \int_{x_s}^x \frac{P}{Q} dx, \quad x > x_s. \quad 3.15$$

Integrating we obtain:

$$1 - c(x)/c_{eq} = (1 - c_0/c_{eq}) \exp\left(-\frac{Pk_1}{Qc_{eq}} x\right), \quad x \leq x_s, \quad 3.16$$

$$\left(1 - c(x)/c_{eq}\right)^{-n+1} = \left(1 - c_s/c_{eq}\right)^{-n+1} + \frac{Pk_n(n-1)(x-x_s)}{Qc_{eq}}, \quad x > x_s. \quad 3.17$$

Inserting $x = x_s$ and $c(x) = c_s$ in Eq. 3.16 we get:





3. THE EVOLUTION OF A SINGLE FRACTURE

$$x_s = \frac{Qc_{eq}}{Pk_1} \ln \left(\frac{1-c_0/c_{eq}}{1-c_s/c_{eq}} \right) \quad 3.18$$

Using Eq. 2.12 we write the term $(1-c(x)/c_{eq})$ as a function of $F(x)$ and reorder the upper expressions to obtain the explicit form for the dissolution rates:

$$F(x) = F(x=0) \exp \left(-\frac{Pk_1}{Qc_{eq}} x \right), \quad x \leq x_s, \quad 3.19$$

$$F(x) = F(x_s) \left[1 + \frac{Pk_n(n-1)(x-x_s)}{Qc_{eq}} (1-c_s/c_{eq})^{n-1} \right]^{\frac{n}{1-n}}, \quad x > x_s. \quad 3.20$$

More generally, if the rate at some point x_1 is known and the non-linear rate law with constant c_{eq} , k_n and n describes the dissolution between point x_1 and some other arbitrary point x_2 , the rate at x_2 is given by

$$F(x_2) = F(x_1) \left[1 + \frac{Pk_n(n-1)(x_2-x_1)}{Qc_{eq}} (1-c(x_1)/c_{eq})^{n-1} \right]^{\frac{n}{1-n}}, \quad x_2 > x_1. \quad 3.21$$

The problem is further simplified by taking a wide fracture, i.e. $b \gg a$. In this case

$$\frac{a+b}{a^3b} \approx \frac{1}{a^3}, \text{ therefore } P/Q = \frac{24\eta}{\rho g} \frac{L}{a^3h}. \quad 3.22$$

For more transparency we define new parameters λ_1 and λ_n with the dimension of length

$$\lambda_1 = \frac{Qc_{eq}}{Pk_1} \quad 3.23$$

$$\lambda_1 = \frac{\rho g}{24\eta} \frac{a^3h}{L} \frac{c_{eq}}{k_1} ; \quad b \gg a, \quad 3.24$$

$$\lambda_n(x) = \frac{Qc_{eq}(1-c(x)/c_{eq})^{1-n}}{Pk_n(n-1)} \quad 3.25$$

$$\lambda_n(x) = \frac{\rho g}{24\eta} \frac{a^3h}{L} \frac{c_{eq}}{k_n(n-1)} (1-c(x)/c_{eq})^{1-n} ; \quad b \gg a. \quad 3.26$$



Note that $\lambda_n(x_s) = \lambda_1/(n-1)$ since $k_n = k_1(1-c_s/c_{eq})^{1-n}$. Eqs. 3.19 to 3.21 now take the form:

$$F(x) = F(0) \exp\left(-\frac{x}{\lambda_1}\right) \quad x \leq x_s \tag{3.27}$$

$$F(x) = F(x_s) \left[1 + \frac{x-x_s}{\lambda_n(x_s)}\right]^{\frac{n}{1-n}}; \quad x > x_s, \tag{3.28}$$

$$F(x_2) = F(x_1) \left[1 + \frac{x_2-x_1}{\lambda_n(x_1)}\right]^{\frac{n}{1-n}}; \quad x_2 > x_1 > x_s. \tag{3.29}$$

These equations will be the “bread and butter” for the later discussions. The parameters λ_1 and $\lambda_n(x)$ define how fast the dissolution rates decrease along the fracture. λ_1 measures how far first order dissolution rates penetrate into the fracture. The expression

penetration lengths will be used to refer to them. For non-linear kinetics, the penetration length $\lambda_n(x)$ increases along the fracture due to increasing concentration. This is not the case for λ_1 , which does not depend on the x coordinate.

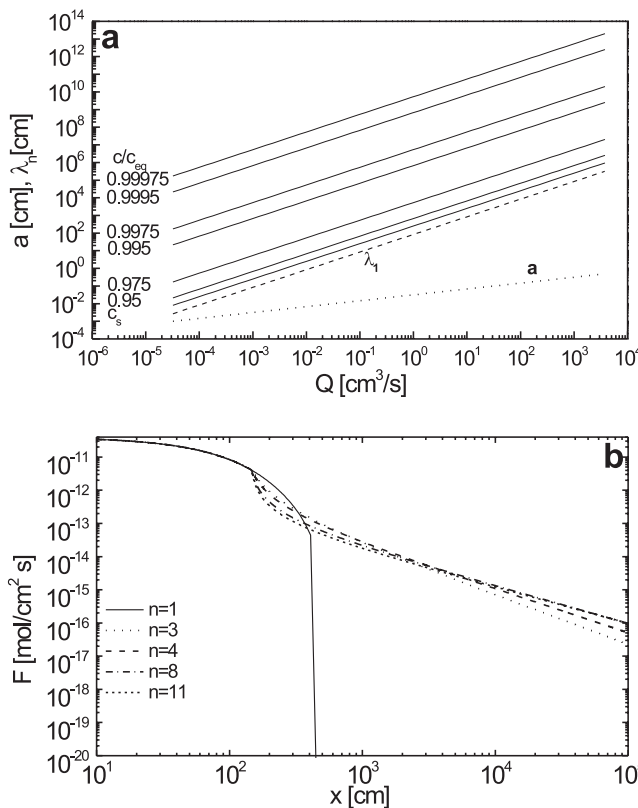


Figure 3.5: a) Dependence of penetration lengths λ_n (solid lines) and λ_1 (dashed line) on Q . λ_n is shown for various values of c/c_{eq} as denoted on the lines. The dotted line shows the aperture widths for the uniform “standard” fracture (see Table 3.1) which correspond to the values of Q at the abscissa. b) Dissolution rates along the uniform “standard” fracture for various order n of the rate equation as denoted in the figure.

Figure 3.5a gives the dependence of λ_n and λ_1 on the flow rate for various values of saturation ratios c/c_{eq} (given in the figure). λ_1 (dashed line) does not depend on c/c_{eq} . The dotted line presents the aperture widths corresponding to the flow rate Q for the uniform fracture. Other parameters are those given in Table 3.1.



3. THE EVOLUTION OF A SINGLE FRACTURE

Figure 3.5b shows the dissolution rates along the uniform fracture. The solid lines present the case where solely linear kinetics acts along the fracture. The other lines (see figure) depict the cases where the rate law switches to higher order at $c > c_s$. The “standard” fracture parameters given in Table 3.1 were used to calculate the rates, except for the varying parameters n and k_n . If only linear kinetics acts, the rates drop exponentially and are reduced by 13 orders of magnitude within a short distance. In contrast, when non-linear kinetics is active the rates are reduced only moderately by about 3 orders of magnitude.

We now assume that a plane parallel uniform fracture ($a_0 \ll b_0$) widens uniformly by the rate at its exit. Its widening is described by:

$$\frac{da}{dt} = 2\gamma F(L, t) \quad 3.30$$

where $F(L, T)$ is obtained from Eq. 3.28. For natural karstification the relations $L \gg x_s$, and $L/\lambda_n(x_s) \gg 1$ are valid. Therefore we neglect the terms “1” and x_s in Eq. 3.28.

For a uniform fracture the time dependence of $\lambda_n(x_s)$ can now be written as

$$\lambda_n(x_s, t) = \lambda_n^0(x_s) \left(\frac{a(t)}{a_0} \right)^3 \quad 3.31$$

We introduce $\lambda_n^0(x_s)$ to denote $\lambda_n(x_s, t = 0)$. Inserting $\lambda_n(x_s, t)$ into Eq. 3.28 we obtain:

$$F(L, t) = F(c_s) \left[\frac{L}{\lambda_n^0(x_s)} \frac{a_0^3}{a(t)^3} \right]^{\frac{-n}{n-1}} \quad 3.32$$

Applying the obtained $F(L, t)$ in Eq. 3.30 gives an easy integrable equation for dissolutional widening:

$$\frac{da}{dt} = 2\gamma F(c_s) \left(\frac{\lambda_n^0(x_s)}{L} \right)^{\frac{n}{n-1}} \left(\frac{a(t)}{a_0} \right)^{\frac{3n}{n-1}} \quad 3.33$$

The rate of widening is proportional to the power $3n/(n-1)$ of the actual aperture width. This explains the strong feedback mechanism seen in the numerical results. Integration of Eq. 3.33 gives the time dependence of the aperture width:

$$a(t) = a_0 \left(1 - t/T_B \right)^{\frac{1-n}{3n-1}}, \quad 3.34$$

where

$$T_B = \frac{1}{\gamma} \cdot \frac{n-1}{2n+1} \left(\frac{1}{a_0} \right)^{\frac{2n+1}{n-1}} \left(\frac{24\eta L^2 (n-1)}{\rho g h c_{eq}} \right)^{\frac{n}{n-1}} k_n^{\frac{1}{n-1}} = \frac{1}{2\gamma} \frac{(n-1)}{(2n+1)} \frac{a_0}{F(L, 0)}. \quad 3.35$$



T_B is the pole of $a(t)$ and represents an estimation for the breakthrough time. It is inversely proportional to the initial widening rate at the exit. It has the same functional dependence on the basic parameters as the numerically obtained expression for T_B given in Eq. 3.12. In the following chapters additional parameters will be added to the model. Then the symbol T_B^0 will be used to refer to the breakthrough time given in Eq. 3.35. Figure 3.6a shows the evolution of fracture aperture widths for the uniform plane parallel fracture as calculated from the Eq. 3.34.

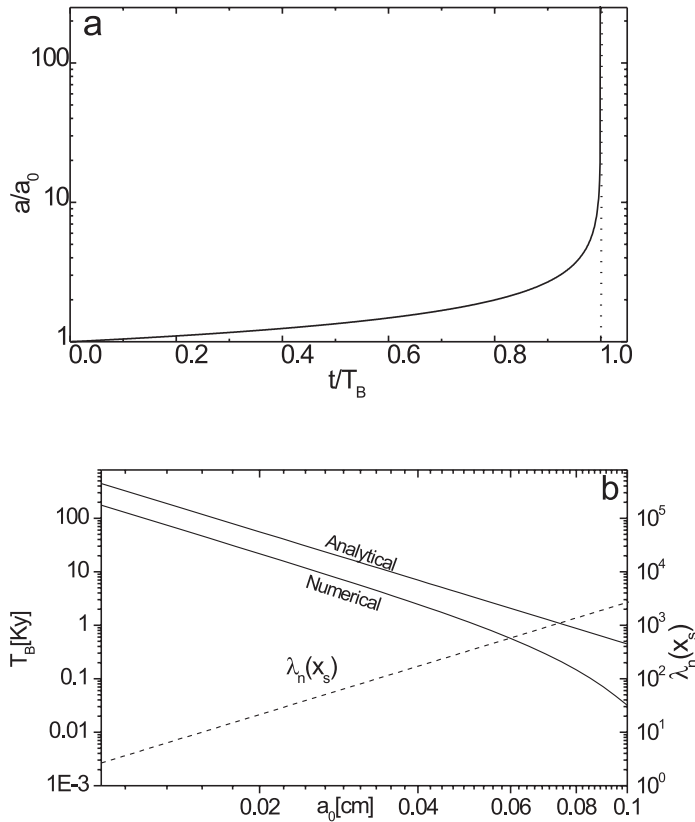


Figure 3.6: **a)** Evolution of fracture aperture widths for the uniform fracture at the exit as given by Eq. 3.34. The dotted vertical line represents the pole of the function $a(t)$. **b)** Dependence of breakthrough time on a_0 for otherwise standard fracture. The upper line gives the T_B from 3.35, the lower line is obtained by the finite difference model. The dashed line gives the value of $\lambda_n^0(x_s)$. Note the logarithmic scale on both axes. The analytical approximation and the numerical solution follow the same power law for $a_0 < 0.06$ cm. The assumptions which lead to the approximation fail at higher a_0 and higher initial penetration lengths. Then both curves start to deviate from each other.

Note, that the T_B given in Eq. 3.35 is an upper limit, since the minimal rates at the exit were taken along the entire fracture to calculate its evolution. This is shown on Figure 3.6b. The upper solid line represents Eq. 3.35, the lower one the results of a numerical run. The initial width is varied between 0.01 cm and 0.1 cm, all the other parameters are kept constant (see Table 3.1). Up to $a_0 \approx 0.06$ cm, the ratio between the analytically and numerically obtained breakthrough times is practically constant. For $a_0 > 0.06$ cm the numerical breakthrough time starts to deviate from the power law and the approximation fails. There the assumptions $L \gg x_s$ and $L \gg \lambda_n^0(x_s)$ are no longer valid.

The dashed line and the scale at the right vertical axis show the initial $\lambda_n^0(x_s)$. Using Eq. 3.26, the variation of any parameter can be expressed as the variation of $\lambda_n^0(x_s)$. It shows out that regardless of which parameter we vary, the approximation given in Eq. 3.35 fails if $L/\lambda_n^0(x_s) < 100$.

An important conclusion: The bottleneck principle

The keystone of the presented approximation is that the breakthrough time is determined by the initial dissolution rates at the “bottleneck” part where the resistance to flow is maximal and the dissolution rates are minimal. Here the bottleneck is at the fracture’s end. When hydrogeochemical conditions favor the formation of a bottleneck somewhere else in the fracture one should focus on the initial rates there to estimate the behavior of the breakthrough time. We will benefit from this fact also when adding further parameters to the basic settings presented in this chapter.

3.1.3 Solutions with high initial saturation ratios. “Switch off” of the feedback mechanism

Before entering the closed system, karst water normally dissolves limestone under open system conditions. Therefore it enters the fractures with a saturation ratio c_0/c_{eq} . The question is how does this affect the evolution of a single fracture.

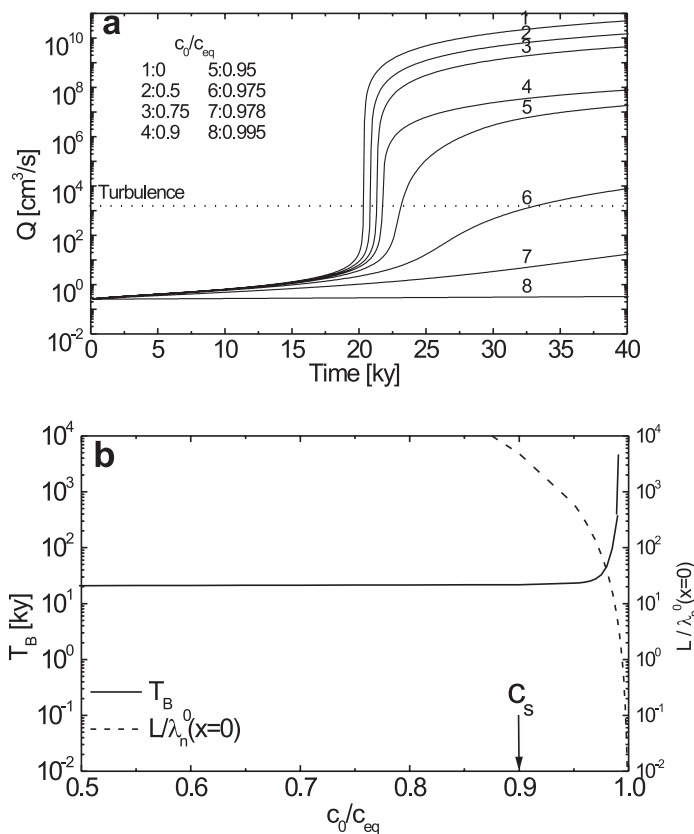


Figure 3.7: a) The evolution of flow rates in the standard fracture for various values of c_0/c_{eq} as denoted in the figure and on the curves. b) The dependence of breakthrough time (solid line) and the parameter $L/\lambda_n(x = 0, t = 0)$ (dashed line) on c_0/c_{eq} . The arrow indicates the value of c_s . No considerable change of breakthrough time is observed for $c_0/c_{eq} < 0.97$.

Figure 3.7a shows the evolution of flow rates for the standard fracture for several ratios c_0/c_{eq} as denoted in the figure. Flow rates beyond turbulence, i.e. above the dotted



3. THE EVOLUTION OF A SINGLE FRACTURE

line, are unrealistic and are given for completeness and support to the later discussion. As long as the initial concentration is below the switch concentration (lines 1–4), no considerable change of T_B is observed. Line 4 shows the case when $c_0 = c_s$. If c_0 is higher than c_s , T_B starts to increase and as c_0 approaches c_{eq} (lines 6–8) breakthrough no longer occurs in the sense of an abrupt jump in flow rates. In these cases the fracture widens uniformly in time from the onset of karstification.

A more general picture of the behavior of T_B on c_0/c_{eq} is given in Figure 3.7b. The solid line denotes the dependence of T_B on c_0/c_{eq} . The dashed line shows the dependence of $L/\lambda_n^0(x=0)$ on c/c_{eq} , both for the standard fracture. The same scale is used for both variables. As stated above, no effect on T_B is observed if $c_0 < c_s$. A considerable increase of T_B is observed once the ratio L/λ_n^0 drops to 10, where $c_0/c_{eq} \approx 0.97$. From thereon T_B increases steeply. No breakthrough occurs if $L/\lambda_n^0 < 0.1$.

This behavior can be derived from Eqs. 3.28 and 3.29. As long as $L \gg \lambda_n$ the summand 1 in the brackets can be neglected and Eq. 3.32 is valid. Consequently breakthrough occurs. If however $L/\lambda_n \ll 1$, the rates are approximated by $F = k_n(1 - c/c_{eq})^n$ and widening is constant and even along the entire fracture.

The presented discussion is not only valid for fractures dissolved by autogenic waters flowing from the surface, but also holds for fractures located deep in the phreatic zone where the parameter $\lambda_n^0(x=0)$ can take a value of several kilometres and even widening in the order of 10^{-9} cm/year can enlarge these fractures in a time scale of several millions of years. When the hydrogeological conditions change, these fractures can become preferential pathways for later karstification. This can provide an explanation for the concept of inception horizons, without assuming mechanisms as those discussed by Lowe (1992) and Lowe and Gunn (1997).

3.1.4 Evolution of a single fracture under linear dissolution kinetics

We have stressed the importance of the higher order ($n > 1$) dissolution kinetics for conduit development. The non-linear rate equation close to equilibrium is valid for natural limestones and dolomites and according to the latest results (Jeschke *et al.*, 2001) also for gypsum. Nevertheless, for historical reasons, for completeness, and for “what if?” we will discuss the conduit evolution under the action of linear dissolution kinetics only. We therefore assume that the linear part of of Eq. 2.11 is valid until c_{eq} :

$$F(c) = k(1 - c/c_{eq}). \quad 3.36$$

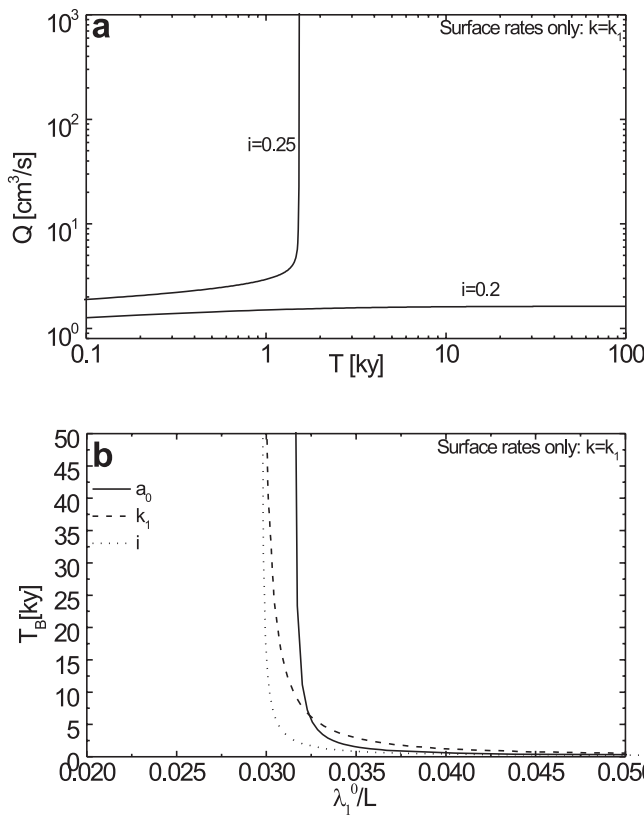
So far we did not consider the diffusion control of dissolution rates. Numerical results show that for karstification with a non-linear rate law, diffusion plays a minor role and does not much alter the breakthrough time. In contrary we will see that for the case with linear kinetics diffusion plays a crucial role.



Now we consider the combined action of surface reaction and diffusional transport of dissolved ionic species. As shown by Dreybrodt (1988) this can be done by using a modified rate constant which yields:

$$k = k_D = k_1 \left[1 + \frac{k_1 a}{6 D c_{eq}} \right]^{-1} \quad 3.37$$

From this equation one can deduce three regions of dissolution. If $k_1 a / 6 D c_{eq} = 1$ we obtain $k \approx k_1$, such that the dissolution rates are controlled by surface reactions. The dissolution is purely diffusion controlled when $k_1 a / 6 D c_{eq} \gg 1$. Between the two extremes the dissolution rates are controlled by both (mixed kinetics).



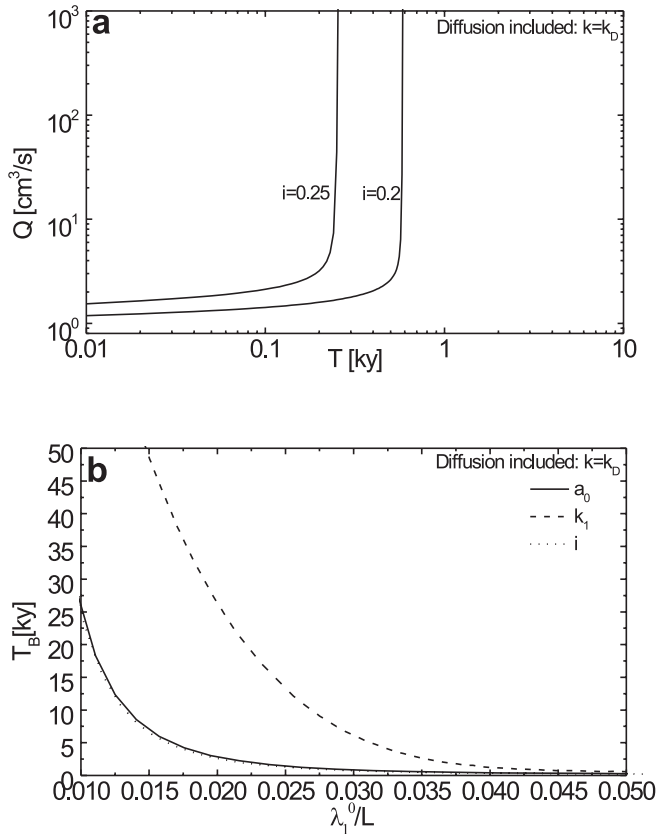
Suppose that the diffusion is not important for the evolution of a fracture, so that $k = k_1$. Figure 3.8a shows the evolution of flow rates for two fractures with different hydraulic gradients i . All the other parameters are identical for both cases (see figure caption).

Figure 3.8: a) Evolution of the flow rate for linear kinetics when only surface rates are considered. $a_0 = 0.02$ cm, $b_0 = 100$ cm, $L = 10^4$ cm, $k_1 = 4 \cdot 10^{-11}$ mol $\text{cm}^{-2}\text{s}^{-1}$, $c_{eq} = 2 \cdot 10^{-6}$ mol/ cm^3 , $i = 0.2$ and $i = 0.25$ as denoted at the lines. b) The dependence of T_B on λ_1^0/L . This is varied by changing a_0 , k_1 and i presented by the solid, dashed and dotted lines respectively. Other parameters are the same as in figure a.

For $i = 0.25$ T_B is 1.2 ky but there is no breakthrough for $i = 0.2$. Figure 3.8b shows the dependence of T_B on λ_1^0/L (see Eq. 3.24). The full line denotes the case where λ_1^0 is varied by varying a_0 and keeping the other parameters constant. The dashed and dotted lines present the cases where k_1 and i are the varying parameters. There is a sharp limit between the region of parameters where breakthrough occurs and the region without breakthrough. All three curves show the same behaviour. Therefore we can take λ_1^0/L as a master parameter determining the breakthrough behaviour. When $\lambda_1^0/L > 0.33$ breakthrough occurs. Otherwise breakthrough is excluded.

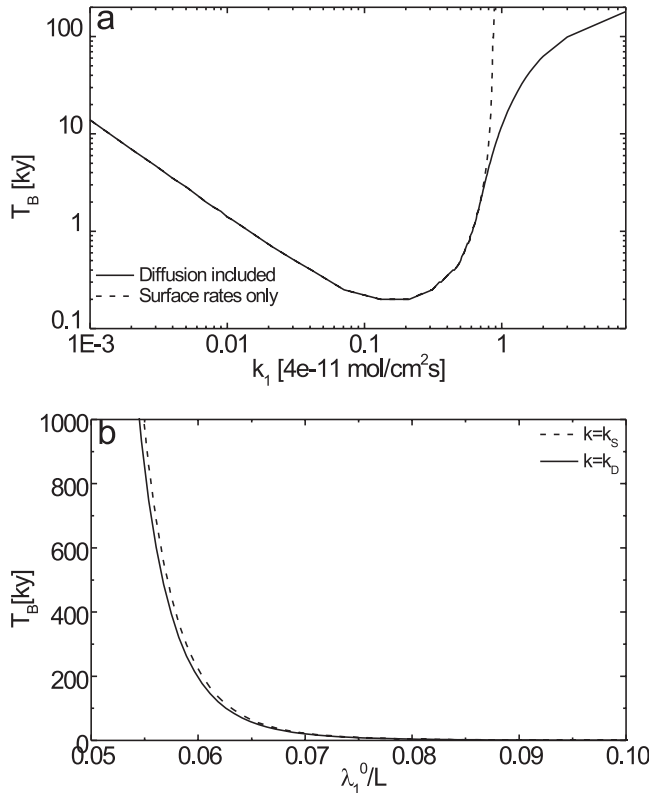
Now we include diffusion by using Eq. 3.37 as the rate equation. Figure 3.9 presents

3. THE EVOLUTION OF A SINGLE FRACTURE



the evolution of flow rates for the same fracture as in Figure 3.9a, but with diffusion included. Now the breakthrough time for $i = 0.2$ is below 1 ky. As shown by Figure 3.9b, there is no sharp boundary dividing the region of parameters with and without breakthrough. In this case we obtain geologically relevant breakthrough times for much smaller values of λ_1^0/L .

Figure 3.9: a) Evolution of flow rate for the case of linear kinetics. Diffusion is included in the rate equation. Parameters are the same as in Figure 3.8. b) The dependence of T_B on λ_1^0/L . See also Figure 3.8b.



Another example is shown on Figure 3.10a, which gives a wide range dependence of T_B on k_1 for the cases with $k = k_1$ and $k = k_D$. Other parameters are the same as in Figure 3.8. As long as $k_1 < 8 \cdot 10^{-12}$ molcm⁻² s⁻¹, the surface reaction determines the rates and both cases coincide. For larger values of k_1 no breakthrough occurs if only surface rates are considered.

Figure 3.10: a) The dependence of T_B on k_1 . Other parameters are as in Figure 3.3. The solid line presents the case when only surface controlled rates are included to the model, the dashed line presents the case where diffusion is also considered. b) T_B dependence on λ_1^0/L obtained by solving Eqs. 3.38 and 3.39.

The question arises whether we can treat the problem with the approximation for the widening rate at the exit everywhere in the fracture. From Eq. 3.27 we get the exit dissolution rate. Introducing it into Eq. 3.30 we obtain:

$$\frac{da}{dt} = 2\gamma k_1 \exp\left(-\frac{La_0^3}{\lambda_1^0 a^3}\right) \tag{3.38}$$

If the rates are controlled by mixed kinetics we obtain:

$$\frac{da}{dt} = 2\gamma \frac{k_1}{1 + \frac{k_1 a}{6Dc_{eq}}} \exp\left(-\frac{La_0^3}{\lambda_1^0 a^3 \left(1 + \frac{k_1 a}{6Dc_{eq}}\right)}\right) \tag{3.39}$$

The results of the integration are given in Figure 3.10b. T_B rises beyond any relevant value $\lambda_1^0/L < 0.05$. There is practically no difference between the case with and without diffusion, since the aperture width at the exit is small. Therefore the difference between Eqs.3.38 and 3.39 is negligible. We see that the approximation with the exit rate does not explain the difference observed in the numerical runs. To explain this difference we have to focus on the entrance part of the fracture. Figure 3.11a shows the evolution of aperture widths for the case with $i = 0.2$ from Figure 3.1. The small graph shows the aperture widths in the first 0.5 m of the fracture. This part exhibits extremely high aperture widths. Then the aperture widths drop fast such that more than half of the fracture keeps its initial flow resistance. High apertures at the entrance and almost constant resistance of the rest of the fracture cause the decrease of dissolution rates in time. For more on this see the discussion in (Dreybrodt, 1996) and in the following section.

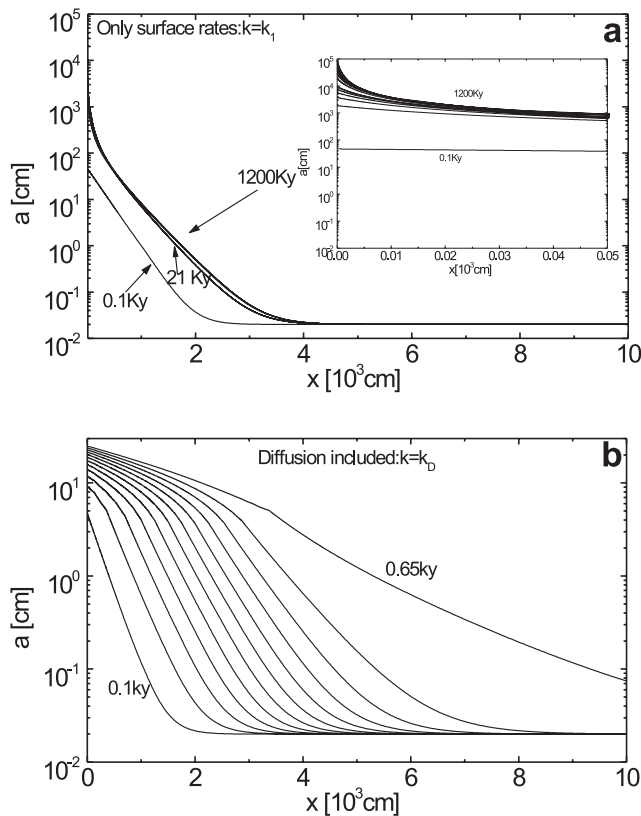


Figure 3.11: a) The profiles of the aperture widths for $i = 0.2$ from Figure 3.8. Only surface rates are considered. The excerpt shows the entrance part, $x < 50$ cm. **b)** Same as in the figure a, but diffusion is also considered. Profiles are taken each 100 y, starting at 50 y.



3. THE EVOLUTION OF A SINGLE FRACTURE

Figure 3.11b shows the aperture widths if diffusion is included in the rate calculation. Diffusion becomes rate limiting once the aperture widths are large (see Eq. 3.37). For mixed control, the penetration length from Eq. 3.39 can be written as

$$\lambda_D = \lambda_1 \left(1 + \frac{k_1 a}{6Dc_{eq}} \right) \quad 3.40$$

Since $\lambda_D > \lambda_1$ widening progresses deeper into the fracture. Furthermore, diffusion prevents the uncontrolled widening at the entrance which causes the retreat of dissolution rates if only surface rates are assumed.

3.1.5 The difference between the evolution of wide fractures and tubes

So far we have discussed only the evolution of wide fractures. This enabled us to obtain analytical results due to the approximation given in Eq. 3.22. Although the obtained results are conceptionally valid also for the tubes, one should be aware of an important difference between the two cases.

To clarify this difference we consider the dissolution rates along a fracture of general shape. This can be obtained the same way as for the parallel fracture, except that the right hand side of Eq. 3.8 is left in the integral form:

$$F(x, t) = F(x=0) \exp \left(- \frac{k_1 \int_0^{x_s} P(x, t) dx}{Q(t)c_{eq}} \right), \quad x < x_s \quad 3.41$$

$$F(x, t) = F(x_s) \left[1 + \frac{k_n (n-1) \int_{x_s}^x P(x, t) dx}{Q(t)c_{eq}} (1 - c_s/c_{eq})^{n-1} \right]^{\frac{n}{1-n}}, \quad x > x_s. \quad 3.42$$

The ratio $\frac{1}{Q(t)} \int_0^x P(x, t) dx$ determines whether the dissolution rates along the fracture increase or decrease in time. If this ratio increases, the rate decreases and vice versa.

In wide fractures the relative change of perimeter in time is small, such that the dissolution rates increase in time with increasing flow rate.

This is not always true for tubes. In this case the time variation of the perimeter and its integral along the fracture might exceed the time variation of flow rate. This is particularly important at the entrance of the fracture, where dissolution rates are high and fast widening occurs. As shown above, if linear kinetics with surface controlled rates can prevent the breakthrough also for the initially wide fractures ($a_0/b_0 = 0.01$).





3.1.6 Some general conclusions on the evolution of a single fracture

We have calculated the evolution of a single fracture by combining the basic flow equations, the knowledge on dissolution rates and the mass conservation law for the dissolved ionic species. The evolution is determined by chemical and physical parameters which define the flow through the fracture and dissolution rates along it. These parameters are given in Table 3.1.

The evolution of a fracture is governed by a feed-back mechanism where an increase of flow rates causes an increase of dissolution rates and vice versa. This mechanism ends in an abrupt jump of flow and dissolution rates, termed as breakthrough. The breakthrough time can be expressed as a function of basic chemical and physical parameters (Eq. 3.35). The dependence of breakthrough time on these parameters follows power laws. Once breakthrough occurs and turbulent flow sets in, the fracture is widened evenly with high dissolution rates.

The problem of the evolution of a single fracture is normally handled numerically. We presented an analytical approximation which gives the correct dependence of breakthrough time on the basic parameters. The approximation assumes an even widening of the fracture with the dissolution rates at the exit.

The initial saturation ratio c_0/c_{eq} does not affect the feedback mechanism if the initial concentration is below the switch concentration. If the ratio c_0/c_{eq} is close to 1, i.e., $c_0/c_{eq} > 0.97$ the evolution is significantly affected and the feedback mechanism is switched off.

If only a linear rate law is assumed, one must consider the diffusional flux of dissolved ionic species as a rate controlling mechanism. If only surface controlled rates are assumed we observe a sharp boundary between the region of parameters where breakthrough occurs and the region with no breakthrough as obtained by Hanna and Rajaram (1998).

3.1.7 Time variation of the hydraulic head

In nature the boundary conditions and the parameters defining karstification change during karst evolution. For reasons of clarity, most of the discussion in this work does not assume any time variation of the parameters given in Table 3.1.

To get some insight into scenarios with time-varying parameters we present the case with a time dependent hydraulic head. One can envisage many scenarios: changes of the hydraulic head e.g. the down-cutting of an erosional base, the change of meteoric precipitation or the change of hydraulic properties of an aquifer.

We assume some explicit time dependence of the hydraulic head $h = h(t)$. To obtain the breakthrough behaviour we can apply the same procedure as for the constant head conditions (Eq. 3.30 – Eq. 3.34). If the head variation is explicitly known it can be included into Eqs. 3.31, 3.30 and 3.34. This gives the following relations:



$$\lambda_n(x_s, t) = \lambda_n^0(x_s) \left(\frac{a(t)}{a_0} \right)^3 \left(\frac{h(t)}{h_0} \right), \tag{3.43}$$

$$\frac{da}{dt} = 2\gamma F(L, t) = 2\gamma F(c_s) \left(\frac{\lambda_n^0(x_s)}{L} \right)^{\frac{n}{n-1}} \left(\frac{a(t)}{a_0} \right)^{\frac{3n}{n-1}} \left(\frac{h(t)}{h_0} \right)^{\frac{n}{n-1}}, \tag{3.44}$$

and by integration

$$a(t) = a_0 \left(1 - H(t)/T_B^0 \right)^{\frac{1-n}{2n+1}}, \text{ where } H(t) = h_0^{\frac{n}{1-n}} \int_0^t h(t)^{\frac{n}{n-1}} dt. \tag{3.45}$$

T_B^0 is the breakthrough time as given in Eq. 3.35 for the constant hydraulic head $h(t) = h_0$. The breakthrough time is obtained from the condition for the pole of the function $a(t)$ which yields:

$$h_0^{n/n-1} T_B^0 = \int_0^{T_B^0} h(t)^{n/n-1} dt. \tag{3.46}$$

The hydraulic head can increase or decrease in time. Depending on the particular situation various forms of its time-dependence can be assumed.

As an example we assume a simple case where the hydraulic head drops exponentially in time as $h = h_0 \exp(-t/\tau)$. We take this dependence for didactical reasons because it gives clear-cut results which can be easily obtained and interpreted. Integrating Eq. 3.46 using this dependence and a bit of reordering gives:

$$T_B = T_B^0 \frac{n-1}{n} \ln \left(1 - \frac{T_B^0 n}{\tau(n-1)} \right)^{-1}. \tag{3.47}$$

The solid line in Figure 3.12 shows the dependence of T_B/T_B^0 on τ/T_B^0 as given by Eq. 3.47, the dashed line depicts the dependence calculated by the finite differences model. The vertical dashed line divides the regions of breakthrough and no breakthrough. The condition for the breakthrough is $\tau > \frac{n}{n-1} T_B^0$.

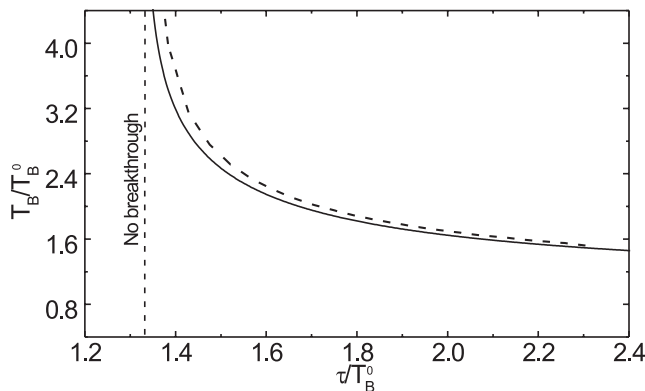


Figure 3.12: Dependence of T_B/T_B^0 on τ/T_B^0 when the hydraulic head drops exponentially with time constant τ . The solid line represents Eq. 3.48, the dashed one the results of the finite differences model. The parameters for the standard fracture are used. The vertical dashed line divides the regions with and without breakthrough.



When assuming a time dependence of other parameters, a similar treatment can be done. One has to bear in mind that these parameters are time dependent when karstification proceeds in nature and that further work on this topic is needed.

3.2 THE INFLUENCE OF FRACTURE ROUGHNESS ON KARSTIFICATION TIMES

Natural fractures exhibit various degrees of roughness. This section investigates the influence of fracture roughness on the breakthrough time of the karst conduits. First estimations on the influence of roughness on cave evolution were performed by Groves and Howard (1994) on two-dimensional fracture networks. They replaced the uniform aperture widths of the initial pathways by statistically distributed apertures and found breakthrough behaviour similar to that in smooth fractures. A more realistic approach is that of Hanna and Rajaram (Hanna and Rajaram, 1998) who performed simulations on a single two dimensional fracture with statistically distributed aperture width.

Using statistically distributed aperture widths along a single one-dimensional fracture we have found that the breakthrough times do not change significantly provided that the standard deviation does not exceed $0.3a_0$. If σ however becomes close to a_0 it is highly probable that the fracture becomes blocked and its flow resistance becomes high enough to increase the breakthrough time dramatically. This approach needs many calculations with different distributions of initial aperture widths, and is thus not well suited. It is also inconvenient for yielding clear-cut results on the influence of roughness to breakthrough times.

A more convenient approximation can be taken by replacing an irregular roughness by a regular one, which allows us to calculate the hydrodynamic resistance analytically. This was done by Ge (1997). He investigated the validity of the cubic law, i.e. the dependence of the flow rate on the third power of the average fracture aperture width \bar{a} , for a general wide $b \gg a$ rough fracture. He gives analytical results for a fracture consisting of one confining ideal plane and the other plane shaped by periodical triangles, as is illustrated in Figure 3.13.

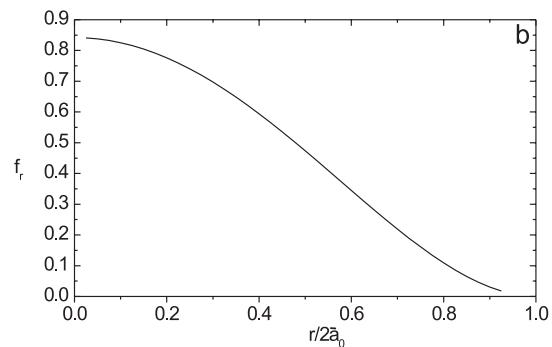
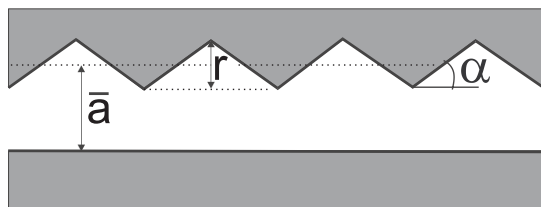


Figure 3.13: a) Geometry of an ideally rough fracture with a saw-toothed upper plane. r is the roughness amplitude. Initial relative roughness is $r/2\bar{a}$. b) The factor f_r , which represents the effect of roughness on the flow rate, as a function of relative roughness $r/2\bar{a}$ for $\alpha = 35^\circ$.



The flow rate for such a fracture can be expressed as

$$Q_r = f_r \cdot Q_s, \tag{3.48}$$

where Q_s is the flow rate of the smooth fracture with aperture \bar{a} , given by:

$$Q_s = \frac{\rho g \bar{a}^3}{12\eta} \cdot \frac{dh}{dx}. \tag{3.49}$$

The factor f_r is a function of the relative roughness $r/2\bar{a}$:

$$f_r(r/2\bar{a}) = \left(2 \frac{r/2\bar{a}}{1-r/2\bar{a}} + 1 \right)^2 \cdot \left(\frac{r/2\bar{a}}{1-r/2\bar{a}} \right)^{-4} \cdot \Phi(\alpha). \tag{3.50}$$

The parameter α is the angle of inclination as depicted in Figure 3.13a. $\Phi(\alpha)$ is a function of this angle (See Ge (1997)). Note from Figure 3.13a that $\alpha \rightarrow 0$ if $r \rightarrow 0$, such that $\Phi(\alpha) \rightarrow 1$. If $30^\circ < \alpha < 60^\circ$ then $\Phi(\alpha)$ varies between 0.7 and 0.9. In our calculations we used $\alpha = 35^\circ$ where $\Phi(\alpha) \approx 0.84$.

The factor f_r is a measure of the flow reduction due to the roughness of the fracture. For a completely rough surface when $r/2\bar{a} = 1$, f_r becomes zero since the fracture is blocked to flow. Figure 3.13b depicts f_r as a function of $r/2\bar{a}$.

The roughness factor can be easily incorporated into the algorithm for single fracture evolution. Again, a typical breakthrough behaviour as that in Figure 3.3 is observed in

all cases, but the breakthrough time increases with relative roughness.

The breakthrough curves for various degrees of roughness are shown on Figure 3.14a.

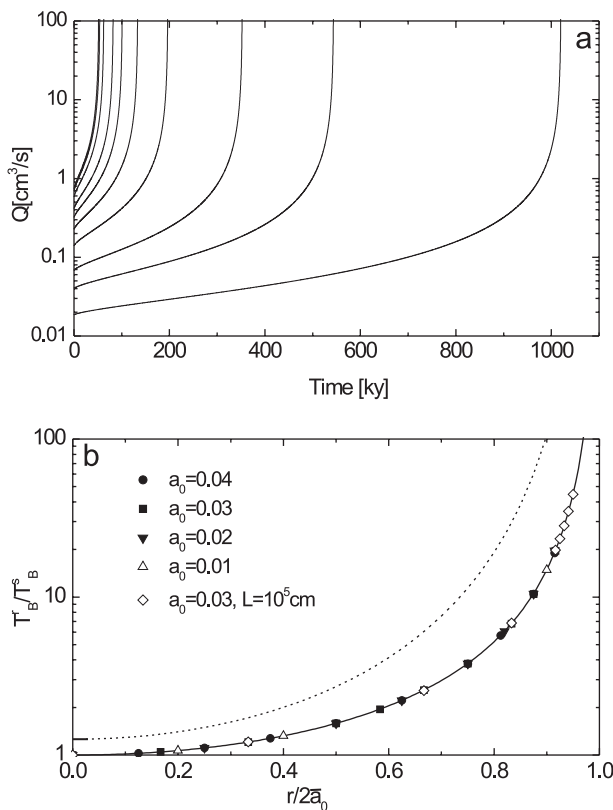


Figure 3.14: **a)** Breakthrough curves for rough fractures with various degrees of roughness: $r/2\bar{a} = 0, 0.166, 0.333, 0.5, 0.583, 0.66, 0.833, 0.875, 0.916$ from left to right respectively. $\alpha = 35^\circ, L = 4 \cdot 10^5$ cm, $\bar{a} = 0.03$ cm, other parameters as for the standard fracture (see Table 3.1). **b)** Dependence of the ratio between breakthrough time of a rough fracture with initial relative roughness $r/2\bar{a}$ and an initially smooth fracture. The symbols represent results of the finite difference model for various initial widths and lengths. The full line shows the result obtained by integrating Eq. 3.30 using Eq. 3.51 for the exit rates. The dotted line represents the crude approximation given by Eq. 3.52.



3. THE EVOLUTION OF A SINGLE FRACTURE

Figure 3.14b presents the ratio between the breakthrough times of the rough and the corresponding smooth fracture versus initial relative roughness.

Results of the finite difference model are presented by the symbols. Various symbols denote various initial aperture widths and lengths as denoted in the figure. Curves present approximations which we discuss latter.

In the calculations the following assumptions are made:

- The roughness amplitude r is maintained during the dissolutional widening.
- Only the aperture widths $a(x)$ change by dissolutional widening.

During the evolution of the conduit the roughness $r/2\bar{a}$ decreases continuously and the correction factor f_r loses its influence. Once $r/2\bar{a}$ has decreased to 0.2, which still is significant, the fracture develops almost like a smooth one.

However, to obtain the upper estimation for the breakthrough time of the rough fracture, we assume that the relative roughness ($r/2\bar{a}$) is kept constant. We justify this assumption by the fact, that the aperture width at the bottleneck is widened only a few times until breakthrough. To obtain the exit dissolution rate for the rough fracture we insert Eq. 3.48 into Eq.3.20:

$$F_r(L) = F(x_s) \left[\frac{LPk_n(n-1)(1-c_s/c_{eq})^{n-1}}{f_r Q_s} \right]^{\frac{n}{1-n}} = F_s(L) \cdot f_r^{\frac{n}{n-1}}. \quad 3.51$$

As in Section 3.1 we neglected terms x_s and 1 in the expression for the dissolution rates. $F_s(L)$ denotes the exit dissolution rate for the corresponding smooth fracture. Inserting the obtained rate into Eqs.3.34 and 3.35 we get an estimation for the breakthrough time:

$$T_B^r = T_B^s \cdot f_r^{\frac{-n}{n-1}}. \quad 3.52$$

This is depicted by the dotted line in Figure 3.14b.

To improve the analytical result, we consider the decrease of relative roughness in time. Including the widening rate from Eq. 3.51 into Eq. 3.30 we get an integral for the T_B^r , which has to be solved numerically. The results obtained are presented by the full line in Figure 3.14b. The ratio T_B^r/T_B^s is in complete accordance with the results of the finite difference model. As can be seen from Figure 3.14b extreme roughness is necessary to exert significant influence to the breakthrough times.

It is difficult to estimate the roughness factor for natural fractures, which exhibit roughness on both confining sides. Nevertheless the idealized rough fracture as depicted by Figure 3.13a can be regarded as a first approach, and it is reasonable to generalize the result in the following way. As long as the initial ratio $Q_0^r/Q_0^s \geq 0.3$ the influence of roughness does not increase the T_B for more than a factor of 2. To increase the breakthrough time by one order of magnitude, a $Q_0^r/Q_0^s = 0.02$ is needed. Therefore an extreme roughness is necessary for a drastic change and it seems that in most natural cases its influence is not very significant. Although this result might appear qualitative it gives a



first estimation on the reliability of smooth fracture models of conduit evolution. Eqs. 3.51 and 3.52 can be generally applied for any type of roughness provided that the function f_r is known.

It is more realistic to consider the fracture as a two-dimensional medium. This was done by Hanna and Rayaram (1998). Their results are apparently in contrast to ours, since they obtained that the breakthrough time decreases with roughness.

In rough two-dimensional fractures flow is channeled along the pathways which exhibit lowest flow resistance (Tsang and Tsang, 1989). These channels are preferential for the breakthrough. Suppose that the roughness is varied in the way that the initial flow rate through the fracture is kept constant as performed by Hanna and Rayaram (1998). Then the flow velocities along the preferential channels increase with the roughness. Also the lengths of these channels increase with the roughness. With respect to the widening rates these two effects oppose each other. Still the effect of flow velocities is stronger so that the breakthrough time is decreasing with roughness.

3.3 EVOLUTION OF A SINGLE FRACTURE WITH VARYING LITHOLOGY

As stated in Section 2.2, the kinetic order n depends on the type of limestone. According to Eisenlohr *et al.* (1999) it takes values between 3 and 11. The breakthrough time depends on the kinetic order n , as can be seen from Eq. 3.35. Figure 3.15a shows this dependence for the standard fracture (see Table 3.1).

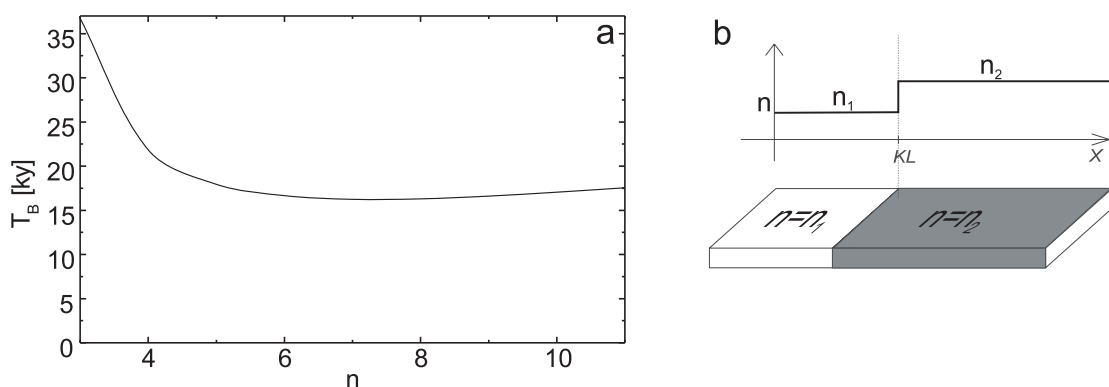


Figure 3.15: a) The dependence of the breakthrough time on the order of reaction kinetics for the standard fracture (see Table 3.1). b) Fracture extending through a boundary separating limestones with different kinetic properties.

Conduits often extend through several limestone formations with different kinetic properties. The concept of a single boundary is shown on Figure 3.15b. The dissolution rates are governed by the kinetic constant k_1 and order n_1 for $x < KL$ and k_2 and n_2 for $x \geq KL$.

How such kinetic boundaries affect the dissolution rates is shown on Figure 3.16. This graph presents the dependence of the logarithm of dissolution rates on the logarithm of undersaturation ($1-c/c_{eq}$). The full line illustrates the chemical evolution of a solution in a setting with two kinetic boundaries between the orders $n = 8$ and $n = 4$. Up to point A ($c = c_s = 0.9c_{eq}$) the linear rate law acts. Then the non-linear rate law with $n = 8$ becomes active until point B. At point B the boundary to the fourth order kinetics boosts the dissolution rate for two orders of magnitude to point C. Between points C and D the dissolution proceeds with the fourth order kinetics. At point D another boundary to the eighth order is faced and the rates drop down to point E, which is more than two orders of magnitude lower than point D. Note from the figure, that the closer to saturation the solution is, the higher is the shift of the dissolution rate.

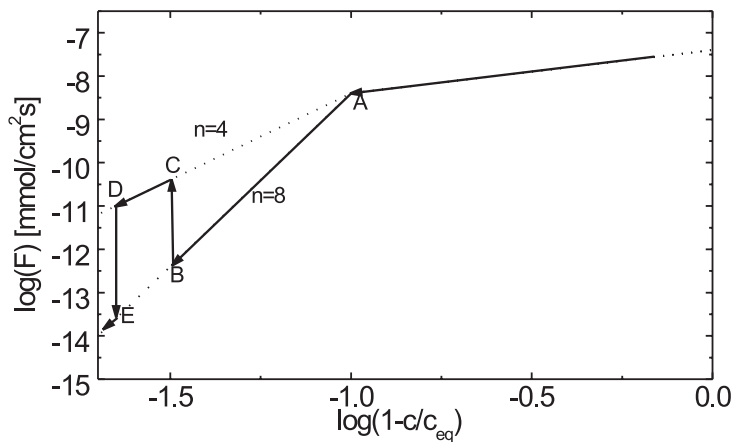


Figure 3.16: Dissolution rates in a system with varying lithology. See text.

3.3.1 Numerical results

Introducing varying lithology does not require many changes in the numerical algorithm for the evolution of a single fracture. Basically, the calculation procedure is the same as described in Section 3.1. Additionally, one has to enter the parameters describing the positions of the boundaries and the rate orders for each lithology.

Let us first assume two different lithologies: n_1, k_{n1} , for $x \leq KL$ and n_2, k_{n2} for $x \geq KL$. We assume the switch concentration for both lithologies as equal; in this case the rate constants are related by $(1 - c_s/c_{eq})^{n_1-n_2}$. This gives only two additional parameters to the basic model presented in Section 3.1: n_2 and K .

Figure 3.17 presents the numerical results for the standard fracture, with $n_1 = 6$, $n_2 = 4$ and $K = 0.5$ (a, b, c) and for the reverse case where $n_1 = 6$ and $n_2 = 4$ (d, e, f). The breakthrough time T_B for the first case (Figure 3.17a) is almost two orders of magnitude higher. Figures b, c, e and f confirm the consideration on Figure 3.16. Dissolution rates and aperture widths at the lithology boundaries face a step change either in the positive ($n_2 < n_1$) or negative directions ($n_2 > n_1$). Therefore the evolution of a fracture strongly depends on the side from which the water enters.

3. THE EVOLUTION OF A SINGLE FRACTURE

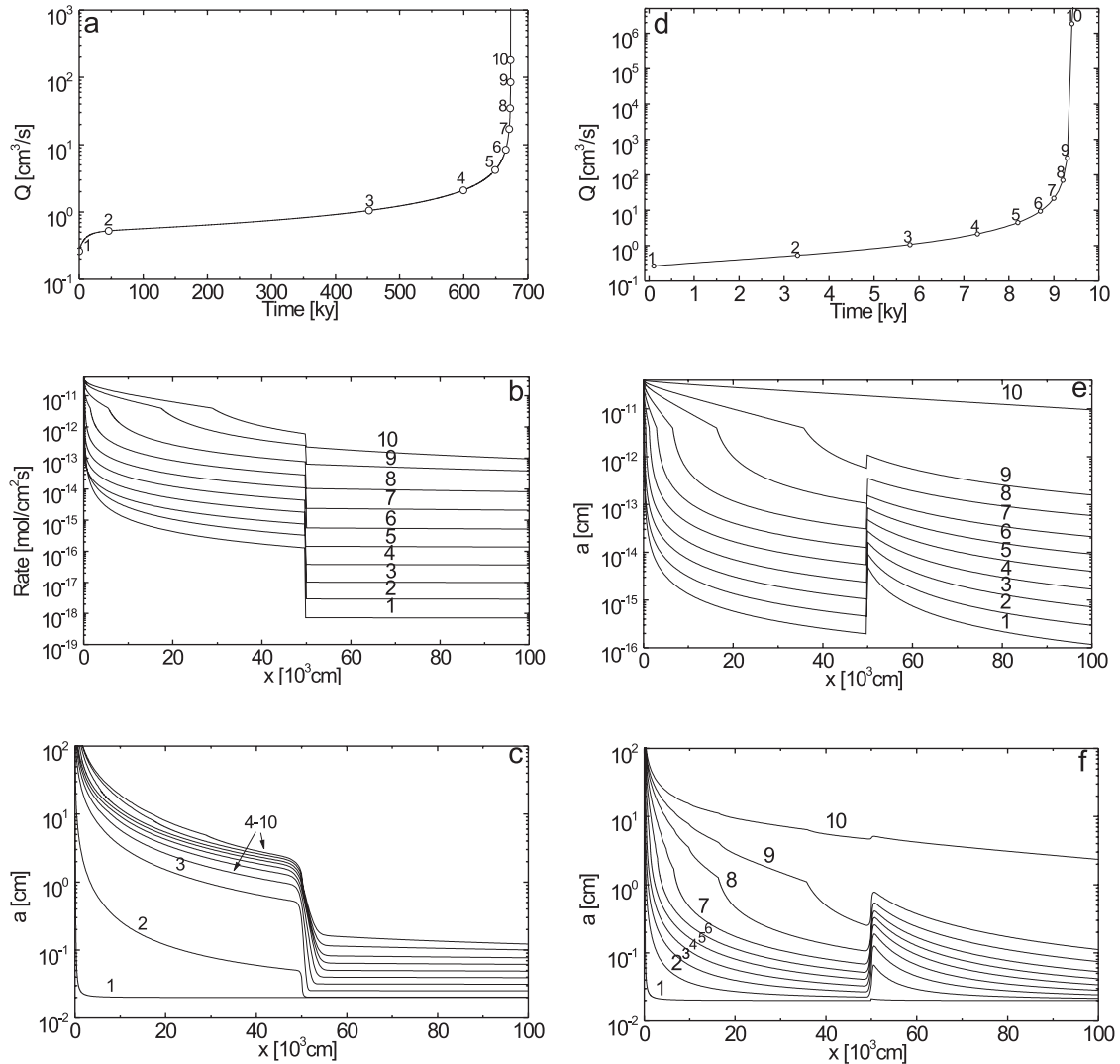


Figure 3.17:

- a) Evolution of flow rates in time for the standard fracture with $n_1 = 4$, $n_2 = 6$ and $K = 0.5$ (see Figure 3.15).
- b, c) Profiles of dissolution rates and aperture widths for $n_1 = 4$, $n_2 = 6$ and $K = 0.5$ plotted at 0.1, 45.8, 452.1, 599.4, 649.1, 665.5, 670.9, 672.5, 673 and 673.1 ky, marked from 1–10 respectively.
- d) Evolution of flow rate in time for the standard fracture with $n_1 = 6$, $n_2 = 4$ and $K = 0.5$.
- e, f) Profiles of dissolution rates and aperture widths for $n_1 = 6$, $n_2 = 4$ and $K = 0.5$ at 0.1, 3.3, 5.8, 7.3, 8.2, 8.7, 9, 9.2, 9.3 and 9.4 ky, marked from 1–10 respectively.

To get some more insight into the problem, we can apply the bottleneck principle described in Section 3.1. As shown there, the initial rate at the bottleneck is required to describe the breakthrough behaviour of the system. We expect bottlenecks either at $x = KL$ or $x = L$, so we focus on the rates there. We use Eq. 3.28 to obtain the initial rates at KL ($b_0 \gg a_0$ and $KL \gg x_s$) at the n_1 side of the lithology boundary.



3. THE EVOLUTION OF A SINGLE FRACTURE

$$F(KL)_{n_1} = F(x_s) \left[1 + \frac{KL}{\lambda_{n_1}(x_s)} \right]^{n_1/(1-n_1)} \quad 3.53$$

Concentration and therefore the saturation ratio are continuous across the boundary. From Eq. 3.53 and Eq. 2.12 we calculate the concentration at KL . Inserting it into the rate equation with n_2 and k_{n_2} we obtain the rate on the n_2 side of the boundary

$$F(KL)_{n_2} = F(x_s) \frac{k_{n_2}}{k_{n_1}} \left[1 + \frac{KL}{\lambda_{n_1}(x_s)} \right]^{n_2/(1-n_1)} \quad 3.54$$

The ratio between the rates on both sides of the boundary at KL is

$$\frac{F(KL)_{n_1}}{F(KL)_{n_2}} = \frac{k_{n_1}}{k_{n_2}} \left[1 + \frac{KL}{\lambda_{n_1}(x_s)} \right]^{(n_1-n_2)/(1-n_1)} \quad 3.55$$

Employing Eq. 3.29, we obtain the rate at the exit:

$$F(L)_{n_2} = F(KL) \left(1 + \frac{(1-K)L}{\lambda_{n_2}(KL)} \right)^{n_2/(1-n_2)} \quad 3.56$$

Depending on n_1 and n_2 the bottleneck is either at the boundary of lithology KL or at the exit of the fracture L .

3.3.2 The case $n_2 > n_1$

If $n_2 \geq n_1$, the bottleneck is always at $x = L$, since the rates at the boundary drop and continue to drop as the solution proceeds towards the exit. To get an estimation for the behaviour of T_B , we make a rather crude approximation and assume the following:

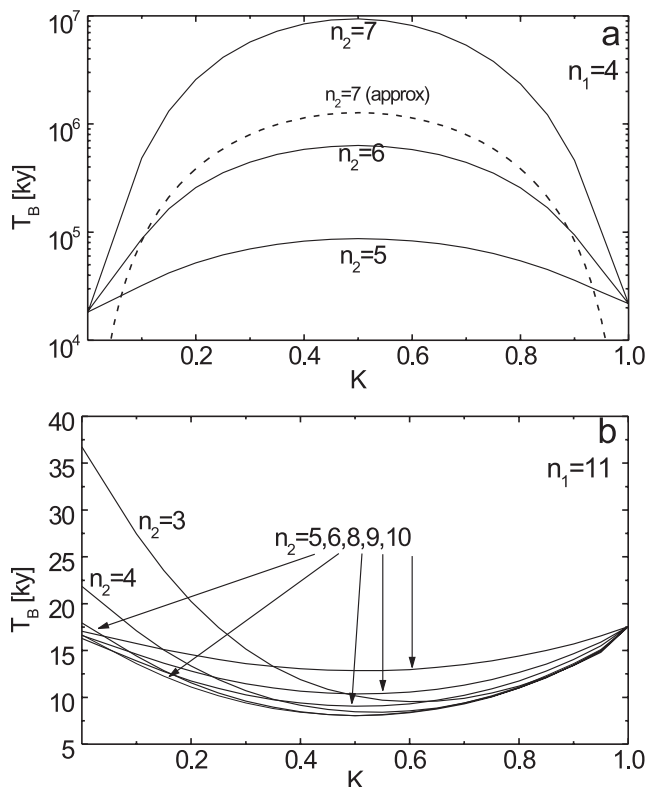
- The penetration length λ_{n_2} is so large, that the rates do not change much between the boundary and the exit. Therefore $F(L) \approx F(KL)_{n_2}$ (see Eq. 3.56).
- The first part of the fracture opens up quickly, therefore the hydraulic head drops mostly along the bottleneck part $x > KL$, i.e. $i = h/((1-K)L)$.

This approximation enables us to get an estimation of T_B for $0.2 < K < 0.8$. Using the same procedure as in Section 3.1, i.e. inserting the rate $F(KL)_{n_2}$ into 3.30 and integrating it, we obtain

$$T_B \approx \frac{n_1 - 1}{3n_2 - n_1 + 1} \cdot \frac{a_0 (K(1-K))^{\frac{n_2}{n_1-1}}}{2\gamma F(c_s)} \left(\frac{n_1 - 2}{2n_1 + 1} \cdot \frac{a_0}{2\gamma F(c_s)} \right)^{-n_2/n_1} \left(\frac{1}{T_B^0} \right)^{-n_2/n_1} \quad 3.57$$



T_B^0 is the breakthrough time if $n = n_1$ along the entire fracture. With increasing K , $F(KL)_{n_2}$ and the length of the bottleneck part $(1-K)L$ decreases. Both effects oppose each other with respect to the breakthrough time, which is maximal at $K = 0.5$ as can be derived



from Eq. 3.57. Figure 3.18a shows the dependence of T_B on K for the standard fracture with $n_1 = 4$ and $n_2 = 5, 6$ and 7 , obtained from the numerical model. The dashed line depicts the analytic approximation given in Eq. 3.57 for $n_2 = 7$.

Figure 3.18: a) Dependence of breakthrough time on the position of the lithological boundary ($x = KL$) for the standard fracture with $n_1 = 4$ and $n_2 = 5, 6, 7$ (denoted on the lines). The dashed line is an approximation given by Eq. 3.57. b) As in figure a, but for $n_1 = 11$ and $n_2 = 10, 9, 8, 7, 6, 5, 4$ and 3 .

3.3.3 The case $n_2 < n_1$

If the rate order at the boundary drops, the dissolution rate is boosted up. The bottleneck can form either at $x = KL$ or at $x = L$ depending on the position of the boundary and the change of the dissolution rate there. For any pair n_1 and n_2 there is a value of K where the rates at both possible bottlenecks are equal – we will call it K_{min} .

If $K < K_{min}$, the bottleneck is at the exit. As K increases, the rate at the exit increases and the length of the bottleneck decreases. Consequently the breakthrough time drops with K .

Once K reaches the value K_{min} the two bottlenecks open simultaneously. Breakthrough time with respect to K is minimal at this point.

For $K > K_{min}$, the bottleneck is at $x = KL$. The rate at KL decreases with increasing K and the length of bottleneck part ($x < KL$) increases. Both variations contribute to the rise of T_B with K .

This behaviour is shown in Figure 3.18b. In this case $n_1 = 11$ and n_2 takes values between 10 and 3.



3.3.4 Multiple boundaries and boundaries with insoluble rock

Arbitrary settings with multiple lithology can be assumed in nature as well as in the model. Figure 3.19 gives an example of a fracture extending through a sequence of limestone sections with $n = 4$ and $n = 6$, starting with $n = 4$.

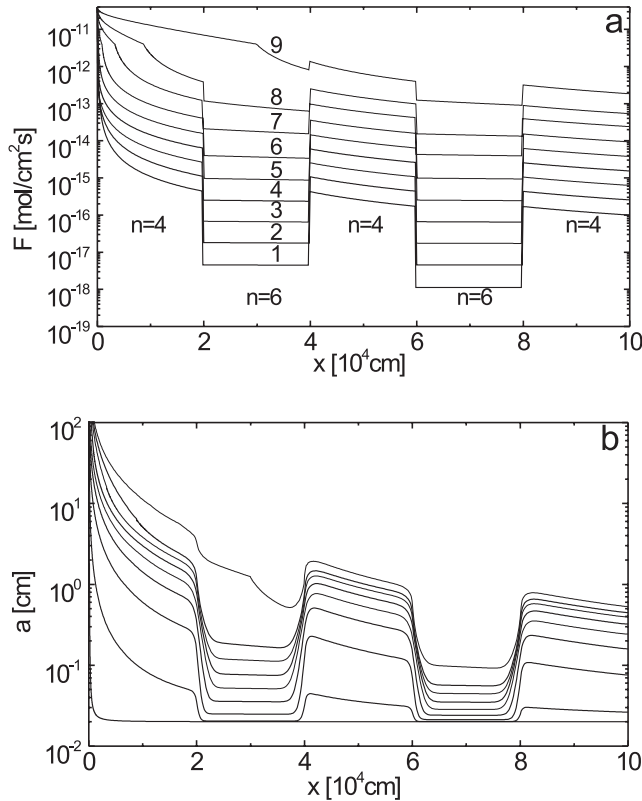


Figure 3.19: a) Evolution of dissolution rates in a fracture extending through four boundaries between $n = 4$ and $n = 6$. Lithology changes every $2 \cdot 10^4$ cm. Profiles were recorded at 0.1, 14.6, 62.3, 99, 113.9, 119.7, 121.8, 122.4 and 122.7 ky, marked from 1–9 respectively. b) Aperture widths at the same times as in figure a.

The bottlenecks form in the region with higher kinetics order $n = 6$. $Q(t)$, not shown here, shows breakthrough behavior. Initially it rises fast due to the opening of $n = 4$ parts, but then builds up a plateau due to the bottlenecks in the $n = 6$ regions which delay the breakthrough event. The rates between successive $n = 4$ borders are almost constant, since the concentration within $n = 6$ regions rises only slightly, thus the aggressivity of the solution with respect to the limestone with $n = 4$ is preserved there.

One can imagine many possible lithology settings. An extreme contrast occurs when one part of the fracture extends through insoluble rock. In this case the flow rate initially rises due to the opening of the soluble part of the fracture, but the constant resistance of the insoluble part switches off the feedback mechanism.

Figure 3.20a shows the evolution of flow rates for the standard fracture with insoluble walls for $x \geq KL$ for three different values of K as denoted on the lines. The flow rate Q converges to the value $1/(1-K)Q_0$, where Q_0 is the initial flow rate and $(1-K)L$ is the length of the insoluble part. Figure 3.20b shows the evolution of fracture aperture widths for $K = 0.5$.





3. THE EVOLUTION OF A SINGLE FRACTURE

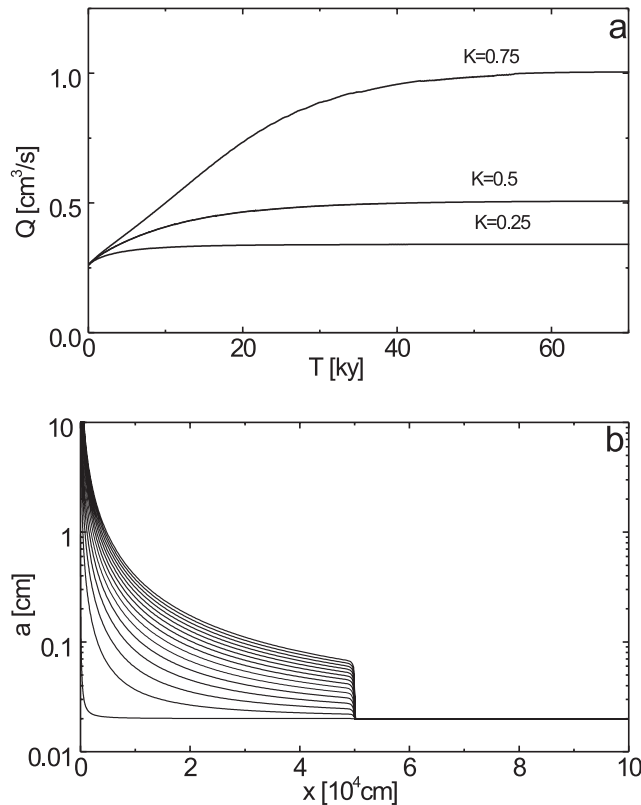


Figure 3.20: a) Evolution of flow rates in a fracture with insoluble walls for $x > KL$ ($K = 0.25$, $K = 0.5$ and $K = 0.75$). b) Aperture width profiles for $K = 0.5$. The lowest line is at 100y, later profiles are taken with 4ky steps between 5 and 70ky.

3.4 THE INFLUENCE OF SUBTERRANEAN CO_2 SOURCES ON THE INITIAL KARSTIFICATION OF A SINGLE FRACTURE

Various geochemical settings can change the parameters of the rate equation within a single karstifying fracture. The change of the kinetic order n was discussed in Section 3.3. Another parameter is the equilibrium concentration. This is determined by the content of CO_2 in the solution as shown in Chapter 2. So far we have assumed that CO_2 stems entirely from the surface and that c_{eq} is constant along the entire fracture. One could assume, however, various sources delivering CO_2 into the fracture and thus shifting c_{eq} . Due to the non-linearity of the rate equation, the dissolution rates are highly sensitive to variations of c/c_{eq} , especially when the solution is close to saturation. During most of the initial karstification $c/c_{eq} > 0.99$ (cf. Figure 3.3c) along almost the entire fracture. Therefore subterranean sources of CO_2 , which increase the value of c_{eq} , might heavily enhance the initial karstification (Gabrovšek *et al.*, 2000). We discuss this topic in this section.

It is not our aim to discuss the mechanisms of CO_2 delivery in detail, but to incorporate the effect of possible CO_2 sources into the model of a single fracture. We will focus on two simple cases:

- A: Point input of CO_2 [Figure 3.21]: Although point sources are a rather unrealistic idealization, one can expect a very focused CO_2 delivery into the karstifying



fractures when volcanic activity is present in the vicinity of evolving karst. The amount of CO_2 delivered by volcanic activity into the solution changes its c_{eq} with respect to calcite by Δc_{eq} .

- B: Extended input of evenly distributed CO_2 [Figure 3.21]: This scenario could refer to the case of microbial activity. If heterotrophic micro-organisms dwell on the walls of the fracture, they oxidize organic carbon constituents of karst water by aerobic metabolism and produce CO_2 along the flow path of the water (Menne, 1998). The consequence is a linear increase of c_{eq} within a part of the fracture where CO_2 input is evenly distributed. The increase of CO_2 concentration delivered by bacteria cannot exceed the concentration of O_2 in the water prior to conversion. The solubility of oxygen in the water is 11.3 mg/l at 10 °C (Freeze and Cherry, 1979). Therefore the maximal increase of CO_2 is about $3.5 \cdot 10^{-7}$ mol/cm³. This corresponds to change of c_{eq} by $\Delta c_{eq} = 2 \cdot 10^{-7}$ mol/cm³ if c_{eq} prior to CO_2 delivery is 2 μ mol/cm³. Extended sources can also result from volcanic origin and may therefore exhibit a much larger Δc_{eq} .

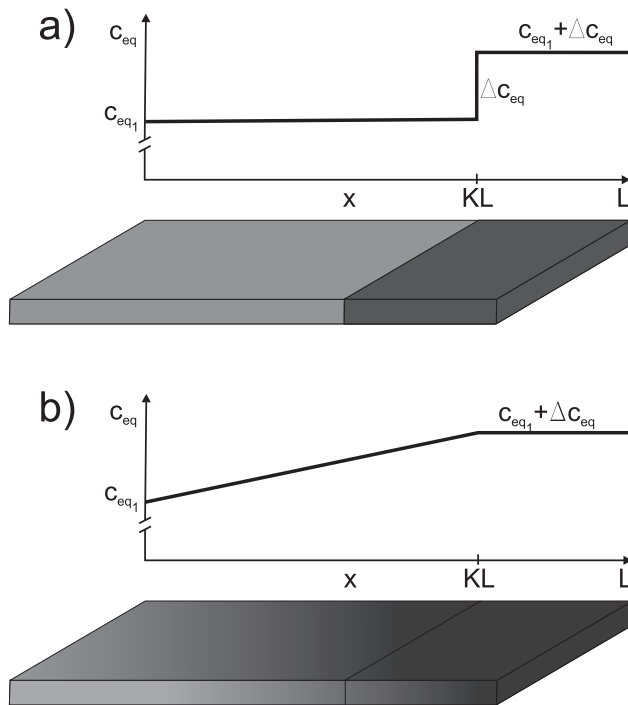


Figure 3.21: Conceptual models of subterranean CO_2 sources: **a)** A point source of CO_2 at position KL causes a step increase of c_{eq} . **b)** Evenly distributed CO_2 input between the entrance of the fracture and the position KL causes a linear increase of c_{eq} in this region.

3.4.1 Point sources of CO_2

Let us suppose that a point CO_2 source is introduced into the karstifying fracture at some position $x_{in} = KL$, where $K \leq 1$. This is depicted on Figure 3.21a.

The chemical picture of the scenario is presented on the Figure 3.22. The thick curve presents the CO_2 - Ca^{2+} equilibrium curve. See Figure 2.1 and the discussion in Chapter 2

for more details. The solution enters into the fracture with some initial Ca^{2+} and CO_2 concentration represented by point A. The chemical pathway proceeds along the line A-CA until at point B' the concentration of CO_2 rises and dissolution proceeds along the parallel pathway B-CB. The net result of the CO_2 input with respect to our model is the change of the equilibrium concentration by Δc_{eq} . Note that point A corresponds to the entrance of the fracture and points B and B' to the input point of CO_2 at $x = KL$. In all the following model runs point B' is very close to the equilibrium curve. In summary: The dissolution rates for $x \leq x_{in}$ are determined by c_{eq1} , the equilibrium concentration related to the CO_2 -concentration of the inflowing water. At $x = x_{in}$ the equilibrium concentration increases due to the input of CO_2 to $c_{eq2} = c_{eq1} + \Delta c_{eq}$.

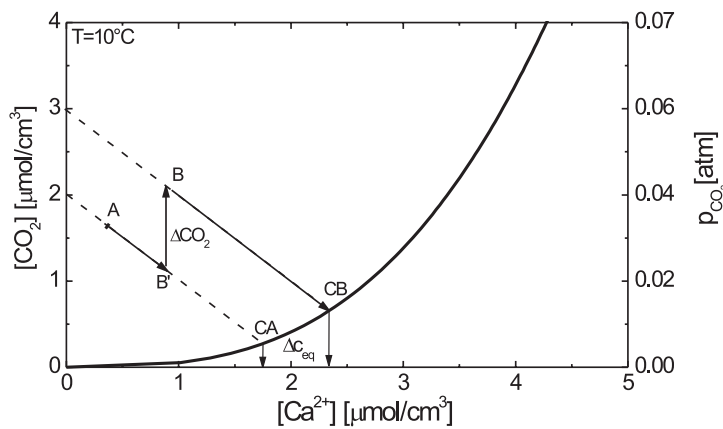


Figure 3.22: Chemical evolution of an $H_2O-CO_2-CaCO_3$ solution flowing in a fracture under closed system conditions with respect to CO_2 . The curve represents equilibrium with respect to calcite. See text for explanation.

Numerical results

To incorporate the above settings into the model of a single fracture we change c_{eq} in the rate equation according to:

$$c_{eq} = \begin{cases} c_{eq1} & x < KL \\ c_{eq2} & x \geq KL. \end{cases} \quad 3.58$$

The new parameters describing this extended model are K and $\alpha = c_{eq1}/c_{eq2}$. We will focus our discussion on the effect of these two parameters on the breakthrough time. Figure 3.23a shows the evolution of flow rates for various values of K denoted on the curves for the standard fracture (see Table 3.1 in Section 3.1 for the basic parameters) and $\alpha = 0.91$ ($\Delta c_{eq} = 0.2 \mu\text{mol}/\text{cm}^3$). All curves exhibit the same behaviour with breakthrough times changing from 21.7 ky at $K = 1$ (standard fracture) to a minimum value of 7.5 ky at $K = 0.5$.

Figure 3.23b illustrates the dependence of the breakthrough time on K for various values of α . All curves exhibit a minimum which depends on α . Note that the breakthrough times at $K = 0$ are related to an inflowing solution with c_{eq2} . Therefore they drop with increasing c_{eq2} as $T_B = \alpha^{4/3} \cdot T_B^0$ (see Eq. 3.35).

3. THE EVOLUTION OF A SINGLE FRACTURE

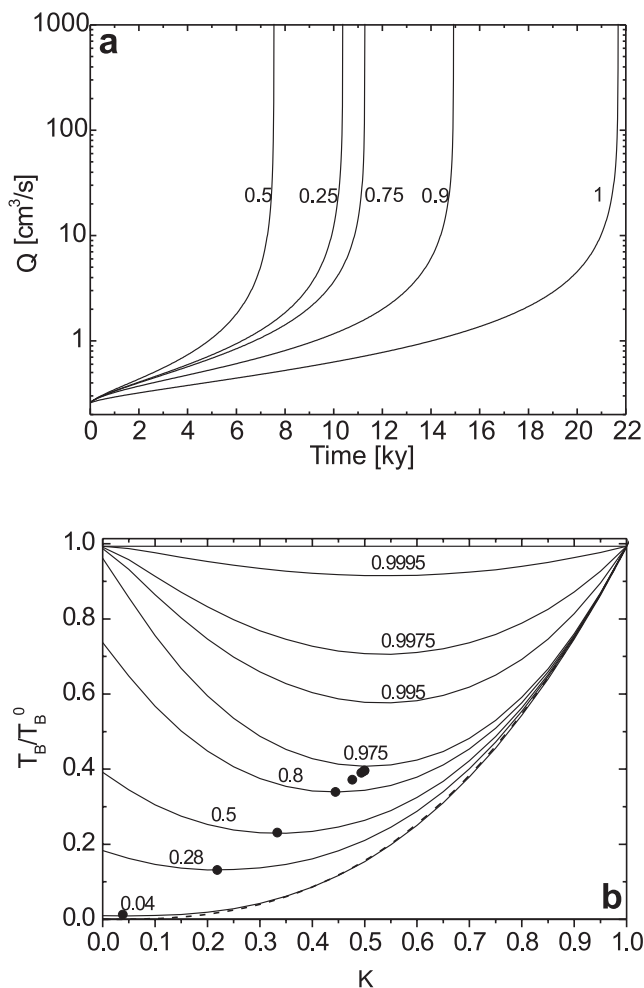


Figure 3.23: a) Evolution of flow rates for the standard fracture with a CO_2 point input for various values of K (denoted on the curves). $\Delta c_{eq} = 0.2 \mu\text{mol}/\text{cm}^3$. The curve for $K = 1$ corresponds to the standard fracture (see Table 3.1). b) Dependence of T_B/T_B^0 on K for several values of α (denoted on the lines). Dots present the approximation given in Eq. 3.66.

Figure 3.24a shows T_B as a function of α for various values of K , denoted on the curves. In all cases there is a drastic drop of breakthrough times in the region between $\alpha=1$ and $\alpha \approx 0.9$. Two sets of curves are observed. For large K ($K > 0.7$) the breakthrough times drop up to a factor of two between $\alpha = 1$ and $\alpha = 0.975$ which corresponds to

$\Delta c_{eq} = 0.05 \mu\text{mol}/\text{cm}^3$. Then only little variation is observed as α decreases. In contrary, for $K < 0.5$ the breakthrough times show a significant continuous decrease also at smaller values of α .

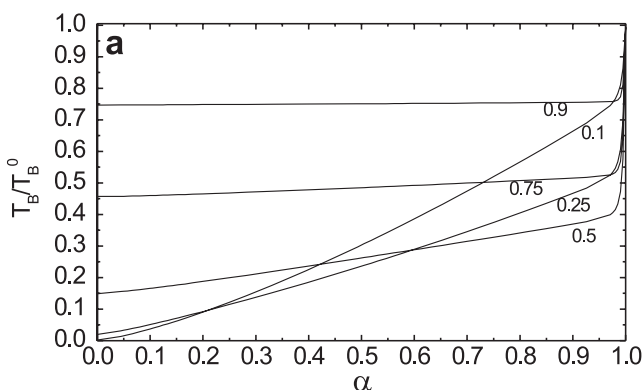


Figure 3.24: a) Breakthrough times as a function of α for various values of K as denoted on the curves.

3. THE EVOLUTION OF A SINGLE FRACTURE

To explain this behavior we focus on two representative cases. Figure 3.24b shows the dissolution rates along the fracture for $K = 0.25$ (dashed lines) and $K = 0.75$ (full lines) for various times of evolution. At the onset of karstification the dissolution rates exhibit a characteristic drop close to the entrance until they are boosted up at $x_{in} = KL$. Then the rates drop again.

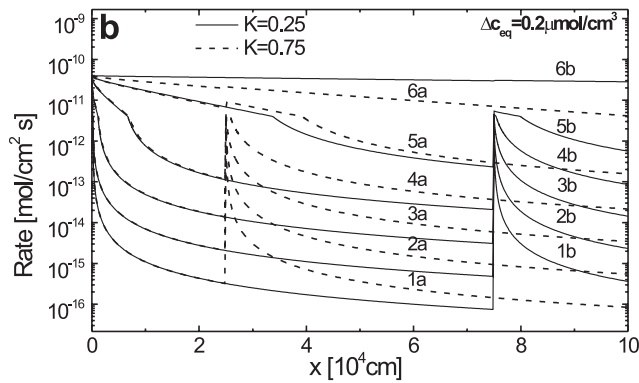


Figure 3.24: b) Dissolution rates for the point input: $\alpha = 0.91$, $K = 0.25$ (dashed lines) and $K = 0.75$ (full lines). For $K = 0.25$ profiles are recorded at 0.1, 6.3, 9.2, 10.11, 10.33, 10.37 ky, marked by 1a–6a. For $K = 0.75$ profiles are recorded at 0.1, 6.93, 10.19, 11.07, 11.27 and 11.31 ky, marked by 1b–6b.

For $K = 0.25$ the rates at the exit are considerably lower than at x_{in} at all times. This forms a bottleneck at the exit as shown by Figure 3.25a.

The situation becomes different for $K = 0.75$ (full lines). Firstly the rates are equal to those above up to $x = 0.25L$, and drop further until they are boosted up at $0.75L$. Now the rates at the exit are higher and the bottleneck is at KL during the entire time span. This is shown by Figure 3.25b.

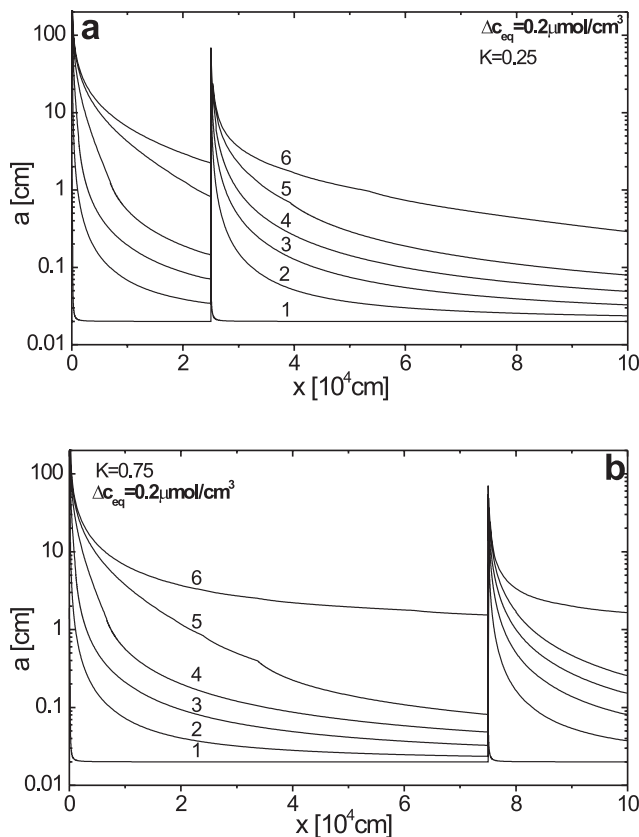


Figure 3.25: Evolution of aperture widths for the case from Figure 3.24. **a)** $K = 0.25$. **b)** $K = 0.75$.



3. THE EVOLUTION OF A SINGLE FRACTURE

From the numerical results the following conclusions can be drawn:

- For any α , a K_{min} exists, where the rates at $x = K_{min}L$ and at $x = L$ are equal, and therefore T_B becomes a minimum
- In the region $K < K_{min}$, the bottleneck is at the end of the fracture: with increasing K , the rate there increases and the length of the bottleneck part $x > KL$ decreases. Thus the breakthrough time decreases in this region
- In the region $K > K_{min}$, the bottleneck is at KL , $F(KL)$ then decreases with increasing K , the length of the bottleneck part decreases, and consequently T_B increases.

Analytical estimation of T_B

To give at least some approximate analytical results and to prove the above statements, we refer to the bottleneck principle. We use Eq. 3.29 to obtain the rates at the both possible bottlenecks, i.e. at $x = KL$ and at $x = L$. The initial dissolution rate at the input of CO_2 is equal to:

$$F(KL)_\downarrow = F(c_s) \left(1 + \frac{KL}{\lambda_n(x_s)} \right)^{\frac{n}{1-n}} \quad 3.59$$

From numerical results we see that for most cases of interest the solution at $x = KL$ is close to c_{eq1} , such that $c_{eq1} - c(KL) \ll c_{eq2} - c_{eq1} = \Delta c_{eq}$. This simplifies the rate at position KL after the CO_2 input to

$$F(KL)_\uparrow = k_n (1 - c_{eq1} / c_{eq2})^n = k_n (1 - \alpha)^n \quad 3.60$$

\downarrow and \uparrow denote the rate at position KL before and after the CO_2 input. Applying Eq. 3.29 we obtain an estimation for the exit rate:

$$F(L) = k_n (1 - \alpha)^n \left(1 + \frac{(1-K)L}{\lambda_n(KL)} \right)^{\frac{n}{1-n}} \quad 3.61$$

For convenience we define a new parameter $\tilde{\lambda}$ as

$$\tilde{\lambda} = \frac{\rho g h c_{eq1} a_0^3}{24 \eta L (n-1) k_n}, \quad 3.62$$

so that the penetration lengths at x_s and $x = KL$ are (see also Eq. 3.26):

$$\lambda_n(x_s) = \tilde{\lambda} (1 - c_s / c_{eq1})^{1-n} \quad 3.63$$

$$\lambda_n(KL) = \frac{\tilde{\lambda}}{\alpha} (1 - \alpha)^{1-n} \quad 3.64$$





3. THE EVOLUTION OF A SINGLE FRACTURE

At K_{min} we have $F(K_{min}L) = F(L)$. Neglecting the term “1” in Eq. 3.61 we get

$$K_{min} = \frac{\left(\frac{\tilde{\lambda}}{L}(1-\alpha)^{1-n} + \alpha\right)}{1+\alpha} \approx \frac{\alpha}{1+\alpha}. \quad 3.65$$

The right side is valid if $(\tilde{\lambda}/L)(1-\alpha)^{1-n} \ll \alpha$ which also means $(1-K)L/\lambda_n(KL) \gg 1$. Then K_{min} becomes independent of $\tilde{\lambda}/L$ and the breakthrough time can be expressed as

$$T_B^{min} = T_B^0 \cdot K_{min}^{n/(n-1)} = T_B^0 \left(\frac{\alpha}{1+\alpha}\right)^{n/n-1}. \quad 3.66$$

The full circles on Figure 3.23b mark this approximation at the minimal breakthrough times T_B^{min} , which are close to the minima of the curves. T_B^0 is the breakthrough time without CO_2 input given by Eq. 3.35 in Section 3.1. Note that T_B^{min} has the same functional dependence on the basic parameters as T_B^0 . The approximation is in good accordance with the finite difference model for $\alpha \leq 0.91$. Then it fails, since the assumption does not hold anymore.

Another limiting case is when c_{eq2} becomes so large, that the dissolution rates at the exit are sufficiently high and the last part of the fracture widens quickly in comparison to the first part. Therefore after a short time the hydraulic head acts only along the region $x \leq KL$. The breakthrough time can then be calculated by replacing L by KL and h/L by h/KL in Eq. 3.35. In this case we obtain

$$T_B^{lim} = T_B^0 K^{\frac{2n}{n-1}}. \quad 3.67$$

This result is presented by the lower dashed curve in Figure 3.23b. Finally for $K = 0$, the T_B dependence on α can be directly obtained from Eq. 3.35 as $T_B^0 \alpha^{n/(n-1)}$.

In all three limiting cases, the dependence of T_B on the basic parameters (c.f. Section 3.1) is, within the limit of our assumption, given by that of T_B^0 . We can conclude, since all the equations solely contain the algebraic group $\tilde{\lambda}/L$, that this is also generally true. One can read T_B for all intermediate cases in Figure 3.23b if T_B^0 is known, provided $n = 4$. For other values of n similar graphs can be constructed. In the region between $n = 3$ and $n = 10$, not presented here, but checked, the deviations are not large.

3.4.2 Extended sources of CO_2

We assume delivery of CO_2 by an evenly distributed population of micro-organisms oxidizing organic carbon into CO_2 . They deliver a constant rate of CO_2 as long as a sufficient amount of oxygen and organic matter is available.



Numerical results

We model the situation by using a linear increase of c_{eq} in the rate equation:

$$c_{eq} = \begin{cases} c_{eq_1} + \frac{\Delta c_{eq}}{KL} x & x < KL \\ c_{eq_2} & x \geq KL \end{cases} \quad 3.68$$

Additional parameters describing the extended model are now K and Δc_{eq} .

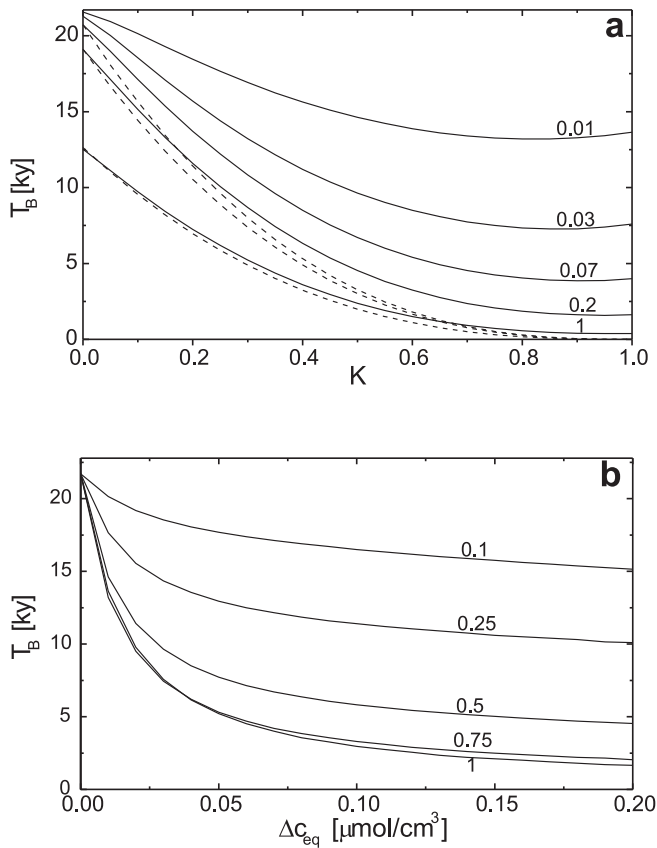
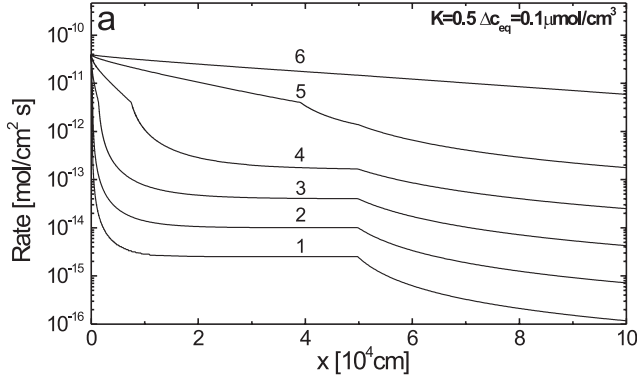


Figure 3.26: Effect of an extended source of CO_2 on the breakthrough time of the standard fracture. **a)** T_B dependence on K for various values of Δc_{eq} [$\mu\text{mol}/\text{cm}^3$] as denoted on the lines. The dashed lines show the approximation by Eq. 3.75 for $\Delta c_{eq} = 0.07 \mu\text{mol}/\text{cm}^3$, $\Delta c_{eq} = 0.2 \mu\text{mol}/\text{cm}^3$ and $\Delta c_{eq} = 1 \mu\text{mol}/\text{cm}^3$ respectively. **b)** T_B dependence on Δc_{eq} for various values of K as denoted on the lines.

Figure 3.26a shows the dependence of the breakthrough times on K for various values of Δc_{eq} . Other parameters correspond to the standard fracture with $c_{eq_1} = 2 \mu\text{mol}/\text{cm}^3$. T_B decreases with increasing K .

Figure 3.26b shows the breakthrough times as a function of Δc_{eq} for various values of K (denoted at the curves). There is a steep decrease at low Δc_{eq} . Most of the reduction occurs for $\Delta c_{eq} \leq 0.05 \mu\text{mol}/\text{cm}^3$. Thus when the organism dwell in the first half of the fracture ($K = 0.5$) and only about 25 % of the maximum available oxygen (11.3 mg/l at 10 °C) is converted to CO_2 , the breakthrough time is reduced from 21.7 ky to 7.5 ky. If only 10 % of O_2 is converted ($\Delta c_{eq} = 0.025 \mu\text{mol}/\text{cm}^3$) the reduction is still to 10 ky.

Figure 3.27a shows the dissolution rates and the aperture widths along the fracture at several timesteps in the evolution. Again, the rates at the entrance drop steeply and then become constant. Beyond



$x = KL$, c_{eq} is constant and in agreement with Eq. 3.21 the rates drop continuously as the solution moves towards the exit. Figure 3.27b shows the corresponding profiles of the aperture widths. The bottleneck for the flow is located at the exit and therefore widening there determines the breakthrough time.

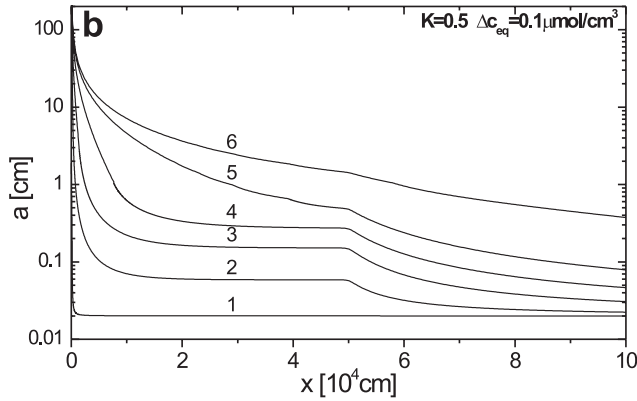


Figure 3.27: a) Profiles of the dissolution rates in the standard fracture with extended CO_2 source at 0.1, 3, 5, 5.6, 5.82 and 5.83 ky, marked from 1–6 respectively. b) Evolution of fracture aperture widths at the same times.

Analytical approximations

To understand this behaviour, we try to obtain some analytical approximations. The bottleneck forms always at the exit. The rate there can be obtained using Eq. 3.29 inserting KL and L for x_1 and x_2 respectively.

To calculate the rates at $x = KL$, one has to solve Eq. 3.7 for the linear increase of c_{eq} as given in Eq. 3.68. For convenience we introduce the variable $\Delta c(x) = c_{eq}(x) - c(x)$. Eq. 3.7 then becomes

$$k_n \left(\frac{\Delta c(x)}{c_{eq}(x)} \right)^n P dx = Q d(c_{eq}(x) - \Delta c(x)) = P \cdot F(x) dx \tag{3.69}$$

We introduce $\kappa = \Delta c_{eq}/KL$ and rewrite the first part of Eq. 3.68

$$c_{eq}(x) = c_{eq_1} + \kappa x = c_{eq_1} \left(1 + \frac{\kappa x}{c_{eq_1}} \right) \tag{3.70}$$

Inserting the upper expression into Eq. 3.69 and reordering it we get:

$$\kappa - \frac{d\Delta c}{dx} = k_n \frac{P}{Q} \left(\frac{\Delta c}{c_{eq1} (1 + \kappa x/c_{eq1})} \right)^n. \quad 3.71$$

The numerical results show, that for the cases of our interest $\kappa \gg d\Delta c/dx$, in other word the variation of $\Delta c(x)$ is small compared to the rise of c_{eq} . Applying this in the upper equation gives:

$$\frac{\Delta c}{c_{eq1} (1 + \kappa x/c_{eq1})} = \frac{\Delta c}{c_{eq}(x)} = \left(\frac{Q\kappa}{k_n P} \right)^{1/n} = \left[\frac{1}{k_n} F(KL) \right]^{1/n}. \quad 3.72$$

The rate at $x = KL$ can now be written as

$$F(KL) = \frac{\kappa Q}{P} = \frac{\Delta c_{eq} Q}{PKL}. \quad 3.73$$

The result is somewhat surprising, since the rate does not depend on c_{eq1} . This is also confirmed by numerical runs. The exit rate can now be calculated by inserting the obtained $F(KL)$ into Eq. 3.29. We obtain

$$F(L) = F(KL) \left[1 + \frac{(1-K)L}{\lambda_n(KL)} \right]^{\frac{n}{1-n}}, \quad \text{where} \quad \lambda_n(KL) = \tilde{\lambda} \frac{c_{eq2}}{c_{eq1}} \left(\frac{F(KL)}{k_n} \right)^{(1-n)/n}. \quad 3.74$$

We need to determine the range of the new parameters, where the enhancement of karstification is considerable. To do this we compare the initial dissolution rates $F(L,0)$ to the initial dissolution rates $F^0(L,0)$ (see Eq. 3.32) for the fracture with no CO_2 input. As a criterion we choose $T_B/T_B^0 \approx 0.5$ and correspondingly $F(L,0)/F^0(L,0) \approx 2$. Therefore we search for $\varepsilon_{crit} = \Delta c_{eq}/c_{eq1}$ where this criterion is achieved. For each K and $L/\tilde{\lambda}$ we obtain a value of Δc_{eq} where T_B is reduced to $1/2$. The full lines on Figure 3.28 show the dependence of ε_{crit} on K for various values of $L/\tilde{\lambda}$ denoted at the corresponding curves. The lowest value of $L/\tilde{\lambda}$ corresponds to a fracture with $a_0 = 0.04$ cm, $L = 10^4$ cm, $h/L = 0.5$, the highest value represents a fracture with $a_0 = 0.01$ cm, $L = 10^6$ cm, $h/L = 0.01$. The middle curve is our standard fracture. Thus the entire region of natural karstification is covered.

The four horizontal dashed lines present the maximal possible values of $\varepsilon_{max} = \Delta c_{eq}^{max}/c_{eq1}$ which can result from micro-organisms when using up all the available oxygen. This causes an increase of the CO_2 concentration by $0.35 \mu\text{mol}/\text{cm}^3$. The corresponding value of Δc_{eq}^{max} depends on c_{eq1} ; $\Delta c_{eq}^{max} = 0.32 \mu\text{mol}/\text{cm}^3$ at $c_{eq1} = 0.5 \mu\text{mol}/\text{cm}^3$, $\Delta c_{eq}^{max} = 0.3 \mu\text{mol}/\text{cm}^3$ at $c_{eq1} = 1 \mu\text{mol}/\text{cm}^3$, $\Delta c_{eq}^{max} = 0.2 \mu\text{mol}/\text{cm}^3$ at $c_{eq1} = 2 \mu\text{mol}/\text{cm}^3$ and $\Delta c_{eq}^{max} = 0.1 \mu\text{mol}/\text{cm}^3$ at $c_{eq1} = 4 \mu\text{mol}/\text{cm}^3$.

3. THE EVOLUTION OF A SINGLE FRACTURE

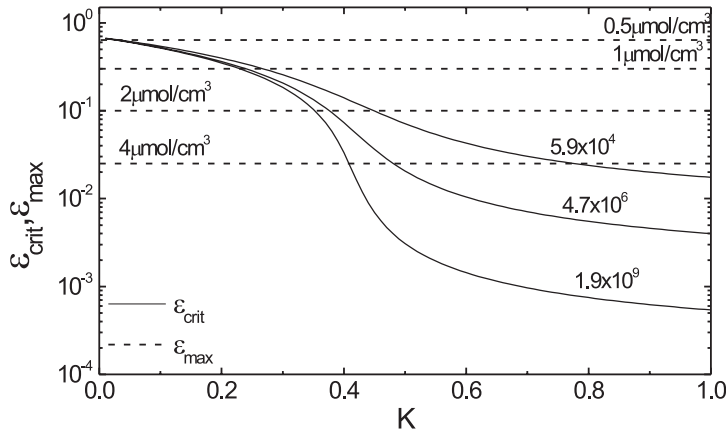


Figure 3.28: The full lines represent the value of $\Delta c_{eq}/c_{eq1}$ where the breakthrough time of the fracture with the extended CO_2 source is reduced to one half of the breakthrough time with no extra CO_2 . Numbers denote the values of L/λ ; the lowest value corresponds to a fracture with $a_0 = 0.04$ cm, $L = 10^4$ cm, $h/L = 0.5$, the highest represents a fracture with $a_0 = 0.01$ cm, $L = 10^6$ cm, $h/L = 0.01$ and the middle curve is the standard fracture. Dashed lines present the $\varepsilon_{max} = \Delta c_{eq}^{max}/c_{eq}$ which can be delivered by microbial activity for four different values of c_{eq1} as given on the lines. If a full line is below some dashed line this means that the bacterial activity can reduce the “intrinsic” breakthrough time for more than one half.

If the curves denoting ε_{crit} are above the corresponding lines representing ε_{max} , karstification is not significantly enhanced. On the other hand, if $\varepsilon_{crit} < \varepsilon_{max}$ a large enhancement is to be expected. From Figure 3.28 one reads that a deep invasion of micro-organisms into the fracture is necessary. In view of the initial flow velocities of the water in the order of several metres/day, such deep invasion seems likely. For the standard case with $c_{eq1} = 2 \mu\text{mol}/\text{cm}^3$, $K > 0.4$ is required. If little external CO_2 is supplied from the surface, i.e., $c_{eq1} = 0.5 \mu\text{mol}/\text{cm}^3$, this value of K is reduced and significant enhancement of karstification can arise solely by the activity of micro-organisms.

It is also possible to give an extreme limit of enhancement for each value of K . If Δc_{eq1} becomes so large that the constant initial dissolution rate becomes very large compared to that of the same fracture with no CO_2 supply, karstification is entirely governed by the evolution of the last part of the fracture which represents the bottleneck for the flow. Then the hydraulic head acts entirely along that part, that

$$T_B(K) = T_B^0(c_{eq2}) \cdot (1 - K)^{2n/h} \quad 3.75$$

$T_B^0(c_{eq2})$ is the breakthrough time of the corresponding fracture with constant $c_{eq} = c_{eq2}$. The lowest dashed curves in Figure 3.26a represent this limit, for the standard fracture. It shows that bacterial activity can be sufficient to approach this limit closely. It should be noted that the approximation breaks down when K is close to 1. The two higher dashed curves show that for smaller values of Δc_{eq} significant deviations occur.

Figure 3.29a represents the dependence of T_B on Δc_{eq} for various values of L and K . Three different lengths are presented; $L = 10^6$ cm by the full lines, $L = 10^5$ cm (standard

fracture) by the dashed lines and $L = 10^3$ cm by the dotted lines. The values of K are denoted at the lines. Other parameters are “standard”. It demonstrates clearly that for $L > 1$ km and $K > 0.5$ an increase of c_{eq} by $1 \mu\text{mol}/\text{cm}^3$ is sufficient to reach the maximum of enhancement. For karstification along short fractures of about 100 m, however, biogenic CO_2 reduces the breakthrough time only to about one half. For low values of $K \approx 0.1$ no significant enhancement arises at all. This again shows that deep invasion of micro-organisms into the initial karst system is necessary.

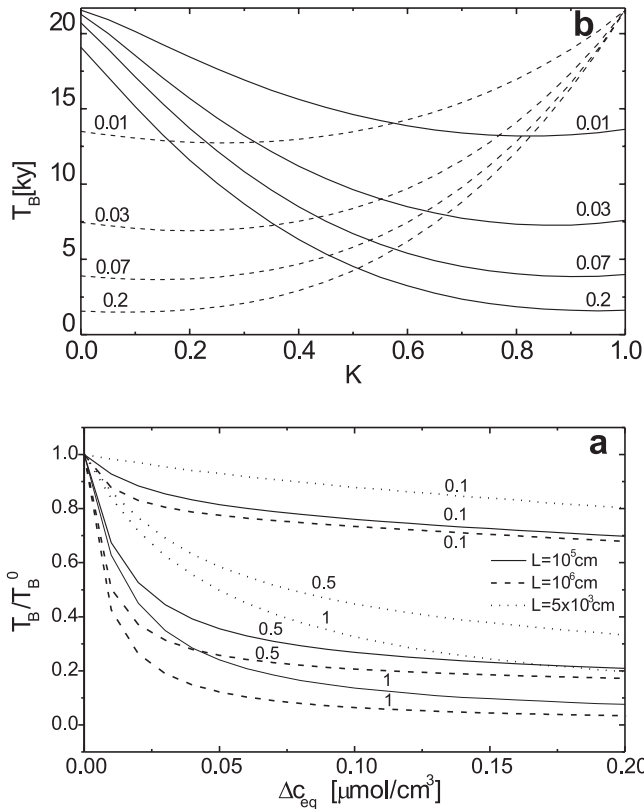


Figure 3.29: a) Breakthrough times for the standard fracture (full lines) and fractures with $L = 10^6$ cm (dashed) and $L = 10^3$ cm (dotted) as a function of Δc_{eq} . The numbers on the curves denote K . The scale is in units of T_B^0 , i.e. the breakthrough times of the respective fractures without CO_2 supply. These are 0.32 ky, 21.7 ky and 467 ky, for $L = 10^3$ cm, $L = 10^5$ cm and $L = 10^6$ cm respectively. **b)** T_B as a function of K for the values of Δc_{eq} [$\mu\text{mol}/\text{cm}^3$] denoted at the lines. The dashed lines denote the case where the input is in the first part of the fracture, as shown in Figure 3.26. The full lines represent the case, when CO_2 input starts at $x_m = KL$.

3.4.3 The reverse case: extended input in the second half of the fracture

The full lines on Figure 3.29b present the dependence of T_B on K for various values of Δc_{eq} if the CO_2 is delivered in the second part of the fracture at $x \geq KL$. In this case $c_{eq} = c_{eq1}$ for $x < KL$, and $c_{eq} = c_{eq1} + \kappa(x - KL)$ for $x \geq KL$. The numbers on the curves denote $\Delta c_{eq}/c_{eq1}$.

For comparison, the dashed lines present the results from Figure 3.26a. When CO_2 is delivered for $x < KL$, the bottleneck is located at the exit part of the fracture. The breakthrough times in this case are a function of $(1-K)$. If, however, CO_2 is delivered at $x > KL$, then the part $x < KL$ represents the bottleneck and the breakthrough time is a similar function, but now of K . At $K \approx 0.5$ breakthrough times for both cases should

not differ much. Moreover the corresponding curves should be mirror like, because breakthrough times should be close to each other if the lengths of the bottlenecks are equal for the two cases. As an example, breakthrough time for the case where CO_2 is delivered at $x < KL$, should be close to the breakthrough time at $1-K$ when CO_2 is delivered at $x > KL$ since the lengths of the both bottlenecks are equal. This is nicely demonstrated by Figure 3.29b and gives further support to the “bottleneck method” which we have used to analyse the numerical results.

So far we have assumed that microbiological oxidation of organic carbon increases with increasing flow through the fracture, such that the increase in c_{eq} is independent of the flow rate. This implies that the overwhelming bulk of bacteria is floating in the solution and their concentration is independent of flow rate. If, however, the bacteria are located at the fissure surfaces forming a biofilm and their rate of production is assumed to be constant, then the concentration of CO_2 decreases as the flow rate increases. If at time $t = 0$, $\Delta c_{eq}(0)$ is the increase in equilibrium concentration with respect to calcite at flow rate $Q(0)$, then at later times t , $\Delta c_{eq}(t) = \Delta c_{eq}(0) \cdot Q_0/Q(t)$. This can be incorporated into the numerical model by employing $\Delta c_{eq}(t)$ in each time step. The results qualitatively resemble those of from Figure 3.26, although the variations are less pronounced. One could envisage many different scenarios of CO_2 input into the karstifying fractures. As a final example we take the case, where CO_2 is supplied between $x_1 = K_1L$ and $x_2 = K_2L$, which causes a constant increase of c_{eq} in this region. For $x > K_2L$, c_{eq} remains constant.

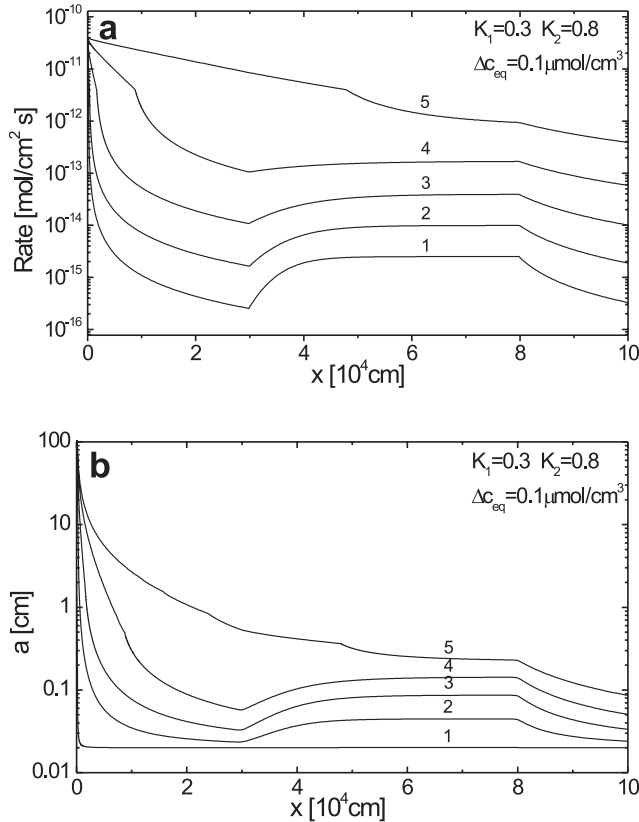


Figure 3.30 shows the evolution of the dissolution rates and aperture widths for the standard fracture with $K_1 = 0.3$, $K_2 = 0.8$ and $\Delta c_{eq} = 10^{-7} \text{ mol/cm}^3$. After an abrupt drop close to the entrance the rates increase in the region where CO_2 is released, and then drop when approaching the exit. Breakthrough is reduced by a factor of almost 7 with respect to the T_B^0 .

Figure 3.30: a) Profiles of the dissolution rates in the standard fracture with extended CO_2 source between K_1L and K_2L , where $K_1 = 0.3$ and $K_2 = 0.8$. Profiles are recorded at: 0.1, 2.1, 2.95, 3.23, 3.4 ky, marked from 1-6, respectively. b) Profiles of the aperture widths at the same times.



4.4.4. Conclusion

Subterranean sources of CO_2 , either supplied at point inputs or continuously along a part of a karstifying fracture, cause a significant enhancement on early karstification. The reduction of breakthrough times depends on the amount of CO_2 supplied and on the position of the inputs.

For point inputs the highest reduction of breakthrough times is observed if the input is located near the center of the fracture. In this case a small increase of p_{CO_2} by about $2 \cdot 10^{-3}$ atm is enough to reduce breakthrough times to about one half. If the input is close to the entrance, an increase of about 0.1 atm is required for a significant reduction of breakthrough times. For inputs close to the exit of the fracture, even a large increase of p_{CO_2} affects breakthrough times only moderately. These values correspond for situations of vegetated karst with $c_{eq1} \approx 2 \mu mol/cm^3$. For bare karst areas with saturation of about $0.5-1 \mu mol/cm^3$, the influence of CO_2 inputs is increased and lower values of additional CO_2 are needed to cause similar decrease of breakthrough times.

Continuous CO_2 input can arise from extended diffuse gas migration from deep volcanic sources or from heterotrophic micro-organisms dwelling at the walls of the karstifying fractures. Micro-organisms can cause an increase of p_{CO_2} by about $6 \cdot 10^{-3}$ atm. For natural karstification this is enough for a significant reduction of breakthrough times, provided the micro-organisms have invaded deep into the fracture, populating at least the first third of length. In this case the influence of CO_2 supply for bare karst areas is even more enhanced. Then karstification can arise even if only atmospheric CO_2 is contained in the inflowing water.

3.5 THE ROLE OF MIXING CORROSION IN EARLY KARST EVOLUTION

3.5.1 Background and model structure

A brief history of mixing corrosion: when and why?

The chemical background of mixing corrosion has been already discussed in Chapter 2. If two saturated solutions with different chemical compositions mix, the aggressivity is renewed due to the nonlinearity of the $Ca^{2+}-CO_2$ equilibrium curve. Although mixing corrosion had been known before, its role in karst was first stressed by Bögli (1964) who suggested it as a possible cave forming mechanism.

Experiments by Weyl (1958) and Erga and Terjesen (1956) revealed a linear rate law for the dissolution kinetics of limestone in H_2O-CO_2 solution and therefore the evolution of extended karst conduits as observed in nature could not be explained by theoretical models (White and Longyear, 1992). Bögli suggested that caves could originate deep in



the rock due to the mixing of saturated solutions. Mixing corrosion was also discussed by Dreybrodt (1981a) who showed that, owing to this mechanism, cave conduits can grow when two saturated solutions mix along an intersection of fractures. This model does not explain the fact pointed out by Ford and Ewers (1978), that most of the caves develop along bedding planes without any intersections by joints.

Mixing corrosion was put into the “back stage”, after it was shown that the action of non-linear dissolution kinetics alone can generate extended karst conduits. In Section 3.1 we have seen that due to the nonlinearity only a small change of parameters in the rate equation causes a large reduction of T_B . From the model point of view we can consider mixing corrosion as an extra source of CO_2 therefore we might expect it to cause a similar enhancement of early karstification (Gabrovšek and Dreybrodt, 2000).

Model structure

To achieve mixing of two solutions, we have to leave the “easy-to-analyse” territory of single fracture models.

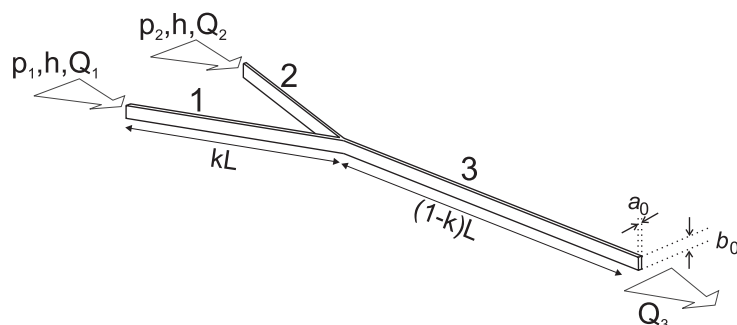


Figure 3.31: Symmetric confluence of two fractures. Conceptual model for the most simple scenario where mixing corrosion is active. p_1 and p_2 denote the p_{CO_2} of solutions at the entrances of the fractures which join at the position KL .

Figure 3.31 shows the simplest case where mixing is possible: Two symmetric fractures joining into a third one. All have initial aperture widths a_0 and widths b_0 . Fractures 1 and 2 join into fracture 3 at distance KL from the entrance, where L is the total length of the system. At the confluence water is mixed completely. The hydraulic heads at the entrances 1 and 2 are h_1 and h_2 , respectively. At the outflow the hydraulic head is set to zero.

Figure 3.32 shows the chemical evolution of the solution in fractures 1 and 2 with respect to CO_2 and Ca^{2+} . The solutions enter at points 1 and 2 with $[Ca^{2+}] = 0$ and different concentrations of CO_2 corresponding to equilibrium with p_1 and p_2 respectively. The evolution of the solutions within the fractures is illustrated by the full lines. Points 1' and 2' depict the chemical composition at the exits of both fractures at the confluence. Point M shows the concentration c_{mix} after immediate and complete mixing at the confluence. The equilibrium of the mixture is given by the intersection of the dashed line representing dissolution by the mixed solution in fracture 3 under closed conditions and the CO_2 - Ca^{2+} equilibrium curve (fat line).

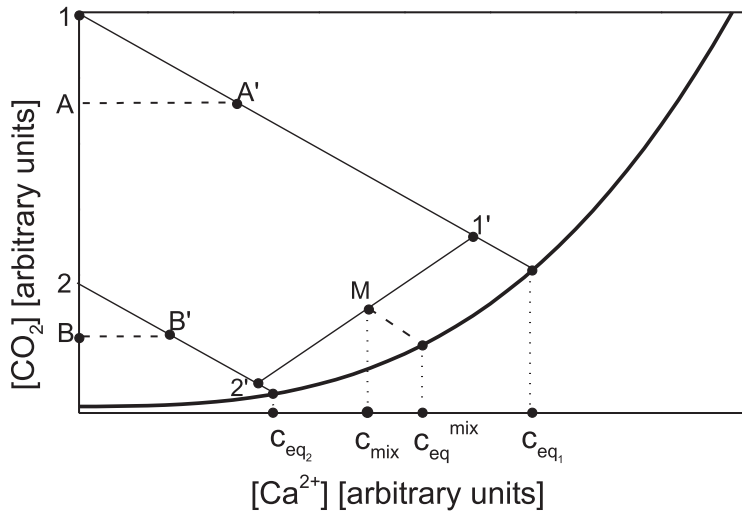


Figure 3.32: Chemical scenario of mixing corrosion. See text.

Another scenario is also possible. Assume that both soils exhibit different soil structures and contain calcite. In that case water seeping down will dissolve calcite under open system conditions designated by the dashed lines BB' and AA' until at points A' and B' , respectively, it enters into the fractures. From then on it dissolves limestone under closed system conditions. This leads to the same amount of undersaturation as in the first scenario given above. Even if the points A and B coincide, this last scenario allows mixing corrosion.

To calculate the evolution of fracture widths for the case $h = h_1 = h_2$, we use the following procedure:

1. Calculate the resistance of each fracture and the head h_j at the junction according to:

$$h_j = h \frac{R_1 R_3 + R_2 R_3}{R_1 R_2 + R_1 R_3 + R_2 R_3}, \tag{3.76}$$

where R_1 , R_2 and R_3 are the resistances of the three fractures calculated by Eq. 3.2.

2. Apply the transport-dissolution model (see Section 3.1) and calculate the widening and chemical evolution of fractures 1 and 2.
3. Calculate the concentration c_{mix} entering into fracture 3 assuming complete mixing, i.e.

$$c_{mix} = (Q_1 c_1^j + Q_2 c_2^j) / (Q_1 + Q_2), \tag{3.77}$$

where c_1^j and c_2^j are the concentrations in the fractures 1 and 2 at the confluence.

4. Calculate the widening of the fracture 3.
5. Repeat steps 1.–3. until the onset of turbulence.

3.5.2 Numerical results and discussion

Model parameters

The following parameters were used in the runs that follow: $a_i(t=0) = 0.02$ cm, $b_i(t=0) = 100$ cm, for $i = 1, 2, 3$. $h = 5000$ cm, $p_1 = 0.05$ atm and p_2 is in the range between 0.003 atm and 0.05 atm. $k_1 = 4 \cdot 10^{-11}$ mol cm⁻²s⁻¹, $k_n = 4 \cdot 10^{-8}$ mol cm⁻²s⁻¹, $c_s = 0.9c_{eq}$, $n = 4$, as in the standard fracture.

Note: from here on the expression “Mixing Corrosion” will be abbreviated as MC.

Linear kinetics with MC vs. nonlinear kinetics without MC

We start with Bögli’s concept of MC, where dissolution rates are defined only by linear kinetics. Figure 3.33a shows the aperture widths of fractures 1 and 3, as they develop in time. $p_1 = 0.05$ atm and $p_2 = 0.03$ atm. Due to the exponential decrease of the dissolution rates, fracture 1 opens at the entrance and the dissolution front progresses very slowly. Mixing corrosion causes opening at the junction, but has only a local importance. There is no breakthrough in a geologically relevant time.

Figure 3.33b shows the evolution of the aperture widths when no MC is present, i.e. $p_1 = p_2 = 0.05$ atm, but nonlinear dissolution rates are assumed. All other parameters are unchanged. It depicts the profiles of all three fractures. Note that fractures 1 and 2 are equal due to the symmetry of the settings. The behavior is, as expected, very similar to that of a single fracture discussed in the previous sections. Breakthrough is achieved after 57 ky.

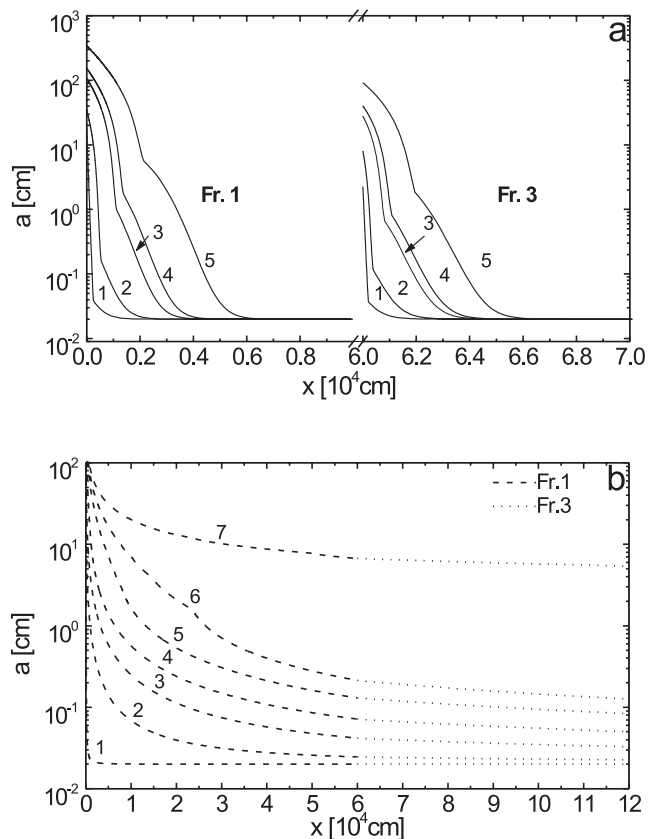


Figure 3.33: a) Profiles of the aperture widths of fractures 1 and 3 if only linear kinetics is operative. Profiles are recorded at 0.2, 2, 20, 40 and 400 ky, marked from 1-5 respectively. $K = 0.5$, $p_1 = 0.05$ atm, $p_2 = 0.003$ atm. Note the breaks in the x-axis. b) Same settings with $p_1 = p_2 = 0.05$ atm. No MC, but non-linear kinetics is active. Profiles at 0.1, 23.9, 48.6, 55.2, 56.9, 57.2 and 57.4 ky are marked by 1-7.

Nonlinear kinetics with MC

In the next step we combine MC ($p_1 = 0.05$ atm and $p_2 = 0.03$ atm) and non-linear dissolution rates. The aperture widths for the three fractures are shown by Figure 3.34a. Due to the larger p_1 and correspondingly larger c_{eq}^1 , the widths in fracture 1 increase faster than those in fracture 2. Thus the resistance of fracture 1 decreases more rapidly. Consequently the head at the confluence rises (see also Eq. 3.76) causing reduced flow rates in fracture 2 compared to those in fracture 1. Therefore dissolution rates at the exit of fracture 2 remain low, and the restriction of this fracture is maintained.

At the confluence MC boosts the dissolution rates. Breakthrough occurs at 17 ky, less than one third of the value without MC.

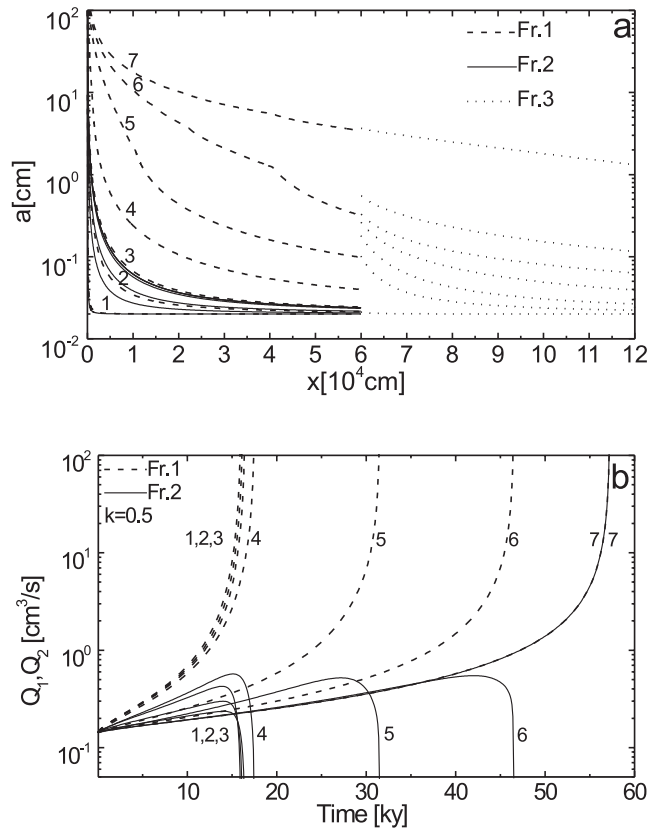


Figure 3.34: a) Profiles of aperture widths for $p_1 = 0.05$ atm and $p_2 = 0.03$ atm. Breakthrough occurs at 17.6 ky. Profiles are taken at: 0.1, 6.3, 11.3, 15.8, 17.2, 17.5 and 17.6 ky, marked by 1–7. b) Flow rates through fracture 1 (dotted lines) and fracture 2 (full lines) as a function of time for $p_1 = 0.05$ atm and $p_2 = 0.003, 0.01, 0.02, 0.03, 0.04, 0.045, 0.05$ atm, marked by 1–7.

To elucidate the processes underlying conduit genesis by the combined action of MC and nonlinear kinetics Figure 3.34b presents the flow rates Q_1 and Q_2 through the fractures 1 and 2 for $p_1 = 0.05$ atm and various values of p_2 in the range from 0.003 atm up to 0.05 atm. In all cases Q_1 shows a slow increase until it is drastically enhanced at breakthrough. Q_2 exhibits a different pattern. The flow rate increases initially, but the increase is suppressed by the rising head at the junction caused by the fast widening of fracture 1. Shortly before breakthrough the resistance of fracture 1 drops to such low values that the hydraulic head at the junction approaches the head at the entrance of fracture 1. Therefore the head difference and consequently the flow rate along fracture 2 decrease until they become zero. In the symmetric case, where $p_1 = p_2$, both fractures behave in the same way and both exhibit breakthrough (cf. curve 7).

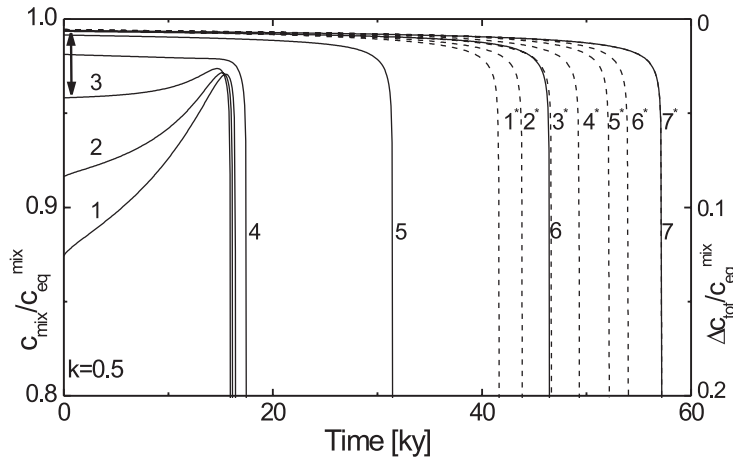


Figure 3.35: Evolution of c_{mix}/c_{eq}^{mix} in time for the same parameters as in Figure 3.34. Dashed lines 1*–7* depict the corresponding curves when MC is switched off numerically. See text.

In the case where $p_1 > p_2$, Q_1 increases more rapidly than Q_2 , therefore the effect of MC decreases until at breakthrough it is switched off completely. This is visualized by Figure 3.35, which shows the saturation ratio of the mixed solution c_{mix}/c_{eq}^{mix} at the confluence as a function of time. Values of p_2 are as in Figure 3.34. For curves 1–3 with $p_2 < 0.03$ atm this ratio increases in time until a drastic drop at breakthrough time is observed. It is interesting to note that for $p_2 < 0.03$ atm the values of T_B are almost equal. A second regime is exhibited for $p_2 > 0.03$ atm. In this region the ratio c_{mix}/c_{eq}^{mix} is only slightly dependent on p_2 and decreases slowly in time until it drops to zero at breakthrough. The value of T_B increases with p_2 . Curve 7 with $p_2 = 0.05$ atm presents the case without MC.

Chemical evolution of the solution in fractures

To obtain more insight into the mechanism of this behaviour, we discuss the chemical composition of the solution at the confluence. Figure 3.36 illustrates the pathways of the chemical evolution. Chemical pathways of the solutions in fractures 1 and 2 (closed system) are represented by the lines through AA_{eq} and BB_{eq} respectively.

The curve through M_0M depicts the evolution of the concentrations at the entrance of fracture 3. The fat line depicts the CO_2 - Ca^{2+} equilibrium. Points A , B and M characterize the concentrations of Ca^{2+} and CO_2 at arbitrary time t . A and B refer to the solutions at the exits of fractures 1 and 2. M refers to the mixed solution at the entrance of fracture 3. Point D gives the concentration of two fully saturated solutions A_{eq} and B_{eq} mixing at the exit of fractures 1 and 2. Point M_{eq} gives the equilibrium composition of the solution entering fracture 3. The subscript 0 indicates the composition at time zero.

The total undersaturation of the mixed solution with respect to Ca^{2+} is Δc_{tot} as shown in the figure. It consists of two contributions, Δc_{mix} and Δc_{eq} . Δc_{mix} results from mixing of the two undersaturated solutions (points A and B) in the diagram. It becomes zero if both solutions are saturated. Δc_{eq} gives the undersaturation by MC due to the curvature of the CO_2 - Ca^{2+} equilibrium curve. Δc_A and Δc_B are the saturation deficits of the solutions at the exit of fractures 1 and 2.

3. THE EVOLUTION OF A SINGLE FRACTURE

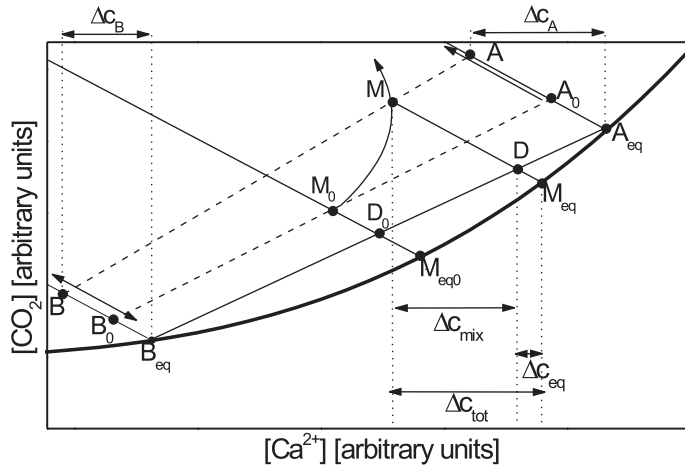


Figure 3.36: Chemical evolution of the solution at the exits of the fracture 1 (point A) and 2 (point B) and at the confluence (point M) after complete mixing. See text.

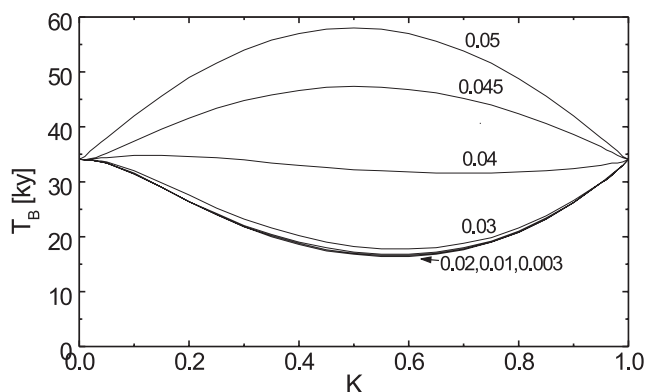
During the evolution of the fractures, Q_1 increases and therefore point A moves to lower calcium concentrations. As long as Q_2 increases B moves into the same direction, which is reversed as soon as Q_2 starts to decrease. As a consequence point M moves along the curve M_0M . As the ratio Q_1/Q_2 increases in time, point M_{eq} moves towards A_{eq} . Then Δc_{eq} approaches zero and MC is switched off.

From Figure 3.35 we can now read the value $\Delta c_{tot}/c_{eq}^{mix}$, where c_{eq}^{mix} refers to the saturation at point M_{eq} . This is indicated on the right vertical axis. Note that $c_{mix}/c_{eq}^{mix} = 1 - \Delta c_{tot}/c_{eq}^{mix}$. For curve 7, where $p_1 = p_2$, Δc_{eq} is zero during the entire evolution. Therefore $\Delta c_{tot} = \Delta c_{mix}$. At time zero Δc_{mix} of all other curves must be smaller, since Δc_B decreases with decreasing p_2 . Furthermore Δc_{mix} is continuously increasing in time. The difference between curves 1–6 to curve 7 represents the corresponding value Δc_{eq} for each of these curves in a reasonable approximation. This, as an example, is indicated by an arrow at curve 3. For curves 1–3, Δc_{eq} is initially much larger than Δc_{mix} . Due to the increasing ratio of Q_1/Q_2 during the evolution of the fracture, $\Delta c_{eq}/c_{eq}^{mix}$ decreases and consequently the curves rise. This is opposed by the increase in $\Delta c_{mix}/c_{eq}^{mix}$, which takes the value of 1 at breakthrough. Therefore a maximum occurs close to breakthrough. In curve 4 the rise in Δc_{mix} cancels the decay of Δc_{eq} , such that Δc_{tot} remains constant during most of the time until breakthrough. For curves 5 and 6 Δc_{eq} is much smaller than Δc_{mix} . Therefore Δc_{tot} increases in time.

To visualize the effect of Δc_{eq} on the breakthrough time we have also calculated the breakthrough behaviour, when MC is switched off, by fixing Δc_{eq} numerically to zero and retaining only Δc_{mix} as contribution to Δc_{tot} . The dashed lines in Figure 3.35, marked from 1* to 7* corresponding to lines 1–7 respectively, present the results. From these it can be seen that for curves 1–4 MC has a significant effect to the reduction of T_B . For curves 5 and 6, although $\Delta c_{eq} < \Delta c_{mix}$, the reduction in T_B is still remarkable. Curves 7 and 7* are identical since $\Delta c_{eq} = 0$ in any case.

3.5.3 The reduction of the breakthrough time due to the mixing corrosion

To answer the question, why does T_B stay constant for $p_2 < 0.03$ atm (see Figure 3.34b), we have calculated T_B as a function of K , denoting the position of confluence, whereby

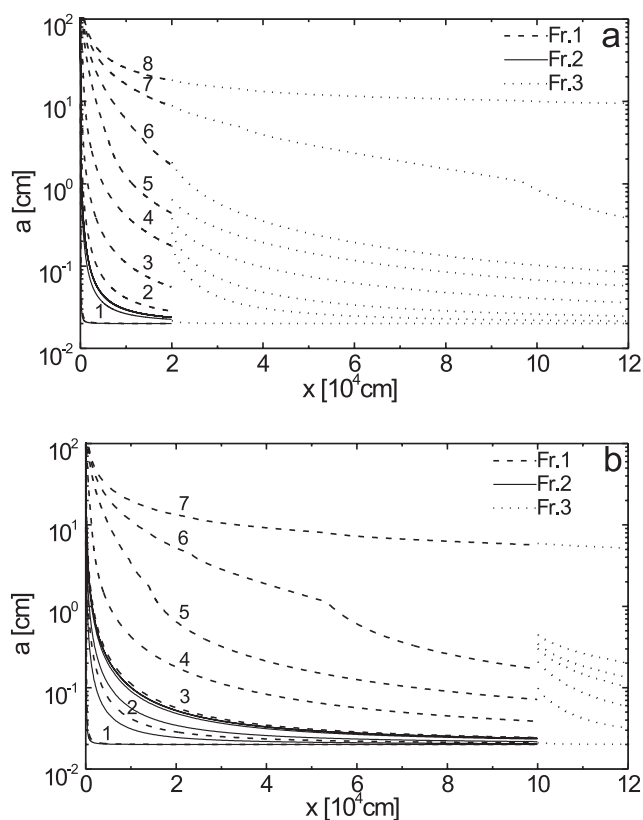


L has been kept to $1.2 \cdot 10^5$ cm.

Figure 3.37 shows the results for various values of p_2 . For $p_2 < 0.03$ atm the curves are crowded to a small region and ex-

Figure 3.37: Breakthrough time as a function of K . $p_1 = 0.05$ atm, the values of p_2 are denoted on the curves.

hibit a minimum close to $k \approx 0.5$. For $p_2 > 0.03$ atm, T_B increases and for $p_2 > 0.04$ atm a maximum arises. The upmost curve represents $T_B(K)$ for $p_2 = p_1$. We have also calculated T_B for $p_1 = 0.07$ atm, varying p_2 from 0.03 to 0.07 atm, and for $p_1 = 0.03$ atm with p_2 from 0.03 to 0.003 atm, and have found a similar behaviour (not shown here).



To elucidate the reason for the limit in the reduction of T_B , Figure 3.38a shows the evolution of the aperture widths in time for a junction with $K = 0.167$ for $p_1 = 0.05$ atm and $p_2 = 0.03$ atm. As can be easily visualized fracture 1 opens up quickly in time such that its flow resistance becomes small against that of fracture 3, which still retains

Figure 3.38: a) Profiles of aperture width for the junction with $K = 0.167$, $p_1 = 0.05$ atm and $p_2 = 0.03$ atm. Profiles are taken at 0.1, 9.6, 17.8, 25.7, 27.8, 28.2, 28.4 and 28.5 ky marked by 1-8, respectively. b) Parameters as in figure a, but $K = 0.833$. Profiles at 0.1, 6.6, 14.5, 20.8, 22, 22.2 and 23.3 ky marked by 1-7, respectively.

its bottleneck at the exit. Fracture 2 due to the lower p_{CO_2} also retains its high resistance. As a consequence the flow rates in this fracture drop quickly.

This is shown by the corresponding curves in Figure 3.39a, which illustrate the flow Q_1 and Q_2 as a function of time for various p_2 . After about 10 thousand years the ratio Q_1/Q_2 has dropped to about 0.1. Therefore at that time MC is switched off almost completely. Due to the decreasing value of Q_2 the dissolution rates in fracture 2 drop and its aperture widths remain restricted. Fracture 1, however, opens quickly. Therefore T_B is determined entirely by the evolution of fractures 1 and 3 which experience dissolution rates independent of p_2 during most of their evolution time. Consequently T_B becomes independent on p_2 .

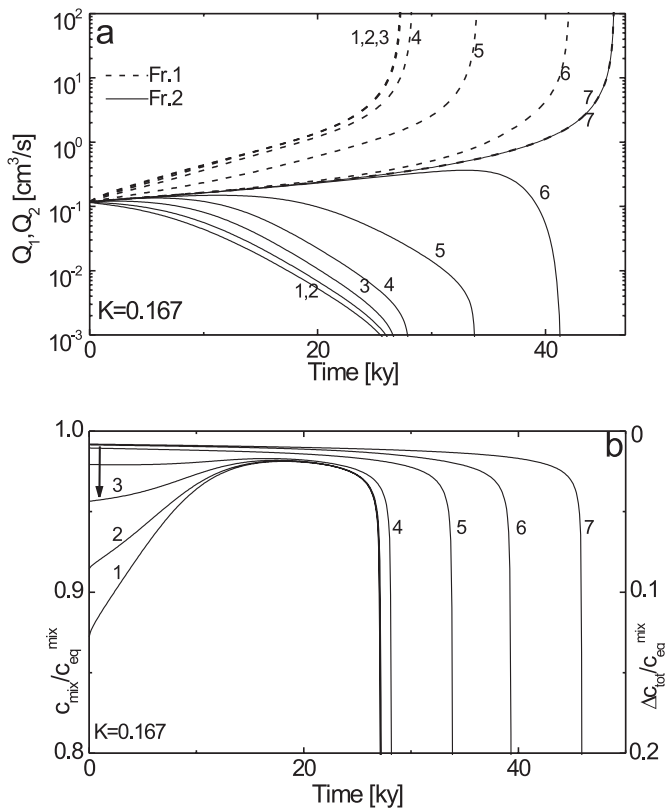


Figure 3.39: a) Flow rates Q_1 and Q_2 as a function of time for $p_1 = 0.05$ atm and various p_2 as in Figure 3.34. Other parameters are the same as in Figure 3.38. b) Evolution of c_{mix}/c_{eq}^{mix} as a function of time for the same setting as in a).

In contrast if p_2 approaches p_1 (i.e. $p_2 > 0.03$ atm) the effect of MC becomes small, since $\Delta c_{eq} < \Delta c_{mix}$. Furthermore fracture 2 opens up more quickly, such that the ratio Q_1/Q_2 drops less rapidly, until it remains constant when $p_1 = p_2$. Nevertheless, the increase of dissolution rates by the action of Δc_{eq} is sufficient to exert a significant influence to the T_B . Figure 3.39b shows c_{mix}/c_{eq}^{mix} as a function of time for the various p_2 . The curves for $p_2 \leq 0.03$ atm (curves 1–3) show a steep rise until MC is switched off and from then on a plateau until breakthrough occurs.

The behavior exhibited by Figure 3.37 for $K \leq 0.5$ is independent on p_j . Therefore the same behavior is expected, e.g. for $p_1 = 0.07$ atm and p_2 -values from 0.003 to 0.07 atm. As has been mentioned above this was verified by computer simulations. If K increases



3. THE EVOLUTION OF A SINGLE FRACTURE

the length of the restricted exit fracture 3 decreases, and as long as the entrance fracture 1 is sufficiently wide T_B decreases.

The situation becomes different for large values of $K > 0.5$. As an example Figure 3.38b illustrates the evolution of the aperture widths for $K = 0.833$ and other parameters as in Figure 3.38a. In contrast to what we have observed above, now fracture 3 opens first, and fractures 1 and 2 both remain restricted during almost the entire time until breakthrough.

As long as p_2 is sufficiently small, T_B is therefore determined by dissolution in fracture 1, independent of p_2 . For sufficiently large p_2 , however both Δc_{mix} and Δc_{eq} determine T_B which rise until $\Delta c_{eq} = 0$, i.e. $p_1 = p_2$. The behaviour of c_{mix}/c_{eq}^{mix} and Q_1 , Q_2 as functions of time resembles very much that with $k = 0.5$ as plotted in Figure 3.35 and Figure 3.39b and is therefore not shown.

The essential result of our model calculations so far is condensed in Figure 3.37. The upper curve depicts T_B with $p_1 = p_2$. Therefore MC is absent. $K = 0$ and $K = 1$ relate either a single fracture or two identical isolated fractures respectively. Therefore the T_B are equal for both K . For each value of $0 < K < 1$, T_B must be higher, because the initial flow rates through each of the entrance fractures are lower than that through the isolated fracture. Due to the higher concentration of Ca^{2+} at the confluence the dissolution rates are lower than in the isolated fractures. Only a slight reduction of p_2 to about 0.04 atm is sufficient to reduce T_B significantly. A limit of reduction is achieved for $p_2 = 0.03$ atm and further decrease of p_2 has no effect.

3.5.4 Asymmetric confluence

The symmetric arrangement depicted in Figure 3.31 is not very likely in a natural setting. First the heads at the entrances 1 and 2 can be different, and furthermore also the lengths and aperture widths of the fractures cause different flow resistances R_1 , R_2 and R_3 . The flow through the fracture 2 is given by

$$Q_2 = \frac{R_3(h_2 - h_1) + R_1 h_2}{R_1 R_2 + R_2 R_3 + R_1 R_3}. \quad 3.78$$

Q_1 is found by interchanging the subscripts 1 and 2. In the following we assume $h_1 > h_2$ and $p_1 > p_2$. Therefore Q_1 is positive, i.e. it is directed towards the confluence. For Q_2 three cases are possible as can be read from Eq. 3.78:

1. $Q_2 > 0$ when $\|h_2 - h_1\| R_3 < h_2 R_1$
2. $Q_2 = 0$ when $\|h_2 - h_1\| R_3 = h_2 R_1$
3. $Q_2 < 0$ when $\|h_2 - h_1\| R_3 > h_2 R_1$

These conditions are independent on the resistance R_2 . Now depending on the evolution of the aperture widths, the following scenarios arise:





3. THE EVOLUTION OF A SINGLE FRACTURE

- Initially condition 1 is valid and remains so until breakthrough. Then both flows are directed towards the confluence. At breakthrough the resistance of the winning path along fractures 1 and 3 drops close to zero ($R_1 \approx R_3 \approx 0$) and consequently the ratio Q_2/Q_1 becomes zero. MC is operative, until $Q_2/Q_1 > 0.1$.
- Initially condition 1 is valid. But as fractures 1 and 3 open up condition 3 is achieved. As soon as that happens Q_2 changes its flow direction. Then MC is no longer effective, and depending on the value of R_2 breakthrough occurs first via fracture 3 or fracture 2 solely by the action of nonlinear kinetics.
- Condition 3 holds at $t = 0$. Then MC is not active from the very beginning. Since under the action of nonlinear kinetics fracture 1 opens more quickly than fractures 2 and 3 condition 3 remains valid and breakthrough occurs either via fracture 2 or 3.

If three fractures with entrance heads h join to a confluence into fracture 4 with head $h = 0$ at its exit, similar situations arise. Q_1 is always positive, assuring $p_1 = \max(p_i)$. Depending on the initial values of the fracture resistances R_1, R_2, R_3, R_4 and their evolution in time Q_2 and Q_3 can take both flow directions, either towards the confluence or opposite. If Q_2 and Q_3 are positive, mixing of three solutions activates MC at the entrance of fracture 3. If $Q_2 > 0$ and $Q_3 < 0$ or vice versa two solutions mix and MC is active in fracture 4 and fractures 3 or 2, respectively. If both Q_2 and Q_3 are negative higher order kinetics determine exclusively the evolution of all aperture widths. Depending on the resistances, the p_{CO_2} , and the heads acting, breakthrough can occur along each combination of two of the four fractures. Thus, there is always a winning pathway which does not only depend on the geological setting (resistances and heads) but also on the chemical compositions of the inflowing solutions. All these possibilities exist in two-dimensional networks, which we present in Chapter 4.

3.5.5 Conclusion

Variations of p_{CO_2} in the soil of the catchment area, different pathways of solutions in the vadose zone, different soil structures etc. can cause different chemical compositions of solutions entering the closed system. When they mix, MC is activated. As shown, mixing corrosion can play an important role in the early karstification. A study on a simple junction presented here shows that already small variations in p_{CO_2} are sufficient to cause MC and to produce large reductions of breakthrough times of the evolving conduits. It was shown that the reduction of breakthrough time depends on the location of confluence and is largest at $K = 0.5$ (see Figure 3.37). The reduction also increases with decreasing p_2 and becomes constant for $p_2 < 0.5p_1$.

When discussing early karstification one also has to consider the geochemical settings such as distribution of CO_2 in the soil and the soil structure. Considering that inflowing solutions are not fully saturated MC is not a crucial factor for cave development though it plays an important role in the early stage of cave evolution.





3.6 EVOLUTION OF A SINGLE FRACTURE WITH CONSTANT RECHARGE ALONG THE FRACTURE

So far we have assumed a constant head driving the water through the fracture. In this section we discuss another important element of more complex settings, a fracture with a constant recharge. Our goal is to present some very basic results which are new with respect to what has been shown so far.

3.6.1 The model structure and numerical results

Figure 3.40 shows the concept: a constant recharge $dQ/dx = q[\text{cm}^2/\text{s}]$, with calcium concentration c_{in} is introduced along the fracture. At the entrance the fracture receives some initial flow Q_0 with concentration c_0 .

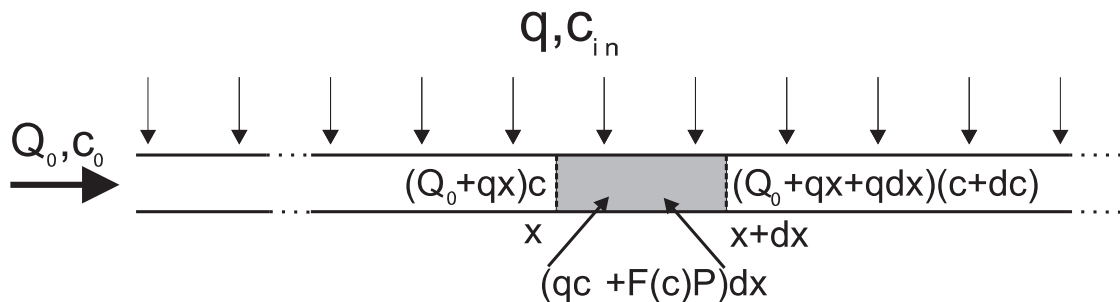


Figure 3.40: Basic parameters and mass conservation between x and $x+dx$ in a single fracture with a constant recharge along it.

To obtain numerical results we proceed as in the fracture with constant head conditions. But we use an adapted mass conservation equation. Instead of 3.7, the conservation of Ca^{2+} ions now demands:

$$(Q_0 + qx)c + F(c)Pdx + c_{in}qdx = (Q_0 + qx + qdx)(c + dc) \quad 3.79$$

The concentration c changes due to dissolution and to mixing with the inflowing water. Therefore, if $c(x)$ is the concentration at position x , $c(x + \Delta x) = c(x) + \Delta c$ is calculated by:

$$c(x + \Delta x) = c_{mix}(x) + \frac{F(c_{mix}(x))P(x)\Delta x}{qx + q\Delta x}, \quad \text{where} \quad 3.80$$

$$c_{mix}(x) = \frac{qxc(x) + q\Delta x c_{in}}{(x + \Delta x)q}$$

There is no breakthrough in this case, since the flow rate is constant in time. Termination of the calculation is thus “user-defined”.



Figure 3.41 shows the evolution of the aperture widths and concentrations along the fracture for various times. The full lines represent the case where only surface reactions control the rates as in the standard fracture. The dotted lines present the case where diffusion limited dissolution was also considered. The difference between both is significant only close to the entrance, where the rates are diffusion controlled.

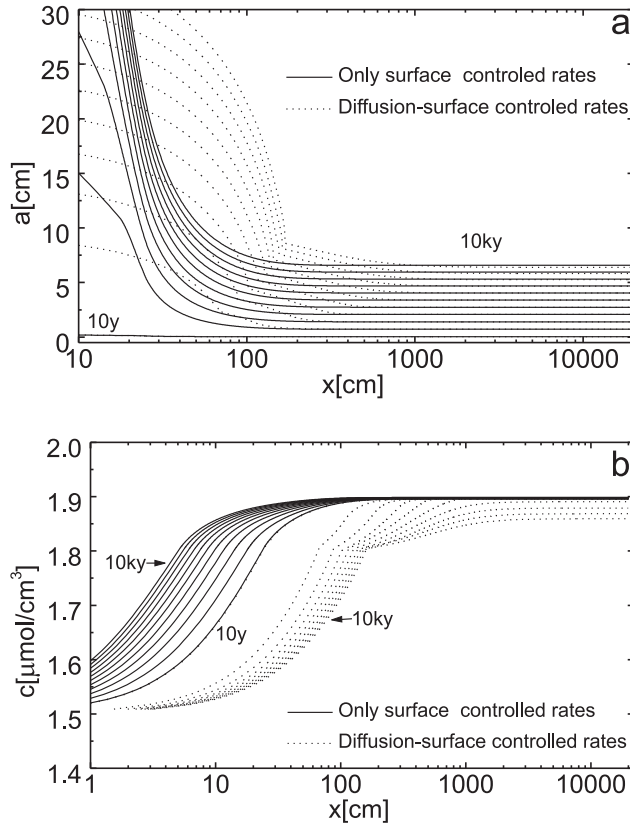


Figure 3.41: Profiles of aperture widths (a) and concentrations (b) for the fracture with constant recharge. $a_0 = 0.03$ cm, $b_0 = 100$ cm, $Q_0 = 0.1$ cm³/s, $q = 1.5 \times 10^{-4}$ cm²/s, $c_0 = c_{in} = 1.5$ $\mu\text{mol}/\text{cm}^3$. Profiles are taken in 1 ky intervals. Dotted lines show the case where surface-transport controlled dissolution is considered. Full lines show the results when only surface control is considered. Note the logarithmic scale in x .

From the model runs we observe the following:

- Provided that the fracture is wide i.e. $b \gg a$, it is widened uniformly in time and the rate of widening does not depend on its initial aperture width.
- The concentration initially exhibits a fast rise to above 99 % of its asymptotic value $c_{sat} < c_{eq}$. We define x_{sat} as the point in the fracture where $c = 0.99c_{sat}$.
- The aperture widths initially drop and then stay constant along the fracture for $x \geq x_{sat}$.
- c_{sat} and x_{sat} do not depend on the initial length and width of the fracture.
- There is no feedback mechanism since the hydraulic head is not constant, but is adapted to the offered recharge.

The evolution of the fracture with constant recharge is thus well described by c_{sat} and x_{sat} . Figure 3.42 shows the dependence of x_{sat} and c_{sat} on q for various c_{in} as denoted on the lines in $\mu\text{mol}/\text{cm}^3$. Since c_{sat} is the asymptotic value for $x \rightarrow \infty$, x_{sat} is taken at the

point where $c = 0.99c_{sat}$. Full lines present the case when only linear kinetics ($c_s = c_{eq}$) was assumed, dashed lines present the results when also nonlinear dissolution rates ($c_s = 0.9c_{eq}$, $n = 4$) are considered.

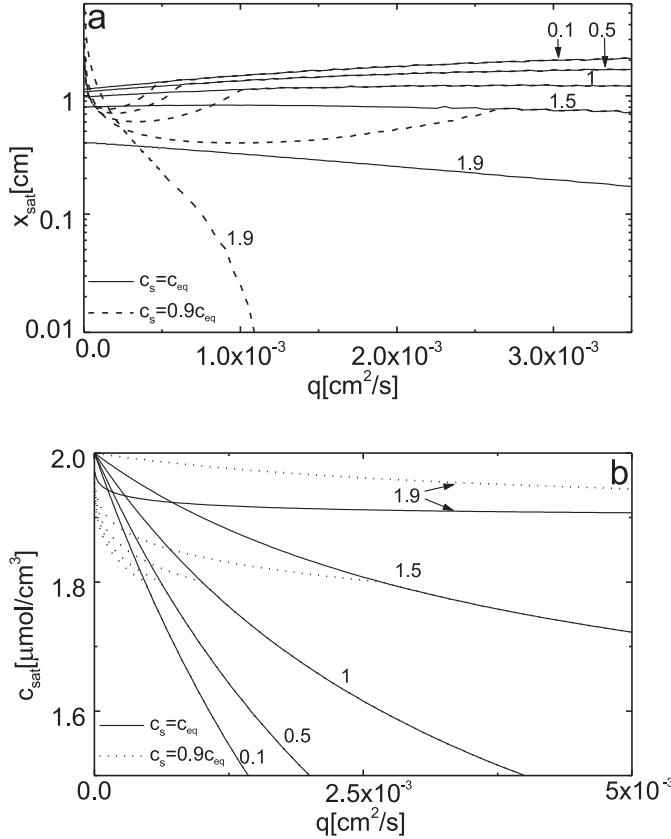


Figure 3.42: The dependence of x_{sat} (a) and c_{sat} (b) on q for various c_{in} (denoted on the lines in $\mu\text{mol}/\text{cm}^3$). In both cases $Q_0 = 10^{-3} \text{ cm}^3/\text{s}$. Other parameters are the same as in Figure 3.41.

3.6.2 Analytical approximations

To gain some more insight into the dependence of c_{sat} and x_{sat} presented in Figure 3.42, we try to get some analytical approximations. Multiplying the terms in Eq. 3.79 and neglecting the higher order differentials ($dxdc$) we get

$$\frac{dx}{Q_0 + qx} = \frac{dc}{q(c_{in} - c) + F(c)P} \tag{3.81}$$

For a wide fracture, where P can be regarded as a constant, the differential equation can be easily integrated for the case of linear kinetics, where $F(c) = \tilde{k}_1(c_{eq} - c)$ with $\tilde{k}_1 = k_1/c_{eq}$. In this case we obtain basic integrals for x and c . The result yields:

$$\left[1 + \frac{qx}{Q_0}\right]^{-(1+\tilde{k}_1P/q)} = \frac{qc_{in} + \tilde{k}_1Pc_{eq} - c(\tilde{k}_1P + q)}{qc_{in} + \tilde{k}_1Pc_{eq} - c_{in}(\tilde{k}_1P + q)} \tag{3.82}$$



3. THE EVOLUTION OF A SINGLE FRACTURE

Note that c_0 was taken equal to c_{in} . Some further algebraic “gymnastics” gives an explicit equation for $c(x)$:

$$c(x) = \frac{qc_{in} + \tilde{k}_1 P c_{eq}}{q + \tilde{k}_1 P} \left[1 - (1 + qx/Q_0)^{-(1+\tilde{k}_1 P/q)} \right] + c_{in} (1 + qx/Q_0)^{-(1+\tilde{k}_1 P/q)}. \quad 3.83$$

If $x \rightarrow \infty$ the term $(1 + qx/Q_0)^{-(1+\tilde{k}_1 P/q)}$ vanishes and an expression for c_{sat} is obtained:

$$c_{sat} = \frac{qc_{in} + \tilde{k}_1 P c_{eq}}{q + \tilde{k}_1 P}. \quad 3.84$$

From Eq. 3.83 we see that $c(x) = c_{sat}$ is constant along the fracture when $Q_0 = 0$.

The value of x_{sat} can then be determined according to some criterion which we choose, e.g. at $c_{crit} = 0.99c_{sat}$. From Eq. 3.82 we obtain:

$$x_{sat} = \frac{Q_0}{q} \left[\left(\frac{1 - c_{in}/c_{sat}}{1 - c_{crit}/c_{sat}} \right)^{\frac{q}{q+\tilde{k}_1 P}} - 1 \right]. \quad 3.85$$

Note that $x_{sat} \propto Q_0$.

Figure 3.42 presents the dependence of x_{sat} and c_{sat} on q for various values of c_{in} . Full lines show the case when only linear kinetics is assumed and represent directly the results from Eq. 3.85 and Eq. 3.84. Dashed lines show the dependence when the kinetics switches at $c_s = 0.9c_{eq}$ to non-linear with $n = 4$, $k_4 = 4 \cdot 10^{-8} \text{ mol cm}^{-2} \text{ s}^{-1}$.

Whenever $c_{in} < c_s$ the results with and without the switch of the kinetic order coincide when q becomes sufficiently large to keep the resulting concentration c_{sat} below c_s .

3.6.3 Fracture with a constant recharge and varying geochemical parameters

In the case of the fracture with constant head conditions we have discussed how variations of geochemical parameters, such as kinetic constants or CO_2 content influence the early evolution. Here we present a few results for the case when the kinetic parameters n and k_n change within the fracture (see Section 3.3) under conditions of constant recharge along the fracture.

As in the constant head conditions, the rates of widening are changed at the lithology boundary if the concentration c_{sat} is above c_s . If $c_{sat} < c_s$ only first order kinetic is active along the entire fracture.

If $c_{sat}^{(1)} > c_s$ then the ratio between the rates on the both sides of boundaries is equal to



$$\frac{F(KL)_{n_1}}{F(KL)_{n_2}} = \frac{k_{n_1}}{k_{n_2}} \left(1 - \frac{c_{sat}}{c_{eq}} \right)^{(n_1 - n_2)/(1 - n_1)} \quad 3.86$$

Figure 3.43a shows the profiles of aperture widths with input concentration $c_{in} = 1.8 \mu\text{mol}/\text{cm}^3$, other parameters are as in Figure 3.41. Dissolution rates and aperture widths at the boundary drop, but then they increase and approach an asymptotic value. The reason for this increase is that $c_{sat}^{(1)} > c_{sat}^{(2)}$, therefore the concentration of solution for $x > x_{sat}^{(2)}$ is lower than the concentration at the boundary. In Figure 3.43b the kinetic parameters change from $n = 8$ to $n = 4$. The aperture widths at the boundary are boosted up. Then they drop to asymptotic value, since the concentration beyond the lithology boundary increases and therefore the dissolution rates and aperture widths decrease.

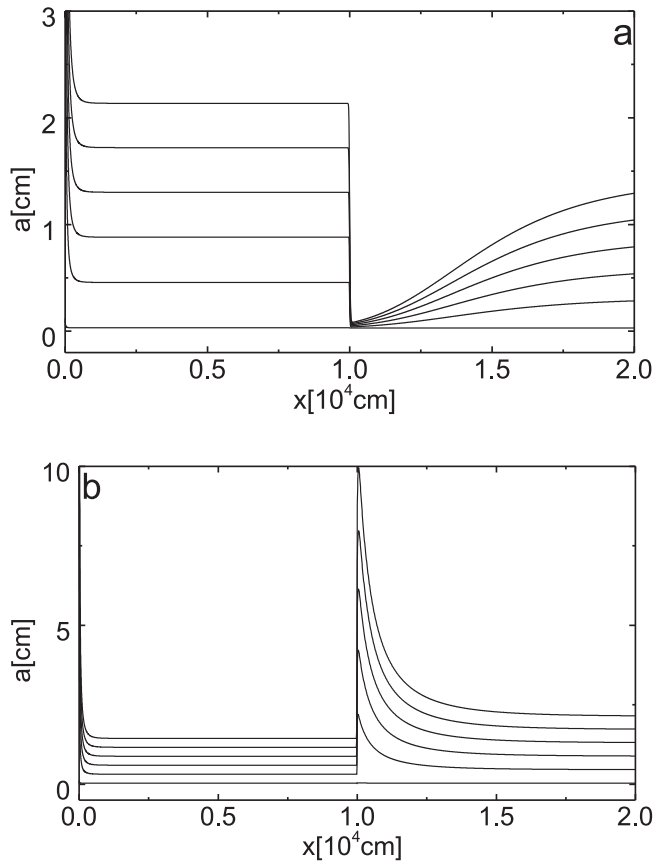


Figure 3.43: Evolution of aperture widths for the fracture with a constant recharge and a lithology boundary. **a)** $n_1 = 4, n_2 = 8, K = 0.5$. **b)** $n_1 = 8, n_2 = 4, K = 0.5$. The first profile is taken at 10 y, than every 2 ky starting at 2 ky. $Q_0 = 0.1 \text{ cm}^3/\text{s}$, $q = 0.0015 \text{ cm}^2/\text{s}$. Other parameters are the same as in Figure 3.41.

In both cases the fracture can be considered as two successive fractures with the initial flow and concentration $Q_0^{(1)}$ and $c_0^{(1)}$ for $x < KL$ and $Q_0^{(2)} = Q_0^{(1)} + qKL$, $c_0^{(2)} = c_{sat}^{(1)}$ for $x > KL$, provided that $KL > x_{sat}^{(1)}$.



3. THE EVOLUTION OF A SINGLE FRACTURE

3.6.4 Conclusion

The main result obtained in this section is a steady state behaviour. The concentrations along the fracture remain constant after some distance x_{sat} from the entrance. Beyond that point the entire fracture opens evenly and widens linearly in time. The concept of a fracture with the constant recharge will be met in Chapter 5 where we shall discuss the evolution in an unconfined aquifer.





4. MODELING KARST EVOLUTION ON TWO-DIMENSIONAL NETWORKS: CONSTANT HEAD BOUNDARY CONDITIONS

Understanding the evolution of single one-dimensional fractures into karst conduits under boundary conditions of constant head or constant recharge is a keystone to all more advanced modeling because it contains the basic concepts of the feedback mechanisms. However, real karst is three-dimensional, which adds extreme complexity. A first step to approach such a system is modeling in two dimensions in order to explore the processes, which occur in nets, but are absent in single conduits. A most simple two-dimensional model can be envisaged as a few 1-dimensional percolating pathways connecting inputs with some outputs of a modeling domain. If these flow pathways are only rarely connected or if in the extreme case they remain completely separated, the flow through the aquifer will exhibit breakthrough behavior of a 1-dimensional conduit. If, however, many interconnected percolating pathways exist, which can exchange flow the evolution of each is influenced by all other evolving conduits. Then we have a system of many interacting single conduits. This is a genuine property of two or three-dimensional models. As we will see in this chapter the basic breakthrough behavior is therefore affected in two-dimensional models.

Two-dimensional modeling allows incorporating local distributions of fracture positions and fracturing aperture widths in real karst. More generally, one could envisage a karst aquifer as a dual-fracture system, where the distribution of fracture aperture widths is bimodal. There are few prominent fractures with large aperture widths and spacing, which may give rise to percolating pathways from input points to discharge points. These fractures are embedded into a dense net of fine fissures with smaller spacing and statistically distributed lower aperture widths. In such aquifers water from prominent fractures can flow into the “continuum” of fine fractures and leave the aquifer through these. This attracts more flow of calcite aggressive water into the input points of the prominent fractures and enhances karstification by reducing breakthrough times. On the other hand, highly saturated water from the fine net of fissures can enter into prominent fractures and reduce dissolution there to such an extent that breakthrough times are enlarged. Mixing corrosion can also become active, when the chemical compositions of inflowing waters differ at different input points. By this way complex evolution patterns result, which are not easy to be predicted.

If one wishes to extract the processes operative in karst from models it is advisable to do the modeling in steps by investigating each mechanism alone and then combine them in the next step.





In this chapter we start with the evolution of percolating networks of fractures as one extreme. Then we deal with dense fracture systems with statistically distributed aperture widths as the other extreme. Finally, we will combine these two different approaches into a dual-fracture model, as a closer approach to reality. To all these three modeling approaches chemical boundary conditions activating mixing corrosion are added, and their influence to the evolution is elucidated.

4.1 MODELING DOMAIN

Two-dimensional modeling can describe karst aquifers only as transects in width and length or in length and depth. In Chapter 4 we deal with a layer of limestone dipping down at some inclination angle. The modeling domain is the plane of this layer, into which the fractures are embedded. In the simplest case, this is regarded as an aquifer confined by impermeable layers below and above the limestone. Recharge to this aquifer is supplied by flow through input points with constant head boundary conditions (or constant recharge, if the head no longer can support the flow). The aquifer discharges through output points at low head, e.g. $h = 0$. Such a geological situation is shown in Figure 4.13, where the upper confining layer is not drawn for better visualization. More details of such conceptual models can be found in the book of Ford and Williams (1989).

There is discussion whether such domains are a sufficiently accurate representation of nature, because they are constructed quite artificially. However, due to the lack of 3-D models at present one has to accept them as one way to model karstification. As we will see in chapter 6 they are well suited to describe karstification below dam sites.

The other alternative is to deal with vertical transects in length and depth, implying unconfined aquifers with a water table. These aquifers contain many properties as these presented in Chapter 4. They will be discussed in Chapter 5.

To visualize the results on the evolution of karst aquifers we have used various codes in the following chapter. These are summarized in the box below as a help to read the figures.

Code box: An assistance to read the figures: bar codes and color codes

To visualize the evolution of karst aquifers in chapters 4–6, we have used bar codes to depict fracture widths and flow rates. In addition, a continuous color code from red-blue-black shows dissolution rates. Flow directions are shown by 4 colors (red = to the right, yellow = to the left, green = down, blue = up).

Usually one set of figures depicts fracture aperture widths by bar code and dissolution rates by a continuous color code. The second set gives flow rates by bar code and flow directions by color code correspondingly.

1. Bar code for fracture aperture widths

All fractures with aperture widths less than $1.01\bar{a}_0$ are not shown. For statistical nets



this means that about half of the fractures are omitted. For uniform nets this implies that only fractures, which have been widened by more than 1 % are shown. Therefore, white regions in figures visualizing aperture widths are locations, where dissolutional widening has not yet been active. The bar code representing aperture widths is shown below. The smallest aperture width is for $1.01\bar{a}_0 < a < 2\bar{a}_0$, the width is doubled for values of aperture widths $2\bar{a}_0 < a < 4\bar{a}_0$, and so on. The widest code is for fractures $a > 512\bar{a}_0$.

a/a_0 <4 <8 <16 <32 <64 <128 <256 <512 >512

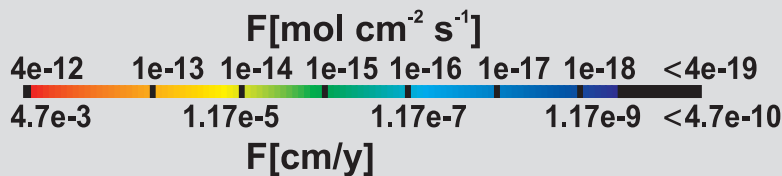
2. Bar code for flow rates:

Since flow rates in the net increase in time a common bar code for all figures cannot be given. Therefore, to display flow rates the bar code gives values of Q/Q_{max} , where Q is the current flow in the selected fracture and Q_{max} the maximal flow at that time occurring in some fracture of the net. All flow rates $Q \leq 10^{-3}Q_{max}$ are omitted for better overview. Therefore, white depicts regions of little flow. The bar code proceeds linearly in the following steps of the normalized values of Q/Q_{max} . The smallest width is for $0.001 < Q/Q_{max} < 0.025$, then second largest width from $0.025 < Q/Q_{max} < 0.05$ continuing with $0.05 < Q/Q_{max} < 0.075$ and $0.075 < Q/Q_{max} < 0.1$. All flow rates $Q/Q_{max} > 0.1$ are designated to the maximum bar width.

Q/Q_{max} >0.001 >0.0025 >0.005 >0.075 >0.1

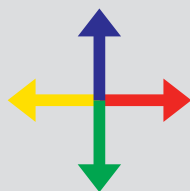
3. Color codes for dissolution rates

Dissolution rates are depicted by a continuous color code. The highest dissolution rate F_{max} is displayed by dark red and the lowest by dark blue $10^{-4}F_{max}$ (Note: F_{max} corresponds to a retreat of bedrock by $5 \cdot 10^{-3}$ cm/year). Black denotes flow rates $F < 10^{-5}F_{max}$. This means that in black regions dissolutional widening is practically zero. These regions are mostly identical to the white regions, where flow rates are practically zero.



4. Color code for flow directions.

This code depicts the flow direction in a fracture and is used to visualize the flow field. It is especially appropriate to present the interaction of flow in the net of fine fissures and that in the prominent fractures of dual-fracture networks. Therefore, it is a good tool to interpret the action of mixing corrosion.



5. Color code for Ca-equilibrium concentrations

In the case of mixing corrosion two types of waters, one with calcium equilibrium concentration c_{eq}^{max} and the other with $c_{eq}^{min} < c_{eq}^{max}$, mix and consequently the equilibrium concentration of the mixed solution is in between these values. This is depicted by a color code with red for the highest concentration c_{eq}^{max} , decreasing down through the optical spectrum to dark blue for concentration c_{eq}^{min} .



6. Isolines of head

In some of the figures we have also included lines of equal head to show changes in the head distribution during aquifer evolution. Flow directions can also be inferred from these isolines, since they are roughly perpendicular to them.

7. Organization of Figures

In all figures showing the evolution of aperture widths and dissolution rates, and also flow rates and flow directions, the left hand side column depicts aperture widths and dissolution rates. The right hand side column shows normalized flow rates Q/Q_{max} and directions of flow. In all cases where other codes are used, these are given in the figures.

4.2 PERCOLATION NETWORKS

In the following, we will use percolation networks of fractures. They are superior to regular rectangular (“brick”) networks as used in the first 2-D-models (Groves and Howard, 1994, Howard and Groves, 1995), because they reflect statistical properties of the spatial distribution of fractures. Figure 4.1 shows a bond percolation network, which is generated in the following way. One starts with a square or rectangular array of points. The nearest neighbor points are then connected by lines (dotted). By this way a network of squares or rectangles is obtained. Next, one assigns a fracture with equal probability p to each of the dotted lines. This way one obtains in a $n \times n$ square net a system of $2pn(n-2)$ fractures, distributed spatially in the net. Some of them are incorporated in a backbone (fat lines), providing a system of fractures that can carry flow from an input to an output point. Other fractures (thin lines) are fractures, which end inside the square net and are not connected to an output. Therefore, they cannot carry flow.



4. MODELING KARST EVOLUTION ON TWO-DIMENSIONAL NETWORKS: CONSTANT HEAD BOUNDARY CONDITION

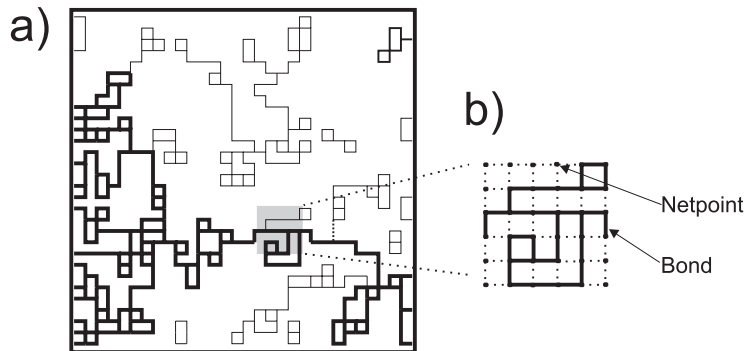


Figure 4.1: An example of a percolation net with $p = 0.5$ **a)** Thick lines denote the percolation backbone. Non-percolating clusters or dead ends of the percolation backbone are presented by thin lines. **b)** Excerpt from the net with net points and bonds. Occupied and non-occupied bonds are marked by full and dotted lines, respectively.

Fractures generated by this way form clusters of various sizes, depending on p . For each lattice type (e.g. triangular, square, honeycomb (see Stauffer and Aharony (1992) or Lee and Farmer (1993) for details) a critical occupation probability P_c exists, where infinite clusters start to form. For the square lattice presented in Figure 4.1 we have used bond percolation with $P_c = 0.5$. Therefore, taking a square net with $p \geq 0.5$ a cluster of fractures is generated that connects the sides of the net and can transmit water.

All generated fractures can be classified into two classes:

1. **Percolating fractures** are connected to the entrance and to the exit of the network by uninterrupted and self-avoiding pathways. They are grouped into the cluster, connecting the left and right boundary of the network and thus they are able to carry flow. They are represented by the thick lines in Figure 4.1.
2. **Non-percolating fractures** do not carry flow within the network. They are either parts of isolated clusters or dead ends. These are depicted by the thin lines in Figure 4.1. Isolated fractures with no connection to any other fracture and dead ends, which have only one connection point, are excluded from the figure. During the process of network generation all non-percolating fractures are omitted by an iterative procedure.

Figure 4.2 shows a typical modeling domain. It represents a percolation backbone with $p = 0.8$, where all fractures which cannot carry flow have been omitted. The upper and lower boundaries are impermeable. The left hand side boundary is at constant head h_{in} , whereas the right hand side boundary contains several discharge points at a constant head $h_{out} = 0$. There are several input points at various heads, which may differ with respect to the chemical composition (p_{CO_2} , Ca^{2+}) of the inflowing water. The aperture widths of the fractures can have any kind of distribution, but in the following we have chosen equal aperture widths A_0 everywhere in the domain.



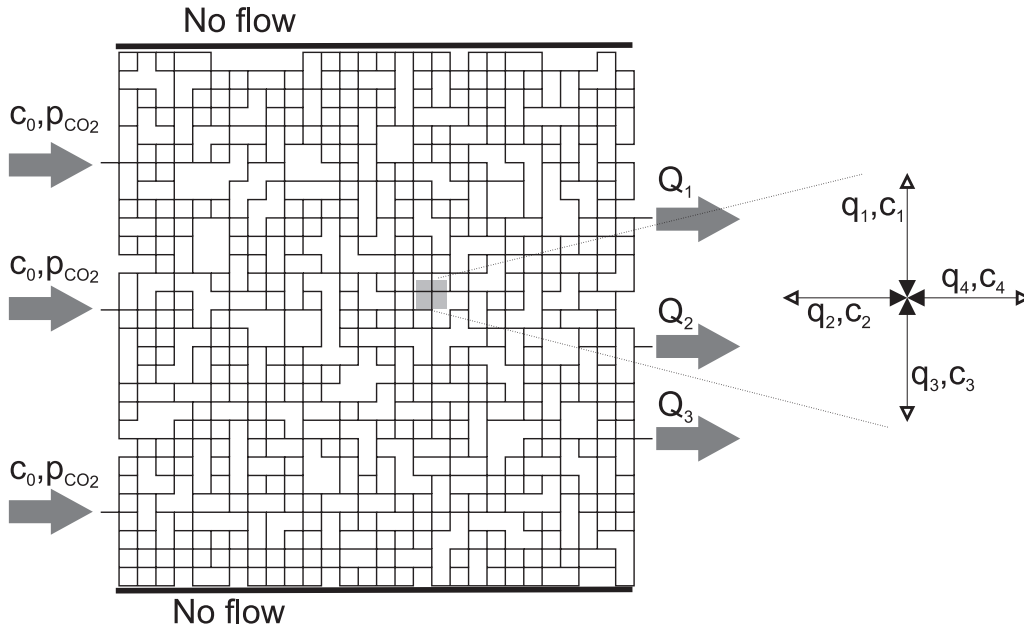


Figure 4.2: Percolation net ($p = 0.8$) with imposed boundary conditions. Inputs are on the left-hand side and outputs on the right-hand side of the net. Upper and lower boundaries are impermeable. Excerpt on the right hand side presents a junction of four fractures; mass conservation is valid for flow and ionic species at all junctions.

4.2.1 Calculation of network evolution

To calculate the widening of each fracture in a network, the flow rate and the concentration of the solution entering must be known as discussed in Section 3.1. Flow through a fracture connecting two next neighbor node points i and j is given by

$$Q_{ij} = \frac{h_i - h_j}{R_{ij}}, \tag{4.1}$$

R_{ij} is the resistance of the fracture, h_i and h_j are the heads at nodes i and j . The calculation of the heads is based on mass conservation for each node point.

$$\sum Q_{in}(i) - \sum Q_{out}(i) = \sum_j Q_{ij} = 0, \tag{4.2}$$

where $Q_{in}(i)$ is the flow rate towards node i and $Q_{out}(i)$ the flow rate away from it. Q_{ij} is the flow rate through the fracture connecting nodes i and j . Eqs. 4.1 and 4.2 give a set of linear equations for the unknown heads in the case of laminar flow. When flow becomes turbulent, the Darcy-Weissbach equation (see Eqns 3.5 and 3.6) has to be used and the set of equations becomes non-linear. Calculation of flow rates is initiated by assuming laminar flow everywhere. The resulting system of linear equations is solved by the Preconditioned Conjugate Gradients method for sparse matrices (Press *et al.*, 2002;



Stewart and Leyk, 1994). Then for each fracture the Reynold's number Re_{ij} is checked. Turbulence is assumed when $Re_{ij} \geq 3000$. As turbulence is detected the system of equations becomes non-linear and is solved by Newton-Raphson-iteration. Once flow rates are known, dissolutional widening is calculated by the following procedure:

1. Apply the one-dimensional dissolution-transport model to all fractures at the input points in the modeling domain. Calculate the new profiles of these fractures for the time Δt .
2. Select the nodes where the concentration of the inflowing solution is known and apply the transport-dissolution model to the fractures draining water from them.
3. Calculate the new profiles for these fractures and the concentrations at their exits. In all presented model runs complete mixing is assumed. The concentration of the solution at node i is then given by

$$c_i = \frac{\sum_j Q_j c_j^{out}}{\sum_j Q_j} \quad 4.3$$

Q_j is the flow rate in a fracture carrying water to node i and c_j^{out} the concentration at its exit.

4. Repeat steps 2 and 3 until new profiles for all conduits have been obtained.
5. Calculate the new head distribution according to the new fracture resistances for the next time steps. Laminar flow is assured through calculation of the Reynolds number for each fracture at each time step ($Re_{ij} \leq 3000$).
6. Repeat steps 1–4 or end the procedure at a user defined condition, e.g. onset of turbulent flow or a prescribed flow rate.

4.2.2 Results for the standard percolation network

In the following various aspects of the evolution of a percolation network shown by Figure 4.2 will be discussed.

The modeling domain is 900 m by 900 m with a grid size of 30 m x 30 m. The occupation probability p is 0.8. The net has three inputs and three outputs marked by A , B and C and A^* , B^* , C^* in Figures 4.3a to 4.7a. The inflowing solutions have the same chemical compositions at all inputs. Flow can leave the net only through output points A^* , B^* , and C^* . The aquifer is confined. It could be viewed as a limestone bed 1 m deep, confined by 2 layers of impermeable rock above and below the bed. The head at the left hand side boundary at entrance points A , B , C is 50 m and zero at output points A^* , B^* , C^* . The upper and lower boundaries marked by no flow in the figure are impermeable. Other parameters are given in the figure caption. We refer to this scenario as standard later on. The input concentration of calcium is $c_{in} = 0$ and $p_{CO_2} = 0.05$ atm. All parameters are listed in Table 4.1.



4. MODELING KARST EVOLUTION ON TWO-DIMENSIONAL NETWORKS: CONSTANT HEAD BOUNDARY CONDITION

Name	Symbol	Units	Typical or initial value
Aperture width	A_0	cm	0.03
Breadth	b	cm	100
Length of individual fracture	l	m	30
Head difference	h	m	50
Second kinetic order	n_2		4
Initial p_{CO_2}	p_{CO_2}	atm	0.05
Domain size		m ²	900 × 900
Initial concentration	c_{in}	c_{in}/c_{eq}	0
Bond occupation probability	p		0.8

Table 4.1: Typical values of parameters used in the calculations of percolation networks

Figure 4.3 to Figure 4.6 show the evolution of the aquifer. Figure 4.3 shows aperture widths in units of the initial aperture width A_0 . Figure 4.4 shows flow rates in units of the maximal flow rate Q_{max} . Note that Q_{max} increases in time. Therefore, same line thickness represent different absolute values at different times. Figure 4.5 shows the distribution of the dissolution rates in units of $F_{max} = 4 \cdot 10^{-12} \text{ mol cm}^{-2}\text{s}^{-1}$. Figure 4.6 shows the contour map of the head distribution together with the fracture widths of Figure 4.3. The figures present four snapshots of the net at different times: 1 ky, 3 ky, 5 ky and breakthrough at 5.81 ky. The situation at 1ky is presented in Figure 4.3a–4.6a. The fractures close to the inputs A, B and C are in the region of high dissolution rates and have therefore been widened considerably. The distribution of flow rates is relatively uniform, except in the vicinity of inputs. Dissolution rates drop continuously from the left to the right hand side. Opening of the fractures close to the inputs has caused the penetration of high hydraulic heads ($h > 0.999h_{in}$) into the net. The distribution of hydraulic heads is uniform, except close to the inputs and outputs.

After 3ky (Figures 4.3b–4.6b), the pathways marked by 1, 2 and 3 on Figure 4.3b have progressed deeper into the network. In this region flow and high dissolution rates are already focused to the fractures comprising these pathways. Flow from the tips of these conduits is dispersed into the net and therefore total flow through the corresponding input is higher, as it would be in the case of an isolated 1-D input of the same length. Therefore the calcium concentration in the net's conduits is lower and dissolution is enhanced. As we will see later, depending on the properties of the net, this can play an important role in the evolution of two-dimensional aquifers. More to the right, where conduits have not yet evolved, the distribution of flow rates is still fairly uniform, but the dissolution rates have increased. The regions of high hydraulic heads (shown by the isolines of head) have penetrated deeper towards the exit, causing high gradients close to the output.

Close to breakthrough at 5 ky (Figures 4.3c–4.6c) pathway 1 starting at input A almost reaches the output A*. Dissolution rates and flow rates are high along this pathway.

4. MODELING KARST EVOLUTION ON TWO-DIMENSIONAL NETWORKS: CONSTANT HEAD BOUNDARY CONDITION

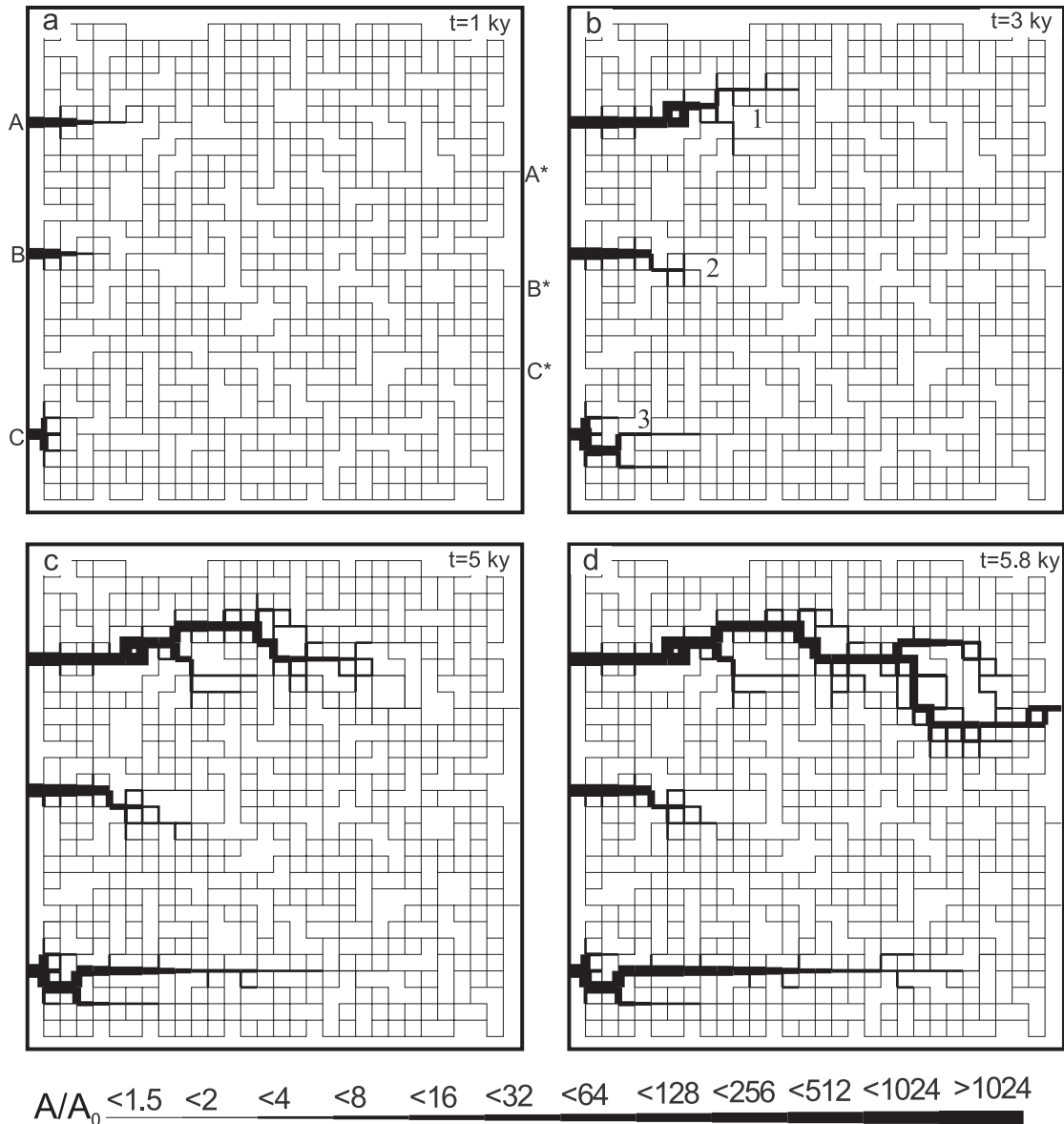


Figure 4.3: Aperture widths of fractures in the standard percolation network in units of A_0 at different stages of its evolution. Times in ky are denoted at the figures. Size of the net: $900 \text{ m} \times 900 \text{ m}$, grid size: 30 m by 30 m , $p = 0.8$, $A_0 = 0.03 \text{ cm}$, $b_0 = 1 \text{ m}$, $\Delta h = 50 \text{ m}$, $c_0 = 0$, $c_{eq} = 2 \text{ } \mu\text{mol/cm}^3$, $k_l = 4 \cdot 10^{-11} \text{ mol/cm}^2\text{s}$, $n = 4$, $k_d = 4 \cdot 10^{-8} \text{ mol/cm}^2\text{s}$. $c_{in} = 0$ and $p_{CO_2} = 0.05 \text{ atm}$ at all inputs. Inputs and outputs are denoted on figure a by A, B, C and A*, B*, C*, respectively. Numbers 1, 2 and 3 at figure b mark three evolving pathways.

Pathway 3 connecting C and C* is less favorable, but has also evolved considerably. The loser of the race to breakthrough is pathway 2, connecting B and B*. The region of high hydraulic heads caused by an efficient widening of pathways 1 and 3 extends almost to the outputs preventing flow along the less developed pathway 2 (BB*).

4. MODELING KARST EVOLUTION ON TWO-DIMENSIONAL NETWORKS: CONSTANT HEAD BOUNDARY CONDITION

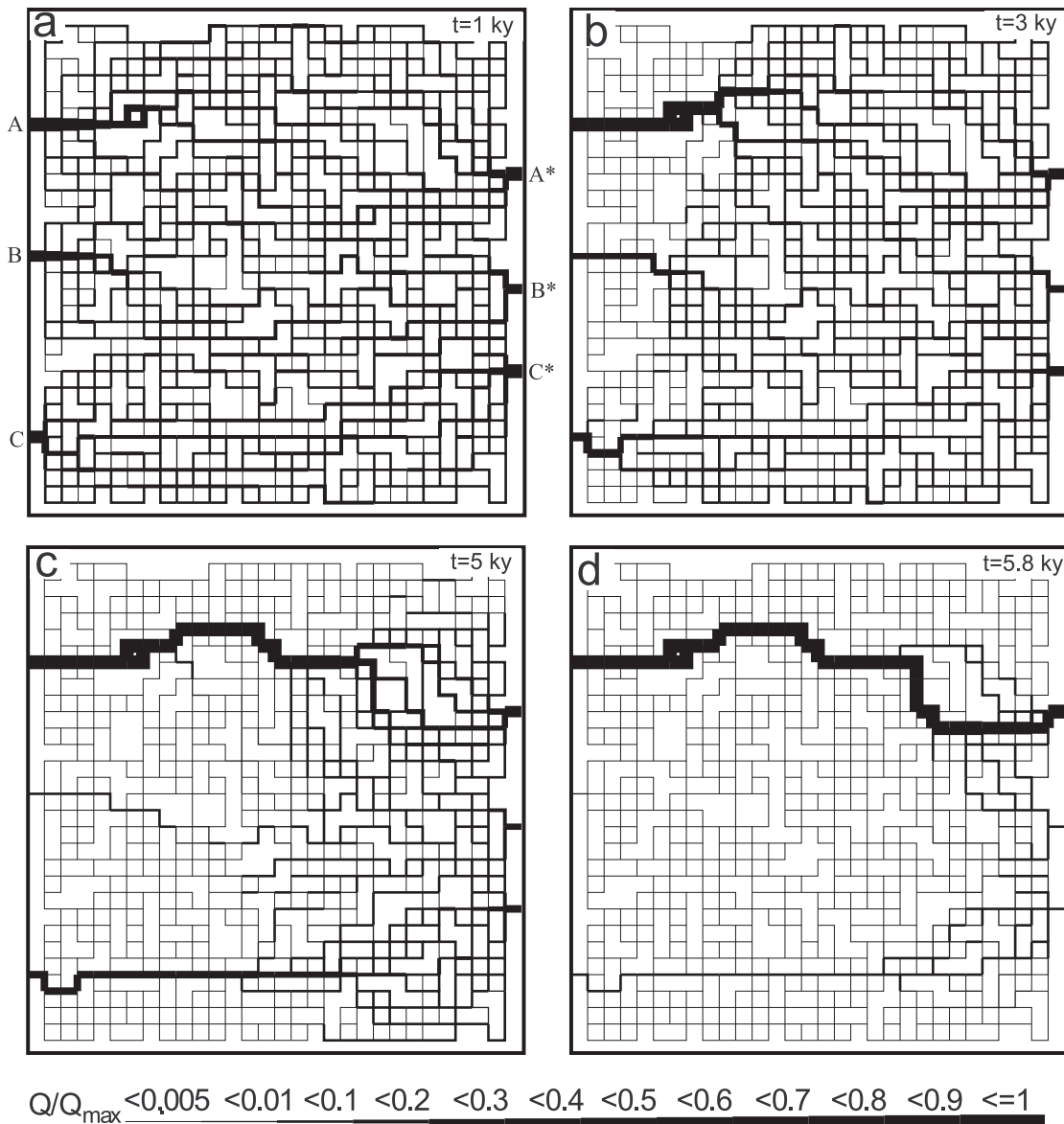


Figure 4.4: Standard percolation network: Evolution of flow rates. Line thickness represents the magnitude of flow rates in units Q/Q_{max} , in which Q_{max} is equal to the flow through the fracture with the highest flow rate. **a)** $Q_{max} = 5.36 \text{ cm}^3/\text{s}$, **b)** $Q_{max} = 10.12 \text{ cm}^3/\text{s}$, **c)** $Q_{max} = 30 \text{ cm}^3/\text{s}$, **d)** $Q_{max} = 172 \text{ cm}^3/\text{s}$.

The breakthrough situation at 5.81 ky is shown by Figures 4.3d–4.6d. At 5.81 ky breakthrough occurs along pathway 1, which carries most of the flow. Pathway 3 has also evolved close to breakthrough, while pathway 2 has not evolved any further. High dissolution rates act along both evolved pathways. Note that some flow with high dissolution rates also leads from pathways 1 and 3 to output B*. Consequently, close to output A* a set of conduits is evolving in the direction towards output B*. The breakthrough of pathway 1 ends our simulation with the onset of turbulence.



4. MODELING KARST EVOLUTION ON TWO-DIMENSIONAL NETWORKS: CONSTANT HEAD BOUNDARY CONDITION

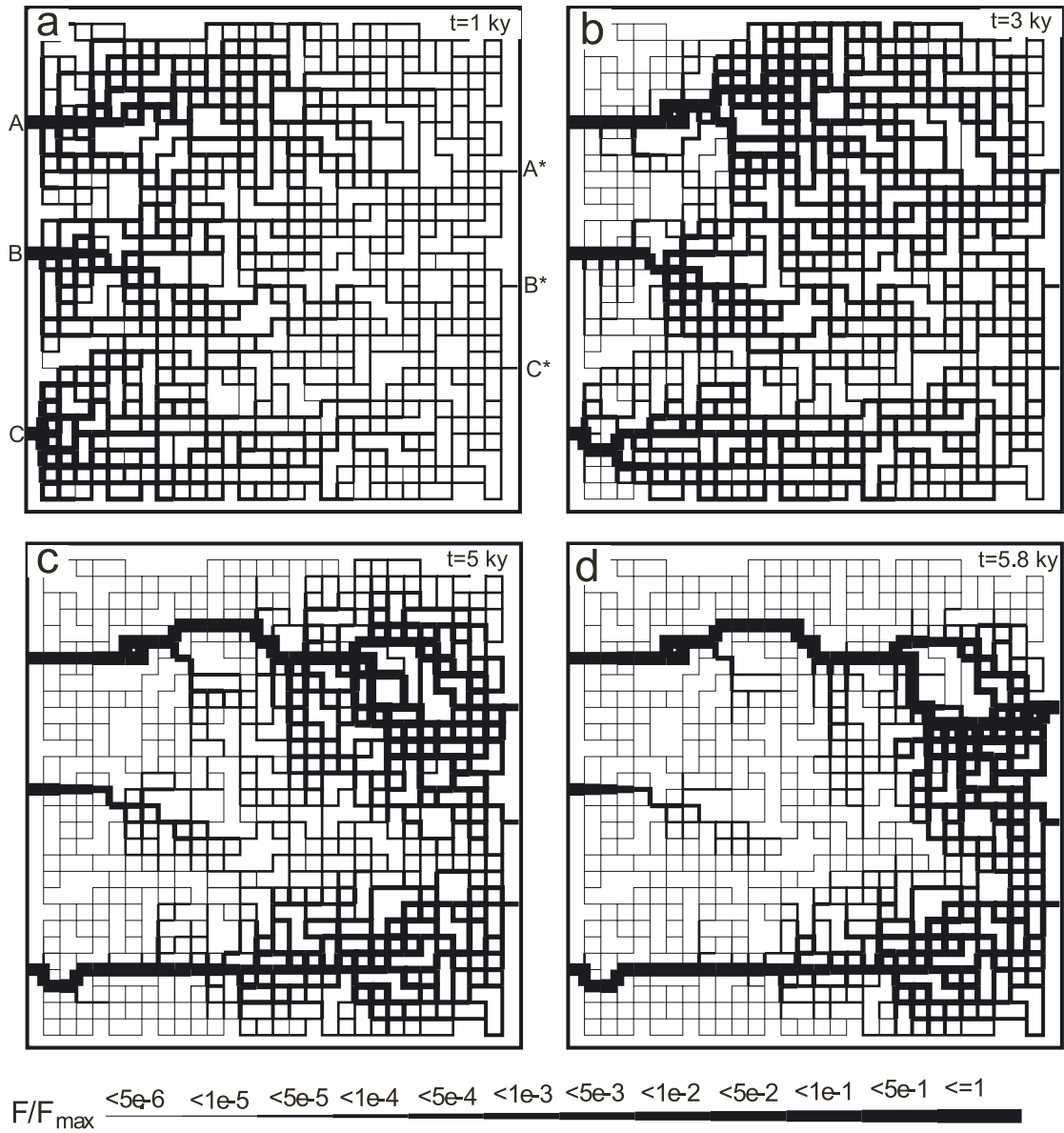


Figure 4.5: Standard percolation network: Evolution of dissolution rates. Line thickness represents dissolution rates in units of F/F_{max} , in which $F_{max} = 4 \cdot 10^{-12}$ mol/cm²s.



4. MODELING KARST EVOLUTION ON TWO-DIMENSIONAL NETWORKS: CONSTANT HEAD BOUNDARY CONDITION

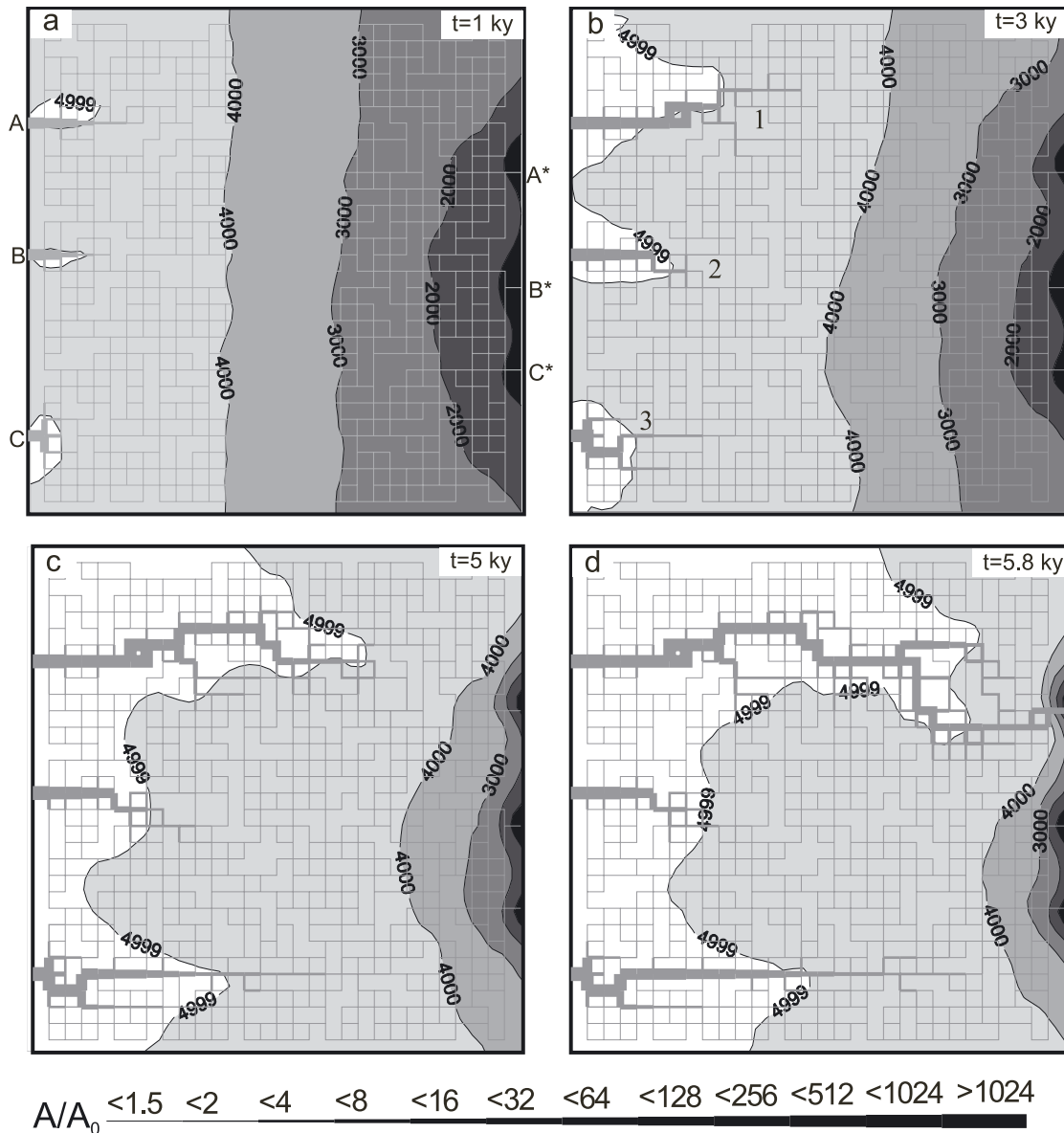


Figure 4.6: Standard percolation network: Evolution of aperture widths and distribution of hydraulic heads. Values of heads are given in centimeters on the isolines.

Figure 4.7 shows the flow rates through each input and output as they evolve in time. Flow through inputs A and C increases continuously until breakthrough. Flow through input B initially increases, but starts to decrease after 2 ky due to the redistribution of hydraulic heads caused by the efficient widening of pathways 1 (AA*) and 3 (CC*). Note that output B* attracts also water from inputs A and B. The flow through input points A and B clearly shows breakthrough behavior as found in 1-D modeling discussed in Chapter 3.

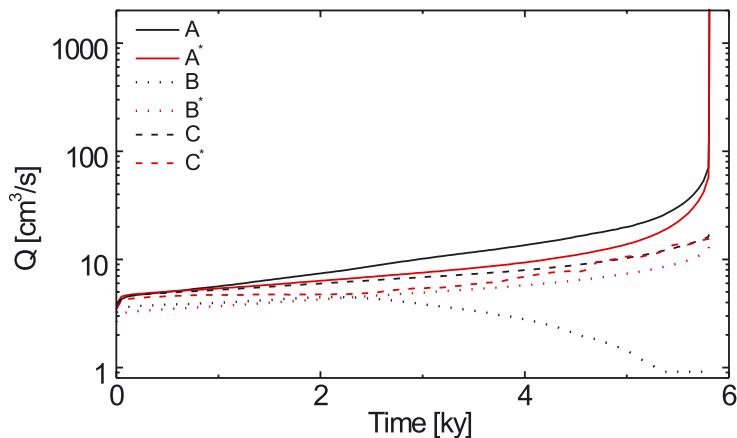


Figure 4.7: Evolution of flow rates through inputs and outputs of the standard percolation net presented in Figures 4.3–4.6. Flow rates at inputs are in black color, flow rates at outputs in red. Different line types denote different inputs and outputs, as shown in the legend.

4.3 EVOLUTION OF 2-D PERCOLATION NETWORKS AND BREAKTHROUGH

These results suggest that the dependence of breakthrough times on the parameters A_0 , L , h , c_{in} , c_{eq} , and k_n of percolation nets might be similar to that of one-dimensional conduits. But one also has to consider that a new parameter has been introduced, the occupation probability p . Siemers and Dreybrodt (1998) have studied the dependence of breakthrough times on this parameter.

Figure 4.8 shows realizations of four percolation networks with $p = 0.5, 0.6, 0.8,$ and 0.9 , respectively and their fracture aperture widths at breakthrough. The parameters are given in the figure caption. Only fractures, which carry flow are shown. At low p (Figure 4.8a) long percolation pathways occur and the evolution follows meandering pathways. As p increases the percolating passages are less distorted and become practically straight at $p = 0.9$. Due to the decreasing effective lengths of the percolating pathways, breakthrough times are long for low and become shorter for high values of p .

For $p = 1$ the net is fully filled with fractures of equal aperture widths. In this case, due to the imposed boundary conditions, flow follows straight pathways parallel to the upper and lower boundaries. There is no vertical flow between these pathways. Therefore, each of them behaves like an ideal isolated one-dimensional fracture and all of them reach breakthrough simultaneously. Since the length of this pathway is shorter or equal to any other percolating pathway in the net, breakthrough time should be at a minimum. For $p = 1$, however, the breakthrough time is not at a minimum as inferred above, but takes a value about twice as large. The reason for this unexpected behavior of breakthrough times is flow from evolving conduits into the net. This attracts more flow with low concentration into the input and therefore higher dissolution rates penetrate deeper. Consequently, breakthrough times are reduced. The exchange of flow is low for low p , because the percolating pathways have only few connections into the net. With

4. MODELING KARST EVOLUTION ON TWO-DIMENSIONAL NETWORKS: CONSTANT HEAD BOUNDARY CONDITION

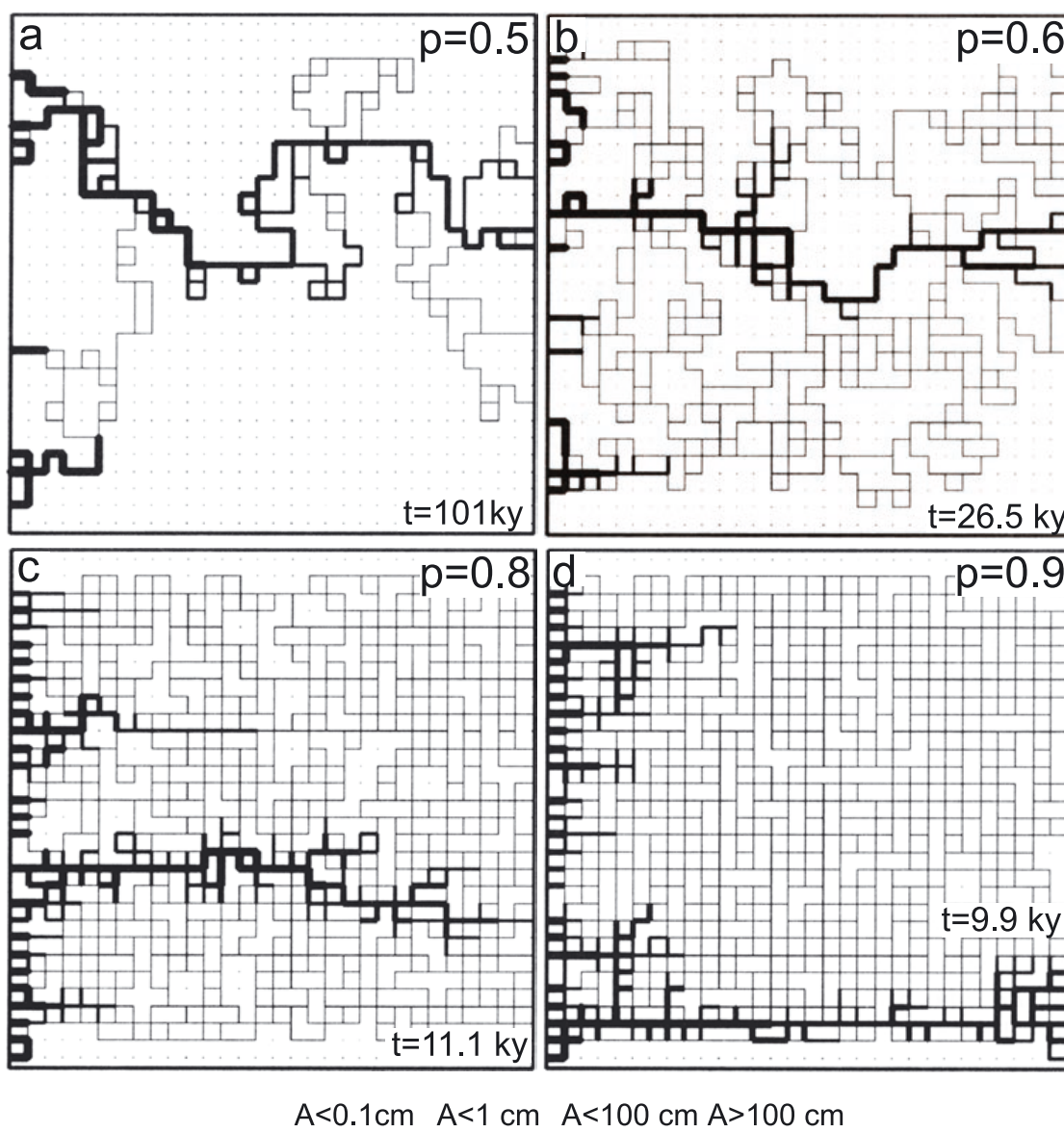


Figure 4.8: Distribution of aperture widths at breakthrough for percolation networks with various occupation probabilities as denoted in the figures. The head difference Δh is 150 m, the extension of the system is 3 km by 3 km, grid size is 100 m by 100 m, $A_0 = 0.03 \text{ cm}$, $b_0 = 1 \text{ m}$. Values of chemical parameters are equal to the standard given in Table 4.1 and Figure 4.3.

increasing p the number of points where flow can be injected into the net increases. At high $p > 0.95$, however, the distribution of hydraulic heads approaches that with $p = 1$. Then, although the evolving channels are well connected to the net, flow vertical to the channels is reduced, and therefore they do not exchange flow into the net. On the other hand the effective lengths of pathways do not longer increase significantly at $p > 0.9$.

As a consequence, breakthrough times increase for values of $p > 0.95$. A note should be given here. In the paper of Siemers and Dreybrodt (1998) the value at $p = 1$ is wrong due to an error in the program in this limiting case. All other values, however, are correct.

To obtain the dependence of breakthrough times on p , Siemers and Dreybrodt (1998) performed 10 different realizations and simulated their evolution until breakthrough. The results shown in Figure 4.9 are the average values of these breakthrough times and the bars designate the standard deviations.

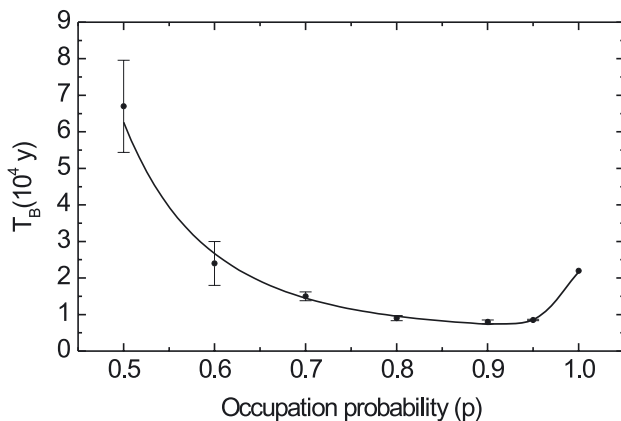


Figure 4.9: Breakthrough times of percolation networks (Figure 4.8) as function of occupation probability.

At low p the variation of the lengths of percolating pathways is high, because long pathways, as shown in Figure 4.8a with $p = 0.5$, have similar probability to arise in one realization as short pathways in another one. Accordingly, breakthrough times also show large variations. On the other hand at very high $p = 0.9$ all percolating pathways (Figure 4.8) have similar effective lengths and therefore the variation in breakthrough times is small. Up to a value of $p = 0.95$ breakthrough times decrease with increasing p .

To find the dependence of breakthrough times on the parameters A_0 , h , c_{eq} , k_n , and L , Siemers and Dreybrodt (1998) have performed a detailed sensitivity analysis for various values of p . The results are summarized in Figure 4.10, in which breakthrough time T_B is plotted double logarithmically as a function of the parameters mentioned above. This sensitivity analysis was performed using the model with parameters as in Figure 4.8. Then only one parameter was changed, such as A_0 to find T_B as function of this parameter. These runs have been performed for $p = 0.5$, $p = 0.6$ and $p = 0.7$. All plots show straight lines, which are parallel to each other. This clearly proves power laws as they are typical for isolated 1-dimensional conduits. The exponents of these power functions are listed in Table 4.2 and are compared to the corresponding powers of 1-D conduits given by Eq. 3.35. In view of the statistical properties of percolation networks one finds excellent agreement. Therefore, breakthrough times can be written as

$$T_B = f(p) T_B^{1D} \quad 4.4$$

4. MODELING KARST EVOLUTION ON TWO-DIMENSIONAL NETWORKS: CONSTANT HEAD BOUNDARY CONDITION

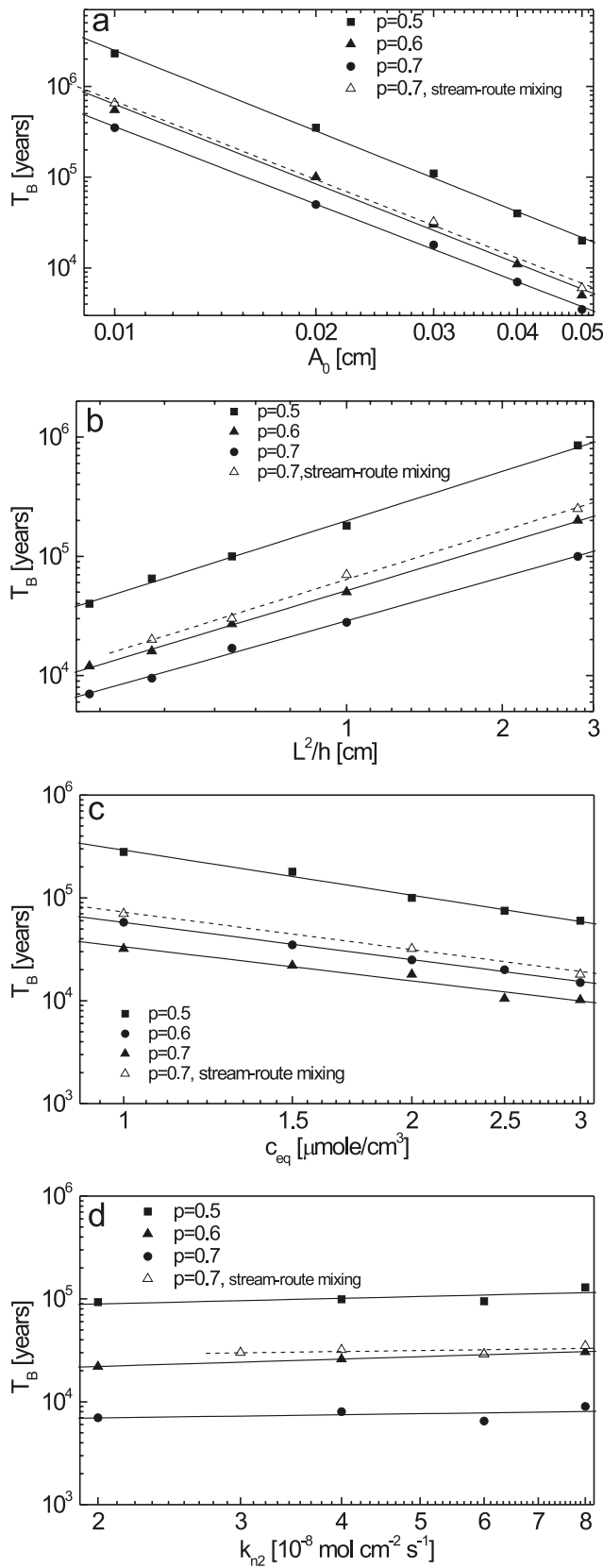


Figure 4.10: Breakthrough times of a percolation network (Figure 4.8) for complete mixing (solid lines) as a function of A_0 (a), L^2/h (b), c_{eq} (c) and k_{n2} (d) for different occupation probabilities p as given in the legend. The dashed line for comparison depicts the dependence for stream route mixing with $p = 0.7$.

T_B^{1D} is the breakthrough time of a corresponding one-dimensional conduit, and is given by Eq. 3.34. There, one has to replace length l of the 1-D-fracture by length L of the modeling domain. It should be noted here that in a percolation net Eq. 4.4 remains also valid for statistical distributions of aperture widths A_0 , if one replaces A_0 by its average value (Siemers and Dreybrodt, 1998).

Parameter	Theoretical values	Numerical values for tubes	Numerical values for fractures
A_0	-3.00	-2.84 ± 0.08	-3.50 ± 0.8
l^2/h	1.33	1.30 ± 0.04	1.22 ± 0.1
c_{eq}	-1.33	-1.20 ± 0.07	-1.16 ± 0.15
k_{n2}	0.33	0.22 ± 0.05	0.27 ± 0.1

Table 4.2: Numerical and theoretical values of exponents of power functions.

4.3.1 Mixing at fracture intersections

One comment must be given here. In all calculations we have assumed complete mixing of the solutions in each node as given by Eq. 4.3. This is an idealization and is mostly used in modeling karst evolution because of its simplicity. Complete mixing in laminar flow is mainly affected by molecular diffusion. The time T_c that a parcel of fluid with velocity v needs to cross an intersection of fractures with aperture widths a is $T_c = a/v$. The time T_D , which is necessary to level out concentration gradients by molecular diffusion, is given by $T_D = a^2/D$. If $T_D \ll T_c$ complete mixing may be assumed. Usually this condition is written in terms of the Peclet number $Pe = va/D = T_D/T_c$. Berkowitz *et al.* (1994) have shown that for $Pe < 10^{-2}$ complete mixing results, whereas for $Pe > 1$ stream route models at an ideal intersection provide good approximations. For such cases Berkowitz *et al.* (1994) have given equations which have been employed as mixing rules by Siemers and Dreybrodt (1998).

As an example Figure 4.11 illustrates the evolution of a karst system at breakthrough time for complete mixing **(a)** and for stream route mixing **(b)** as extreme cases. Otherwise the parameters and boundary conditions are identical. The breakthrough time for stream route mixing has increased to 31 ky in comparison to 18 ky for complete mixing. Also the evolution patterns are significantly different. This shows that the distribution of calcium concentrations in the net influences the pathways of evolution.

The basic behavior of the evolution, however, is not changed. This is also reflected in Figure 4.10, which shows (dotted line) that Eq. 4.4 is also valid, if one assumed stream-route mixing. A better approximation in between these two extremes is to calculate the Peclet number at each node and then use the according mixing rules.

However, since there is no basic difference in the processes governing the evolution between those two extremes, we restrict our modeling to the case of complete mixing as used by other modeling groups as well.

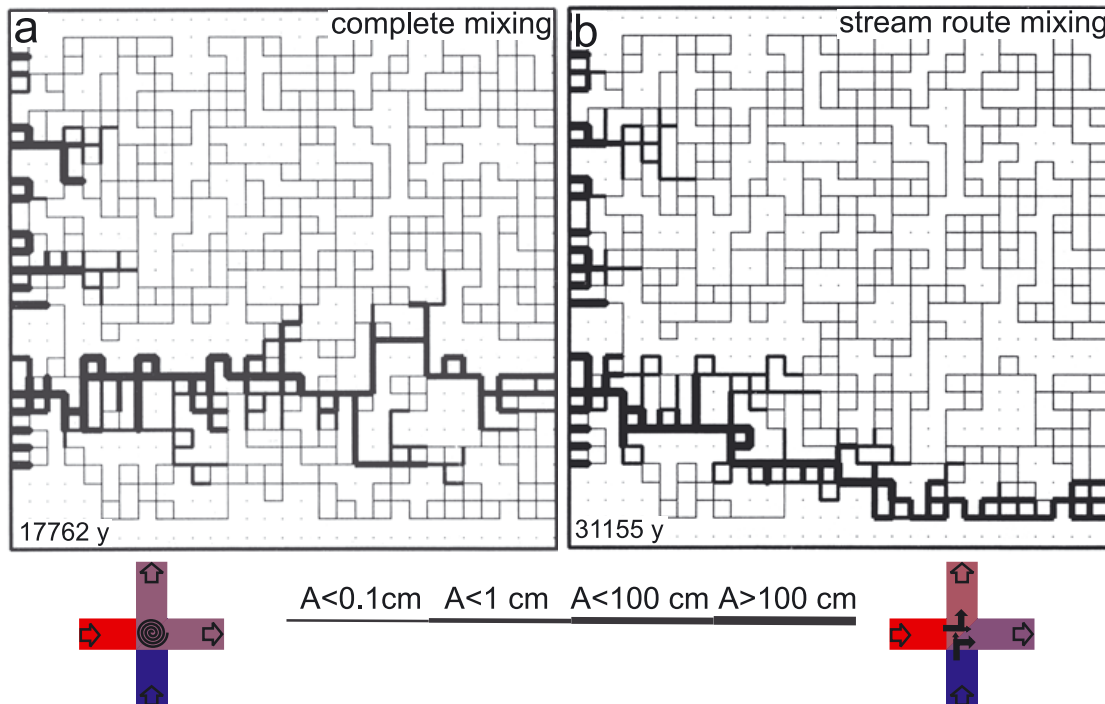


Figure 4.11: Aperture widths at breakthrough for identical percolation networks (Figure 4.8) with different mixing rules. All parameters as in Figure 4.8, except $p = 0.7$. **a)** Complete mixing at 17762 y, **b)** Stream route mixing at 31155 y.

4.3.2 Validity of constant head boundary conditions

The results presented so far show that karst evolution with constant head boundary conditions is governed by a competition of conduit evolution along various percolating pathways. In a crude approximation, the effective length determines the breakthrough time of each pathway. Therefore, conduits penetrate most easily along the shortest effective lengths, whereas due to the redistribution of heads by faster growing conduits, pathways with longer effective lengths are abandoned by flow and stop growing.

At that point one has to ask the question whether constant head boundary conditions are realistic during the evolution until breakthrough. To discuss this we return to the basic case illustrated by Figures 4.3 to 4.7. Shortly before breakthrough the amount of flow Q , leaving the system via the exit points A^* , B^* , and C^* is about $100 \text{ cm}^3 \text{ s}^{-1} = 3.15 \cdot 10^3 \text{ m}^3/\text{year}$. To maintain constant head conditions this value must be lower than the annual infiltration into the system. If we assume an infiltration of 300 mm/year into the aquifer with a catchment area of 900 m by 900 m, total recharge to the area is $2.43 \cdot 10^5 \text{ m}^3/\text{year}$. Some of this recharge is stored in the aquifer with 1 m depth in the standard scenario. Storage in the initial karst aquifer is 10.8 m^3 . Therefore, most of the water will leave the system by surface run-off and rivers or lakes can exist as efficient input points.

This justifies the assumption of constant head until breakthrough, when all our model runs have been terminated.

After breakthrough of a channel the constant head at its input can no longer be supported. Because of the limited supply of water, a boundary condition of limited recharge must be applied. The consequences of this to the further evolution will be discussed in Section 4.11. In the following sections the model runs are terminated at breakthrough, when flow through the aquifer exceeds its initial value by a factor of 1000.

4.4 STATISTICAL 2D-NETWORKS

The high-dip model

An alternative to percolation networks are nets with an occupation probability $p = 1$, i.e. all net points are connected by fractures. But the aperture widths of these are given by some geostatistical distribution.

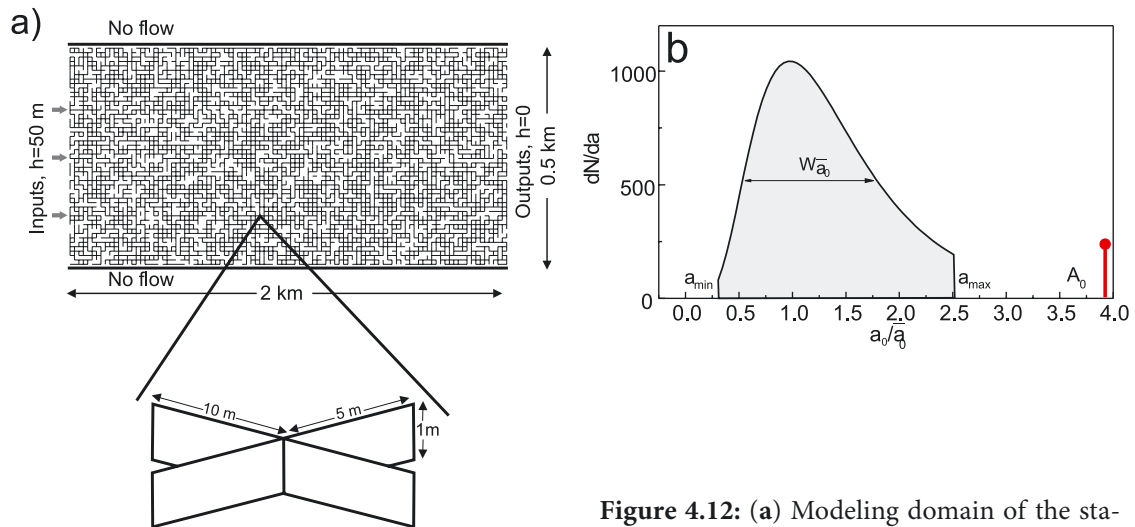


Figure 4.12: (a) Modeling domain of the statistical 2-dimensional fracture network. The

length L of the domain is 2 km, the width $w = 0.5$ km. Fracture spacing is 10×5 m². There are three inputs on the left side of the domain at $h = 50$ m and a series of outputs on the right hand side at $h = 0$. Each fracture has an initial aperture width, which is determined by a truncated lognormal distribution, shown in (b), for the entire set of fractures.

Figure 4.12a shows the domain for such a net. In the following we use a lognormal distribution. The probability density dN/da , which gives the number N of fractures per interval da in this distribution, is shown in Figure 4.12b. It is derived from a lognormal distribution, with average value \bar{a}_0 and a width $W_{a_0} = 1.25\bar{a}_0$. Furthermore, the lognormal distribution is restricted to values between $a_{min} = 0.25\bar{a}_0$ and $a_{max} = 2.5\bar{a}_0$. The realization of this distribution as presented by Figure 4.12a will be used in all corresponding scenarios in chapter 4.

The modeling domain in Figure 4.12 can be translated into a geological setup shown by Figure 4.13. A limestone bed dissected by fractures is dipping to a valley, where some river drains the system. The limestone is overlain by impermeable material (not shown). At some locations a lake or a river is in contact with the limestone bed and provides inputs of constant head. This scenario corresponds to the high dip-model of Ewers and Ford (Ford and Williams, 1989).

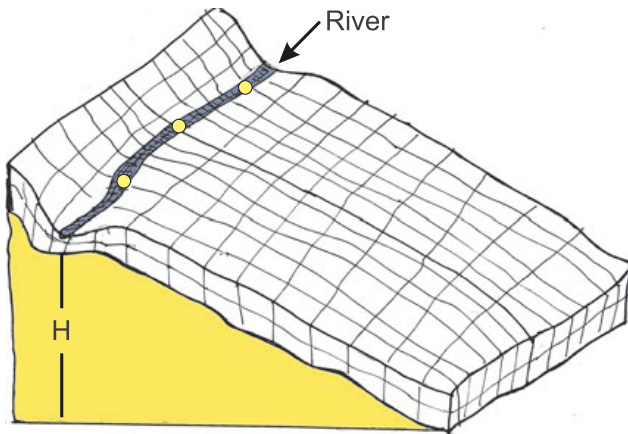


Figure 4.13: Geological setting of the modeling domain in the previous Figure 4.12. High-dip model. The limestone bed is covered by an impermeable layer to keep the aquifer confined (not shown). The underlying rocks (yellow) are impermeable. The input points at the river are shown as yellow circles. Outflow is at the lowest boundary at the right hand side.

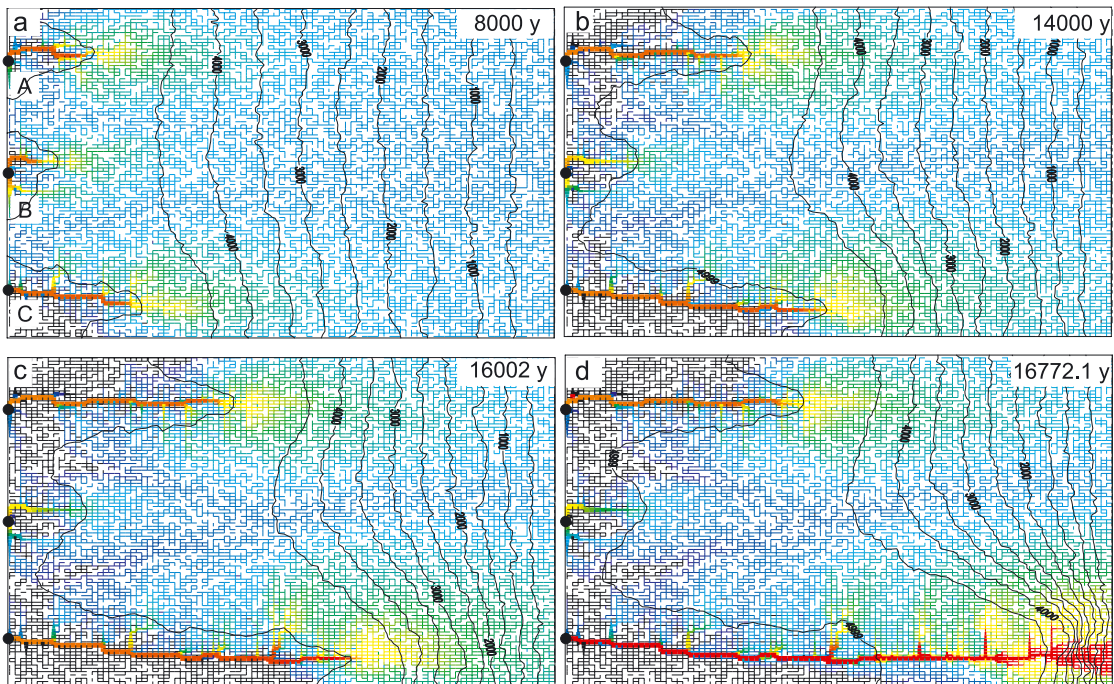
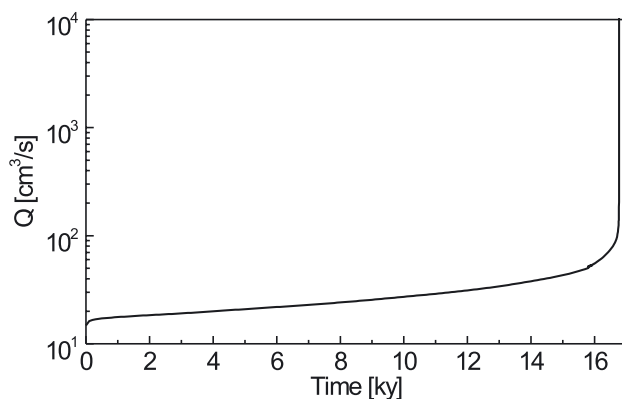


Figure 4.14: Evolution of fracture aperture widths and dissolution rates for the high-dip model, as in the previous Figures 4.12 and 4.13. Initial fracture aperture widths $\bar{a}_0 = 0.02$ cm, $p_{CO_2} = 0.05$ atm and $c_{in} = 0$ at all inputs. For explanation of color and bar codes see Code box. Isolines of head are given in cm in steps of 500. $h = 50$ m.

The evolution of the aquifer with $\bar{a}_0 = 0.02$ cm is illustrated by Figures 4.14a–d. These show the aperture widths, dissolution rates and head contour lines. Since flow is roughly perpendicular to the latter, flow directions can be visualized. Dissolution rates are highest at red color. Black areas are abandoned by dissolutional widening since the rates are extremely low there ($F < 10^{-5}F(c_s)$). For bar and color code see Code box.

After 8000 y three competing channels have propagated downstream. The upper and the lower channel continue to penetrate downstream with high dissolution rates, whereas due to the redistribution of heads, the central channel is abandoned by flow, and consequently experiences little dissolution (b, c). Breakthrough occurs after 16.772 y (d). At that time the constant head condition breaks down and must be replaced by constant flow into the input of the lower channel.

Figure 4.15 illustrates the evolution of total flow through the net, which exhibits typical breakthrough behavior. The behavior of statistical networks resembles that of



percolation networks shown in Figures 4.3, 4.6, 4.7.

Figure 4.15: Evolution of total flow rate for the high-dip model in Figure 4.14.

The spatial distribution of flow rates is also similar. Figure 4.16 illustrates flow rates in the statistical net shown in Figure 4.14. At the beginning flow enters into all input points. At the tips of the evolving passages water is injected into the net of fine fractures and dispersed widely. This enhances flow through the main passage by attracting more aggressive solution. Therefore, one expects breakthrough times to be lower than for a comparable isolated tube. The middle conduit evolves more slowly. Because of this retardation the hydraulic gradient drops along it, and the passage becomes abandoned. After breakthrough flow from the lower input is focused to the lower passage, from which it leaves the aquifer. A similar pattern is also found in percolation networks with $p > 0.6$ (see Figure 4.4).

Percolation and statistical networks represent quite different geological situations: The percolation network mimics coarse nets with only few long fractures, whereas the statistical model resembles highly fractured rock. Their behavior, however, appears to be similar. The evolution of both is based on the evolution of single conduits, which are the basic elements of the net. To confirm this we have performed a sensitivity analysis on the modeling scenario of Figure 4.14, equal to that reported by Dreybrodt and Siemers (1998) shown by Figure 4.10. The results are basically the same and can be summarized by Eq. 4.4. Therefore, they are not shown here.

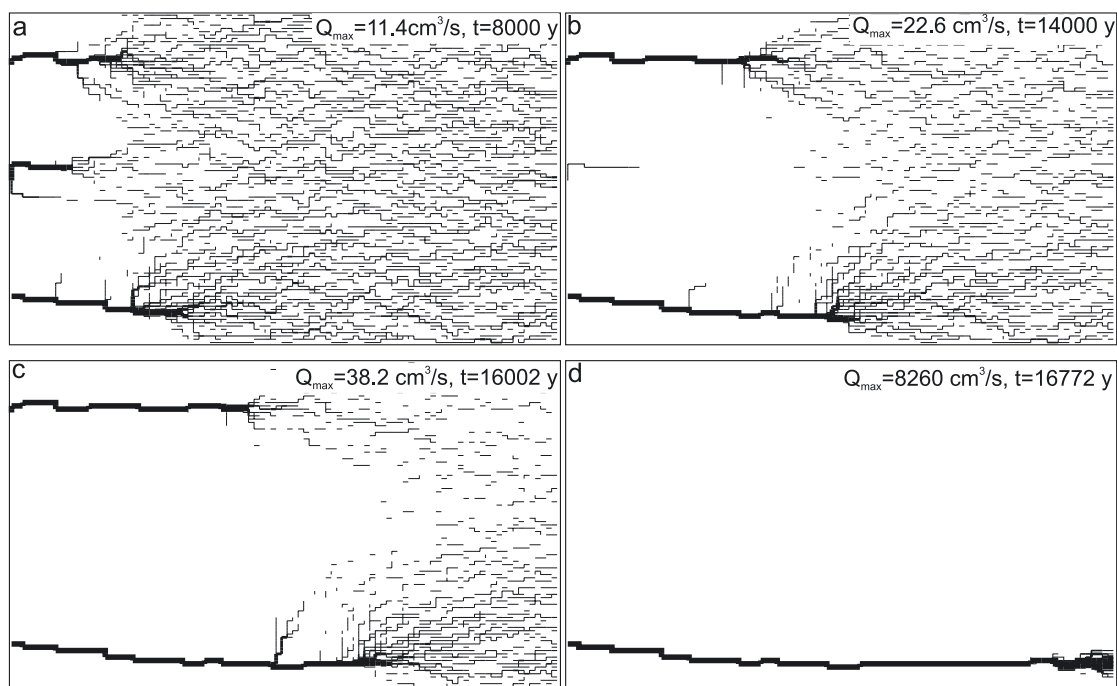


Figure 4.16: Distribution of flow rates in the high-dip model of Figure 4.14 at various times.

4.4.1 Applications of 2-D network simulations

To obtain a high flexibility in simulating varying geological and hydrochemical settings the program allows to assign individual values of a_0 , k_n , n , l , k_n , n and c_{eq} to each fracture, and also to assign a fixed head or a fixed input flow to selected nodes. The concentration of Ca^{++} and the p_{CO_2} at each input node can also be chosen individually.

This allows the investigation of the influence of various external boundary conditions as well as that of the lithology, determined by k_n and n , on the evolution of karst aquifers. It is also possible to model the influence of insoluble rocks embedded into the aquifer. Impermeable rock within the modeling domain can be taken into account by assigning extremely low values (10^{-6} cm) to the aperture widths of the corresponding fractures, or by omitting them from the net. In this chapter we apply these options.

The low-dip model

As a first example, we discuss the low-dip model by Ewers and Ford ((Ford and Williams, 1989). In this case, two inputs D and E, shown as black dots in Figure 4.17, are added in the central region of the modeling domain (Figure 4.12, Figure 4.14). These are at equal heads as the three input points A, B, C at the left hand side boundary. The concentration c and p_{CO_2} of the solutions as well as the heads are equal at all input points.

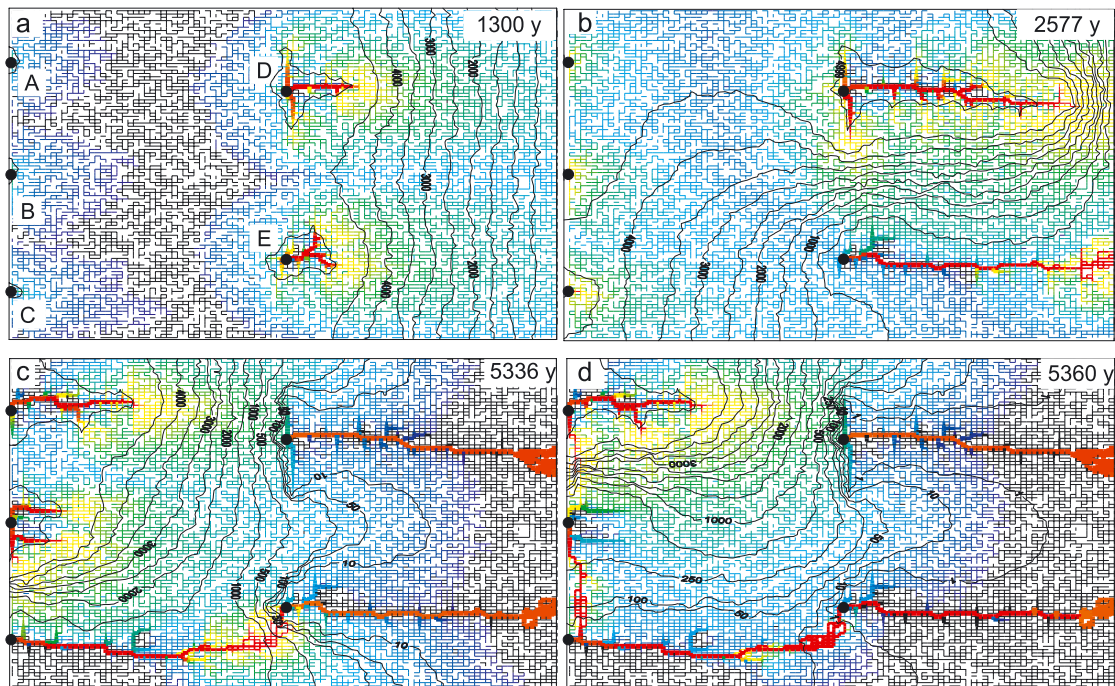


Figure. 4.17: Evolution of low-dip model. Two input points D and E marked by black dots have been added in the middle of the aquifer shown in Figure 4.14. Their heads are equal to those of the input points at the left hand side boundary. Other parameters and boundary conditions as in Figure 4.14.

Figure 4.17 a–d illustrates the results. It depicts fracture aperture widths, dissolution rates and head contours. In the beginning (1300 y) channels from input points D and E penetrate downstream. There is little flow from the input points A, B and C at the left hand side boundary to the central ones because they are at equal head. Accordingly, dissolutional widening is almost absent in this region (a). After 2600 y the lower channel has reached the output and a constant flow boundary condition is assigned to its input point E. This redistributes the hydraulic heads, as shown by the isolines. Therefore, flow from inputs B and C is directed to the region of low hydraulic head along the breakthrough conduit (b). After 5835 y a channel from input A is connected to the first breakthrough conduit. During this time the uppermost channel from the central input D has reached the outflow boundary and constant recharge is imposed to its input, causing again a redistribution of heads. A steep hydraulic gradient connects input point B to the channel originating from point C, causing breakthrough after 5360 y (c). Due to the change of boundary conditions steep hydraulic gradients arise between points A and B and also between A and D. From what has been discussed follows that breakthrough subsequently will connect these points (not shown). Finally, all input points are connected by an integrated cave system (d).

One comment is necessary here. In all cases, in which the constant head condition is replaced by a constant recharge condition, we have assumed that all tubes remain

completely filled with water. However, at steeply dipping conduits flow becomes vadose following gravity as open channel flow. Due to the problems handling this, all modelers have used flow in completely filled conduits, when assigning constant recharge conditions. To deal with this problem correctly is one of the challenges to future modeling. More details on the integration of conduits by changing subsequently to constant recharge conditions are discussed in Section 4.11.

To compare the behavior of the high-dip and the low-dip model, the evolution of total flow through both networks is illustrated in Figure 4.21.

Due to the shorter distance between central input points and output, the breakthrough time for the first breakthrough in the low-dip case is almost one order of magnitude lower than in the high dip model. This again reflects the role of single conduits as a basic element. For the low-dip model first breakthrough occurs in the lower half of the net, because there is no flow in the upstream half, due to the equal head at all input points. Therefore, the effective domain length is half that of the high-dip setting. Since breakthrough time for 1-D conduits is proportional to $L^{8/3}$ (cf. Eqs. 3.35 and 4.3) for $n = 4$, the ratio of low-dip to high-dip breakthrough times becomes 0.16, close to the modeling result.

The low dip model can be expanded by inserting input points in several parallel rows. Then first breakthrough happens from the array closest to the output boundary and a net of conduits propagates upstream by breakthrough events between neighboring arrays.

Bauer (2005) has used such a setting to simulate the interaction between conduit systems and surface conditions.

High-dip model with varying lithology

In Section 3.3 we have discussed the influence of varying lithology in a single fracture by assuming locally different dissolution kinetics, expressed by the parameters n and k_n . In networks the influence of lithology can be investigated assigning these parameters to the fractures of selected regions in the modeling domain.

Figure 4.18 shows the evolution of the standard aquifer in Figure 4.14, where the central part of the aquifer is replaced by limestone with dissolution kinetics of $n = 8$ instead of $n = 4$, and $k_{n_2} = k_{n_1} \cdot (1 - c_s/c_{sq})^{1-n_2}$. In our standard case this equals $k_{n_2} = k_{n_1} \cdot 10^{n_2-n_1}$. Everything else remains unchanged.

Due to this change, dissolution rates drop in the region of $n = 8$ (confer to Figure 3.16). In the early stage channels start to migrate down head. When they encounter the region of reduced dissolution rates, they form branches with conduits growing parallel along the border (a). Later the upper and the lower conduit penetrate into the $n = 8$ region (b). Finally, the lowest one traverses this region and achieves breakthrough (c). Then constant recharge conditions are applied and the conduits are integrating into one connected system(d). This will be discussed in more detail in Section 4.10.

The situation becomes different if the regions with $n = 4$ are replaced by $n = 8$, and the region with $n = 8$ becomes $n = 4$. This is illustrated by Figure 4.19. After 8000 y

4. MODELING KARST EVOLUTION ON TWO-DIMENSIONAL NETWORKS: CONSTANT HEAD BOUNDARY CONDITION

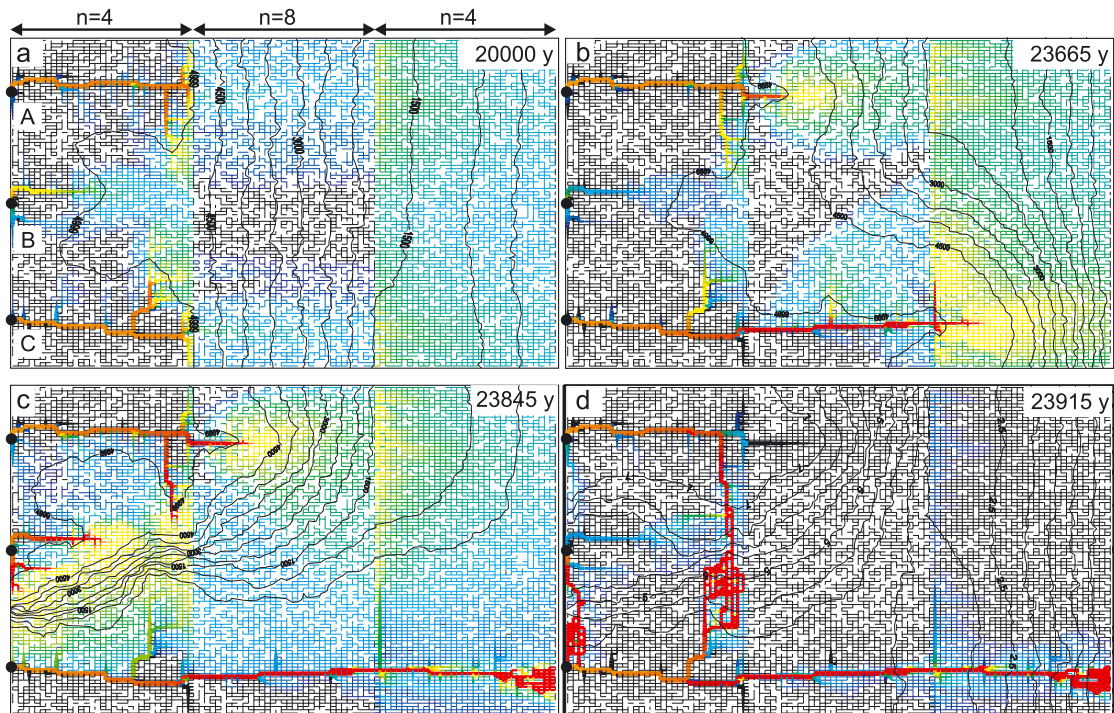


Figure 4.18: High-dip model with changing lithology. Evolution of fracture aperture widths and dissolution rates. The center region is replaced by limestone with 8th order kinetics. Other parameters and boundary conditions as in high-dip model of Figure 4.14.

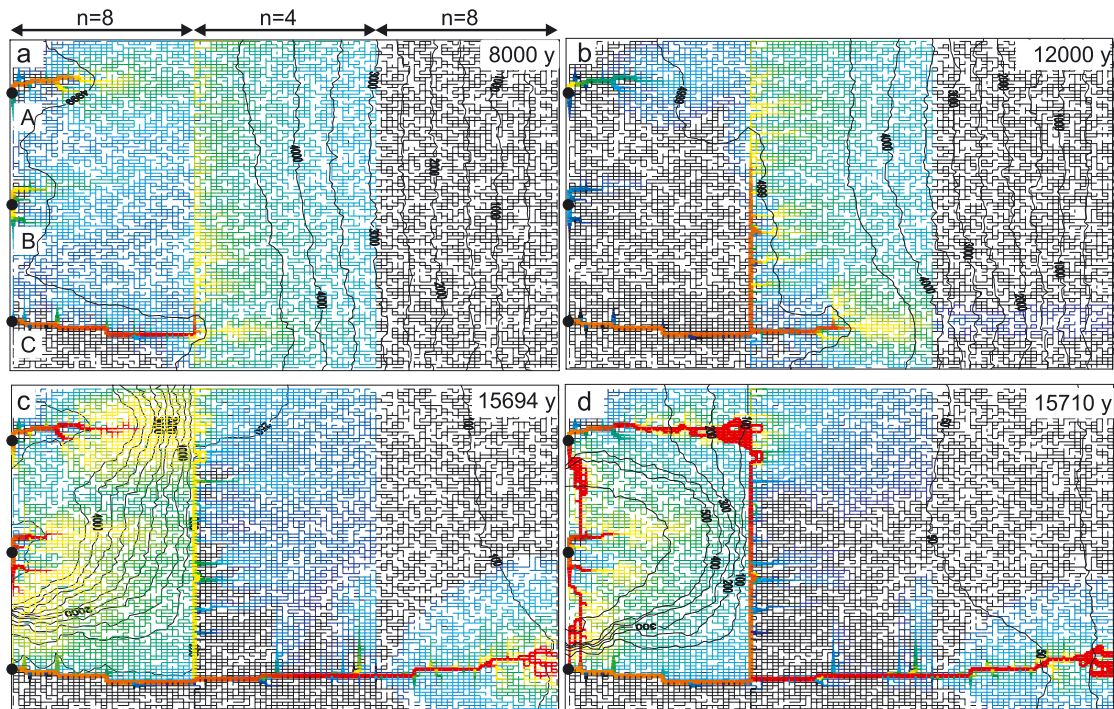


Figure 4.19: High-dip model with changing lithology. Evolution of fracture aperture widths and dissolution rates. Center region $n = 4$, left and right regions $n = 8$. Other parameters and boundary conditions as in high-dip model of Figure 4.14.

three conduits, originating from input points A, B and C, have penetrated down head. The channel from input B has migrated the shortest distance. It has been abandoned by flow and its dissolution rates are low. The lowest channel has reached the border with $n = 4$, and consequently dissolution rates increase, where the solution enters into this region. This creates a fringe of increasing permeability along the border (a). After 12 ky the lower conduit enters into the region with $n = 4$. Simultaneously, a branch grows parallel to the boundary in this region. This redistributes the hydraulic heads, and both competing conduits from A and B do no longer carry flow. After 15700 y the lower channel breaks through and a constant recharge boundary condition is imposed to its input. This reactivates flow into the upper conduits (c). Shortly thereafter the channel from A utilizes the highly permeable region at the boundary between $n = 8$ and $n = 4$ and connects to the lowest channel by a breakthrough event (d). Figure 4.21 shows the evolution of flow rates for both cases.

In contrast to the previous case of 4–8–4 lithology of Figure 4.18 the time for the first breakthrough event is shorter by 8000 y.

High-dip model containing a region of insoluble rock

Another interesting situation arises if the central part of the aquifer is replaced by fractured insoluble rock. In this case, flow through the aquifer is limited by the resistance of this insoluble layer.

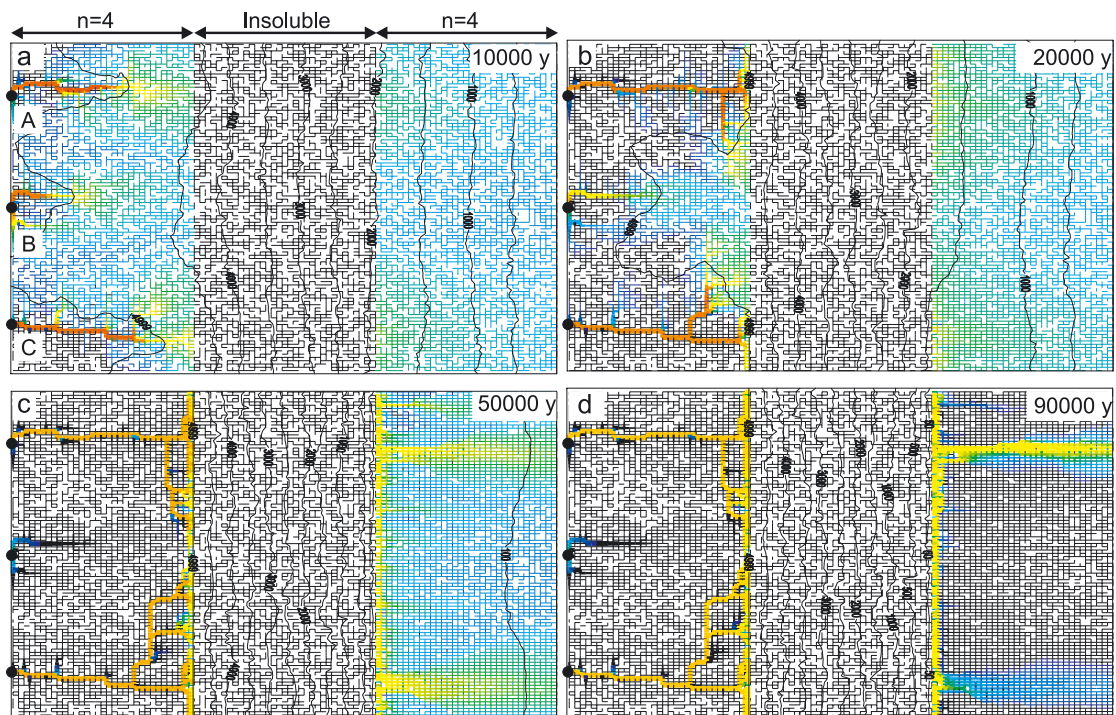


Figure 4.20: High-dip model with insoluble rock in the central region. Evolution of aperture widths and dissolution rates. Other parameters and boundary conditions as in Figure 4.14.

Figure 4.20 shows the evolution of the aquifer. After 10 ky channels have propagated downstream. When they reach the insoluble region of the aquifer, the water is spread into this part and labyrinth-like structures arise at the upstream border. Water flowing through the insoluble region does not change its concentration. When it discharges diffusively into the downstream soluble region small channels start to grow there. These evolve slowly, because the constant resistance of the insoluble region restricts flow to a constant value after 50 ky, and therefore the positive feedback-loop is switched off. After 90 ky the upper channel reaches the outflow boundary and efficiently drains the aquifer. Therefore, dissolution rates become small in all other downstream regions (blue and black).

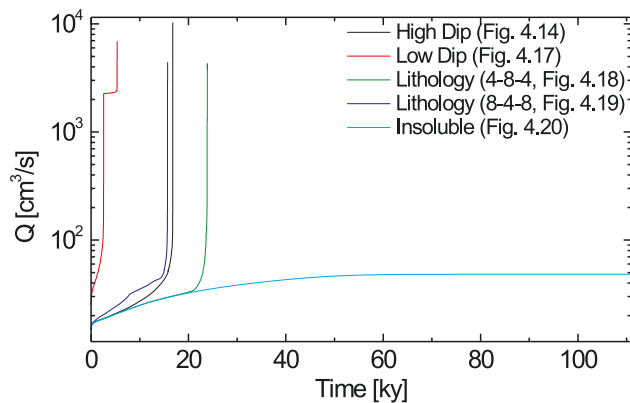


Figure 4.21: Evolution of total flow rates for the model runs in Figures 4.14 and 4.17–4.20.

Figure 4.21 shows the evolution of flow rates as a function of time. Initially, the flow rates rise, due to the dissolutional widening in the limestone regions. When their resistance to flow becomes smaller than that of the unaltered insoluble rock, the resistance of this layer determines flow and the rates become constant in time.

4.5 ONE STEP CLOSER TO REALITY: THE DUAL-FRACTURE SYSTEM

Karst aquifers evolve in fractured soluble rock, such as limestone, dolomite or gypsum. Such rocks contain a variety of primary fractures penetrable by water, for example bedding planes and master joints, which we will term prominent fractures in the following. These fractures are characterized by their large extensions and comparatively wide aperture widths of several 10^{-2} cm (Dreybrodt, 1988; Ford and Williams, 1989; White, 1988). They are embedded into a dense net of narrow fissures and are in hydraulic contact to them. The fractures in this net exhibit smaller aperture widths and are less extended than the prominent ones. We term such a constellation a dual-fracture system.

Such a system can be modeled the following way. First one generates a percolation network on a square lattice of large dimensions with grid sizes of, e.g. 50×50 m² and aperture width A_p . The modeling domain is then further subdivided into squares of 5×5 m², and to each position of the net, not occupied by a prominent fracture of the percolation net, an aperture width is assigned.

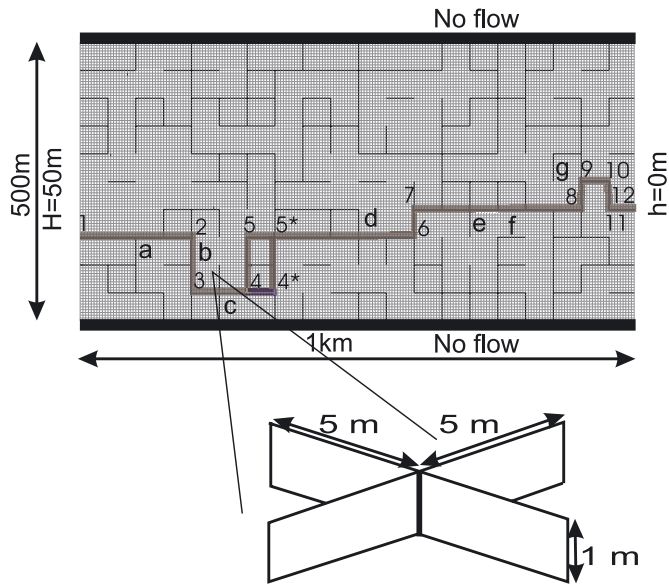


Figure 4.22: Structure of a dual-fracture aquifer. Fat lines mark prominent fractures of 50 m length with an aperture width A_0 . Thin lines represent the net of fine fissures of 5 m length with lognormally distributed aperture widths a_0 . The gray shaded pathway 1–12 along prominent fractures connecting input (1) and output (12) shows the pathway of breakthrough for $\bar{a}_0 = 0.005$ cm and is depicted here for later discussion. Letters a–g designate points of confluence within the net of prominent fractures.

Figure 4.22 shows such a modeling domain. The aperture widths in the dense net are statistically distributed, lognormally in our case, with an average $a_0 < A_0$. The probability density dN/da gives the number N of fractures per interval da in this distribution and is shown in Figure 4.12b. The percolation net of prominent fractures has equal aperture widths A_0 in all fractures as indicated by the red bar denoted with A_0 . Its occupation probability is $p = 0.6$.

The upper and lower boundaries are impervious, whereas the left hand side boundary is open to flow at a constant head of 50 m. All flow leaves the aquifer at the right hand side boundary at head zero. The length of the aquifer is 1000 m and its width 500 m. It is divided by fine fractures into squares of $5 \times 5 \text{ m}^2$ (200×101 nodes). The thickness of the aquifer is 1 m, i.e. all fractures have a height of 1 m. Solution entering at the left hand side boundary is in equilibrium with a partial pressure $p = 0.05$ atm of carbon dioxide. Its calcium concentration c is equal to zero. The gray shaded pathways will be used later to depict profiles of dissolution rates along them.

Since the two nets are connected hydraulically, exchange of flow between them is possible. One may envisage that exchange of flow between these nets becomes larger with increasing ratio $M = \bar{a}_0/A_0$ which we term the hydraulic coupling ratio. If flow from a prominent fracture, located in a percolating pathway is injected into the net of fine fissures, more water must enter at the input. This new aggressive solution penetrates deeper into the aquifer retaining more dissolutional power and therefore, in comparison to an isolated percolation net ($\bar{a}_0 = 0$ cm), breakthrough should be enhanced. On the other hand water entering from the net into a prominent fracture may be significantly closer to saturation than the solution flowing in the wider prominent fractures. When both solutions mix, dissolution rates drop and breakthrough is retarded. These two mechanisms can counterbalance, and it is not easy to recognize them in a modeling domain such as that shown by Figure 4.22.

Therefore we first discuss simple scenarios, which clearly show the mechanisms mentioned above, and later we will approach more complex scenarios.

4.5.1 Single prominent fracture embedded in the net: Enhancement of karst evolution

Figure 4.23 shows the geological setting for our first simple scenario. It depicts a highly fractured limestone terrain with a single major fracture in its center. The river on top of the limestone acts as an input region. Water discharges along the wider central fracture, but also through the dense fissure system. A layer of impermeable cap rock on top of the limestone (not shown) keeps the aquifer confined.

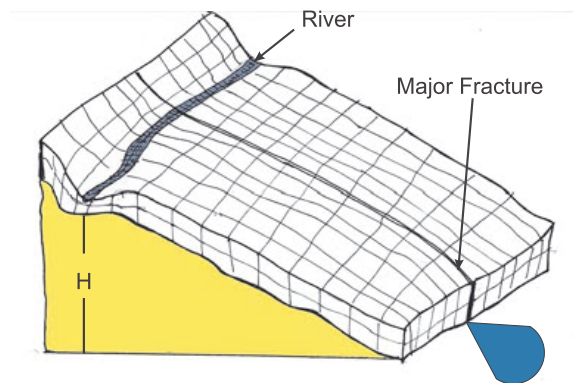


Figure 4.23: Geological setting of a dipping limestone bed with a central prominent fracture. A river supplies water to the input boundary. Most of the outflow is through the prominent central fracture, but the fractures of the net end also at outflow points with constant head zero.

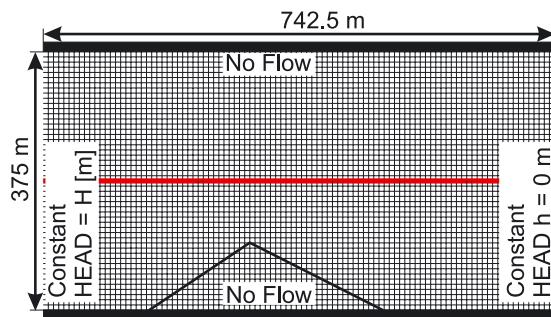
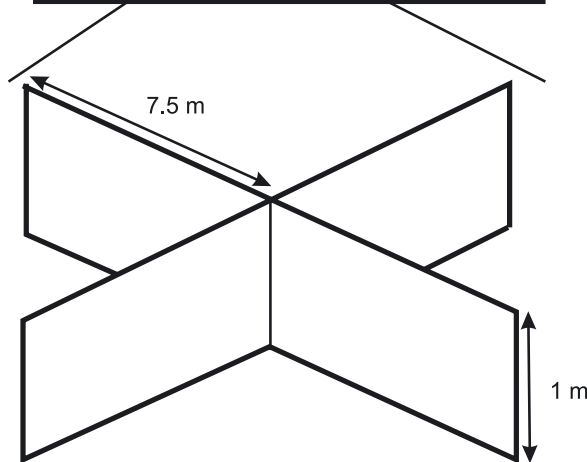


Figure 4.24: Modeling domain for the setting shown in Figure 4.23. The red line depicts the prominent fracture of width A_0 located in the center. The black lines depict the narrow fissures of width a_0 . Boundary conditions can be read from the figure. $H = 100$ m.



From this setting, the modeling domain is constructed as shown by Figure 4.24. The dense net of fissures is simulated by a square net of fractures with squares of 7.5×7.5 m². The length of the limestone bed is 742.5 m, its width is 375 m. The major prominent fracture is represented by a straight central fracture with aperture width

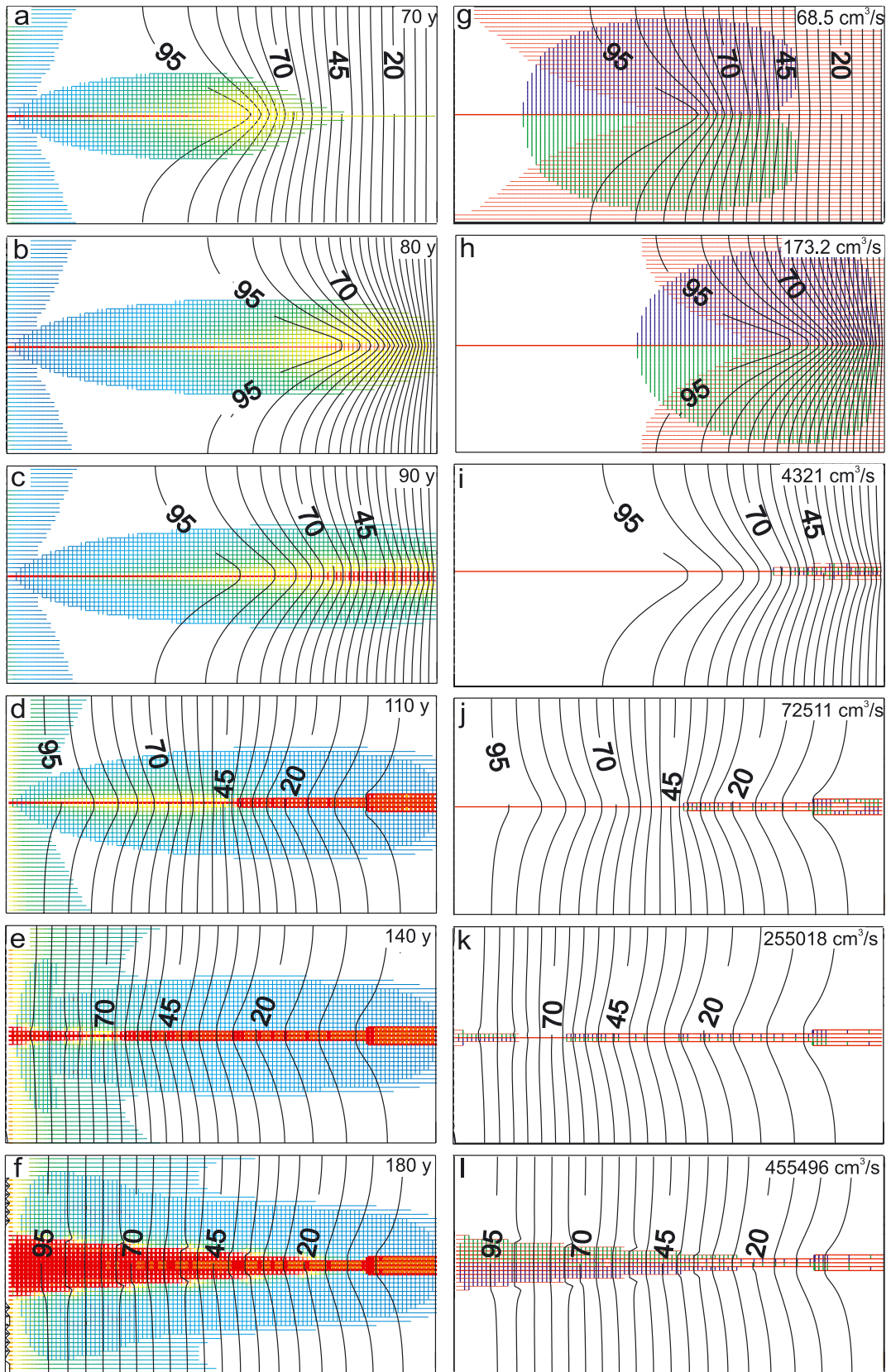
$A_0 = 0.03$ cm. The fractures in the net exhibit equal aperture widths $a_0 = 0.02$ cm. Upper and lower boundaries are impermeable. The head H , which drives water from the left hand side downstream, is 100 m. From the symmetry of this setting it is evident that initially there is no exchange of flow between the central fracture and the dense net of fissures. However, when the central fracture widens, hydraulic heads are redistributed such that flow from the fracture is injected into the net.

Figure 4.25 shows the evolution of the system beyond breakthrough under constant head conditions. The left hand side column shows the evolution of fracture widths and dissolution rates. The bar code designates fracture widths and the color code gives dissolution rates. The right hand side depicts flow rates and flow directions through the domain. There the color code depicts the directions of flow (blue up, green down, red to the right, and yellow to the left). The bar code illustrates the amount of flow rate in each fracture. Note, that for each time step this bar code is normalized to the maximal flow rate occurring somewhere in the domain. Therefore, bar codes at different times are not comparable. In addition, head isolines are given. Note, that flow is roughly perpendicular to them.

In the early stage (a, b) a conduit propagates down the central fracture. Because of its larger aperture width it migrates faster downstream than the conduits along fine fractures. The high hydraulic head penetrates deeply into the widened central fracture close to its tip and high hydraulic gradients inject water into the adjacent fissure system. This can be seen from the head lines and also from the flow directions. Green regions of flow below the fracture and blue regions above show where flow leaves the central prominent fracture. Shortly before breakthrough after 80 y (b) the tip of the central conduit has approached nearly the output boundary. Due to steep hydraulic gradients a large amount of water is injected into the net. Most of it is flowing where the gradient is steepest, preferentially in the fissures adjacent to the central fracture. As will be shown in Figure 4.27 the calcium concentration of the solution injected into the adjacent fissures is about $0.6c_{eq}$. Therefore, these fractures are widened by high dissolution rates. At breakthrough (90 y, c) flow is entirely restricted to the central channel and a few adjacent fissures. The hydraulic gradient is still sufficiently steep to maintain flow until a series of consecutive breakthrough events produces an exit fan of fast widening fissures. This fan propagates upstream (110 y, d). As a consequence, hydraulic heads are redistributed such that water, almost saturated from the net, enters the downstream part of the exit fan and prevents its further expansion (d, e, f and j, k, l). After 140 y (Figure 4.25e) another fan has developed close to the entrance point. There, aggressive solution entering into the nearest neighboring fractures flows into the central tube. Therefore, breakthrough occurs along this short pathway. After this event, similar to the evolution of the exit

Figure 4.25: Evolution of the aquifer in Figure 4.24 with one single prominent fracture embedded into a uniform net. ($A_0 = 0.03$ cm, $a_0 = 0.02$ cm). The left hand side column illustrates aperture widths (bar code) and dissolution rates (color code). The right hand column shows corresponding flow rates (bar code) and flow directions (color code). See Code box. →

4. MODELING KARST EVOLUTION ON TWO-DIMENSIONAL NETWORKS: CONSTANT HEAD BOUNDARY CONDITION



fan, a series of breakthrough events creates an entrance fan, which drains water into the central conduit. After sufficient time this fan conquers the whole domain. The exit fan, as mentioned above, cannot expand vertically (green or blue) but grows only upstream. It keeps its vertical shape, because the inflowing water from the net is almost saturated and there is no flow of highly aggressive solution out from the central fracture.

With these observations it is now easy to understand the evolution for a lognormal statistically distributed dense net with $\bar{a}_0 = 0.02$ cm (Figure 4.12). The evolution of fracture widths for such an aquifer is illustrated by Figure 4.26. Its basic pattern is similar to the uniform net shown in Figure 4.25. But there are some differences in the evolution after breakthrough. Some fissures initially wider than 0.02 cm can form pathways, which are connected fast to the central channel by little breakthrough events. This is seen in the area marked with a black rectangle in (e) at 140 y, where steep hydraulic gradients direct flow into the central fracture.

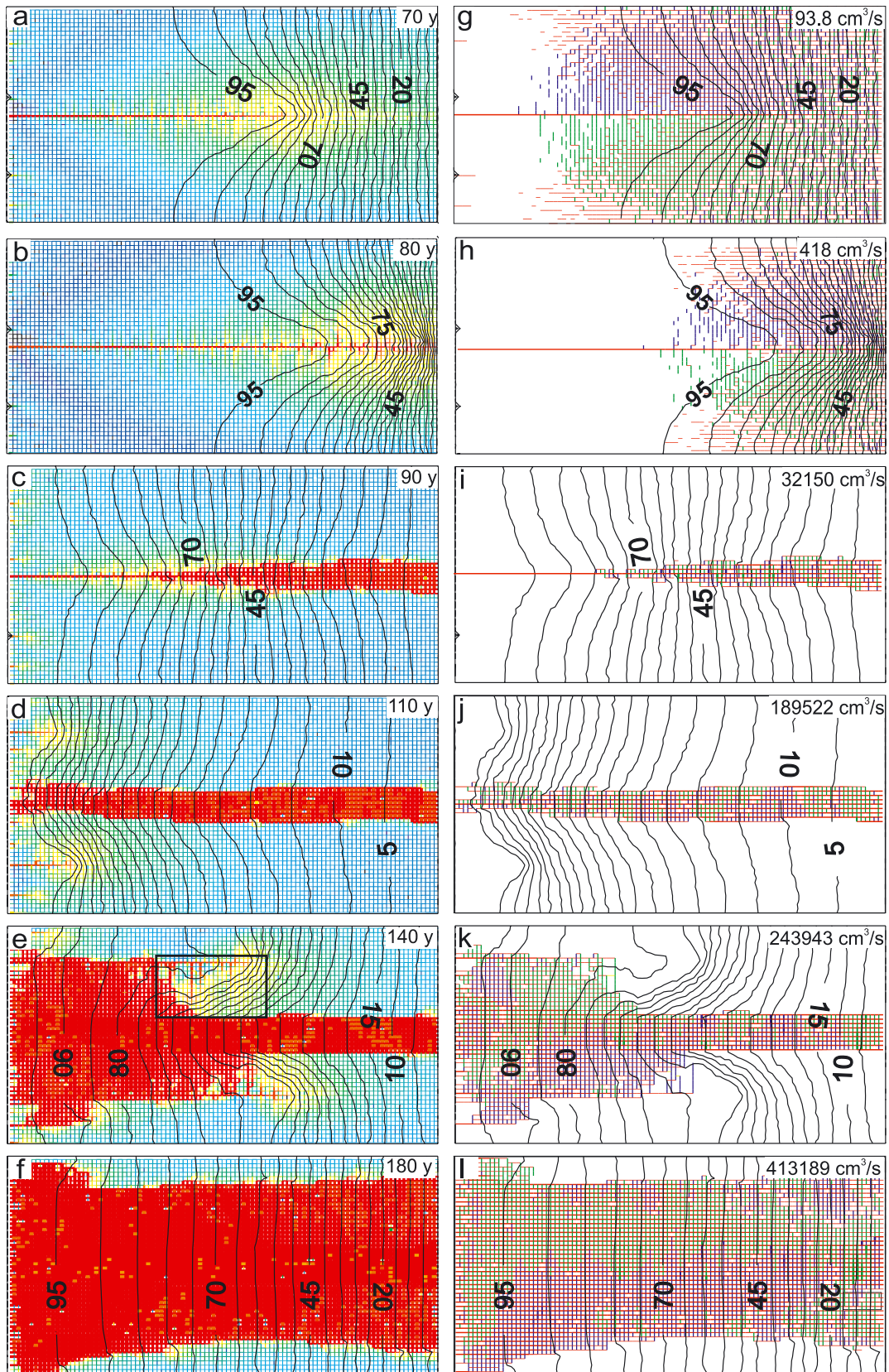
To further illustrate the role of exchange, in Figure 4.27 we compare the profiles of head distribution, flow, aperture widths, and calcium concentration along the central conduit for the uniform net of Figure 4.24 with those of an isolated one-dimensional conduit of identical dimensions and boundary conditions. The latter is realized by setting $a_0 = 10^{-6}$ cm everywhere in the fine net. The left hand side in Figure 4.27 shows the profiles along the central fracture embedded into the net ($a_0 = 0.02$ cm) and the right hand side those for the isolated conduit.

First we discuss the evolution of flow rates along the central fracture (c, d). Times are listed in the figure caption. In the beginning ($t = 0$), flow through the central fracture is identical for both cases. But after only 10 y flow at the input of the central fracture in the net has increased by one order of magnitude compared to the isolated fracture. This flow is then lost to the net, seen by the reduced flow along the fracture. (Naturally it stays constant in the isolated fracture.) The region where the loss occurs moves down head until breakthrough happens after 90 y. In case of the isolated fracture it takes 800 y until the breakthrough event. The formation of the exit fan is also reflected by the flow profiles after breakthrough (blue curves). The small steps close to the exit show that water is lost to the neighboring fracture elements. These steps move head wards indicating the spreading of the exit fan. The evolution of the entrance fan at a later time (blue curve) causes some increase of flow rates downstream from the entrance. This is the result of breakthrough events along fine fractures close to the central channel at the input boundary. These deliver flow to the central channel.

The evolution of aperture widths exhibits a fast downstream penetration of the central channel (e, f). Because of its interaction with the surrounding net head distributions are more complex than that of the isolated fracture. Due to the large amount of fresh water

Figure 4.26: Evolution of the aquifer of Figure 4.24 with one single prominent fracture ($A_0 = 0.03$ cm) embedded in a statistical net with $\bar{a}_0 = 0.02$ cm. The left hand side column illustrates aperture widths (bar code) and dissolution rates (color code). The right hand column shows corresponding flow rates (bar code) and flow directions (color code). See Code box. →

4. MODELING KARST EVOLUTION ON TWO-DIMENSIONAL NETWORKS: CONSTANT HEAD BOUNDARY CONDITION



4. MODELING KARST EVOLUTION ON TWO-DIMENSIONAL NETWORKS: CONSTANT HEAD BOUNDARY CONDITION

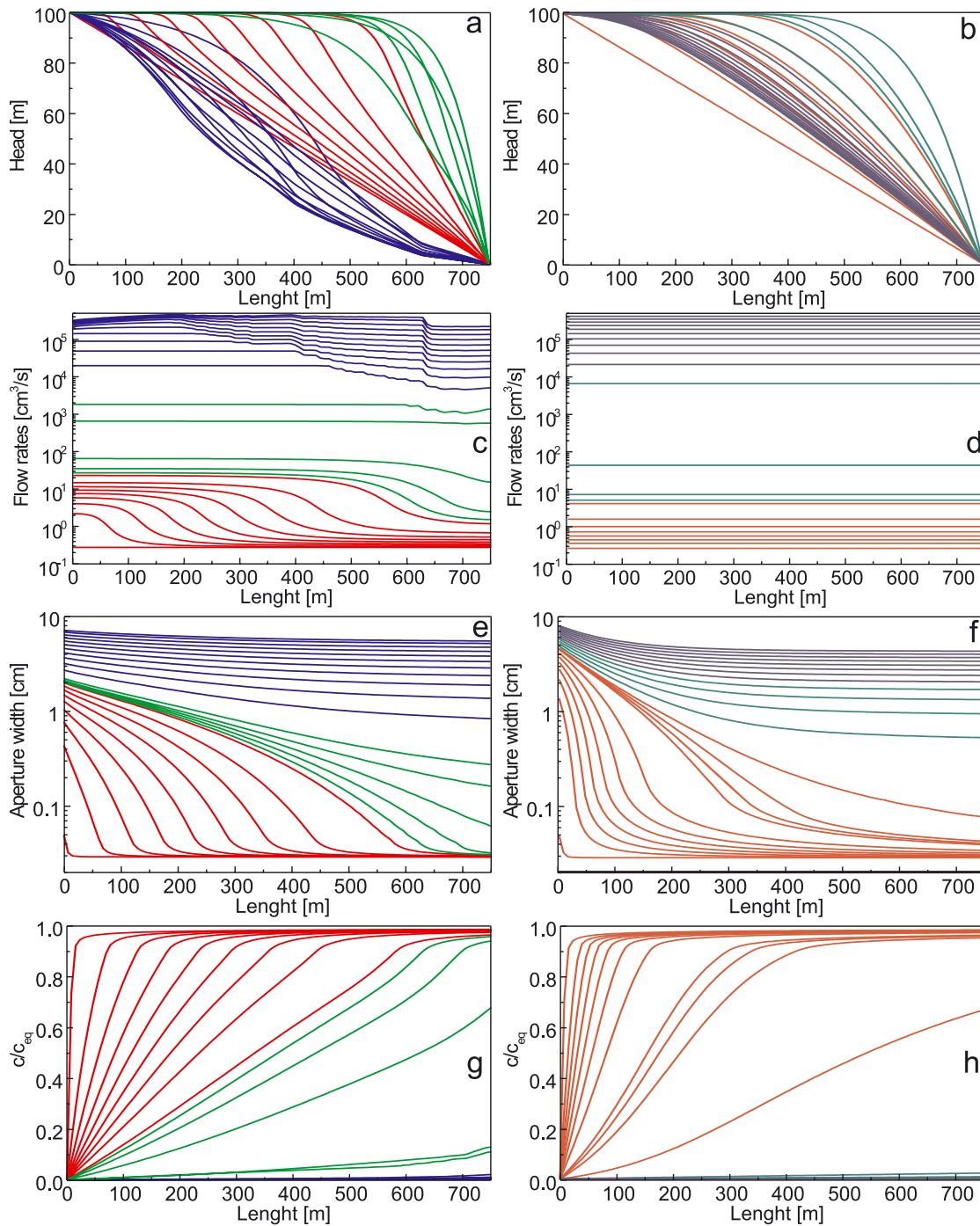


Figure 4.27: Profiles of **a, b**) hydraulic head, **c, d**) flow rate, **e, f**) aperture width and **g, h**) calcium concentration along the central prominent fracture of the aquifer with uniform net of Figure 4.25) (left hand side column) in comparison to the corresponding profiles of an isolated single fracture (right hand side column). In the left hand side column: Red: 0–80 years, every 10 years; green: 82 to 90 years, every 2 years; blue: 90 to 190, every 10 years. In the right hand side column: Red: 0 to 700 years, every 100 years; green: 710–740 years, every 10 years; blue: 750–850 years, every 10 years.

at the input, the increase in calcium concentration is much slower than for the isolated case. Therefore, a deeper zone of effective dissolution widens the profiles faster along the central fracture. These findings clearly demonstrate that the increasing flow into the central fracture enhances karstification. This is a property of 2-D nets. 1-D channels can lose water only at the exit.

The next question to be asked is: How do breakthrough times depend on the coupling ratio $M = \bar{a}_0/A_0$? Figure 4.28 shows the result for $A_0 = 0.03$ cm and 10^{-5} cm $\leq \bar{a}_0 < 0.03$ cm for both a uniform and a statistically distributed net. Breakthrough times drop significantly, if fracture widths increase from 10^{-6} cm ≈ 0 (isolated fracture) to 0.02 cm (i.e. 2/3 of the width of the central fracture). It is interesting to note that although there are clear differences in the evolution of uniform and statistical nets, breakthrough times remain unaffected. One exception is evident, however, for the uniform case. If $a_0 = A_0$ in the uniform case, all fractures are equal and parallel during the entire evolution. No flow can cross perpendicular to the fractures. Therefore, breakthrough time switches to that of an isolated conduit. For statistical nets, however, it remains low even if $\bar{a}_0 = A_0$. More detailed information is available in the thesis of Romanov (2003) and in Romanov *et al.* (2004 a, b). Kaufmann (2003b) has used the scenario presented here as a benchmark for his modeling approach and has confirmed our results. Recently Bauer and Liedl (2003) have reported a similar scenario and found also the same behavior. This gives evidence that different modeling approaches are basically consistent.

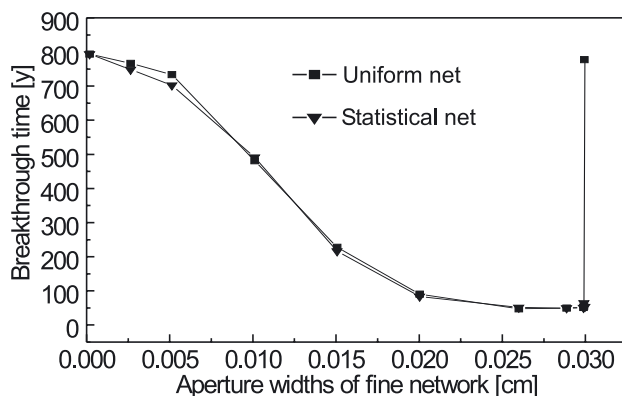


Figure 4.28: Breakthrough times of the scenarios in Figure 4.25 (central fracture, uniform net) and Figure 4.26 (central fracture, statistical net) in dependence on aperture width \bar{a}_0 in the fine net.

4.5.2 Retardation of karstification by flow into prominent fractures

The scenarios of one single prominent fracture exhibit flow from the prominent fracture into the net, but exclude flow from the net into the fracture. In virtually all more complex cases both happens and the effects could counter balance.

Therefore to understand the influence of saturated solutions entering from the net into a prominent fracture we construct a simple confluence. At some position in the prominent fracture which carries flow Q with concentration c , a flow rate q with concentration $c = c_{eq}$ is injected. The new concentration c_m after mixing is then

$$c_m = \frac{Qc + qc_{eq}}{Q + q} \quad 4.5$$

From this one finds the reduction of dissolution rates

$$F(c_m) = F(c) \cdot (Q/(Q + q))^n \quad 4.6$$

where n is the order of dissolution kinetics. For $q = Q$ and $n = 4$ the rates are reduced to $1/32$ of the corresponding rate in an isolated tube. This gives an example of delay for karstification by inflowing solutions close to equilibrium with respect to calcite.

4.5.3 A loop of prominent fractures: An example with inflow and outflow

Before we discuss the dual-fracture aquifer in Figure 4.22 we construct a much simpler system which already shows all features we will find in more complex systems (Gabrovšek *et al.*, 2004).

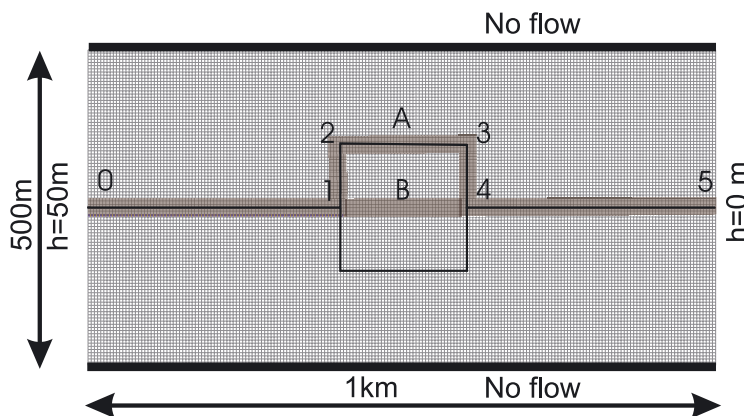


Figure 4.29: The central loop: Modeling domain. Fat lines show a simple system of prominent fractures. Thin lines depict the net of fine fractures with equal aperture widths a_0 . The gray shaded pathway will be used in the following discussion. Boundary conditions can be read from the figure.

Figure 4.29 depicts the modeling domain (standard loop). It consists of a uniform net of dense fissures with aperture widths a_0 . Embedded into this is a central fracture and in addition a square loop in the central part of the domain. In this setting, flow leaving the central fracture at point 1 into the net via the region close to B can reenter the fracture at point 4. Since the available surface area in the net is by orders of magnitude higher and flow rates are much lower than in the central fracture the solutions in the net are very close to saturation with respect to calcite when they reenter the prominent fracture.

In the following, we study the evolution of this simple model in dependence on fracture widths a_0 , whereby $A_0 = 0.03$ cm. Figure 4.30 shows breakthrough times (full circles) as a function of a_0 . For the isolated case ($a_0 = 1 \cdot 10^{-5}$ cm) breakthrough time is about 35 ky. It stays almost constant for $a_0 < 0.00625$ cm. A maximum is attained for $a_0 = 0.005$ cm, and with increasing a_0 the breakthrough time drops by more than one order of magnitude.

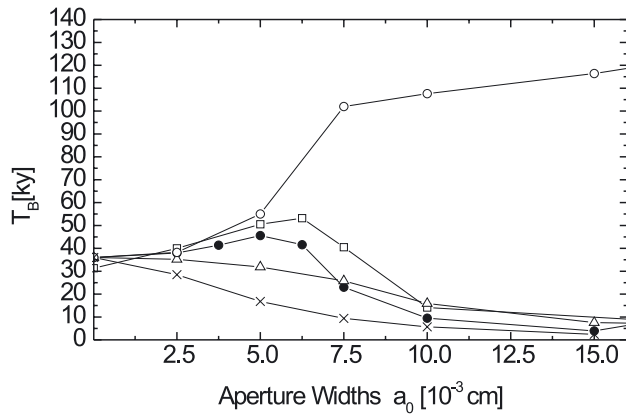


Figure 4.30: Breakthrough times for dual-fracture aquifers with $A_0 = 0.02$ cm as a function of \bar{a}_0 . (•) central loop, (x) central loop with dissolution only in the prominent fractures, (o) central loop, all fractures outside of the square are removed. Exchange of flow is possible only in the interior of the square. (Δ) central loop, all fractures inside the square are removed, (⊗) percolation net embedded into a net of fine fissures.

In the following, we will illustrate the evolution of fracture aperture widths, dissolution rates and flow rates for this scenario with $a_0 = 5 \cdot 10^{-3}$ cm, $a_0 = 0.00625$ cm and $a_0 = 0.01$ cm, respectively (Figures 4.31, 4.32, 4.33).

Figure 4.31 ($a_0 = 5 \cdot 10^{-3}$ cm) depicts the aperture widths by a bar code and the dissolution rates by a color code. The flow rates and flow directions are shown by the right hand side column, with the codes as used in the last chapter (see code box).

In the beginning dissolution rates are high along the first part of the central fracture, which carries a high amount of flow (a, e). There is also flow in the net. Close to the square the fracture loses flow into the net. Highly saturated flow from the net enters into the square at the upstream corners. At the downstream corner fractures of the square lose flow, but then flow from the net enters into the central fracture. After 10 ky a channel propagates down head (b, f), draining most of the flow. After some distance, considerable amounts of this flow are dispersed into the nets. Some of it reenters into the fracture at the downstream side of the loop. After 25 ky the evolving channel along the prominent fracture has invaded the loop (c, g). Most of the flow is attracted by the loop. But a minor part flows along the central pathway until it is injected into the net after a short distance. Some of the flow in the loop enters the net at its downstream part, whereas the remaining flow is drained by the central channel downstream. After 45 ky breakthrough is reached (d, h). Breakthrough time is not much different from that of the isolated loop with $a_0 = 1 \cdot 10^{-5}$ cm, because the enhancement by the out flowing solution is balanced by the reduction of dissolution rates in the downstream region of the central fracture, where almost saturated water enters from the net. Note that the color code for dissolution rates is also indicative for the state of saturation (red highly undersaturated, blue-black close to equilibrium).

4. MODELING KARST EVOLUTION ON TWO-DIMENSIONAL NETWORKS: CONSTANT HEAD BOUNDARY CONDITION

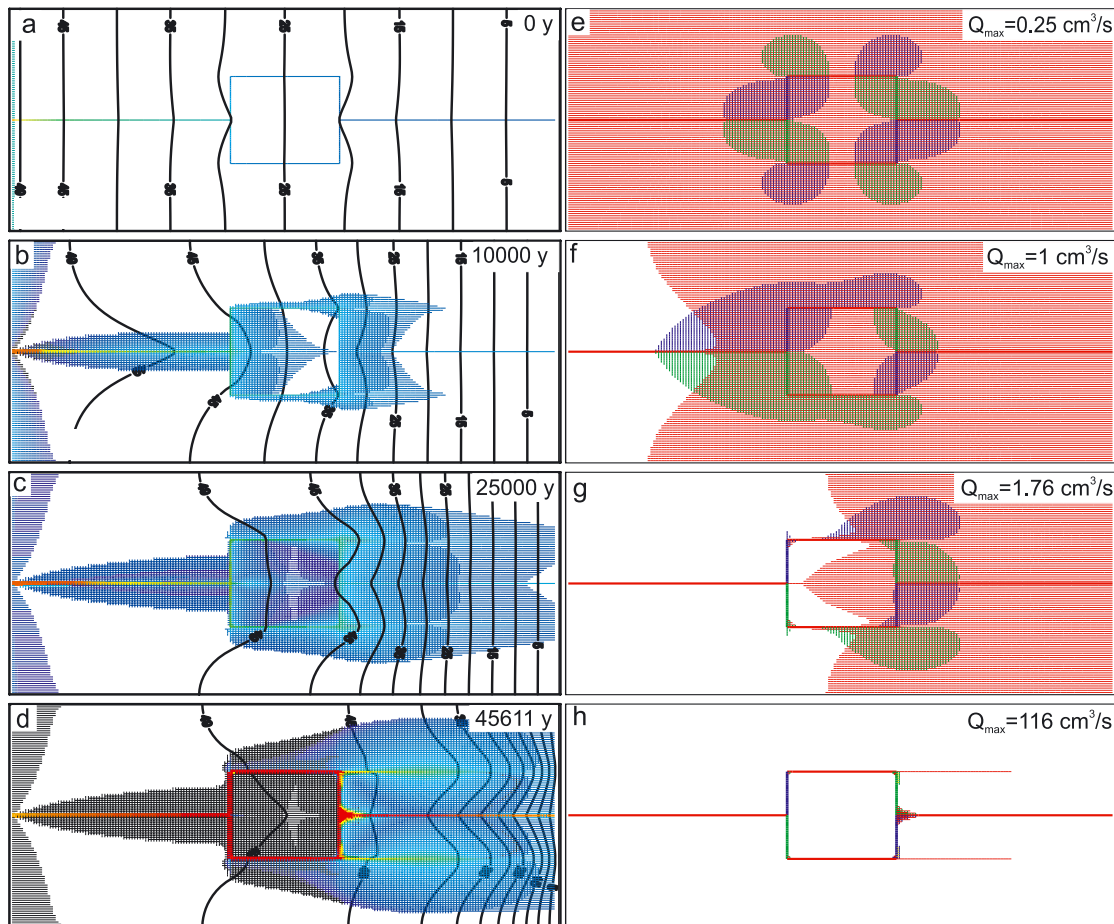


Figure 4.31: Evolution of the central loop scenario in Figure 4.29. Uniform net of fine fissures with $a_0 = 0.005$ cm, $A_0 = 0.02$ cm. Left hand side: aperture widths and dissolution rates. Right hand side: flow rates and flow directions. $p_{CO_2} = 0.05$ atm, $c_{in} = 0$ at all input points.

The next series of Figure 4.32 illustrates the evolution for $a_0 = 0.00625$ cm. For the first 20 ky it is similar to that of Figure 4.32 (a, e, b, f). At 30 ky a new feature arises (c, g). A considerable amount of aggressive flow is lost from the downstream corners of the square loop. Some of this solution flows straight through the net, to the output boundary. On the other hand flow from the downstream side of the square reenters the fracture and inhibits dissolution there. By this way channels evolving from the downstream corners of the square straight through the net are more competitive, although they are much narrower. They become the winners in the race for breakthrough at 40 ky (d, h).

As a_0 is further increased to 0.01 cm, initially, much more flow is carried in the net. As the central channel propagates downstream, due to the high coupling, much of its flow is lost into the net, accelerating its downstream migration (a, e). After 4 ky the conduit has reached the square (b, f). A more favorable region for dissolution is now the inner part of the square where hydraulic gradients are steep and where a small (yellow) zone of relatively high dissolution rates has developed. After 8 ky (c, g) flow is channeled

into a straight conduit in the center of the loop, which joins the downstream prominent fracture. The flow lost into the net is drained by fine fissures and does not return into the central fracture. Therefore, breakthrough occurs after 9.2 ky through the square and then along the central fracture (d, h). Flow now is limited to this central channel.

It is remarkable what variety of evolution patterns become possible even in such a simple dual-fracture model. They are determined by the interplay between exchange of flow, but also by the competition of alternative pathways through the net of fine fractures. Increasing coupling favors the latter mechanism and is the main reason for reduced breakthrough times.

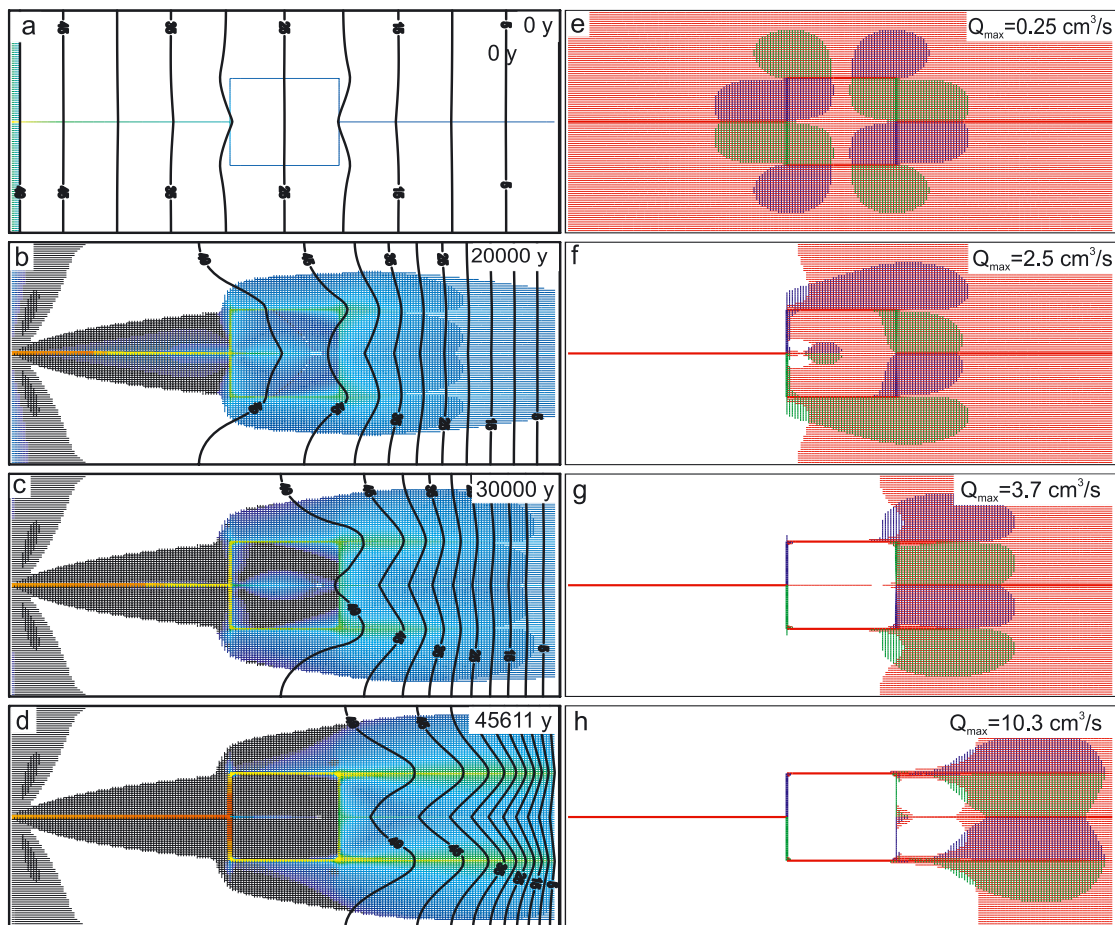


Figure 4.32: Evolution of the central loop aquifer in Figure 4.29. Other parameters and boundary conditions as in previous Figure 4.31 except fracture widths a_0 of fine fissures, $a_0 = 0.00625$ cm.

To further elucidate the role of saturated solutions reentering into prominent fractures we have performed two more simulations on the loop. In the first case we allow dissolution only in prominent fractures. The corresponding breakthrough times are depicted by crosses in Figure 4.30. In all cases they are lower than in the standard loop, because water reenters prominent fractures now with the same concentration it left them and therefore does not reduce dissolution rates.

The opposite behavior is found, if one removes all fine fractures outside the square. Then exchange flow from the central fracture is restricted to the region inside the square loop. When flowing through fractures inside the square the solution attains a high calcium concentration. Consequently, when it flows back to the prominent fracture dissolution rates are reduced there. In all these cases one therefore expects breakthrough times higher than those of the standard loop of Figure 4.29. This, indeed is the case, as can be seen from the open circles in Figure 4.30.

If we remove all fractures inside the square but keep those outside, flow into the center of the square is avoided. In consequence less saturated solution enters the prominent fractures and breakthrough times are smaller than in the previous scenario. This is shown by open triangles in Figure 4.30.

Profiles of dissolution rates

Another way to show the inhibition of dissolution rates is to investigate their profiles along the prominent fractures in the pathway 0–1–2–3–4–5 (see Figure 4.29). These are shown by dotted lines in Figure 4.34 for the scenario with $a_0 = 5 \cdot 10^{-3}$ cm depicted in Figure 4.31. For comparison full lines depict profiles of dissolution rates for the isolated loop, $a_0 = 10^{-5}$ cm.

At the onset of karstification rates are equal to those of the isolated system for the first 400 m from the input point 0 to point 1. Due to the almost saturated solution flowing from the net into the fracture between points 1 and 2, the rates drop drastically there. They stay almost constant between points 2 and 3 and drop again between points 3 and 4 because solution close to equilibrium enters from the net. In the last section, rates are lower by almost two orders of magnitude compared to the isolated case. After 10 ky, however, rates at the entrance have become higher compared to the isolated case, because of increasing exchange flow leaving the fracture. Due to the injection of saturated solution, rates still drop in regions 1–2 and 3–4. This pattern persists but smoothes out during time until breakthrough. It is evident that the advantage of flow leaving the fracture is overcompensated by returning flow inhibiting dissolution.

The evolution of the aquifer becomes even more complex, when short cuts through the net arise. This is the case for $a_0 = 0.01$ cm, depicted by Figure 4.33a–d. Here, rates along two pathways are compared (see Figure 4.29). Pathway 1 is along the points 0–1–2–3–4–5 of the prominent fractures. Pathway 2 takes the short cut between points 1–4 through the net. Figure 4.35 illustrates the dissolution rates along these two pathways. Full lines illustrate dissolution rates along pathway 1. Dotted lines show the dissolution rates in the short cut between 400 and 600 m. Otherwise pathway 1 and 2 coincide. The length of pathway 1 is 1200 m, that of pathway 2 is 1000 m.

4. MODELING KARST EVOLUTION ON TWO-DIMENSIONAL NETWORKS: CONSTANT HEAD BOUNDARY CONDITION

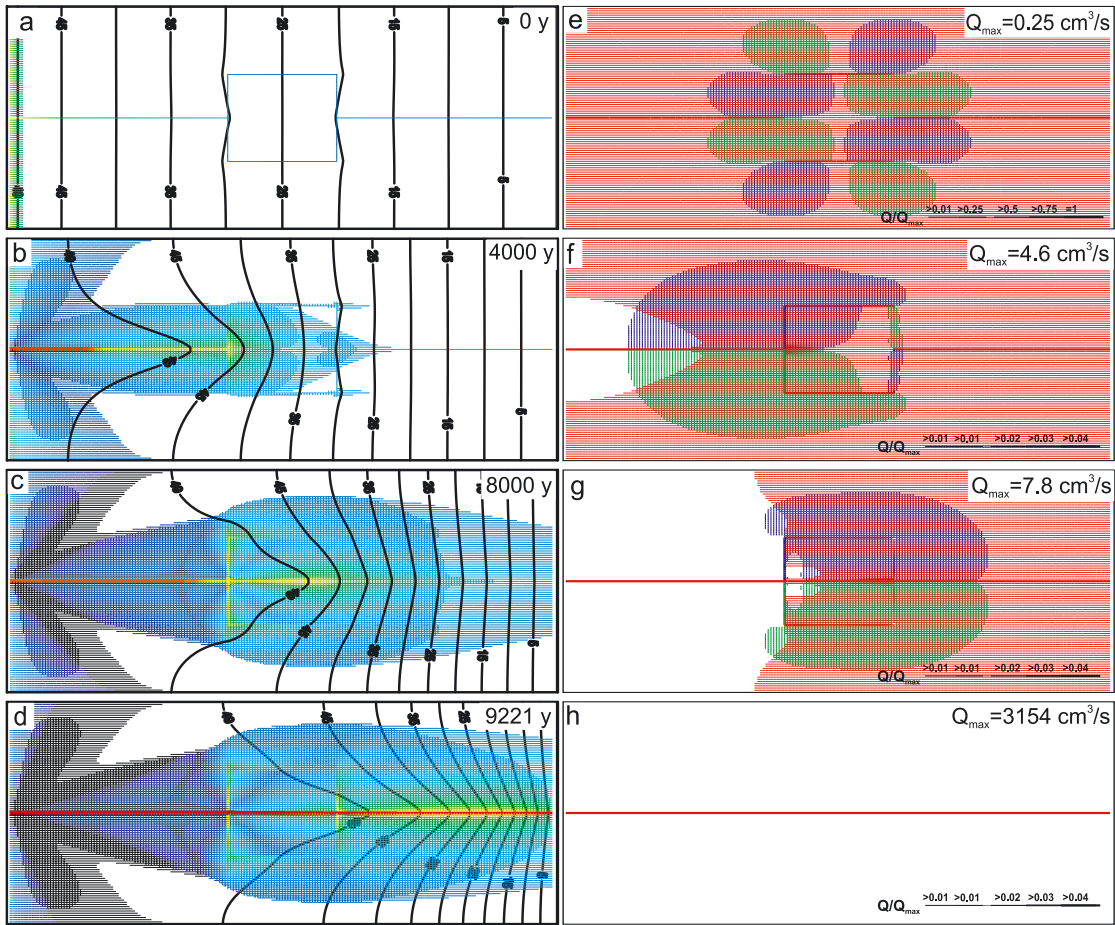


Figure 4.33: Evolution of the central loop aquifer in Figure 4.29. Now $a_0 = 0.01$ cm. Other parameters and boundary conditions as in Figure 4.31.

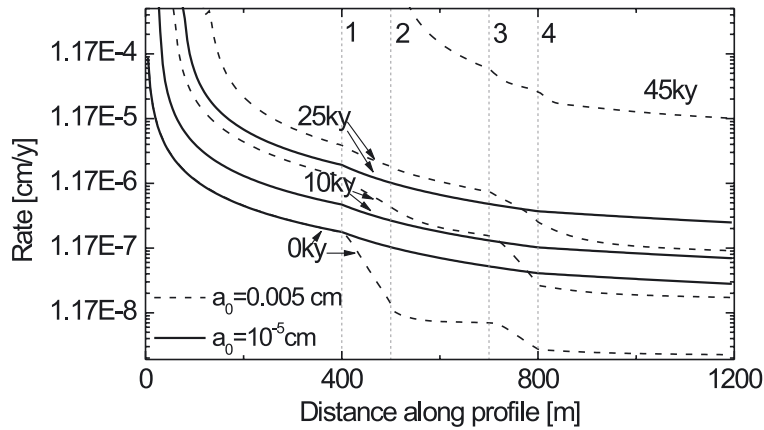


Figure 4.34: Dissolution rates in the central loop scenario along the pathway 0–1–2–3–4 marked in Figure 4.29. The dashed line depicts the profiles taken from Figures 4.31 a–d, $a_0 = 0.005$ cm. Full lines show the flow rates for an isolated system of prominent fractures ($a_0 = 0$ cm) for comparison.

4. MODELING KARST EVOLUTION ON TWO-DIMENSIONAL NETWORKS: CONSTANT HEAD BOUNDARY CONDITION

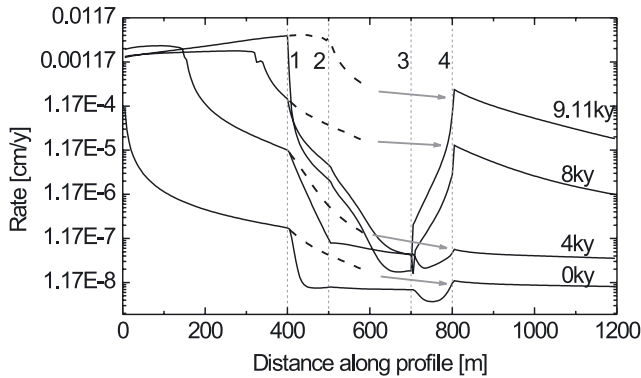
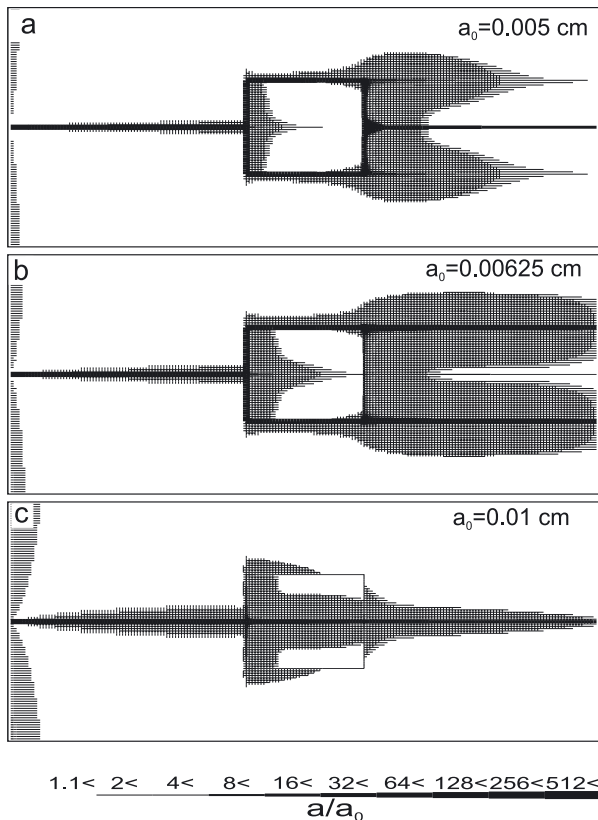


Figure 4.35: Dissolution rates in the central loop scenario along pathway 0–1–2–3–4 of Figure 4.29 for the evolution in Figures 4.33 a–d, $a_0 = 0.01$ cm (full lines). Dashed lines show the profiles through the short cut 1–4.

At the onset ($t = 0$), dissolution rates along section 0–1 drop by almost three orders of magnitude. Along section 1–2 a further decrease by one order of magnitude occurs. Then, along section 2–3, dissolution rates remain low and constant. They even drop further at the beginning of section 3–4. Due to inflowing water that passed the net along the later short cut 1–4, dissolution rates begin to rise at the exit of section 3–4. This water has a lower degree of saturation as that to which it mixes in section 3–4. This can also be seen from the profile of higher dissolution rates along the short cut 1–4 (dotted line). After 4000 y the profile remains similar, although dissolution rates have increased significantly. After 8000 y dissolution rates are high in the region of the shortcut. When

water of comparatively low calcium concentration from this region enters into section 3–4 rates along pathway 3–4 rise significantly to meet those along the shortcut at point 4. This scenario clearly elucidates the competitive role of short cuts between prominent fractures.



To summarize and to illustrate the sensitivity of aquifer evolution to the hydraulic coupling parameter a_0/A_0 , Figure 4.36 shows the aperture width at breakthrough for the standard loop with $a_0 = 0.01$ cm, $a_0 = 0.00625$ cm, $a_0 = 0.005$ cm. Detailed information on dual-fracture aquifers and the mechanisms described above is given by Gabrovšek *et al.* (2004).

Figure 4.36: Aperture widths at breakthrough for the central loop aquifers of Figures 4.31 – 4.33.

4.5.4 The dual-fracture aquifer: A percolation-net of prominent fractures embedded into a statistical net of fine fractures

We now proceed to a modeling domain much closer to nature. The dimensions and boundary conditions are identical to the modeling domain scenario of Figure 4.29. What has been changed is the structure of the aquifer (Figure 4.37). We have first created a system of prominent fractures (fat lines) by constructing a percolation net on a coarse grid of $50\text{ m} \times 50\text{ m}$. The occupation probability for a prominent fracture is $p = 0.6$. The width of all prominent fractures is $A_0 = 0.02\text{ cm}$. The fine fracture net on a grid size of $5\text{ m} \times 5\text{ m}$ is created by assigning statistically distributed (see Figure 4.12b) aperture widths \bar{a}_0 to all fractures, which are not occupied by prominent fractures. This aquifer contains isolated prominent fractures, but also percolating pathways. One of them is shown by a gray shade along the points 1 to 12. It is obvious that the structure of scenario A is contained as an element in this net.

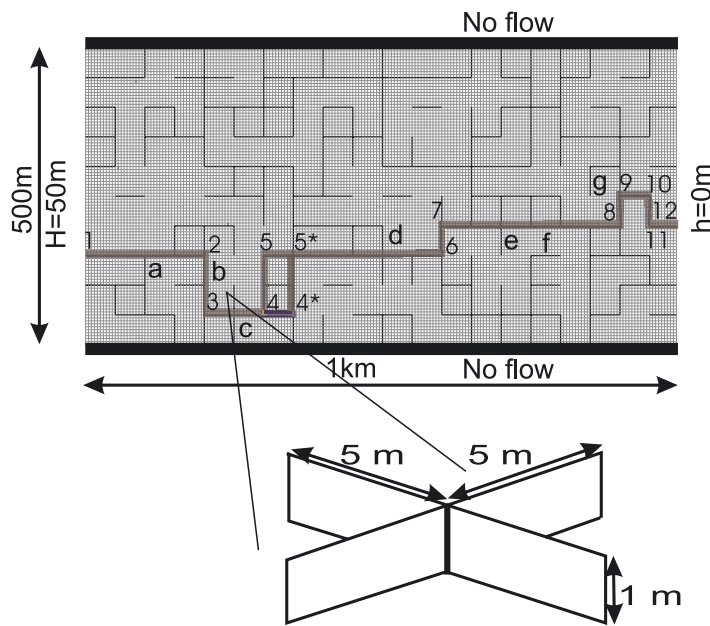


Figure 4.37: Modeling domain of a dual-fracture aquifer. Fat lines mark prominent fractures of 50 m length with an aperture width $A_0 = 0.02\text{ cm}$. Thin lines represent the net of fine fissures of 5 m length with lognormally distributed aperture widths a_0 . The gray shaded pathway 1–12 along prominent fractures, connecting input 1 and output 12, shows the pathway of breakthrough for $\bar{a}_0 = 0.005\text{ cm}$ and is depicted here for later discussion. Letters a–g designate points of confluence within the net of prominent fractures. Boundary conditions can be read from the figure.

4.5.5 Results and discussion

In the following we will show the results of model runs for various aperture widths \bar{a}_0 . In all these simulations the chemical composition of the input solution is $c_{in} = 0$ and $p_{CO_2} = 0.05$ atm.

Figure 4.38a–h shows the evolution of the isolated net of prominent fractures ($A_0 = 0.02$ cm, $a_0 = 0$ cm). The left hand side column shows aperture widths and dissolution rates. The right hand side column depicts flow rates and their directions. At the beginning ($t = 0$) flow through input point 1 (see Figure 4.37) is high and is distributed along some favorable fractures (e). Dissolution rates are high at entrance point 1 (a). After 12 ky the flow pattern remains similar, but the front of high dissolution rates has further invaded into the aquifer. Competing pathways still transport most of the flow similar as at time zero (Figure 4.38b, f). After 20 ky (Figure 4.38c, g) water preferen-

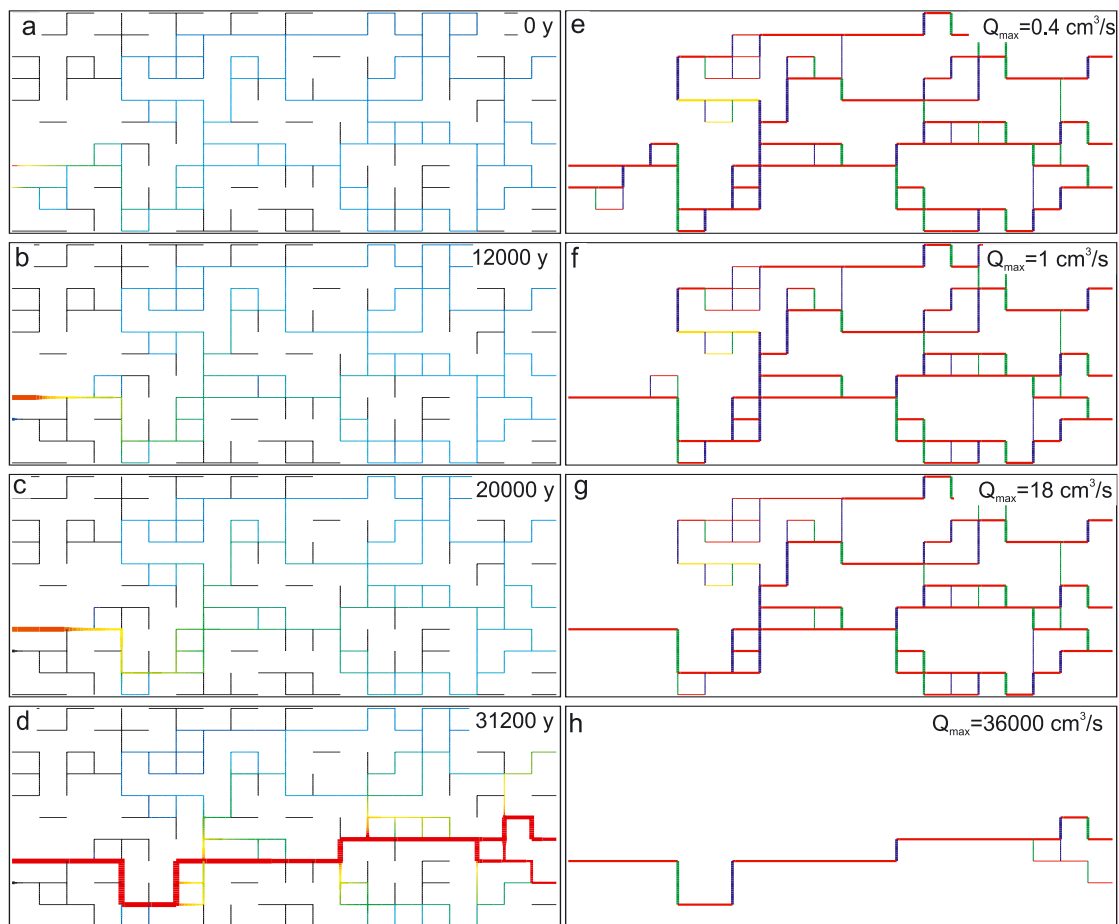


Figure 4.38: Evolution of aperture widths and dissolution rates (left hand side) and flow rates and directions (right hand side) for the dual-fracture aquifer shown in Figure 4.37. In this case prominent fractures are isolated by setting $\bar{a}_0 = 0$, $A_0 = 0.02$ cm, $p_{CO_2} = 0.05$ atm, $c_{in} = 0$.

tially flows along the lower pathway and high dissolution rates have penetrated further. At breakthrough after 31 ky (Figure 4.38d, h) all flow is carried by one single pathway. This behavior is well known from earlier modeling.

In Figure 4.39a–h \bar{a}_0 has been changed to 0.0025 cm. At time zero, in contrast to the isolated net of prominent fractures, especially in the entrance region, flow is more evenly distributed in prominent fractures, because the net of fine fractures carries flow between them. After 20 ky (Figure 4.39b, f) the evolution of dissolution rates along prominent fractures is similar to that of the isolated case at the same time. After 35 ky (Figure 4.39c) dissolution is active in the lower part of the domain and at 40 ky breakthrough occurs on a pathway, which, although not identical, is very similar to that of Figure 4.38d. The hydraulic coupling by fine fractures has not changed the overall behavior, but has retarded breakthrough by 9000 y.

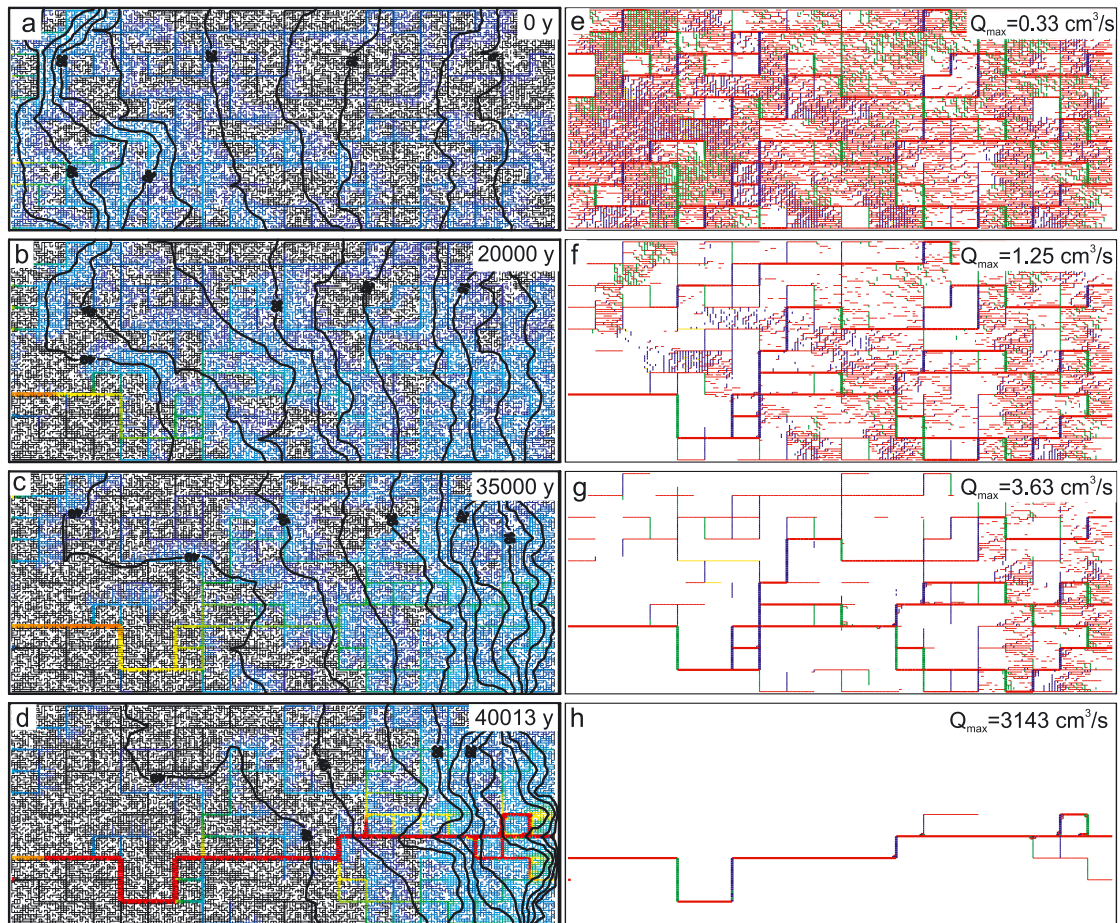


Figure 4.39: Evolution of aperture widths and dissolution rates (left hand side) and flow rates and directions (right hand side) for the dual-fracture aquifer shown in Figure 4.37. Weak hydraulic coupling, $\bar{a}_0 = 0.0025$ cm, $A_0 = 0.02$ cm, $p_{CO_2} = 0.05$ atm, $c_{in} = 0$.

Figure 4.40a–h shows the evolution caused by a further increase in the hydraulic coupling ($\bar{a}_0 = 0.005$ cm). There is intensive exchange of flow between prominent fractures and the net. Although this does not change the evolution in the first 20 ky (Figure 4.40a, e), one can see that the dissolution front has been retarded. Redirected flow into fractures delays breakthrough, which occurs at 50500 y (Figure 4.40d, h). In contrast to the evolution with $\bar{a}_0 = 0.0025$ cm, the exit region shows a complex structure, indicating shortcuts through the net.

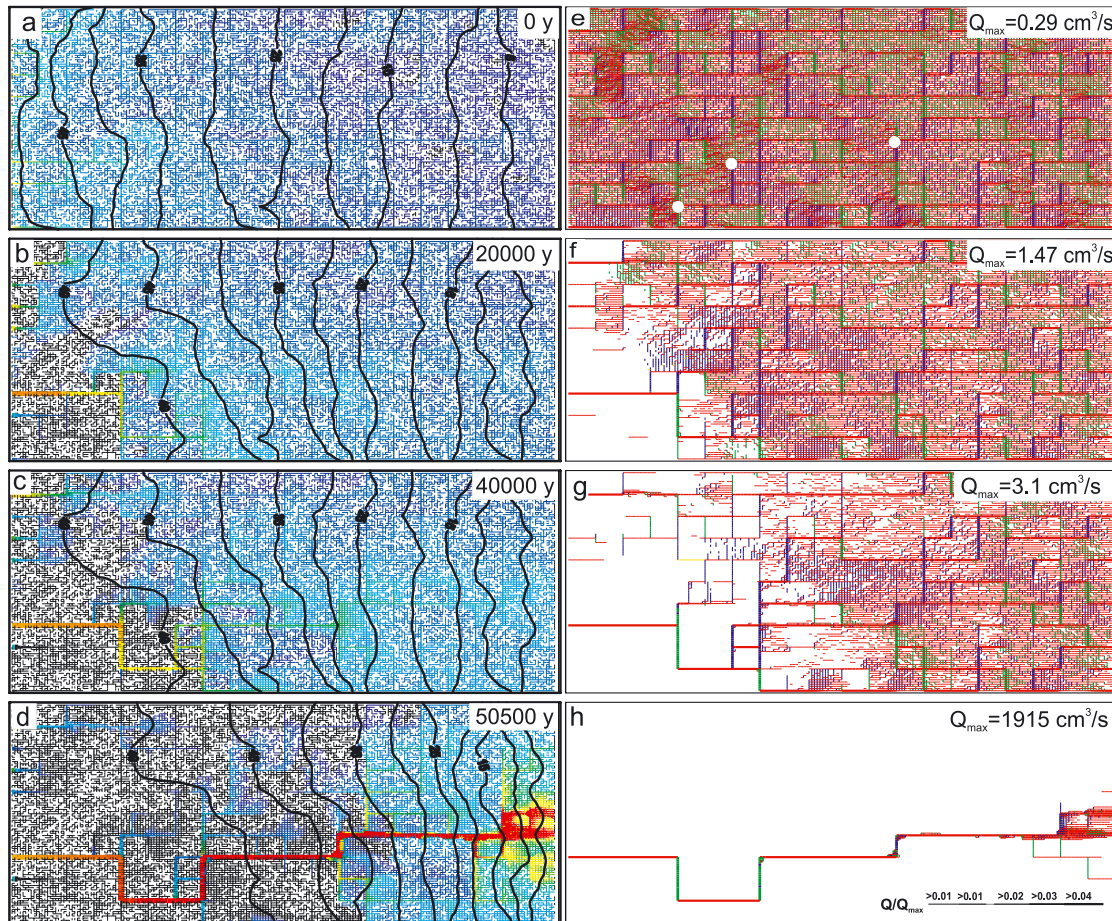


Figure 4.40: Evolution of aperture widths and dissolution rates (left hand side) and flow rates and directions (right hand side) for the dual-fracture aquifer shown in Figure 4.37. Moderate hydraulic coupling, $\bar{a}_0 = 0.005$ cm, $A_0 = 0.02$ cm, $p_{CO_2} = 0.05$ atm, $c_{in} = 0$. The white dots in (e) mark sites where flow from the net enters prominent fractures. The bar code for the flow rates differs from the one given in code box and is given in figure h.

Figure 4.41 shows profiles of dissolution rates along the pathway 1–12 for the isolated case and along pathway 1–12 via 4*–5*, which has been taken at breakthrough for $\bar{a}_0 = 0.005$ cm (see Figure 4.37, and Figure 4.40). Dissolution rates for the isolated case show some minor drops at the positions a, b, c, d, e, f and g, which are also denoted in Figure 4.37. At these points, junctions of prominent fractures occur and the mixed solutions exhibit increased calcium concentrations. The reason for this is that

the percolation pathways, joining pathway 1–10, are much longer, and therefore their Ca-concentration is higher.

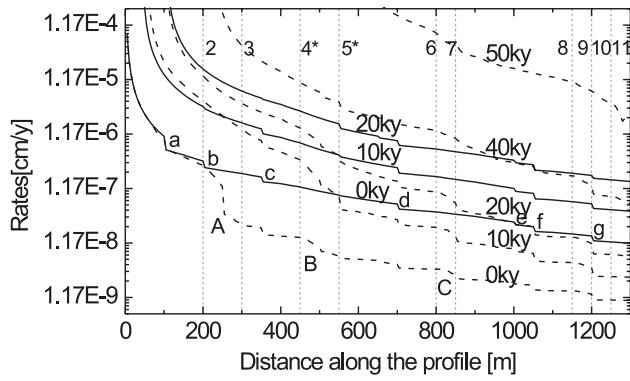


Figure 4.41: Dissolution rates in the dual-fracture aquifer of Figure 4.37 along pathway 1–12. The isolated case, $\bar{a}_0 = 0$ cm, of Figures 4.38 a-d is shown by full lines. Dashed lines designate moderate hydraulic coupling of $\bar{a}_0 = 0.005$ cm, Figures 4.40 a-d. The pathway is now taken via 1–4–4*–5*–6–12 as depicted in Figure 4.37. Points a-g denote junctions of prominent fractures. Points A, B and C, marked by arrows in Figure 4.40, are locations where flow almost saturates from the net enters into a prominent fracture and causes reduced dissolution rates.

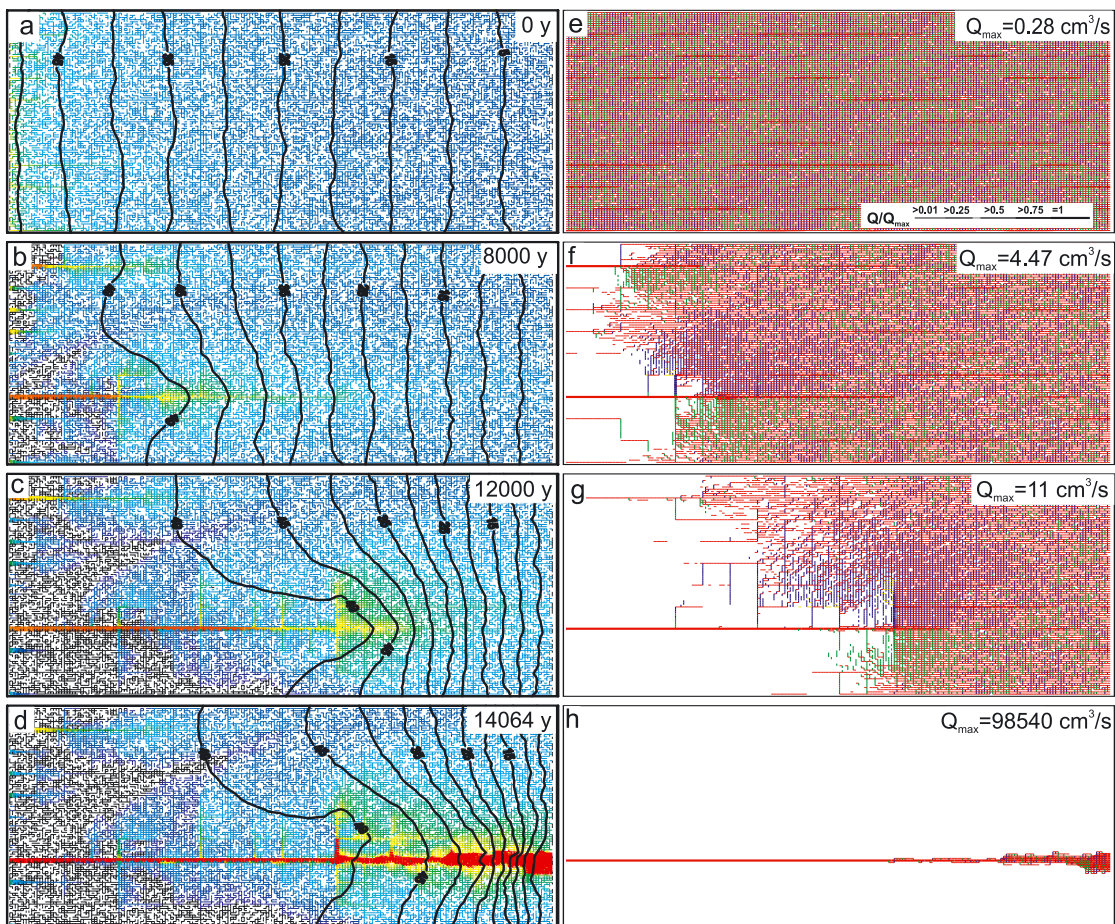


Figure 4.42: Evolution of aperture widths and dissolution rates (left hand side) and flow rates and directions (right hand side) for the dual-fracture aquifer in Figure 4.37. Strong hydraulic coupling, $\bar{a}_0 = 0.01$ cm, $A_0 = 0.02$ cm, $p_{CO_2} = 0.05$ atm, $c_{in} = 0$.

If the system of prominent fractures is embedded into the net, flow from prominent fractures is injected into the net, but then again flows back. A, B and C mark such points and are also shown by white dots in Figure 4.40e. It can clearly be seen that at these points solution from the net flows into the fracture. This causes a drastic decrease of dissolution rates. Although more complex, the dissolution rates in principle show the same behavior as those of the simple standard loop (see Figure 4.34). With increasing time, the exchange of flow in the upstream part of the winning pathway is diminished. Therefore, profiles smooth out. It is also interesting to note that for dual-fracture nets the dependence of breakthrough times on the aperture widths a_0 of the continuum resembles that of the loop. This is shown by the open squares in Figure 4.30.

The last figure in this section shows the evolution for $\bar{a}_0 = 0.01$ cm, when alternative pathways through the net become more likely. (Figure 4.42a–h). At $t = 0$ flow is evenly distributed in the net (a, e). At the entrances dissolutional activity has created a narrow fringe along the fine fractures and a dissolution front enters deeper via the prominent ones. After 8000 y the lower fracture 1–2 is more competitive and a shortcut through the net between points 2 and 5 is more favorable than following the loop. After 12 ky the dissolutional channel has followed the prominent fracture along 5 to 6. But instead following the pathway 6–7–8–9–10–11–12 along the fracture, breakthrough occurs by a shortcut from point 6 straight to the exit boundary.

In summary Figure 4.43a–d for comparison illustrates the patterns of the fracture widths at breakthrough for the four cases of the dual-fracture aquifer shown by Figure 4.38, Figure 4.39, Figure 4.40 and Figure 4.42.

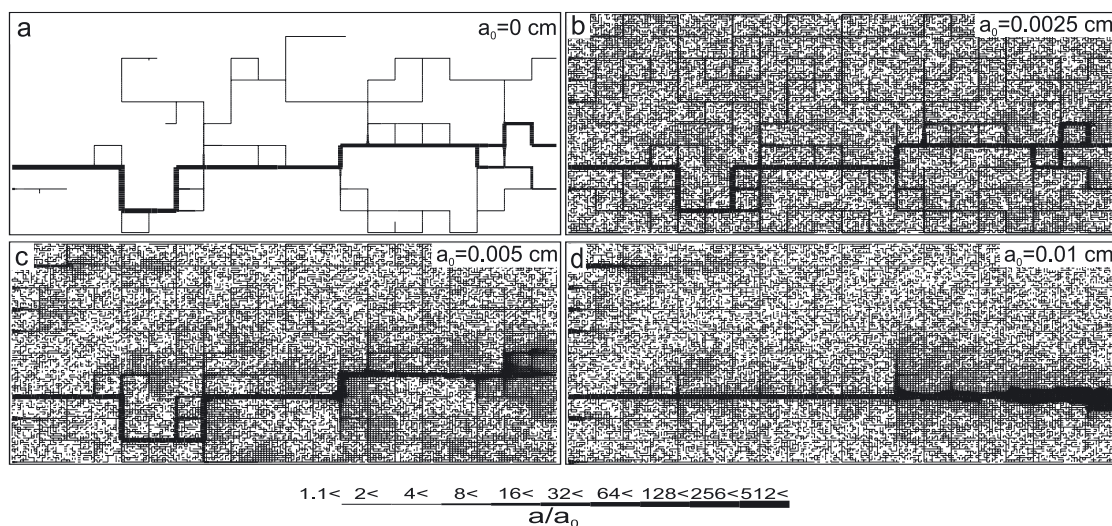


Figure 4.43: Distribution of fracture aperture widths at breakthrough in the dual-fracture aquifer in Figure 4.37 with various hydraulic coupling: **a)** $\bar{a}_0 = 0$ (Figure 4.38), **b)** $\bar{a}_0 = 0.0025$ cm (Figure 4.39), **c)** $\bar{a}_0 = 0.005$ cm (Figure 4.40) and **d)** $\bar{a}_0 = 0.01$ cm (Figure 4.42).

To conclude this section it should be stated that changing hydrological conditions in a simple constant head domain, such as the structure of the fracture net, and the

aperture widths of fractures, or imposing additional boundary conditions leads to an overwhelming variety of resulting structures. To understand these it is necessary to know the basic mechanisms underlying them. This can be achieved by analyzing simple structures before tackling complex ones.

4.6 GEOCHEMICAL BOUNDARY CONDITIONS

So far, we have assumed simple chemical boundary conditions with $c_{in} = 0$ and equal initial p_{CO_2} at all the inputs to the aquifer.

If these conditions are relaxed a variety of new features occurs. When c_{in} approaches c_{eq} the breakthrough mechanism could be switched off, as we have shown already for single 1-D conduits. Furthermore if the compositions of the inflowing solutions vary in space mixing corrosion occurs deep in the aquifer and can become of high significance for its further evolution. In this section we will study the influence of such changes to the evolution of karst aquifers.

4.6.1 Influence of the input concentration

Up to now, in all our considerations, we have assumed that the water entering into the fracture is in equilibrium with some p_{CO_2} , but has not yet dissolved limestone. This may not be realistic because there is dissolution in the subcutaneous zone and it might well be that water with concentrations close to equilibrium enters into the fracture system of the compact bedrock below. We have discussed this for a single fracture in Section 3.1.3. We have seen that breakthrough times are only little affected, when the inflowing water has a concentration not higher than c_s , the concentration where the kinetics switches to a non-linear regime. The reason for this is that the penetration depth, where linear dissolution kinetics is active, is short in comparison to the length of the one-dimensional fracture. Therefore, high order kinetics governs almost along the entire fracture.

For input concentrations $c_{in} > c_s$ the positive feedback mechanism becomes continuously weaker with increasing c_{in} . This can be seen from Eq. 3.28. If the input concentration comes closer to equilibrium with respect to calcite the higher order penetration length λ_n approaches infinity (see Eqs. 3.24, 3.25). Therefore, rates become low at high input concentrations, but they do no longer drop significantly, when the solution flows downstream. In other words: If the higher order penetration distance λ_n exceeds the length of the fracture by more than one order of magnitude, the summand containing λ_n in Eq. 3.28 can be neglected and the rate becomes low and almost constant along the entire length of the fracture.

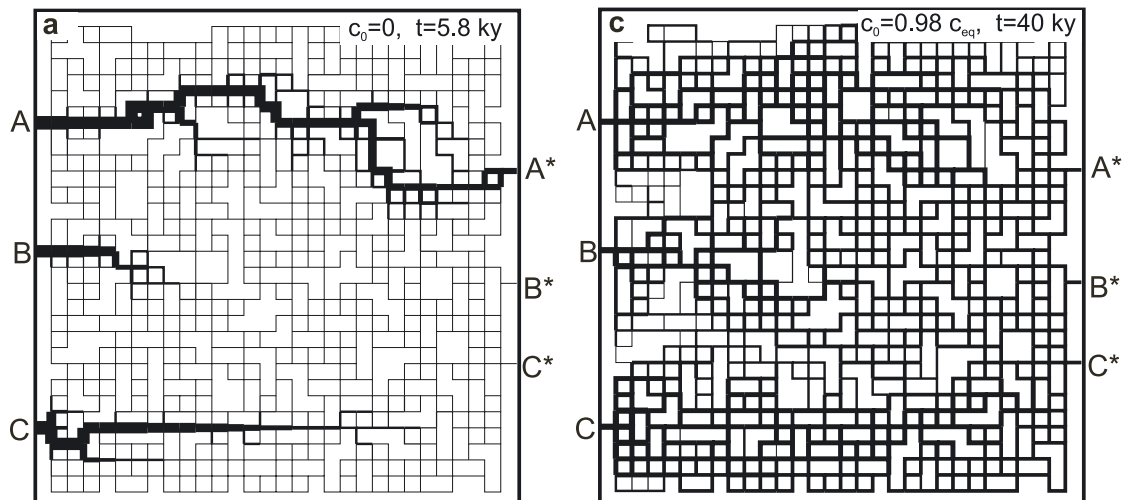
Once again, considering that the basic element of nets is the single one-dimensional conduit, one could expect a similar behavior in two-dimensional nets.

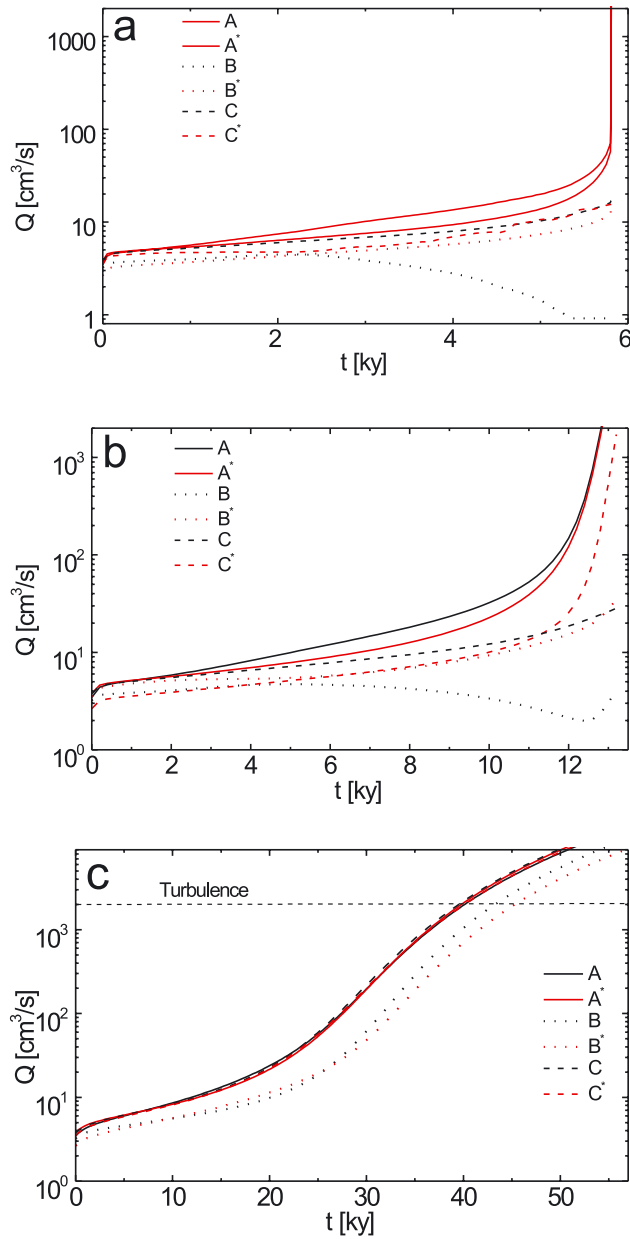
Percolation networks

We now investigate the influence of c_{in} on the evolution of karst aquifers in percolation nets. Therefore, we have fixed the input concentrations c_{in} to values of $c_{in} = 0$ (a), $c_{in} = 0.95c_{eq}$ (b) and $c_{in} = 0.98c_{eq}$ (c) at all three input points in the percolation net of Figure 4.3. Other parameters and boundary conditions are as in Figure 4.3.

Figure 4.44 shows the aperture width of the aquifers for these scenarios at breakthrough, when flow becomes turbulent. For $c_{in} = 0$ (a), breakthrough occurs at 5.81 ky in the upper branch along a preferential pathway with little ramification. The aquifer shows three restricted areas of conduit formation. Increasing c_{in} to $0.95c_{eq}$ (b) changes the pattern considerably. First, the upper branch becomes more braided and connects to both output points A* and B*, in contrast to the previous case. Furthermore, the lower channels have penetrated deeper downstream and show many side branches. Breakthrough time has increased to 12.8 ky. The differences between (b) and (a) reflect that dissolution rates are lower for a higher c_{in} and are more evenly distributed in the neighborhood of leading conduits. Changing c_{in} to $0.98c_{eq}$ (c) enhances this effect. Now, almost all fractures in the net experience slow widening and a highly integrated maze like network is obtained at a time of 40 ky, when flow becomes turbulent.

Figure 4.44: Percolation network of Figure 4.3 at breakthrough with different calcium input concentrations. Distribution of aperture widths. **a)** $c_{in} = 0$, **b)** $c_{in} = 0.95c_{eq}$, **c)** $c_{in} = 0.98c_{eq}$. Note increasing breakthrough time when c_{in} approaches equilibrium. Other parameters and boundary conditions as in Figure 4.3. $p_{CO_2} = 0.05$ atm.





The decreasing strength of the feedback loop is also illustrated by Figure 4.45a–c, which depicts flow rates through the three input points A, B, C and the output points A*, B*, C* respectively. For $c_{in} = 0$ (a) there is a clear steep breakthrough through A–A*, whereas the flow through input B is low and decreases in time. For $c_{in} = 0.95c_{eq}$ (b) we find high flow rates at points A, A* and C*, but flow through input B is still low. The rise of flow, although still rapid, is less steep. Finally, for $c_{in} = 0.98c_{eq}$ (c) all input and output points carry flow increasing smoothly in time. This behavior reflects the switch off of the feedback loop and resembles that of single conduits discussed in Chapter 3.

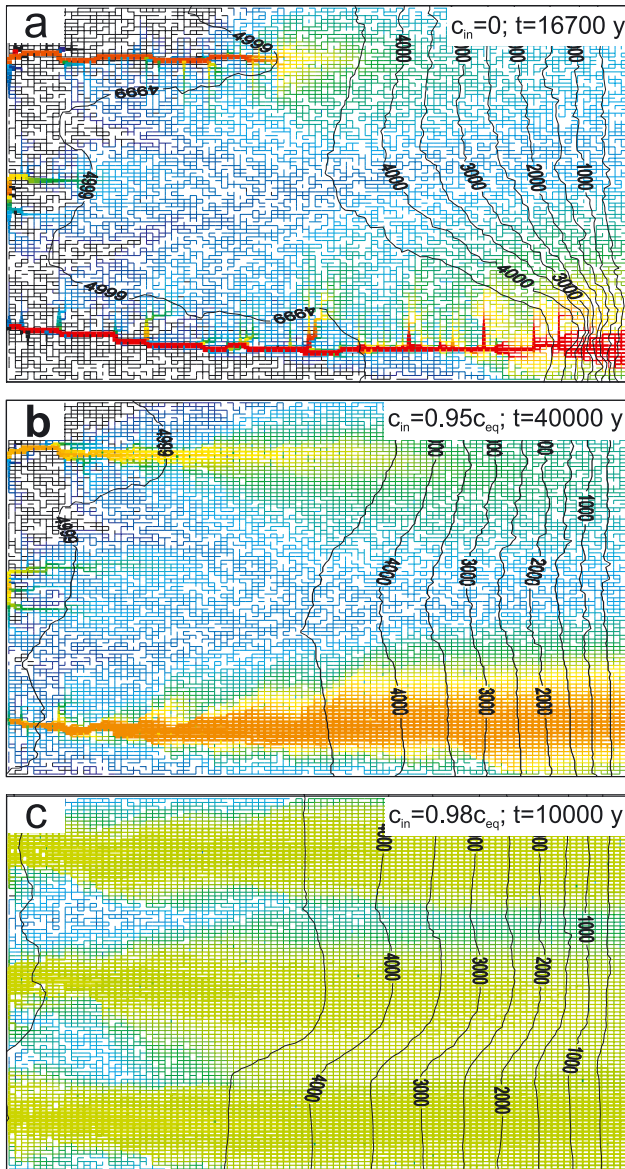
Figure 4.45: Evolution of flow rates in the percolation net through input points A, B, C and output points A*, B*, C* as depicted in previous figure. **a)** $c_{in} = 0$, **b)** $c_{in} = 0.95c_{eq}$, and **c)** $c_{in} = 0.98c_{eq}$.

Statistical networks

We now turn to statistical networks. The influence of the input concentration on the evolution of the standard statistical net with $\bar{a}_0 = 0.02$ cm and $p_{CO_2} = 0.05$ atm (Figure 4.12 and Figure 4.14) is shown by Figure 4.46a–c, for input concentrations of $c_{in} = 0$, $c_{in} = 0.95c_{eq}$, and $c_{in} = 0.98c_{eq}$.

Figure 4.46 shows the structure at the time, when flow becomes turbulent (see code box). The bar code depicts aperture widths and the color code dissolution rates. The behavior is very similar to that of the percolation nets. The closer c_{in} approaches c_{eq} the longer

4. MODELING KARST EVOLUTION ON TWO-DIMENSIONAL NETWORKS: CONSTANT HEAD BOUNDARY CONDITION



is the time to reach turbulent flow, and with increasing c_{in} the regions affected by dissolutional widening spread out. It is evident that with increasing c_{in} rates become lower and more widely distributed in the net. Figure 4.47 shows the time dependence of the total flow rate through the domain for the three c_{in} in Figure 4.46.

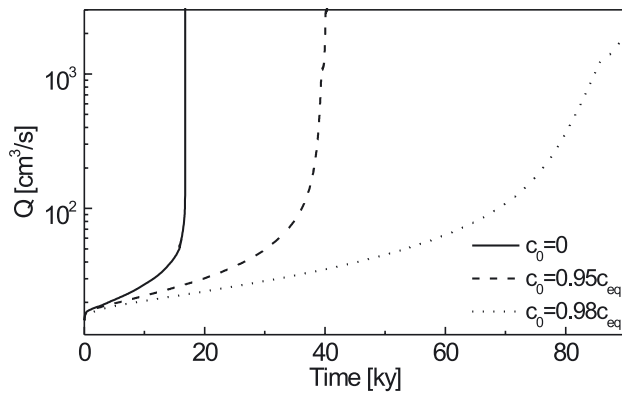


Figure 4.46: The statistical 2D-net aquifer of Figure 4.14 at breakthrough for various calcium input concentrations c_{in} . Distribution of aperture widths and dissolution rates. **a)** $c_{in} = 0$, **b)** $c_{in} = 0.95c_{eq}$, and **c)** $c_{in} = 0.98c_{eq}$. Other parameters and boundary conditions as in Figure 4.14.

Figure 4.47: Evolution of total flow for the statistical 2D-net aquifers presented in the previous Figure 4.46.

For $c_{in} = 0$ the steep breakthrough curve is typical. For higher $c_{in} = 0.95c_{eq}$ breakthrough is retarded and the increase is less steep. Eventually, for $c_{in} > 0.98c_{eq}$ breakthrough is replaced by a smooth increase of flow rates.

4.6.2 Mixing corrosion in 2-D nets: The chemical pathways

In Section 3.5 we have already discussed that mixing corrosion enhances breakthrough at confluences of 1-D conduits. In 2-D-networks mixing corrosion can be considered by assigning different chemical compositions to waters entering at different input points. This way mixing corrosion becomes active at the confluences of fractures deep in the aquifer.

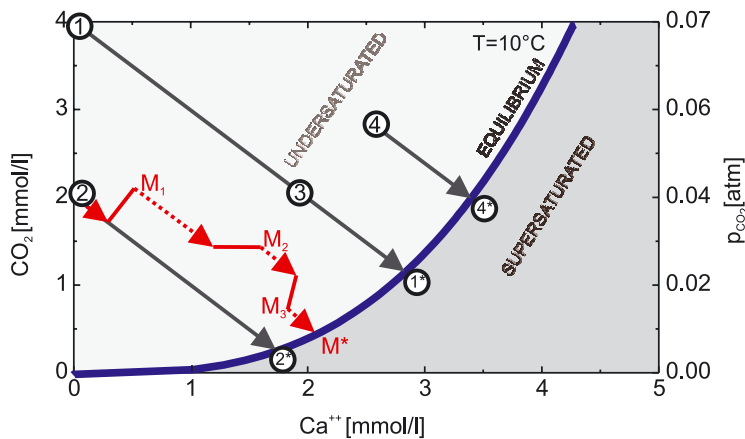


Figure 4.48: Chemical pathways for undersaturated solutions 1, 2, 3, 4, when they approach equilibrium with respect to calcite in the closed system with respect to CO_2 . Solutions 1 and 2 differ in initial p_{CO_2} . Solutions 2 and 3 differ in their initial calcium concentrations, but have equal initial p_{CO_2} . Solution 4 differs in both initial calcium concentration and initial p_{CO_2} from all other solutions. The dashed lines from M_1 , M_2 and M_3 represent chemical pathways after mixing events of solution 2 with solutions 1, 3 or 4, respectively.

Figure 4.48 shows the chemical pathways of solutions flowing in fractures under chemically closed conditions with respect to CO_2 . The figure shows the equilibrium curve (cf. Eq. 2.5) of the Ca -concentration with respect to p_{CO_2} . In the simplest case only two input points 1 and 2 are present. We assume that the solutions at both input points enter with calcium concentrations $c_{in} = 0$, but they are in equilibrium with different p_{CO_2} values. Inside the net closed conditions with respect to CO_2 are operative, and solutions 1 and 2 will evolve on separate parallel straight lines. These pathways reflect the fact that each Ca^{2+} released into the solution consumes one molecule of CO_2 (Eq. 2.6). If on their way to the outflow these solutions never mix, they just will continue on their separate chemical pathways and approach equilibrium at points 1* and 2*, respectively. If, however, at some confluence the solutions mix (red line), the chemical evolution of the mixed solution M_1 continues on a parallel red line (dashed). It may experience

further mixing events, M_2 , M_3 and so on, and will finally approach on a zig-zag like pathway some point M^* on the equilibrium curve. By this way many different pathways to equilibrium are possible. As a consequence, sufficiently far from the input points, different regions in the net carry solutions, which are close to saturation, but have different equilibrium concentrations with respect to calcite. When these mix, they again become undersaturated by mixing corrosion as described in Figures 2.2, 3.32, and 3.36 and cause dissolution deep in the aquifer.

Mixing corrosion becomes also active, when the two entering solutions are in open system equilibrium with equal p_{CO_2} , but differ in their input concentrations of calcium. This is shown by points 2 and 3. The evolving pathways then are analogue to those discussed already. From these arguments it is also evident that MC is active, whenever the chemical input (e.g. the pair 2 and 4) concentrations differ in either, Ca^{2+} or p_{CO_2} , or in both simultaneously (point 4 in Figure 4.48). Mixing corrosion is excluded for points (e.g. 1 and 3) on a common pathway.

Generally, mixing corrosion occurs if solutions with different equilibrium concentrations mix.

Various chemical compositions at input points cause mixing corrosion in the net. One therefore has to know the value of c_{eq} after mixing in each individual fracture of the net. To trace the equilibrium concentration it is necessary to calculate the CO_2 -concentrations in the same way as the calcium concentration. The corresponding value of c_{eq} is calculated by Eqs. 2.5 and 2.6. For details see Gabrovšek (2000) and Gabrovšek and Dreybrodt (2000).

4.6.3 Mixing corrosion in a 2-D statistical network: Two modes of evolution

A simple geological setting, in which mixing corrosion can arise is shown in Figure 4.49. A gently dipping limestone bed underlain by impermeable rock is overlain by two areas of different vegetation. At point A an intense vegetation causes a $p_{CO_2} = 0.05$ atm of infiltrating waters, whereas in the poorly vegetated area input point B receives water with

lower $p_{CO_2} = 0.01$ atm. The waters are driven by head h down to the base level at the river.

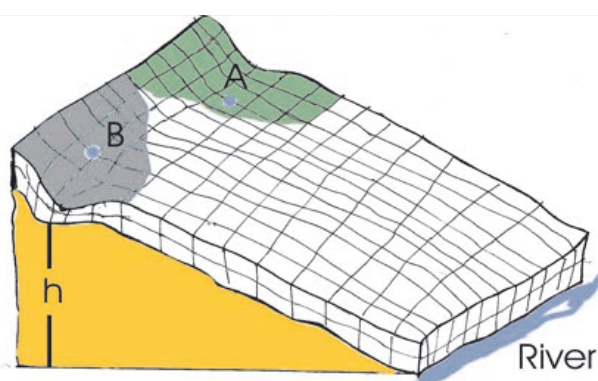


Figure 4.49: Geological setting of a high-dip model with two input points located in differently vegetated areas (green and gray). Consequently, the input p_{CO_2} of solutions entering A and B is different.

Figure 4.50 depicts the modeling domain translating this geologic setting. The domain is 500 m long, 225 m wide and is divided into blocks of $5 \times 1 \times 1 \text{ m}^3$. A lognormal distribution of the aperture fracture width with average $\bar{a}_0 = 0.015 \text{ cm}$ and is employed for the realization of the distribution of aperture widths. It will be kept for all future scenarios in this section. A constant head $h = 25 \text{ m}$ is applied to both input points A and B. Outflow at $h = 0$ is through the right hand side margin. The black rims in Figure 4.50 denote no flow boundary conditions.

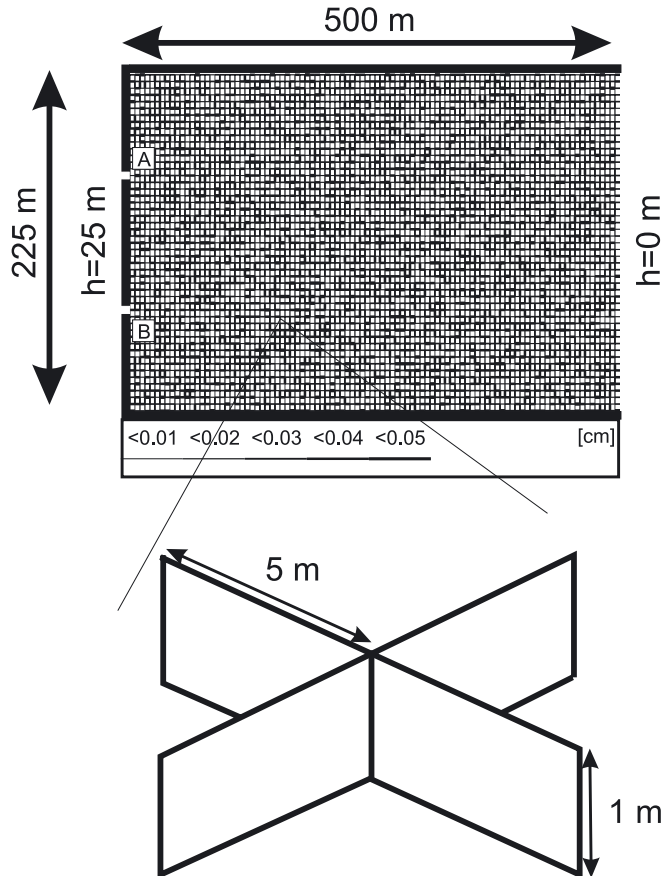


Figure 4.50: Modeling domain of the geological setting in the previous Figure 4.49. Only two input points A and B provide water to the aquifer. Dimensions and boundary conditions can be read from figure.

Two extreme cases

If both input waters have identical chemical compositions, their equilibrium concentrations with respect to calcium are equal $c_{eq}^A = c_{eq}^B$ and, as we have discussed already, mixing corrosion is excluded. In this case, at sufficiently low input concentrations, we expect the well-known breakthrough behavior.

On the other hand, when the p_{CO_2} -values are different $c_{eq}^A \neq c_{eq}^B$ and if both solutions are already saturated when they enter into the aquifer, solutional widening is possible only where these solutions mix. Figure 4.51 illustrates the evolution of these two extreme cases. The bar code depicts fracture widths and the color code dissolution rates in the corresponding fractures. The isolines of heads are also presented.

4. MODELING KARST EVOLUTION ON TWO-DIMENSIONAL NETWORKS: CONSTANT HEAD BOUNDARY CONDITION

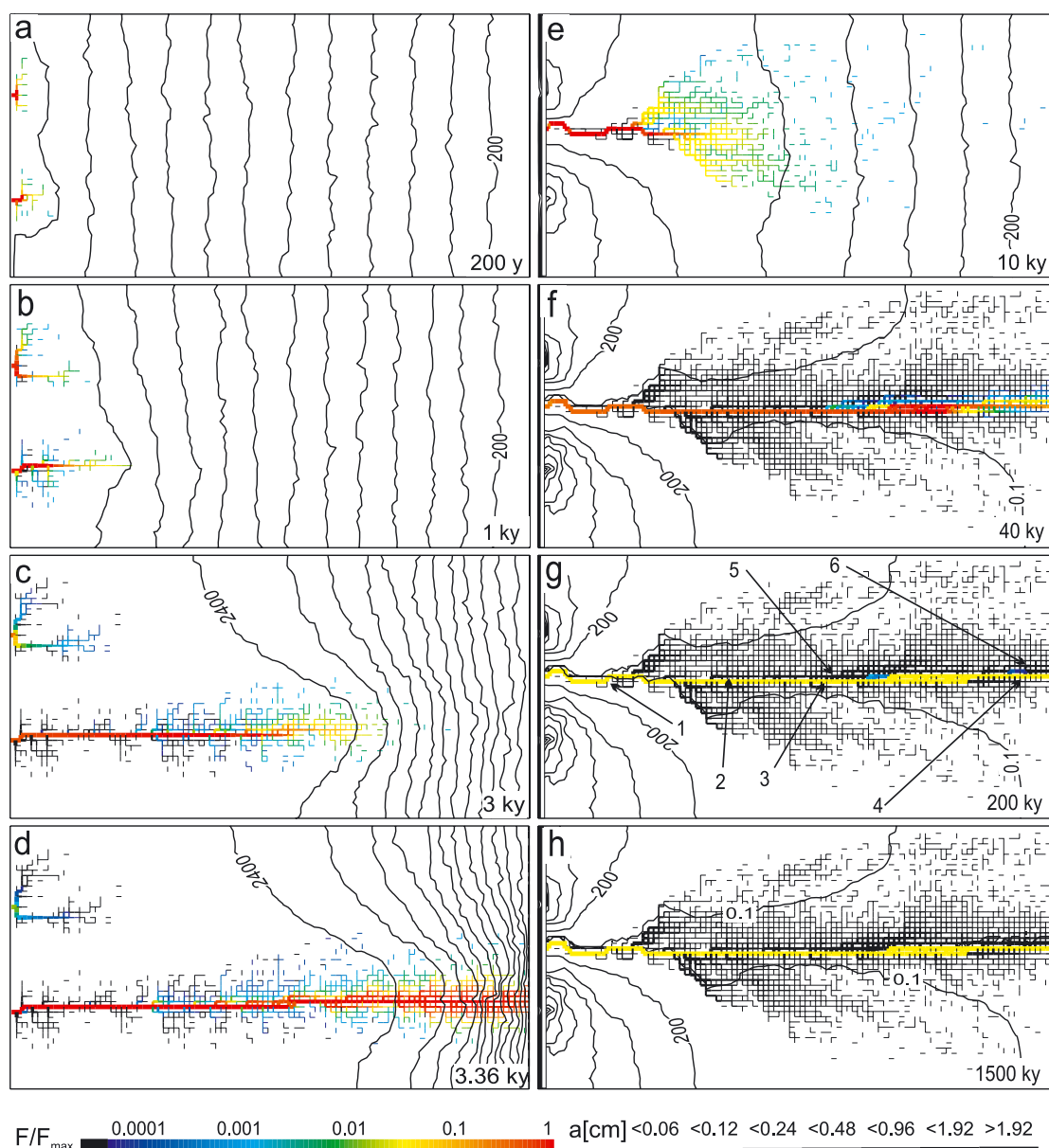


Figure 4.51: Evolution of dissolution rates and aperture widths for the modeling domain in Figure 4.50 for the two extreme limits. a–d: breakthrough mode: $c_{in} = 0.75 c_{eq}$, $p_{CO_2} = 0.05$ atm at both input points. e–h: Pure mixing corrosion: $c_{in} = c_{eq}$, $p_{CO_2} = 0.05$ atm at the upper and $p_{CO_2} = 0.01$ atm at the lower input point. The isolines of head are given in distances of 200 cm. Times of evolution are given at the lower corner of the right hand sides. Dissolution rates are depicted in colors as in the color code in units of maximal dissolution rates during the evolution. Black denotes rates smaller than $10^{-5} F_{max}$. $F_{max} = 0.0034$ cm/y for a–d and $F_{max} = 1.6 \times 10^{-4}$ cm/y for e–f. Fracture widths are given in cm by the bar code below. Fractures with aperture widths below 0.06 cm are not shown.

Figure 4.51a–d represents the evolution of the system, when both solutions entering have equal chemical compositions, $p_{CO_2} = 0.05$ atm and $c_{in} = 0.75 c_{eq}$, $c_{eq} = 2.14 \cdot 10^{-6}$ mol/cm³. Then mixing corrosion is not active. Two conduits start to grow and the lower

one reaches breakthrough after 3360 y. A zone of high dissolution rates penetrates into the aquifer. After breakthrough rates are high and constant along the winning conduit, whereas they drop in the losing one. Note that input point A is connected to the output by the conduit.

The scenario shown by Figure 4.51e–h illustrates what happens, when both input solutions are saturated with respect to calcite but have different p_{CO_2} ($p_{CO_2} = 0.05$ atm and $c_{eq} = 2.14 \cdot 10^{-6}$ mol/cm³ at the upper input A; $p_{CO_2} = 0.01$ atm and $c_{eq} = 0.55 \cdot 10^{-6}$ mol/cm³ at the lower input B)

Widening of fractures is now driven by mixing corrosion solely. Waters flowing from the input points are directed towards the middle region of the aquifer (as can be seen from the head lines). There they mix in fracture nodes close to the left-hand side border. Mixing corrosion becomes active and high dissolution rates increase hydraulic conductivity. Because of its increasing permeability, this region attracts flow. In consequence, the central region, where input waters mix, propagates down head creating a channel, which drains the saturated input waters from the net along its entire length and grows evenly at medium rates. This channel finally reaches the outflow border. It remains connected to the input points only by narrow, unwidened fractures of the net. Note that MC can become operative only at the first node after each input point, where solutions can mix for the first time. Note also that the time scale of this mixing-corrosion mode is several orders of magnitude larger than that of the breakthrough-mode.

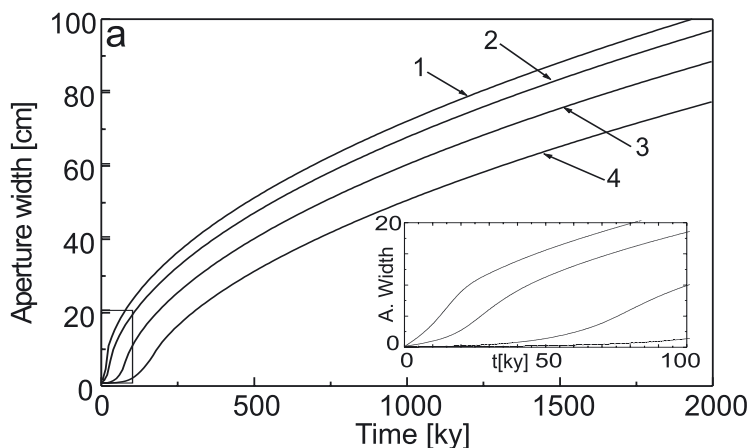


Figure 4.52: a) Evolution of aperture widths of 4 selected fractures as depicted by arrows 1–4 in Figure 4.51g. b) Evolution of aperture widths of two fractures indicated by arrows 5 and 6 in Figure 4.51g.

To further illustrate the evolution of some selected fractures, indicated by arrows 1–6 in Figure 4.51g, Figure 4.52 depicts their aperture widths as they grow in time. In Figure 4.52a the evolution of four fractures in the later central channel can be seen. These are indicated by arrows 1 to 4 in Figure 4.51g. Fracture 1 located closest to the input starts to grow first. Fractures 2 to 4 located further downstream start to grow later in sequence of their locations. Growth rates are high initially and become constant after about 1 million years, when aperture widths of about 50 cm have been reached. Then the rates amount to a widening of 30 cm per million years. Figure 4.52b shows the growth of fractures, which become abandoned by aggressive solution. Their locations are depicted

by arrows 5 and 6 in Figure 4.51g. These fractures first grow quickly. After 40 ky and 80 ky, respectively, they are no longer in the region of MC and stop widening, when aperture widths on the order of 1 cm have been reached. This behavior is common to all fractures in regions where dissolution has stopped (black color in Figure 4.51e–h).

The evolution of flow rates through the aquifer for both limiting cases (breakthrough and MC) is shown in Figure 4.53 by curves *a* and *h* respectively. Curve *a* shows a typical breakthrough behavior with steeply rising flow rates, because input and output become connected by wide conduits.

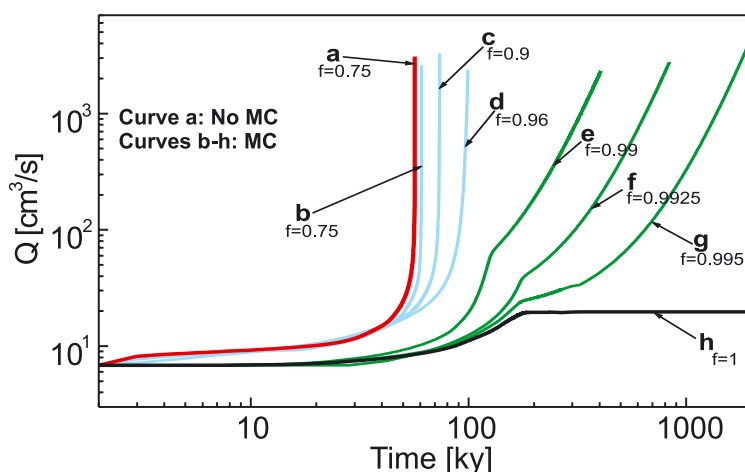


Figure 4.53: Evolution of flow rates through aquifers with identical geological conditions as depicted by the model domain in Figure 4.50, but different chemical boundary conditions for the solutions in upper and lower inputs. **a)** $p_{\text{CO}_2} = 0.05$ atm and $c_{\text{in}} = 0.75c_{\text{eq}}$ at both inputs. No MC. All other curves **b–h** show the time dependence of flow rates, when $p_{\text{CO}_2} = 0.05$ atm at the upper input and $p_{\text{CO}_2} = 0.01$ atm at the lower one. Input concentrations are given by $f c_{\text{eq}}$ with respect to the corresponding equilibrium concentrations at inputs. **b)** $c_{\text{in}} = 0.75c_{\text{eq}}$, **c)** $c_{\text{in}} = 0.9c_{\text{eq}}$, **d)** $c_{\text{in}} = 0.96c_{\text{eq}}$, **e)** $c_{\text{in}} = 0.99c_{\text{eq}}$, **f)** $c_{\text{in}} = 0.9925c_{\text{eq}}$, **g)** $c_{\text{in}} = 0.995c_{\text{eq}}$, and **h)** $c_{\text{in}} = c_{\text{eq}}$ (pure MC).

The behavior is entirely different for the other extreme with MC active solely (curve *h*). Dissolutional widening occurs only distant from the inputs in fractures, where solutions mix. No dissolution is active elsewhere. Higher permeability is created only at some distance from the inputs, in the region of MC, which drains water from the inputs through narrow unwidened fractures. As this region extends down head flow rates increase. After some time the central area has been integrated to a conduit system with low resistance to flow, extending to the output. Then the region of not widened fractures, leading water from the inputs to the center, limits flow rates. Therefore, they become constant after 40 ky. It should be pointed out again that the hydrological settings for both runs are identical. Only the changes in the hydrochemical conditions at inputs A and B are responsible for the extreme difference of aquifer evolution.

Our considerations show that two entirely different modes of karstification can be active. The breakthrough mechanism is fast and connects input and output. The MC

mode is extremely slow and creates central channels in the order of tenths of centimeters in times of several million years. These, however, are connected to the input point only by fractures, which have not experienced dissolutional widening and limit flow during almost the entire evolution.

The intermediate cases

To study the simultaneous action of both mechanisms, the positive feedback-loop of breakthrough and increasing permeability by mixing corrosion, the following scenarios are investigated.

As in the case with pure mixing corrosion we assume different p_{CO_2} of 0.05 and 0.01 atm. at the input points A and B respectively. This corresponds to different equilibrium concentrations with respect to the closed system. These are $c_{eq}^A = 2.14$ mmol/l and $c_{eq}^B = 0.55$ mmol/l, respectively. But now input waters are undersaturated. This can be expressed by a factor $f \leq 1$ by which $c_{in}^A = f \cdot c_{eq}^A$ and $c_{in}^B = f \cdot c_{eq}^B$. In the following we will find that f is an important controlling parameter.

The evolution of the aquifer with $f = 0.75$ is shown by Figure 4.54 a–d. After 400 y, similar to the evolution shown in Figure 4.51a and b, a conduit starts to grow from the upper input. The water from the lower input, with $p_{CO_2} = 0.01$ atm is considerably less aggressive. Therefore, the channel from there has grown only a short distance (Figure 4.54a). Figure 4.54b reveals a new important aspect. In the region close between the two inputs some isolated fractures have grown sufficiently wide by MC. This implies higher hydraulic conductivity in this region. Therefore the conduit growing from the upper input separates into two branches, with one directed into this area of lower permeability. The other keeps its former direction. The lower conduit is more competitive than the upper one because MC is active along the center of the aquifer, where waters from the two inputs mix. In average, aperture widths become larger in the mixing zone than in the region of the upper channel, where no MC is active. Therefore, the central conduit propagates through this more favorable region and consequently needs less time for breakthrough (cf. Eqn. 3.35). This is seen in Figure 4.54c (3000 y). The lower channel has gained significant lead and breakthrough occurs at 3800 y as illustrated by Figure 4.54d. Clearly a breakthrough behavior is seen, but with the help of MC the pathways of conduit growth are now directed into the region where MC is active. Therefore a different pattern of conduits arises, compared to Figure 4.51d, where MC is excluded, but all other conditions are entirely identical. The evolution of flow rates in time is shown by Figure 4.53, curve *b*.

The influence of the breakthrough mechanism is reduced, when input solutions are closer to saturation. Therefore, one expects a more dominant role of mixing corrosion. To this end, we have performed computer runs with c_{in} increasing from $0.75c_{eq}$, $0.9c_{eq}$, $0.96c_{eq}$, $0.99c_{eq}$, $0.9925c_{eq}$ and $0.995c_{eq}$. The evolution of flow rates in time is shown in Figure 4.53. Curves *b–d* exhibit typical breakthrough behavior, such as curve *a* where MC is absent, and the evolution of the respective aquifer is similar to that shown by

4. MODELING KARST EVOLUTION ON TWO-DIMENSIONAL NETWORKS: CONSTANT HEAD BOUNDARY CONDITION

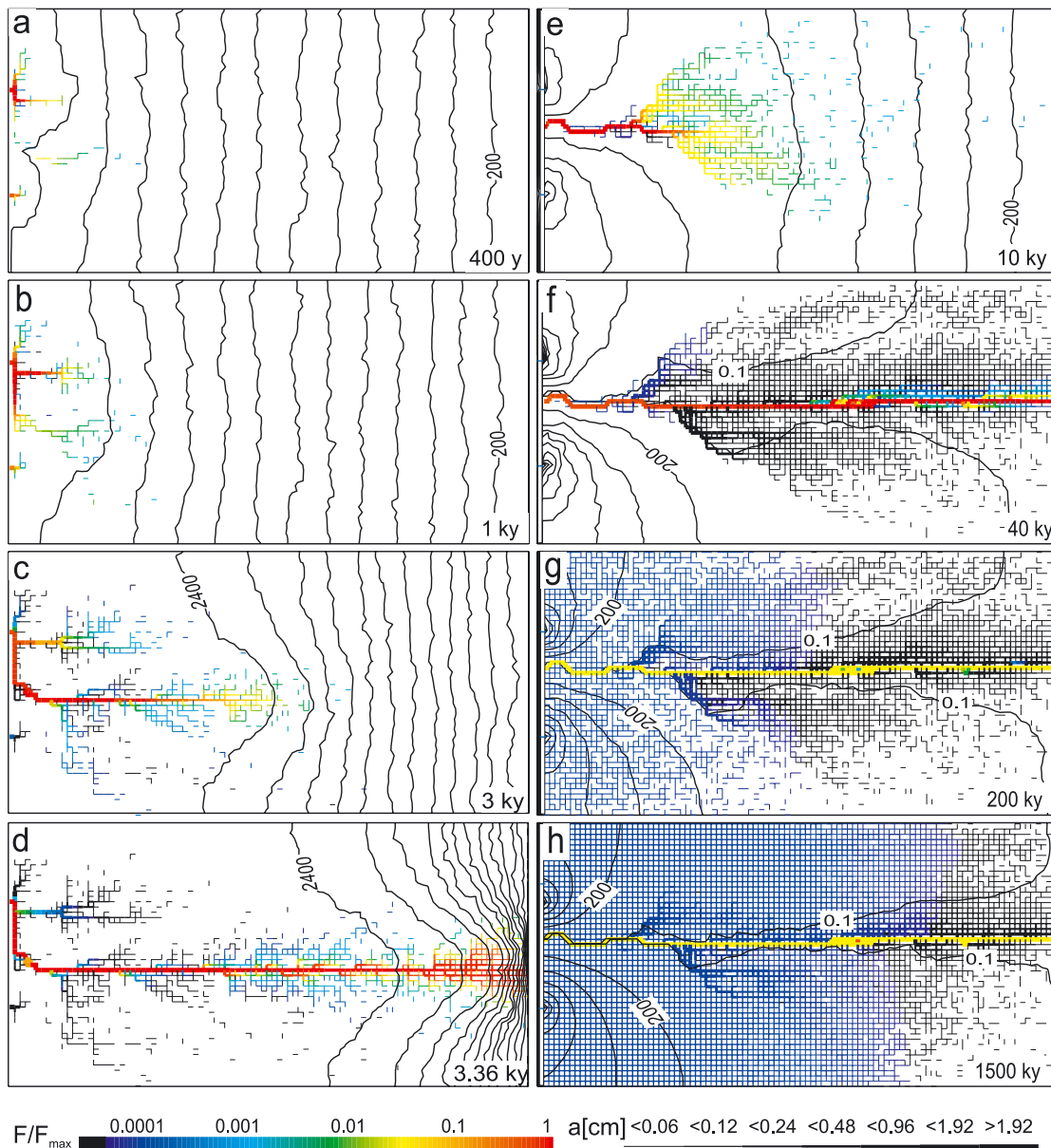


Figure 4.54: Evolution of dissolution rates and fracture aperture widths for the modeling domain of Figure 4.50. (a-d) Breakthrough mode with MC (see Figure 4.53, curve b) $c_{in} = 0.75c_{eq}$, $p_{CO_2} = 0.05$ atm at the upper input and $p_{CO_2} = 0.01$ atm at the lower input. (e-h) reduced influence of breakthrough: $c_{in} = 0.995 c_{eq}$, p_{CO_2} as in (e-d). Codes as in Figure 4.51.

Figure 4.54a–d. At higher input concentrations ($c_{in} \geq 0.99c_{eq}$) the shape of the curves changes as shown by curves e to g. All curves first exhibit a steady increase of flow rates, which becomes steeper indicating breakthrough. But then the rates increase less steeply in curves e–h and breakthrough does not occur. For $c_{in} = c_{eq}$, when only MC is active (curve h) flow rates become constant. Evidently, breakthrough does no longer dominate the evolution of the aquifer.

Figures 4.54e–h, show the evolution of the aquifer for $c_{in} = 0.995c_{eq}$. In this case MC acts similarly as in Figure 4.54e–h but the inflowing solution is slightly undersaturated and therefore all fractures in the net experience very slow, even widening. During the first 40 ky this widening has no effect and therefore the evolution of the aquifer is almost identical to that of pure MC, as shown by Figures 4.51e–f. This can be seen by comparing Figure 4.51e with Figure 4.54e, both at 10 ky and Figure 4.51f with Figure 4.54f at 40 ky. After several 10 ky slow widening of fractures has increased their widths (blue areas in g and h). Therefore more flow can enter into the domain. This is the reason for a further increase in flow rates shown in Figure 4.53g. The evolution of the aquifer departs from that of pure MC at times of several 100 ky. This is seen from the system of fractures (blue), which extend from the input after 500 ky (Figure 4.54g) and 1.5 million years (Figure 4.54h). On such time scales dissolutional widening by the slightly undersaturated input solution opens those fractures, where MC remains absent, by several times their initial aperture width. Therefore, in contrast to pure MC flow rates increase continuously.

Summing up, we can state that two modes of karstification are possible. Up to input concentrations of $0.96c_{eq}$ the positive breakthrough feedback loop is dominant. Even in this region of concentrations MC can play an important role, because deep in the aquifer, where the solutions are practically saturated, mixing corrosion becomes active when they mix. From the very beginning of karstification this creates areas of increased fracture aperture widths, through which channels propagating downstream can be diverted. As a consequence the patterns of evolution become different from those, which would arise, if both input solutions had equal chemical composition, i.e. MC was absent.

It is evident from Figure 4.53 that the steep rise, marking breakthrough, is maintained up to values of $f = 0.96$, although breakthrough times increase slightly. For higher values, $f > 0.99$, flow rates increase slowly, because dissolution rates become lower with increasing f and are practically equal everywhere in the net. Mixing corrosion gains a dominant role. It creates a channel, which drains many slowly evolving fractures. The initial rise of flow rates is caused by this. When the channel has opened up sufficiently, its resistance to flow becomes so low, that the further slower rise of flow is caused solely by slow solutional widening of the fractures in the net, which carry solutions close to equilibrium.

The interplay between breakthrough and mixing corrosion can create a remarkable variety of patterns of dissolution widening. Summarizing Figure 4.55 depicts the fracture widths of all scenarios (Figure 4.53a–h) at the termination of the model runs. More detailed information on this topic is given by Romanov *et al.* (2003b) and by Romanov (2003).

4. MODELING KARST EVOLUTION ON TWO-DIMENSIONAL NETWORKS: CONSTANT HEAD BOUNDARY CONDITION

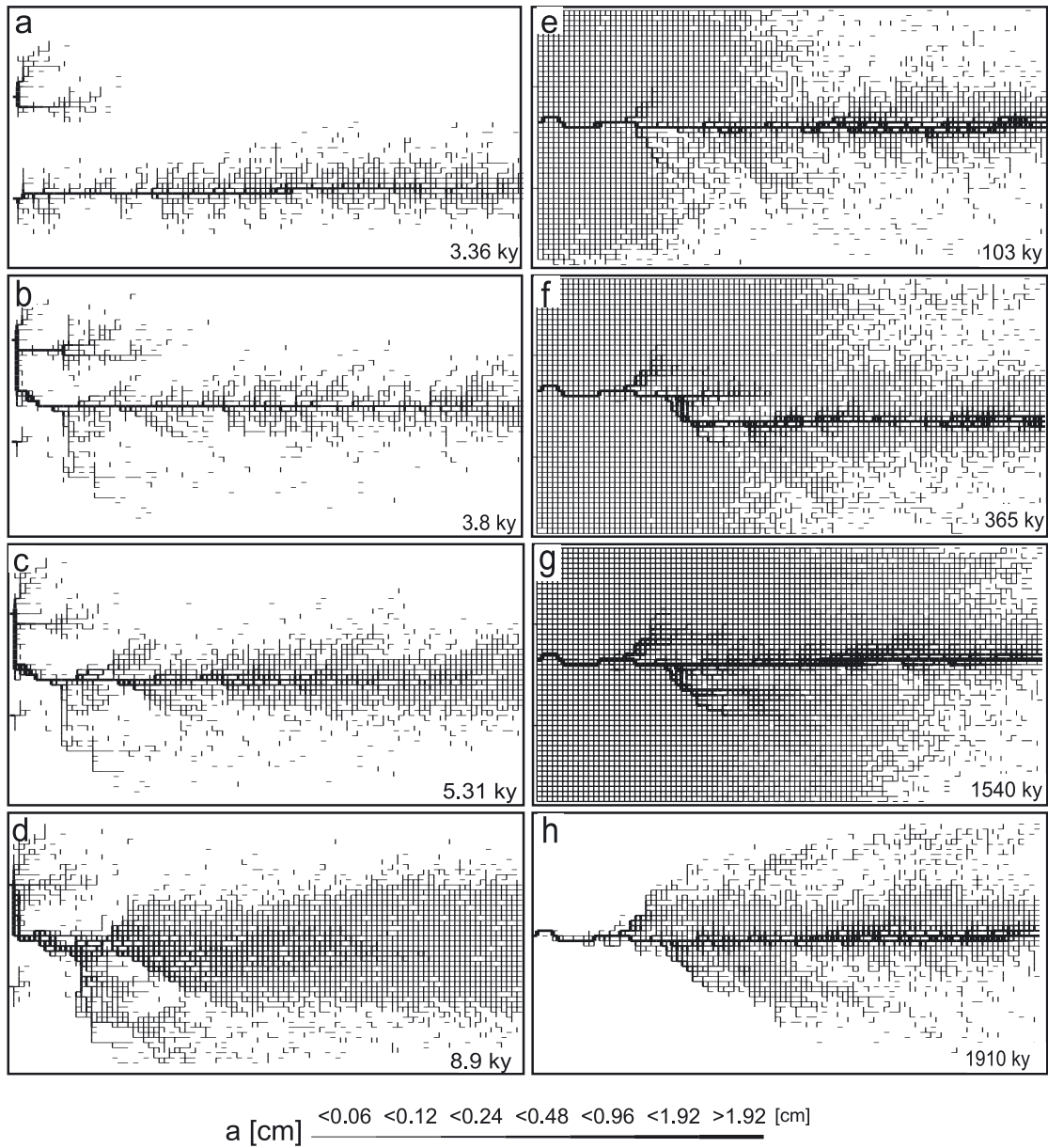


Figure 4.55: Aperture widths of all aquifers at the terminations of model runs. The letters in the figures relate to the corresponding curves in Figure 4.53. Aquifers a-d are breakthrough-dominated, whereas aquifers e-g are controlled by mixing corrosion.

4.6.4 Mixing corrosion in percolation nets

Percolation nets with low occupation probability $p \leq 0.8$ are different from statistical nets, because they exhibit only few points of confluence where waters from different inputs mix.

Such a net with $p = 0.8$ is shown by Figure 4.56. It is a 30×30 net with grid size of $30 \times 30 \text{ m}^2$. Two input points at a head of 50 m supply water to the aquifer. The output fractures at the right hand margin are at head zero. The aperture width of all fractures is $A_0 = 0.03 \text{ cm}$. There is one point of confluence noted by a black circle, about one third of the domain length distant from the input boundary. All other points of confluence are close to the output boundary, such that no further mixing is possible in the central part of the aquifer.

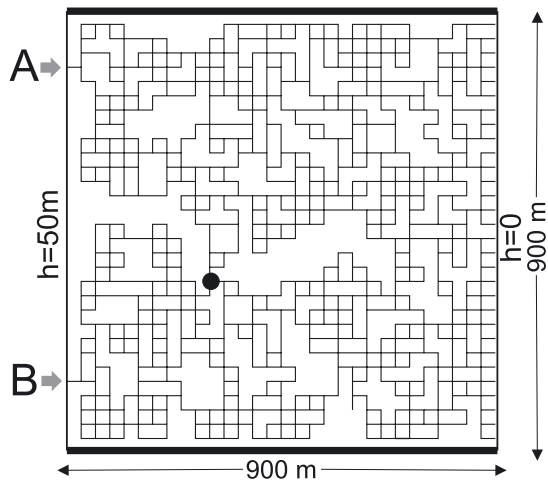


Figure 4.56: Modeling domain of the percolation network used in the following computer runs. There are two inputs A and B with head of 50 m. Outflow is at all fractures at the right hand-side boundary at head zero. $A_0 = 0.03 \text{ cm}$. Dimensions and boundary conditions can be read from figure.

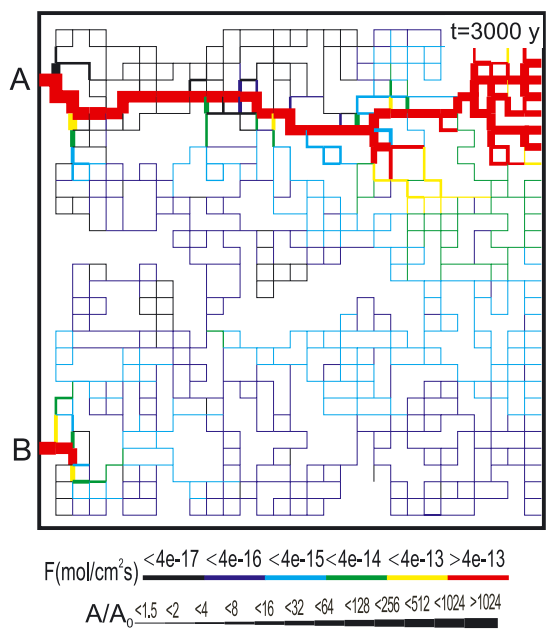


Figure 4.57 shows the situation at breakthrough, when both input points are at $p_{CO_2} = 0.05 \text{ atm}$. and $c_{in} = 0$. A channel from input A has evolved and reached breakthrough.

Figure 4.57: Distribution of aperture fracture widths and dissolution rates in the percolation network shown in Figure 4.56 at breakthrough. $c_{in} = 0$ and $p_{CO_2} = 0.05 \text{ atm}$ at both input points. Breakthrough mode, no MC. Other parameters and boundary conditions as in Figure 4.56.

4. MODELING KARST EVOLUTION ON TWO-DIMENSIONAL NETWORKS: CONSTANT HEAD BOUNDARY CONDITION

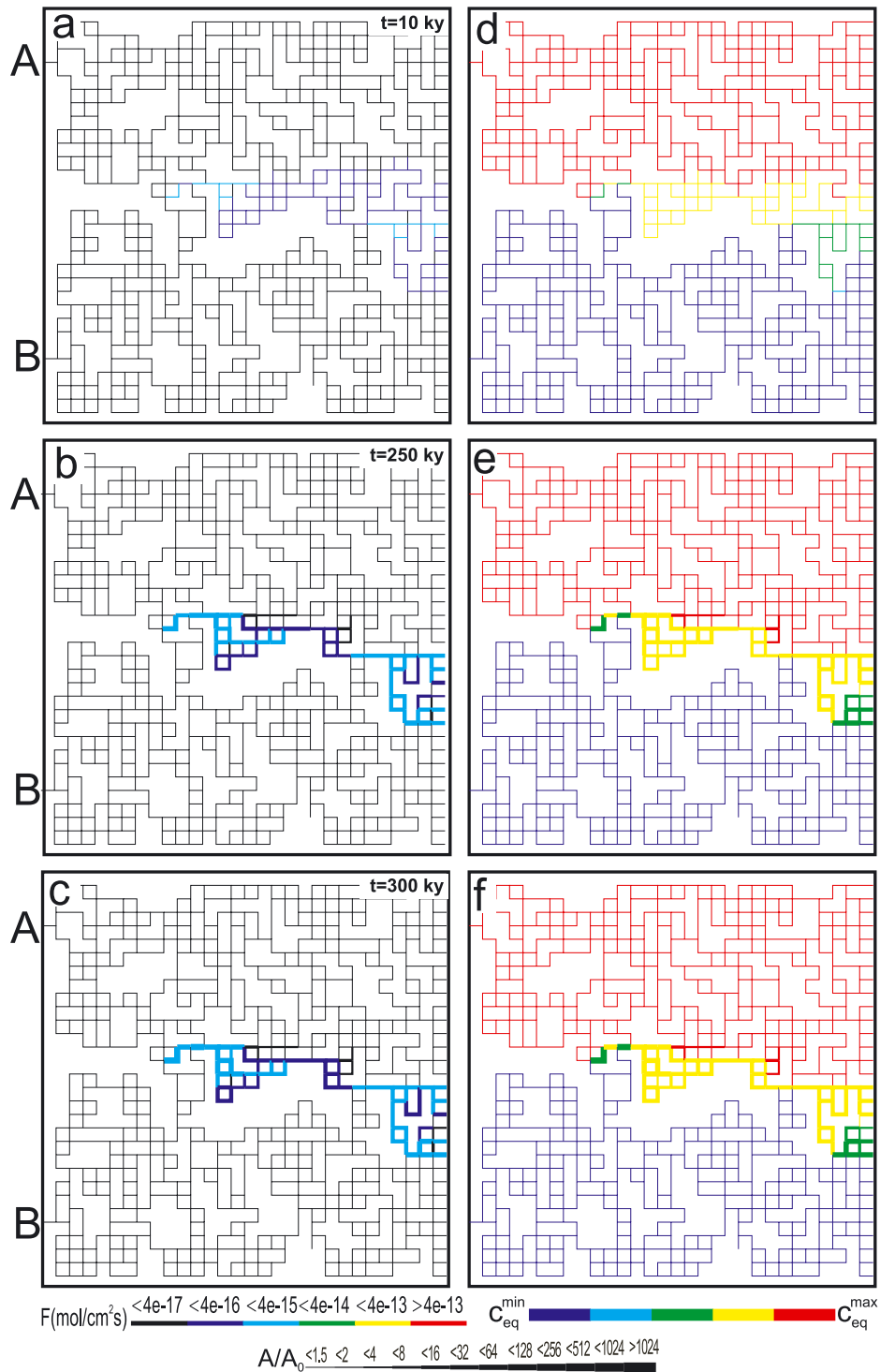


Figure 4.58: Evolution of percolation net (Figure 4.56) with $p_{CO_2} = 0.05$ atm at the upper input and 0.03 atm at the lower one. Pure MC-mode with $c_{in} = c_{eq}$. The left hand side shows the distribution of aperture widths and dissolution rates. The right hand side depicts equilibrium concentrations of the mixed solutions and aperture widths, $A_0 = 0.03$ cm. Other parameters and boundary conditions as in Figure 4.56.

In contrast, Figure 4.58 shows the evolution, if $p_{CO_2} = 0.05$ atm is left unchanged at the upper input, but p_{CO_2} is changed to 0.03 atm at the lower one. Input concentrations of calcium $c_{in} = c_{eq}$ are in closed system equilibrium with these p_{CO_2} , i.e. only mixing corrosion can lead to widening of fractures. The two equilibrium concentrations are designated in the right hand side column by red color for $p_{CO_2} = 0.05$ atm and by blue for 0.03 atm. Where the solutions mix, the calcium equilibrium concentration takes values between those two extremes, shown by the color code. The dissolution rates are illustrated in the left hand side column by color code. Fracture aperture widths are depicted by the bar code in both columns.

Only in those regions, where waters from both inputs mix (regions of yellow and green in the corresponding panels in the right hand side column), dissolutational widening occurs. This is designated by light and dark blue colors in the left column. In those regions without mixing (red and blue in right hand side) dissolution rates are zero as shown by black on the left column.

This way, the region where mixing corrosion is active is clearly depicted. Fracture widths are indicated by the bar code. Mixing occurs at the first confluence (green), and a zone down head (yellow), which extends continuously. This pattern changes only slightly in time. It exhibits, however, continuous widening of fractures. Regions, close to the entrance and outside the mixing zone, remain unaffected and limit flow through the system. This can also be seen from the right hand side column in Figure 4.58, which depicts zero dissolution rates by the black regions.

Figure 4.59 shows the evolution of the flow rates through the upper and lower inputs. They become constant due to the unwidened fractures connecting the channel to the input.

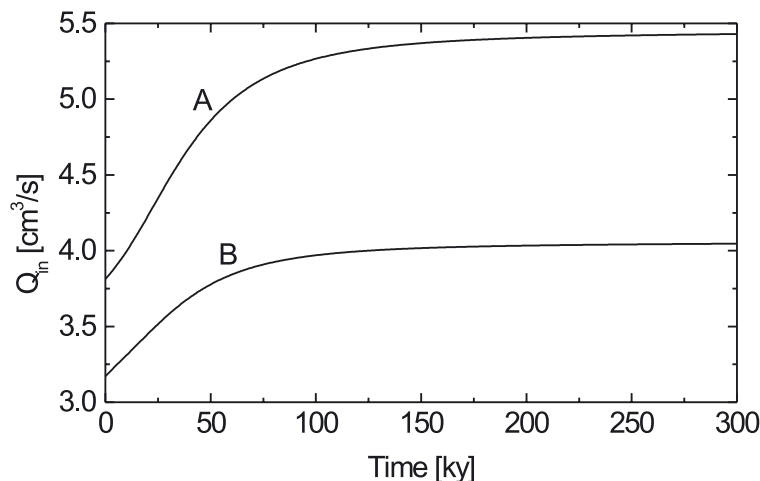


Figure 4.59: Evolution of flow rates through input points A and B in the previous scenario (Figure 4.58).

In the next scenario (Figure 4.60) we still allow mixing corrosion by setting the upper input to $p_{CO_2} = 0.05$ atm and the lower one to 0.03 atm, but now we change c_{in} to $0.97c_{eq}$. The results are similar to those of statistical nets.

4. MODELING KARST EVOLUTION ON TWO-DIMENSIONAL NETWORKS: CONSTANT HEAD BOUNDARY CONDITION

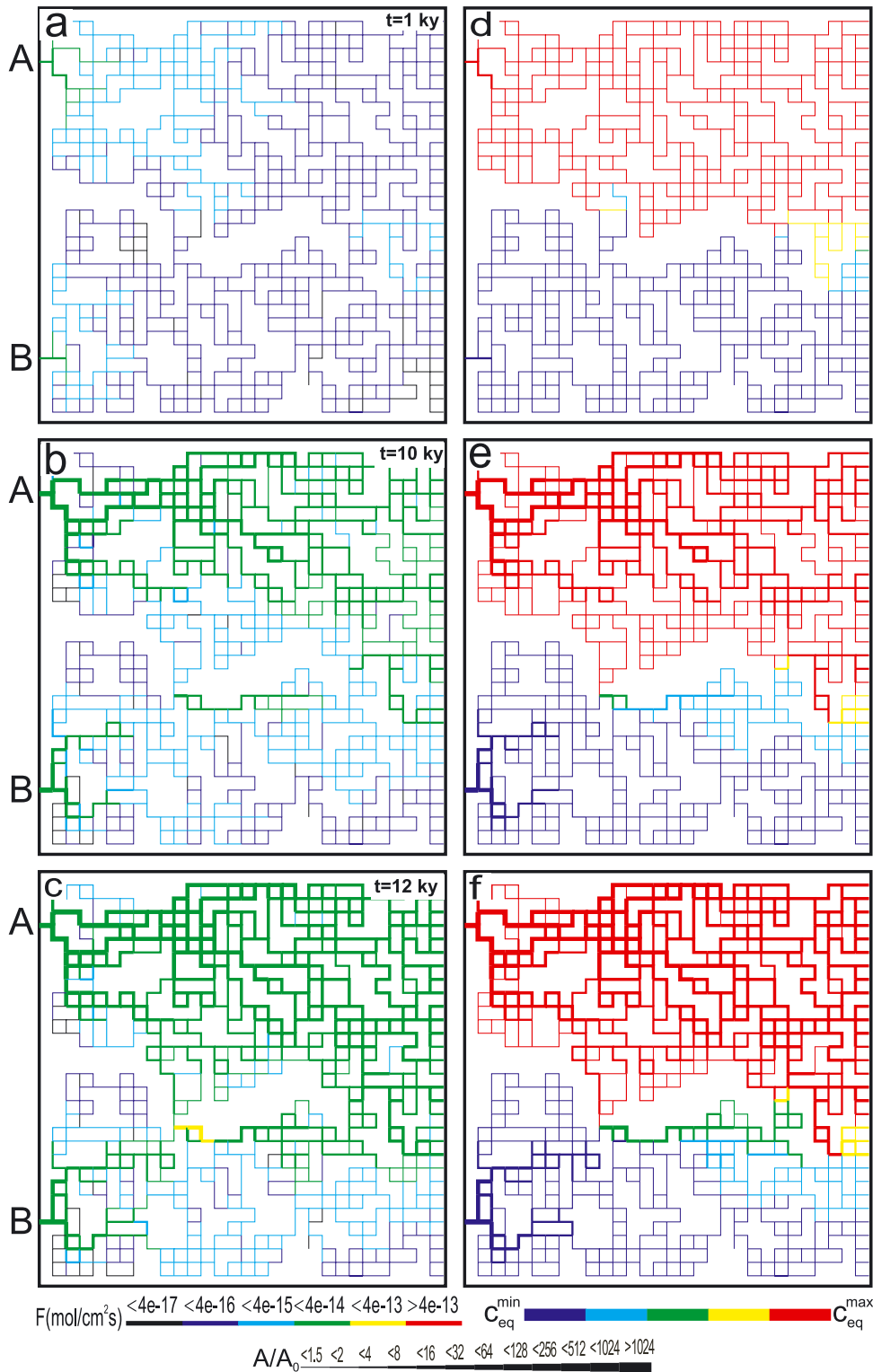


Figure 4.60: Evolution of the percolation net (Figure 4.56). Left hand column: aperture widths and dissolution rates. Right hand column: equilibrium concentrations of mixed solutions and aperture widths. $A_0 = 0.03$ cm, p_{CO_2} at upper input is 0.05 atm and at the lower one 0.03 atm, $c_{in} = 0.97c_{eq}$.

Initially, mixing is seen at the first confluence and also close to the output border. After 10 ky dissolutional widening from the undersaturated input solution in the upper part has created a net of conduits, but also some channels have evolved from the lower input, which because of the lower p_{CO_2} are not so well developed. Both channel systems attract flow from the inputs toward the first point of confluence. There, mixing of these waters creates a zone of dissolution, extending down head towards the exit boundary. Finally, a maze like structure is established when flow becomes turbulent. One should stress here that dissolution rates in the region of MC are similar to those in the regions marked by red and blue on the right column, because these carry slightly undersaturated input solutions with $c_{in} = 0.97c_{eq}$.

Figure 4.62 shows the evolution of flow rates through the upper and lower input points by the dotted curves. The comparatively slow rise of both flow rates indicates dominance of mixing corrosion.

If mixing corrosion is switched off by putting both inputs to $p_{CO_2} = 0.05$ atm and by using $c_{in} = 0.97c_{eq}$, one obtains similar results as for the statistical nets and percolation nets with $c_{in} = 0.98c_{eq}$ (see Figure 4.40 and Figure 4.46c). Due to the low but evenly distributed rates a maze like structure results, as shown by Figure 4.61. The evolution of flow rates is shown in Figure 4.62.

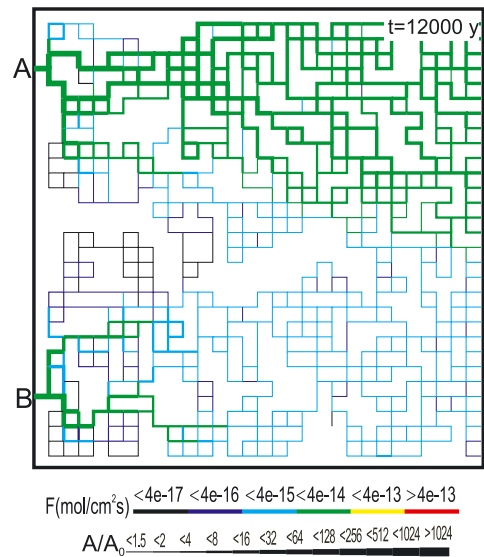


Figure 4.61: Distribution of fracture aperture widths and dissolution rates of the percolation net (Figure 4.56) at breakthrough. Mixing corrosion is excluded by setting p_{CO_2} to 0.05 atm and $c_{in} = 0.97c_{eq}$ at both inputs.

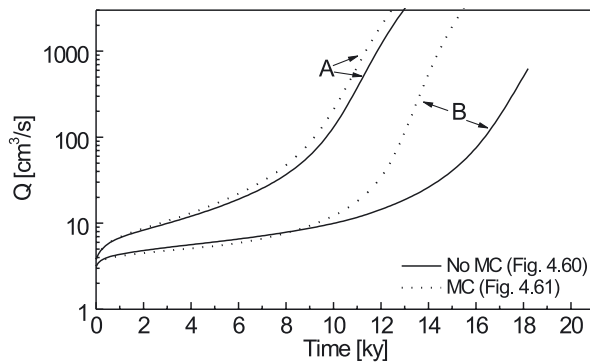


Figure 4.62: Flow rates in time for scenarios shown in Figures 4.60 and 4.61.

4. MODELING KARST EVOLUTION ON TWO-DIMENSIONAL NETWORKS: CONSTANT HEAD BOUNDARY CONDITION

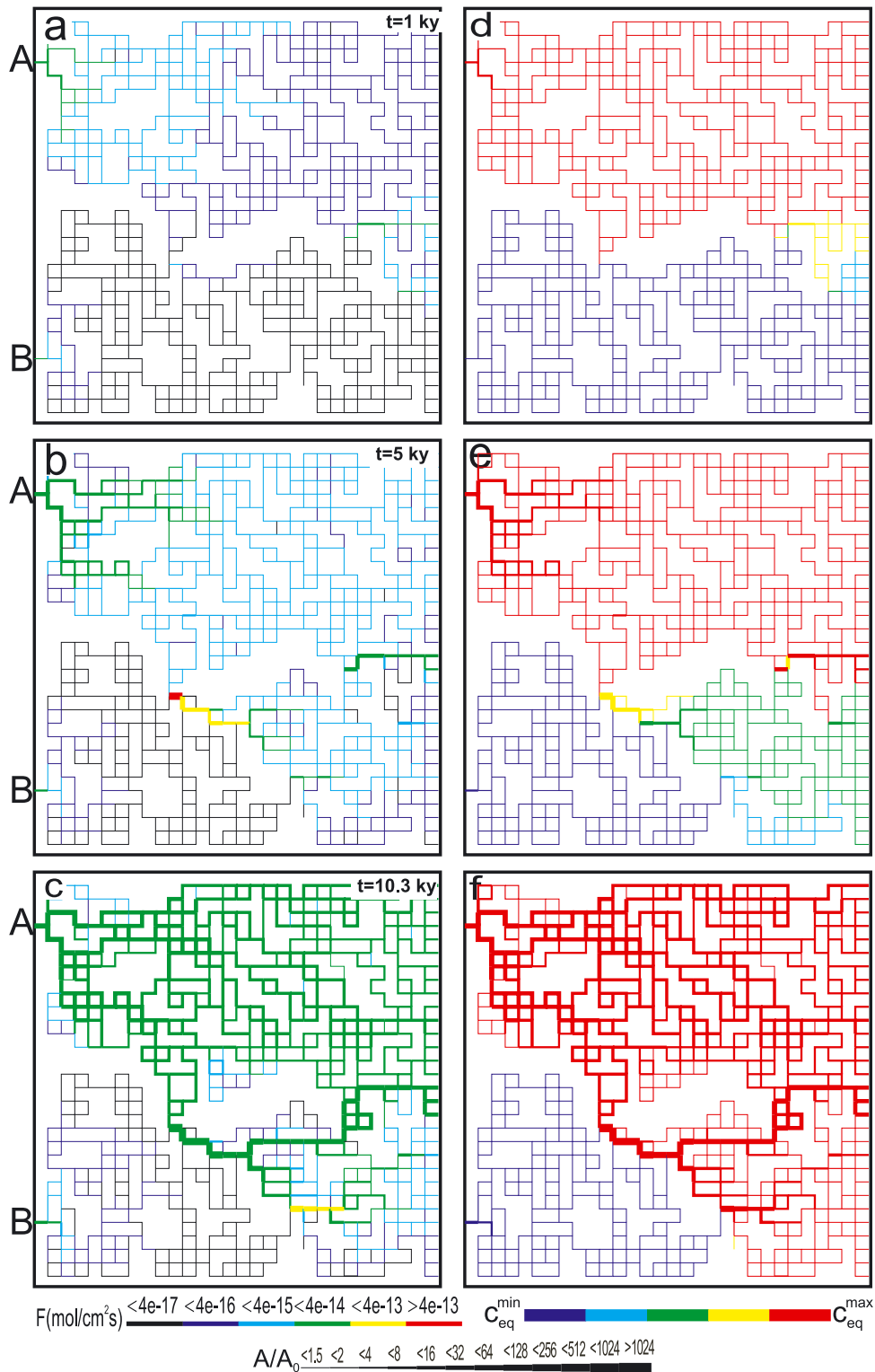


Figure 4.63: Evolution of model aquifer (Figure 4.56). Left hand column: aperture widths and dissolution rates. Right hand side: equilibrium concentrations of mixed solutions and aperture widths. p_{CO_2} at upper input is 0.05 atm and at the lower one 0.003 atm; $c_{in} = 0.97c_{eq}$.

The patterns of karstification are highly sensitive to the boundary conditions. To show an example we have changed p_{CO_2} to 0.003 atm at the lower input of the domain. Otherwise, boundary conditions remain as those of the scenario shown in Figure 4.60. The result is illustrated by Figure 4.63. Due to the smaller value of p_{CO_2} at the lower input point, mixing corrosion is stronger at the first point of confluence (b). In comparison to Figure 4.60 solutions from the upper input invade deeper into the lower part of the aquifer and change the pattern of conduits.

To summarize so far, we have discussed the processes activated by MC. They are operating in statistical nets and in percolation networks as well. But due to the sensitivity of their details, percolation nets can show results, which have not been expected in the more evenly distributed statistical networks.

To explore all possible patterns is difficult, because each new boundary condition requires new parameters. Consequently the number of variations to explore the whole realm of evolution patterns becomes so large, that only keyhole views are possible.

4.7 MIXING CORROSION IN DUAL-FRACTURE AQUIFERS

We have experienced that the combination of statistical networks with percolation nets embedded into them gave rise to a series of new features, although no basically new mechanisms became operative. But the complex interplay of the same mechanisms acting in percolation and statistical networks, showed new, so far unexpected patterns of evolution. Aware of these problems, in this section we will take a few snapshots of what MC can do in dual-fracture aquifers.

The introduction of prominent fractures into a dense net of fissures gives rise to many new combinations of chemical input boundary conditions:

- A) Water percolating through the soil is highly loaded with CO_2 and may preferably enter into the net of narrow fissures. In contrast, prominent fractures may be fed from rivers or small creeks with considerably lower p_{CO_2} . Consequently, one can construct a scenario, in which all (or some) prominent fractures receive water with an initial p_{CO_2} of 0.01 atm, whereas all fine fractures are fed by water with a higher p_{CO_2} of 0.05 atm.
- B) One could also envisage areas of different vegetation on top of the aquifer. In this case, all prominent and narrow fractures in one region would receive water with some p_{CO_2} , whereas other regions would have different p_{CO_2} -values.
- C) Finally, a combination of scenarios A and B is also feasible.

These considerations show the overwhelming variety of possibilities. In view that each scenario is controlled by many further input parameters, such as \bar{a}_0 , A_0 , head h , and the degree of saturation $f \cdot c_{eq}$ of the input solutions, only a few examples can be presented.

4.7.1 Pure mixing corrosion: One prominent fracture in a statistical network

The most simple scenario is shown by Figure 4.64. A straight fracture with aperture width $A_0 = 0.02$ cm is added to the standard statistical network ($\bar{a}_0 = 0.0625$ cm), similar as in Figure 4.24. But now p_{CO_2} of the input solution into the middle fracture is 0.01 atm, whereas it is 0.05 atm into all fissures of the net. All input solutions are saturated with respect to calcite. By these boundary conditions limestone is dissolved exclusively by MC.

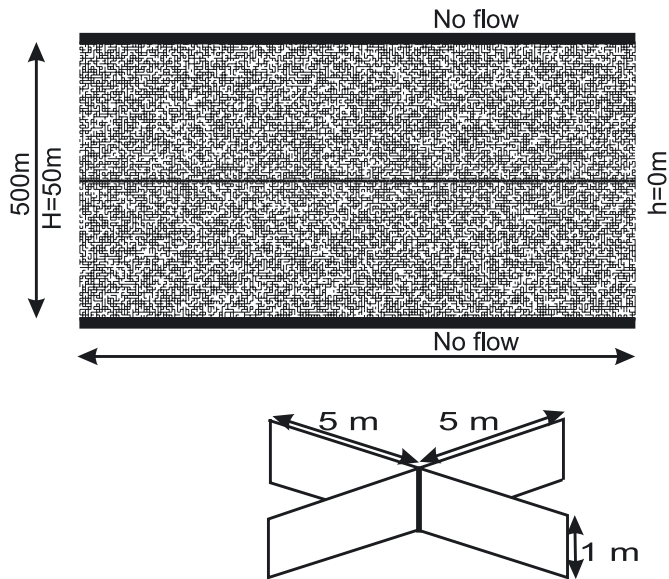


Figure 4.64: Model domain: Network of fine fissures of aperture width \bar{a}_0 with only one prominent fracture of aperture width A_0 in its center. p_{CO_2} at this fracture is 0.01 atm, whereas all other entrance fissures of the net receive water with $p_{CO_2} = 0.05$ atm. Head at the entrance of all fractures and fissures is $H = 50$ m and zero at the outflow. Other parameters and boundary conditions can be read from figure.

The evolution of this aquifer is shown by Figure 4.65. The left hand side column presents fracture aperture widths (bar code) and dissolution rates (color code). The right hand side column depicts the flow rates (bar code), which are normalized to Q_{max} , the actual maximal flow rate in the domain. Note that Q_{max} changes in time. The color code shows the flow directions (blue = up, green = down, red = right, yellow = left). From this code one can envisage where flow enters or leaves prominent fractures.

Initially ($t = 0$) (a, f), water from the net enters the fracture. But there are also sites, where water flows from the fracture into the net. Consequently, a wide zone of mixing is established. This region is shown by the blue fringe of dissolution rates in the net and by the high rates in the fracture (green).

The largest dissolution rates occur after the first node in the prominent fracture connecting to the entrance. Note, that the entrance part reaching to the first node of all fracture does not experience any widening, since mixing can only occur after the first node. This has an important consequence. Flow into the fracture and into the fine fissures remains limited by the resistance of this entrance part of the aquifer during the entire evolution. In the region, where mixing occurs, however, the permeability of the net and

4. MODELING KARST EVOLUTION ON TWO-DIMENSIONAL NETWORKS: CONSTANT HEAD BOUNDARY CONDITION

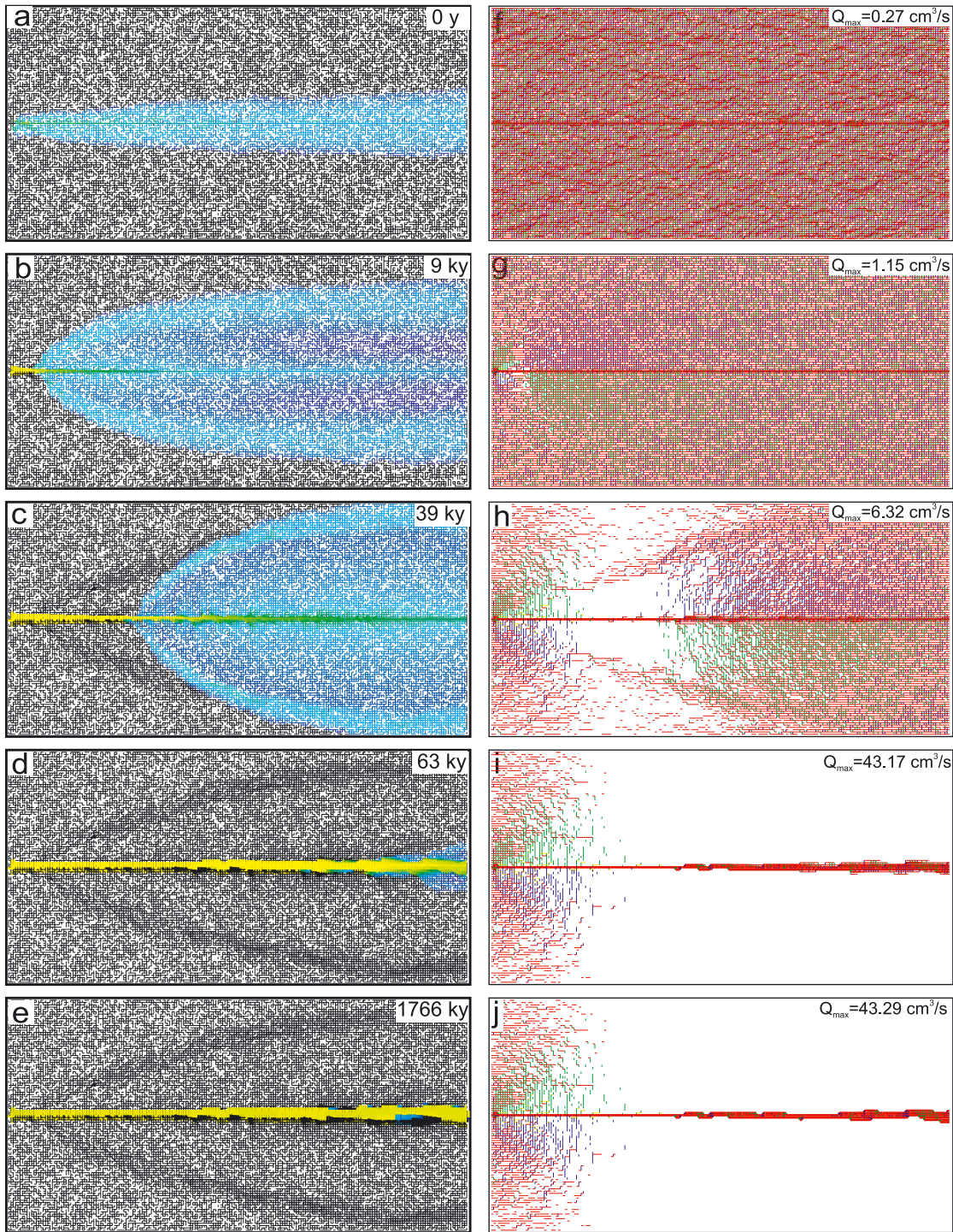


Figure 4.65: Evolution of the aquifer with one central single fracture (Figure 4.64) in the mode of pure MC. $c_{in} = c_{eq}$, $\bar{a}_0 = 0.0625$ cm, and $A_0 = 0.02$ cm, $p_{CO_2} = 0.01$ atm at the input of the prominent fracture and 0.05 atm at all other fissures. Figures a-e: fracture widths and dissolution rates. Figures f-g illustrate flow rates and flow directions.

also that of the fracture increases. This way a region of higher hydraulic conductivity is embedded into an environment of lower conductivity. In such situations, flow from the upstream region is attracted into the central fracture, which is the region of highest conductivity. It is expelled at its tip downstream of the widened central conduit. This can be visualized in g, h, i and j, where one finds flow from the net entering into the upstream part of the fracture. This enhances mixing in the fracture as can be seen in c and h. At the tip of the central channel water is injected into the net and a wide fringe of mixing corrosion is created (c, h). After 63 ky inflow into the net is drained by the central channel, which has reached the output border (d, i). Finally, dissolutional widening is restricted to the central channel and some fissures close to it (e, j).

At the rims of the former mixing fan a region of widened fractures has been created. The region of inflow in the upstream part still delivers water from the net with $p_{CO_2} = 0.05$ atm into the fracture. There it mixes with the water in the fracture (0.01 atm). Otherwise flow is restricted to the fracture and some fissures parallel to it (Figure 4.65i). This situation remains stable as shown by Figure 4.65e, j until 1.77 million years. Now rates of widening are equal and constant in time along the central region.

The evolution of total flow through the domain is depicted by the full line in Figure 4.66. It increases slowly during the first 40 ky. But as soon flow becomes channeled to the central fracture the rates increase rapidly. After 56 ky they remain stable, because flow is now restricted through those fractures of the net, which are located close to the input in the vicinity of the central channel and cannot experienced any widening.

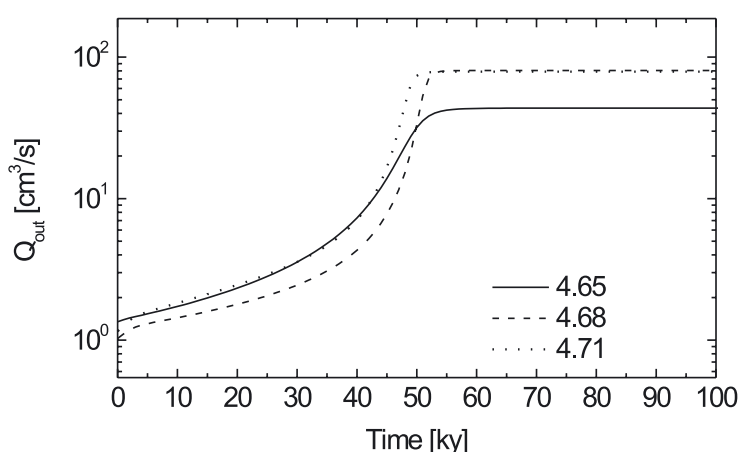


Figure 4.66: Flow rates as a function of time for the scenarios in Figures 4.65, 4.68 and 4.71.

One comment should be given here. If one uses a uniform net (i.e. a net where all fine fractures are of equal aperture widths) instead of the statistical one no mixing can occur. Because of symmetry, there is no flow vertical to the central fracture, and mixing is excluded.

4.7.2 Pure mixing corrosion. Two prominent fractures in a uniform network

Figure 4.67 shows a domain with two straight prominent fractures with $A_0 = 0.02$ cm inserted into the net of Figure 4.64. The lower one penetrates through the entire domain from input to output, whereas the upper one ends blind. The net of fine fissures is uniform with $a_0 = 0.00625$ cm. All other boundary conditions are equal to those in Figure 4.64. Input p_{CO_2} into prominent fractures is 0.01 atm and in all others 0.05 atm. All input waters are saturated with respect to calcite.

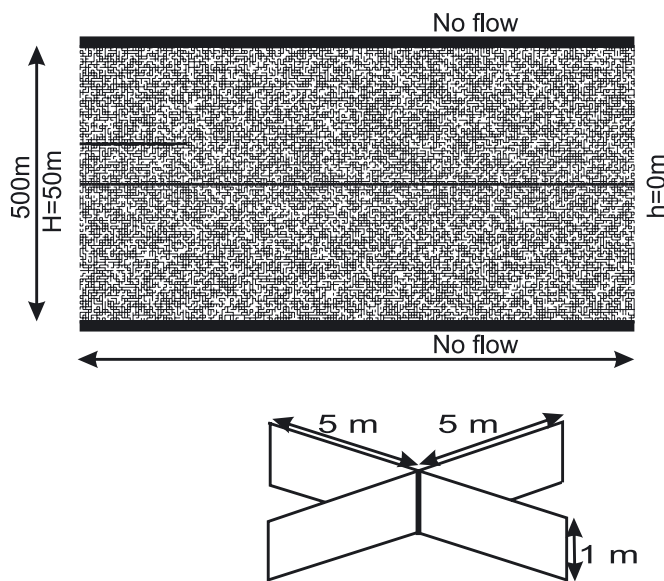


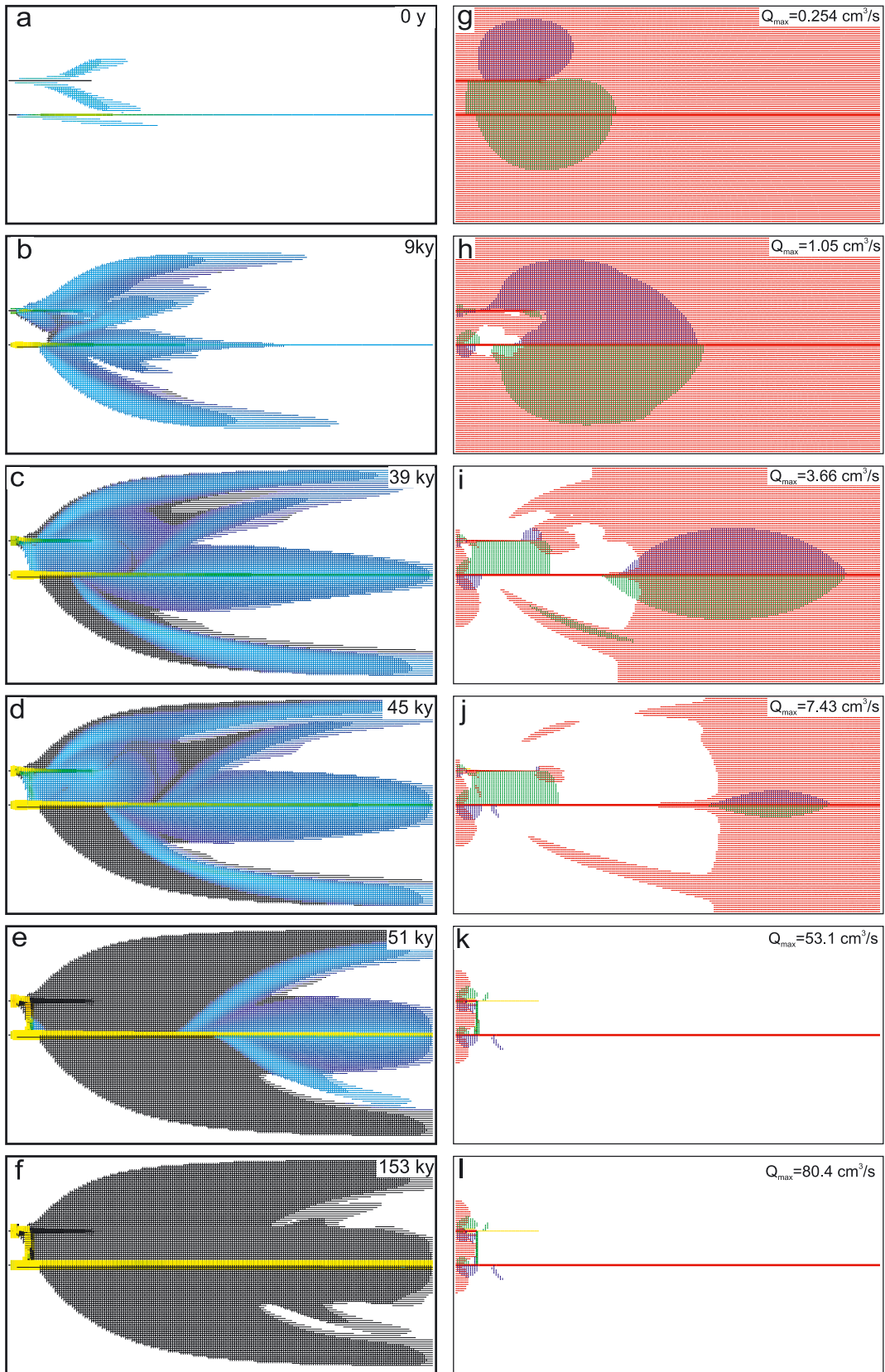
Figure 4.67: Network as in Figure 4.64 with two prominent fractures. p_{CO_2} at these fractures is 0.01 atm, whereas all other entrance fissures of the net receive water with $p_{CO_2} = 0.05$ atm. Head at the entrance of all fractures and fissures is $H = 50$ m and zero at the outflow. Dimensions and boundary conditions can be read from figure. Other conditions as in Figure 4.64.

The evolution of this scenario is depicted in Figure 4.68a–e.

At $t = 0$ (Figure 4.68a) the high head at the tip of the upper fracture injects water into the aquifer. Part of it enters into the lower fracture, which exhibits lower values of head in this region. Close to its entrance there is also flow from the lower fracture into the net (green and blue regions at the fracture). As can be seen in Figure 4.68a by the color code, MC occurs in the region of out flowing waters, where these waters mix with those of the net. MC is also active along the penetrating fracture close to its entrance part, where it receives flow from the net (Figure 4.68b–e).

After 9000 y (Figure 4.68b, h) due to the widening of the lower fracture by MC at its entrance region, high hydraulic heads migrate downstream into the aquifer and water from the lower fracture flows out into the net. However, there is some inflow of water from the net in the entrance region similar as in Figure 4.65. Therefore, MC is active and dissolutional widening occurs along the central fracture. There is also dissolutional widening in the upper blind fracture receiving water from the net. In the regions, where flow from the prominent fractures mixes with water in dense fractures (light and dark blue), a fan of low dissolution rates creates widening by MC (Figure 4.68b).

4. MODELING KARST EVOLUTION ON TWO-DIMENSIONAL NETWORKS: CONSTANT HEAD BOUNDARY CONDITION





After 39 ky (Figure 4.68c, i) this fan of MC has extended and propagated downstream. Mixing corrosion along the lower prominent fracture is still driven by inflow of waters from the net close to the input and by water from the upper fracture flowing downwards. To a lower extent MC is also active along the upper blind fracture. The main region of outflow from the lower fracture has penetrated downstream and creates a large fan of MC in the net. The upstream region, however, is abandoned by flow (Figure 4.68i), and consequently dissolutional activity is absent, reflected by the black and white regions in Figure 4.68c and i. White regions in the right hand column designate extremely low flow rates less than $10^{-5} Q_{max}$, whereas they depict fractures, which never have experienced dissolutional widening on the left hand column.

After 45 ky (Figure 4.68d and j) most of the flow is transported through the lower fracture. There is still significant inflow into its entrance part, from both the net and from the upper fracture. This keeps MC active. There is also inflow of water from the net into the upper fracture at its entrance. More downstream flow is lost from the upper fracture into the net.

After 51 ky flow through the lower fracture dominates (Figure 4.68e and k). The upper fracture now receives water from the net and flow in it is directed backwards (yellow) and towards the lower channel. The upper and lower fractures are connected by a narrow region of MC (Figure 4.68e). In the net, the region, where MC is still active, has propagated downstream, but most of the net is abandoned by flow.

Finally, after 153 ky a stable mode develops (Figure 4.68f and l). Most of the flow is through the lower fracture. There is some flow from the net backwards (yellow) along the upper fracture and mixing is active in the entrance regions. This is sufficient to maintain moderate dissolution rates along the entire channel. There is no flow from the fractures into the net in the downstream part as can be seen by the white regions in Figure 4.68e.

Flow through the net is shown as a function of time by the dashed line in Figure 4.66. It behaves, as one expects, like that of the single penetrating fracture in Figure 4.65.

4.7.3 Pure mixing corrosion: Two fractures in a statistical net

As we have seen in the last section use of uniform nets delivers results, which can be nicely interpreted. However, in nature such aquifers are not realistic. We therefore return to the domain of Figure 4.67 where the uniform net discussed in the last section is replaced by the standard statistical net.

← **Figure 4.68:** Evolution of the aquifer of Figure 4.67, with uniform net ($\bar{a}_0 = 0.00625$ cm) and two prominent fractures ($A_0 = 0.02$ cm) in the mode of pure MC, $c_{in} = c_{eq}$. Note that white areas depict regions where dissolutional widening did not yet operate (a-f). White regions in g-l carry only little flow ($Q < 10^{-5} Q_{max}$).



4. MODELING KARST EVOLUTION ON TWO-DIMENSIONAL NETWORKS: CONSTANT HEAD BOUNDARY CONDITION

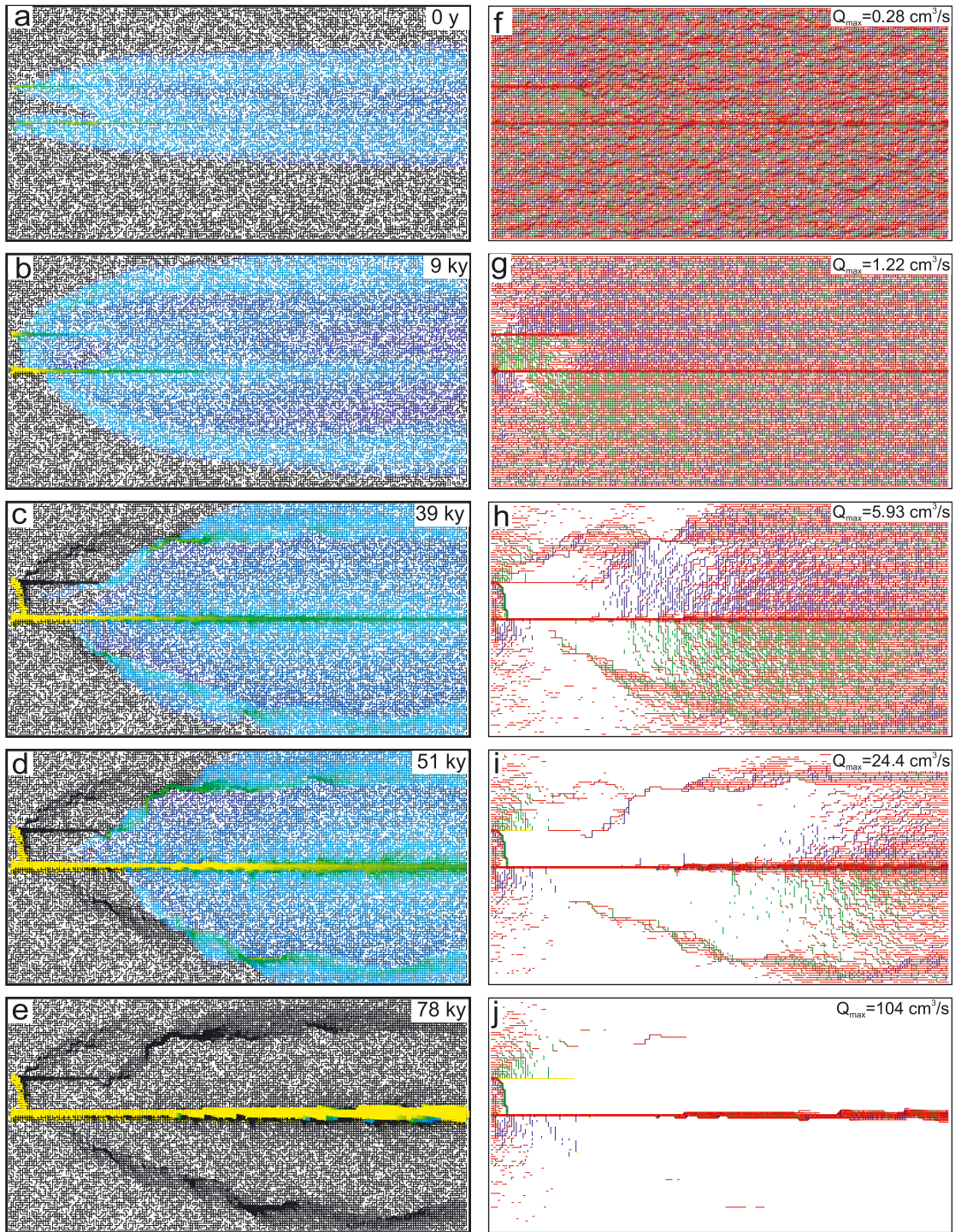


Figure 4.69: Evolution of the aquifer as shown in Figure 4.68. The uniform network is replaced by the standard statistical network with $\bar{a}_0 = 0.00625$ cm. Other parameters and boundary conditions are as in Figure 4.68.

The results are shown in Figure 4.69. At the beginning, we have two overlapping fans, widely extending from both fractures. Mixing corrosion is strongest in the upstream part of the lower, penetrating fracture (Figure 4.69a, f). Flow rates are not so easy to read as in the case of the uniform net. Nevertheless, they are similar. There is flow through the net from the upper fracture into the lower one (green lines), and outflow from the upper fracture into the net. Also the lower fracture feeds flow into the net. But due to the heterogeneity of the statistical net one finds also flow from the net into the central fracture. This can be seen from the statistically distributed green and blue fissures connected to it.

After 9000 y (Figure 4.69b, g) close to the input a region (yellow) of highly active MC arises. It is fed by flow out of the net into the input region of the lower fracture. Although not so easily to be seen, the situation is similar to that in Figure 4.68b and g.

At 39 ky (Figs. Figure 4.69c, h) MC is strong in the region between the upper fracture and the entrance part of the central fracture (yellow). As can be seen from panel h, this is a region of inflow into the central fracture and of outflow from the upper one. The downstream region shows flow leaving this fracture creating a wide fan of MC, which is strongest close to its rims. Close to the entrance region MC has created a connection between the upper and lower channel.

After 51 ky (Figure 4.69d, i) the region of high dissolution rates (yellow) has further propagated downstream. A wide fringe of increased permeability has been created in the net, as shown by the patterns of fat black lines. This has not been observed in the uniform net. The statistical net gives rise to more efficient mixing, creating this phenomenon. The flow into the input region does not show significant changes and flow is drained by the lower channel.

After 78 ky (Figure 4.69e, j) dissolution occurs mainly in the lower channel. But a region of increased permeability has been created (black fringe). Flow now is focused to a narrow region around the lower fracture, which widens slowly.

4.7.4 Pure mixing corrosion: A more complex case by adding isolated fractures and dead ends

Dual-fracture networks contain percolating pathways consisting of prominent fractures. Some pathways of prominent fractures are connected to the input. Some of them are connected to the input, but not to the output. Some are connected neither to inputs nor outputs. These elements have not been regarded so far.

For further completion we now add some isolated fractures and one fork- like branching with $A_0 = 0.02$ cm from the lower fracture into the net of Figure 4.67. This new domain is shown by Figure 4.70.

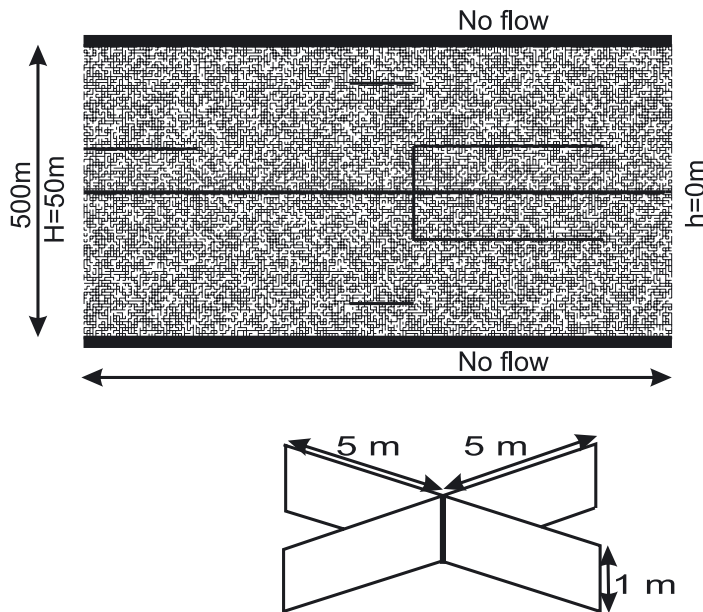


Figure 4.70: Modeling domain: Network of fine fissures as in Figure 4.64, which carries additional prominent fractures. p_{CO_2} at the input points of prominent fractures is 0.01 atm, whereas all other entrance fissures of the fine net receive water with $p_{CO_2} = 0.05$ atm. Hydraulic head $h = 50$ m. Dimensions and boundary conditions can be read from figure. Other conditions as in Figure 4.64

Figure 4.71 shows the evolution of the aquifer with a uniform net. It behaves very similar to the previous scenario. Therefore, we will only comment new features, which are caused by the new fractures. In the beginning, again fans of active MC develop. Some of the flow is attracted by the new prominent fractures. But the entrance region is not seriously affected. After 9000 y (Figure 4.71b, g) there is some flow through the isolated fractures to the neighboring fractures of the fork. This creates a region of permeability growing towards the corners of these fractures. Furthermore, at their downstream part and their tips, water is injected into the net, creating a fringe of growing fractures. After 39 ky (Figure 4.71c, h) dissolutional widening at the entrance of the central fracture migrates downstream. At the same time flow is redirected by the prominent fractures and a complex pattern of active mixing corrosion is obtained.

At 51 ky (Figure 4.71d, i) the dissolutional activity directed towards the isolated fractures has moved downstream, leaving significant porosity (black) in the upstream region. Note that in the black regions dissolutional widening is absent because they are abandoned by flow. After 58 ky (Figure 4.71e, j) dissolutional widening is restricted to the central channel. But the pattern of fracture aperture widths clearly shows the influence of the added prominent fractures. A diagonal pathway connects the central fracture to the lower isolated fracture as a new feature. Figure 4.66 depicts the flow rate as function of time by the dotted curve.

These few scenarios served as an introduction to be able to interpret the evolution of our standard dual-fracture aquifer in the following section.

4. MODELING KARST EVOLUTION ON TWO-DIMENSIONAL NETWORKS: CONSTANT HEAD BOUNDARY CONDITION

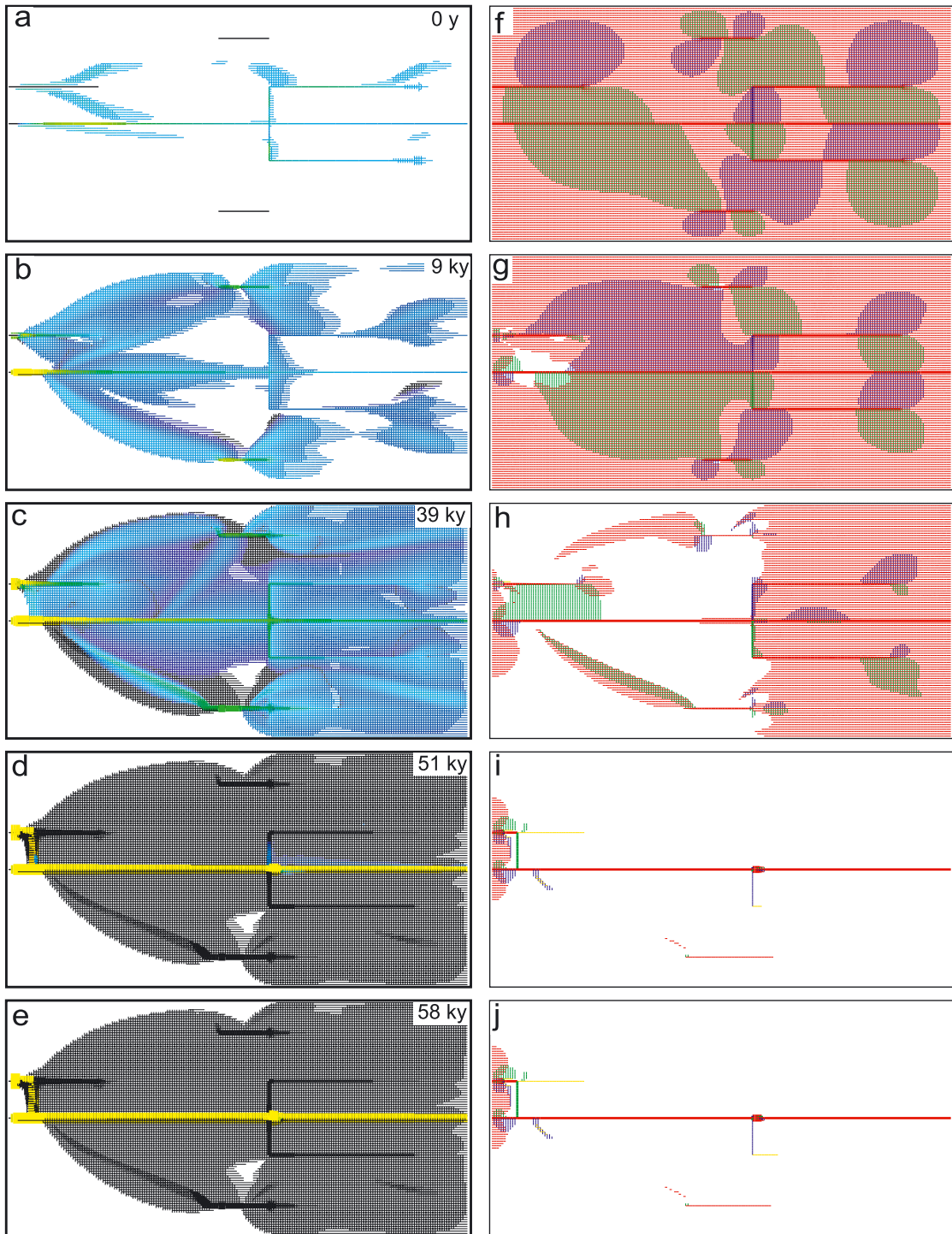


Figure 4.71: Evolution of the aquifer in Figure 4.70. $\bar{a}_0 = 0.00625$ cm, $A_0 = 0.02$ cm, $c_m = c_{eq}$. Other boundary conditions as in previous Figure 4.70.

4.8 MIXING CORROSION AND BREAKTHROUGH

In the previous section we have discussed the extreme situation where all solutions entering the aquifer are fully saturated and mixing corrosion is the only mechanism to cause dissolutional widening. In this section we will discuss scenarios, where mixing corrosion and the breakthrough mechanism are both operative.

4.8.1 One prominent fracture in a statistical network

We combine MC and breakthrough for the case of a single prominent fracture, embedded into a statistical net as shown by Figure 4.64 and 4.65. This is accomplished by putting all input concentrations to $c_{in} = 0$, instead of $c_{in} = c_{eq}$, $p_{CO_2} = 0.01$ atm at the input points of the prominent fracture and 0.05 atm at the input points of the net. Everything else is left unchanged. Figure 4.72 depicts the evolution. After 9000 y (Figure 4.72a) highly aggressive solution has penetrated into the entrance of the prominent fracture, causing high dissolution rates. Therefore, the head becomes high in this entrance region and water flows from the central fracture out into the net (Figure 4.72f). Consequently, mixing corrosion by this way occurs solely outside the fracture in the net.

After 21 ky (Figure 4.72b, g) the conduit along the central fracture has further penetrated downstream and loses water into the net, which activates mixing corrosion and creates a region of small channels.

After 30 ky (Figure 4.72c, h) a highly active region has developed (green) where conductivity is enhanced (Figure 4.72c). The region of water loss from the central fracture into the net has migrated downstream (Figure 4.72h). Since there is no flow into the fractures upstream, MC is not active there.

After 40 ky (Figure 4.72d, i) flow is concentrated in the central fracture and along the channels, which have been created in the highly active mixing zone. These channels are now fed by highly aggressive waters ($c_m = 0$) from the input points. A competition between different breakthrough pathways becomes visible. The first pathway is along the central fracture fed by waters with low $p_{CO_2} = 0.01$ atm. Others are along the small conduits in the fringes, which attract flow from the central fracture. There is a region of inflow from the net into the middle part of the central fracture, such that MC is activated there (yellow). This favors the central fracture as a breakthrough pathway and breakthrough happens after 46.4 ky as depicted by Figure 4.72e and j.

To summarize, a complex interplay between breakthrough behavior and slow widening by MC creates new unexpected features.

It should also be mentioned that in this case the CO_2 -input values are of extreme importance. If p_{CO_2} would be higher in the middle fracture, but lower at the input points in the net, the middle fracture will need shorter time for breakthrough. But the opposite would be true for the channels in the net.

4. MODELING KARST EVOLUTION ON TWO-DIMENSIONAL NETWORKS: CONSTANT HEAD BOUNDARY CONDITION

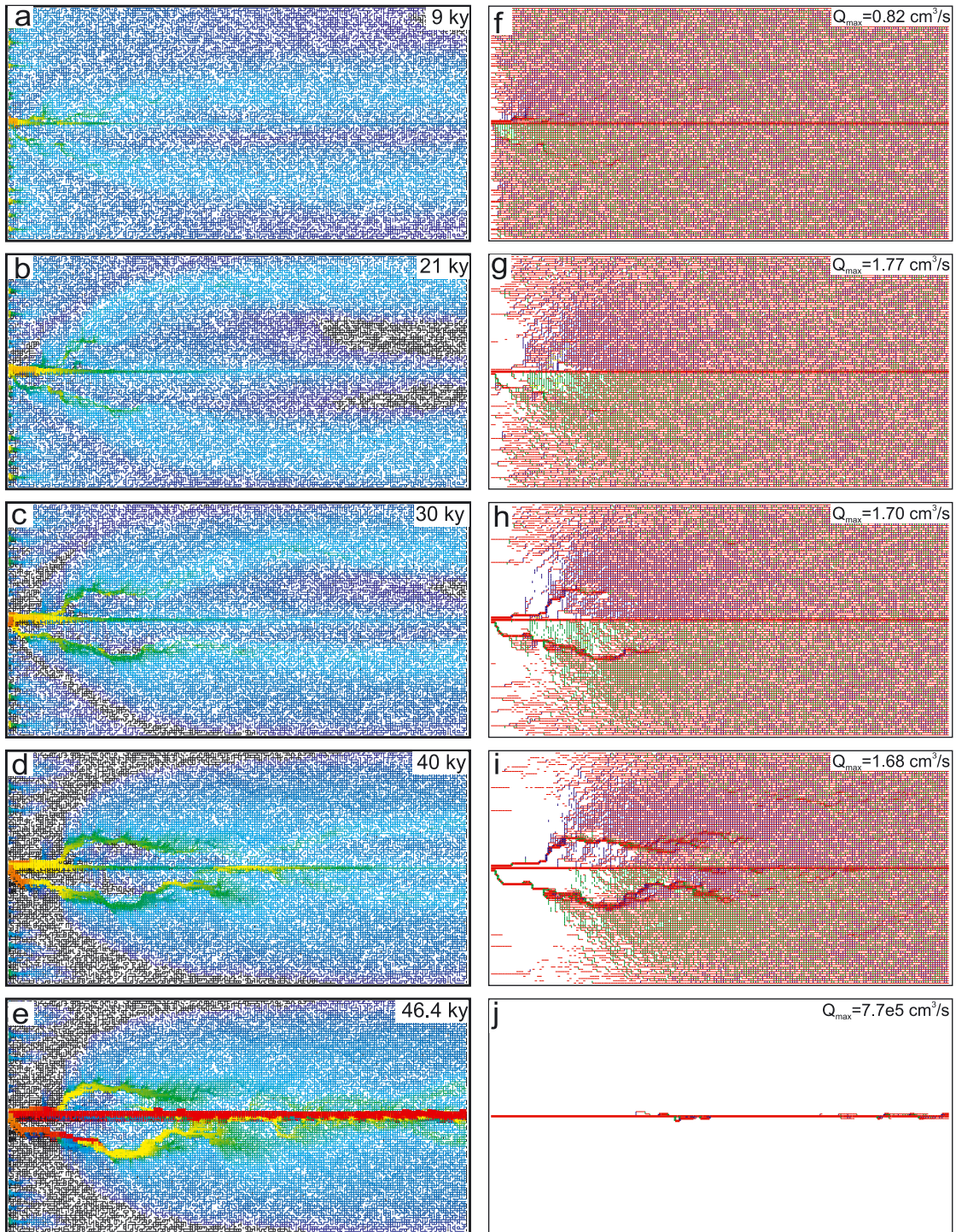


Figure 4.72: Evolution of the aquifer of Figure 4.65 (one single fracture in standard statistical network). But now $c_m = 0$ at all inputs. p_{CO_2} at the input points of prominent fractures is 0.01 atm, whereas all other entrance fissures of the fine net receive water with $p_{CO_2} = 0.05$ atm. MC and breakthrough behavior operate simultaneously. All other parameters and boundary conditions as in Figure 4.65.

4. MODELING KARST EVOLUTION ON TWO-DIMENSIONAL NETWORKS: CONSTANT HEAD BOUNDARY CONDITION

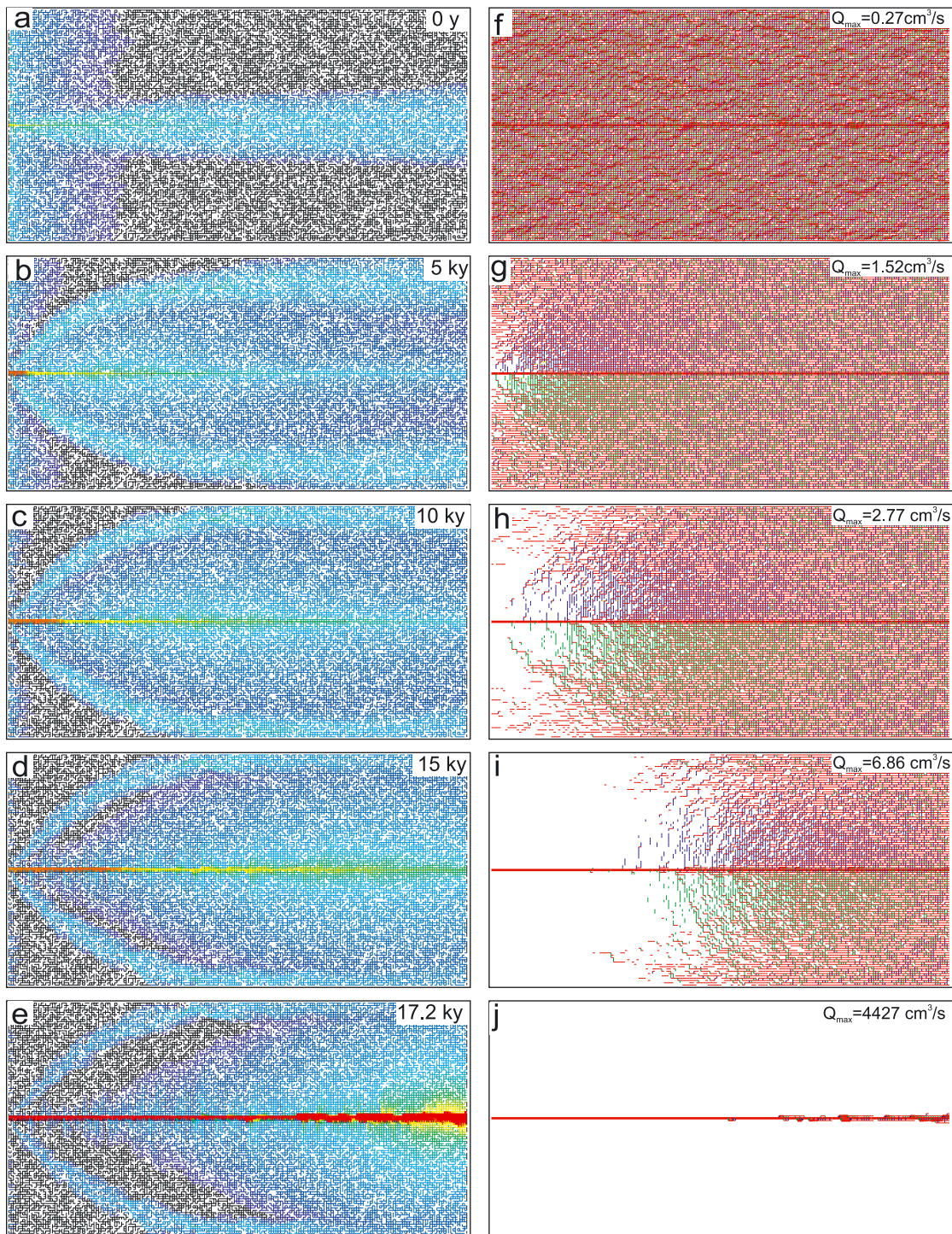


Figure 4.73: Evolution of the aquifer in Figure 4.72. p_{CO_2} at prominent fractures is raised to $p_{CO_2} = 0.05$ atm and in fissures it is lowered to 0.01 atm. Other parameters and boundary conditions as in Figure 4.72.

Figure 4.73 gives this as an example, with $p_{CO_2} = 0.05$ atm in the prominent fracture and $p_{CO_2} = 0.01$ atm in the net. Due to the higher p_{CO_2} in the input of the central prominent fracture, evolution of a channel is accelerated. Although MC is active in the net, time is not sufficient to create significant permeability, because breakthrough along the central conduit occurs already after 17 ky.

We now turn back to the scenario of Figure 4.73. We model the case, where the entering solution is close to equilibrium ($0.99c_{eq}$). All other parameters and boundary conditions are as in Figures 4.73. For such high input concentrations we have seen (confer to section 4.4.1) that dissolution rates are low and even everywhere in the net, so that independently of MC a slow widening, almost linear in time is present.

Figure 4.74a and d show the situation after 9000 y. Dissolution rates from the slightly undersaturated solutions are depicted by dark blue. MC is seen close to the entrance (yellow), along the middle fracture (green, light blue) and also at the fringes of the mixing zone, quite similar to pure MC (Figure 4.65).

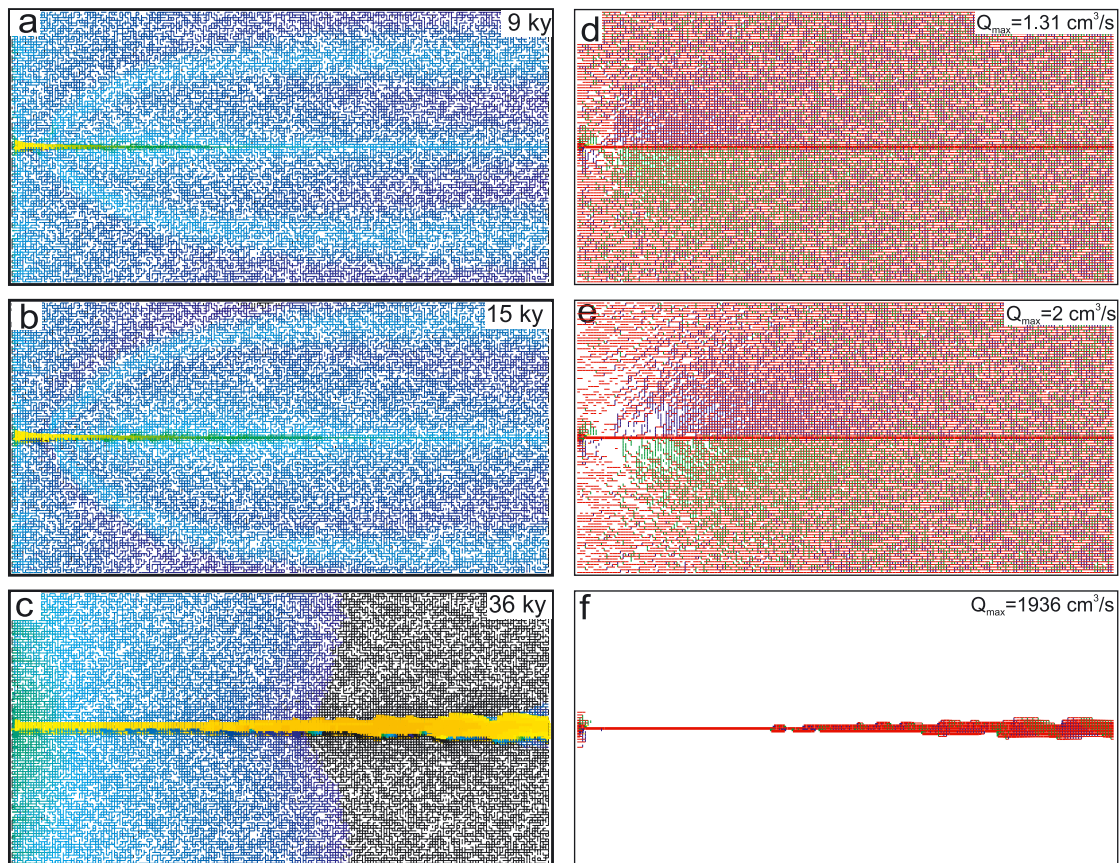


Figure 4.74: Evolution of the aquifer in Figure 4.72. But now $c_{in} = 0.99c_{eq}$. Other parameters and boundary conditions as in Figure 4.72.

After 15 ky there is still no significant change. There is flow from the net into the entrance of the fracture causing MC (Figure 4.74b, e). More downstream there is outflow from the fracture into the net. In the last third of the fracture some inflow again enhances MC. Finally, a stable state of evolution is reached from 36 ky on (Figure 4.74c, f). Flow is concentrated in the central channel, which drains the fracture system. Therefore, dissolution rates by MC are high there, especially at the end of the channel, which receives an optimal amount of water from the net to boost up MC.

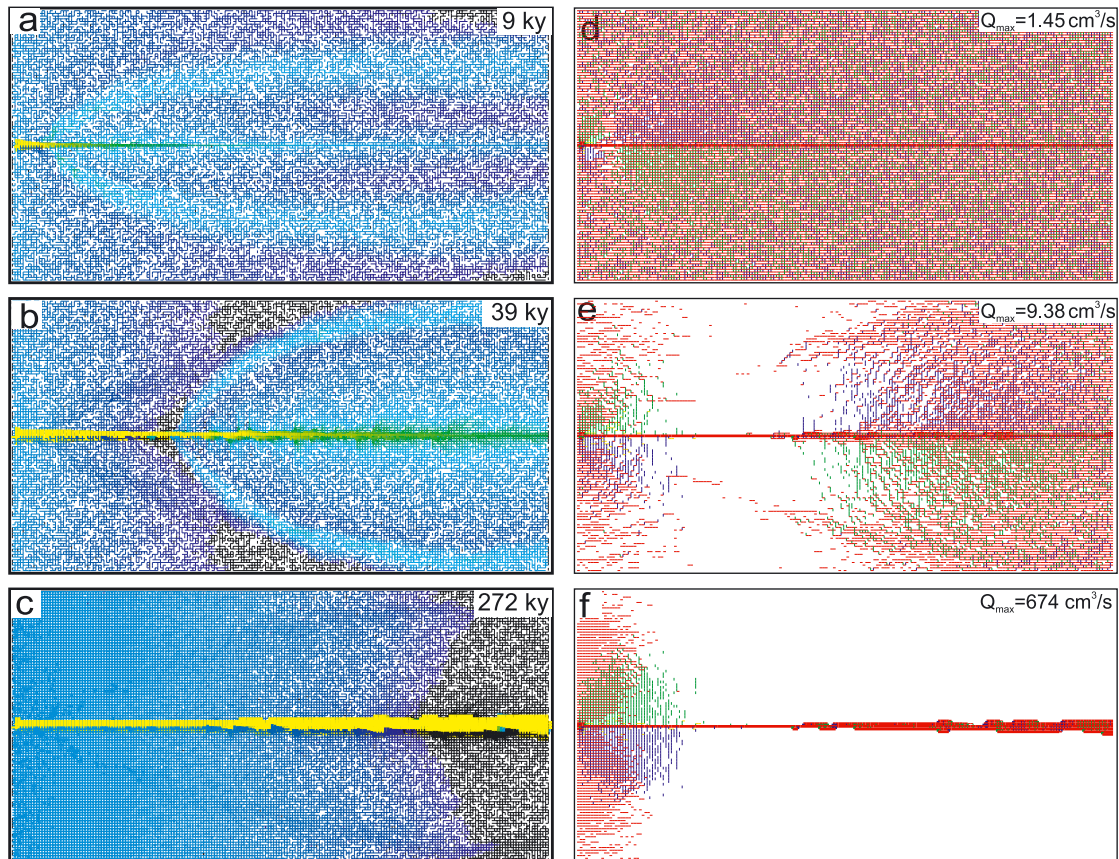


Figure 4.75: Evolution of aquifer as in Figure 4.74. But now $c_{in} = 0.995 c_{eq}$. Other parameters and boundary conditions as in Figure 4.74.

If the input solution is taken closer to saturation with $c_{in} = 0.995 c_{eq}$ the influence of dissolution in the net is reduced. Figure 4.75 shows the evolution in this case. It is very similar to the evolution with pure MC in Figure 4.65. But due to the slightly undersaturated solution, entering into the fissures of the net, slow dissolutional widening is active (blue regions in Figure 4.74), in contrast to the black regions in Figure 4.65).

Figure 4.76 shows flow rates as a function of time for the single fracture scenario with $c_{in} = 0$, $c_{in} = 0.99 c_{eq}$, $c = 0.995 c_{eq}$, and $c_{in} = c_{eq}$, respectively. Their behavior is similar to that found in Figure 4.53. This shows that the interplay of MC and dissolution from undersaturated input solutions plays a generally important role.

4. MODELING KARST EVOLUTION ON TWO-DIMENSIONAL NETWORKS: CONSTANT HEAD BOUNDARY CONDITION

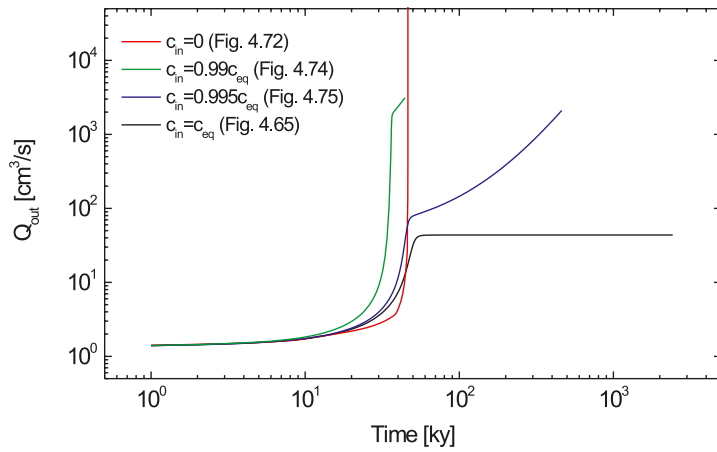


Figure 4.76: Flow rates as a function of time for the scenarios of Figure 4.65 ($c_{in} = c_{eq}$); Figure 4.72 ($c_{in} = 0$); Figure 4.74 ($c_{in} = 0.99c_{eq}$) and Figure 4.75 ($c_{in} = 0.995c_{eq}$).

The importance of MC can also be demonstrated by considering an aquifer, where it is avoided. This is achieved by changing the conditions in the scenario of Figure 4.75, using equal input concentrations of CO_2 everywhere and leave all other conditions unchanged. Figure 4.77 illustrates the evolution.

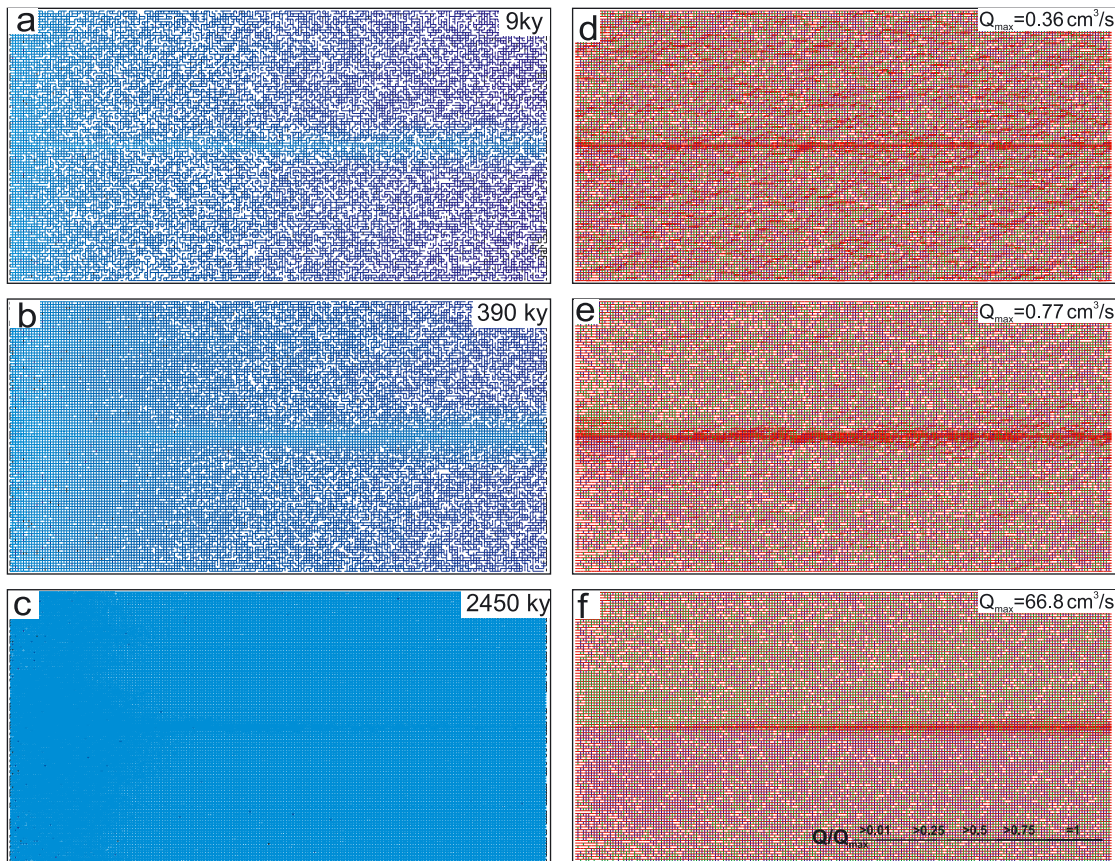


Figure 4.77: Evolution of the aquifer in Figure 4.75. $c_{in} = 0.995c_{eq}$. Now MC is excluded by putting $p_{CO_2} = 0.05$ atm in prominent fractures and narrow fissures. Aperture widths and dissolution rates, left hand side column; flow directions and flow rates, right hand side column.

There is a region of moderate dissolution (light blue) at the beginning of the net. Because of the higher flow in the central fracture, this region of moderate rates penetrates deeper into the aquifer (a, b). Deeper in the net the rates drop (dark blue). As the fracture opens up it attracts flow from the net. After about 2 million years all fractures and fissures have widened to an extent that the penetration lengths λ_n (cf. Eq. 3. 25) exceed the length of the domain. Therefore, dissolution rates become maximal and equal everywhere in the domain, which now experiences equal widening everywhere (c).

To summarize, we can identify two important mechanisms. At all places where flow is directed out of a prominent fracture, dissolution inside this fracture cannot be enhanced by MC. But water leaving the fracture will mix with water flowing inside the net, most efficiently at the rim of the region occupied by out flowing water. This rim is the place, where MC is most active. On the other hand, at all sites, where water enters from the net into a prominent fracture, MC is not active in the net, but enhances widening in the fracture. By these mechanisms MC creates increased permeability in the net and in the prominent fractures. This redistributes flow and can create aquifers entirely different from those without MC, but with otherwise identical initial properties.

4.8.2 Two prominent fractures in a 2D-network

To further investigate the action of those mechanisms, we examine the scenario with two prominent fractures from Figure 4.67. ($A_0 = 0.02$ cm, $\bar{a}_0 = 0.00625$ cm. Input p_{CO_2} into prominent fractures is 0.01 atm and in all others 0.05 atm).

If not otherwise stated in the following all parameters and boundary conditions are as in the scenario of Figure 4.68.

To first illustrate the influence of MC, we investigate the evolution of the aquifer for $c_m = 0$ with and without MC. The right hand side on Figure 4.78 shows the evolution, when MC is switched off by putting $p_{CO_2} = 0.05$ atm everywhere in the net and in the prominent fractures. The left hand side shows what happens, when MC is present, because $p_{CO_2} = 0.05$ atm in the fine fissure net and 0.01 atm in the prominent fractures. Note that this is the only difference between these two scenarios.

After 6000 y (Figure 4.78a, e) a highly active region has penetrated downstream in both prominent fractures. Since in the case without MC p_{CO_2} is higher at the entrance of the central fracture, the channel there has developed faster than for the case of MC, where $p_{CO_2} = 0.01$ atm is lower at the entrances of the fractures. Tiny channels evolve close to the entrance boundaries. In contrast to Figure 4.78e a fringe of dissolutional widening (light blue) is shown where waters mix in Figure 4.78a.

After 10 ky, in case of no MC (Figure 4.78f), the lower channel has penetrated further downstream, but the upper channel due to redistribution of heads loses flow at its input. Therefore, the dissolution rates drop. The further evolution is shown by Figure 4.78g to h. After 15 ky the lower channel is shortly before breakthrough, whereas the upper channel exhibits low dissolution rates.

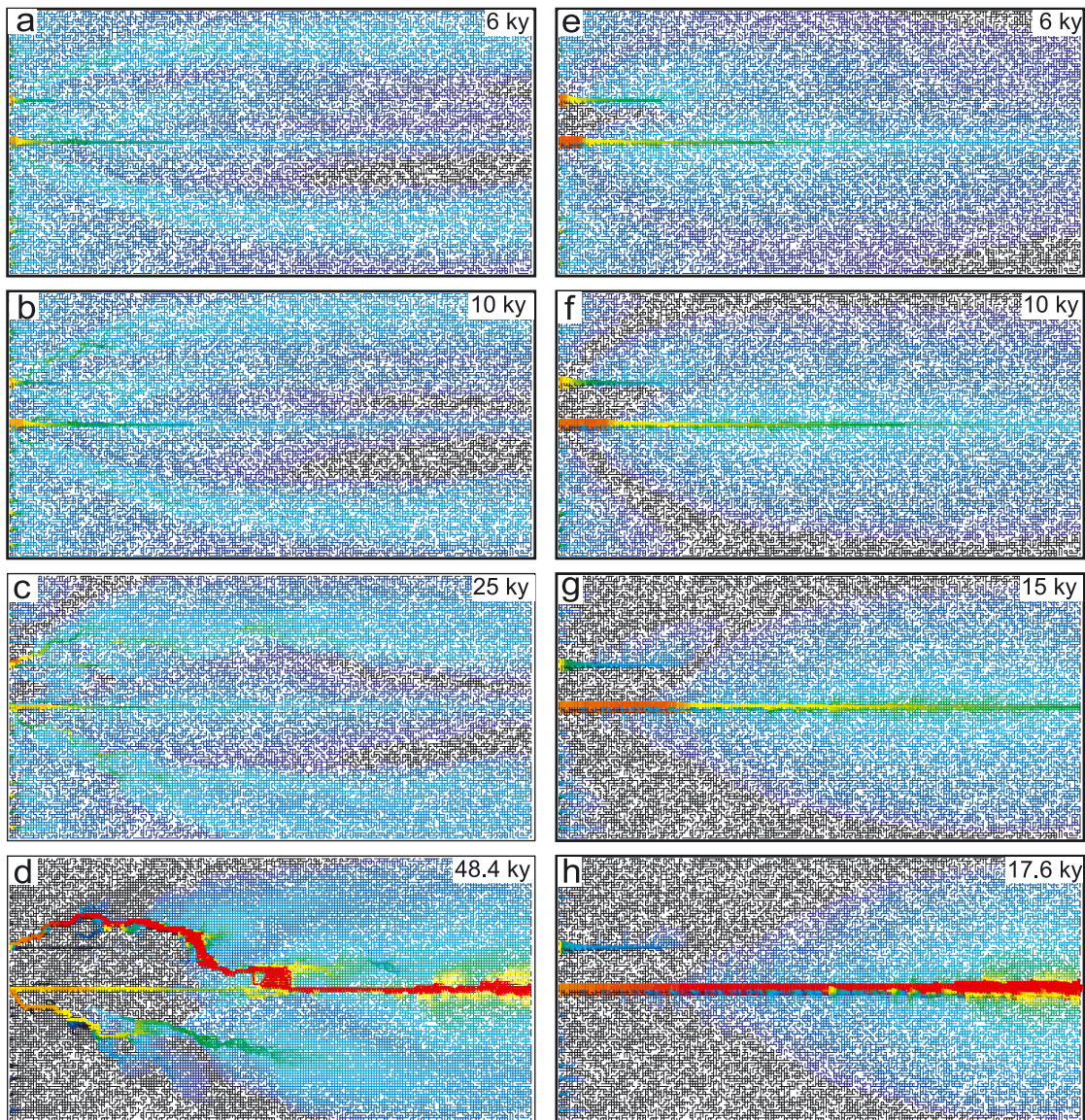


Figure 4.78: Evolution of the aquifer of Figure 4.67 (standard statistical net with two fractures: $\bar{a}_0 = 0.0064$ cm, $A_0 = 0.02$ cm). Left hand side column: Evolution of fracture aperture widths and dissolution rates when $c_{in} = 0$ at all inputs. p_{CO_2} at the input points of prominent fractures is 0.01 atm, whereas all other entrance fissures of the fine net receive water with $p_{CO_2} = 0.05$ atm. MC and breakthrough behavior is present. All other parameters and boundary conditions as in Figure 4.68. Right hand side column: Evolution of the aquifer, when MC is switched off by setting $p_{CO_2} = 0.05$ atm in both fracture systems.

After 17.6 ky breakthrough is accomplished through the more competitive lower channel and an exit fan develops as described in Section 4.4.1.

The evolution of the aquifer with MC is entirely different and needs longer time (Figure 4.78a, b, c, d). As already stated, because of the lower p_{CO_2} , the channel has penetrated only a small distance, but solutional widening occurs in the mixing zone. This

changes the hydraulic properties and attracts flow into this region (Figure 4.78b, 10 ky). Two competing pathways become visible, one through the lower channel and the other along the mixing zone above (Figure 4.78c). Finally, at 48 ky breakthrough utilizes the upper, highly permeable fringe and the downstream section of the prominent fracture (Figure 4.78d). A comparison between Figure 4.78d and h reveals the tremendous influence of MC. Even for the input concentration $c_{in} = 0$ the water quickly comes close to saturation, and in this region of low dissolution rates (dark blue) MC can boost up the rates. This changes the hydraulic conductivity, thereby redistributing flow and creating new pathways competing for breakthrough.

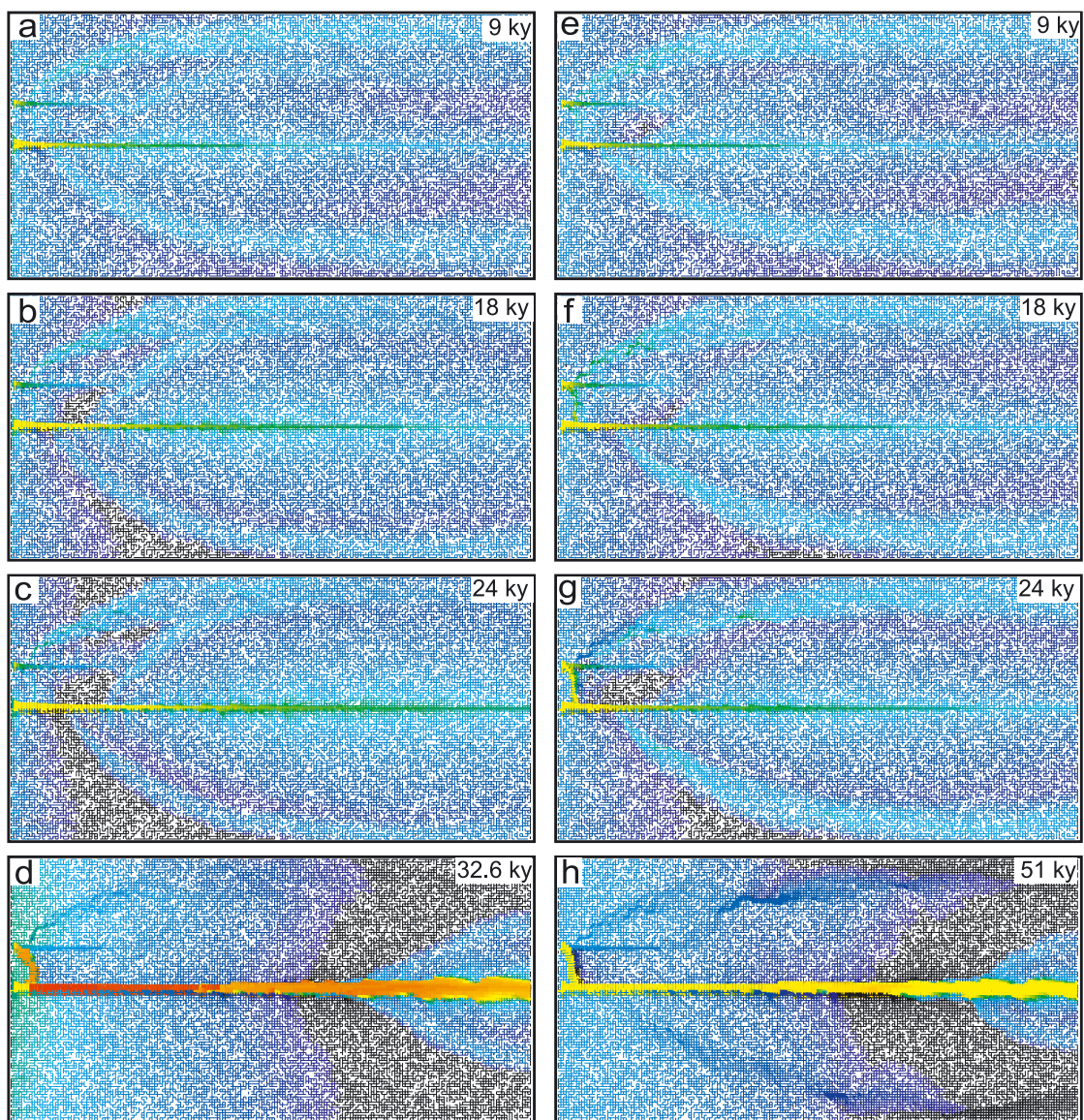


Figure 4.79: Evolution of the aquifer of Figure 4.78 with c_{in} changed to $0.99c_{eq}$ in the left hand column, and to $c_{in} = 0.995c_{eq}$ in the right hand side. MC is active.

In the next step we explore what happens at input concentrations $c_{in} = 0.99c_{eq}$ (Figure 4.79a–d) and $c_{in} = 0.995$ (Figure 4.79e–h), when the breakthrough feedback is reduced, but MC is active in both cases. Up to 9000 y the evolution of both aquifers is very similar (Figure 4.79a, e). After 18 ky the aquifer with $0.99c_{eq}$ (Figure 4.79b) shows more permeability in the vicinity of the central fracture, but at its entrance region it is less developed than the one with $0.995c_{eq}$ (Figure 4.79f). This becomes more pronounced after 24 ky (Figure 4.79c, g). After 32.6 ky (Figure 4.79d) high dissolution rates by MC are found for $c_{in} = 0.99c_{eq}$ creating widening in the central region. For the higher input concentration a very similar shape evolves more slowly with dissolution rates lower by one order of magnitude (Figure 4.79h, 51 ky). Figure 4.80 shows total flow rates through the aquifer as a function of time for $c_{in} = 0.99c_{eq}$, $0.995c_{eq}$, and c_{eq} respectively. It shows a very similar behavior as that of the single fracture in a statistical net for the same reasons explained there.

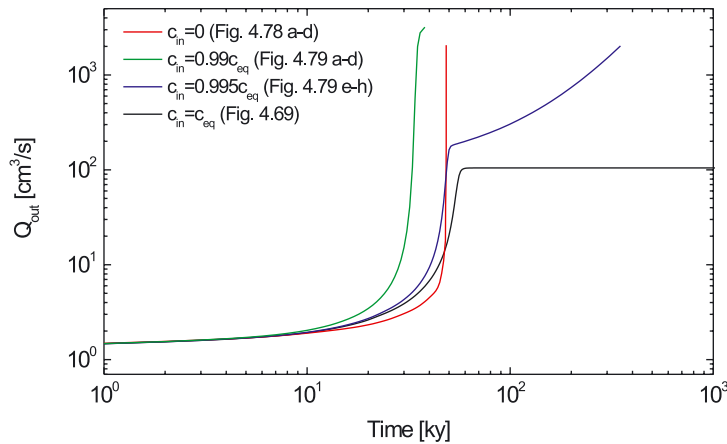


Figure 4.80: Time dependence of flow rates in the standard statistical net with two fractures (Figure 4.67) for Figure 4.78 ($c_{in} = 0$), Figure 4.79 ($c_{in} = 0.99c_{eq}$ and $c_{in} = 0.995c_{eq}$), and Figure 4.69 ($c_{in} = c_{eq}$). All parameters and boundary conditions as in Figure 4.69.

4.8.3 The more complex case by adding isolated fractures and dead ends

Finally, we turn to the more complex scenario by adding isolated fractures and dead end fractures as in Figure 4.70. If not stated all boundary conditions and parameter are as in Figures 4.70 and 4.71. ($A_0 = 0.02$ cm, $\bar{a}_0 = 0.00625$ cm). Input p_{CO_2} into prominent fractures is 0.01 atm and 0.05 atm into those of the net.

We compare the evolution of the aquifer with MC, and without MC. Input concentration $c_{in} = 0$ for both cases. The left hand side column of Figure 4.81 shows the evolution with MC (p_{CO_2} in prominent fractures 0.01 atm and 0.05 atm in the fine net) and the right hand side without MC ($p_{CO_2} = 0.05$ atm everywhere).

4. MODELING KARST EVOLUTION ON TWO-DIMENSIONAL NETWORKS: CONSTANT HEAD BOUNDARY CONDITION

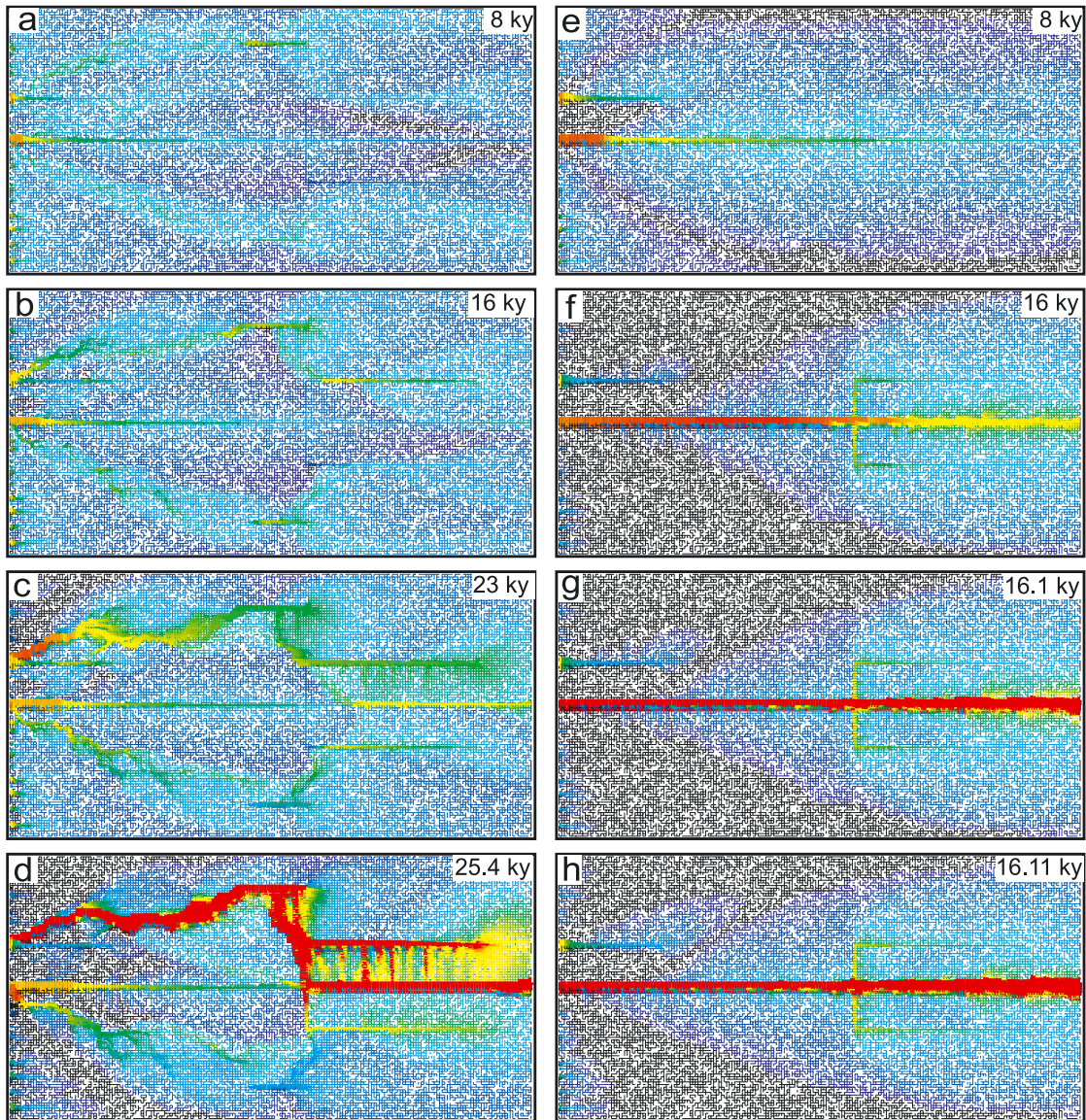


Figure 4.81: Evolution of fracture widths and dissolution rates in the aquifer of Figure 4.70 (network carrying a more complex pattern of prominent fractures, $a_0 = 0.00625$ cm, $A_0 = 0.02$ cm). Left hand side column: $p_{CO_2} = 0.01$ atm at prominent fractures and $p_{CO_2} = 0.05$ atm at all other ones. MC active. Right hand side column: $p_{CO_2} = 0.05$ atm at both fracture systems. MC switched off. $c_{in} = 0$ in both cases.

We first focus on the evolution with MC active shown by Figure 4.81 a, b, c, d. After 8000 y (Figure 4.81a) the central channel has slowly propagated downstream. Note that p_{CO_2} at the entrances of the prominent fractures is 0.01 atm. At the same time MC is active on the fringes and the isolated fractures. After 16 ky (Figure 4.81b) this pattern emerges more clearly. Comparatively large dissolution rates in the upper fracture and in the region of MC close to the upper isolated fracture have created a competitive pathway. After 23 ky (Figure 4.81c) highly aggressive input waters enter this upper pathway, where they

mix efficiently. Then these mixed waters flow along the upper isolated fracture. From there they traverse the net to join the upper prominent fracture of the fork. Finally they cross the net again and are drained by the central channel. The central channel guides water of low p_{CO_2} , which mixes with high p_{CO_2} waters flowing down from the upper dead end fracture. MC is activated in this downstream end of the central fracture (yellow). Finally, after 25.4 ky (Figure 4.81d) breakthrough occurs through the downstream part of the central fracture. To visualize this interpretation, Figure 4.82a–d shows the corresponding flow rates and flow directions.

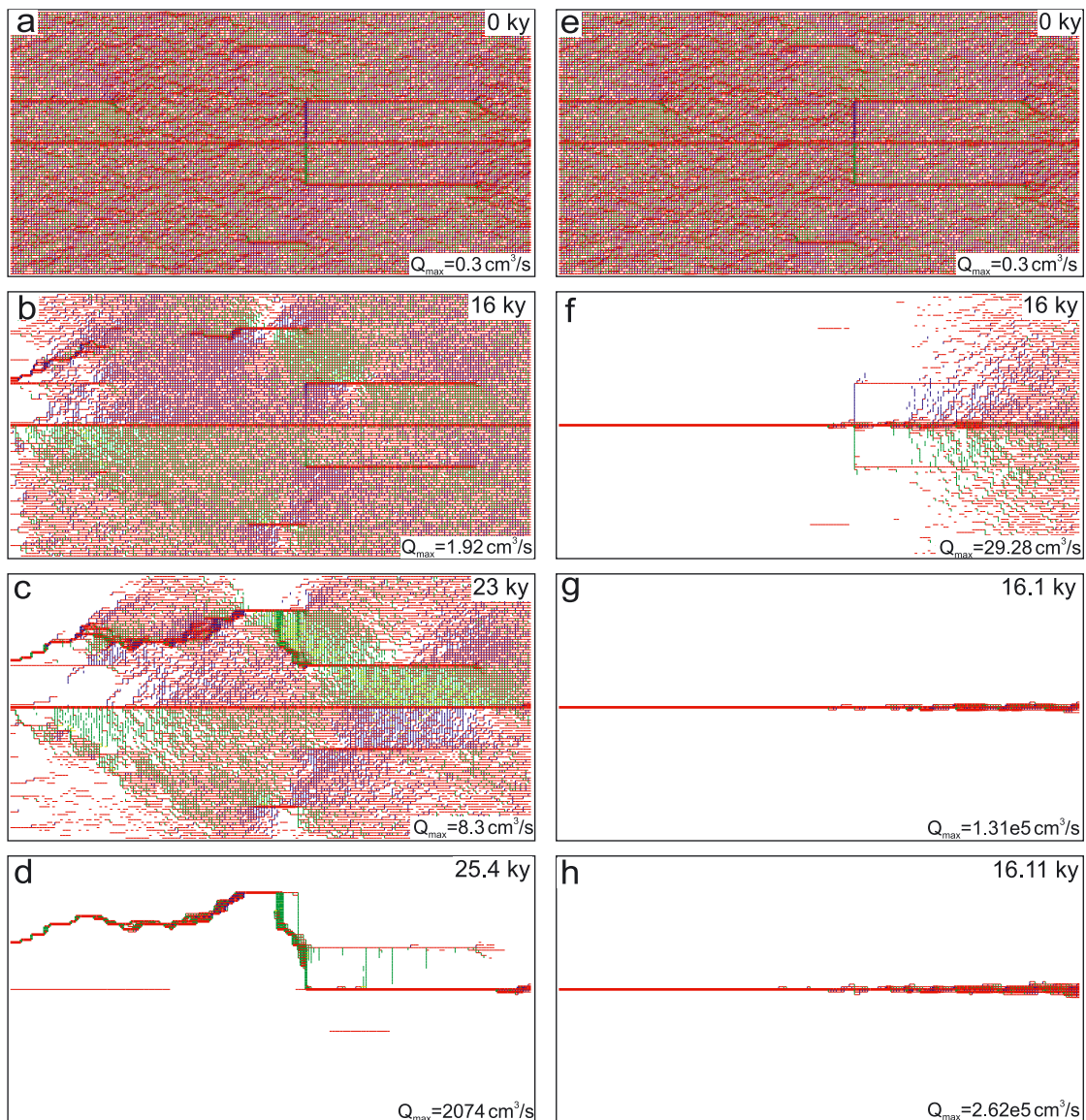


Figure 4.82: Evolution of flow rates and flow directions for the aquifers of the Figure 4.81. Left hand side MC active, right hand side MC switched off. All parameters and boundary conditions as in Figure 4.81.

The evolution without MC ($p_{CO_2} = 0.05$ atm at all inputs) is shown by Figure 4.81e–h and Figure 4.82e–h. A channel propagates downstream along the central fracture exhibiting regular breakthrough behavior at 16.11 ky. Also some widening occurs along the dead end channels and the neighborhood of the downstream part of the main conduit.

Once more, in contrast to this result, the complexity that is created by MC is fascinating.

4.8.4 The dual-fracture system

In the examples given so far, we have used very simple scenarios to clarify the processes active when MC is present. We have seen that hydraulic coupling determines the regions where different waters mix. There, dissolutional widening becomes active altering the pathways of flow. The interaction between MC and hydraulic coupling then determines the evolution. We will now turn to the more realistic modeling domain, which we have discussed in Section 4.1 and which is shown by Figure 4.37.

Again we put the p_{CO_2} to 0.01 atm at the inputs of all prominent fractures and to 0.05 atm at the inputs of net fissures. Since we have studied the mechanism in detail already in the simple scenarios, in the following we will present only the last step of our computations. The criterion for this last step is reached, when the total flow rate through the aquifer exceeds a given value of Q_{max} , which can be taken from the corresponding breakthrough curves.

Figures 4.83a–c show these stages of evolution for $c_{in} = 0$ and MC present. The aperture widths \bar{a}_0 (narrow fissures) in the net are 0.005 cm, 0.00625 cm, and 0.01 cm, respectively. In all cases the fracture width A_0 of the prominent fractures is 0.02 cm. In comparison the right hand side column (Figure 4.83d–f) shows the result if MC is switched off by putting $p_{CO_2} = 0.05$ atm also at the entrances of the prominent fractures.

We first discuss the case with MC in Figure 4.83a–c. For large aperture widths $\bar{a}_0 = 0.01$ cm hydraulic coupling $M = \bar{a}_0 / A_0$ is large (Figure 4.83c). Therefore, water from the prominent percolating pathway is injected into the net, and mixing in the fractures of the percolating pathway is not significant. The water injected at the first corner of the first loop is sufficiently aggressive to bypass this loop straight through the net, such that breakthrough occurs in a straight line through the aquifer and also bypassing some loops in the downstream part of the percolating pathway. This gives some hint that high hydraulic coupling ratios reduce the impact of MC on the final patterns. This is confirmed by Figure 4.83f, which shows the same scenario with MC switched off. Evidently, patterns and breakthrough times are quite similar. However, the breakthrough time in the case of MC is lower by about 20 % from that without MC. This shows that MC enhances dissolution rates in regions of exchange flow.

For $\bar{a}_0 = 0.00625$ cm (Figure 4.83b) the action of MC at the entrance region has created a diagonal pathway connecting to the upper part right through the net. The pattern

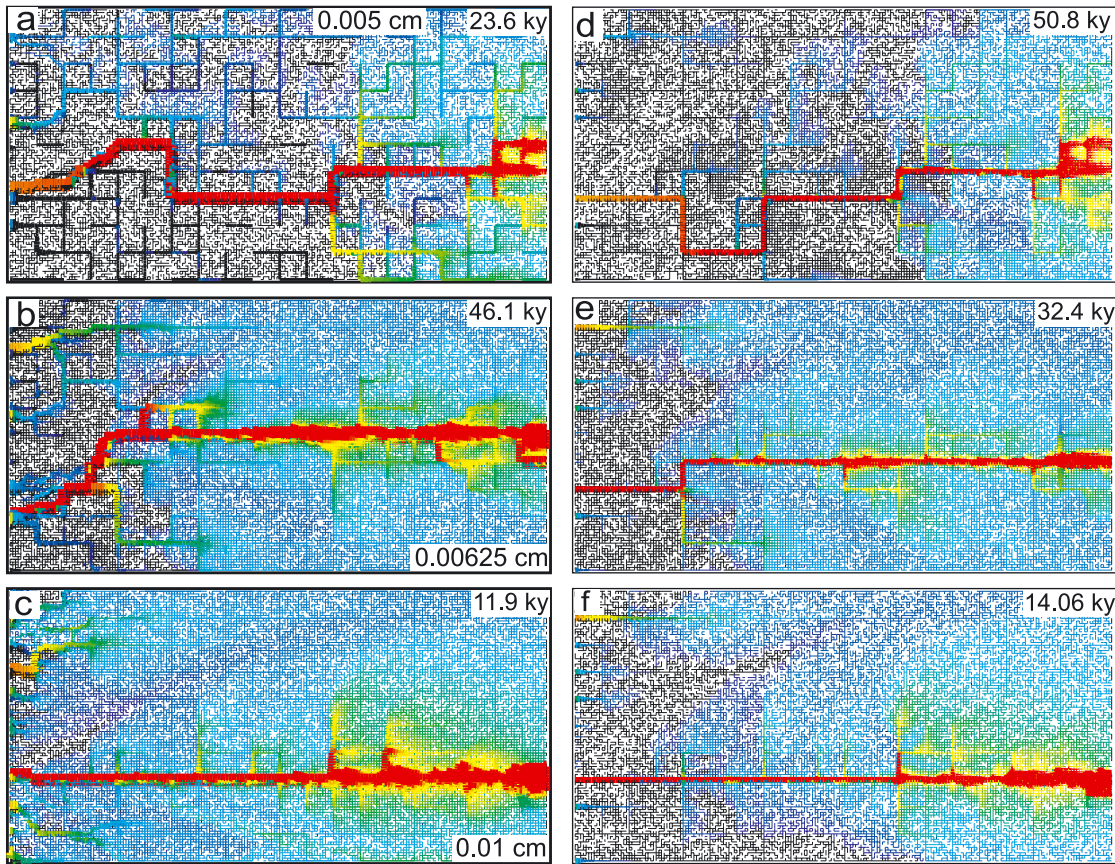


Figure 4.83: Aperture widths and dissolution rates at breakthrough of the dual-fracture aquifer of Figure 4.37 for various values of aperture width \bar{a}_0 depicted in panels a, b, and c. $c_{in} = 0$, $A_0 = 0.02$ cm, $p_{CO_2} = 0.01$ atm at prominent fractures and 0.05 atm at fissures in the net for various values of aperture widths \bar{a}_0 [cm]. $c_{in} = 0$. Left hand side MC active, right hand side MC switched off by setting $p_{CO_2} = 0.05$ atm at both fracture systems.

for $\bar{a}_0 = 0.00625$ cm without MC, shown in Figure 4.83e, is quite different, because it mostly contains prominent fractures and also some cutting through the net.

If hydraulic coupling is reduced further to $a_0 = 0.005$ cm (Figure 4.83a) and MC is active, the pattern once more exhibits significant changes. In the upstream part at the input boundary the channel evolves through the net, turns up diagonally and is then guided by prominent fractures. Then it cuts through the net again, and finally it employs the pathway of prominent fractures leading straight to the output boundary. If MC is excluded (Figure 4.83d) the pattern evolves entirely through the percolating pathway of prominent fractures, leading from the input to the output boundary.

To conclude, we state that coupling a coarse net of prominent fractures with aperture width A_0 to a dense net of narrow fractures with aperture widths $\bar{a}_0 < A_0$, and allowing different chemical input compositions for solutions entering these nets, creates an overwhelming variety of complex patterns solely by changing the hydraulic coupling ratio $M = \bar{a}_0 / A_0$.

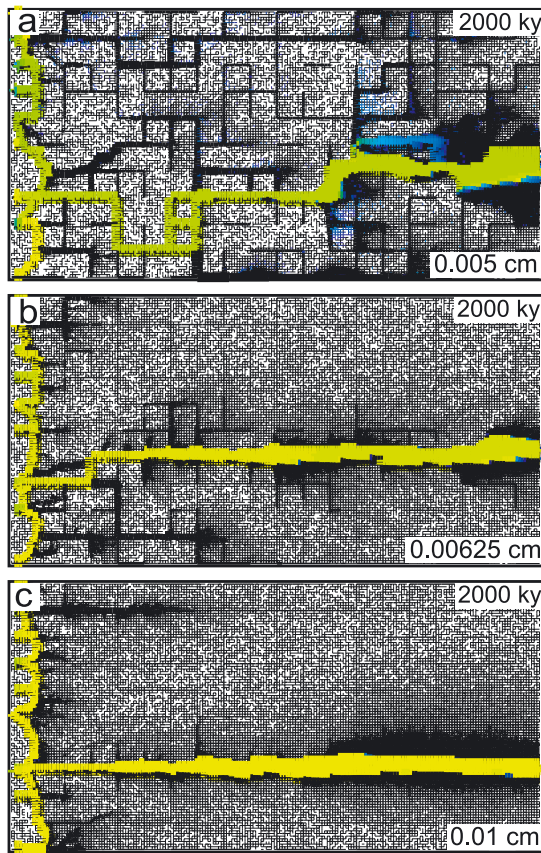


Figure 4.84: Aperture widths and dissolution rates after 2 million years in the dual-fracture aquifer of Figure 4.37 for various values of aperture widths \bar{a}_0 depicted in panels a, b, and c. Pure MC ($c_{in} = c_{eq}$), $p_{CO_2} = 0.01$ atm in prominent fractures and 0.05 atm in fissures of the net.

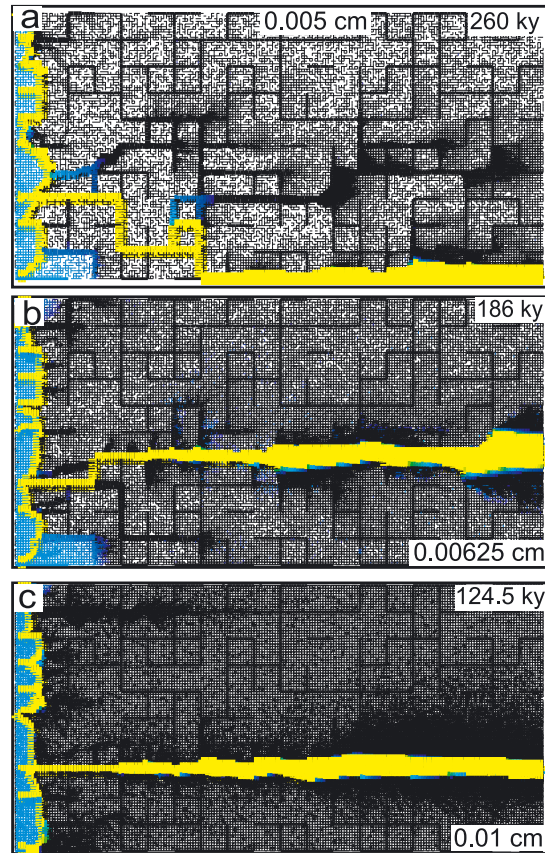


Figure 4.85: Aperture widths and dissolution rates of the aquifers in Figure 4.84 with $c_{in} = 0.995c_{eq}$ at times when total flow through the aquifer is 2000 cm³/s.

We now turn to the case of pure mixing corrosion by changing $c_{in} = c_{eq}$ in the scenarios of Figure 4.84a–d. The results are shown by Figure 4.83 for different aperture widths \bar{a}_0 in the net. For $\bar{a}_0 = 0.01$ cm (Figure 4.84c) a large central zone (yellow) of wide fractures has been created. At the same time at the entrance boundary mixing corrosion has formed an integrated system of conduits. It is obvious in this case that the main channel drains the net and dissolutional widening is therefore active along its entire length. For $\bar{a}_0 = 0.00625$ cm the entrance pattern is very similar (Figure 4.84b), but a somewhat different pathway is taken by the main channel. The situation is quite different for $\bar{a}_0 = 0.005$ cm (Figure 4.84a), where the main channel takes a completely different route. Note that for all cases the time to reach Q_{max} is 2 million years, a time scale two orders of magnitude larger than for the breakthrough mode.

If one reduces the concentration c_{in} at the input to $c_{in} = 0.995c_{eq}$ the patterns differ only in detail as shown by Figure 4.85a–c. The time to reach the same maximal flow rate as in the previous scenario shown in Figure 4.84, however, is one order of magnitude lower.

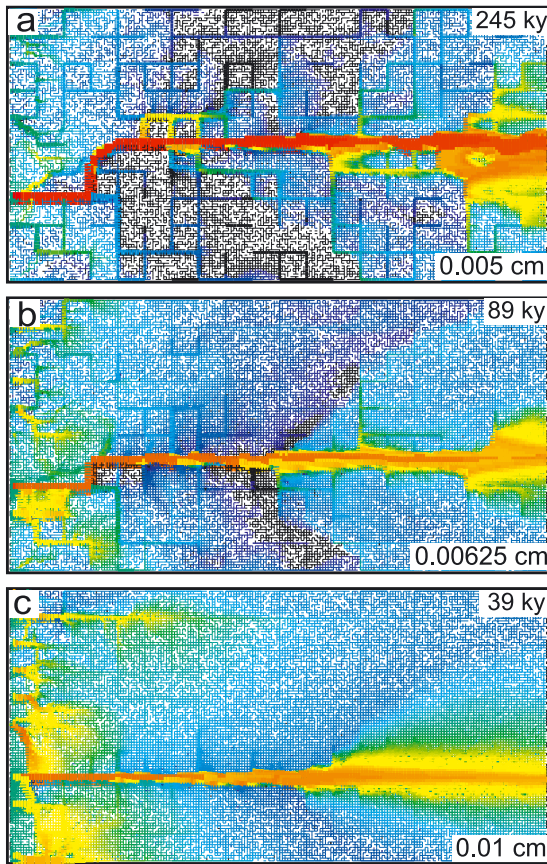


Figure 4.86: Aperture widths and dissolution rates for the aquifers in Figure 4.84 at times when total flow exceeds $2000 \text{ cm}^3/\text{s}$, $c_{in} = 0.99c_{eq}$.

For a lower input concentration $c_{in} = 0.99c_{eq}$ the patterns are shown in Figure 4.86a–c. Times to reach Q_{max} depend on \bar{a}_0 , increasing from 39 ky for

$\bar{a}_0 = 0.01 \text{ cm}$ to 245 ky for $\bar{a}_0 = 0.005 \text{ cm}$. For this input concentration dissolution rates in the net, caused by MC, are high. But comparison to the evolution of the aquifer with $c_{in} = 0$ in Figure 4.83a–d reveals that the breakthrough mechanism gains influence.

The evolution of all these aquifers is quite complex and cannot be presented here in pictures for reasons of space, but all details of widths, dissolution rates at various times and little movies on the evolution can be viewed from the accompanying CD.

From these pictures one can envisage that the mechanisms, which we have discussed in simple scenarios, are also operative in the complex aquifer, and no other principles are necessary to understand the genesis of more complex karst aquifers of this type.

Figure 4.87 shows the breakthrough curves for all considered values of input concentrations and aperture widths \bar{a}_0 in the dual-fracture aquifer with MC. Again, these complex aquifers exhibit a very similar behavior of breakthrough curves as the more simple scenarios discussed in the previous chapters.

A further point should be noted. Independently of the input concentrations, all breakthrough curves with $c_{in} \neq 0$ are identical during the first stage of evolution. This shows that mixing corrosion is the reason for the initial widening of fractures in the entrance region. Due to the low $p_{CO_2} = 0.01 \text{ atm}$ in the prominent fractures, penetration lengths are short and initially do not contribute significantly to the total conductivity of the aquifer.

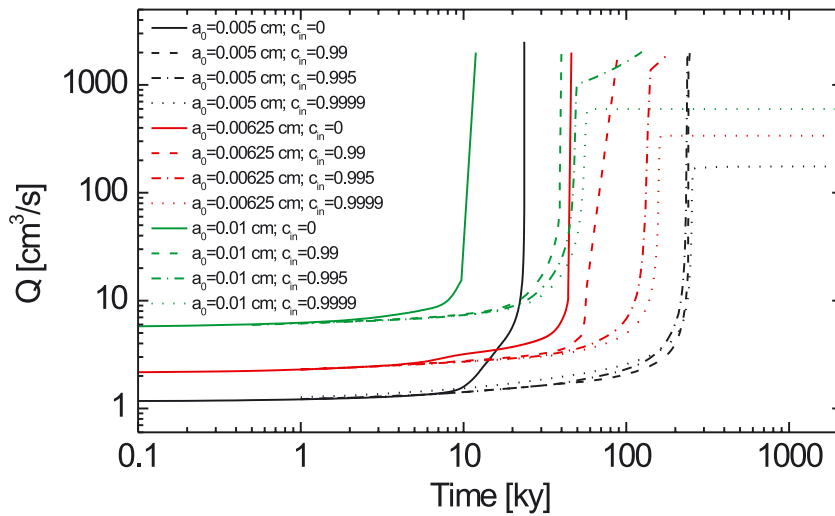


Figure 4.87: Evolution of flow rates in the dual-fracture aquifers of Figures 4.83 a, b, c, 4.84, 4.85 and 4.86 for various aperture widths \bar{a}_0 in the net and various input concentrations. $p_{CO_2} = 0.01$ atm in prominent fractures and 0.05 atm in fissures of the net.

4.9 DUAL-FRACTURE AQUIFER: MIXING CORROSION FROM DIFFERENTLY VEGETATED AREAS

As pointed out already, one could also envisage a scenario, where two different zones of vegetation on top of a karst plateau deliver water with differing p_{CO_2} into both, prominent fractures and fissures, in each of these zones.

This can be accomplished by a simple change of chemical boundary conditions in the standard scenario of Figure 4.37 ($A_0 = 0.02$ cm, $\bar{a}_0 = 0.00625$ cm). We assume a p_{CO_2} of 0.05 atm in all fissures and fractures in the upper half of the input boundary. This region is shown by the arrows in Fig. 4.88a and by red in e. In the lower input region (blue) $p_{CO_2} = 0.01$ atm. The input concentration of calcium is zero everywhere, $c_{in} = 0$.

Figure 4.88a–h shows the evolution aperture widths and dissolution rates on the left hand side column and the equilibrium concentrations of the water and its flow rates on the right hand side. Red color depicts the equilibrium concentration of waters entering the upper half with $p_{CO_2} = 0.05$ atm and blue that of water entering the lower half with 0.01 atm. Yellow, green and light blue represent mixed solutions with a c_{eq} between the two extremes (red, blue).

During the entire evolution the upper half (red) is supplied with water of high c_{eq} and the lower one with water of low c_{eq} . These waters mix in a central region (Figure 4.88e–f). There, the dissolution rates are enhanced, as shown by panels a and e. On the other hand, as in the ordinary breakthrough mode, small channels start to penetrate downstream (Figure 4.88a and b). Because of the higher p_{CO_2} in the upper half, these channels penetrate deeper than in the lower half.

4. MODELING KARST EVOLUTION ON TWO-DIMENSIONAL NETWORKS: CONSTANT HEAD BOUNDARY CONDITION

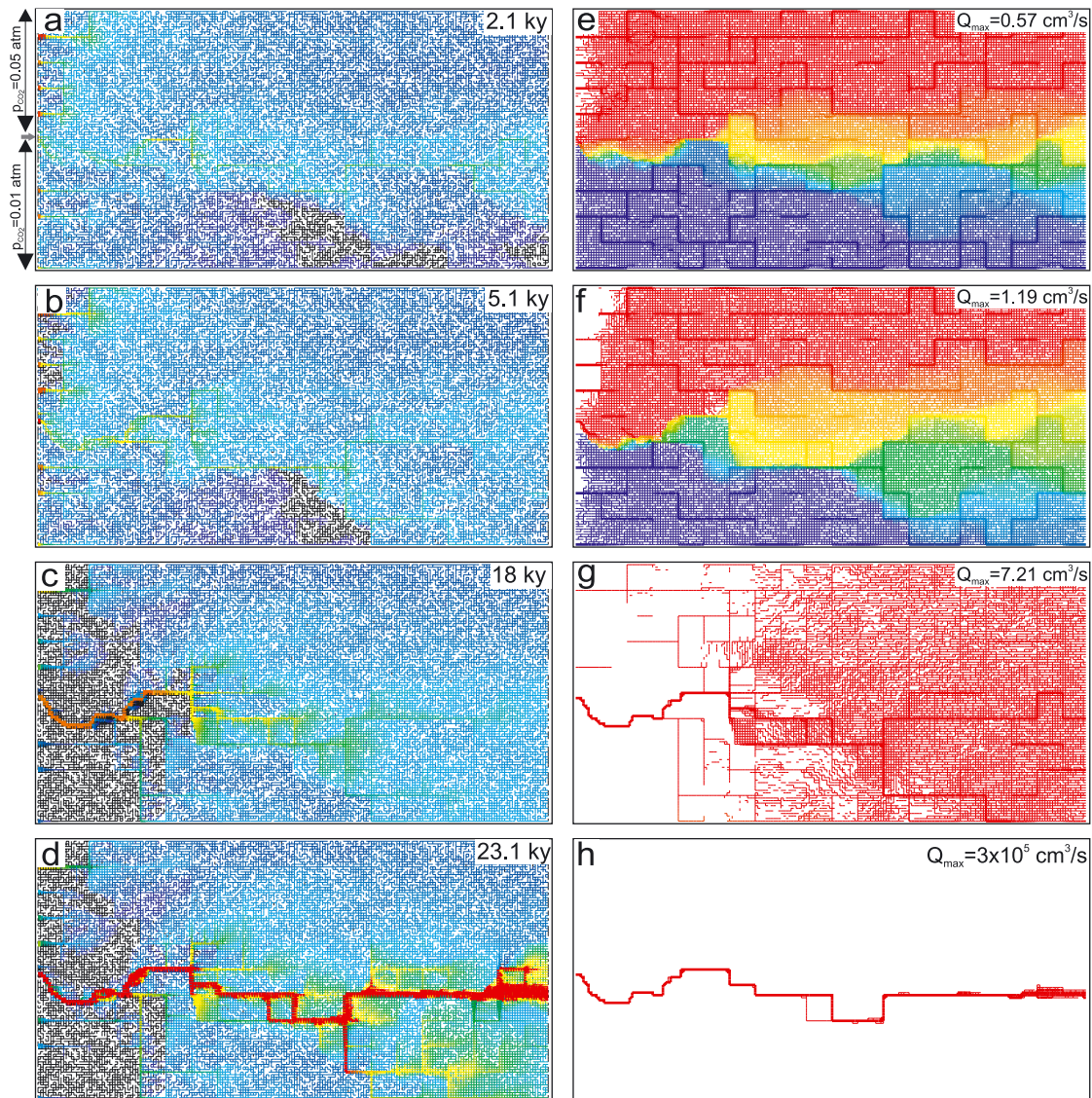


Figure 4.88: Evolution of the dual-fracture-aquifer (Figure 4.37) with mixing corrosion from differently vegetated areas. The upper half of the aquifer (red in the right hand side column) receives recharge with a p_{CO_2} of 0.05 atm into both fracture systems, whereas the p_{CO_2} into both fracture systems of the lower part (blue) is 0.01 atm. Left hand side column: aperture widths and dissolution rates; right hand side column: values of c_{eq} and flow rates. Calcium input concentration $c_{in} = 0$, $\bar{a}_0 = 0.00625$ cm, $A_0 = 0.02$ cm. Other parameters and boundary conditions as in Figure 4.37.

In parallel, mixing corrosion mainly widens fissures of the net in the mixing zone. After 18 ky (Figure 4.88g) water from the upper input with 0.05 atm has invaded almost the entire aquifer. Redistribution of the higher heads penetrating into the aquifer inhibits inflow of water with low p_{CO_2} and therefore MC is switched off (see also chapter 3). Consequently, from this moment the aquifer evolution switches into the breakthrough mode and breakthrough is accomplished after 23 ky (Figures 4.88c, d, g, h)

Now we turn to the mode of pure mixing corrosion with saturated input waters in equilibrium with the corresponding p_{CO_2} -values of the two different zones of vegetation. Everything else is left as in the previous Figure 4.88.

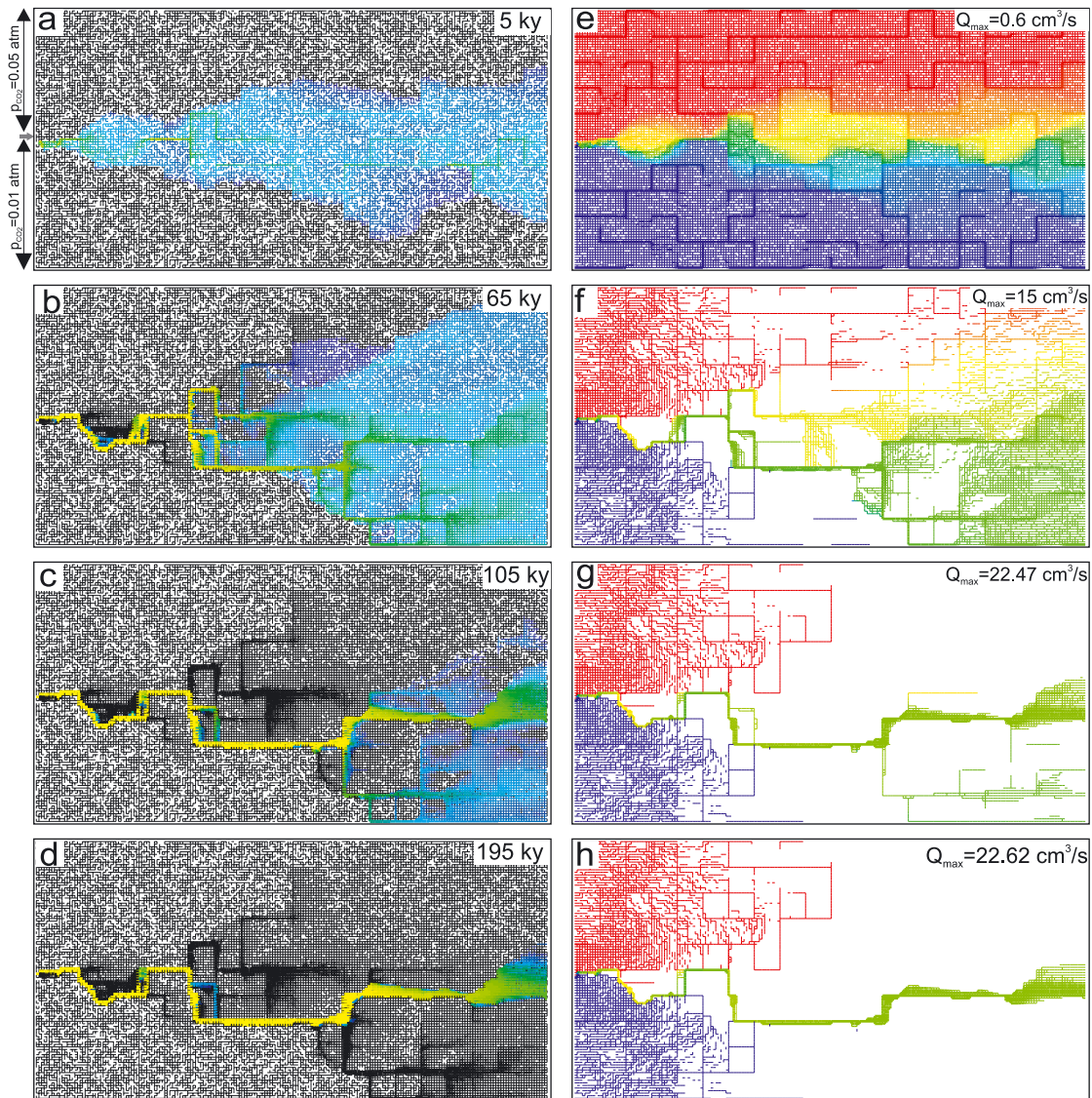


Figure 4.89: Evolution of the dual-fracture aquifer with mixing corrosion as in the previous Figure 4.88 for pure MC. $c_{in} = c_{eq}$. Other parameters and boundary conditions as in Figure 4.88.

The result is shown by Figure 4.89. Since the inflowing solutions are saturated, dissolution occurs only where waters mix, and large regions (black) remain unaffected. At 5000 y (a, e) a wide mixing zone, similar to that in Figure 4.88a, has evolved. High dissolution rates are present at the entrance and at the border between the two regions of vegetation. Furthermore, prominent fractures are widened efficiently (green) by MC, as can be seen from Figure 4.89a and b. After 65 ky (b, f) this region has gained suf-

ficient permeability to focus flow from the two different vegetation zones into a few confluences, where they mix. After 105 ky a central channel drains the aquifer (c, d), and consequently, the mixing zone (g, h) becomes restricted to this central channel and to fissures close to it. From then on the flow pattern remains stable and dissolutional widening is slow and linear in time.

If one uses $c_{in} = 0.995c_{eq}$, this way allowing some dissolution in zones with no mixing corrosion we find a similar behavior. This is shown by Figure 4.90. However, the final pathway taken is different from that of Figure 4.89 with $c_{in} = c_{eq}$, and also the pattern of enlarged fractures abandoned by dissolution (black) is different. This again emphasizes how sensitively details of aquifer evolution react to slight changes in boundary conditions.

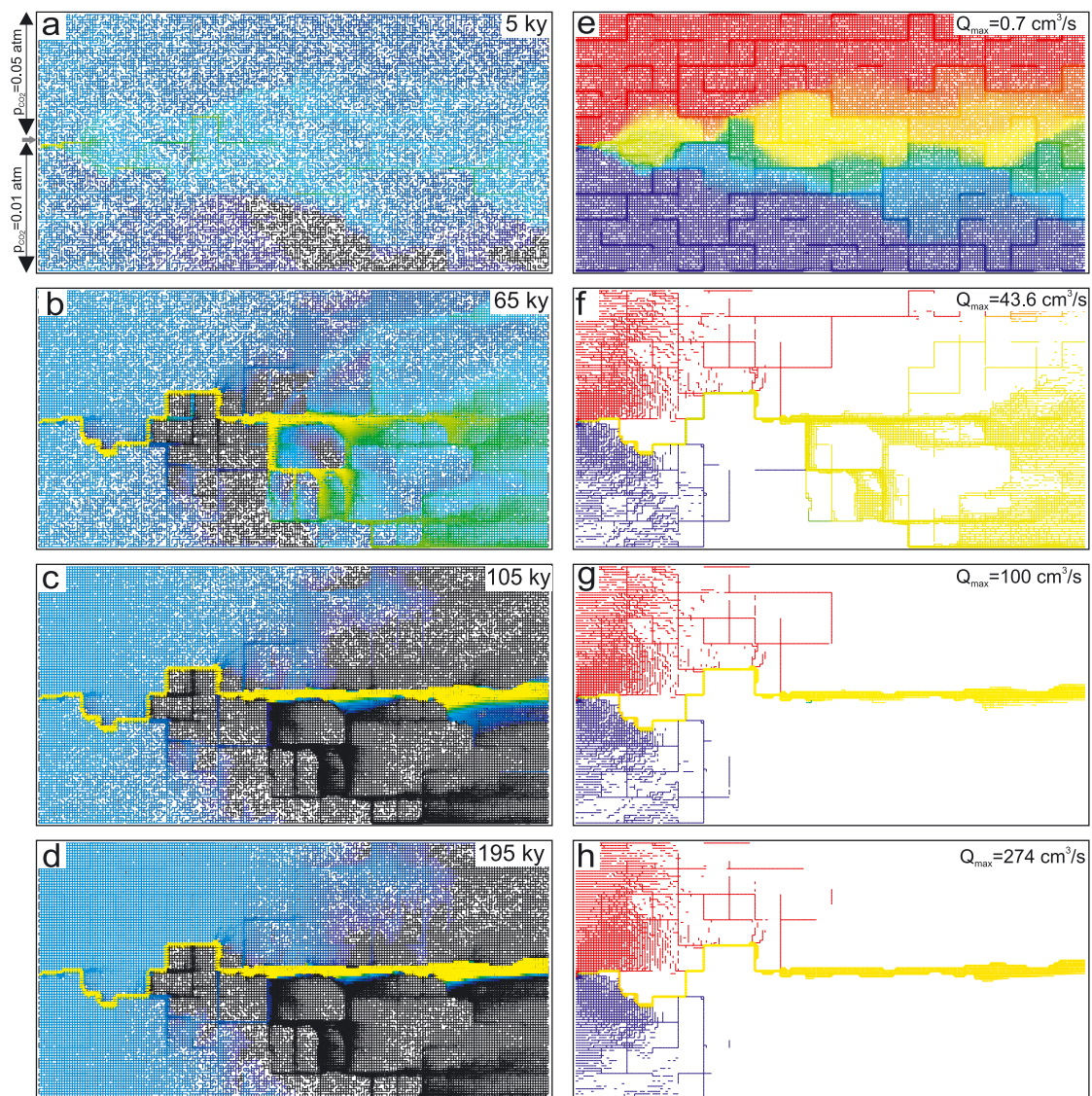


Figure 4.90: Evolution of the dual-fracture aquifer with mixing corrosion as in the previous Figure 4.89, $c_{in} = 0.995c_{eq}$. Other parameters and boundary conditions as in Figure 4.88.

4.10 DUAL-FRACTURE AQUIFER: SUBTERRANEAN INPUT OF CO_2

In chapter 3.4.1 we have discussed the influence of CO_2 -point inputs to the evolution of the 1-D fracture evolution. We have found that breakthrough times are reduced. Therefore in some region, where either volcanic CO_2 invades karstifiable rocks, or where microbiological action releases CO_2 to the water, karstification should be enhanced and patterns should be modified.

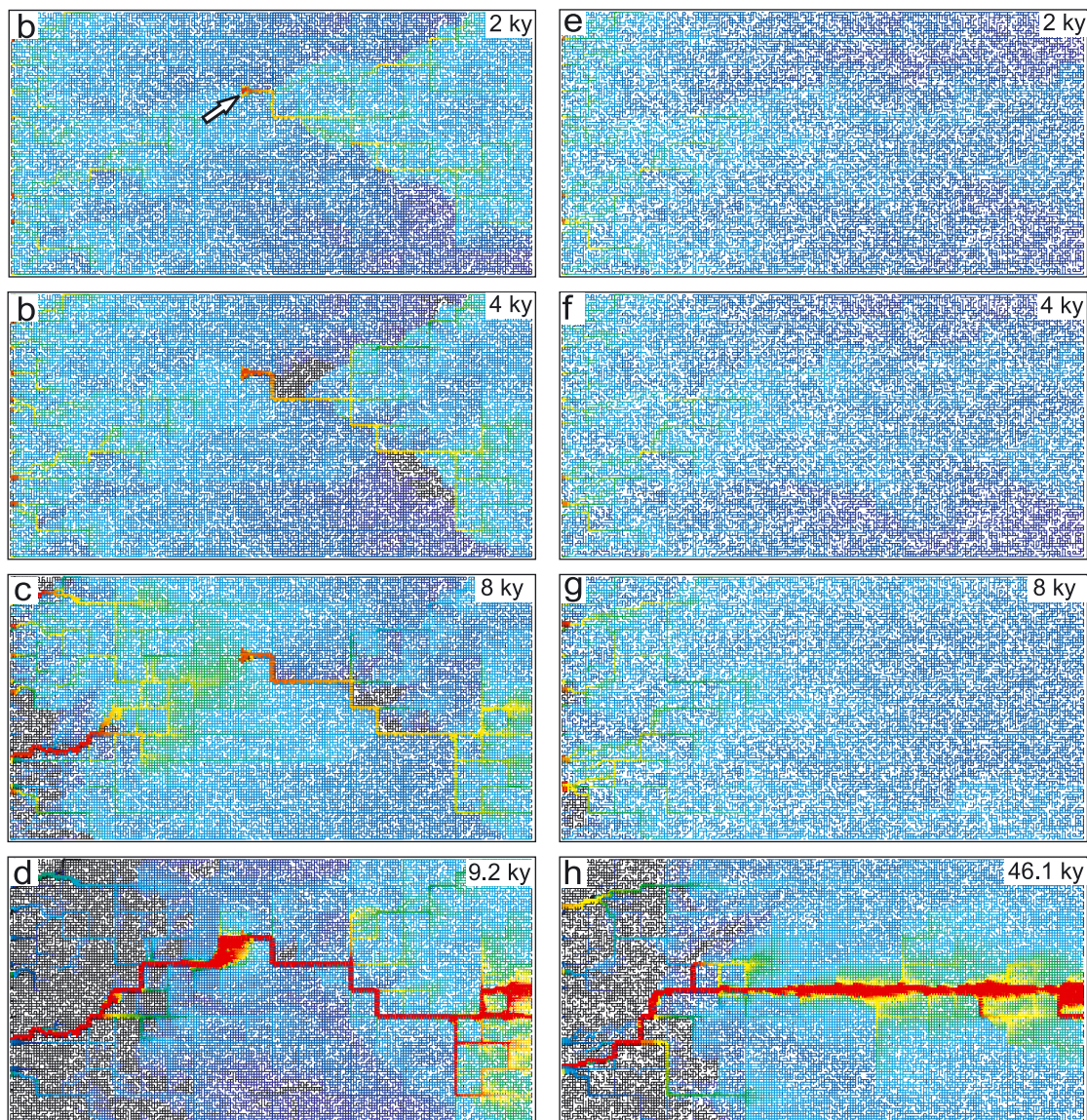


Figure 4.91: Evolution of aperture widths and dissolution rates for the dual-fracture aquifer of Figure 4.83b with $p_{CO_2} = 0.05$ atm in net fractures and $p_{CO_2} = 0.01$ atm in prominent fractures. $c_{in} = 0$, $\bar{a}_0 = 0.00625$ cm, $A_0 = 0.02$ cm. Left hand side column: In addition, subterranean CO_2 with $p_{CO_2} = 0.03$ atm is present (marked by the arrow in the upper panel a). Right hand side column: Subterranean CO_2 is missing.

We therefore turn to the evolution of the dual-fracture network of Figure 4.88b, when a source region with CO_2 -input is added. This region is located in the center of the domain and marked by an arrow in Figure 4.91a. The p_{CO_2} at the inputs of fissures in the net is 0.05 atm and 0.01 atm at prominent fractures. In the source region the CO_2 concentration of the inflowing solution is raised to open system equilibrium with p_{CO_2} of 0.03 atm. When the solution flows out of this region it attains c_{eq} under closed system conditions. Consequently, mixing corrosion between all three water types with different p_{CO_2} becomes active, but also dissolution rates are boosted up at the sub-terrestrial CO_2 -input.

The left hand side column of Figure 4.91 shows the evolution of aperture widths and dissolution rates with $c_{in} = 0$. At the input boundary small channels grow along the prominent fractures injecting water into the net, where small meandering channels are created by MC as indicated by green (a, b). Some of these channels are directed towards the CO_2 -source.

At the same time the solution, flowing out of the region of the CO_2 -input, has boosted up its dissolution rates by uptake of CO_2 and a conduit originates along a percolating pathway of prominent fractures (a, b, c). Conduits, which have grown from the entrance fracture toward the CO_2 -source, due to the redistribution of heads, now connect to the channel growing from the CO_2 -source to the output. Breakthrough is achieved after 9200 y on a pathway combining both conduits.

For comparison the right hand side column of Figure 4.91 depicts the evolution aperture widths and dissolution rates of the aquifer, when the CO_2 -source is absent, but everything else is as in the left hand side. Note that this scenario has already been discussed in Figure 4.83b at breakthrough. Here, its complete evolution in time is presented. In the initial state of the evolution (Figure 4.91e, f) small channels evolve from the input of prominent fractures typical for the breakthrough mode. Due to the low input $p_{CO_2} = 0.01$ atm, this process is slow. Mixing corrosion by the solution, injected from the prominent fractures into the net, creates regions of increasing permeability in the net and also in the prominent fractures. The patterns, evolving up to 4000 y, are almost identical to those evolving from the entrance, when the CO_2 -source is present. During this time of the evolution, the CO_2 -source, has not yet changed the downstream permeability of the aquifer in a significant way. Patterns start to deviate from each other at 8000 y, when a higher density of channels has been created in the presence of the CO_2 -source (compare c and g). If the source is missing the further evolution is a usual breakthrough mode, as shown by Figure 4.91h. Breakthrough utilizes a similar pathway at the entrance, but then, due to the absence of the CO_2 -source, propagates on a different, now more favorable and shorter pathway straight through the net. The time to achieve breakthrough has increased to 46 ky, compared to 9000 y, when the CO_2 -source is present.

We now turn to the other extreme with $c_{in} = c_{eq}$ in the boundary inputs allowing MC only in the region upstream the CO_2 – source and forcing the system into the pure MC-mode there. Downstream the subterranean CO_2 -source, however, allows enhance-

4. MODELING KARST EVOLUTION ON TWO-DIMENSIONAL NETWORKS: CONSTANT HEAD BOUNDARY CONDITION

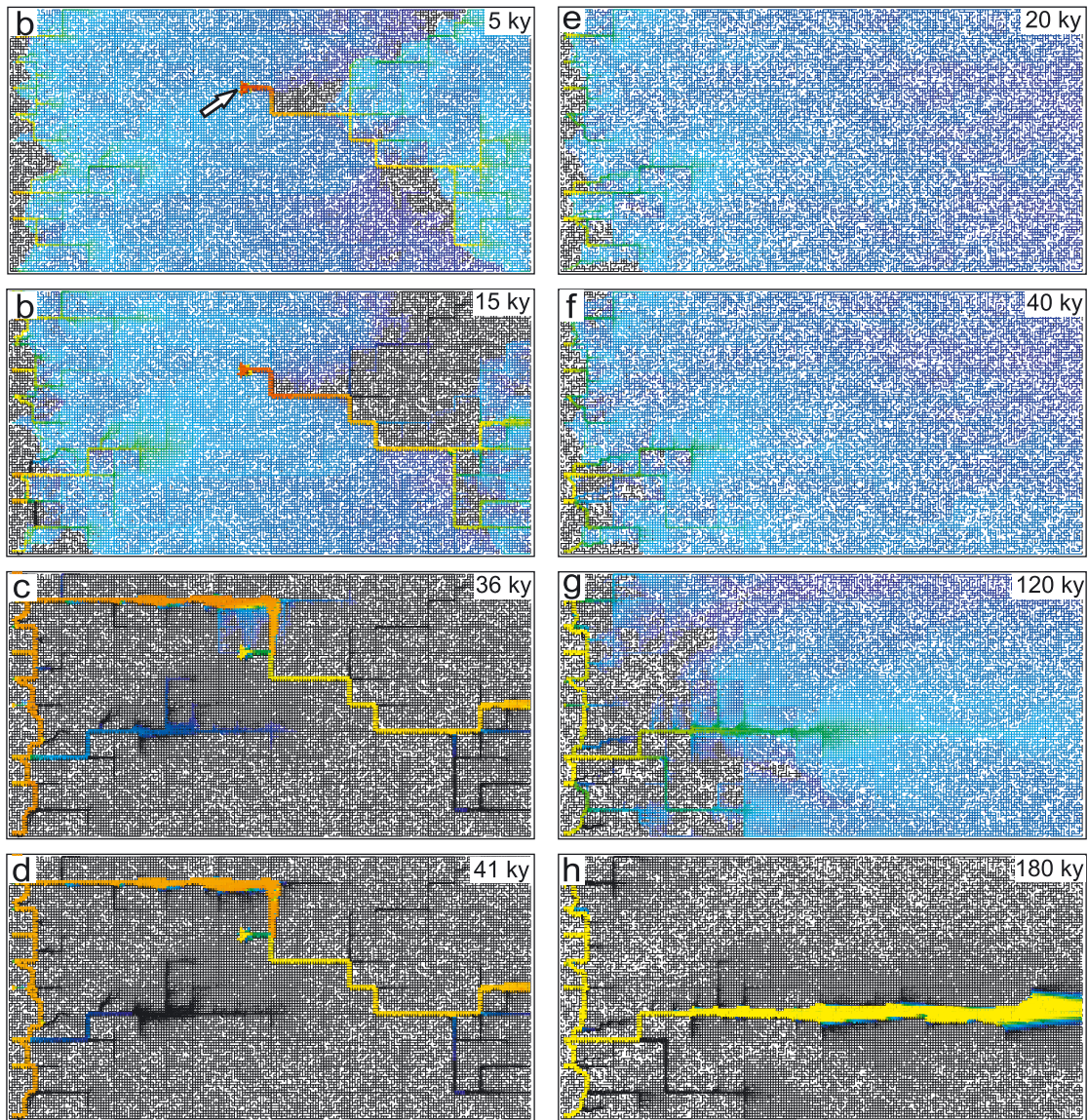


Figure 4.92: Evolution of aperture widths and dissolution rates for the aquifer of Figure 4.91. The left hand side column shows the evolution, when subterranean CO_2 is present. The concentration of the inflowing solution now is $c_{in} = c_{eq}$. The right hand side column shows the evolution with $c_{in} = c_{eq}$, but the CO_2 -source is missing.

ment of dissolution rates beyond that of MC. The left hand side column of Figure 4.92 shows the evolution for these conditions. A channel starts to grow from the CO_2 -source, due to the undersaturated solution originating from CO_2 -uptake. This channel travels along a percolating pathway of prominent fractures towards an exit point. Breakthrough, however, is prevented, because the upstream region of the aquifer with its low conductivity limits flow, and the positive feedback loop there is switched off. In the upstream region MC is the only cause for dissolutional widening (Figure 4.92a, b). The channel

originating from the CO_2 -source becomes sufficiently wide to drain water from the net (Figure 4.92c). Therefore, more flow is attracted through channels widened by MC and one of them migrates toward the CO_2 -source. Once both channels are connected, all flow in the system is focused to the chain of integrated channels (Figure 4.92d). This channel bypasses the CO_2 -source and drains only little flow from it. When this mixes to the water in the main channel, dissolution rates are reduced. This can be seen from the change of orange to yellow.

For comparison we also show on the right hand column of Figure 4.92 the evolution of the aquifer with $c_{in} = c_{eq}$, but without CO_2 -source of Figure 4.92 (compare Figure 4.84b). Again in the beginning, similar as in the case with CO_2 -source, at the entrance a region of MC creates solutional widening in both the net and the fractures. This process, however, takes a much longer time because flow must transverse the downstream part of the aquifer, where due to the lack of the CO_2 -input, the enlargement of fractures is at a slow pace. Finally, the central channel cuts straight through the net.

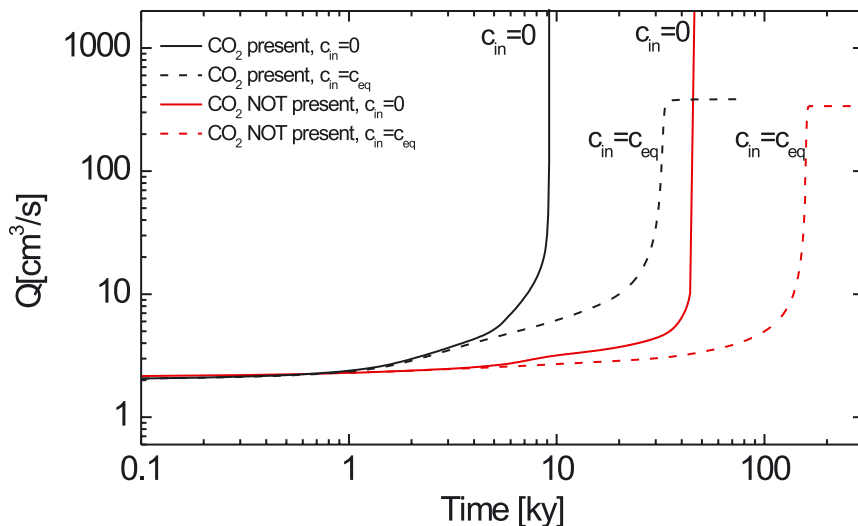


Figure 4.93: Evolution of the flow rates for the cases presented by Figures 4.91 and 4.92.

To show the differences in the initial evolutions Figure 4.93 depicts the flow rates for the cases $c_{in} = 0$ and $c_{in} = c_{eq}$ with and without CO_2 -source (Figures 4.91 and 4.92).

4.11 EVOLUTION OF DUAL-FRACTURE AQUIFERS AFTER BREAKTHROUGH: INTEGRATION OF CONDUITS

Most of our model runs so far have been terminated at breakthrough, when turbulence is setting in. After breakthrough the flow rates increase so dramatically that further calculations become meaningless because such huge amounts of water will be not available.

A way out of this is to change the constant head boundary conditions at all input points, which are connected to the output by a breakthrough event. Therefore, whenever flow at some input point reaches a predefined value $Q_{max} = 10^3 \cdot Q(t=0)$, the constant head condition there is changed to a constant input condition with Q_{max} . This changes the distribution of heads in such a way that heads become low along the entire breakthrough pathway. Therefore, flow from other pathways, either in the percolation net or through the net of narrow fractures, which are connected to a breakthrough channel, is directed to these locations of low head.

First we discuss this for a simple isolated percolation net with 4 input points. Otherwise the conditions are equal to those of the domain in Figure 4.37 ($A_0 = 0.02$ cm, $a_0 = 0$ cm, $h = 50$ m, $p_{CO_2} = 0.05$ atm, and $c_{in} = 0$ at all inputs) with all fractures of the statistical net omitted.

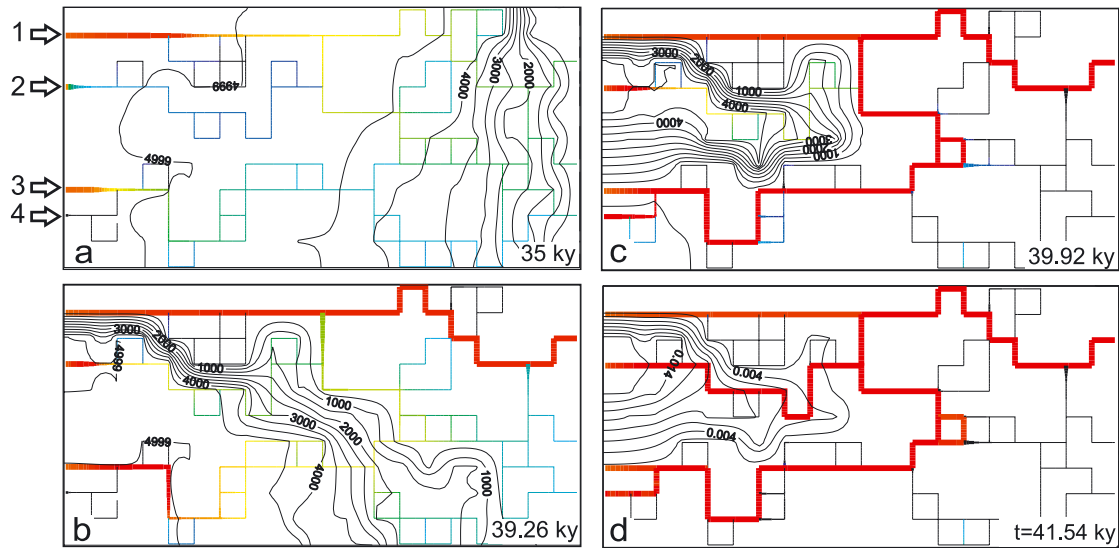


Figure 4.94: Evolution of a dual-fracture aquifer ($A_0 = 0.02$ cm, $a_0 = 0$ cm) after breakthrough. Four input points at prominent fractures with constant head $h = 50$ m are present. $c_{in} = 0$ and $p_{CO_2} = 0.05$ atm at all input points. Other parameters and boundary conditions as in Figure 4.37.

The result of the model run is shown in Figure 4.94, which illustrates aperture widths and dissolution rates. After 35 ky the upper conduit is close to breakthrough at 37 ky through the uppermost input point 1. At that time conduits growing from the lower input points have penetrated only short distances. (a) When the boundary condition is changed

to constant input after breakthrough, the head in the breakthrough channel drops, and flow from the lower channels 3 and 4 finds more favorable ways connecting to this channel rather than through the output boundary (b). Therefore, the two lowest input points 3 and 4 feed a channel connecting to the upper breakthrough channel. At the moment of breakthrough along this pathway the fixed head boundary conditions at points 3 and 4 must be changed to constant input conditions as well (c). This redistributes the heads, which become low also along the new conduits and attract flow from input point 2, which still has a fixed head boundary condition. After a short time (d) the channel originating from input point 2 experiences breakthrough to the channel from points 3 and 4. After that event the integrated network becomes stable. Heads are low everywhere in the cave system such that practically no flow is driven through not yet widened fractures.

It is interesting to pay some attention to the distribution of the heads, shown by the head isolines, which are given in steps of 5 m in Figure 4.94. Before breakthrough gradients are directed towards the output boundary (a). After the first breakthrough heads are low in the upper channel 1 (< 5 m), and hydraulic gradients are directed steeply from the evolving channel 2 towards channel 1 (b). After breakthrough of channels 3 and 4 hydraulic gradients are directed from channel 2 to the surrounding conduits. Outside this region heads are below 5 m (c). Finally, after breakthrough of channel 2, there is some flow from channel 2 to the surrounding channels but heads have dropped now to 0.014 m. Due to the constant input everywhere and due to the low flow resistance of the conduits only very small heads are necessary to drive flow through them. This example shows, how conduits are integrated into more complex cave patterns after breakthrough.

The solid line in Figure 4.95 illustrates the flow rates through the output point of channel 1 as a function of time. The step like increase of flow rates after the first

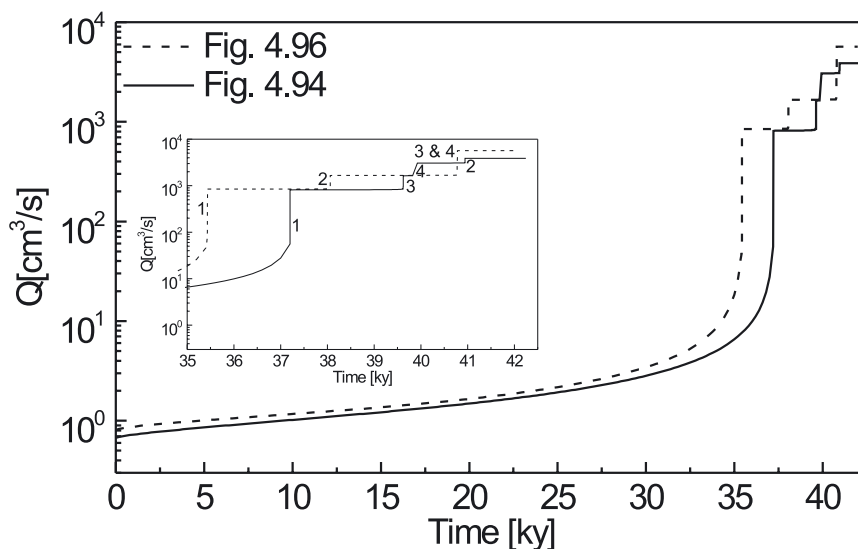


Figure 4.95: Evolution of flow rates for the aquifers of Figures 4.94 and 4.96. Numbers at the steps mark the input points through which the corresponding breakthrough has happened.

breakthrough indicates the subsequent breakthrough events from channel 3 to 1, 4 to 3 and then from channel 2 to 3. At each subsequent breakthrough the increase in Q is by Q_{max} , due to the constant input recharge applied as new boundary condition. Note that the scale in Q is logarithmic.

Now we return to the dual-fracture aquifer by filling the previous percolation net of Figure 4.94 with a statistical network of fractures with $\bar{a}_0 = 0.0025$ cm. All fractures of the statistical network at the left hand side border are subject to no-flow conditions. Input is restricted to the 4 input points as in the previous figure. The right hand side boundary is at fixed head $h = 0$ for all fractures.

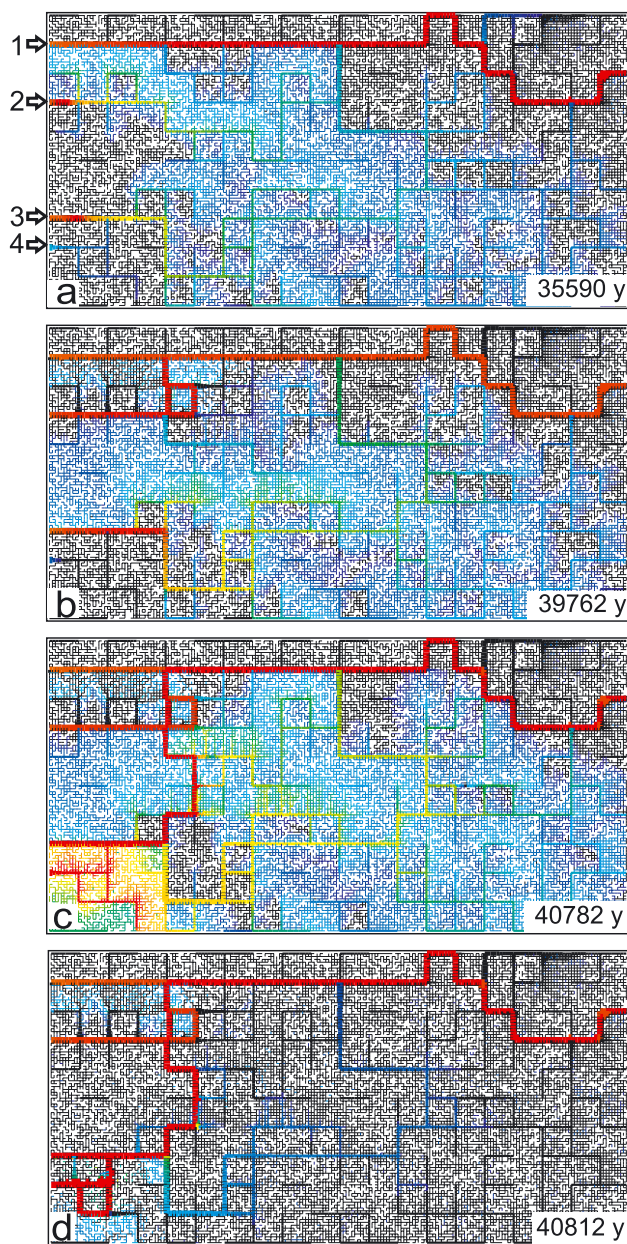
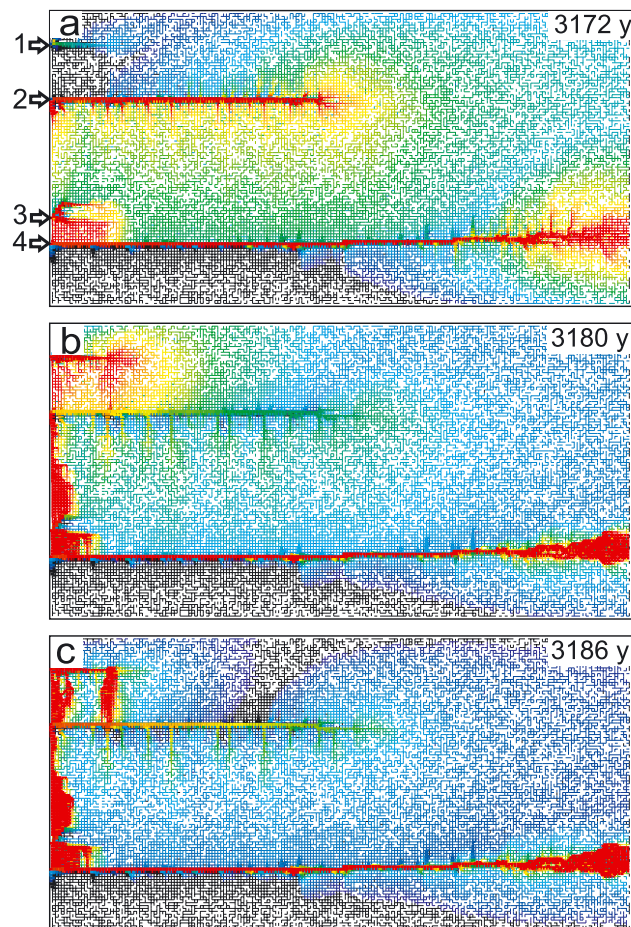


Figure 4.96: Evolution of the dual-fracture aquifer in Figure 4.94 after breakthrough. The percolation network of Figure 4.94 now is embedded into a statistical network with $\bar{a}_0 = 0.0025$ cm. $A_0 = 0.02$ cm. $c_m = 0$ and $p_{CO_2} = 0.05$ atm at all input points. Other parameters and boundary conditions as in Figure 4.94.

The evolution is shown in Figure 4.96, which again depicts aperture widths and dissolution rates. Breakthrough has happened after 35 ky. The breakthrough pathway is identical to that in the previous scenario shown in Figure 4.94. Due to the exchange of flow between the percolation net work and the statistical net, now the channel, growing from input 2, finds more short, competitive pathways cutting through the net and achieves breakthrough to channel 1 first (b). After this event a channel from inputs 3 and 4, which are already connected, joins channel 2 (c). From then on, rates are high only in these channels and the system becomes stable. The pattern, however, due to the presence of the statistical net, has become different. Figure 4.95 illustrates the evolution of flow rates for completeness.

One question remains to be answered. How does integration of breakthrough pathways look like in a the dual-fracture network with maximal hydraulic coupling? To this end, we have repeated the run of the previous scenario by using a large aperture width of $\bar{a}_0 = 0.02$ cm in the statistical net. Everything else is kept as in Figure 4.9.

Figure 4.97 shows the results. Two parallel channels 1 and 4 have migrated downstream and the lower one (4) has reached breakthrough. Since the head is low, flow is directed from input 3 through parallel fractures to channel 4. This is shown by



red fissures in (a) indicating high dissolution rates. Consequently, a series of breakthrough events connects fractures from input 3 to channel 4.

Figure 4.97: Evolution of the dual-fracture aquifer in Figure 4.94 after breakthrough. The percolation network of Figure 4.94 now is embedded into a statistical network with $\bar{a}_0 = 0.02$ cm, $A_0 = 0.02$ cm. Other parameters and boundary conditions as in Figure 4.94.

This can also be seen from the evolution of flow rates depicted in Figure 4.98. In contrast to the step like increase in the two previous scenarios, total flow out of the aquifer rises more smoothly. Integration is completed at the edge marked by (3.4). After the integration between inputs 4 and 3, the fixed head at input 3 is replaced by constant recharge and the head drops such that now flow from input 2 is directed down to the integrated region close to input 3 (b). Similarly as between 3 and 4 integration proceeds between 2 and 3. Because of the longer distance, this takes a longer time as shown in the evolution of the total flow out. Integration is completed at the point marked by (2.3). Then integration from input 1 to 2 begins. Since the head is low at input 2, the channel from input 1, which had been abandoned by flow before, now attracts flow (c). Parallel channels start to migrate toward conduit 2 and a region of breakthrough fractures is integrated to input channel 2 (c). This is shown by a further increase of total flow between points (2, 3) and (1, 2). From then on the aquifer develops with boundary conditions of constant recharge without significant change of its structure.

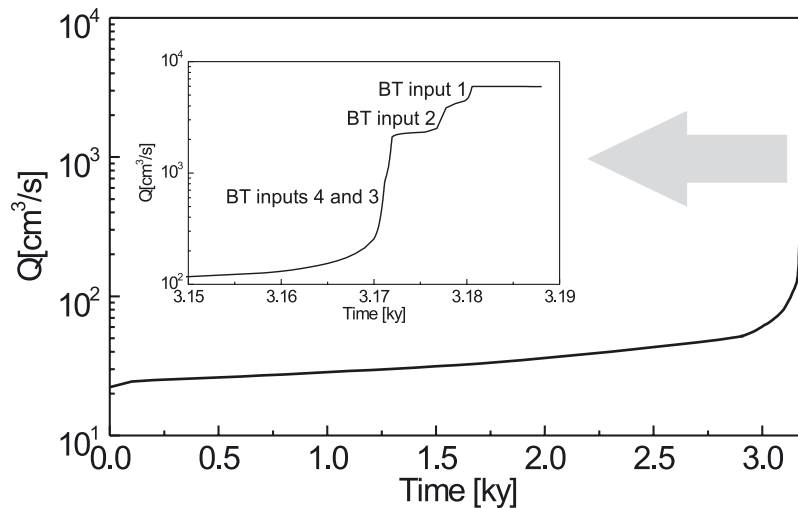


Figure 4.98: Evolution of flow rates for the aquifer of Figure 4.97. Embedded graph shows an excerpt between 1.19 ky and 3.15 ky with successive breakthrough events. Numbers at the steps mark the input points through which the corresponding breakthrough has happened.

From the last two examples it is clear that large integrated cave systems can grow only where the spacing of the leading fractures is sufficiently wide. Densely fractured rocks offer so many equally competing pathways that integration of passages into a net is limited to the entrance regions.

This is also true in dual-fracture nets, when one allows constant head conditions to all fractures, those of the net and the prominent ones. In that case, shortly after breakthrough along some pathway and the subsequent head drop, breakthrough events from the nearest neighboring fractures occur and an entrance fan will develop, similarly as discussed in Figure 4.26.

One critical comment, however, must be given to the considerations in this section. In all model runs we have assumed that all channels and fractures are entirely filled with water. Strictly this is true only, when the aquifer is horizontal, and the recharge offered to it is sufficiently high to produce a head at least equal to the heights of the conduits. If these two conditions are not fulfilled flow will become vadose, and the flow equations of phreatic flow have to be replaced by those for open channel flow. On the other hand the integration of pathways with input points of constant head to a potentially vadose conduit proceeds under high heads. Flow there is phreatic and directed towards the low head in the vadose channel. Therefore, even when details will be different (e.g. pressure in vadose channels is equal to zero and the head is only given by the elevation) the way of integration should be reasonably well approximated. Currently, all modeling groups working on the evolution of karst aquifers tacitly use this approximation. But it is a challenge for future work to handle the late stage of mature karst more exactly.

4.12 CONCLUDING REMARKS

The aim of this chapter has been to elucidate karstification in dual-fracture aquifers under constant head conditions taking into account both hydrodynamical boundary conditions as well as the impact of chemical boundary conditions, such as those activating mixing corrosion. In a first step dual-fracture aquifers were investigated, where chemical boundary conditions exclude mixing corrosion. Dual-fracture aquifers are constructed by nesting a percolation network of prominent fractures with wide spacing and fracture aperture width A_0 into a net of densely spaced fractures with aperture widths $\bar{a}_o < A_0$. This way exchange of flow between the two subsystems causes new phenomena in karst evolution. Depending on the ratio $M = \bar{a}_o/A_0$ the patterns of conduit systems are as in isolated percolation networks for $\bar{a}_o \ll A_0$. They resemble those of statistical 2D-networks for $\bar{a}_o \approx A_0$, (confer Figure 4.43). For intermediate M exchange of flow between the two sub-systems increases. Flow entering from prominent fractures into the net generally has lower calcium concentration than the solutions flowing more slowly in the net. Furthermore due to the leakage of flow from prominent fractures into the net, more aggressive solution is entering into their inputs and the evolution of conduits is enhanced. But the opposite can be true also. Prominent fractures can drain water close to equilibrium from the net. When this water enters these fractures the dissolution rates drop and evolution of conduits is retarded at such locations. This way the rules providing most favorable pathways until breakthrough are changed and in consequence the evolution of the aquifer will depend on the patterns of exchange of flow. We have tried to illustrate this by presenting simple examples of dual-fracture aquifers.

When the chemical boundary conditions are changed, such that waters entering into the prominent fractures have a different CO_2 -concentration from waters entering into the net of fine fractures, mixing corrosion becomes active deep in the aquifer where these waters mix. If the input concentrations are all saturated with respect to calcite but their

equilibrium concentrations differ, only where the waters mix dissolutional widening is active. In such cases breakthrough is not possible because the unaffected entrance regions of the aquifer limit flow. Inside the aquifer, where waters of different chemistry mix, mixing corrosion creates regions of increasing permeability, which drain water from the net, thereby enhancing mixing corrosion. These regions propagate downstream until they reach the outflow boundary. At small coupling ratios M , prominent fractures are utilized. With increasing M the evolving channels cut through parts of the net until at still higher values they leave prominent fractures at all and use pathways straight through the net (see Figure 4.84). This mode of karstification, due to the missing feedback loop, is much slower and needs about 1 million of years to create conduits of a meter or so. If the waters are undersaturated with respect to calcite, but still differ in their input CO_2 -concentrations breakthrough behavior becomes active, but also mixing corrosion is present. Therefore during the evolution of breakthrough-conduits mixing corrosion inside the aquifer creates enhanced permeability. This can render alternative pathways more favorable, and divert the evolving channels through these regions (see Figures 4.81, 4.82, and 4.83).

The evolution of such aquifers is controlled by a rather simple principle: If water flows from the prominent fracture into the net mixing corrosion is activated in the net. Otherwise water flowing from the net into prominent fracture activates mixing corrosion there. To which extent this happens depends on the ratio M . It should be noted here, that the latter principle can conflict with the reduction of dissolution rates, when water from the net enters into a prominent fracture.

This shows that a strategy to explore firstly simple scenarios and adding more complexity later, is most useful. Otherwise such conflicting processes could not be separated from each other.

As a final remark we would like to point out that it is of utmost importance to model dissolution in both, the net of prominent fractures and in the dense net of fine fractures. As we have seen the mutual interaction of both subsystems determines the evolution of the aquifer. Allowing only hydraulic coupling, by restricting dissolution solely to the prominent fractures, as in the concepts of Bauer *et al.* and Kaufmann (see guest contributions) limits conduit evolution entirely to this system. This modeling concept is acceptable for weak coupling ($\bar{a}_0 \ll A_0$), but it fails for medium and strong coupling.

5. UNCONFINED AQUIFERS UNDER VARIOUS BOUNDARY CONDITIONS

In Chapter 4 we have discussed confined aquifers subjected to constant head conditions. Although this situation might not be so common in geological settings the modeling of such aquifers has revealed many insights into the processes determining the evolution of karst.

Much more common in nature are deep limestone strata, which are exposed to the surface and receive recharge from meteoric precipitation. Under such conditions the aquifers are unconfined and exhibit a water table. In this chapter we will deal with these aquifers. The processes, which determine the evolution of confined aquifers, are also operative here. Therefore the findings of chapter 4 will help to understand the results more easily.

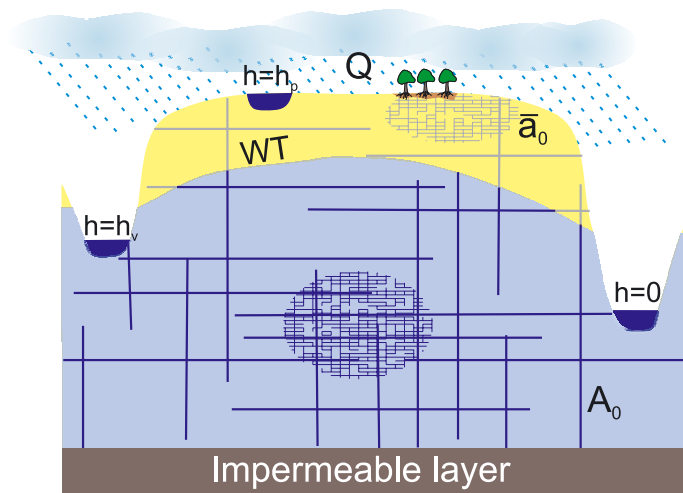


Figure 5.1: Basic concept for modeling unconfined aquifers. A net of prominent fractures with aperture widths A_0 is embedded into a net of narrow fissures with average aperture widths \bar{a}_0 . The karst plateau is bordered by two valleys with rivers flowing in them. At the top of the plateau a lake or river delivers water into the fractures of the rock massive. Otherwise meteoric recharge evenly distributed seeps through the vadose zone (yellow) to the water table. Differing vegetation on the plateau gives rise to varying p_{CO_2} of the inflowing waters. An impermeable layer of rock underlies the limestone strata.

Figure 5.1 shows a vertical section of a limestone plateau bordered by two valleys at different altitudes, where rivers of some depths are flowing. We can also imagine a lake or river on top of the plateau fed by allogenic water. The plateau receives recharge by

meteoric rain, which seeps through the various fractures and fissures to the base levels constituted by the rivers. Most obviously different zones of vegetation (e.g. covered and bare rock) can give rise to input waters with differing contents of carbon dioxide and consequently mixing corrosion becomes active. Also waters seeping through the vadose zone along different pathways will attain different chemical compositions and activate mixing corrosion in the phreatic zone. The rock is dissected into a dense net of narrow fissures with initial average aperture widths \bar{a}_0 between 0.004 cm up to 0.025 cm. Prominent fractures are embedded into the fissure network and form a percolation network with aperture widths A_0 of several tenths of a millimeter. An impermeable layer of rock underlies the limestone.

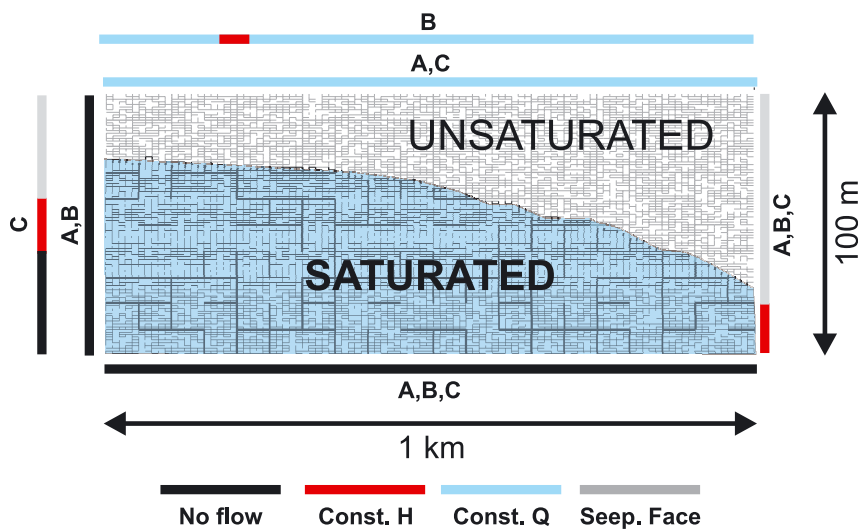


Figure 5.2: Model domain of the conceptual model shown in Figure 5.1. The colored border lines and bars given below depict the boundary conditions. By this way scenarios A, B, and C can be visualized. (See text).

Figure 5.2 shows the modeling domain constructed from the conceptual setting depicted in Figure 5.1. Several combinations of boundary conditions can be chosen. The black border lines depict no flow boundary conditions implied by a watershed or impermeable rock. The gray borderlines mark seepage faces. The red bars denote boundary conditions of constant head. The blue border line on top designates locations of constant recharge to the water table of the aquifer. The latter separates the vadose and phreatic zones. This way three scenarios A, B, and C can be designed.

Scenario A can be envisaged by employing all border lines, which carry the letter A. It can be seen as a plateau bordered by impermeable rock or a watershed at its left hand side boundary and impervious at its bottom. The right hand side boundary consists of a seepage face and a region of constant head conditions, where the rock is below the water of the river. The top of the aquifer is an area of equally distributed constant recharge to the water table.

Scenario B is constructed by considering all border lines, carrying the letter B. This adds a region of constant head input to scenario A at the top of the aquifer (red).

Finally in scenario C one uses all border lines carrying the letter C, thus replacing the left hand side boundary of scenario A by the border line with letter C. This illustrates an impermeable boundary at the lowest part, a region of constant head input from the river above and a seepage face in the uppermost part

Description	Name	Unit	Typical or initial value
Aperture width of fine fractures	\bar{a}_0	cm	0.003 to 0.025
Aperture width of prominent fractures	A_0	cm	0.02, 0.03, 0.04
Length of vertical and horizontal fine fractures	l_v, l_h	m	1, 10
Length of vertical and horizontal prominent fractures	L_v, L_h	m	10, 100
Dimension of the domain		m ²	1000×100
Input concentration	c_{in}	c_{in}/c_{eq}	0.9
Annual recharge	Q	mm/year	400

Table 5.1: Parameters of the unconfined model

The grid size of the net is 10 m in the horizontal and 1 m in the vertical direction. The grid size of the percolation net of prominent fracture is 10 m by 100 m correspondingly. Its occupation probability is $p = 0.6$. the height of the domain is 100 m, its length 1 km. The surface of the lower river is at elevation $h = 0$. The region of constant head reaches down to -20 m. The top of the plateau is at an elevation of 80 m. The recharge to the water table is 400 mm/year.

To estimate the initial hydraulic conductivity k of the pristine aquifer we use the relation (Lee and Farmer, 1993)

$$k = \frac{\rho g \bar{a}_0^3}{12\mu s} , \quad 5.1$$

where \bar{a}_0 is the initial average fracture width, s their spacing, ρ is the density of water, μ its dynamic viscosity, and g is the gravitational acceleration. This way we find $k_n = 6 \cdot 10^{-7} \text{ ms}^{-1}$ for the set of horizontal fractures with $a_0 = 0.009$ cm. The conductivity k_v of the vertical set of fractures is lower by a factor of ten due to wider spacing. These are reasonable numbers for non-karstified limestone.

5.1 CALCULATION OF THE WATER TABLE AND THE EVOLUTION OF AN UNCONFINED AQUIFER

Our model implies an unconfined aquifer, i.e. an aquifer with a water table (WT) which separates a saturated phreatic and an unsaturated vadose zone (see Figure 5.1). Recharge is infiltrating vertically through the surface and the vadose zone down to the phreatic zone at the WT. The position of the WT depends on recharge and on the permeability of the rock. With increasing time, when the permeability of the rock increases by dissolutional widening of the fractures it will drop.

To each fracture in the net we assign aperture width, length, and chemical parameters such as input calcium concentration c_{in} , p_{CO_2} and the constants of the dissolution rates (confer Eqs. 2.10–2.13 and Table 2.1), and information whether the rock is soluble or not. Furthermore, boundary conditions can be applied to each node, such as a constant head or a constant input of flow.

To obtain the flow through the fractures, the position of the WT must be known, since it defines the boundary conditions for flow and separates the saturated zone from the unsaturated one. The position of the WT and the height of the seepage face are calculated by the following procedure:

1. An initial guess for the WT is assumed, e.g. the surface of the plateau.
2. Recharge by precipitation is equally distributed to the points of the assumed WT.
3. The heads of all the net-points below and at the assumed WT are calculated with the boundary conditions defined by the assumed WT and seepage face, i.e. $h = z$. z is the elevation of the water table or of a point located at the seepage face.
4. The heads of the points on the WT are checked for the boundary condition. Their head must be, within a given error, equal to their elevation. If this condition is valid for the point, the WT is kept there, otherwise the WT is either shifted to the node above, if $h > z$ or to the node below if $h < z$. Thus a new approximation for the WT is obtained.
5. Procedure 1–3 is iterated until all the points on the estimated WT fulfill the condition $h = z$.

Once the WT and the seepage zone are obtained, the flow through the fractures in the phreatic zone is calculated and the transport-dissolution model is applied. This is done in the same way as described for confined networks.

During percolation through the vadose zone, the solution attains some saturation state. This is taken into account by choosing the concentration c_{in} at which the solution enters the water table between c_s and c_{eq} . The choice of the parameter c_{in} is rather arbitrary. It influences the evolution of an aquifer, but does not change the results conceptually. A sensitivity analysis will be performed at the end of this chapter.



There are some approximations, which could be criticized:

1. Recharge is put directly to the nodes of the water table, thus assuming that flow is vertical through the vadose zone. This helps to keep modeling efforts moderate. Kaufmann (2002) has applied flow in the vadose zone to a similar model, by using Richards' equation for a variably saturated zone. His results show that our approximation is reasonable.
2. Most of the dissolution in nature takes place in the vadose zone, especially in the upper ten meters forming the epikarst. In this model, this is taken into account by recharging the water table with a solution of concentration c_0 as mentioned above. Dissolutional widening is only considered in the phreatic zone. The vadose zone left behind, when the water table drops, has experienced solutional widening only during the time when it was phreatic. It simply shows the early evolution and could give some hints, how the vadose zone would evolve, if these early structures serve as pathways guiding the aggressive solution down to the water table.

5.2 SCENARIO A: THE EVOLUTION OF UNCONFINED AQUIFERS UNDER CONDITIONS OF CONSTANT RECHARGE

In this chapter we first investigate the evolution of a network with lognormally distributed fractures with $\bar{a}_0 = 0.009$ cm, as shown in Figure 4.12b. The realization of this distribution will be kept in the following computer runs. Then we will turn to a dual-fracture aquifer, which also contains prominent fractures of width $A_0 > \bar{a}_0$ and we will explore the influence of the coupling parameter $M = \bar{a}_0/A_0$.

5.2.1 Statistical network

Figure 5.3 shows the evolution of our model aquifer with a recharge of 400 mm/year, evenly distributed to the input nodes of the water table. The average aperture width of the statistically distributed fractures is $\bar{a}_0 = 0.009$ cm. p_{CO_2} of the infiltrating water on top is 0.05 atm. The solution enters the water table with $c_{in} = 0.9c_{eq}$. Gray lines show the vadose zone, whereas in the phreatic zone a color code depicts the dissolution rates (left hand side column) or otherwise the flow rates and flow directions (right hand side column). Aperture widths and flow rates are given by the bar codes as explained in the code box. In the beginning the water table is high and reaches up to the surface of the plateau at its left hand side. Then it drops towards the right hand side margin, leaving behind a vadose zone and establishing a seepage face in the phreatic zone.

At the left hand side flow into the aquifer is directed deep downwards to the bottom of the aquifer and then towards the output seepage face or the zone of constant head conditions. In other words flow lines of particles entering at the left hand side no-flow



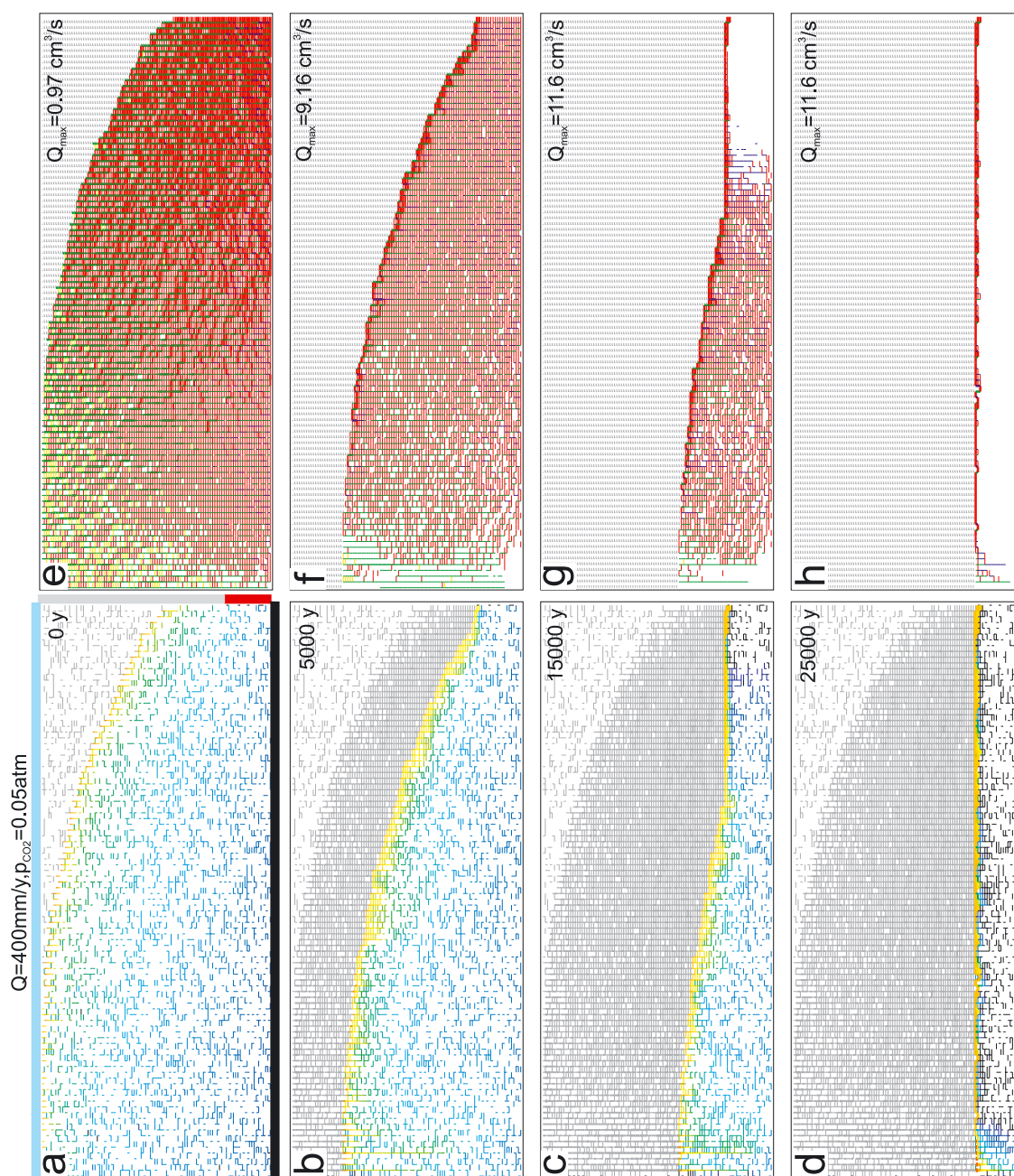


Figure 5.3: Evolution of scenario A: Simple statistical net with $\bar{a}_0 = 0.009$ cm, $c_m = 0.9c_{ef}$. Recharge of 400 mm/year is evenly distributed to the plateau. A watershed provides no flow conditions at the left hand side margin. The river at base level provides constant head boundary conditions with $h = 0$ from $z = 0$ m down to $z = -20$ m. The right hand margin above the river in the phreatic zone is a seepage face. The evolution of fracture aperture widths (bar code) and dissolution rates (color code) is shown in the left hand side column. The corresponding flow rates (bar code) and flow directions (color code) are depicted on the right hand side column.



boundary penetrate to the bottom of the aquifer and are then bended towards the output. Flow lines of particles more to the right are similar, but do not reach that deep and are stacked on top of each other when they bend to the outflow. Therefore flow is relatively evenly distributed in the outflow region (e). As can be seen from the yellow-green fringe (a) dissolutional widening is most active in a restricted region below the water table. This creates increased permeability and causes a slow lowering of the water table. After 5000 y (b) the water table has dropped by about 25 m leaving behind a region of widened fractures in the vadose zone. Flow is now concentrated at the top of the water table, where regions of higher permeability are underlain by not yet widened fractures (f). Note that we do not apply dissolutional widening to a fracture when it is located in the vadose zone. As time continues there is further lowering of the water table. Lowering of the water table is limited by the base level, in other words the head in the network cannot fall below the elevation of the base level. The water table reaches base level after 15 ky and the entire flow is focused into fractures close to base level (g). This evolving conduit also attracts all flow from the left hand side of the aquifer. Almost no flow is observed below this conduit as can be seen from the white region below (g, h). Finally, upon further drop of the water table the channel migrates backwards into the aquifer and a water table cave develops after 25 ky (h). Its width increases continuously because dissolution stays active there (d). After 25 ky the maximal aperture widths of the fractures at the water table are about 2.5 cm. Dissolutional widening is about 10^{-3} cm/year. Due to dissolutional widening in the vadose zone, which is not considered in our model, it could well happen that water reaches the water table with lower c_{in} and the widening could then, at this stage of evolution increase significantly.

5.2.2 Dual-fracture network

For a better approach to nature we introduce a percolation network with occupation probability $p = 0.6$ into the statistical network as described in Section 4.3. The aperture width of the prominent fractures is $A_0 = 0.03$ cm, the net contains statistically distributed aperture widths with $\bar{a}_0 = 0.009$ cm and is identical to that of Figure 5.3. $p_{CO_2} = 0.05$ atm.

Figure 5.4 illustrates the results. Due to the average increase of hydraulic conductivity induced by the prominent fractures, we find the water table initially somewhat lower than in the pure statistical net of Figure 5.3. The dissolution rates are highest at the water table and then drop continuously to the bottom (a). A part of the otherwise continuous flow is attracted by some prominent fractures in an up-and-down-looping pattern (e). After 5000 y the water table has dropped to about half of its initial height (f). Dissolutional widening is focused to a narrow fringe below the water table (b) that carries most of the flow now (f). After 10 ky (c) the right hand side of the water table has reached base level and finally a water table cave, similar to that of Figure 5.3 is created after 20 ky (d, h).



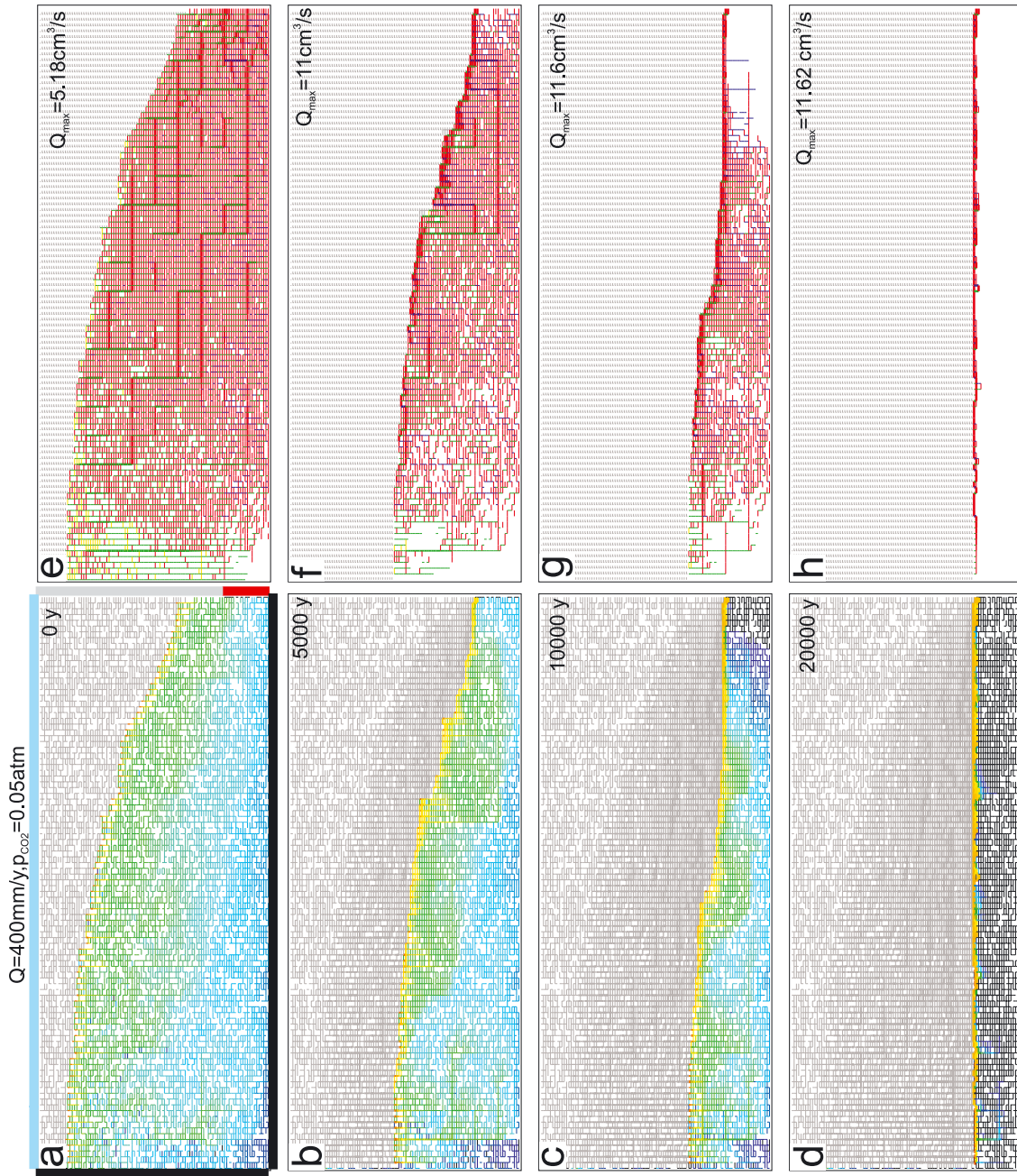


Figure 5.4: Evolution of scenario A (dual-fracture aquifer): A network of prominent fractures with aperture widths $A_0 = 0.03$ cm is added. Other parameters and boundary conditions as in Figure 5.3.



Comparable calculations to those shown in Figure 5.3 and 5.4 have already been performed on a smaller modeling domain by Gabrovšek and Dreybrodt (2001). More detailed information on the distribution of fracture aperture widths and other details can be found there.

5.3 SCENARIO B: A COMBINATION OF CONSTANT RECHARGE AND CONSTANT HEAD BOUNDARY CONDITIONS IN A DUAL-FRACTURE AQUIFER

In the following we assume an allogenic river encountering the plateau. Consequently, a region of constant head boundary conditions marked by the red bar in Figure 5.5a, replaces the constant recharge boundary conditions there. p_{CO_2} of both the river water and the recharge is 0.05 atm.

As we have already seen in Chapter 4 the hydraulic coupling has a significant influence on the evolution of confined aquifers. Therefore, we study the evolution of scenario B for various hydraulic coupling ratios $M = \bar{a}_0/A_0$.

Figure 5.5 shows the evolution of an aquifer with $A_0 = 0.04$ cm and $\bar{a}_0 = 0.005$ cm. In this case hydraulic coupling is low. Initially the water table is rugged because the prominent fractures are efficient in draining the aquifer (a). This can be easily seen from the initial distribution of flow rates (e). Because of constant head conditions the water table cannot drop and dissolutional widening creates a fringe of increasing permeability (b). This renders the water table smoother (f). The prominent fracture located at the left of the constant head region now receives most of the flow (f, g) and a conduit system migrates towards base level in the well-known breakthrough mode. But there is also competitive dissolutional widening at the water table. Finally, after 2650 y breakthrough occurs through the prominent fractures and the flow rate of about $30 \text{ cm}^3/\text{s}$ at 2000 y is increased by almost two orders of magnitude (d, h).

If the hydraulic coupling is raised slightly, using $\bar{a}_0 = 0.006$ cm, the basic pattern of evolution remains very similar. However, due to higher flow rates along the water table the permeability in the downstream part of the net increases sufficiently fast to become a competitive alternative breakthrough pathway attracting a significant part of the total flow, as is shown by Figure 5.6 d, h. Therefore a region of diffuse flow connects the prominent fractures to the output.

If hydraulic coupling becomes strong with $\bar{a}_0 = 0.009$ cm the fringe of rapidly increasing permeability along the water table attracts almost all of the flow and the downstream part of the percolating pathway of prominent fractures becomes almost abandoned by flow. Therefore breakthrough occurs through the net of finer fissures. This behavior is illustrated by Figure 5.7 where breakthrough migrates along a pathway of prominent fractures in the upstream left hand side of the aquifer and then continues through the net down to base level in its right hand part. The region of diffuse flow in the net of widened fractures now occupies almost the entire right half of the domain.



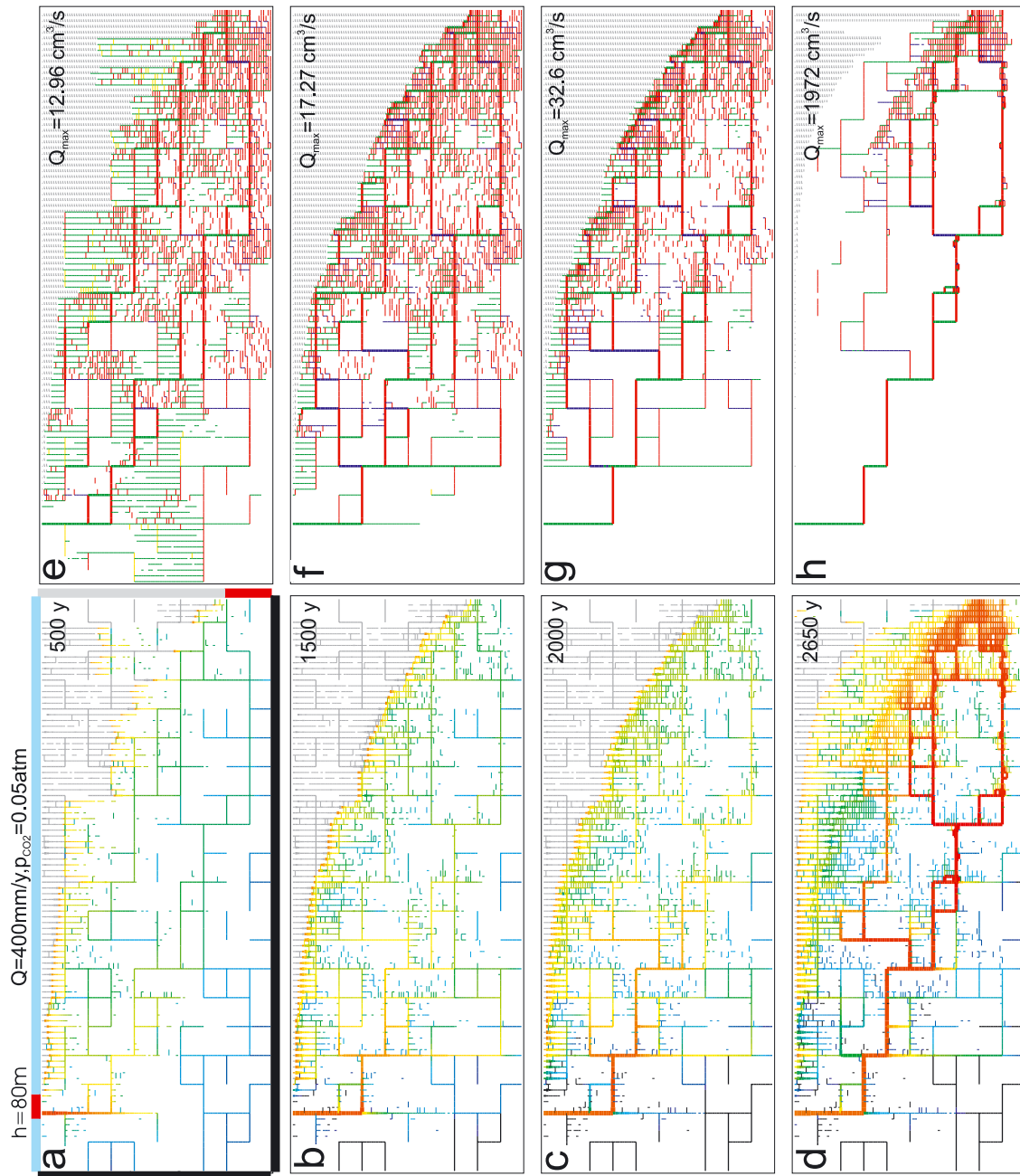


Figure 5.5: Evolution of scenario B: Dual-fracture aquifer. A constant head input, designated by a red bar, at the left hand side of the plateau is added to a dual-fracture aquifer with $A_0 = 0.04$ cm, $\bar{a}_0 = 0.005$ cm. Other parameters and boundary conditions as in Figure 5.4.

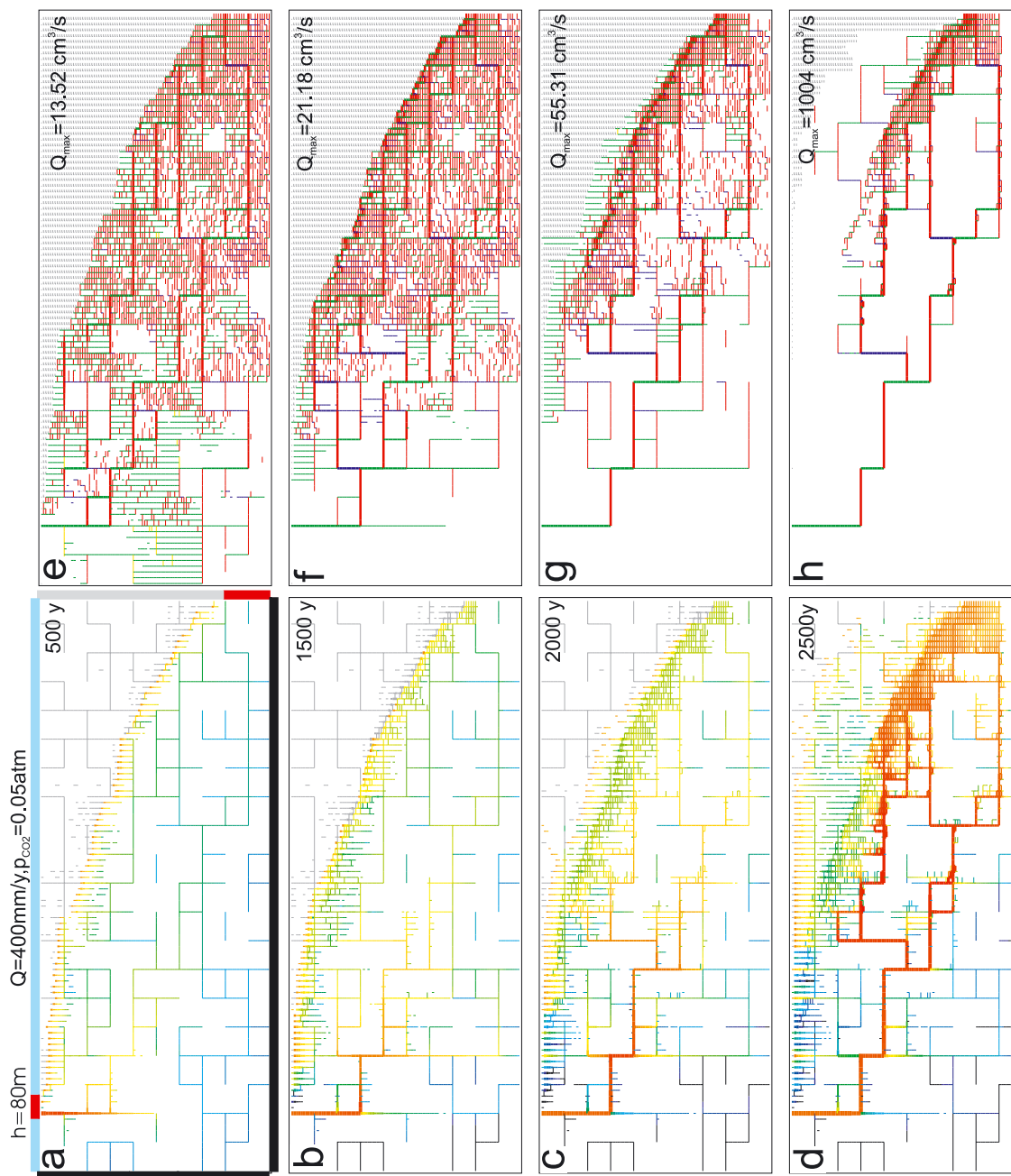


Figure 5.6: Evolution of scenario B: Dual-fracture aquifer with $A_0 = 0.04$ cm, $\bar{a}_0 = 0.006$ cm. Other parameters and boundary conditions as in Figure 5.5.

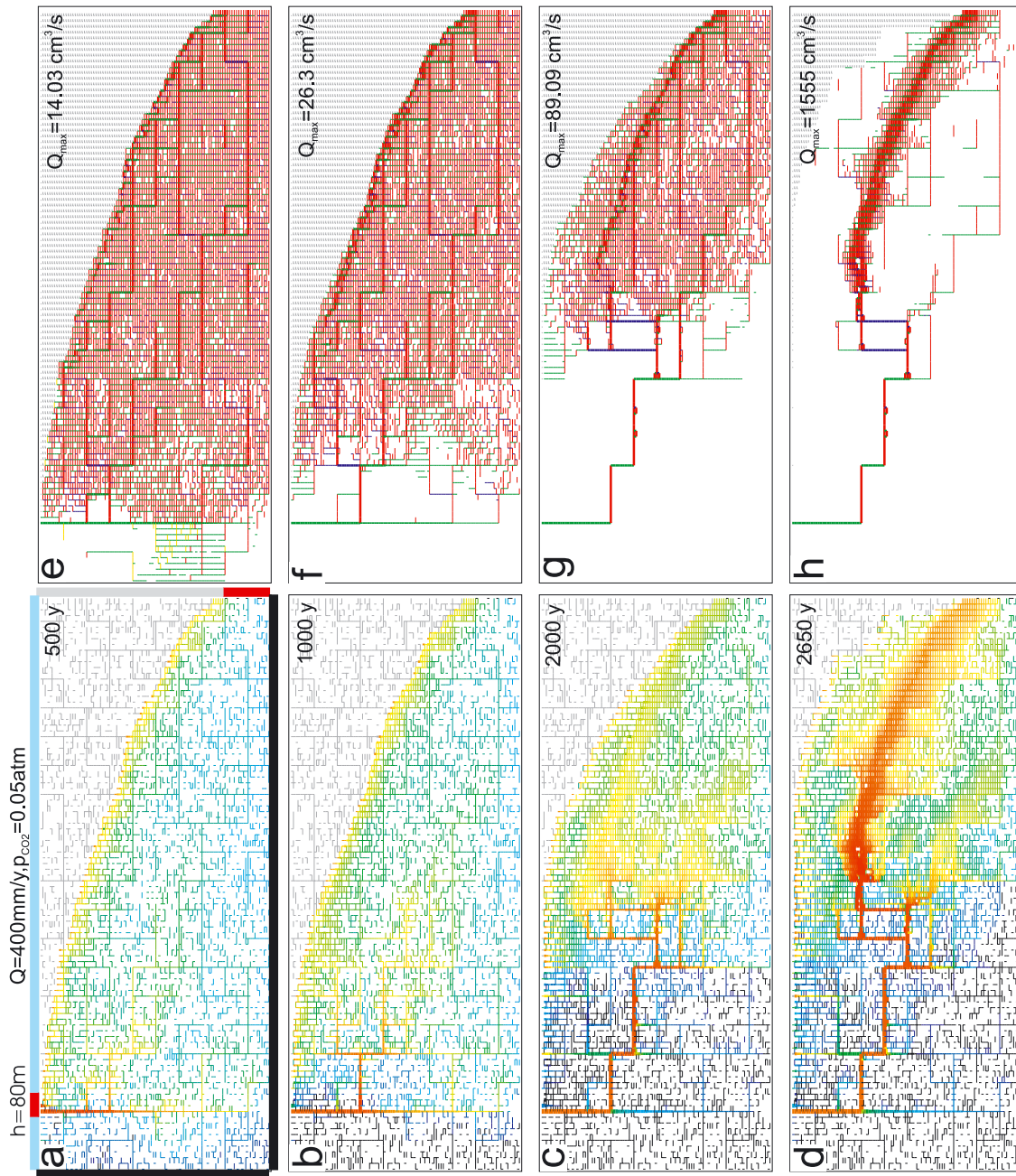


Figure 5.7: Evolution of scenario B: Dual-fracture aquifer with $A_0 = 0.04$ cm, $\hat{a}_0 = 0.009$ cm. Other parameters and boundary conditions as in Figure 5.5.

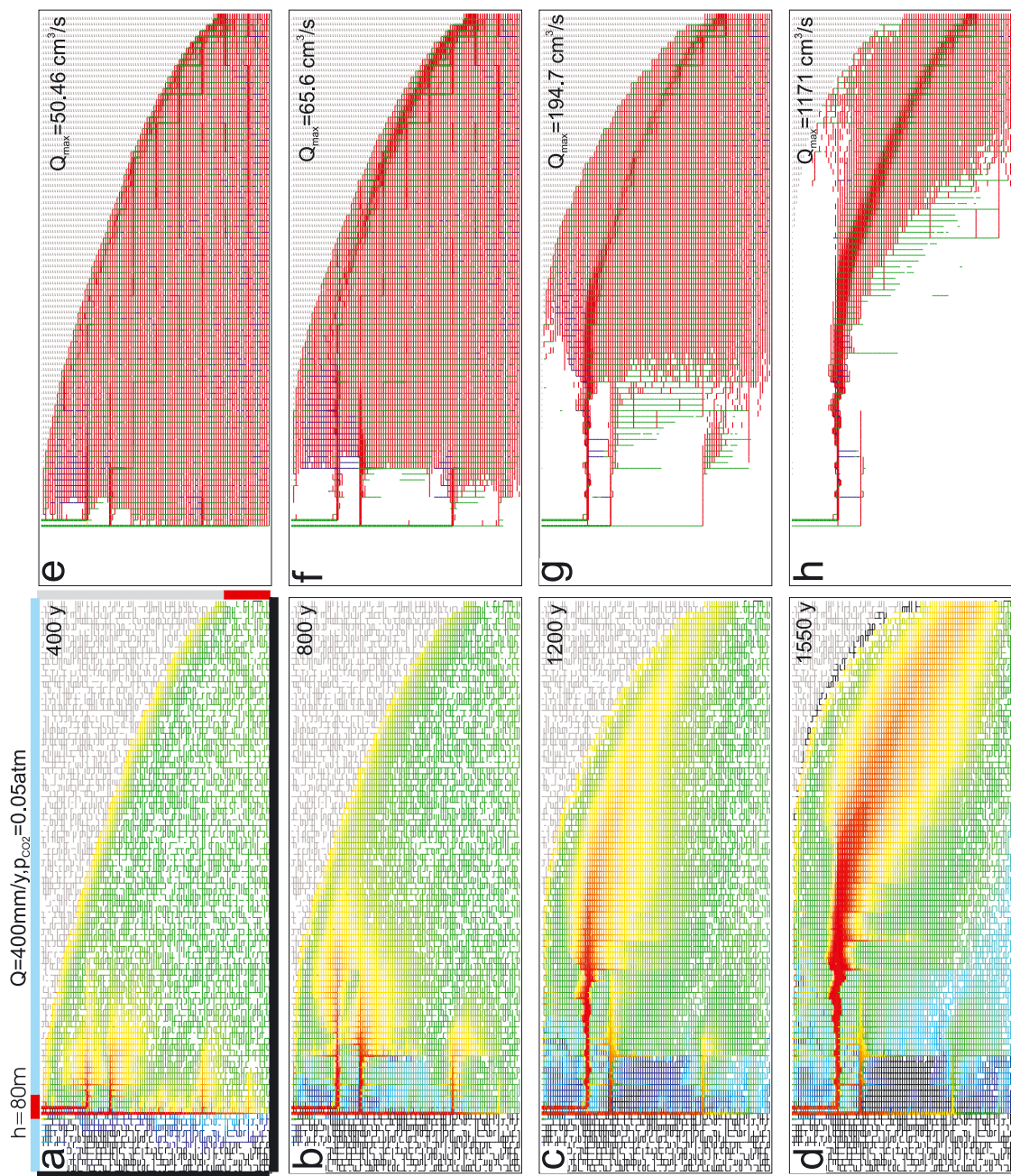
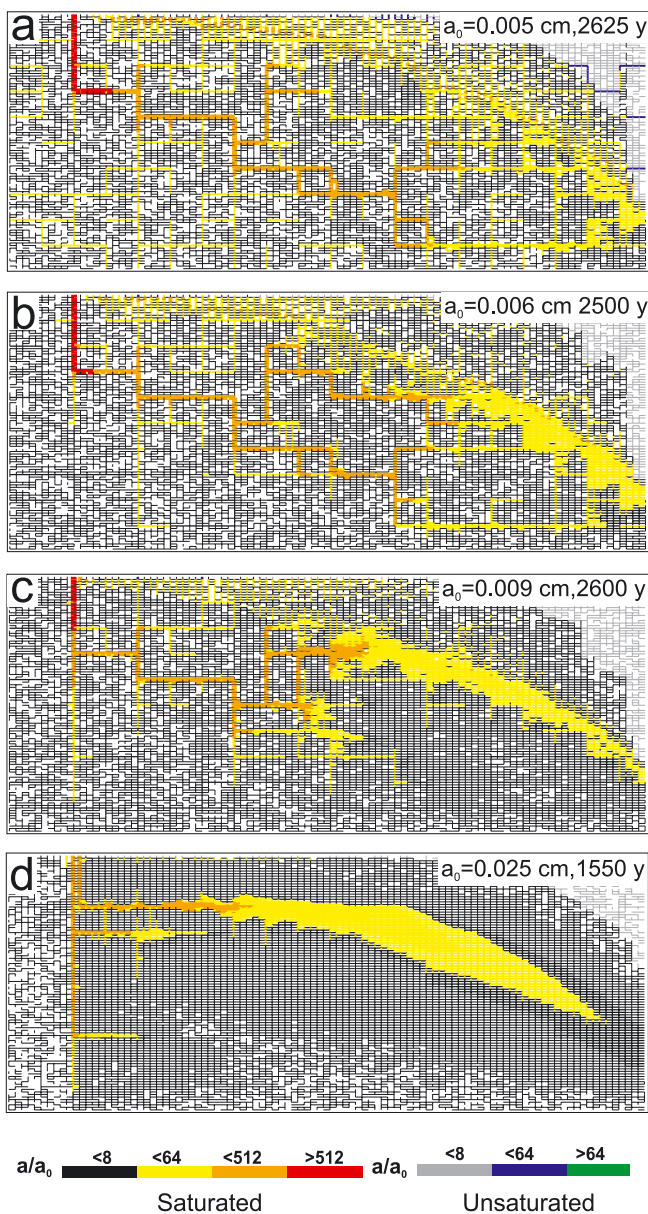


Figure 5.8: Evolution of scenario B: Dual-fracture aquifer with $A_0 = 0.04$ cm, $\hat{a}_0 = 0.025$ cm. Other parameters and boundary conditions as in Figure 5.5.

It is easy to conclude that with further increase of hydraulic coupling breakthrough will be entirely through the net along the water table. Figure 5.8 illustrates an example. Here we have chosen $\bar{a}_0 = 0.025$ cm, and $A_0 = 0.04$ cm. Now only the very first part of the percolation net is employed in the breakthrough pathway that continues through the net along the water table. Breakthrough occurs after 1550 y.

Two processes are operative in all these examples: a) The recharge to the aquifer creates a fringe of increasing permeability along the water table. b) The system of fractures can be regarded as a constant head system confined by the water table, and therefore shows breakthrough behavior. The mutual interaction of these two mechanisms is the reason for the competition in breakthrough pathways either along the percolation pathways or through the net.



To gain some idea on the distribution of fracture widths at breakthrough Figure 5.9 depicts aperture widths at that time for Figures 5.5 to 5.8 by a code of colors. Black denotes $a < 8\bar{a}_0$, yellow $8\bar{a}_0 < a < 64\bar{a}_0$, orange $64\bar{a}_0 < a < 512\bar{a}_0$ and red $a > 512\bar{a}_0$ in the phreatic zone. For the vadose zone we have used gray, $a < 8\bar{a}_0$, blue $8\bar{a}_0 < a < 64\bar{a}_0$, and green $a > 64\bar{a}_0$. Within the percolation pathways conduit widths are in the order of 1 cm (orange). The widths along the water table are one order of magnitude lower, at about 1 mm (yellow). One also can see that with increasing hydraulic coupling dissolution along the water table affects more extended regions and reduces dissolutional widening in the prominent fractures below.

Figure 5.9: Scenario B: Comparison of the distribution of fracture aperture widths at breakthrough for $\bar{a}_0 = 0.005$ cm (Figure 5.5), $\bar{a}_0 = 0.006$ cm (Figure 5.6), $\bar{a}_0 = 0.009$ cm (Figure 5.7), and $\bar{a}_0 = 0.025$ cm (Figure 5.8). The aperture widths can be read from the color code shown below.

Finally, in Figure 5.10 we show the evolution of total flow rates for Figures 5.5 to 5.8. It is interesting to note that for low coupling ($\bar{a}_0 \leq 0.006$ cm) we find a regular breakthrough through the prominent fractures under the constant head fixed by the stable water table. For $\bar{a}_0 = 0.009$ cm the ordinary breakthrough evolution of flow rates is conserved for the first 600 y. From thereon a steeper increase in flow rates illustrates that flow along the water table also contributes. For $\bar{a}_0 \geq 0.025$ cm this significant contribution is high from the very beginning of the aquifer evolution.

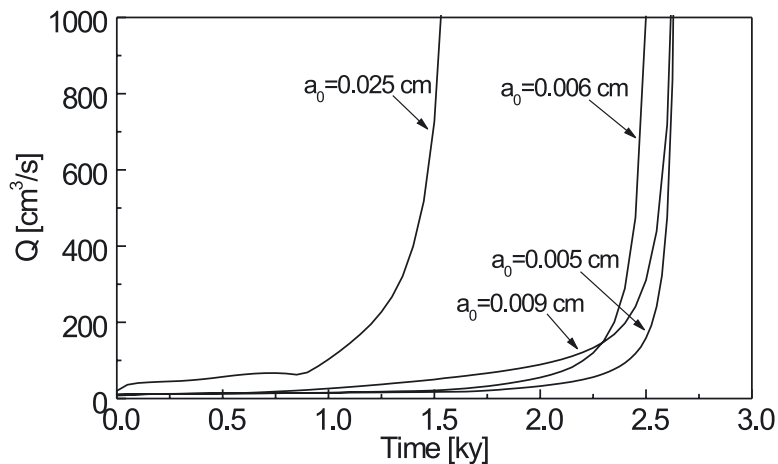


Figure 5.10: Scenario B: Evolution of flow rates for the model runs of Figures 5.5 – 5.8.

5.4 SCENARIO C: TWO VALLEYS OF DIFFERENT ALTITUDE AT THE MARGINS OF THE PLATEAU

As shown in Figure 5.1 two valleys are located at the margins of the plateau. They contain rivers, which define regions of constant head. h is 40 m between the altitudes 30 m and 50 m at the left hand margin. At altitudes between -20 m and base level at 0 m at the right hand side h is zero. Recharge to the plateau is 400 mm/year, evenly distributed to the water table with a p_{CO_2} of 0.05 atm. The water of the river in the upper valley also has a p_{CO_2} of 0.05 atm.

The evolution of the aquifer under such boundary conditions is shown in Figure 5.11. In this case a double-fracture network with $A_0 = 0.03$ cm and $\bar{a}_0 = 0.003$ cm is used. At the onset of the evolution all of the water flowing through the aquifer is derived from the recharge on top. Initially due to the narrow fractures there is no flow from the upper valley down to the lower one. The water table exhibits a maximum, which indicates a watershed and prohibits flow from the upper valley across it (a, e).

Under these conditions the water table drops as in scenario A until it reaches the upper valley. Then a water table caves starts to grow from there on and drains the left part of the aquifer (b, e). Note that flow is still directed to the left (yellow). Once the fractures comprising the water table cave have been widened sufficiently, such that the

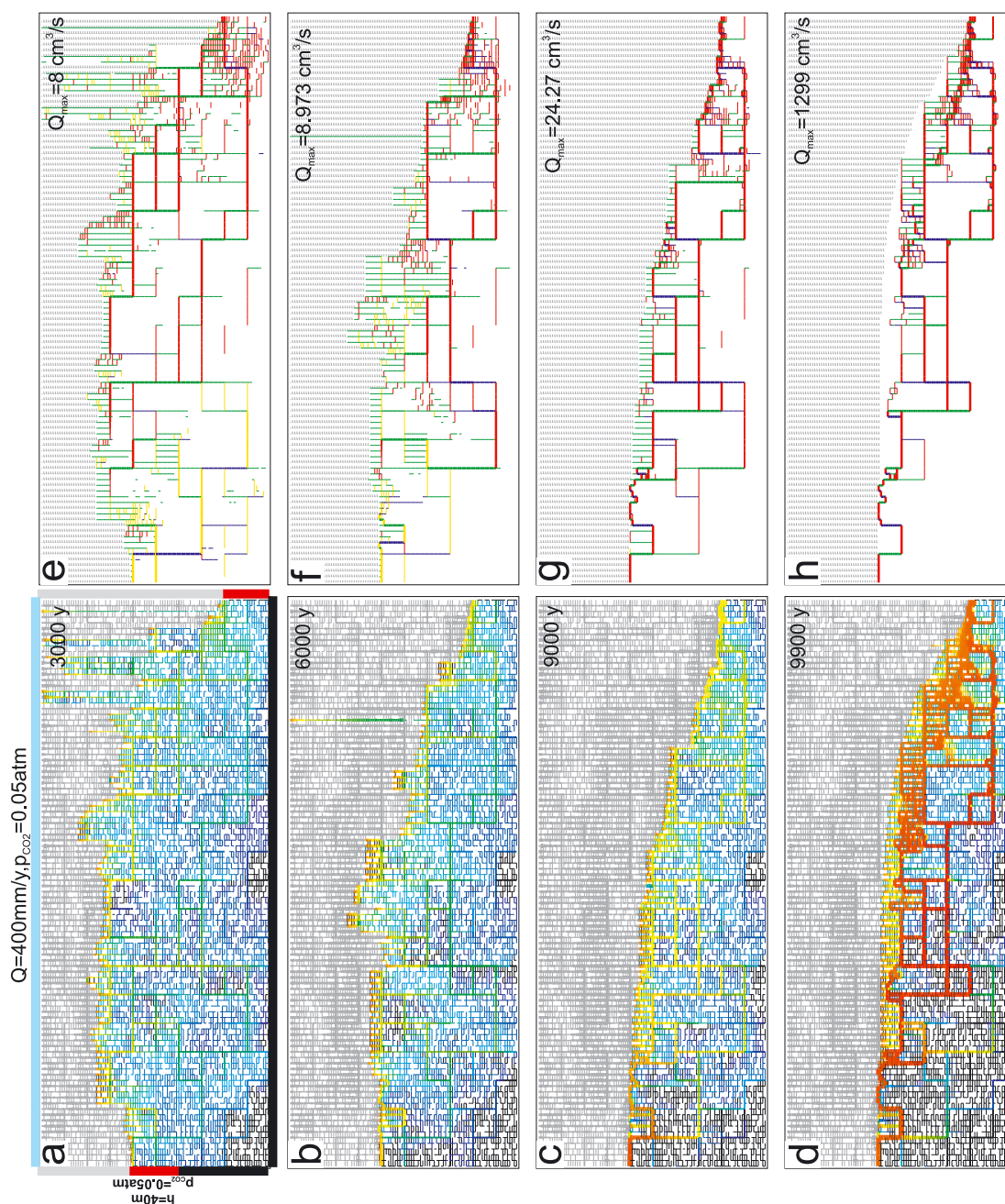


Figure 5.11: Evolution of scenario C: Dual-fracture aquifer as in scenario A (Figure 5.4) with $A_0 = 0.03$ cm, but with $\bar{a}_0 = 0.003$ cm. Recharge is evenly distributed on the plateau, but now two valleys, which deliver boundary conditions of constant head, border the aquifer. The margins of the domain above the rivers are seepage faces in the phreatic zone. Other parameters and boundary conditions as in Figure 5.4.



5. UNCONFINED AQUIFERS UNDER VARIOUS BOUNDARY CONDITIONS

water table has reached the river the flow direction is reversed and the constant head condition imposed by the river at the upper valley takes over. From then on the evolution is very similar to that of scenario B with constant recharge and constant head at the top (c, g).

In consequence the further evolution proceeds in a comparable way. Since the narrow fractures due to their small aperture widths $\bar{a}_0 = 0.003$ cm are not favorable breakthrough pathways the conduits grow along the prominent fractures connected to the water table and a through-cave with deep loops propagates towards base level at the right hand side valley (d, h).

In summary, the evolution is split into two modes. Initially, when flow is dominated by recharge a watershed is established and both parts evolve independently similar to scenario A. After the water table has reached the upper valley, flow driven by constant head between the two valleys takes over and the aquifer is dominated by constant head boundary conditions as in scenario B and our model runs are terminated at breakthrough.

As in examples of Chapter 4 (Figures 4.38, 4.39, 4.40, 4.42 and 4.43) the hydraulic coupling ratio \bar{a}_0/A_0 determines, whether the conduits grow along the prominent fractures or cut through the net. At low values of hydraulic coupling the patterns of conduits resemble the isolated case in Figures 4.38 and 4.39. This is also the case in unconfined settings with constant head boundaries.

Consequently, when increasing the hydraulic coupling one expects that pathways through the net along the water table will be more dominant. Figure 5.12 shows the evolution with $\bar{a}_0 = 0.005$ cm, and $A_0 = 0.03$ cm. Clearly at the beginning a watershed is established. As in the previous case the water table drops and develops along prominent fractures, but cuts also through the net of narrow fissures. By this way the left part of the aquifer resembles closely an isolated conduit system with deep phreatic loops, whereas its right side consists mostly of a fringe of narrow fractures close to the water table.

If \bar{a}_0 is raised further to $\bar{a}_0 = 0.009$ cm these features are enhanced. Because of the higher initial permeability of the net the water table is initially lower and drops much faster. The evolution is shown in Figure 5.13. At 3000 y (c, g) the water table has joined the upper valley. Flow from there utilizes a horizontal prominent fracture. After a short distance it is dispersed into the aquifer. Most of the flow, however, is focused to fractures and fissures close to the water table. In this region dissolutional widening in the net creates a narrow zone of high permeability. At 4010 y this region has attracted the entire flow through the aquifer (d, h).

A further increase of \bar{a}_0 to 0.012 cm does not affect this evolution, because in the previous scenario the aperture widths \bar{a}_0 are already sufficiently high to allow breakthrough through the net and the prominent fractures do no longer play an important role. This is shown in Figure 5.14.



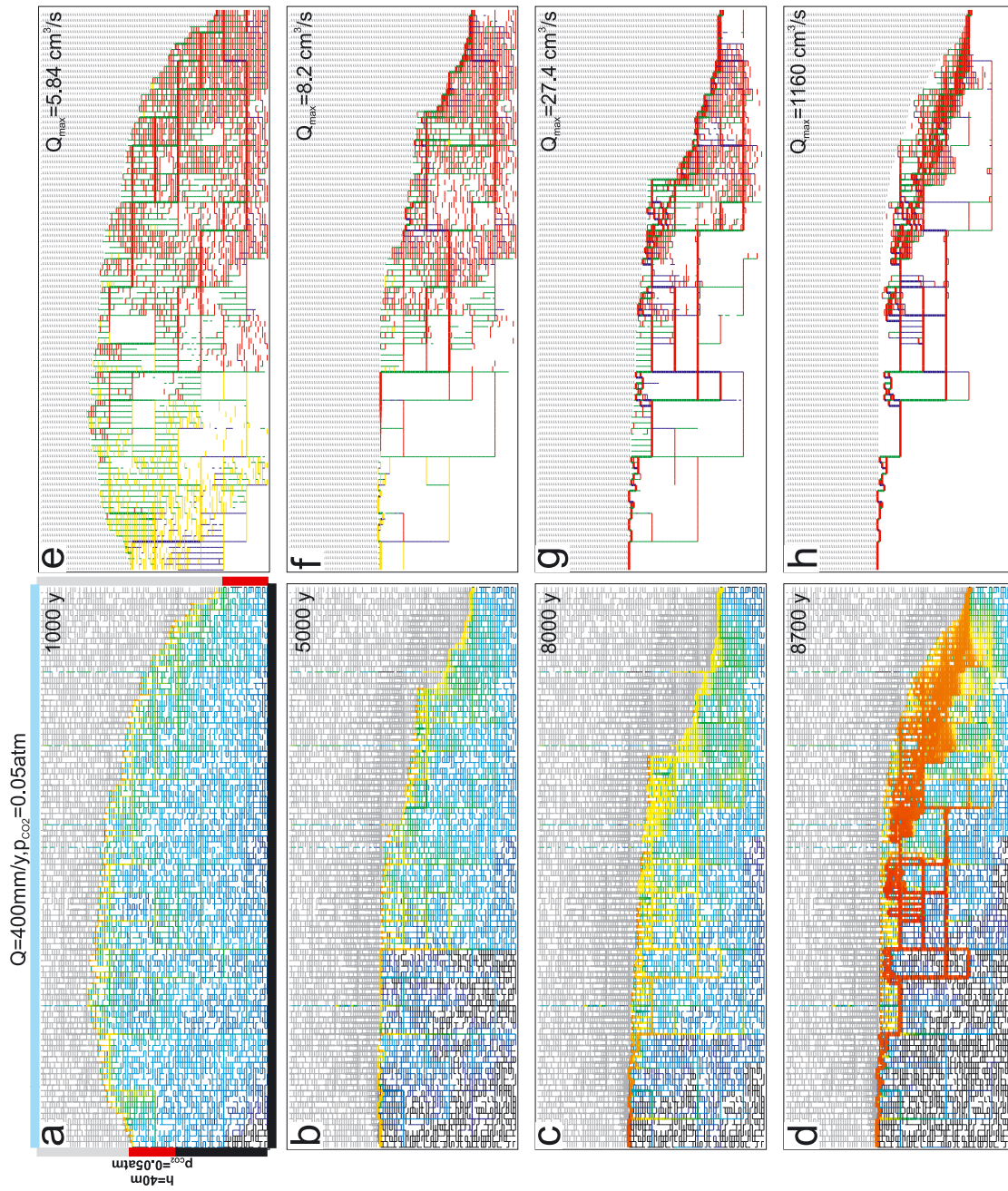


Figure 5.12: Evolution of scenario C: Dual-fracture aquifer with $A_0 = 0.03$ cm, $\hat{a}_0 = 0.005$ cm. Other parameters and boundary conditions as in Figure 5.11.

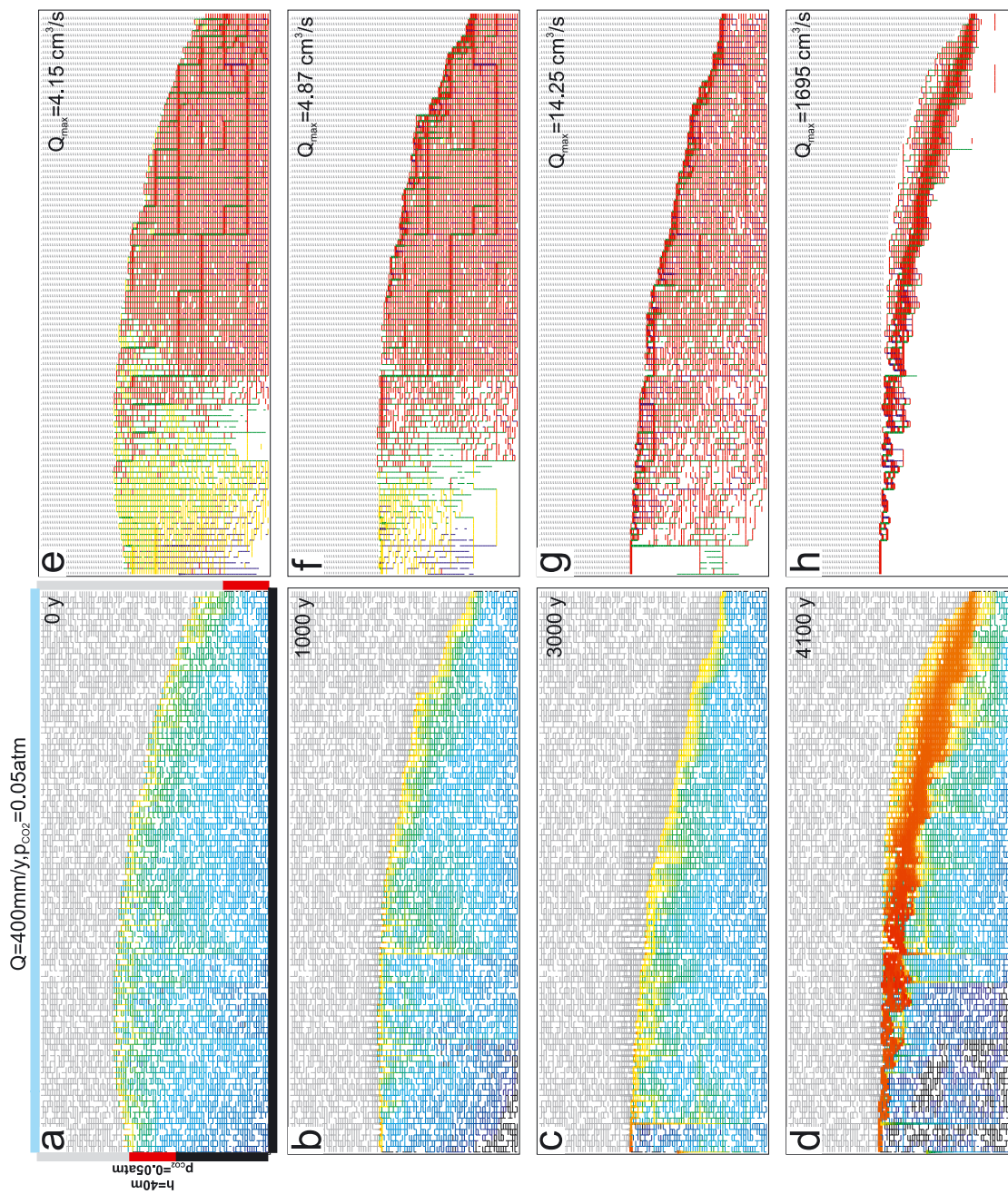


Figure 5.13: Evolution of scenario C: Dual-fracture aquifer with $A_0 = 0.03$ cm, $\bar{a}_0 = 0.009$ cm. Other parameters and boundary conditions as in Figure 5.11.

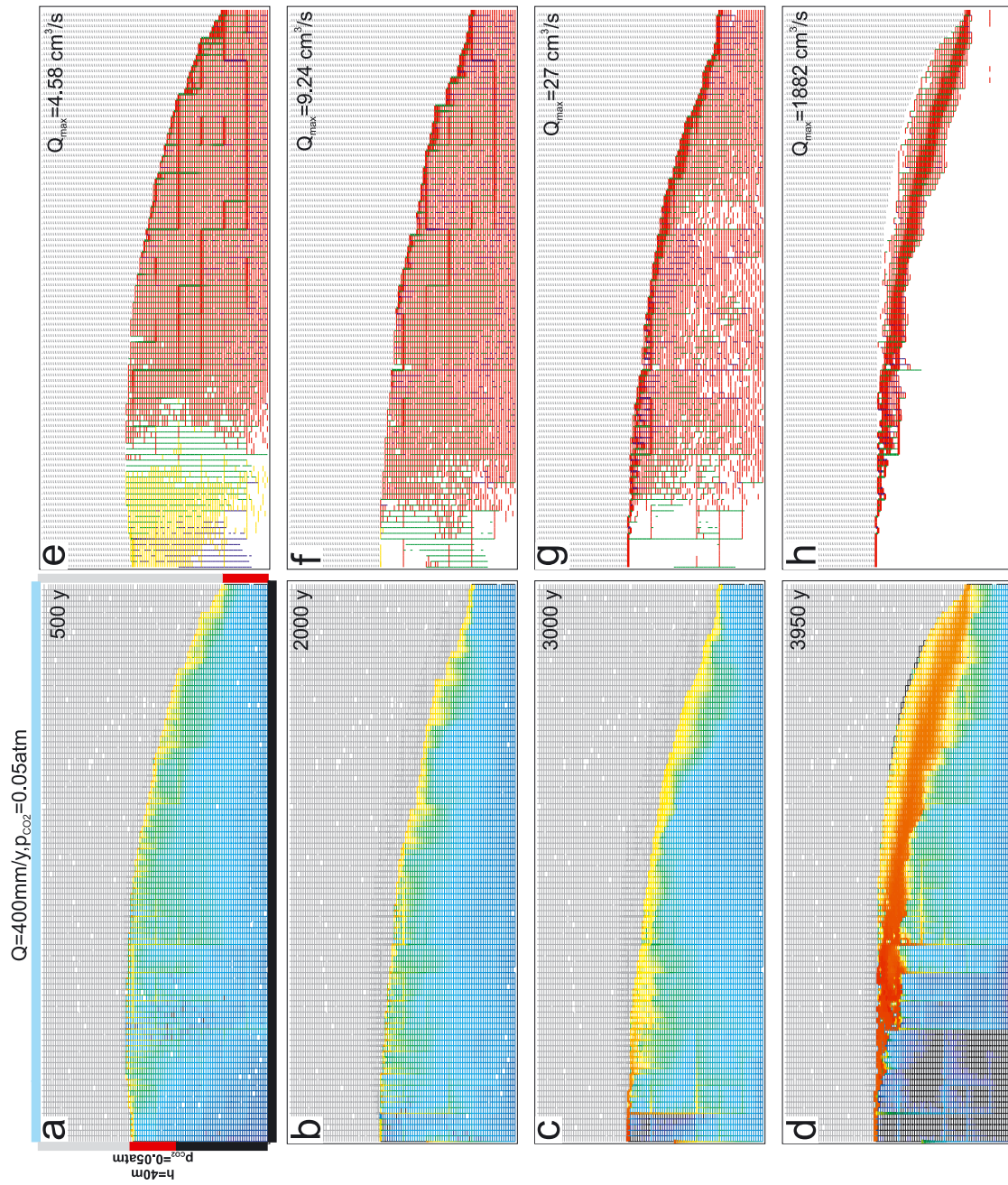
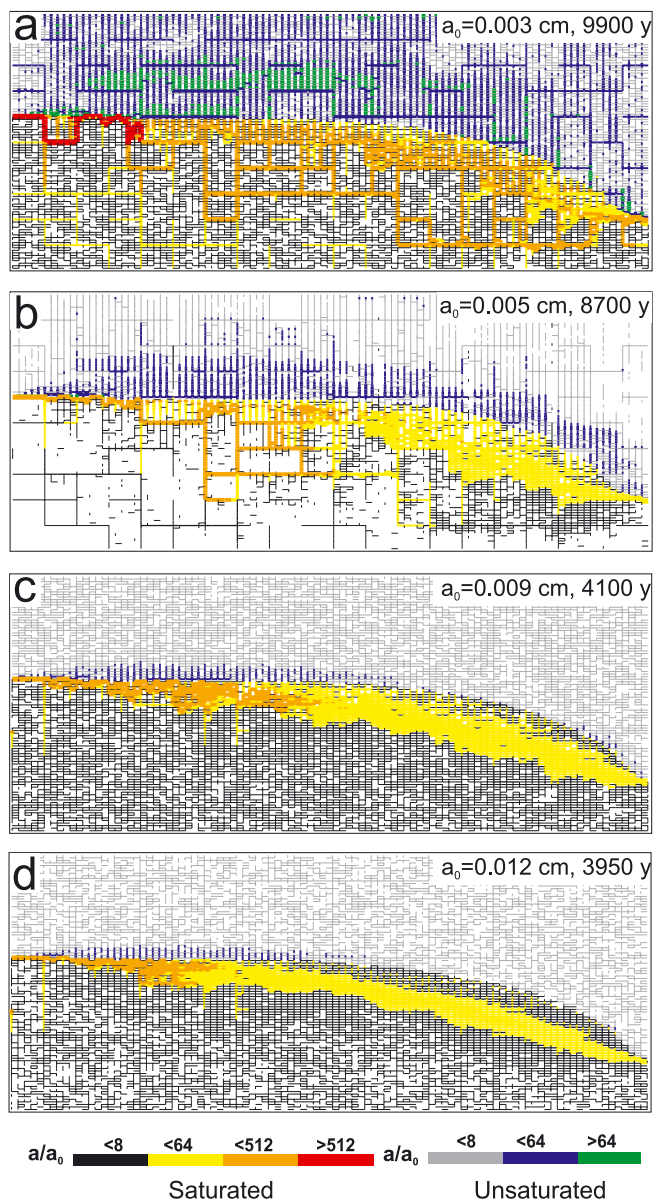


Figure 5.14: Evolution of scenario C: Dual-fracture aquifer with $A_0 = 0.03$ cm, $\bar{a}_0 = 0.012$ cm. Other parameters and boundary conditions as in Figure 5.11.



The distribution of fracture aperture widths at breakthrough is illustrated in Figure 5.15 for the scenarios of Figures 5.11 to 5.14. The color code for the distribution of aperture widths in the phreatic zone is the same as that used in Figure 5.9. Finally Figure 5.16 depicts the evolution of flow rates as a function of time for completeness. All curves show a typical breakthrough behavior.

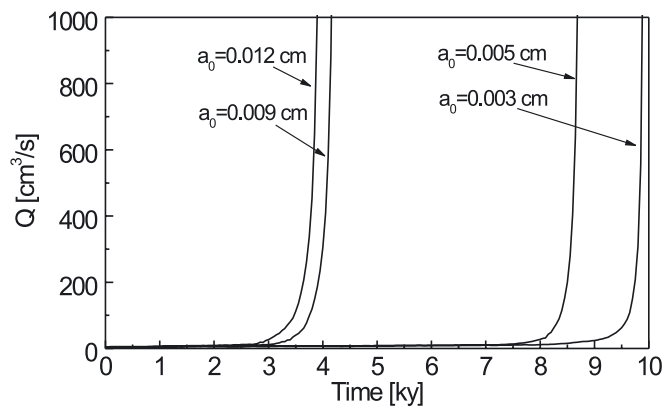


Figure 5.15: Scenario C: Comparison of the distribution of fracture aperture widths at breakthrough for Figures 5.11 to 5.14. The aperture widths in the phreatic and vadose zones can be read from the color codes below.

Figure 5.16: Scenario C: Evolution of flow rates for the model runs of Figures 5.11 – 5.14.



5.5 MIXING CORROSION IN UNCONFINED AQUIFERS

As we have learned in the discussion on the evolution in confined aquifers in Chapter 4 mixing corrosion can be an important factor. Therefore, we now turn to the influence of mixing corrosion in the examples of the unconfined aquifers of scenarios A, B, and C.

There are many ways to define boundary conditions and whatever one selects may appear arbitrary. For scenario A we assume that the karst plateau is vegetated in different ways. Some areas are poorly vegetated with a correspondingly low $p_{CO_2} = 0.01$ atm. Other regions with a higher p_{CO_2} input value of 0.05 atm are covered by grassland or trees. For scenarios B and C one may assume that the input p_{CO_2} of the allogenic water is low (0.01 atm), whereas the meteoric recharge seeping through the soil in vegetated areas has a higher p_{CO_2} (0.05 atm).

Furthermore, we can vary the concentration of the solution when it enters the water table. In this case it is of particular interest to see what happens, when the water enters with $c_{in} = c_{eq}$. Then the only mechanism that may lead to dissolution is mixing corrosion.

From what has been said above an incredible variety of scenarios and boundary conditions can be designed. Only a few very simple cases will be discussed here to introduce into the new patterns arising.

5.5.1 Unconfined aquifers under conditions of constant recharge including mixing corrosion (Scenario A)

We start with scenario A (statistical net) with $\bar{a}_0 = 0.009$ cm as depicted in Figure 5.3. We assume a region of vegetation with $p_{CO_2} = 0.05$ atm located in the left half of the karst plateau.

Figure 5.17 shows the evolution for this case. The pictures on the left hand side column present fracture aperture widths by the bar code and dissolution rates by the color code, as explained in the code box in Chapter 4. The right hand side column illustrates the flow rates by the bar code and the equilibrium value c_{eq} of the mixed solution by the color code. This way an idea is given how and where mixing occurs. The red color stands for the calcium equilibrium concentration of the solution with $p_{CO_2} = 0.05$ atm, whereas blue gives the equilibrium concentration for waters entering with $p_{CO_2} = 0.01$ atm. The colors in between represent the intermediate values of c_{eq} in the mixed solutions. c_{eq} decreases from red to blue.

All solutions enter the water table with $c_{in} = 0.9c_{eq}$ and a fringe of dissolutional activity is created along it (a). In addition to this, as seen on the right hand side column (e) a plume of water with a high concentration flows down from the region of high p_{CO_2} into the aquifer. At the fringes of the plume (yellow) mixing corrosion becomes active and creates a zone of comparatively high dissolution rates penetrating deep into the aquifer (green regions in (a)).



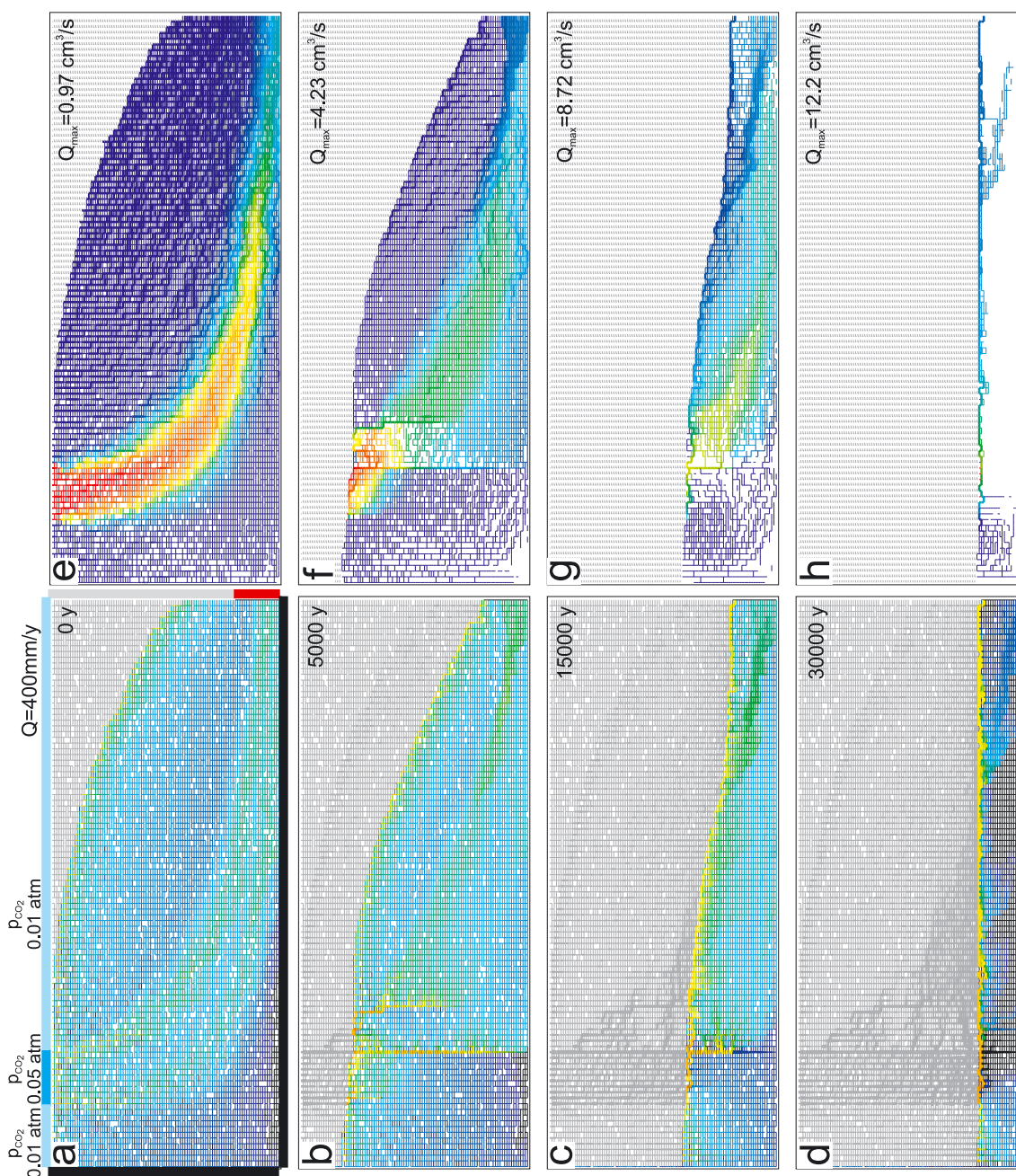


Figure 5.17: Evolution of scenario A (simple statistical Cornet, Figure 5.3): Mixing Corrosion. New chemical boundary conditions are introduced into the constant recharge area of Figure 5.3. At the left side of the plateau a vegetated area with a $p_{CO_2} = 0.05$ atm is assumed. Otherwise bare rock covers the plateau with low $p_{CO_2} = 0.01$ atm of the input waters. $c_{in} = 0.9c_{eq}$, $\bar{a}_0 = 0.009$ cm. Other parameters and boundary conditions as in Figure 5.3. The left column illustrates aperture widths and dissolution rates. The right column shows flow rates and the equilibrium concentrations of the mixed solutions.

After 5000 y (b) the water table has dropped, leaving behind higher fracture aperture widths in the region below the high p_{CO_2} input area (b, f). After 15 ky the flow from the left towards the region of high p_{CO_2} is concentrated along the water table, and high dissolution rates are operative there (c). Therefore mixing is also restricted to this region of high flow rates. The mixed solutions deep in the aquifer become less aggressive as time proceeds (c, g). This is shown by the colors on the right hand side. At the same time the dissolution rates along the water table increase (yellow) in c and d. The water table continues to drop and a water table cave is created as in Figure 5.3. But in contrast to this, where a rather homogeneous permeability is left behind in the vadose zone, now higher permeability is found only in the region below high p_{CO_2} inputs (c, d). Because of the lower p_{CO_2} of 0.01 atm the evolution until a water table cave is established is retarded to about 30 ky compared to 20 ky in scenario A with $p_{CO_2} = 0.05$ atm everywhere.

We now proceed to the case of pure mixing corrosion by assuming that the solutions entering the water table are fully saturated. ($c_{in} = c_{eq}$). The evolution is shown by Figure 5.18. Initially, flow rates and mixing concentrations are equal to those in Figure 5.17. Because of the saturated solutions dissolution rates are zero at the water table and below (black area) (a). Only where water with high p_{CO_2} mixes with the surrounding waters of low p_{CO_2} dissolution is active by mixing corrosion (a, e).

After 10000 years most of the flow is concentrated through fissures close to the water table. These are two vertical fractures at the borders between waters of high and low p_{CO_2} input regions and horizontal ones below the high p_{CO_2} -region. Mixing is high in these fractures and consequently also the dissolution rates (b, f). At the downstream side of the high p_{CO_2} -region water mixes with low p_{CO_2} -water and dissolution rates are high at fractures located at the water table (b, f). Because of the redistribution of flow rates the plume of high p_{CO_2} -water does no longer penetrate deep into the aquifer (b, f)

After 20 ky (c, g) the water table has dropped further and almost all flow is channeled into fractures close to it. Mixing corrosion is active below high p_{CO_2} -region and downstream of it (yellow fractures in c). Further downstream flow is dispersed into the net, where dissolution rates are low. After 40 ky (d, h) the water table has reached base level (g). A water table cave grows, but it is restricted to the region where waters with high and low p_{CO_2} -input mix (d). Downstream dissolution rates are high (orange, yellow) until flow becomes diffuse at the center of the domain towards base level (h).

It seems as if the patterns of pure mixing corrosion of Figure 5.18 and dissolution of unsaturated solutions as in Figure 5.3 can be combined to deliver the patterns seen in Figure 5.17 where both modes are active.

We now turn to scenario A with a percolation network of primary fractures as in Figure 5.4 ($\bar{a}_0 = 0.009$ cm, $A_0 = 0.03$ cm). We assume a region of elevated $p_{CO_2} = 0.05$ atm at the same place as in Figure 5.17. The input concentration at the water table is $c_{in} = 0.9c_{eq}$. Figure 5.19 shows the results. At the onset similar as in Figure 5.17 there is a plume of a solution with a high p_{CO_2} migrating downstream (a, e). Close to the water table dissolution is caused by the undersaturated input solutions. Mixing corrosion is active at the rims of the plume. After 5 ky the water table has dropped and a long

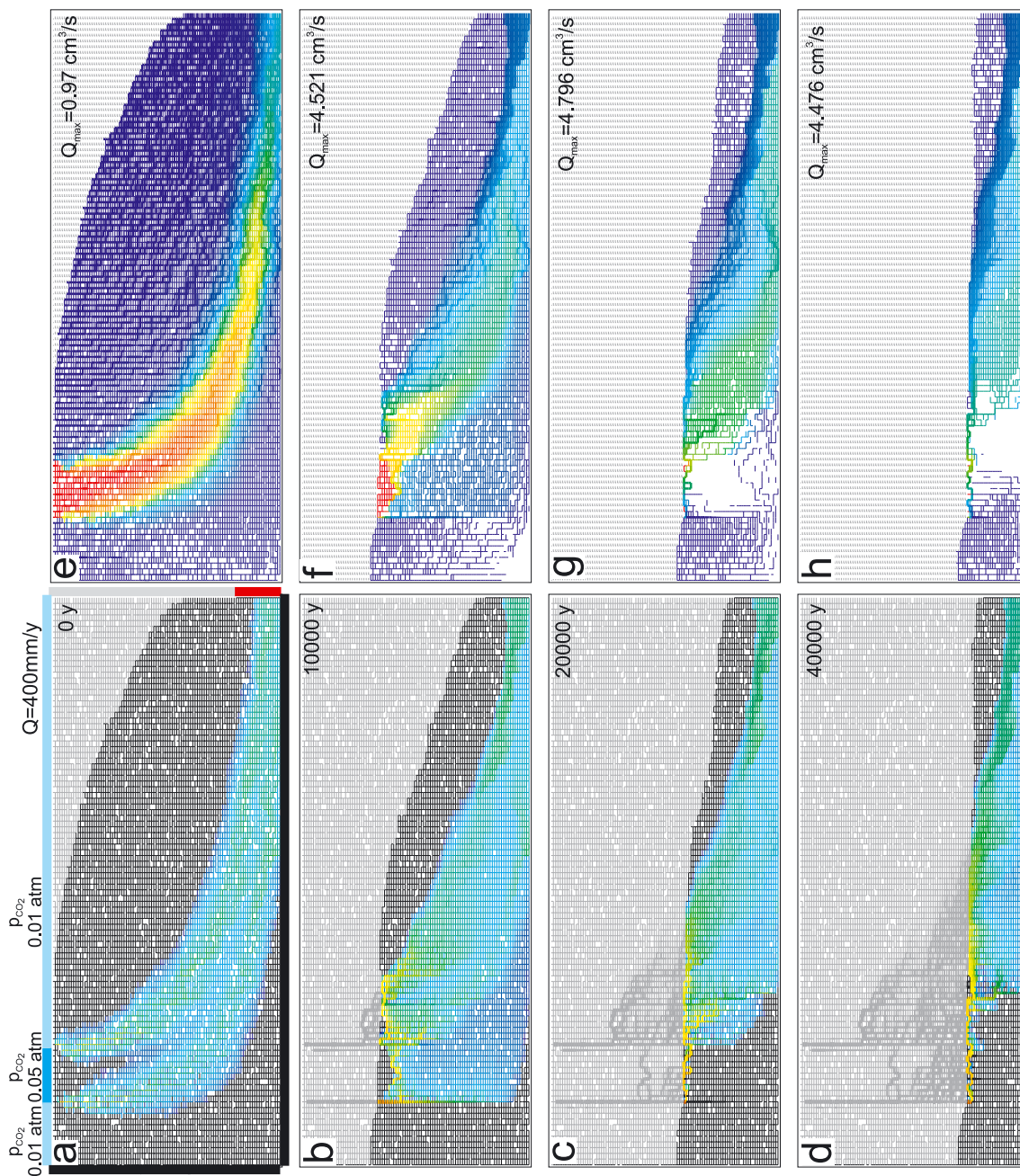


Figure 5.18: Evolution of scenario A (simple statistical net, Figure 5.3): Mixing corrosion. Other parameters and boundary conditions as in the previous Figure 5.17. But now the inflowing solutions are saturated, $c_{in} = c_{eq}$ at all input points. MC is the only cause for dissolution (pure MC). Left hand column: aperture widths and dissolution rates. Right hand column: equilibrium concentrations of mixed solutions.

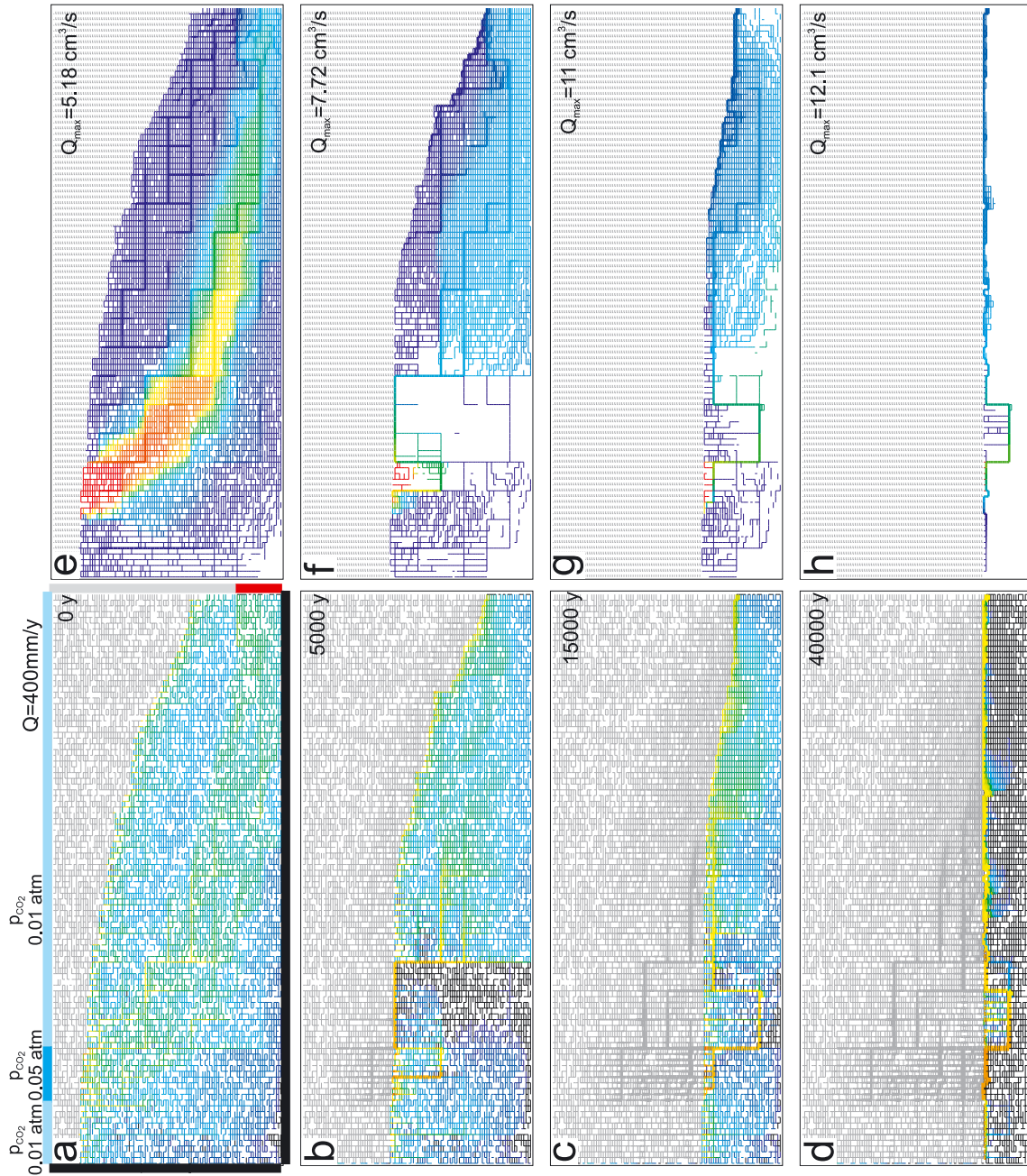


Figure 5.19: Evolution of scenario A (dual-fracture aquifer, Figure 5.4): Mixing corrosion. Regions of $p_{CO_2} = 0.05$ atm (vegetated area) and $p_{CO_2} = 0.01$ atm (bare rock) input waters are located on top of the plateau as in Figure 5.1. $c_{in} = 0.9c_{ef}$. Other parameters and boundary conditions as in Figures 5.4 and 5.17. Left hand column: aperture widths and dissolution rates. Right hand column: equilibrium concentrations of mixed solutions.



pathway of percolating fractures carries flow to the exit (b, f). As the water table drops further other percolating pathways are utilized to carry flow downstream. Dissolution widening occurs predominantly along the prominent fractures (c, g). Finally, base level is reached everywhere and a water table cave with a looping conduit will grow further on to maturity (d, h).

To gain some idea how the distribution of p_{CO_2} influences the aquifer we have modeled the case where the p_{CO_2} -values of Figure 5.19 are changed such that the high p_{CO_2} region is now replaced by a low $p_{CO_2} = 0.01$ atm, and the low p_{CO_2} regions become areas with a high p_{CO_2} of 0.05 atm. Figure 5.20 gives the results of a model run with these boundary conditions.

Basically, the evolution is similar to that of Figure 5.19. At the right hand side column the colors are interchanged due to the change of CO_2 -inputs. Similar to Figure 5.19 a water table cave with a loop has originated. But due to the higher p_{CO_2} in the extended region of the aquifer the time of evolution has dropped from 40 ky (Figure 4.19 with low p_{CO_2} in the extended region) to only 15 ky.

Figure 5.21 shows the evolution of the dual-fracture aquifer in Figure 5.19 in the case of pure mixing corrosion, when $c_{in} = c_{eq}$. The behavior is very similar to that of a statistical net shown in Figure 5.18, and therefore not further explained here. At the end we find a looping cave close to the water table, which is not connected to the output and remains isolated. The remnants in the vadose zone show a structure dominated by prominent fractures.

5.5.2 Mixing corrosion in a combination of constant recharge and constant head boundary conditions (Scenario B)

To study the influence of mixing corrosion in scenario B (conf. to Figure 5.7) the simplest change is to keep the input from meteoric recharge at a p_{CO_2} value of 0.05 atm, but to reduce the value from the allogenic water at the constant head region to $p_{CO_2} = 0.01$ atm instead of 0.05 atm in Figure 5.7 everywhere ($A_0 = 0.04$ cm, $\bar{a}_0 = 0.009$ cm, $c_{in} = 0.9c_{eq}$).

Figure 5.22 shows the results. In the beginning (at $t = 0$ y) low p_{CO_2} water enters in the region with constant head conditions and forms a plume (blue) penetrating into the aquifer creating a wide zone of mixing and dissolution widening at its margins (a, e). However, in contrast to the case without MC (Figure 5.7) the dissolution rates along the prominent fractures are severely reduced due to the low p_{CO_2} in this zone.

Because of the low p_{CO_2} at the constant head input dissolution in the deep reaching prominent fractures is low. MC is restricted to the region close to the water table, but also active in the prominent fractures. Highest dissolution rates from the water entering by recharge appear close to the water table. Therefore, breakthrough along the water table becomes more favorable (b, f). After 1200 y flow from the constant head region along the water table has become dominant and highly dilutes the water from recharge. Thus



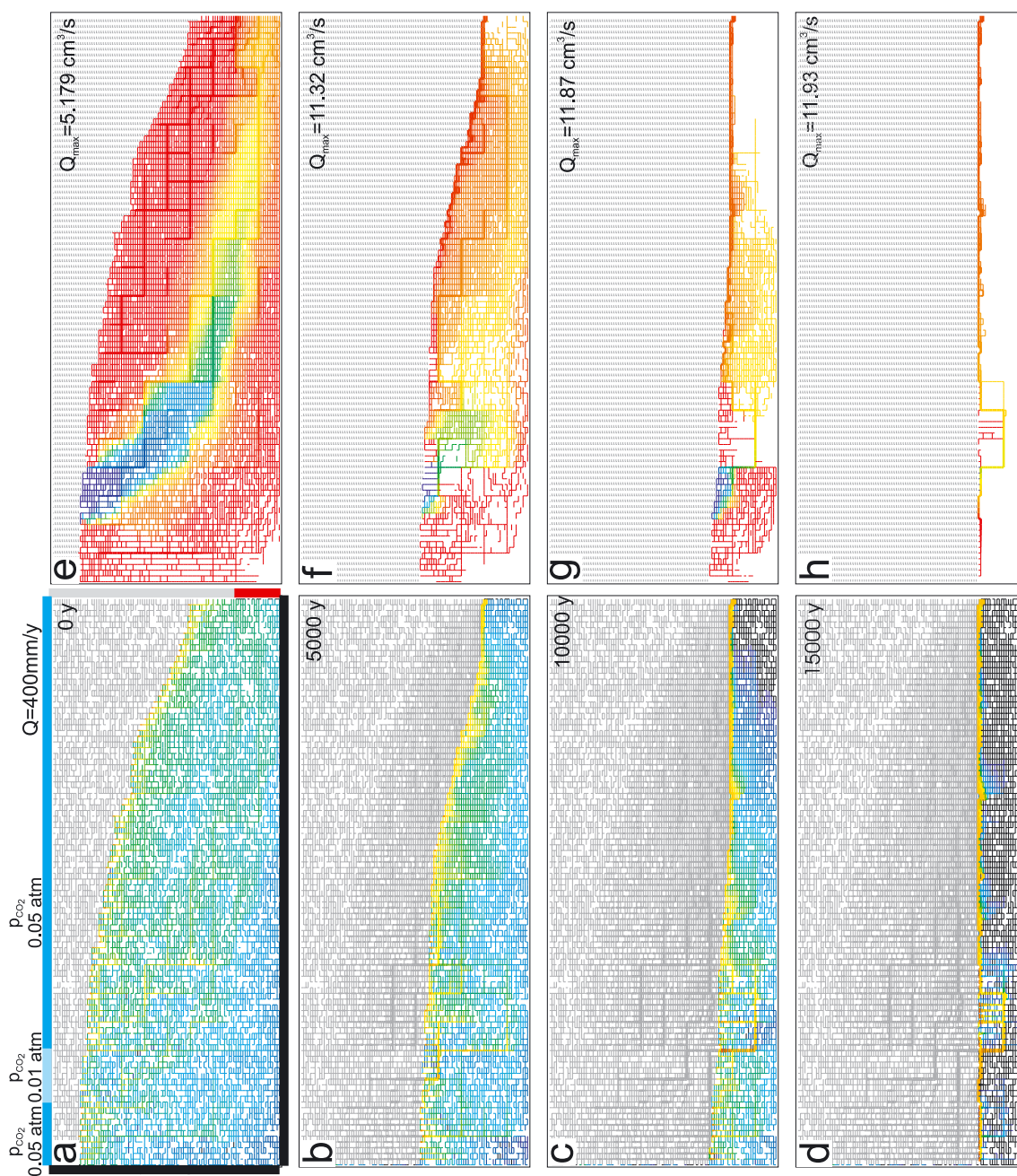


Figure 5.20: Evolution of scenario A (dual-fracture aquifer, Figure 5.4): Mixing corrosion. Other parameters and boundary conditions as in the previous figure. But now the regions of p_{CO_2} are inverted. Low $p_{CO_2} = 0.01$ atm at the left hand side input (bare rock now), elsewhere on the plateau $p_{CO_2} = 0.05$ atm (vegetated). $c_{in} = 0.9c_{eq}$. Left hand column: aperture widths and dissolution rates. Right hand column: equilibrium concentrations of mixed solutions.

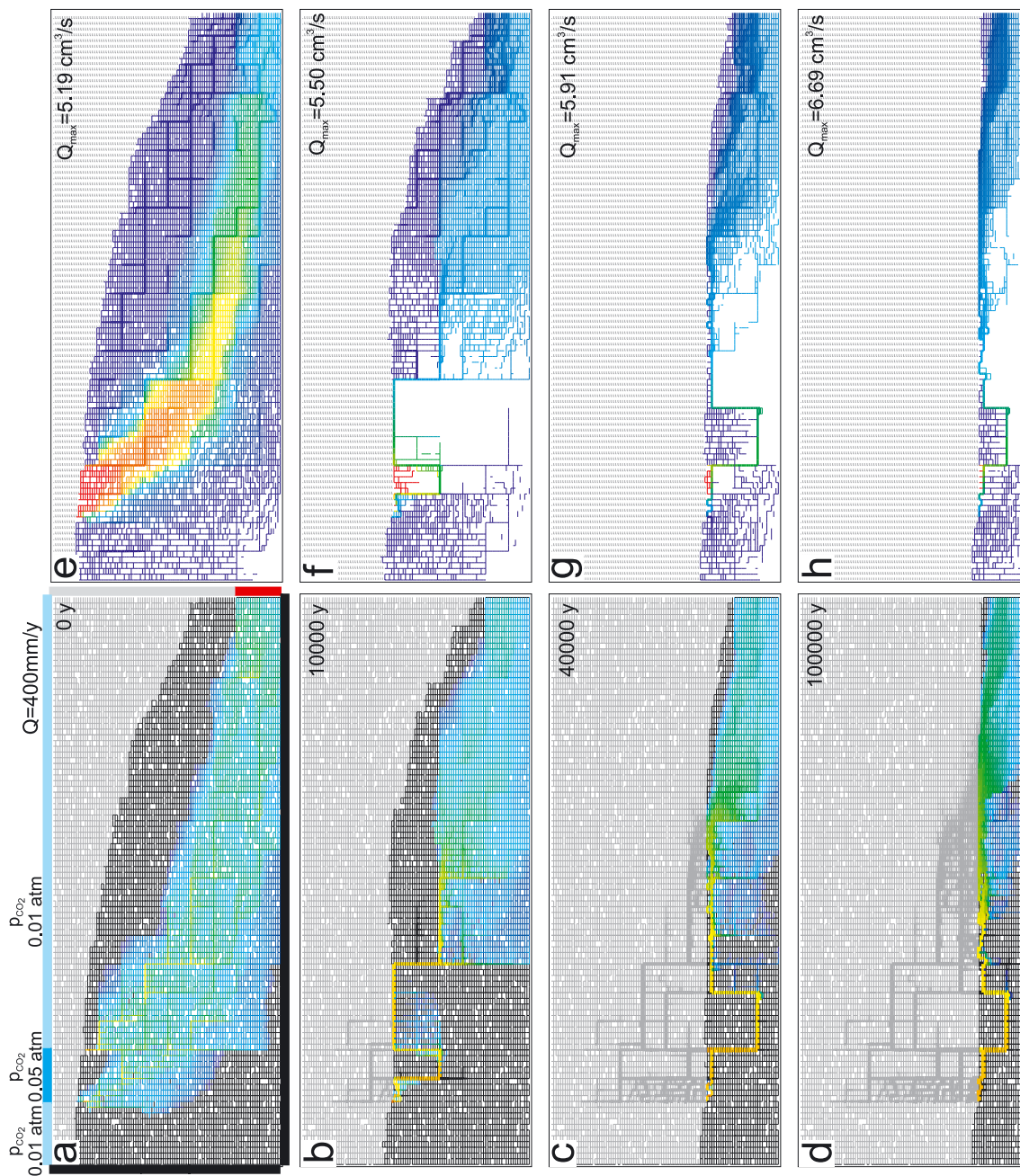


Figure 5.21: Evolution of scenario A (dual-fracture aquifer, Figure 5.4): Mixing corrosion. Other parameters and boundary conditions as in Figure 5.17, but now the inflowing solutions are saturated, $c_{in} = c_{eq}$. MC is the only cause of dissolution (pure mixing corrosion). Left hand column: aperture widths and dissolution rates. Right hand column: equilibrium concentrations of mixed solutions.

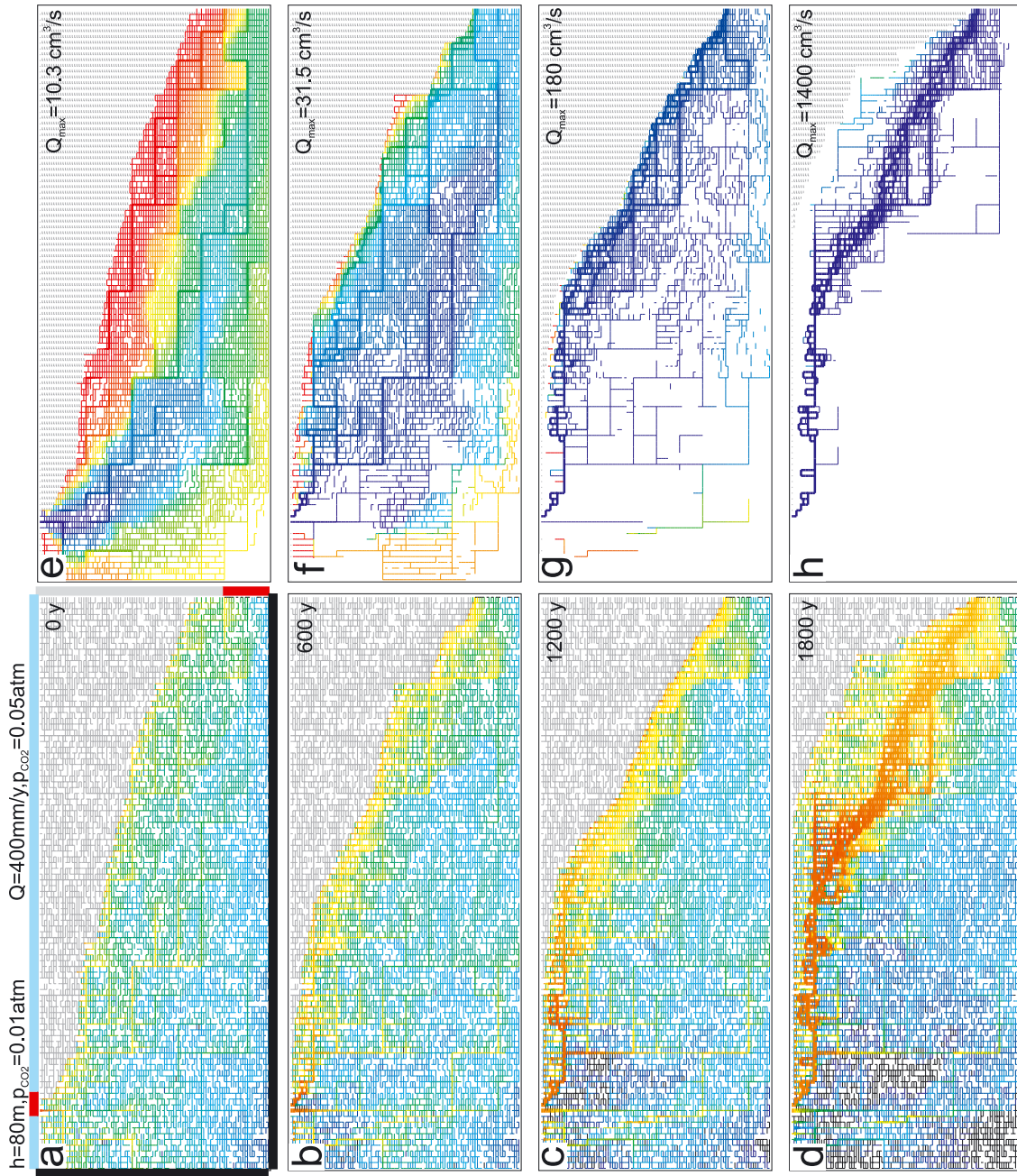


Figure 5.22: Evolution of Scenario B (dual-fracture aquifer, Figure 5.7): Mixing corrosion. Now p_{CO_2} at the constant head boundary (river or lake) is reduced from 0.05 atm to 0.01 atm. Other parameters and boundary conditions on the plateau $p_{CO_2} = 0.05$ atm as in Figure 5.7 $c_m = 0.9c_{eq}$. Left hand column: aperture widths and dissolution rates. Right hand column: equilibrium concentrations of mixed solutions.



5. UNCONFINED AQUIFERS UNDER VARIOUS BOUNDARY CONDITIONS

mixing corrosion is practically switched off by the huge amount of water with low p_{CO_2} invading the aquifer (g, h). Breakthrough occurs after 1800 y mainly along the water table, in contrast to the case without MC (see Figure 5.7), where breakthrough is directed through deep looping prominent fractures and then along the water table.

This mechanism is switched off in the next scenario. We assume that the calcium concentration of the water in the constant head region remains $c_{in} = 0.9c_{eq}$, whereas the water from recharge with $p_{CO_2} = 0.05$ atm enters the water table fully saturated, with $c_{in} = c_{eq}$. This way dissolution rates at the top of the water table are zero (black region), as shown in Figure 5.23a, e. Dissolution is active from the aggressive waters of the allogenic river, and by mixing corrosion, where they mix with the meteoric recharge. Thus breakthrough along prominent fractures is favored (b, f) and flow along conduits determines the evolution. Again, as in the previous scenario mixing corrosion is switched off after 1800 y by the large inflow from allogenic water (c, g). Breakthrough is caused by the unsaturated, low p_{CO_2} waters from the river (d, h).

We now turn to a scenario, in which all input waters, those from recharge and those from the constant head region are saturated. This is accomplished by changing c_{in} from $0.9c_{eq}$ in the proceeding scenario, Figure 5.23, to $c_{in} = c_{eq}$ in the constant head region, leaving everything else unchanged. The evolution under such conditions is illustrated by Figure 5.24. In the beginning a plume of low p_{CO_2} input water from the constant head region penetrates down into the aquifer (blue in the right hand column). Then it mixes readily with the waters from recharge (red). Dissolution rates are now widely distributed in the aquifer. Close to the water table they are low because recharge water is saturated (a, e).

The rates are somewhat higher (yellow) in some of the prominent fractures, where flow is high. After 2500 y the water table has dropped. The saturated solution from the constant head input has invaded a larger part of the aquifer. High dissolution rates (yellow, green) are widely distributed throughout the aquifer. They are especially high in the prominent fractures connected to the water table (b, f and c, g). After 5000 y the water table has reached base level at the right hand side, but stays somewhat higher inside the aquifer. Of course, in the area of constant head the water table reaches the surface. However, the water flowing there is saturated such that in this region dissolution rates are zero and permeability is not increased. Only at the margins of this narrow zone widened fractures have been created and are left behind in the vadose zone. At all times prominent fractures close to the actual water table are preferred pathways of flow and exhibit the highest dissolution rates. Furthermore, in the net of fine fractures dissolution rates are always higher close to the dropping water table. In contrast to the scenario in Figure 5.21 where the water table stays high due to the increasing flow from the constant head region, here the water table drops to base level (d, h). The reason for this is that in the uppermost zone of the aquifer below the constant head region dissolution rates are zero at all time steps ($c_{in} = c_{eq}$). This can be seen from the small black regions in every panel on the left hand side. Consequently inflow from the constant head region remains limited, and the increasing permeability in the constant recharge region



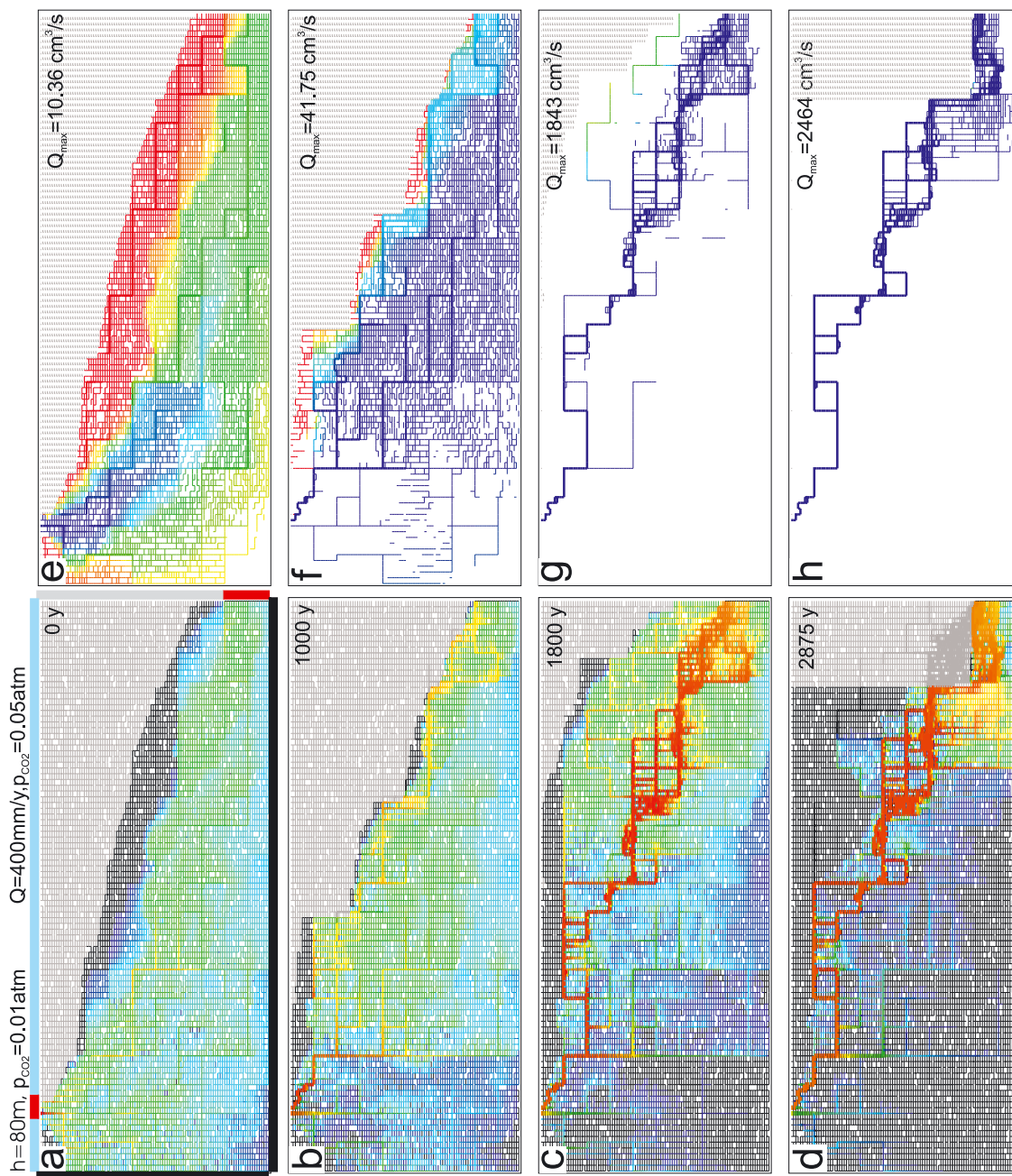


Figure 5.23: Evolution of Scenario B (dual-fracture aquifer, Figure 5.7): Mixing corrosion. Now the inflowing solution from the evenly distributed recharge is saturated, $c_{in} = c_{eq}$. Other parameters and boundary conditions as in previous Figure 5.22. Left hand column: aperture widths and dissolution rates. Right hand column: equilibrium concentrations of mixed solutions.

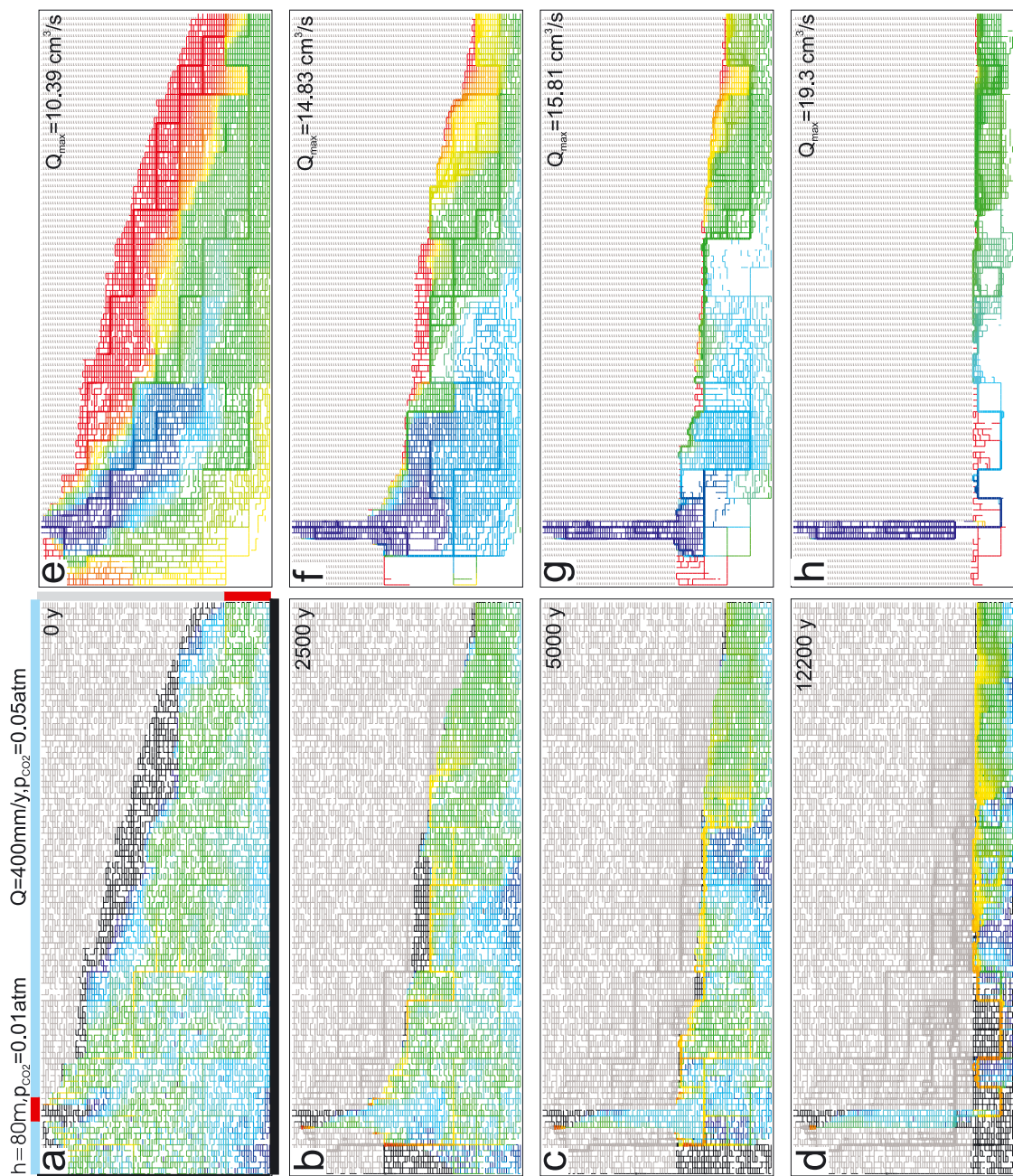


Figure 5.24: Evolution of Scenario B (dual-fracture aquifer, Figure 5.7): Mixing Corrosion. Now $c_m = c_{eq}$ everywhere. Other parameters and boundary conditions as in previous Figure 5.23. Left hand column: aperture widths and dissolution rates. Right hand column: equilibrium concentrations of mixed solutions.

is sufficient to drain those limited amounts of water. Figure 5.25 depicts the evolution of flow rates through the aquifer of Figures 5.22–5.24.

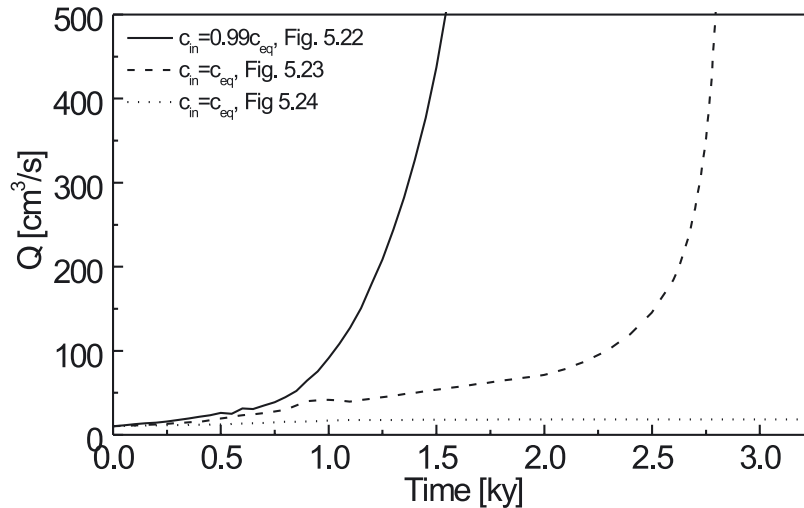


Figure 5.25: Scenario B: Evolution of flow rates for the model runs of Figures 5.22, 5.23 and 5.24.

5.5.3 Mixing corrosion for an aquifer bordered by two valleys (Scenario C)

In scenario C shown in Figure 5.13 ($\bar{a}_0 = 0.009$ cm, $A_0 = 0.03$ cm), we change the p_{CO_2} -value at the constant head input in the upper valley from 0.05 atm to 0.01 atm. Everything else is left unchanged and $c_{in} = 0.9c_{eq}$ for all inputs. The results are shown in Figure 5.26.

At the onset of evolution up to a time of about 2000 y (a, e) the water table exhibits a maximum as discussed already in scenario C. Therefore, only water from recharge flows through the aquifer and MC cannot be active (b, f). When the water table drops further (8 ky) flow enters from the upper river and mixes with water from recharge as can be seen from the blue color in the left hand side panel (c, g). There is a comparably large mixing zone (see the upper margin with red input from recharge), which enhances dissolution rates. The right hand side exhibits a region of dissolution rates very similar to that in Figure 5.13. Shortly after this time breakthrough occurs and due to the large amount of water from the valley mixing corrosion is switched off. The aquifers of Figure 5.11 and Figure 5.26 have developed very similar, because mixing corrosion was active for only a very short time. Breakthrough happens when the permeability at the water table has increased sufficiently. This is caused by the water from meteoric recharge.

If one further assumes that the recharge water enters fully saturated to the water table the aquifer will stay completely unaffected and no karstification will result at all. At the onset of water input all water flowing through the aquifer comes from meteoric recharge and prevents any flow of water from the upper river. If the recharge water is saturated no dissolutional widening is active and the water table stays where it is for all times.

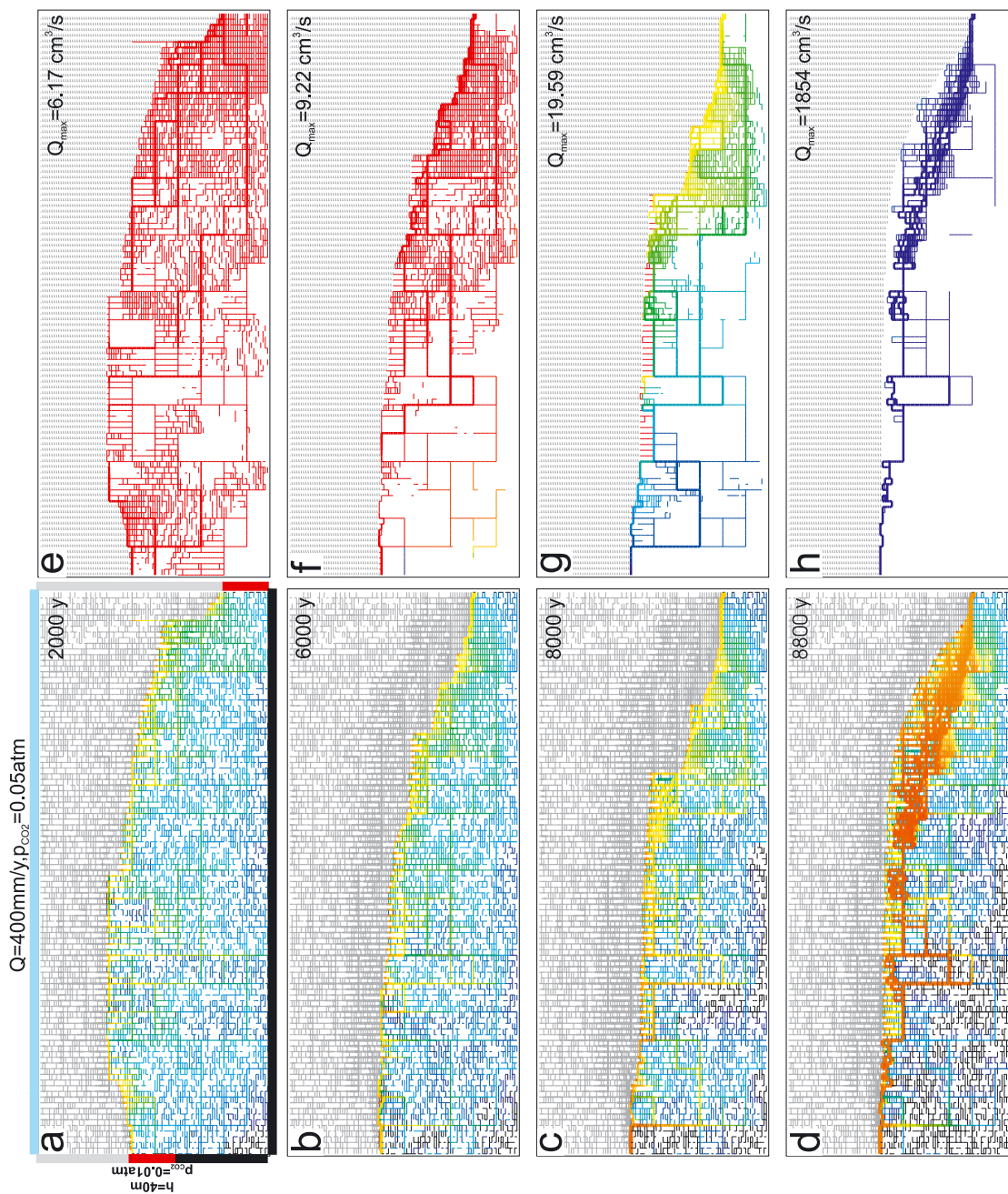


Figure 5.26: Evolution of scenario C (dual-fracture aquifer, Figure 5.13): Mixing corrosion. $\bar{a}_0 = 0.009$ cm, $A_0 = 0.04$ cm. Now the inflowing solution from the upper river (left hand side) has $p_{CO_2} = 0.01$ atm instead of 0.05 atm in Figure 5.13. Other parameters and boundary conditions as in Figure 5.13. $c_{in} = 0.9c_{eq}$. Left hand column: aperture widths and dissolution rates. Right hand column: equilibrium concentrations of mixed solutions.



5.6 EVOLUTION OF UNCONFINED AQUIFERS UNDER UNEVENLY DISTRIBUTED RECHARGE

So far we have dealt exclusively with scenarios, in which recharge is distributed evenly to the water table such that each input point receives the same amount of flow. This is a highly idealistic simplification, but it turned out to be useful to understand the basic patterns of the evolution.

If the karst plateau consists of regions with cap rocks of varying permeability and also of bare limestone surfaces, it may well happen that recharge is focused to some regions of high permeability, whereas in other regions recharge is inhibited by impermeable cap rock. Also small depressions and valleys can focus recharge to preferred regions.

Figure 5.27 shows the evolution of the aquifer of scenario A, with statistical net only, when all recharge is focused to the central part of the aquifer. Otherwise everything is equal to the scenario shown in Figure 5.4, which can be referred to for comparison. Note that the total recharge offered to both aquifers is identical; only the local distributions are different.

Because recharge is now restricted to the central region of the plateau the water table reaches up to the surface at the onset of karstification. There is some flow to the left (yellow in the right hand side column) toward the impervious border, which then turns down (green) and flows on to the right. Dissolution rates are high in the central recharge region (a, e). After 10 ky the water table has dropped due to the high permeability created below this region of the plateau. There is no more flow to the left and therefore the further evolution of the aquifer proceeds only in the region of recharge and in its right hand side (b, f). After 15 ky (c, g) the water table has dropped almost to base level. Dissolution rates remain high below the recharge area and some looping conduits evolve. When the water flows out from that conduit it is diffused into the many fractures, which have widened sufficiently to carry this flow. They exhibit dissolution rates lower by about one order of magnitude. After 25 ky flow is through a single conduit, which is connected to the output by many narrow conduits (d, h).

Most probably recharge will not be restricted to one single zone on the plateau, but will be distributed over several regions. Therefore, we assume that the total precipitation on the plateau is distributed to two separate regions as shown in Figure 5.28. Everything else remains as shown in Figure 5.4 and Figure 5.27.

At the onset the water table reaches the surface of the plateau and some of the flow circulates to the left and then downwards and out of the aquifer. After 7 ky the water table has dropped. The dissolution rates are comparatively high along the water table below the recharge areas but low in the regions where recharge is absent.

In comparison to the case of evenly distributed recharge (Figure 5.4) widening in this region is low and due to its high resistance to flow the water table on the left hand side remains high and almost horizontal (c, g). Finally after 20 ky a water table cave with some loops on its left hand side reaches the exit. In comparison to evenly distributed recharge, its time of evolution is longer by about 10 ky, owing to the before mentioned



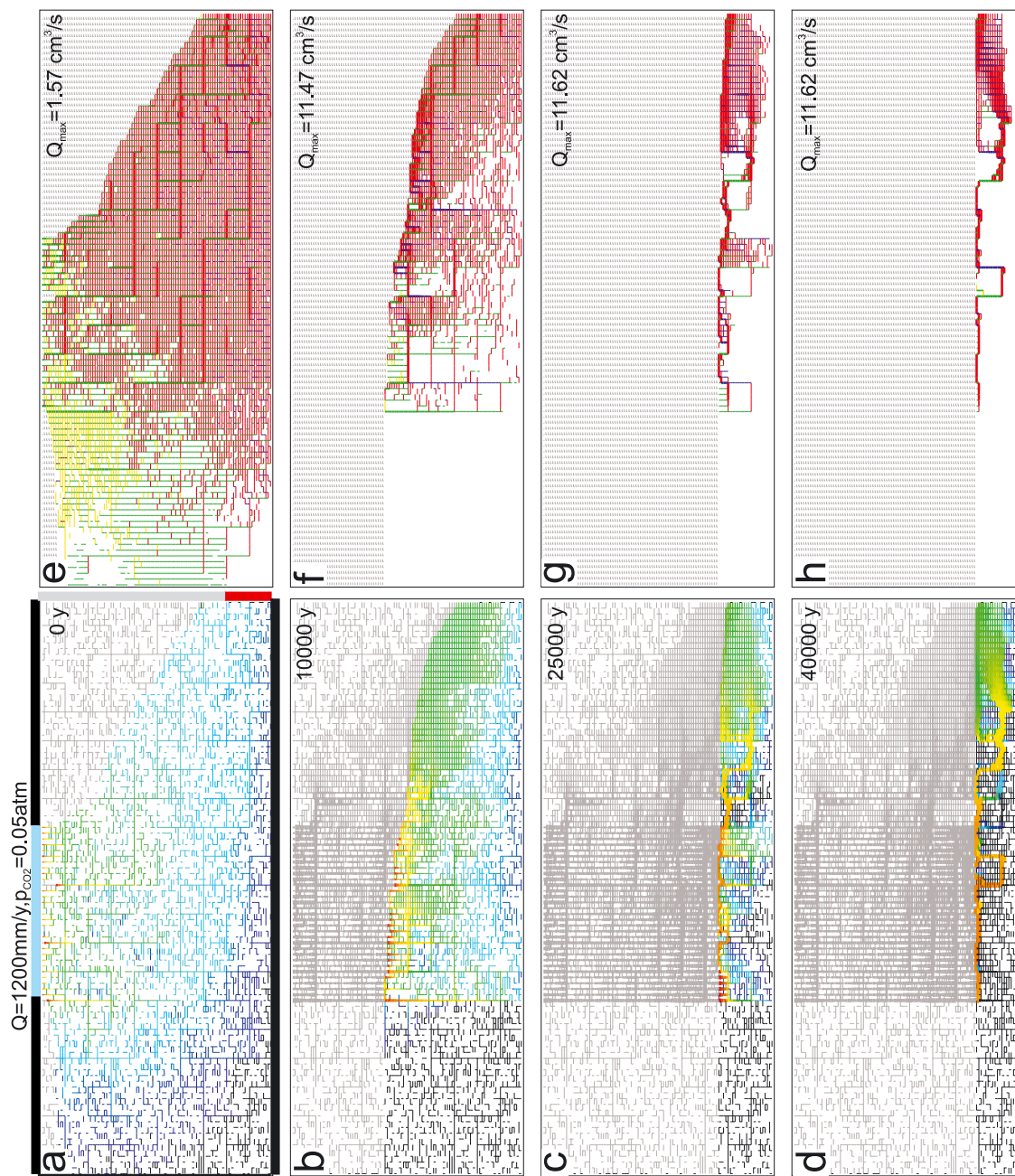


Figure 5.27: Evolution of Scenario A (dual-fracture aquifer, Figure 5.4): Recharge unevenly distributed. Now all recharge to the plateau is limited to the middle region covering one third of the plateau. Impervious rocks cover the remaining regions. Other parameters and boundary conditions as in Figure 5.4.

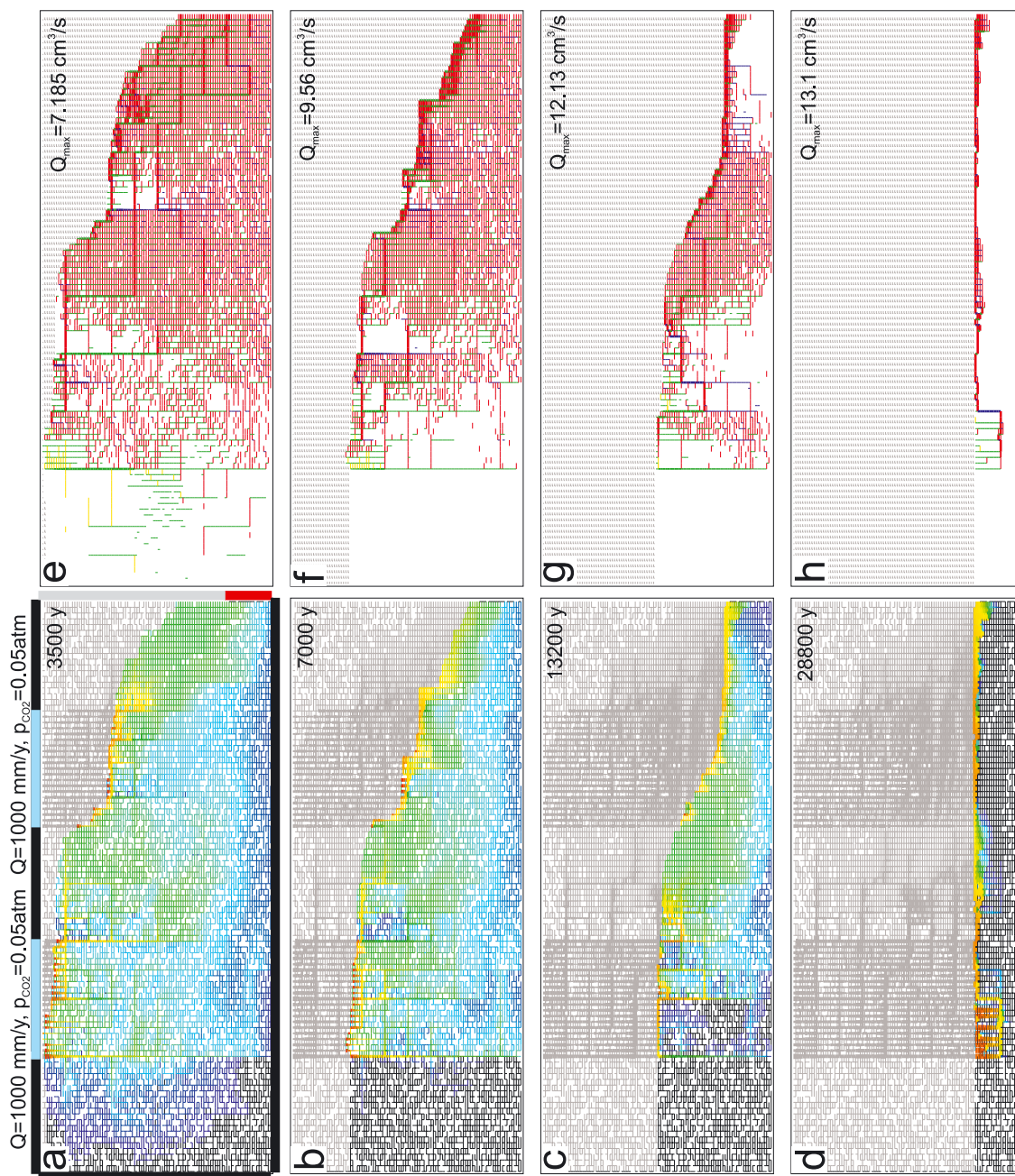


Figure 5.28: Evolution of Scenario A (dual-fracture aquifer, Figure 5.4): Recharge unevenly distributed. Now all recharge to the plateau is distributed to two regions on top of the plateau, which cover 40 % of the plateau. Other parameters and boundary conditions as in previous Figure 5.27

region of lower dissolution rates. One could furthermore take account of the action of mixing corrosion by assigning different p_{CO_2} to different recharge zones. This way a huge selection of new scenarios could be designed.

5.7 UNCONFINED AQUIFERS UNDER MISCELLANEOUS BOUNDARY CONDITIONS

So far in all model runs of Chapter 5 several parameters or conditions remained unchanged. In all cases we used the same realization of the dual-fracture aquifer. The question could be asked, how an aquifer will evolve, if additional prominent fractures are added, such as deep reaching master joints or a fault. Furthermore, we have assumed that only in a short distance below base level the limestone is underlain by impervious rock. What would happen if the aquifer extends deeper in permeable limestone?

Finally, the calcium concentration of the input solutions at the water table is an important parameter. Intuitively it is clear that with increasing c_{in} the evolution will be retarded. Furthermore, the input concentrations at the water table can depend on the hydraulic properties of the vadose zone and could be unevenly distributed. This section will present some keyhole views on such problems by selecting some examples.

5.7.1 The influence of input concentrations on the simple scenario A

We have performed several runs with the domain of Figure 5.3, using different input concentrations $c_{in} = 0.98c_{eq}$, $0.96c_{eq}$, $0.94c_{eq}$, $0.93c_{eq}$, and $0.9c_{eq}$ respectively. The aim of these calculations was to compare the evolution times until a defined state of evolution was reached. This state was defined, when the node located 100 m from the left hand side boundary and 1 m above base level falls dry. In all cases the evolution of the aquifer was similar to that shown in Figure 5.3. But with increasing c_{in} the dissolution rates become lower and as we have discussed in Chapter 4 their spatial variation becomes less pronounced. As a consequence the heterogeneity left behind in the vadose zone smoothes out with increasing c_{in} .

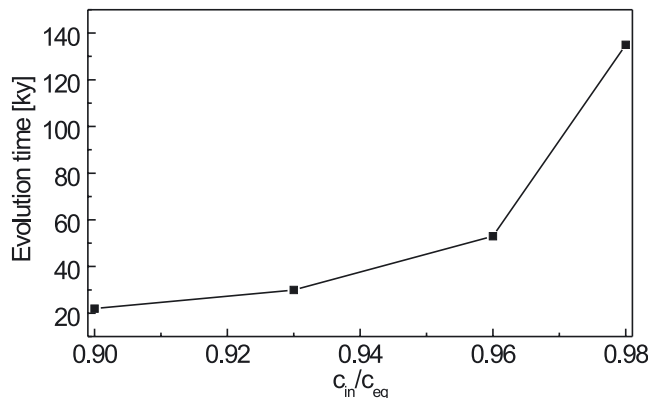


Figure 5.29: Evolution times of scenario A (simple statistical net, see Figure 5.3) for various values of c_{in}/c_{eq} . The evolution time is defined as the time, when the node located 100 m from the left hand side boundary and 1 m above base level falls dry.



Figure 5.29 depicts the evolution times defined above as a function of c_{in} . This time of evolution increases steeply by about one order of magnitude, if the concentration rises from $0.9c_{eq}$ to $0.98c_{eq}$. However, this does not mean that the fracture widths in the aquifer are comparable. Due to the nonlinear fourth order rate law the dissolution rates decrease by three orders of magnitude. Therefore, effective times of karstification depend severely on c_{in} . Nevertheless we have used $c_{in} = 0.9c_{eq}$ throughout this chapter to save computational time, because the processes which have been unraveled are not basically affected.

5.7.2 Influence of the depth of the limestone aquifer

In Figure 5.4 we have illustrated the evolution of scenario A (dual-fracture aquifer) under constant recharge. The limestone reaches down from base level at 0 to -20 m. The rock beneath is assumed impervious. We now extend the domain 50 m deeper, thus allowing limestone to reach down to 70 m below base level. Below the river at base level a watershed renders the right hand side margin to no flow boundary conditions. Everything else is unchanged. The evolution of the aquifer, shown in Figure 5.30 is very similar to that of Figure 5.4. Flow and dissolution rates are mainly close to the water table. Due to the deeper aquifer its transmissivity is higher, and consequently it is drained more rapidly. Therefore the initial height of the water table is lower and it drops more quickly to base level. After only 10 ky the entire flow and dissolution is restricted to the water table at base level.

We now turn to scenario B, in which a region of fixed head input is added to the plateau. We compare all results to Figure 5.5, but now the domain is changed by increasing the vertical length of the grids in the net of fine fractures and also in the net of prominent fractures by a factor of five. In other words the domain is stretched in the vertical direction by a scaling factor of five, but is not changed in the horizontal direction. It now reaches down 500 m from the top and 350 m below base level. Everything else is unchanged.

The evolution can be visualized from Figure 5.31. In the initial state flow reaches down deep into the aquifer. But dissolution rates due to the large distance from the input points are low (green, blue). High dissolutional widening (yellow) occurs only at a fringe close to the water table similar to the situation in Figure 5.5 (a, e). After 1200 y dissolutional widening in the constant head region allows more flow along prominent fractures (b, f). A long prominent horizontal fracture located close to the water table finally attracts most of the flow and dissolutional widening is high (red) (c, g). Break-through occurs along this fracture and then along the water table (d, h). Again as in scenario B the evolution exploits prominent fractures close to the constant head region, but then proceeds close to the water table through many fine fractures. The aquifer is more similar to that of Figure 5.7 with $a_0 = 0.009$ cm. The basic patterns, however, are not much dependent on the depth of the aquifer.



5. UNCONFINED AQUIFERS UNDER VARIOUS BOUNDARY CONDITIONS

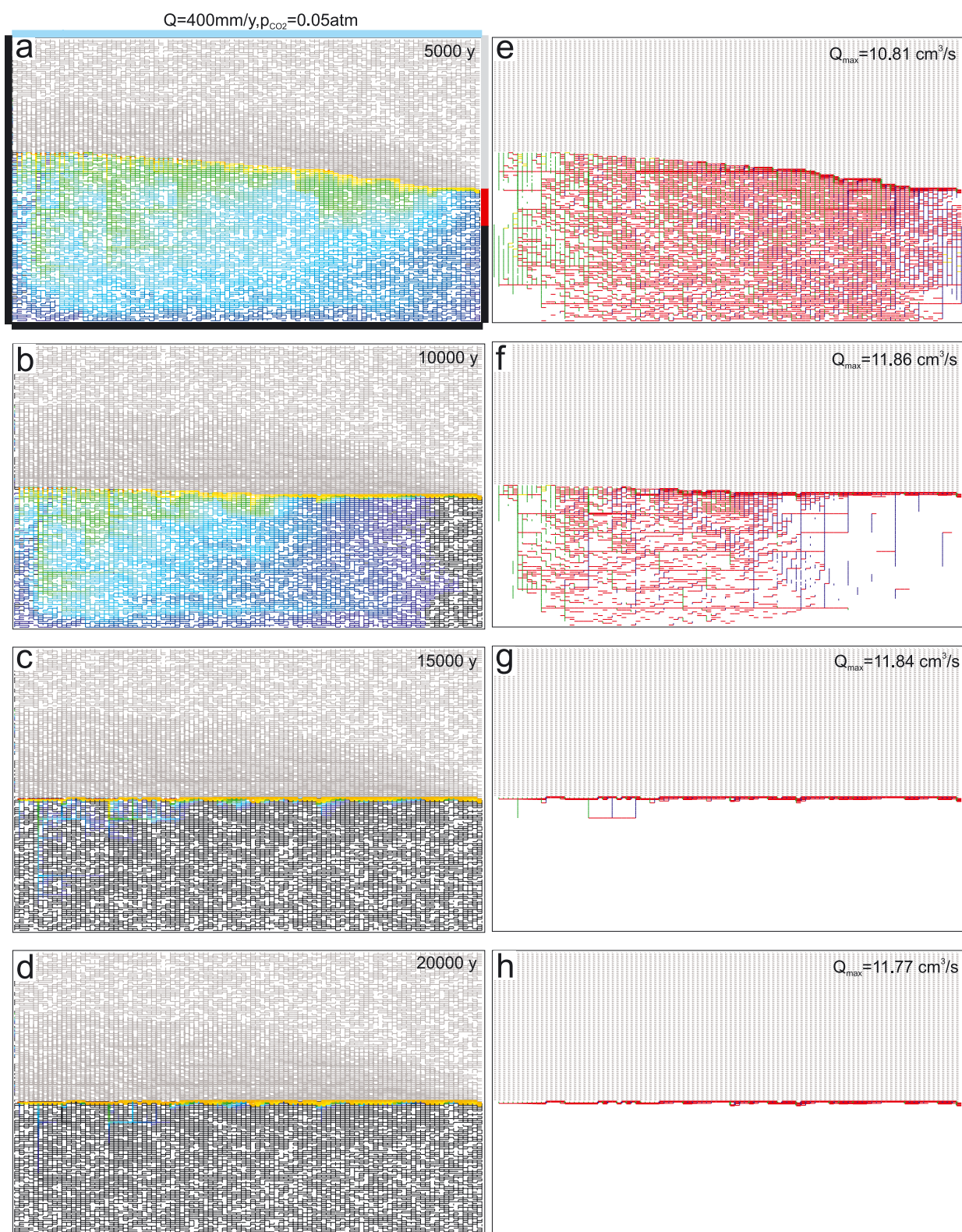


Figure 5.30: Evolution of Scenario A (dual-fracture aquifer, Figure 5.4) with limestone layers extending deep below base level. $\bar{a}_0 = 0.009$, $A_0 = 0.03\text{ cm}$, $c_{in} = 0.9c_{eq}$. Compare with Figure 5.4.

5. UNCONFINED AQUIFERS UNDER VARIOUS BOUNDARY CONDITIONS

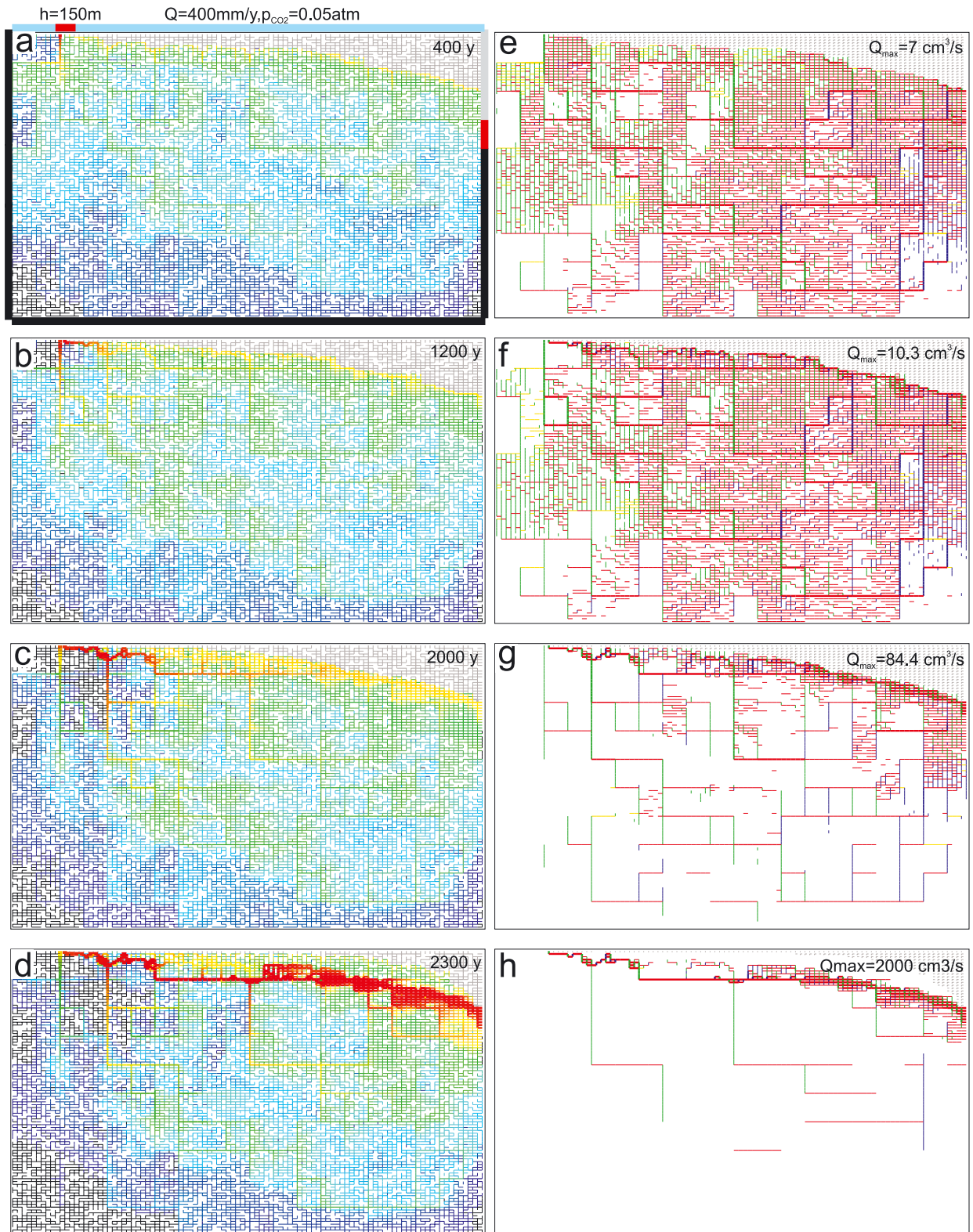


Figure 5.31: Evolution of Scenario B (dual-fracture aquifer, Figure 5.5) with limestone extending deep below base level. $\bar{a}_0 = 0.005 \text{ cm}$, $A_0 = 0.04 \text{ cm}$, $c_{in} = 0.9c_{eq}$. Compare with Figure 5.5.



5.7.3 Adding master joints and bedding planes

The network of prominent fractures in Figure 5.32 possesses a long continuous pathway of prominent fractures, which begins close to the constant head region and ends close to the impermeable right hand side at a depth between 300 to 200 m below base level. This can be seen particularly well in the upper right hand side panel of Figure 5.32 which depicts the initial flow rates. If one connects the dead end of this pathway by a long vertical fracture (depicted by arrows in Figure 5.32a) directly to base level, a new highly competitive percolating pathway has been created and the evolution could be forced into a breakthrough mode along this new pathway of prominent fractures. Arrows show the new vertical fracture in the upper panel for flow rates and flow directions of Figure 5.32. Everything else is equal to the scenario shown in Figure 5.31. The new percolating pathway carries a high amount of flow to the output. After 800 y the flow rate is $10.5 \text{ cm}^3\text{s}^{-1}$, large compared to the amount that is carried by the other fractures fed by the total recharge of $12.7 \text{ cm}^3\text{s}^{-1}$ to the catchment's area. In comparison maximal flow Q_{max} is below $10 \text{ cm}^3\text{s}^{-1}$ in Figure 5.31.

The connection from the constant head zone to the exit fixes the water table at a high level. There are no prominent fractures along the water table and the competing new pathway therefore wins. Breakthrough occurs after 3300 y. This is longer than in the scenario depicted in Figure 5.31, although the new pathway has been added. The reason is the hydraulic coupling of the head distribution in this pathway to the position of the water table. In Figure 5.31 the water table is lower and its fringe contains a long horizontal prominent fracture. This is employed and this pathway along the water table is more competitive than that along the raised water table in Figure 5.32 where prominent fractures are absent.

If one adds a prominent horizontal fracture (e.g. a bedding plane) which cuts through the entire aquifer and is connected to the former percolating pathway one would expect an amplification of the above described behavior. This is illustrated in Figure 5.33. A horizontal fracture located at a depth of 175 m below the top of the domain is connected to the constant head output 25 m below base level. It is shown by black arrows in the up-most left picture. After 800 y the fracture carries a flow of $21.8 \text{ cm}^3\text{s}^{-1}$, larger than Q_{max} in Figure 5.31. This pushes the water table further up to the surface of the plateau. The shorter pathway connecting the constant head reaching via the bedding plane to base level achieves breakthrough after 1600 y.

Again these examples show that the structure of prominent fractures determines the pattern of karst evolution and the structure of the resulting cave system. However, the processes acting remain unaffected.



5. UNCONFINED AQUIFERS UNDER VARIOUS BOUNDARY CONDITIONS

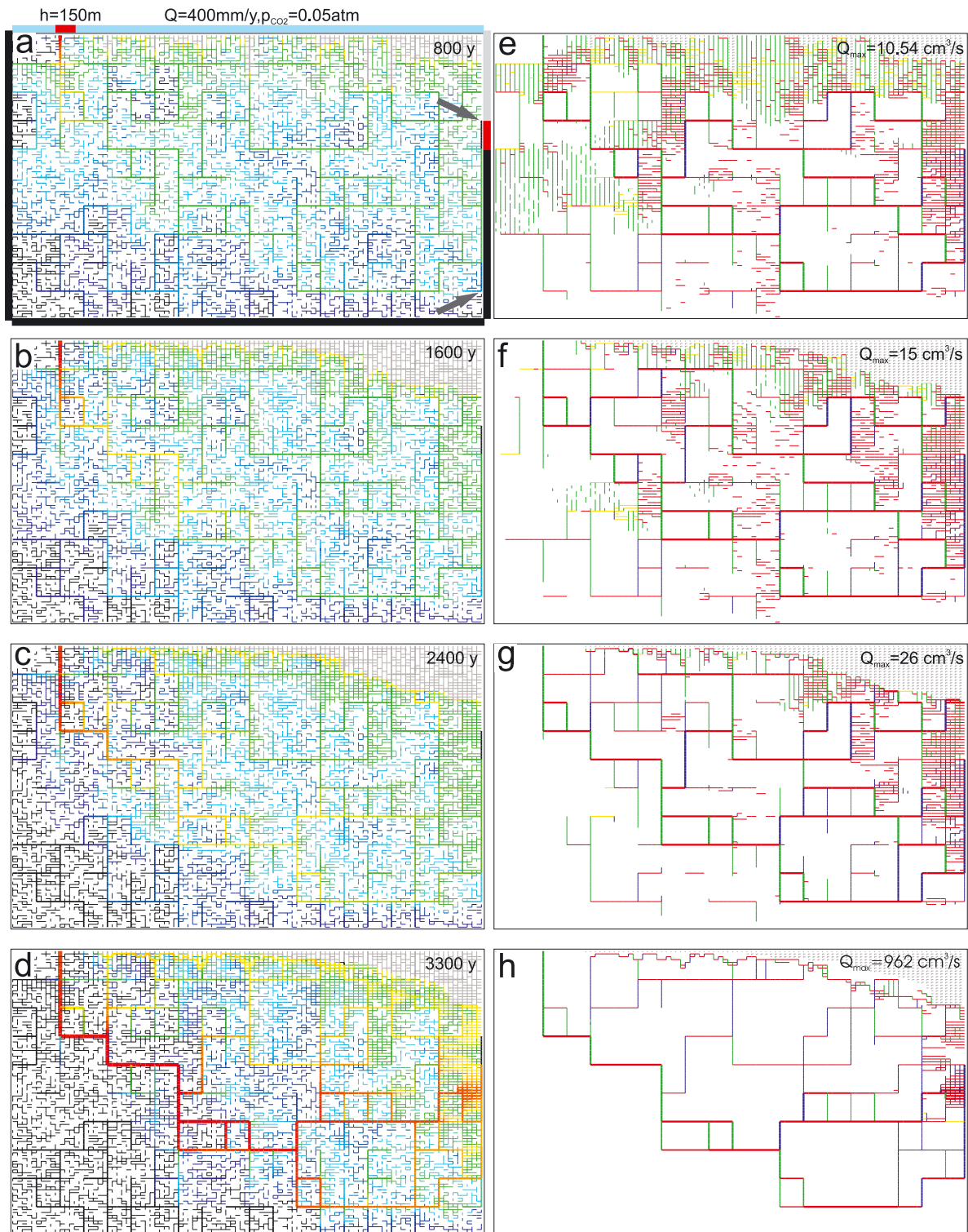


Figure 5.32: Evolution of Scenario B (dual-fracture aquifer, Figure 5.5): Other parameters and boundary conditions as in previous figure (5.31), but one vertical prominent fracture is added at the right hand margin, reaching from -80 m up to -20 m. It connects the constant head input by a pathway to the output. Arrows mark the two end points of the fracture.

5. UNCONFINED AQUIFERS UNDER VARIOUS BOUNDARY CONDITIONS

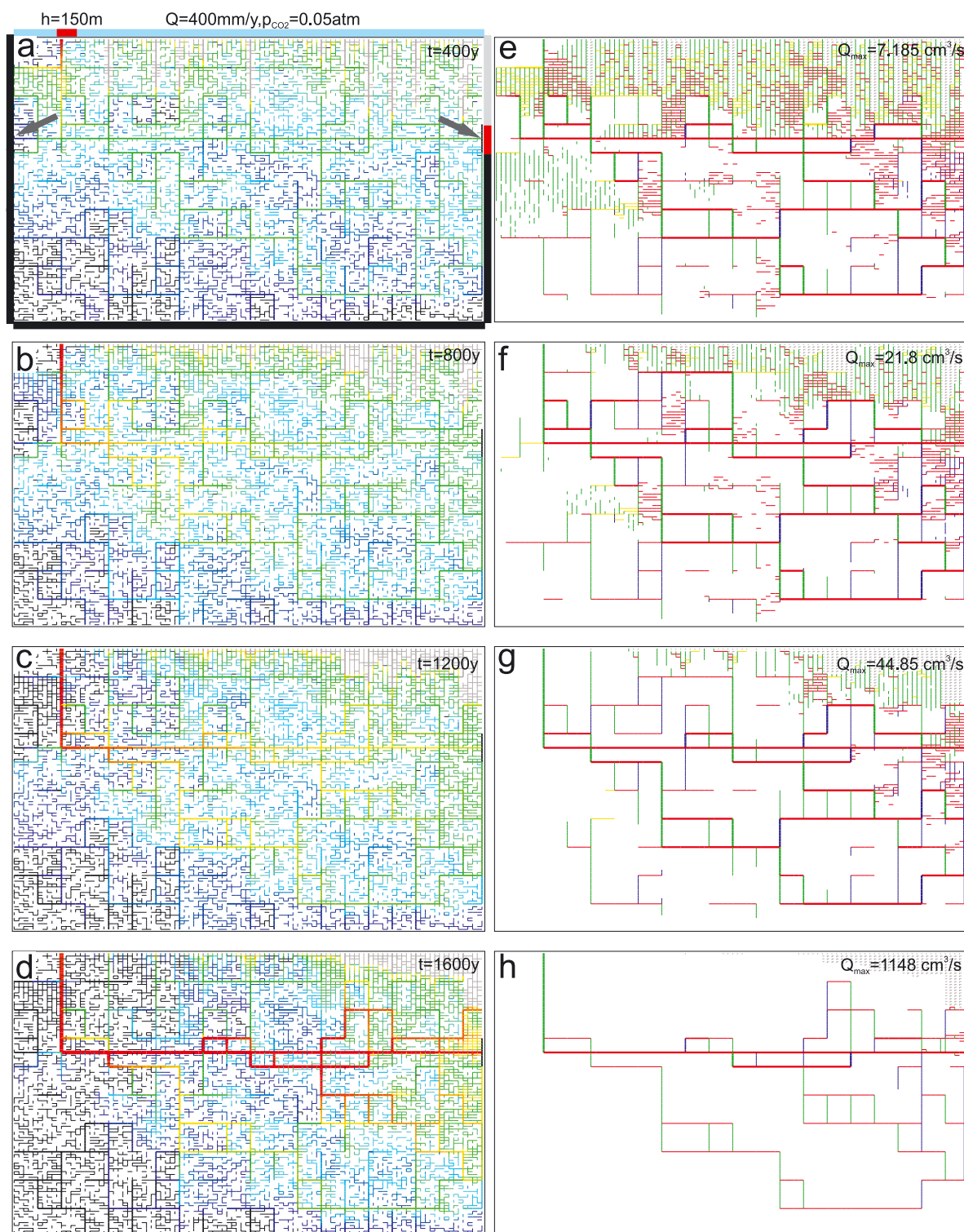


Figure 5.33: Evolution of Scenario B (dual-fracture aquifer, Figure 5.5). Other parameters and boundary conditions as in Figure 5.32. But one additional bedding plane located at 10 m penetrates through the entire aquifer and short cuts other percolating pathways of prominent fractures. The bedding plane is marked by arrows.

5.7.4 Down-cutting and up-filling of a valley

In all considerations in this chapter the boundary conditions have been treated as being independent of time. This was necessary to understand the processes governing the evolution. Of course climate exerts a strong influence on the boundary conditions, such as annual recharge to the aquifer or the p_{CO_2} -pressures of input waters, which are determined by vegetation. An incredible amount of new scenarios could be designed. However, this, would not give more insight into the governing processes, as has already been achieved. And from what we have found so far, it may be possible to infer what would happen in simple scenarios.

Another change of boundary conditions is caused by geological events, which change the location of base level. One example shall be given here. As we have seen in Figure 5.4 for Scenario A (double fracture aquifer) it takes about 10 ky until a water table cave has developed along base level. Now we consider the following case. Due to some uplift there is down cutting of the valley. Initially the base level and correspondingly the constant head output is 20 m below ground. During the time from 10 ky to 20 ky down cutting is linear in time with 0.5 m in 100 y. Therefore, after 20 ky base level is located at 80 m below ground. The next 10 ky it stays stable until 30 ky. From then on up filling of the valley rises the base level by 0.5 m per 100 y until after 40 ky it has reached its initial position, where it stays stable for the next 10 ky. Figure 5.34 shows the depth of base level as a function of time.

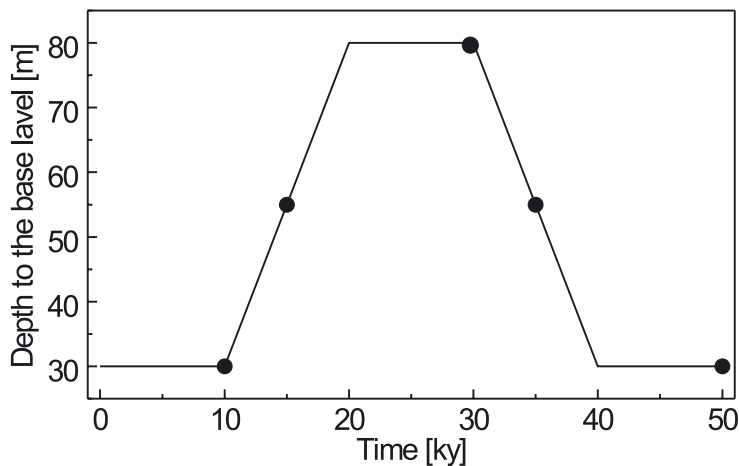


Figure 5.34: Down-cutting and up-filling of a valley: Location of base level below the top of the plateau. The dots mark the times of the evolution of the aquifer shown in Figure 5.35

The evolution of the aquifer depicted in Figure 5.4 for this type of time dependent boundary conditions is shown in Figure 5.35. Note that all other parameters are as in Figure 5.4. The only change is that of boundary conditions as depicted in Figure 5.34. After 10 ky a water table cave is established (a, f). During down cutting (15 ky) of the valley the water table drops and flow penetrates deep into the aquifer below it. Dissolution rates are high at its top and the prominent fracture close to it (b, g). After 30 ky sufficient time has passed to establish a water table cave at the lower base level. (c, h).

5. UNCONFINED AQUIFERS UNDER VARIOUS BOUNDARY CONDITIONS

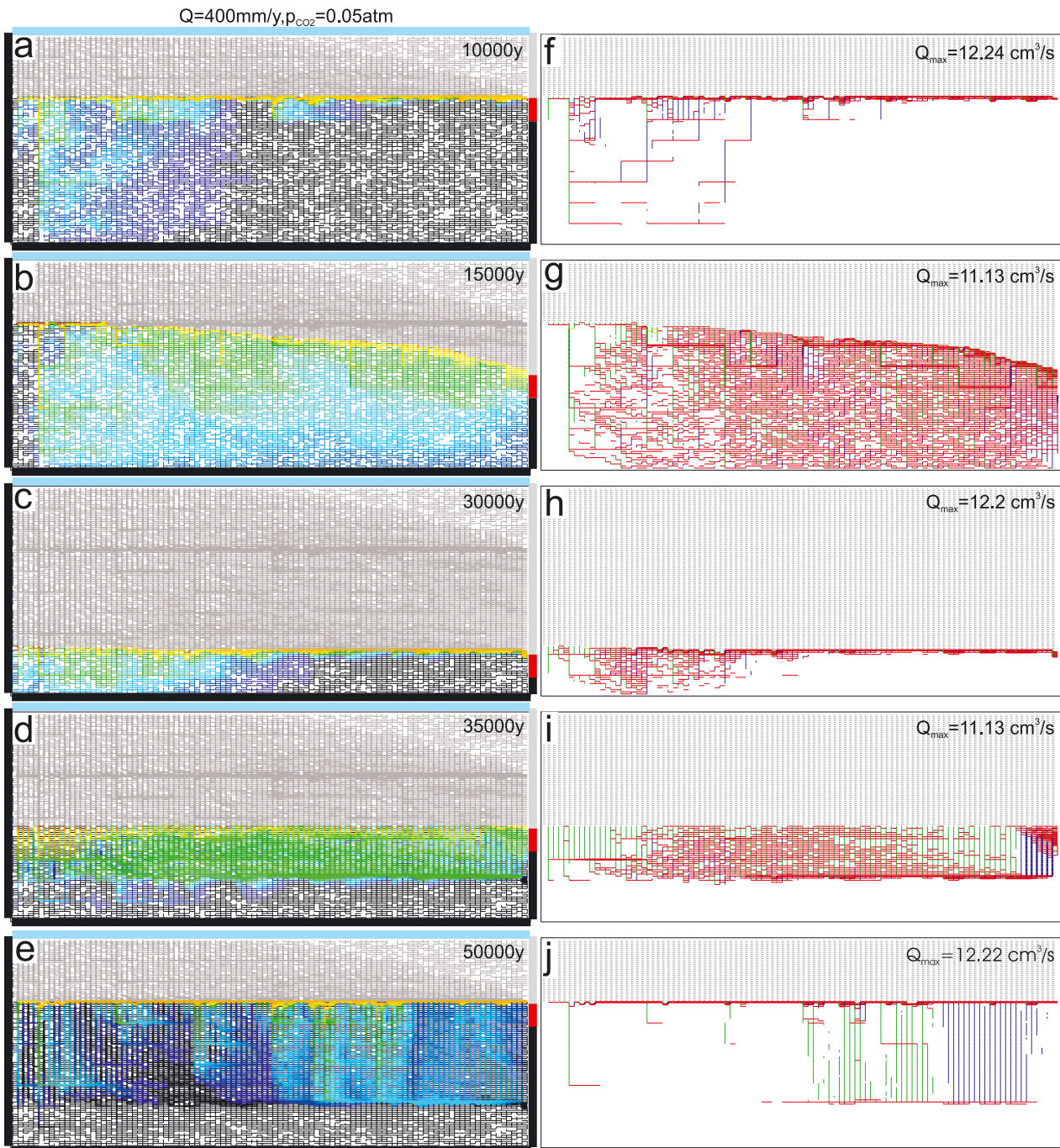


Figure 5.35: Evolution of the aquifer in Figure 5.4 (dual-fracture aquifer) with down-cutting and up-filling of the valley: (a, f) initial water table cave, (b, g) aquifer during down-cutting, (c, h) water table cave on lower level after 10 ky of stable base level, (d, i) aquifer during up-filling of valley, and (e, j) water table cave after 10 ky of stable base level at the initial position.

The permeability of the aquifer above this level has increased significantly. Therefore the water table stays horizontal at actual base level during the entire phase of up filling (d, j) until 40 ky. Between 40 ky and 50 ky the initial water table cave coincides with the water table and evolves further. Below it in contrast to its first phase of evolution after 10 ky a deep zone of high permeability has been created (e, j).

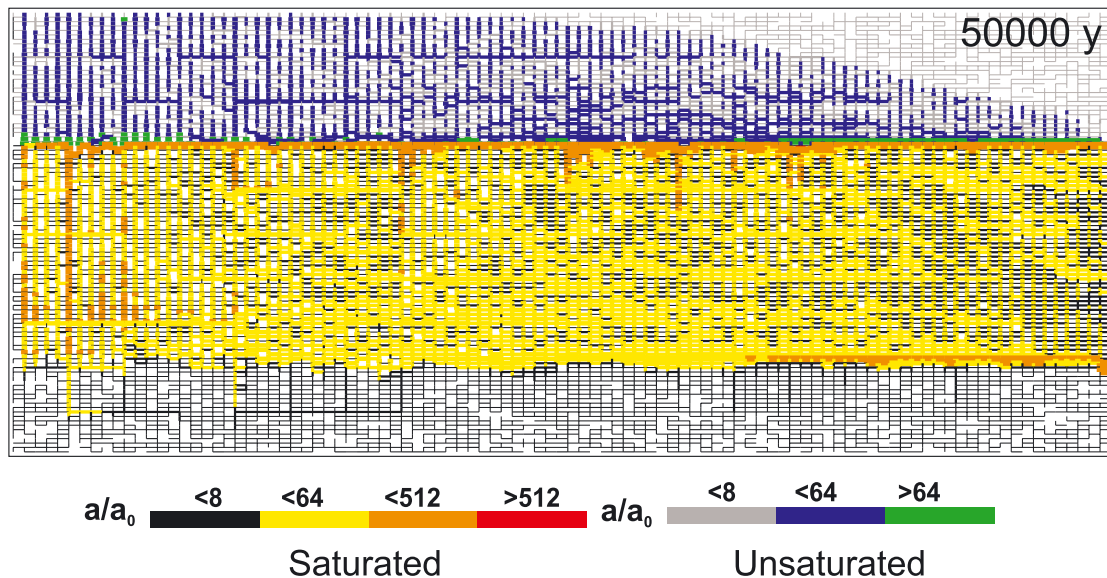


Figure 5.36: Distribution of fracture aperture widths after 50 ky in the aquifer in the previous Figure 5.35 (e, j).

To illustrate fracture aperture widths in this region Figure 5.36 depicts these by the color code already used in Figure 5.15. Yellow depicts fracture aperture widths between 0.072 cm up to 0.58 cm, and orange gives widths between 0.58 cm up to 4.6 cm. Note that also in the vadose zone aperture widths are present up to 0.5 cm as depicted by blue and green.

5.7.5 Subterranean sources of CO₂ in Scenario A

In Section 4.8 we have discussed the influence of subterranean CO₂-inputs under constant head conditions. We now assume that in scenario A (dual-fracture aquifer, Figure 5.4) a region of CO₂-input is added shown by the gray shaded area in Figure 5.38a. p_{CO_2} is 0.1 atm in that region. Water flowing into this region attains equilibrium with respect to $p_{CO_2} = 0.1$ atm under open system conditions. When it leaves its chemical pathway proceeds under closed system conditions and the solution approaches some value of c_{eq} between c_{eq}^{\min} and c_{eq}^{\max} .

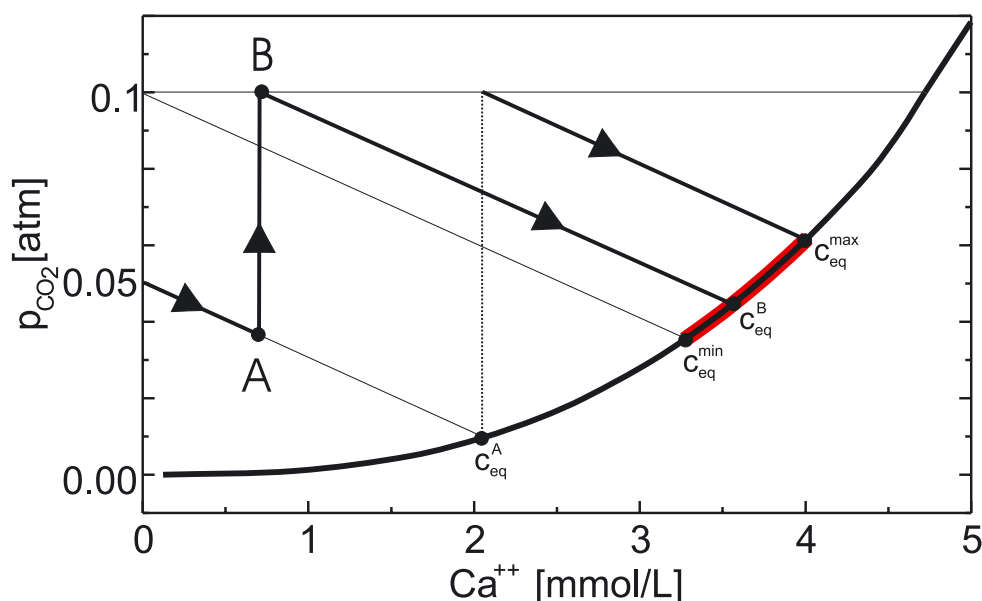


Figure 5.37: Chemical evolution of water entering into a region of elevated subterranean CO_2 . The solution seeps through the aquifer under closed system conditions. When it enters into the region of elevated CO_2 (A) it absorbs CO_2 (B). Then its further evolution proceeds in closed system conditions until equilibrium c_{eq}^B is attained.

This is illustrated by Figure 5.37, which depicts the chemical pathways of the solutions. When the solution from recharge flows into the p_{CO_2} -input region with chemical composition A it boosts up its CO_2 -concentration to composition B in equilibrium with the p_{CO_2} of the input region. Then it leaves this region under closed system conditions and approaches c_{eq}^B . The red part on the equilibrium curve depicts the possible range of values of c_{eq}^B . If these waters are mixed with water from the surface of the plateau mixing corrosion will become active, too.

Figure 5.38 illustrates the evolution of the aquifer. The left hand side column shows fracture aperture widths and dissolution rates. The right hand side column gives flow rates and c_{eq} . The position of the water table after 400 y is shown in (a). Water flowing down into the aquifer (blue) is close to saturation when it enters the p_{CO_2} -input region (e). There it is channeled into a horizontal prominent fracture located there and then flows downstream. Because the entering solution is almost saturated after CO_2 uptake it reaches c_{eq}^{max} (red region). Downstream this solution mixes with water from recharge and lower values of $c_{eq} < c_{eq}^{max}$ are obtained. Therefore a region of renewed dissolution originates below the water table (a, b). After 2 ky the water table has dropped to base level and all water flowing from the left hand side of the CO_2 -region must pass through it (c, g). Mixing corrosion is active along the pathway on its right hand side. Dissolution is active at the water table by recharge from the plateau, but also by mixing corrosion. The channel, which carries most of the flow, drops below base level. It drains water from the water table and small vertical conduits evolve (d, h).

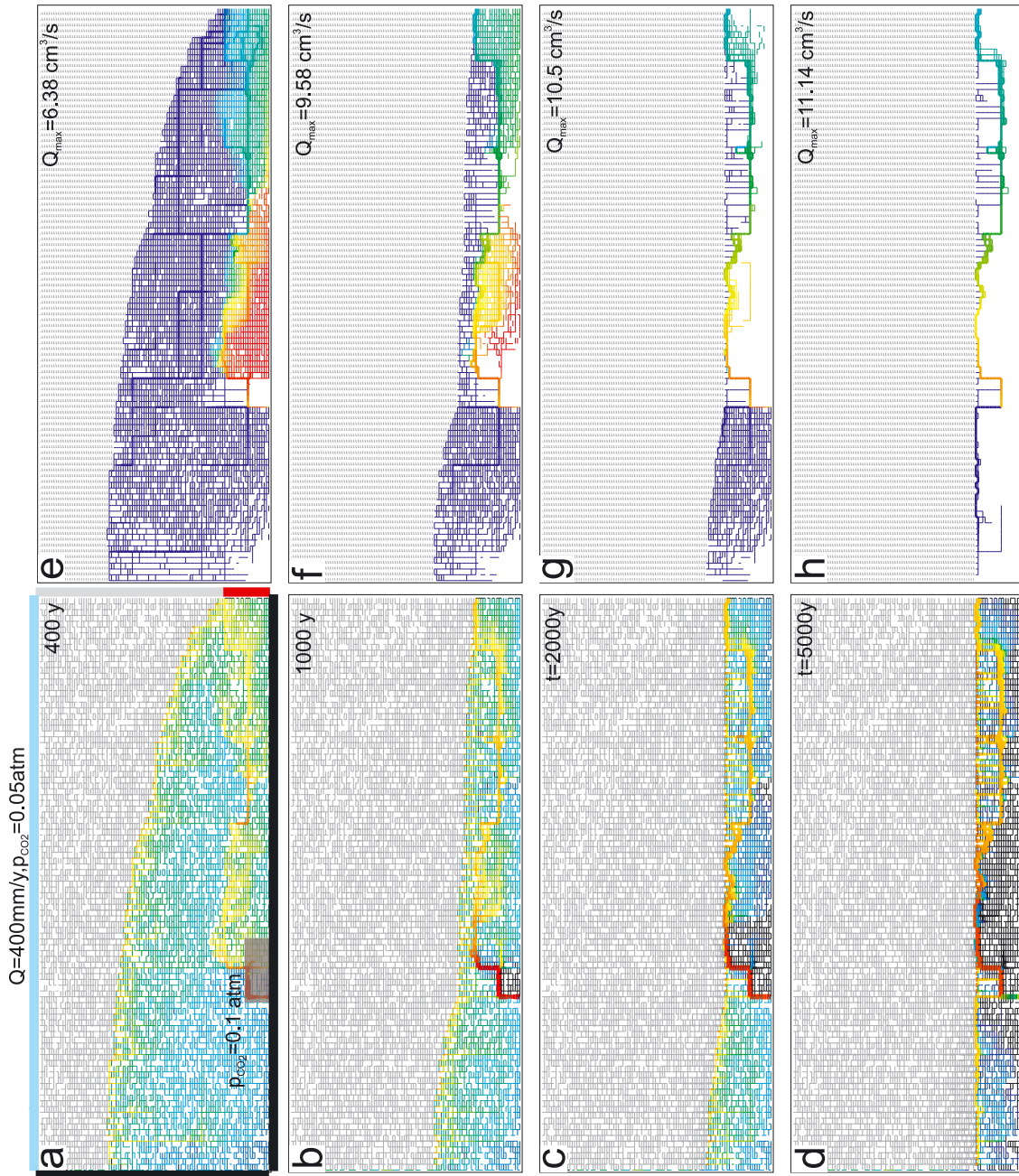


Figure 5.38: Evolution of scenario A (dual-fracture aquifer, Figure 5.4) with a region of elevated CO_2 input (0.1 atm) as shown by the shaded area in (a). Other parameters and boundary conditions as in Figure 5.4.



5.7.6 The influence of lithology on the evolution of unconfined karst aquifers

We now assume that the limestone massif is built out of three layers of differing limestone, which also differ with respect to their dissolution kinetics. We assume layers with $n = 4$ and $n = 8$. For $c = 0.9c_{eq}$, the dissolution rates of both kinetics are equal. But the rates with $n = 8$ drop much more rapidly with increasing c than those with $n = 4$ (confer Figure 3.16).

The left hand side column of Figure 5.39 shows the evolution of scenario A (Figure 5.4) in which a layer with $n = 8$ has been inserted and everything else is left unchanged. The right hand side column (e–h) shows the evolution, if the kinetic orders n have been interchanged. The regions of different n are shown in Figure 5.39, a, e.

At $t = 0$ the water tables of both modifications are identical to that of Figure 5.4, because the initial hydraulic properties are identical (a). We first discuss the evolution of the 4–8–4 case shown on the left hand side. In the beginning the water table drops similar to the basic case of scenario A, Figure 5.4. Since water enters into the water table with $c_{in} = 0.9c_{eq}$ the dissolution rates at the water table are high, as shown by the yellow rim along it. Therefore in the beginning the water table drops similarly as in Figure 5.4. At the places where the water table in the region with $n = 4$ is located above the rock with $n = 8$, the dissolution rates drop, when the water enters the rock with higher order kinetics. This is shown by the black and dark blue areas in figures a and e. When passing through the $n = 8$ region the solution remains aggressive with respect to $n = 4$, as shown by the green area on top of $n = 4$ region in figure b. After 10000 y the water table has dropped into the lower region with $n = 4$ and the further evolution to a water table cave proceeds as in scenario A. In contrast to the situation shown in Figure 5.4 porosity in the vadose zone is created mainly in the lower layer with $n = 4$. In the region with $n = 8$, where dissolution rates are inhibited by the 8th order kinetics only a small change of porosity is created.

We now turn to the inverse case shown on the right hand side. After 1000 y the water table cuts through all three layers. In all of them a fringe of dissolutional activity is established. Dissolution rates are low in the bottom layer with $n = 8$, which receives water almost saturated with respect to calcite. Since this lowest part of the aquifer remains hydraulically almost unchanged the water table cannot drop into it. After 20 ky the major part of the water table is located in the rock with $n = 4$. At its right hand side it cuts into the bottom layer with $n = 8$. There dissolutional widening is active along the entire water table because the concentration of the inflowing solution is $0.9c_{eq}$. Therefore it drops closer to base level through the $n = 8$ layer. But this takes a long time from 20 ky to 50 ky (f, g). At 50 ky the water table has reached base level and a water table cave migrates upstream. After 80 ky the water table has dropped to base level everywhere (h).

Figure 5.40 shows the distributions of fracture aperture widths for the vadose (blue, green) and the phreatic zones (orange, yellow) at the end of the runs, when the water table has reached base level everywhere. For the 4–8–4 case (a) most of porosity in



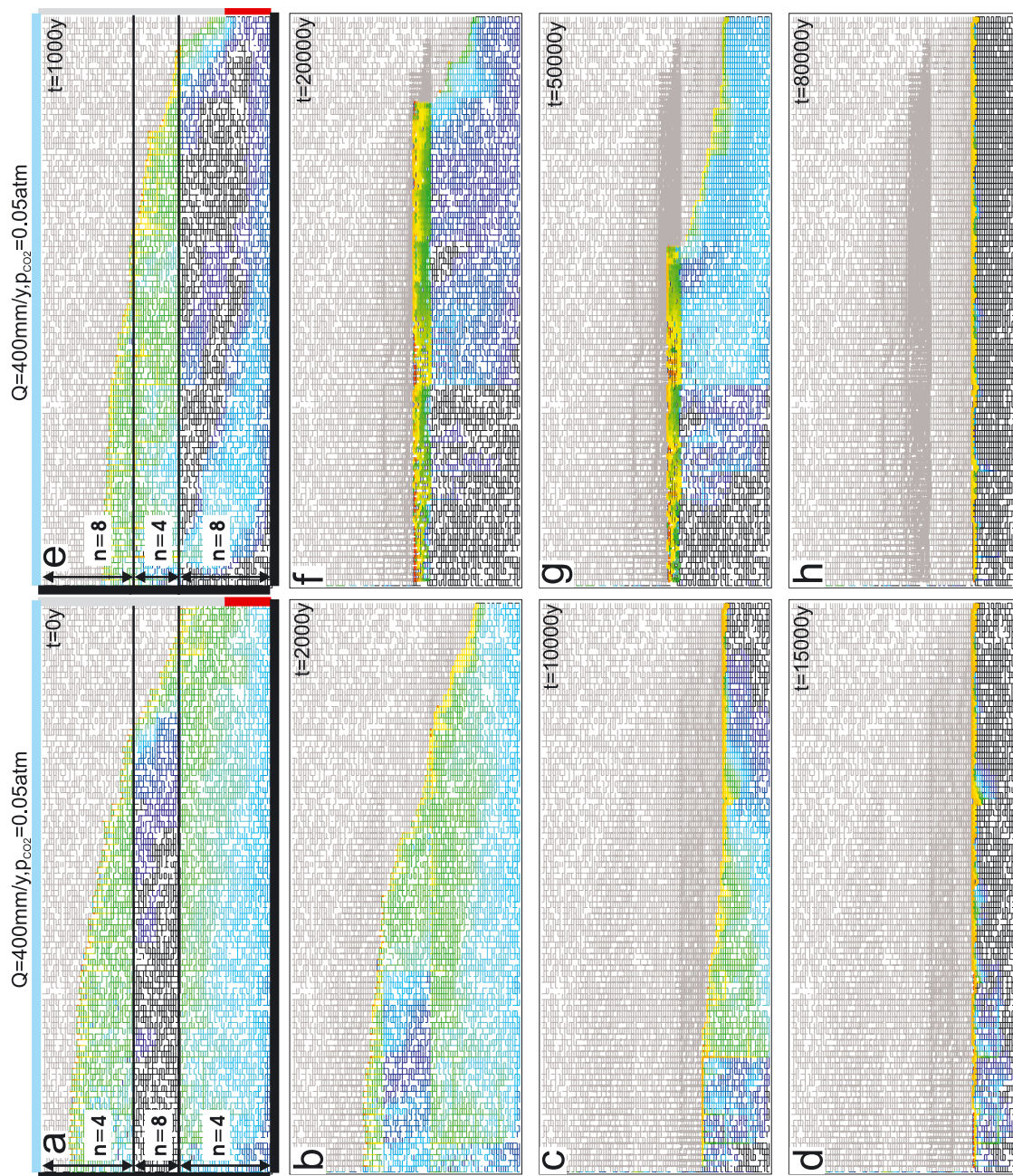


Figure 5.39: Evolution of Scenario A (dual-fracture aquifer, Figure 5.4) with varying lithology. In the center rock with 4th - order kinetics ($n = 4$) is replaced by a layer of rock with 8th-order ($n = 8$). Other parameters and boundary conditions as in Figure 5.4. The right hand side column shows the inverse case, where the regions with $n = 4$ are replaced by $n = 8$ and vice versa.



5. UNCONFINED AQUIFERS UNDER VARIOUS BOUNDARY CONDITIONS

the vadose zone is in the region between the lower 8–4 border and the water table with aperture widths of several millimeters. The inverse case exhibits high fracture widths of several centimeters (green region), which are located at the position, where the water table was held between 20 ky to about 80 ky.

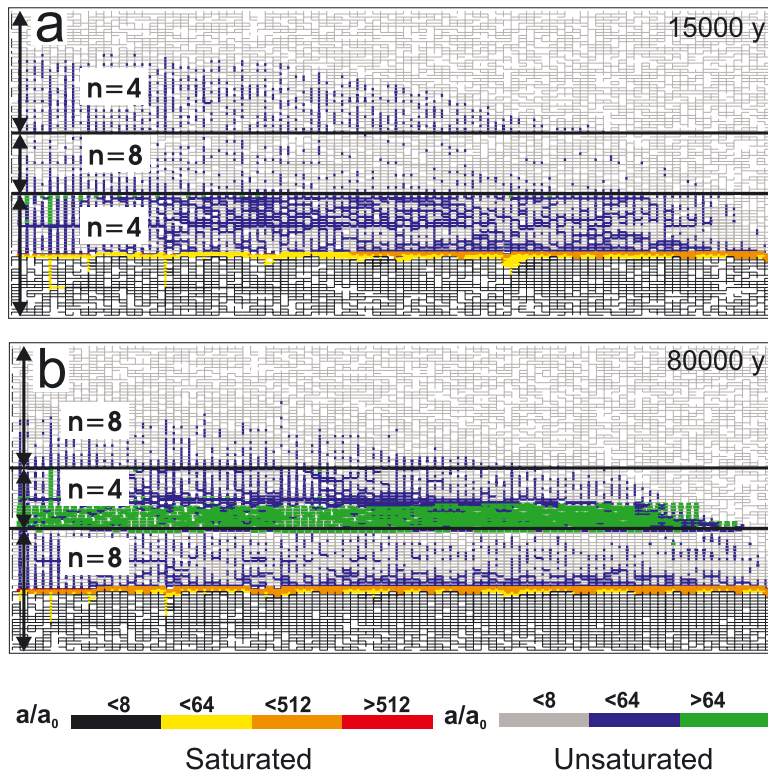


Figure 5.40: Distribution of fracture aperture widths for the previous Figure 5.39 (d, h).

5.7.7 The evolution of karst aquifers at the contact of limestone to insoluble rocks

Where regions of limestone encounter insoluble rock karstification remains limited to the limestone and one expects that dissolutional widening will be focused to the border between the two regions. In the following we will discuss two simple scenarios of aquifer evolution in the case of contact karst.

Figure 5.41 shows the evolution of the aquifer of Figure 5.4, if its right part is replaced by insoluble material, but the structure of all fractures is left unchanged. This is indicated in Figure 5.41a by the gray region. In the beginning the water table has the same shape as in Figure 5.4. But now dissolution is restricted to the region of limestone, whereas the hydraulic resistance of the insoluble part remains unaltered. After 5000 y the water table has dropped. Due to dissolutional widening at the border to the insoluble



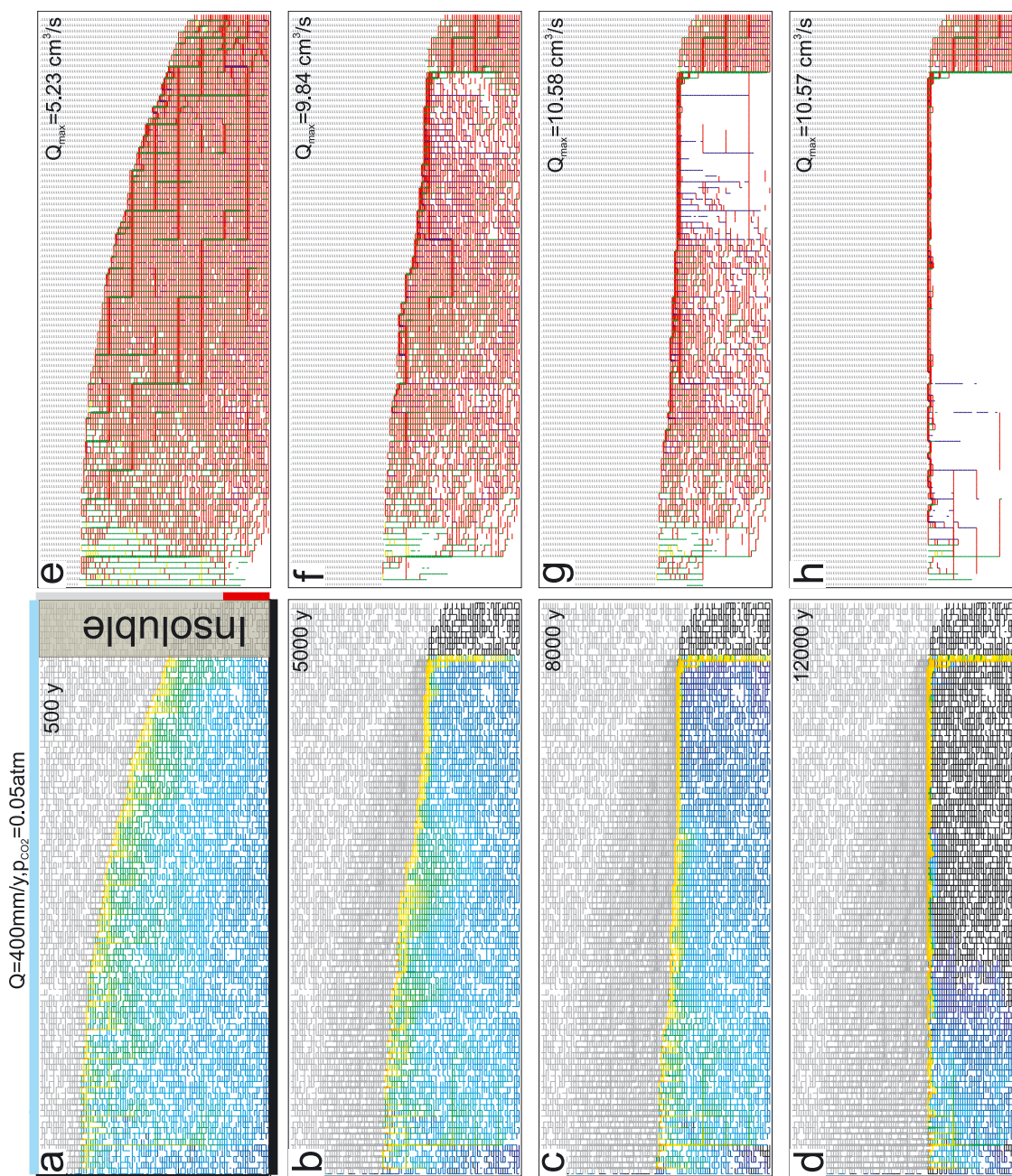


Figure 5.41: Evolution of a contact karst aquifer. Other parameters and boundary conditions as in scenario A (dual-fracture aquifer, Figure 5.4), but the right hand side of the aquifer is replaced by insoluble rock.

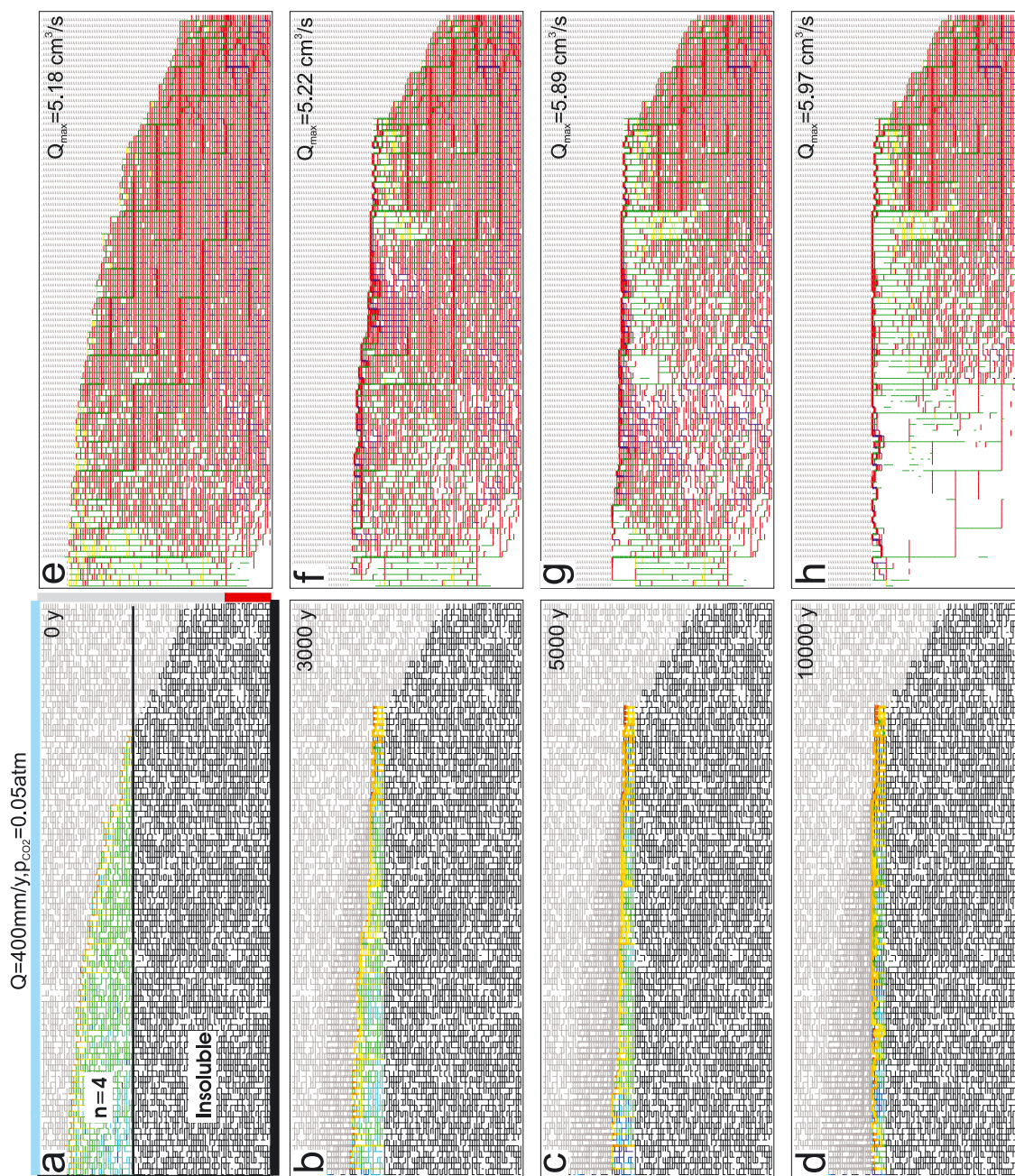


Figure 5.42: Evolution of a contact karst aquifer. Other parameters and boundary conditions as in scenario A (dual-fracture aquifer, Figure 5.4), but now the lower part of the aquifer is replaced by insoluble rock.



material vertical flow develops along the border. After 8 ky the water table has dropped further down. There is still deep flow in the limestone region. However it is channeled to the vertical conduit at the border. After 12 ky the water table has reached a stable position, well above base level. All flow is focused through the conduit evolving along it. Then the water flows down the vertical shaft from where it is dispersed through the insoluble rock to the seepage face and the constant head region at base level. Note that the water table remains horizontal and stays trapped above base level, because the resistance of the insoluble rocks prevents fast outflow, thus keeping the hydraulic heads high. Therefore in contrast to a pure limestone aquifer a water table cave develops but it is located above base level. At the contact between the different rocks a vertical shaft drains the water from the aquifer.

In Figure 5.42 we illustrate what happens if limestone is underlain by insoluble rock. The aquifer shown in Figure 5.41 is equal to the one in Figure 5.4 but now its lower part consists of insoluble material with the same hydraulic properties as the initial properties of the limestone in the scenario of Figure 5.4. Everything else is unchanged. At the beginning the water table cuts through the border of limestone and insoluble rock. Dissolution is restricted to the region, where the water table is located in limestone (a). After 3 ky the water table has dropped to the contact between the rocks and a water table cave evolves there (b). Due to the resistance of the insoluble rock the water table remains stable in time and the flow along the conduit evolving in the limestone above the contact is dispersed outwards through the insoluble rock. Again conduit evolution is restricted to the region of contact.

5.8 CONCLUSION AND SUMMARY

The most important new features in unconfined aquifers can be summarized by the following essentials:

- 1) Dissolutional widening is most active close to the actual water table and consequently a significant part of recharge is drained by the permeable fringe created there. This mechanism causes lowering of the water table to its hydraulic lowest possible location, where dissolutional widening stays active, creating high permeability there.
- 2) If prominent fractures are present phreatic loops below the final water table originate and complex patterns of the distribution of hydraulic conductivities within the aquifer are created.

These principles are valid in any case of architecture of the initial aquifer, for constant recharge or constant head conditions. One important consequence is that water table caves can originate under constant recharge conditions without the guidance by prominent fractures.





5. UNCONFINED AQUIFERS UNDER VARIOUS BOUNDARY CONDITIONS

This resembles very close to older concepts of speleogenesis by Rhoades and Sinacori (1941), who proposed that dissolution occurs close to the actual water table in the epiphreatic zone. Therefore the water table should drop and the cave starts to develop, once the water table has reached base level. Cave development is therefore restricted to this region and conduits propagate headwards from the spring into the rock. These serve later as drainage of the water seeping through the vadose zone.

In the case of allogenic recharge by rivers constant head conditions arise. Therefore the water table is tied to this constant head region and remains restricted to a narrow region, where it can move slightly as recharge increases due to increasing permeability. Consequently increased permeability originates in a fringe close to the water table, almost stable in time as long constant head conditions prevail. Conduits can propagate from the input at constant head towards the spring. In this case the water table is fixed in space before any evolution of karst conduits has taken place. This scenario had been suggested by Swinnerton (1932). A short review of the models of Swinnerton, and Rhoades and Sinacori is given by Ford (1999).

When prominent fractures are available this water table concept breaks down, because a complex competition starts. Conduits start to grow under constant head conditions along the wide prominent fractures, and also in a fringe in the epiphreatic zone close to the water table. The increasing permeability of the latter can direct conduits growing along wide fractures towards the water table. Two extreme cases are possible. If the breakthrough time for conduits propagating along prominent fractures is short compared to the time required for breakthrough along the water table fringe, complex conduit systems can originate in depth and length. As soon as breakthrough has occurred the constant head condition breaks down and the water table will drop to base level. On the other hand if breakthrough along the water table is effected first, a water table system is left. After breakthrough again constant recharge has to be assumed and the water table will drop towards base level.

Our model, although applicable in its present state only to cave evolution in depth and length, reconciles conflicting hypotheses and theories of cave genesis. It contains the four-state model of Ford (1999, 1989) as well as the water table hypotheses by Swinnerton (1932) and Rhoades and Sinacori (1942). Which of those concepts is valid depends on the boundary conditions and the structure of the initial aquifer. Prominent fracture systems and constant head conditions favor evolution, which is well described by the four-state model by Ford and Ewers. Where initial porosity is sufficient for drainage of annual precipitation water table caves seem more likely. Constant recharge to karst plateaus favors the model of Rhoades and Sinacori.





6. KARSTIFICATION BELOW DAM SITES

The time scale of the evolution of a karst aquifer under natural boundary conditions – in general low hydraulic gradients – is in the range of ten thousands to several hundred thousands of years. Changes in the aquifer are so slow that it remains practically unaffected during the life times of generations of people. Under man made hydraulic boundary conditions, such as dam sites, this needs no longer to be true. Here, extremely high hydraulic heads and comparatively short pathways from input to output accelerate the process of karstification. The evolution time may then become comparable with the lifetime of the hydraulic structure. The dynamics of changes in the aquifer can endanger the function of the construction.

For example the Great Falls Reservoir in the USA showed an increase in leakage from 0.47 m³/s in 1926 to 6.6 m³/s in 1939 and to 12.7 m³/s in 1945. This caused a decrease of its water level by 8.1 m (Milanović, 2000). There are examples of dam sites, whose initial leakage was so high that they could never be filled to their planned capacity. An interesting case study describing problems associated with the construction of the Lar Dam in Iran has been published (Uromeihy, 2000). It describes the interplay between man made high hydraulic gradients and naturally calcite aggressive water in this construction.

As soon as the dam site is filled with water, boundary conditions of the karst aquifer change dramatically to very high hydraulic gradients. Therefore, the flow rates through fractures and joints in the soluble rock below the dam increase with respect to the natural situation. Consequently, dissolution rates are enhanced and changes in the aquifer are considerably faster. To study the reaction of the dam sites to meteoric flooding events is not sufficient. It is necessary to investigate the process of enhanced karstification below as well.

James and Kirkpatrick (1980) and James (James, 1992) discuss four major classes of soluble rocks found at dam sites. They describe the risk in terms of potential settlements and leakage paths, caused by dissolution of these materials within the foundation of dams. Site investigation procedures and a quantitative basis for the design of safe structures are described and proposed for future use in engineering design. James (1992) created models based on one-dimensional conduits. His work investigates the enhanced dissolution in limestone and in gypsum terrains and its relation to the failure of dams. James (1992) reports several case histories of failures due to excessive water losses, which he believes are due to dissolution of gypsum.



Palmer (1988) proposes a one-dimensional model of limestone dissolution and concludes that the increase of water loss of the Great Falls Reservoir, USA, resulted from dissolutional widening of fracture pathways, connecting the bottom of the reservoir to the valley downstream. He suggests a crude estimation for hydraulic conditions under which a pathway in limestone with aperture widths of about 0.01 cm would suffer dissolutional widening, leading to significant water losses.

Dreybrodt (1992; 1996) confirms these estimations. His work describes the crucial parameters, determining the failure of hydraulic structures. These are the aperture widths a_0 of fractures comprising a percolating pathway and the hydraulic ratio given by H/L^2 , where H is the height of the impounded water and L is the length of the pathway from its input at the bottom of the reservoir below the dam to its output. For hydraulic structures with $H/L^2 > 0.2 \text{ m}^{-1}$ water losses of about $0.5 \text{ m}^3\text{s}^{-1}$ can arise within 50 years for a single pathway with an initial aperture width of 0.01 cm and a width of 1 m.

These single conduit models neglect the exchange of flow between single percolating pathways and the surrounding network of fractures. It was already shown in Chapter 4 that this exchange has a strong influence on the evolution of karst aquifers. Because of the mechanisms discussed above, the evolution is accelerated. Consequently, estimations on the values of the crucial parameters derived by single conduit models can sometimes be misleading. First approaches to avoid these problems are reported by Bauer *et al.* (1999). Dreybrodt and Siemers (2000), Dreybrodt *et al.* (2002), and Romanov *et al.* (2003a) demonstrate first attempts in two-dimensional modeling, and a systematic study of the processes governing the evolution of a karst aquifer under the boundary conditions of a dam site. In a recent study, Kaufmann (2003a) discussed the effect of mixing corrosion on the evolution of a karst aquifer in an artificial environment.

The topic of this chapter is karstification below dam sites, and the timescales of its evolution under boundary conditions of short pathways subjected to high hydraulic gradients.

6.1 BASIC SETTINGS AND MODELING DOMAIN

Figure 6.1 presents an idealized model of a dam site, located in a narrow valley underlain by karstifiable soluble rock. The slopes of the valley consist of insoluble and impermeable rocks extending below the surface down to the soluble rock. The dam site impounds water to height H . The width of the dam site on the impermeable basis (sealing apron) is W . An impermeable grouting curtain below the dam extends down into the soluble rock to depth G .

The height of the impounded water is kept constant during the evolution of the system. We assume that there is enough water, flowing from the catchment area to keep the level constant until the end of the simulation. We stop the calculations, when leakage reaches a prescribed maximal allowed value of $2 \cdot 10^5 \text{ cm}^3/\text{s}$ per meter of the dam's width. In the case of a dam site 100 meters wide, this corresponds to a leakage rate of $20 \text{ m}^3/\text{s}$, which is regarded as unbearable.



6. KARSTIFICATION BELOW DAM SITES

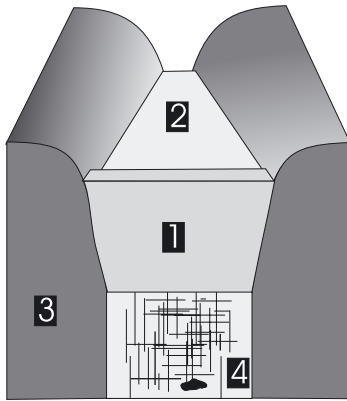


Figure 6.1: Geological setting. 1) Dam site; 2) Impounded water; 3) Valley – impermeable rocks; 4) Bottom of the valley – soluble rock dissected by a net of fractures. Larger voids and a cave are also presented.

As in the scenarios of the preceding chapters, there is a net of primary, yet unwidened fractures and fissures, which comprise percolating pathways from the bottom of the reservoir to the valley downstream. This network is characterized by the average spacing s of the fractures, their aperture widths a_0 and their widths b_0 . As already discussed, the hydraulic conductivity of such a fracture system is given by Eq. 5.1 (Lee and Farmer, 1993). In reality, not all of the fractures have equal initial aperture widths. Therefore, in addition to the network with equal initial aperture widths of its fractures (Uniform scenario), we also use a statistical distribution of the initial aperture widths of fractures (Statistical scenario).

There is one important difference to the geological settings discussed in Chapter 4. The soluble rock is extending to a certain depth below the dam. The average aperture widths of primary joints are about 0.015 cm, and are decreasing exponentially with depth to values of about 0.008 cm. In already karstified rocks these numbers may be higher, but in any case aperture widths in the range between several 10^{-2} cm to $3 \cdot 10^{-3}$ cm are considered reasonable. At the same time the average spacing s of fractures is decreasing from 5 m at the surface to about 10 m at depths below 50 meters (Lee and Farmer, 1993).

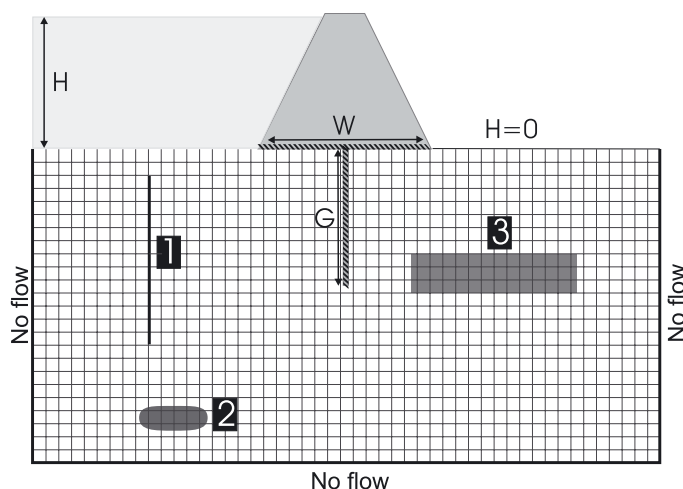
In the statistical scenario we use a net of fractures with a lognormal statistical distribution of the initial aperture widths (Gale, 1987). In this way we meet the requirements discussed so far. We are also able to take into account the influence of some initially significantly larger fractures forming preferential pathways through the rock. Some regions where dams are constructed are highly karstified (Milanović, 2000). Our model is designed to consider such situations and to simulate the behavior of dam sites in the presence of large cave conduits below the grouting curtain.

Figure 6.2 depicts the modeling domain, a two-dimensional cross section of the scenario shown in Figure 6.1. It is a rectangular network – $750 \text{ m} \times 350 \text{ m} \times 1 \text{ m}$ – divided into blocks of 7.5 m by 7.5 m by 1 m by fractures and fissures. Different properties, such as fracture aperture width, the chemical parameters of dissolution kinetics, or insoluble rock at the fracture walls can be assigned to each individual fracture. This way any kind of heterogeneity in the aquifer can be modeled. At places where the bedrock is impermeable (the region of the grouting curtain for example) fractures are omitted from the network.



6. KARSTIFICATION BELOW DAM SITES

Figure 6.2: Model domain of a dam site. A slice of 1 m width is taken along the valley. It is dissected by fractures and fissures into blocks of $7.5 \times 7.5 \times 1 \text{ m}^3$. The domain is 750 m in horizontal extension and 350 m in vertical. The bottom and the edges are impermeable. The dam, the sealing apron of width W and the grouting curtain with depth G are impermeable. The upper left hand side is at constant head H , which is the depth of impounded water. The upper right hand side is at constant head 0 m. 1) Widened fracture; 2) Cave conduit; 3) Region of rock with different solubility than the rest of the network.



Two basic scenarios are discussed:

- Scenario A: The width W (sealing apron) of the dam is 262 meters and the grouting depth G is 97 meters
- Scenario B: The width W (sealing apron) of the dam is 82 meters and grouting depth G is 187 meters

Table 6.1: Basic parameters used in the models presented in Chapter 6

Description	Symbol	Unit	Numerical values
Network parameters			
Initial fracture aperture width	a_0	cm	0.02
Fracture width	b	cm	100
Fracture length	L	cm	750
Domain dimension		m	750×375
Parameters of dam site			
Hydraulic head	H	m	150
Grouting depth	G	m	97 (A), 187 (B)
Apron width	W	m	262 (A), 82 (B)
Limestone: Chemical parameters			
Order of nonlinear kinetics	n		4
Nonlinear kinetics constant	k_n	$\text{mol cm}^{-2}\text{s}^{-1}$	$4 \cdot 10^{-8}$
Calcium concentration	c	mol/cm^3	$c_{in} < c < c_{eq}$
Initial concentration	c_{in}	mol/cm^3	0
Switch concentration	c_s	mol/cm^3	$0.9 c_{eq}$
Equilibrium concentration	c_{eq}	mol/cm^3	$2 \cdot 10^{-6}$



6. KARSTIFICATION BELOW DAM SITES

We present two sets of calculations for both basic scenarios:

- Uniform initial distribution of fracture aperture width $a_0 = 0.02$ cm
- Lognormal distribution with average fracture aperture width $\bar{a}_0 = 0.02$ cm and width $\Delta a_0 = 0.025$ cm.
- In all simulation runs the sealing apron of width W below the dam and the grouting curtain are considered impervious.

The hydrological boundary conditions are:

- Hydraulic head (height) H of the impounded water is 150 meters
- Hydraulic head on the valley side is 0 meters

No flow boundary conditions exist on left and right hand side boundaries and at the bottom of the domain. The bottom of the modeling domain is 375 meters below the ground. Even if the soluble rock extends further in vertical direction, its permeability at depths close to 400 meters is so low that it can be considered as practically impermeable ((Milanović, 1981; 2000)). The boundary conditions at the upstream and downstream side boundaries need some comment. According to Figure 6.1 the rock is not impermeable. To model this, we would have to extend the modeling domain by kilometers in both, the upstream and downstream directions. Since our computer capacity is limited, this is not possible at present. On the other hand, most flow to the valley is carried through a finite region below the dam. Consequently, the influence of the upstream and downstream boundaries on the evolution decreases relatively fast with increasing extension of the modeling domain. Several test runs for a domain with dimensions of 1500 meters by 750 meters revealed no change in comparison to the evolution of a domain with 750 meters by 375 meters. Therefore, we regard the impervious boundaries as appropriate for the dimension of the modeling domain (750 meters by 375 meters) and the dimension of the hydraulic structure.

The concentration of inflowing water is assumed to be $c_0 = 0$. All chemical and hydrological parameters used for the basic scenarios are depicted in Table. 6.1.

6.2 NUMERICAL RESULTS FOR SCENARIOS WITH UNIFORM NETS

Figure 6.3 depicts the initial flow rates and the pressure head distribution for scenario A with uniform net. The color code represents the flow rates through the current fracture, normalized to the maximal flow carried by some fracture in the network. The scale is logarithmic. Flow through fractures, colored blue is four orders of magnitude less than flow through the red ones. Dashed black lines depict the pressure head distribution at steps of 1.25 meters and the full ones at steps of 10 meters.

The pressure lines show a symmetrical pattern with respect to the grouting curtain. Hydraulic gradients are steepest for pathways close to the structure. The amount of flow through fractures close to the dam is almost two orders of magnitude higher than that through fractures more distant and towards the right hand side boundaries of the domain.



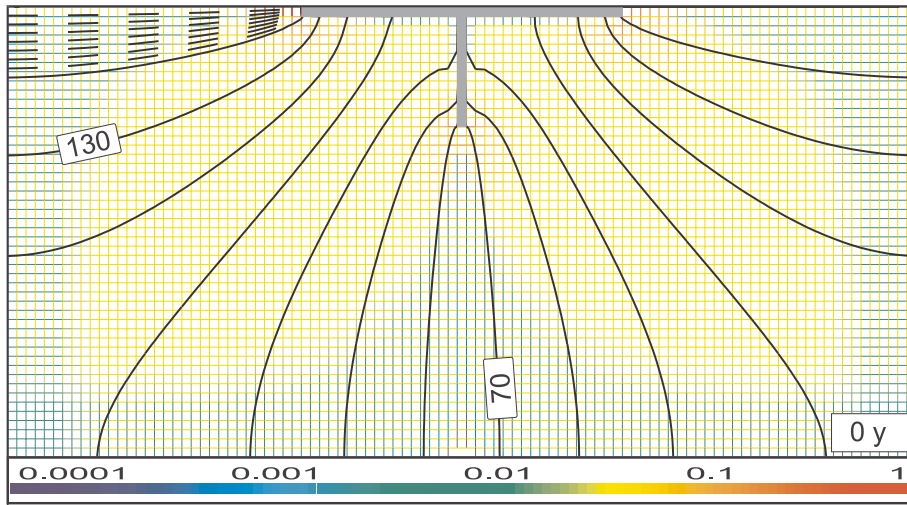


Figure 6.3: Initial distribution of flow rates – Scenario A (uniform net). See text. Thick black lines represent the distribution of hydraulic heads – starting at 150 m every 1.25 m (dashed lines) and every 10 m (solid lines). The color code designates the flow rates in a logarithmic scale. The maximal flow rate Q_{max} [cm^3/s] is depicted at the upper right corner and by the red color. Dark blue means $0.0001 \cdot Q_{max}$. Note that all fractures carrying flow smaller than $0.0001 \cdot Q_{max}$ are omitted in the figure.

6.2.1 Scenario A

All the following figures on the evolution of aquifers below the dam sites in this chapter show fracture aperture widths and flow rates on the left hand side columns. The right hand side columns illustrate the corresponding dissolution rates and repeat the fracture widths.

Flow rates are depicted by a color code from dark blue ($0.0001 \cdot Q_{max}$) to red (Q_{max}). Q_{max} is the maximal flow rate at some fracture in the network at that time of the evolution and is shown in the corresponding panel. All fractures with flow rates less than $10^{-4} \cdot Q_{max}$ are omitted (white regions).

The color code on the right hand side column similarly depicts dissolution rates from $10^{-4} \cdot F_{max}$ to F_{max} , where F_{max} is constant in time and gives the dissolution rate for a solution with $c = 0$, i.e. $F_{max} = k_j = 4 \cdot 10^{-11} \text{ mol cm}^2 \text{ s}^{-1}$. This corresponds to a widening of the fractures by 0.1 cm/year. All fractures with rates smaller than $10^{-4} \cdot F_{max}$ are omitted from the figure (white regions).

The black lines represent the hydraulic head distribution every 1.25 meters (dashed lines) and every 10 meters (full lines).

Figure 6.4a and b depict the situation after 31 years of evolution. A channel grows down vertically in the region with the highest initial flow and steepest hydraulic gradient (see Figure 6.3), close to the rim of the sealing apron and parallel to the grouting. There is flow out from this widened channel into the surrounding network, increasing with depth and maximal at the tip. This behavior looks similar to the early evolution of

6. KARSTIFICATION BELOW DAM SITES

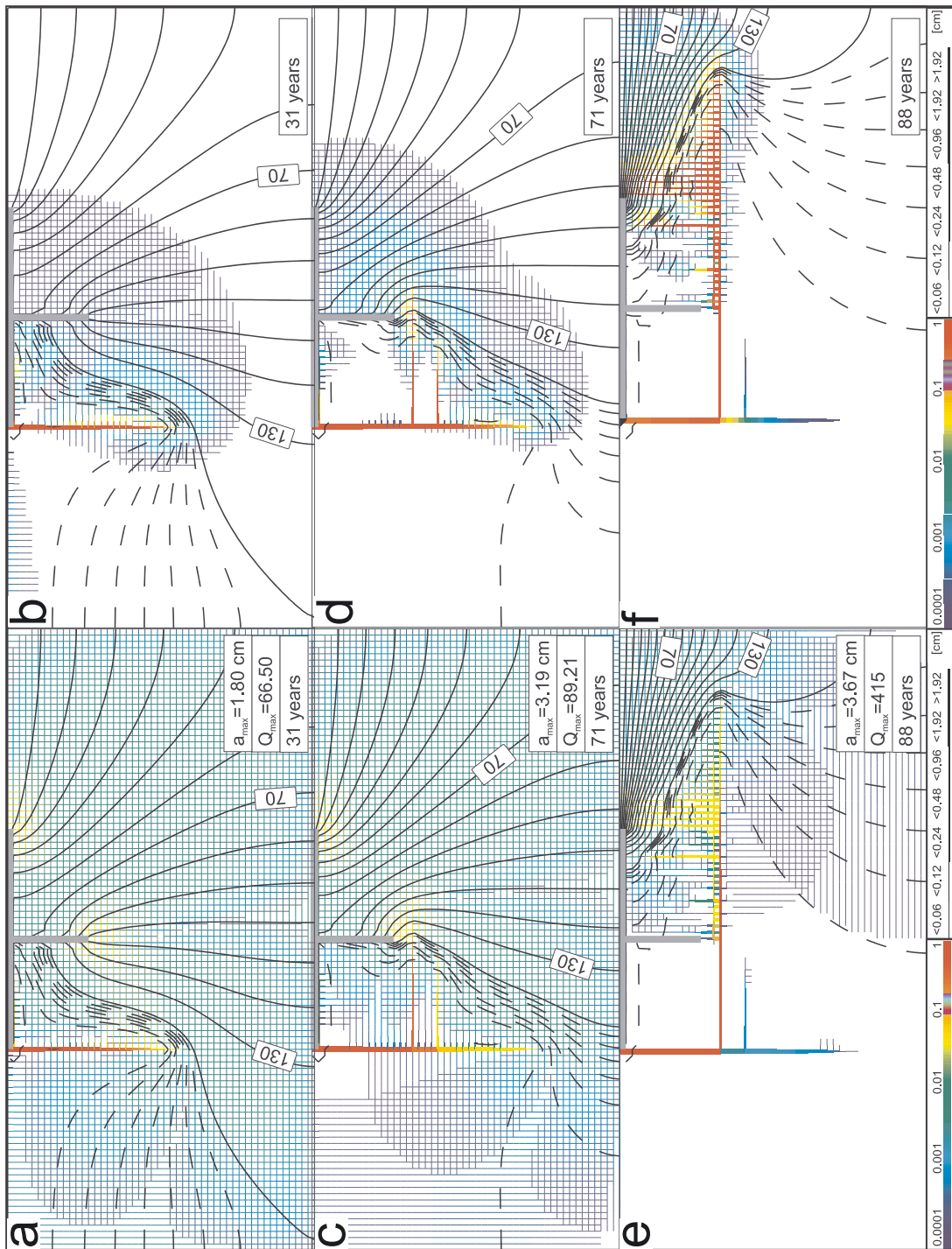
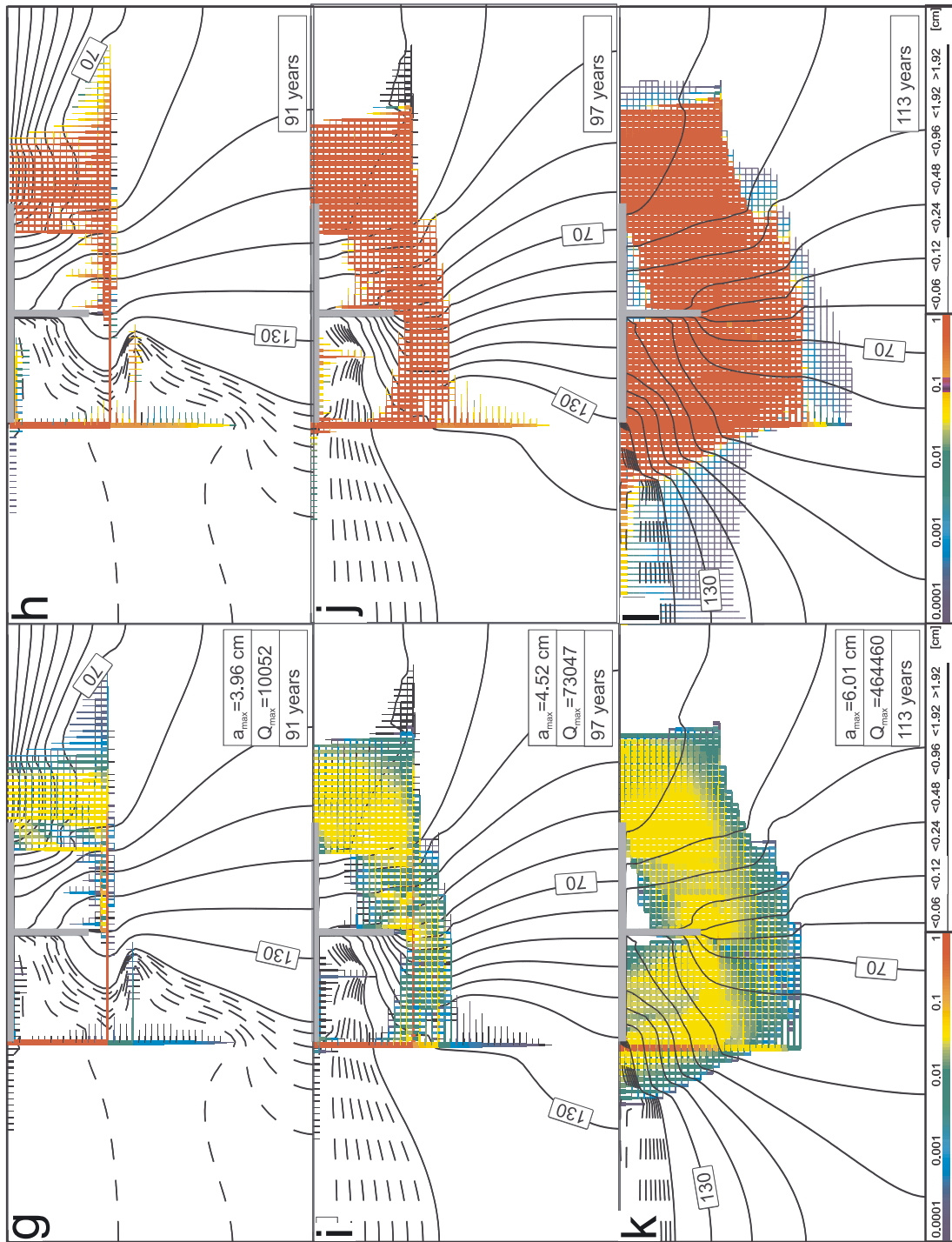


Figure 6.4: Evolution of fracture aperture widths, pressure heads, flow rates, and dissolution rates for Scenario A (uniform net) See text. The bar code in both columns represents the fracture aperture widths in centimeters. The maximal aperture width a_{max} [cm] and the time are depicted at the lower right corner. Thick black lines represent the isolines of the pressure head distribution starting at 150 m at every 1.25 m (dashed lines), and every 10 m (solid lines). The color code in the left hand column designates the flow rates in a logarithmic scale. The maximal flow rate Q_{max} [cm³/s] is

6. KARSTIFICATION BELOW DAM SITES



depicted at the lower right corner and by the red color. Dark blue means $0.0001 \cdot Q_{max}$. Note that all fractures carrying flow rates less than $0.0001 \cdot Q_{max}$ are omitted from the figure. The color code in the right hand column designates the dissolution rates in a logarithmic scale. The maximal dissolution rate F_{max} ($4 \cdot 10^{-11} \text{ mol cm}^{-2} \text{ s}^{-1}$) is depicted by the red color. Dark blue means $0.0001 \cdot F_{max}$. Note that all fractures with dissolution rates smaller than $0.0001 \cdot F_{max}$ are omitted from the figure.



6. KARSTIFICATION BELOW DAM SITES

the standard scenario in Chapter 4 (see Figures 4.13, 4.14, and 4.23 to 4.27). The flow out from the tip accelerates the evolution of the channel in comparison to the rest of the network. Once it is created, it behaves in the same way as the central conduit discussed in Chapter 4. The widened part of the channel causes a redistribution of the pressure head along it. Highest hydraulic gradients are at the tip. The rest of the network is still unaffected. Flow from the channel follows the direction of steepest hydraulic gradient located downstream close to its tip. Consequently, dissolution rates (b) are high at the outflow nodes from the channel (red, yellow) but low (blue) everywhere else.

After 71 years (Figure 6.4c and d) a horizontal channel has grown towards the bottom of the grouting curtain. It attracts large amounts of flow. The region of high hydraulic gradients has moved downstream and flow is concentrated below the bottom of the grouting. A second horizontal channel grows parallel below and competes for flow.

After 88 years (Figure 6.4e and f) the upper horizontal channel has attracted practically all flow and has migrated downstream close below the grouting. Since hydraulic gradients are directed upwards to the downstream part of the dam, all flow is dispersed upwards, and parallel channels compete to reach an output. Therefore, a comb like structure grows upwards with one of its teeth reaching breakthrough first. Breakthrough occurs close to the downstream base of the dam at the rim of the apron along the geometrically shortest pathway, as to be expected. This is demonstrated particularly convincing in uniform networks, which were selected for this reason.

Figure 6.4g and h depict the situation at 91 years, shortly after breakthrough when flow has become turbulent. Some of the vertical growing channels are already connected to the exit. There is a clearly visible region of parallel horizontal channels, which connect to vertical fractures of the comb and transmit flow to the valley downstream. The pressure heads are redistributed in the whole domain. Highest flow rates are along the widened conduits (see Figure 6.4g). Solutions with very low Ca -concentrations are entering into these channels and dissolution rates along them are almost constant (see Figure 6.4h). This causes continuous further growth. There is no zone of outflow of aggressive solution from widened channels into the surrounding net (Figure 6.4h). Consequently, an exit type fan cannot grow.

Figure 6.4 i and j depict the situation after 97 years. The pressure head is more evenly distributed along the entire domain. A net of widened fractures has extended below the sealing apron and the grouting curtain. These fractures mark the beginning of evolving entrance fans. Because of the asymmetrical setup, the fans grow unsymmetrically on both sides of the pathway.

Continuing growth of the fans and their incorporation into the widened pathway is depicted in Figure 6.4k and l, which shows the situation after 113 years. The region of widened pathways carries most of the flow through the domain (see Figure 6.4k). The dissolution rates are even and maximal along the whole pathway – Figure 6.4l. This assures continuous, fast widening. Because of the evolution of the fans, this zone expands radially around the impervious structure, finally conquering the whole modeling domain.



6.2.2 Scenario B

The dimensions of the dam structure are: $W = 82$ m, $G = 187$ m. By this way we keep the distance $W+2G$ equal to that of scenario A. Consequently, the lengths of evolving pathways are similar for both scenarios. The hydrological and chemical boundary conditions for scenario B are shown in Table 6.1.

The evolution of fracture aperture widths, flow rates, dissolution rates, and the pressure head distribution is depicted in Figure 6.5. Figures 6.5a and b depict the situation after 26 years. A vertical channel is growing from the bottom of the reservoir similar to the evolution of scenario A (see Figure 6.4a). This channel changes the head

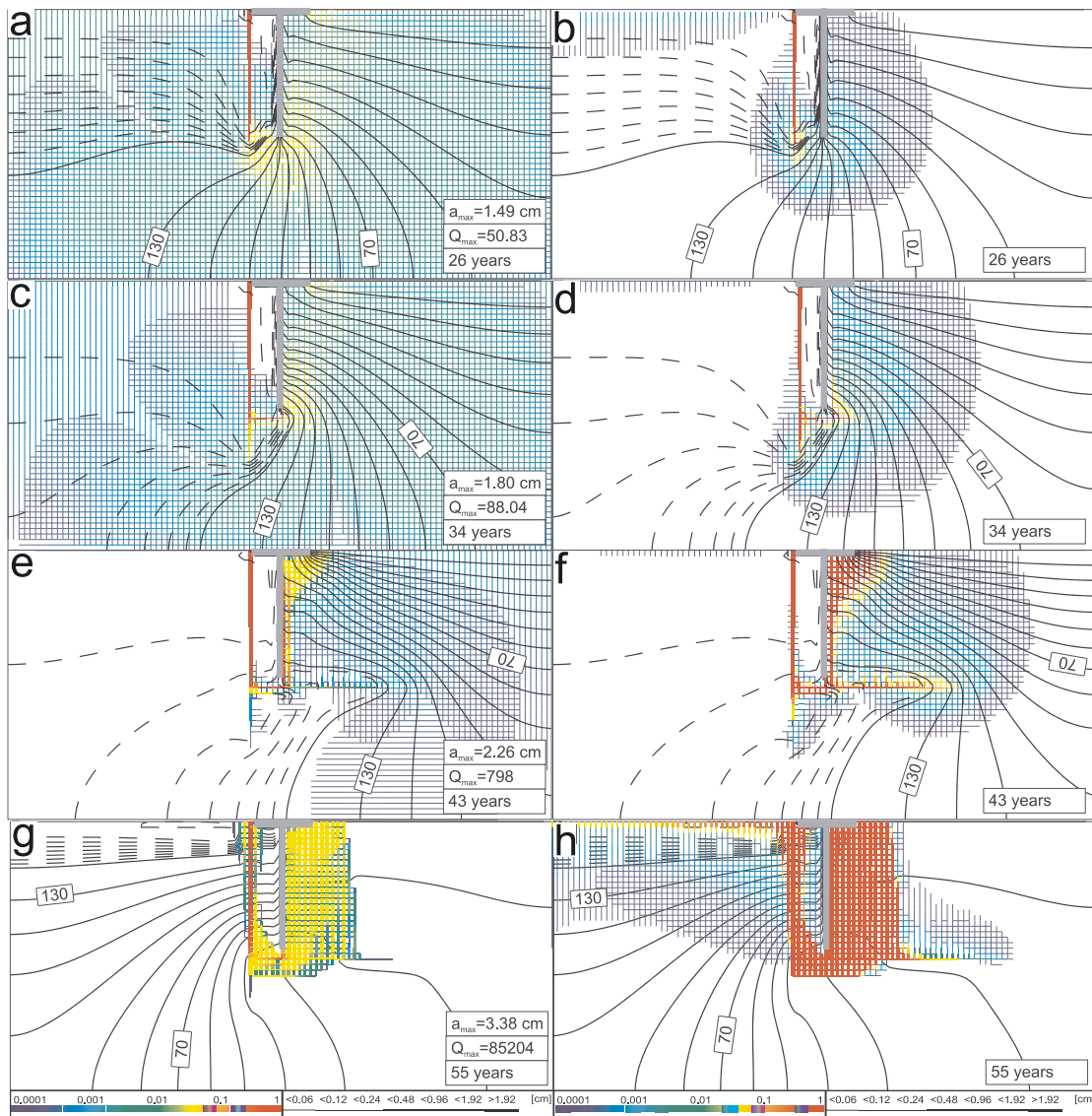


Figure 6.5: Evolution of fracture aperture widths, pressure heads, flow rates, and dissolution rates for Scenario B (uniform net). Bar and color codes as in Figure 6.4



6. KARSTIFICATION BELOW DAM SITES

distribution in the neighboring area and flow rates are maximal along it. The pressure distribution depicts the outflow of water from the channel into the surrounding network. This outflow is maximal at the tip of the conduit. Dissolution rates are maximal along the channel and on the right hand side of the tip. This marks the area of further growth of pathways.

After 34 years (Figure 6.5c and d) the channel has propagated vertically. Flow from its tip is directed through parallel fractures below the grouting. Consequently, a horizontal channel grows into the direction of the grouting curtain. Dissolution rates are highest in this region of horizontal flow. After 43 years (Figure 6.5e and f) the horizontal channel has penetrated below the grouting. Hydraulic gradients are directed upwards and a channel propagates vertically upwards parallel to the downstream side of the grouting and close to it. Below the impermeable apron flow from the horizontal channel is dispersed into the net.

At 55 years (Figure 6.5g and h), shortly after breakthrough a large zone of widened fractures has developed below the construction. Flow is already turbulent and dissolution rates are high and even everywhere in this region. In the upstream part channels start to grow from the floor of the lake. These will connect to the region where flow is high and consequently, the heads are low and an entrance fan will develop. In a similar way, a fan of breakthrough pathways penetrates upwards at the downstream side of the horizontal channel creating a second fan.

6.3 NUMERICAL RESULTS FOR SCENARIOS WITH STATISTICAL NETS

In order to model scenarios closer to natural conditions, we extend our set-ups by introducing a statistical distribution of the initial aperture widths of fractures used to build the networks. The mean value of the lognormal distribution is set to $\bar{a}_0 = 0.02$ cm. We use the same boundary and geometrical conditions as in the simulations so far (see Table. 6.1).

6.3.1 Scenario A

The evolution of fracture aperture widths, flow rates, dissolution rates and the pressure head distribution is depicted in Figure 6.6a–l. The basic behavior of the evolution is similar to the uniform scenario A. A vertical channel evolves downwards on the left hand side of the sealing apron, along the grouting curtain.

This is depicted in Figure 6.6a and b. As already discussed, this channel evolves in zones favored by the geometry of the setup, and by its initial boundary conditions. The main difference to the uniform scenario, resulting from the statistical distribution of the initial aperture widths, is the existence of several competing pathways, which are favored



because of their initially wider aperture widths. This is the reason for diversion of the vertical pathway into the diagonal direction towards the grouting curtain. The existence of such initially wider pathways also causes growth of vertical channels in upstream areas away from the impermeable dam site structure. These channels are depicted in Figure 6.6c and d. They start from the bottom of the reservoir and grow independently of the evolution of the zone with low resistance below the dam site. After the breakthrough event, when the growth of entrance type fans starts to extend this zone, these channels are integrated into it (Figure 6.6e–h).

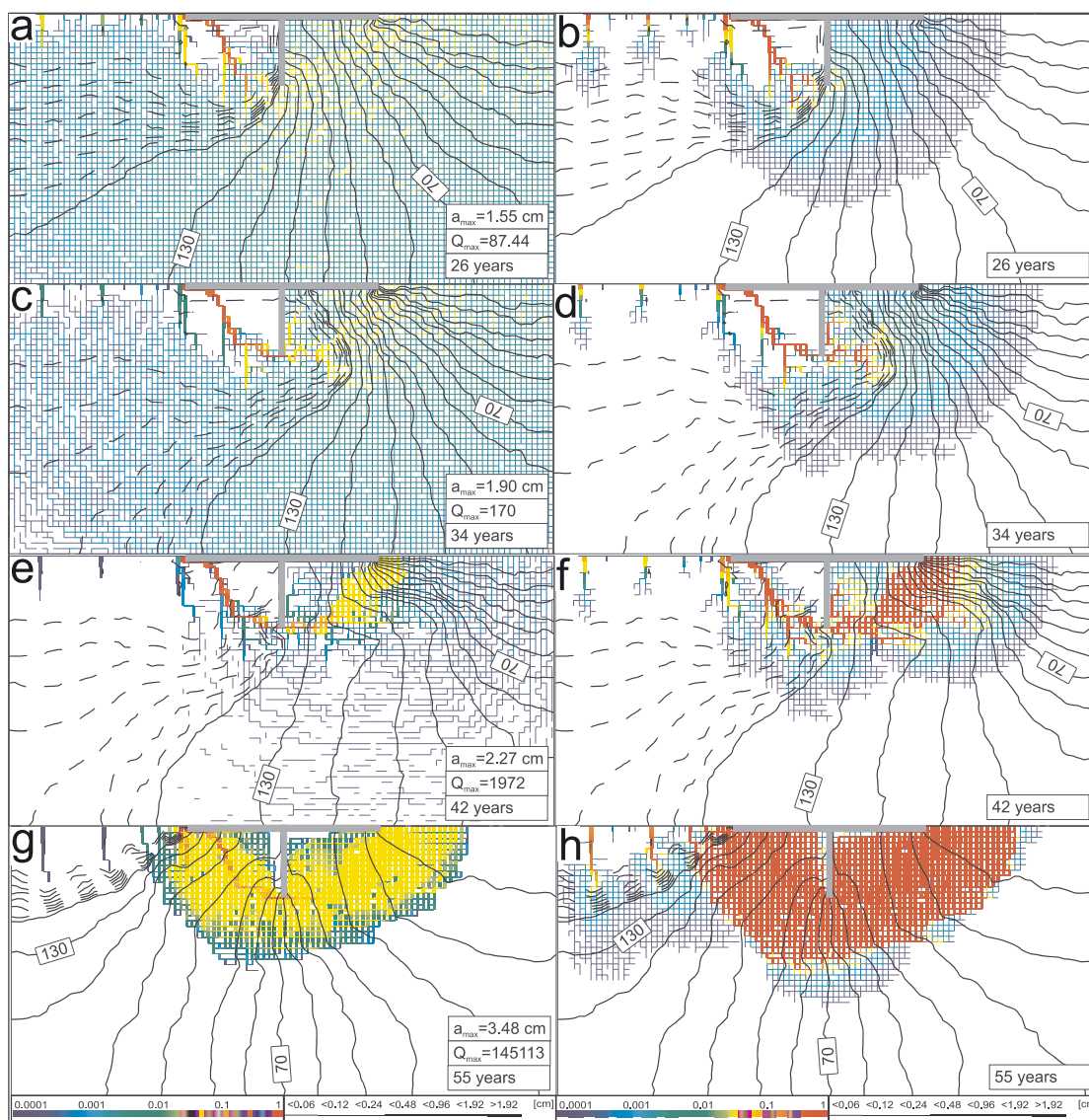


Figure 6.6: Evolution of fracture aperture widths, pressure heads, flow rates, and dissolution rates for Scenario A (statistical net). Bar and color codes as in Figure 6.4

6.3.2 Scenario B

In scenario B – statistical net, we use the same realization of the net of initial fractures as in the statistical scenario A. Only the geometry of the construction is changed. The evolution is very similar to the uniform scenario B (see Figure 6.7). A vertical channel propagates downstream vertically, turns then horizontally and migrates upwards close to the grouting curtain. From the bottom of the reservoir channels grow downwards from the onset of the evolution along initially wider pathways. They are caused by the statistical properties of the net and will become integrated later into the region of high flow.

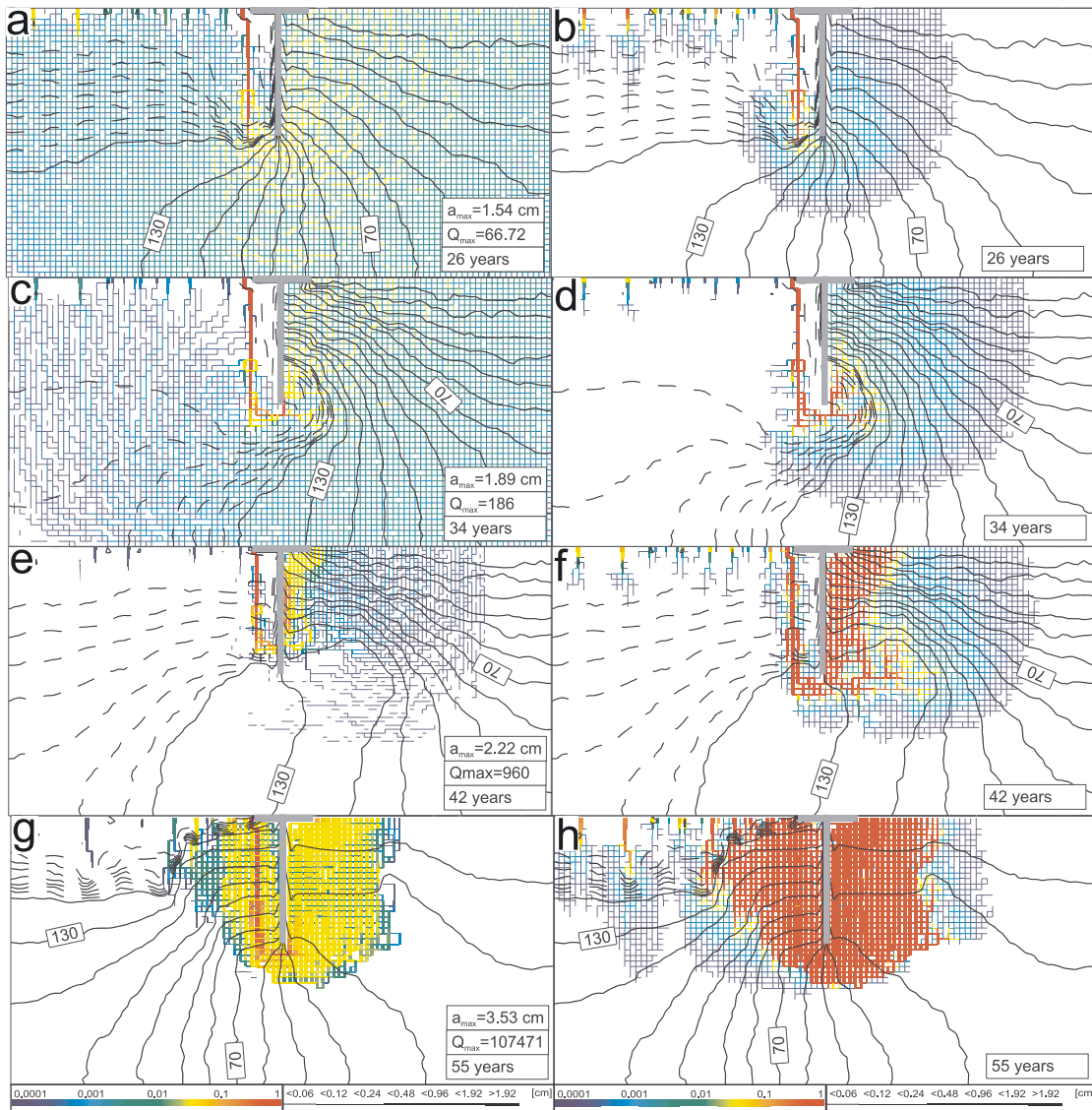


Figure 6.7: Evolution of fracture aperture widths, pressure heads, flow rates, and dissolution rates for Scenario B, statistical net. Bar and color codes as in Figure 6.4

6.3.4 Evolution of flow rates for statistical scenarios A and B

Because of the closer similarity of the statistically distributed nets to natural aquifers we restrict the discussion of the evolution of flow rates shown by Figure 6.8 to these. Figure 6.8 depicts total seepage through 1 m of the dam's width. For a dam one hundred meters wide a seepage of $2 \cdot 10^5 \text{ cm}^3/\text{ms}$ corresponds to a total leakage of $20 \text{ m}^3\text{s}^{-1}$. When this is reached computer runs are terminated.

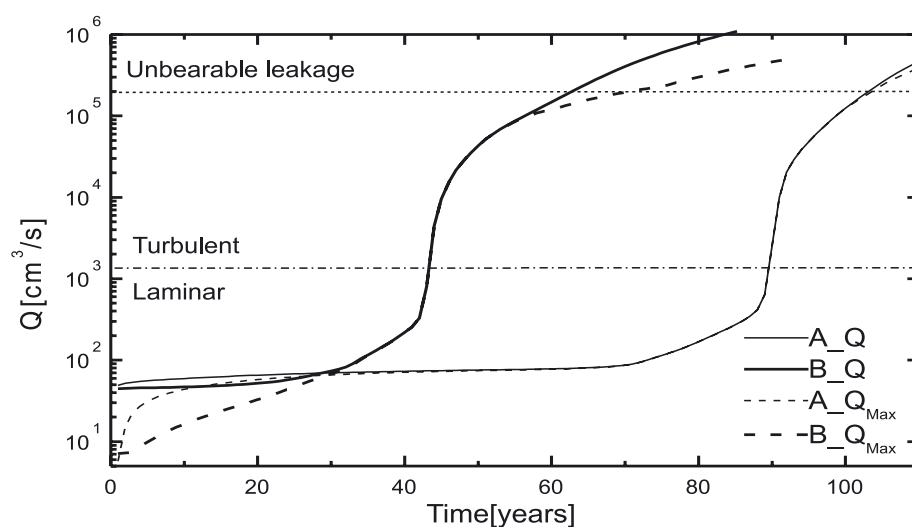


Figure 6.8: Evolution of flow rates Q and Q_{max} for Scenarios A and B, both with statistical net.

It shows total flow Q and for comparison the flow Q_{max} , which is the maximal flow occurring in some fracture of the domain. Shortly after filling the reservoir Q increases steeply, whereas the total flow remains fairly constant. This means that flow Q is distributed over many fractures. One of them located on a preferential path is more competitive than all others and attracts more and more flow from neighboring fractures until all flow is channeled through it. This is the case at about 30 years, when Q_{max} and Q , (total flow) become equal. During further evolution to breakthrough a pathway including the fracture with maximal flow carries all flow. After breakthrough Q_{max} becomes smaller than total flow. This indicates, that now flow employs many parallel fractures at the downstream side.

Another feature is also interesting. In contrast to breakthrough curves evolving under constant head through statistical networks (see Figures 4.13–4.15), shortly before breakthrough (at about 30 years) flow rates rise but still need ten years until breakthrough. An increase of seepage, therefore, gives advanced warning to serious problems several ten years later.



6.4 INFLUENCE OF BASIC HYDROLOGICAL AND GEO-CHEMICAL PARAMETERS ON BREAKTHROUGH TIME

The aperture widths of fractures and their distribution are not known in nature. Furthermore, the chemistry of inflowing water is also not easy to determine. It is therefore of utmost importance to carry out a sensitivity analysis of breakthrough times on these parameters.

Before this can be done one has to know the influence of different realizations of the statistical distribution. To this end, ten different realizations all with equal $\bar{a}_0 = 0.02$ cm have been carried out for the statistical scenarios A and B. Although not in detail the evolutions of these aquifers below the dam site were found to be very similar. The breakthrough times turned out to vary by no more than 15 %. These findings render a sensitivity analysis on other parameters a meaningful tool.

We have performed this analysis for all four scenarios discussed in this chapter by changing one of the parameters of the corresponding case and leaving everything else unchanged.

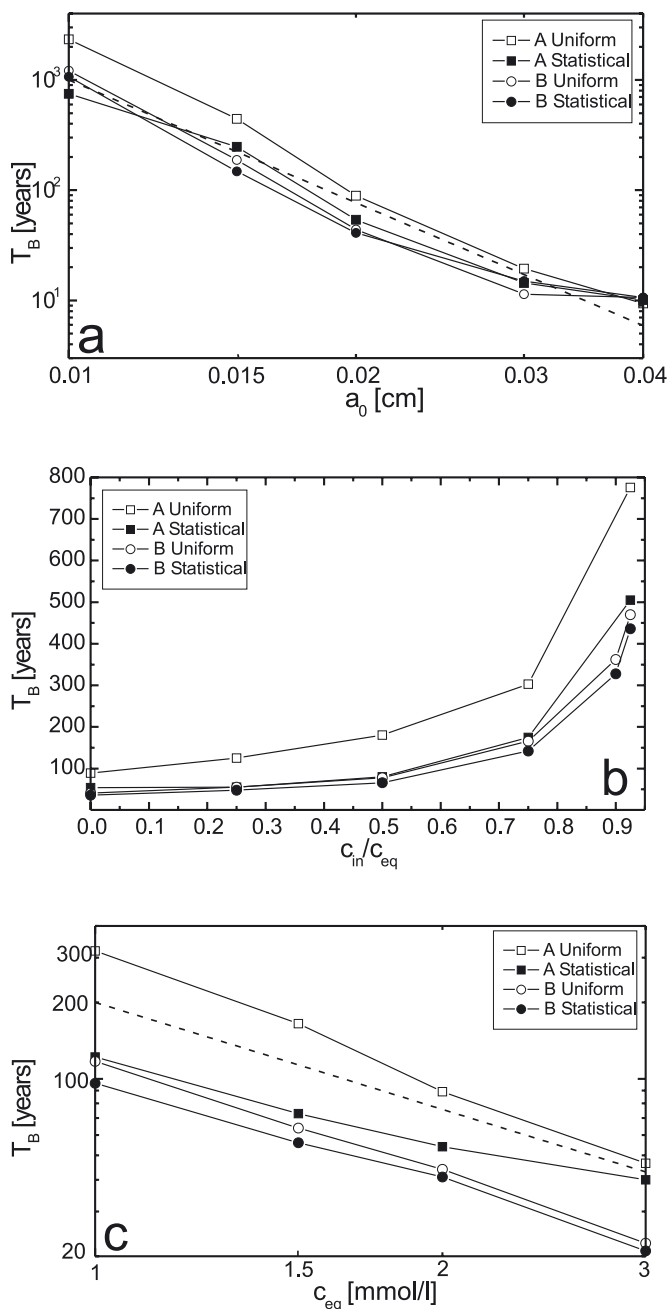
First we discuss the influence of fracture aperture widths \bar{a}_0 . To gain some estimate of their influence on breakthrough time, we have varied \bar{a}_0 between 0.01 cm and 0.04 cm in scenarios A, B with uniform net. Everything else is unchanged. We have also performed this procedure on the statistical nets of the scenarios A and B, whereby we have also scaled $\Delta\bar{a}_0$ accordingly. Figure 6.9a shows breakthrough times in dependence on \bar{a}_0 in a double logarithmic scale. Note that for fracture widths smaller than 0.03 cm the curves can be reasonably well approximated by $T_B \propto \bar{a}^{-3.7}$. The straight dashed line in Figure 6.9a shows such a dependence. Such power laws for breakthrough times have already been found on one-dimensional conduits (Dreybrodt, 1996; Dreybrodt and Gabrovšek, 2000) and for breakthrough on two-dimensional percolation nets by Siemers and Dreybrodt (1998). They are discussed in Chapters 3 and 4. For aperture widths larger than 0.03 cm breakthrough times are reduced to values of about 10 years, and dams could be regarded as critical. On the other hand fractures of 0.01 cm aperture widths yield breakthrough times of about 1000 years.

In all scenarios so far, we have assumed that the water entering has not yet dissolved the soluble rock and consequently $c_{in} = 0$. To investigate what happens when water enters with a higher Ca-concentration, we have plotted breakthrough times as a function of c_{in}/c_{eq} in Figure 6.9b. For $c_{in}/c_{eq} < 0.5$ little variation is found. The closer, however, c_{in}/c_{eq} approaches saturation, the higher are breakthrough times. Therefore, the saturation state of the reservoir water is a parameter of utmost importance. If water entering the fractures is close to saturation ($c/c_{eq} > 0.8$) karstification below the dam site is delayed.

A second important chemical parameter in limestone is the equilibrium concentration c_{eq} , which depends on the concentration of CO_2 at the bottom of the reservoir. The dependence of breakthrough times on c_{eq} is shown by Figure 6.9c. Breakthrough



6. KARSTIFICATION BELOW DAM SITES



times roughly follow a power law $T_B \propto c_{eq}^{-1.4}$, similar to what has been found on single tubes and percolation networks. It should be noted here that c_{eq} is the equilibrium concentration for dissolution of calcite in a system closed with respect to CO_2 . It depends on the CO_2 and calcium concentration of the reservoir water (Dreybrodt, 1996) when entering the fractures.

Figure 6.9: a) Breakthrough times for Scenarios A and B in dependence of initial aperture width a_0 . b) Breakthrough times for Scenarios A and B in dependence on the calcium concentration c_{in} of the impounded water. c) Breakthrough times for Scenarios A and B in dependence on the equilibrium concentration c_{eq} of the impounded water.

Another critical parameter is the height H of the impounded water. Figure 6.10a depicts double-logarithmic plots for breakthrough times as a function of H . Again we find a power law $T_B \propto H^{-1.8}$ similar to what has been found earlier for single channels Dreybrodt (1996) and percolation nets (Siemers and Dreybrodt, 1998).

In the construction of dams grouting plays a most important role. Figure 6.10b illustrates the dependence of breakthrough time on the depth G of the grouting curtain. Breakthrough times increase steeply if the grouting depth is larger than height H .

6. KARSTIFICATION BELOW DAM SITES

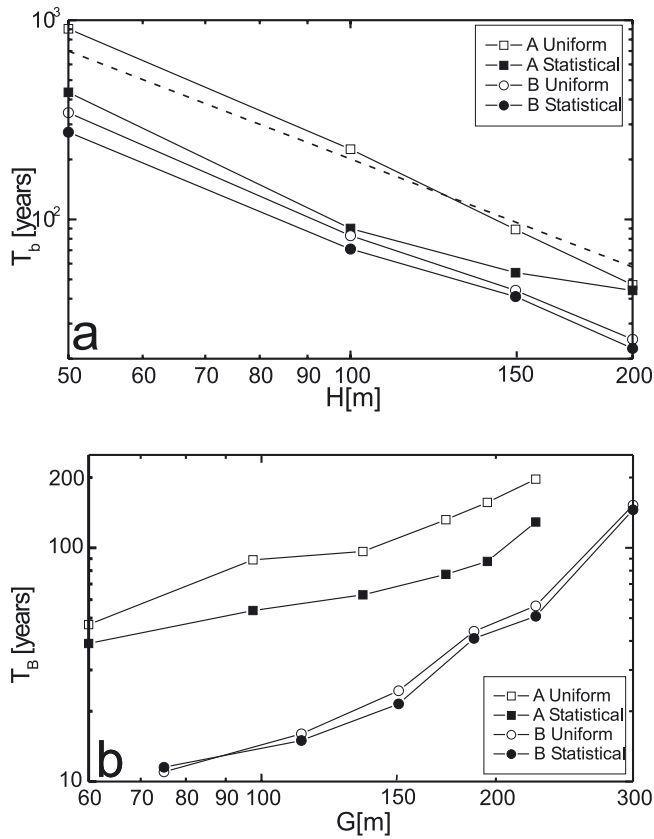


Figure 6.10: a) Breakthrough times for all Scenarios A and B in dependence on the hydraulic head H . b) Breakthrough times for Scenarios A and B in dependence on the depth G of the grouting curtain.

In scenarios A and B we have assumed a domain of 750 m width and 375 m depth. As we have noted earlier the width of the domain could be critical to our calculations, because of the artificial boundary conditions (up and down stream side are regarded impermeable). Therefore, we have extended the domain to 1500 m width, keeping the depth at 375 m. The size of the grids was kept at 7.5 by 7.5 m². Breakthrough times and channel patterns remained unaffected. This asserts that the domain of our scenarios is reasonable. Reducing this domain, however, by a factor of one half to a 50 by 50 net, with a horizontal width of 375 m shows an increase of breakthrough times by about 30 %.

To obtain some idea on the breakthrough behaviour of smaller dams we have scaled H , G , and W by a common factor f_s . In other words, we reduce the dimensions of the structure by the factor f_s . Figure 6.11 shows the breakthrough time in dependence of the scaling factor f_s . Breakthrough times decrease for all scenarios with decreasing size of the structure. They follow a power law close to $f_s^{4/3}$ as shown by the dashed line. At $f_s = 0.5$ breakthrough times are reduced to about one half compared to the standard scenarios. This means that especially for smaller structures comparatively deeper grouting is necessary to prevent karstification below the dam. Again, this behavior reflects breakthrough properties of single conduits and percolation nets. Their breakthrough times follow a power law $T_B \propto (L^2/H)^{4/3}$, in which L is the length of the channel (Dreybrodt, 1996; Dreybrodt and Gabrovšek, 2000). In our cases L is close to $W+2G$. Scaling W , G , H by a common factor f_s scales T_B by a factor of $f_s^{4/3}$.

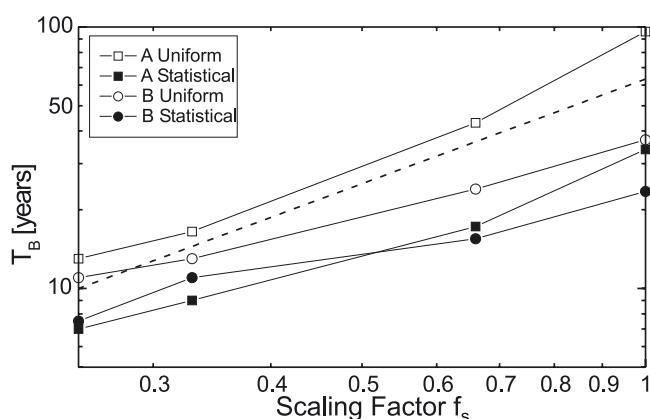


Figure 6.11: Breakthrough times for Scenarios A and B in dependence on the scaling factor f_s . The dashed line depicts the power law $f_s^{4/3}$.

6.5 EXAMPLES OF MORE COMPLEX GEOLOGICAL SETTINGS

So far we have considered a very simple geological setting with a net of narrow fractures solely. This corresponds to the ideal situation, where grouting has sealed all open voids, fractures or even cave conduits. To see the influence of a phreatic cave conduit below the dam, we have modeled such a situation. We have introduced a phreatic cave conduit well below the dam into the scenario A with statistical net. This is indicated by the white square in Figure 6.12. The boundary conditions at all fractures comprising this area are set to 0.1 m. This corresponds to a phreatic cave conduit, which has its spring somewhere down stream of the dam site. Figure 6.12 depicts headlines and fracture widths after 26 years. There are two competitive routes to breakthrough. One is leading below the dam and grouting to the outputs downstream with head zero. The other one is directed towards the cave conduit with similarly low head. In our scenario this last pathway is more competitive and breakthrough into the conduit arises after 26 years, much earlier than for scenario A with statistical net at 42 years. Figure 6.15 illustrates the evolution of total leakage.

In our models we assumed that the rock is homogeneous with respect to its dissolutional properties. We now relax this by inserting a horizontal layer of insoluble rock extending from the left hand side boundary below the dam to the right hand side border. Its thickness is 67.5 m. The fracture widths distribution remains unchanged, as in scenario A (statistical net).

Figure 6.13 shows a setting, where the grouting curtain has not reached this layer and a thin layer of soluble rock remains between grouting and insoluble rock. It further depicts isolines of head and fracture widths distribution after breakthrough at 45 years. Breakthrough has occurred via the small soluble fringe between the tip of the grouting and the layer of insoluble rock. Head distribution and structure of flow conduits resemble very much that of extended the statistical scenario A, depicted in Figure 6.6b and c. The evolution of total leakage is depicted in Figure 6.15.

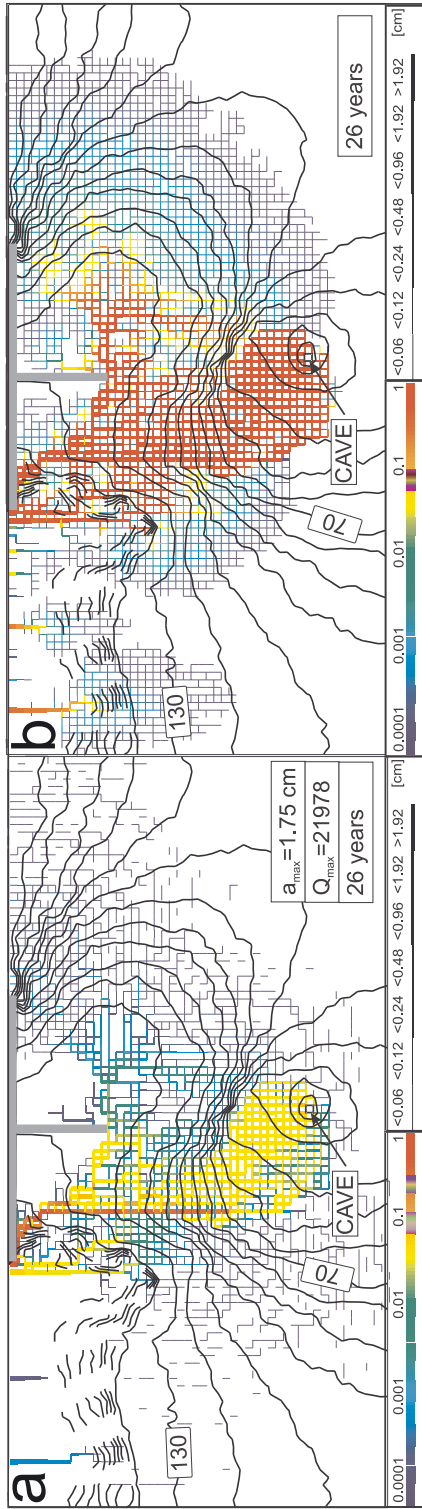


Figure 6.12: Evolution of fracture aperture widths, pressure heads, flow rates, and dissolution rates for Scenario A (statistical net) extended by a cave conduit deep below the dam site. Bar and color codes as in Figure 6.4

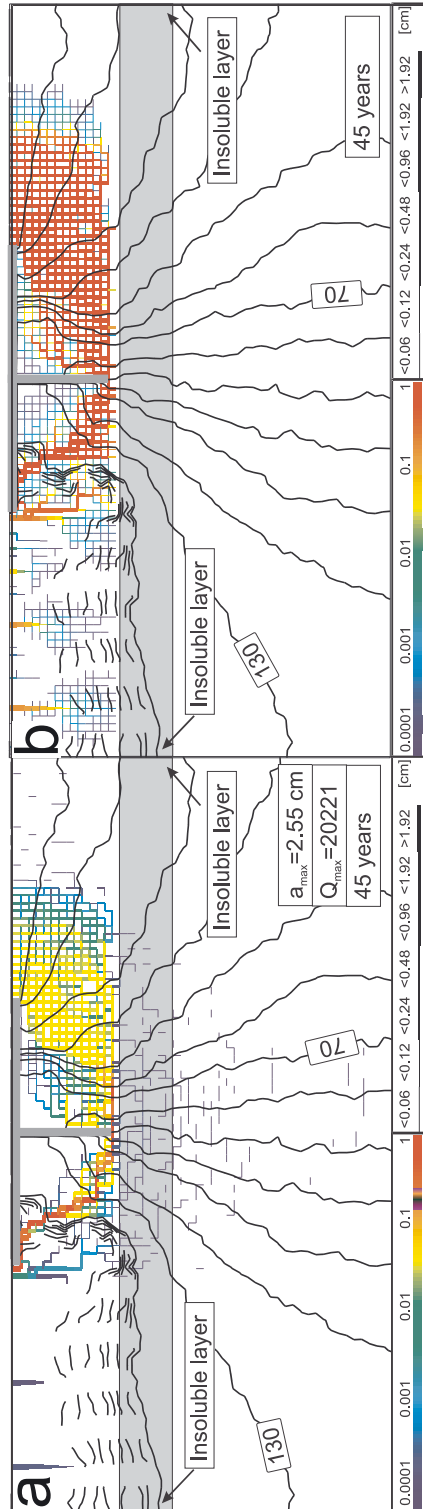


Figure 6.13: Fracture aperture widths, pressure heads, flow rates, and dissolution rates at breakthrough for Scenario A (statistical net), extended by an insoluble layer below the dam structure. The grouting curtain does not reach into the insoluble layer. Bar and color codes as in Figure 6.4

6. KARSTIFICATION BELOW DAM SITES

A completely different behavior results, if the grouting reaches into the insoluble layer as shown in Figure 6.14. Now the pathway to breakthrough below the dam is blocked. Widening of fractures occurs above the insoluble layer and also at its lower border. But breakthrough is prevented because all water leaking below the dam must pass through the insoluble layer, where fractures are not enlarged. Therefore, this layer limits flow rates, even if the permeability of the rock above increases significantly. This is also shown by the evolution of flow rates shown in Figure 6.15.

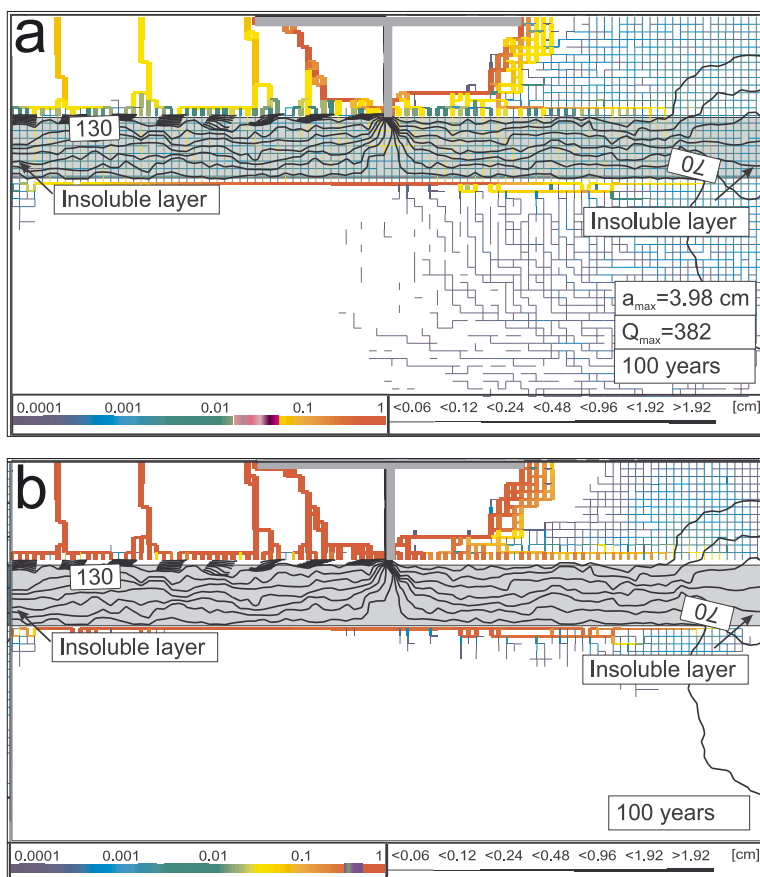


Figure 6.14: Fracture aperture widths, pressure heads, flow rates, and dissolution rates at breakthrough for Scenario A (statistical net) extended by an insoluble layer below the dam structure. The grouting curtain reaches down into the layer. Bar and color codes as in Figure 6.4.

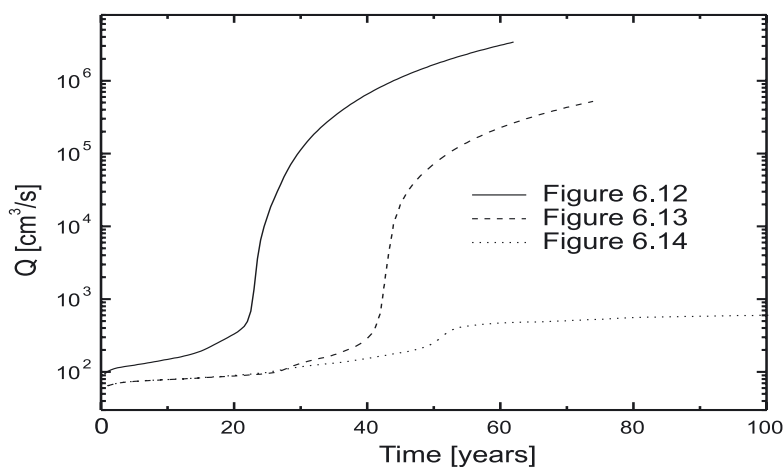


Figure 6.15: Evolution of total leakage in time for the geological settings in Figures 6.12, 6.13 and 6.14.



6. KARSTIFICATION BELOW DAM SITES

The head distribution also illustrates that flow from the reservoir passes the insoluble layer and emerges through this layer downstream. These few examples show the wide field of applications of our modeling, but also underline that it is necessary to understand the more simple scenarios to interpret more complex geological situations.

6.6 CONCLUSION

We have presented a model of the evolution of karstification under high hydraulic heads and unnaturally short pathways of flow from an input to an output in limestone terrains. Such conditions exist at dam sites. But also other hydraulic structures present similar conditions, e.g. impounded water in cave systems by blocked outflows (Milanović, 2000).

In the model we simulate the initial conductivity by a fracture network with average aperture widths of several 10^{-2} cm. This is highly idealized. Nevertheless, nets with fracture aperture widths of 0.02 cm with spacing of 10 m correspond to hydraulic conductivities of $8 \cdot 10^{-7}$ m s⁻¹, which is not unrealistic in karst. All our model runs show that under such conditions large dam sites exhibit increasing leakage rates within their life times. More complex geological settings can be incorporated into the model, such as open phreatic or vadose cave conduits beneath the dam. It is also possible to model stratigraphic layers of rock with varying properties with respect to hydraulic conductivity or dissolution kinetics. For instance, regions of low hydraulic conductivity, diverting flow paths to longer detours, will reduce leakage considerably and breakthrough times will be much longer. Furthermore, regions of insoluble rock under favorable conditions can prevent breakthrough.

To model a real situation detailed knowledge of the specific geological situation is needed. It is not a major problem to include this into the computer model where fracture widths, dissolution rate laws, lengths etc. can be assigned to each fracture individually. Blockage of fractures by clays, either in flow or dissolutional widening, is also inhibitors for karstification. In the model runs discussed here clay blockage is neglected. Therefore a conclusion that karstification below dam sites in any case must lead to problems within their lifetimes cannot be regarded as generally valid. On the other hand, however, in view of the results presented here, one should not exclude the possibilities that enhanced karstification may lead to problems and this should be considered in risk assessment. Natural processes, which are not common in terrains of insoluble rocks could cause problems in karst regions.





7. CONCLUSION AND FUTURE PERSPECTIVES

Within a time of only 15 years modeling of karst evolution from its initial state has achieved considerable progress. The first papers dealing with the evolution of single one-dimensional conduits until breakthrough were published by Dreybrodt (1990) and Palmer (Palmer 1991). In 1994 Groves and Howard presented a two dimensional model of an aquifer under conditions of laminar flow and expanded this to turbulent flow one year later (Groves and Howard 1994; Howard and Groves 1995).

These early papers motivated further work by our working group, and in this book we have summarized these results. We also have added a variety of new scenarios, which have not yet been published before.

In 1997 the group of Sauter and Liedl at the University of Tuebingen published their first results on the evolution of karst aquifers. They used a double permeability approach by coupling hydraulically a continuum representing the dense net of narrow fractures to a system of cylindrical pipes with diameters of few tenths of a millimeter. They allowed dissolution only in these pipes, which then evolve to karst conduits. Within the continuum dissolutional widening is not taken into account. A summary of the development of this work is given in the guest article by Bauer, Birk, Liedl and Sauter in this book.

Two years later Kaufmann and Braun (1999) suggested a model much more flexible by use of finite elements instead of finite differences. In a series of publications Kaufmann has used this tool to model scenarios of confined and unconfined aquifers and has also included flow in the vadose zone. An overview of this work is found in the second guest article in this book.

Karst evolution is governed by the initial boundary conditions. These are the hydrological parameters such, as length of karstifying pathways, their aperture widths, the hydraulic heads at input and output points, input of recharge into the aquifer etc. The chemical boundary conditions comprise the chemical composition of the input solutions, which depends on climate and on the present vegetation on the top of a karst plateau.

Finally the dissolution kinetics can vary from one type of rock to another one (Eisenlohr *et al.* 1999). One also has to take into account geological formations of insoluble rock within a karst system.

Any modeling therefore must use programs, which enable one to assign these many variables to each grid element (e. g. a selected fracture) individually. The results of such complex initial conditions are complex systems of conduits and karstified fractures, which cannot easily be interpreted.





7. CONCLUSION AND FUTURE PERSPECTIVES

To understand the processes, which are operative in the formation of karst one has to start with simple systems, such as a confined aquifer with properties uniform in all its fractures and with some input and output points at given heads. After having studied its evolution, more details are added. Instead of uniform aperture widths one can use statistically distributed ones and percolating networks of prominent fractures can be incorporated. This way hydraulic coupling between the statistically distributed net and the prominent fractures causes new interactions. Flow injected into the continuum of the net enhances dissolution, whereas water flowing back from the net into a prominent fracture inhibits it. Once this process has been worked out chemical boundary conditions can be added, such that mixing corrosion becomes active. This way new patterns of karstification emerge. Mixing corrosion can work deep inside the aquifer, where waters from different input points mix. There, the increasing permeability offers new ways for the evolution of channels and compared to an identical aquifer without mixing corrosion the patterns of evolving channels changes.

Each type of added complexity involves new parameters. In order to study the new processes one has to vary each of them. A large set of model runs is therefore unavoidable. Such runs are discussed in Chapter 4 for confined aquifers and in Chapter 5 for unconfined aquifers. From these results one can learn some general rules, which can help to understand some basic principles and to find out, which parameters are of relevance. It is the aim of this book to contribute to a better understanding of karst evolution not only in the world of models. By understanding the underlying processes and principles some of the knowledge may be helpful also in the field.

First applications are emerging at present. Dam sites constructed in limestone terrains impose new boundary conditions to the rock below. Extremely high hydraulic gradients are created by the impounded water, which could speed up karstification and could endanger the hydraulic structures during their lifetimes. This issue has been addressed in Chapter 6 and also to less extend in the guest contributions. With detailed knowledge on the geology of a special site further development of such programs could support construction of hydraulic structures.

Karst aquifers are hydrologically extremely complex. Prediction of their reactions to storm events and the transport of pollutants cannot simply be given. By use of karst modeling one may be able to create a virtual aquifer, where all the details are exactly known. Such aquifers could then be used to study their responses to input of contaminants and to meteoric events, or both simultaneously. Kaufmann in his contribution has taken first steps towards this target.

At present, however, the existing models are incomplete. Firstly they do not model the evolution in the vadose zone, which has a significant mutual interaction with the phreatic zone. Secondly all models are only two-dimensional projections. Hopefully in the future these problems will be addressed and possibly virtual karst aquifers can be generated at all stages of their evolution. They could replace the black box systems, which are examined at present.





8. BIBLIOGRAPHY

- Appelo, C.A.J. and Postma, D., 1993. *Geochemistry, groundwater and pollution*. A.A. Balkema, Rotterdam; Brookfield, VT, xvi, 536 pp.
- Bauer, S., Birk, S., Liedl, R. and Sauter, M., 1999. Solutionally enhanced leakage rates of dams in karst regions. In: A. Palmer, M.V. Palmer and I. Sasowsky (Editors), *Karst Modelling: Special publication 5*. Special Publication. Karst Waters Institute, Charles town, West Virginia.
- Bauer, S., Liedl, R. and Sauter, M., 2003. Modeling of karst aquifer genesis: Influence of exchange flow. *Water Resources Research*, 39(10): art. no.–1285.
- Bauer, S., R. Liedl, and M. Sauter, 2005. Modeling the influence of epikarst evolution on karst aquifer genesis, submitted to *Water Resources Research*.
- Bear, J. and Verruijt, A., 1987. *Modelling groundwater flow and pollution*. D. Reidel publishing company, Dordrecht, 414 pp.
- Beek, W.J., Mutzall, K.M.K. and Heuven, J.W.v., 1999. *Transport phenomena*. John Wiley & Sons, Chichester; New York, xii, 329 p. pp.
- Berkowitz, B., Naumann, C. and Smith, L., 1994. Mass-Transfer at Fracture Intersections – an Evaluation of Mixing Models. *Water Resources Research*, 30(6): 1765–1773.
- Bird, R.B., Stewart, W.E. and Lightfoot, E.N., 2002. *Transport phenomena*. John Wiley & Sons, Inc., New York; Chichester, xii, 895 p. pp.
- Bögli, A., 1964. Mischungskorrosion: Ein Beitrag zum Verkarstungsproblem. *Erdkunde*, 18: 83–92.
- Buhmann, D. and Dreybrodt, W., 1985a. The kinetics of calcite dissolution and precipitation in geologically relevant situations of karst areas.1. Open system. *Chemical geology*, 48(1–4): 189–211.
- Buhmann, D. and Dreybrodt, W., 1985b. The kinetics of calcite dissolution and precipitation in geologically relevant situations of karst areas.2. Closed system. *Chemical geology*, 53(1–2): 109–124.
- Dreybrodt, W., 1981. Mixing corrosion in $\text{CaCO}_3\text{-CO}_2\text{-H}_2\text{O}$ systems and its role in the karstification of limestone areas. *Chemical geology*, 32(3–4): 221–236.
- Dreybrodt, W., 1988. *Processes in karst systems: physics, chemistry, and geology*. Springer-Verlag, Berlin; New York, xii, 288 p. pp.
- Dreybrodt, W., 1990. The role of dissolution kinetics in the development of karst aquifers in limestone – A model simulation of karst evolution. *Journal of Geology*, 98(5): 639–655.





8. BIBLIOGRAPHY

- Dreybrodt, W., 1992. Dynamics of karstification: A model applied to hydraulic structures in kars terranes. *Applied Hydrogeology*, 1: 20–32.
- Dreybrodt, W., 1996. Principles of early development of karst conduits under natural and man-made conditions revealed by mathematical analysis of numerical models. *Water Resources Research*, 32(9): 2923–2935.
- Dreybrodt, W., 2000. Equilibrium chemistry of karst waters in limestone terranes. In: A. Klimchouk, D.C. Ford, A. Palmer and W. Dreybrodt (Editors), *Speleogenesis: Evolution of karst aquifers*. National Speleological Society, Huntsville, pp. 130–136.
- Dreybrodt, W. and Gabrovšek, F., 2000. Dynamics of the evolution of a single karst conduit. In: A. Klimchouk, D.C. Ford, A. Palmer and W. Dreybrodt (Editors), *Speleogenesis: Evolution of karst aquifers*. National Speleological Society, pp. 184–193.
- Dreybrodt, W., Lauckner, J., Liu, Z.H., Svensson, U. and Buhmann, D., 1996. The kinetics of the reaction $\text{CO}_2 + \text{H}_2\text{O} \rightarrow \text{H}^+ + \text{HCO}_3^-$ as one of the rate limiting steps for the dissolution of calcite in the system $\text{H}_2\text{O}-\text{CO}_2-\text{CaCO}_3$. *Geochimica Et Cosmochimica Acta*, 60(18): 3375–3381.
- Dreybrodt, W., Romanov, D. and Gabrovšek, F., 2002. Karstification below dam sites: a model of increasing leakage from reservoirs. *Environmental Geology*, 42(5): 518–524.
- Dreybrodt, W. and Siemers, J., 2000. Cave evolution on two-dimensional networks of primary fractures in limestone. In: A. Klimchouk, D.C. Ford, A. Palmer and W. Dreybrodt (Editors), *Speleogenesis: Evolution of karst aquifers*. National Speleological Society, Huntsville, pp. 201–211.
- Eisenlohr, L., Meteva, K., Gabrovšek, F. and Dreybrodt, W., 1999. The inhibiting action of intrinsic impurities in natural calcium carbonate minerals to their dissolution kinetics in aqueous $\text{H}_2\text{O}-\text{CO}_2$ solutions. *Geochimica Et Cosmochimica Acta*, 63(7–8): 989–1001.
- Erga, O. and Terjesen, S., 1956. Kinetics of the heterogenous reaction of calcium bicarbonate formation, with special reference to copper inhibition. *Acta Chimica Scandinavica*, 10: 872–875.
- Ewers, R., 1982. Cavern development in the dimension of length and breadth. PhD Thesis, McMaster University.
- Ford, D.C., 1999. Perspectives in karst hydrogeology and cavern genesis. In: A. Palmer, M. Palmer and I. Sasowsky (Editors), *Karst modeling: Special publication 5*. The Karst Waters Institute, Charles town, West Virginia, pp. 17–29.
- Ford, D.C. and Ewers, R., 1978. The development of limestone caves in the dimensions of length and depth. *Canadian Journal of Earth Sciences*, 15: 1783–1798.
- Ford, D.C. and Williams, P., 1989. *Karst geomorphology and hydrology*. Unwin Hyman, London, 601 pp.
- Freeze, R.A. and Cherry, J.A., 1979. *Groundwater*. Prentice-Hall, Englewood Cliffs, N.J., xvi, 604 p. pp.
- Gabrovšek, F., 2000. *Evolution of Early Karst Aquifers: From Simple Principles to Complex Models*. Založba ZRC, Ljubljana, 150 pp.
- Gabrovšek, F. (Editor), 2002. *Evolution of karst: From prekarst to cessation*. ZRC Publishing, Ljubljana, 448 pp.
- Gabrovšek, F. and Dreybrodt, W., 2000. Role of mixing corrosion in calcite-aggressive

8. BIBLIOGRAPHY

- H₂O-CO₂-CaCO₃ solutions in the early evolution of karst aquifers in limestone. *Water Resources Research*, 36(5): 1179–1188.
- Gabrovšek, F. and Dreybrodt, W., 2001. A model of the early evolution of karst aquifers in limestone in the dimensions of length and depth. *Journal of Hydrology*, 240(3–4): 206–224.
- Gabrovšek, F., Menne, B. and Dreybrodt, W., 2000. A model of early evolution of karst conduits affected by subterranean CO₂ sources. *Environmental Geology*, 39(6): 531–543.
- Gabrovšek, F., Romanov, D. and Dreybrodt, W., 2004. Early karstification in a dual-fracture aquifer: the role of exchange flow between prominent fractures and a dense net of fissures. *Journal of Hydrology*, 299(1–2): 45–66.
- Gale, J.E., 1987. Comparison of coupled fracture deformation and fluid flow models with direct measurement of fracture pore structure and stress-flow properties, 28th U. S. Symposium of Rock Mechanics, pp. 1213–1222.
- Ge, S.M., 1997. A governing equation for fluid flow in rough fractures. *Water Resources Research*, 33(1): 53–61.
- Groves, C.G. and Howard, A.D., 1994. Early development of karst systems.1. Preferential flow path enlargement under laminar-flow. *Water Resources Research*, 30(10): 2837–2846.
- Halihan, T., Sharp, J. and Mace, R., 1999. Interpreting flow using permeability at multiple scales. In: A. Palmer, M. Palmer and I. Sasowsky (Editors), *Karst modeling: Special publication 5*. Karst Waters Institute, Charles town, West Virginia, pp. 82–95.
- Hanna, R.B. and Rajaram, H., 1998. Influence of aperture variability on dissolutional growth of fissures in karst formations. *Water Resources Research*, 34(11): 2843–2853.
- Howard, A.D. and Groves, C.G., 1995. Early development of karst systems.2. Turbulent-flow. *Water Resources Research*, 31(1): 19–26.
- Incropera, F.P. and DeWitt, D.P., 2002. *Fundamentals of heat and mass transfer*. J. Wiley, New York, xix, 981 p. pp.
- James, A.N., 1992. *Soluble materials in civil engineering*. Ellis Horwood series in civil engineering. Ellis Horwood, Chichester, 434 pp.
- James, A.N. and Kirkpatrick, I.M., 1980. Design of foundations of dams containing soluble rocks and soils. *Quart. J. Eng. Geol.*, 13(3).
- Jeschke, A.A., Vosbeck, K. and Dreybrodt, W., 2001. Surface controlled dissolution rates of gypsum in aqueous solutions exhibit nonlinear dissolution kinetics. *Geochimica et cosmochimica acta*, 65(1): 27–34.
- Kaufmann, G., 2002. Karst aquifer evolution in a changing water table environment. *Water resources research*, 38(6): art. no.–1090.
- Kaufmann, G., 2003a. Numerical models for mixing corrosion in natural and artificial karst environments. *Water Resources Research*, 39(6): art. no.–1157.
- Kaufmann, G., 2003b. A model comparison of karst aquifer evolution for different matrix-flow formulations. *Journal Of Hydrology*, 283(1–4): 281–289.
- Kaufmann, G. and Braun, J., 1999. Karst aquifer evolution in fractured rocks. *Water Resources Research*, 35(11): 3223–3238.
- Kaufmann, G. and Braun, J., 2000. Karst aquifer evolution in fractured, porous rocks. *Water Resources Research*, 36(6): 1381–1391.



8. BIBLIOGRAPHY

- Klimchouk, A., Ford, D.C., Palmer, A. and Dreybrodt, W. (Editors), 2000. *Speleogenesis: Evolution of karst aquifers*. National Speleological Society, Huntsville, 527 pp.
- Lauritzen, S.-E., Odling, N. and Petersen, J., 1992. Modelling the evolution of channel network in carbonate rocks. In: J.A. Hudson (Editor), *ISRM Symposium: Eurock ,92*. Thomas Telford, pp. 57–62.
- Lee, C.-H. and Farmer, I.W., 1993. *Fluid flow in discontinuous rocks*. Chapman & Hall, London; New York, vi, 169 pp.
- Liedl, R., Sauter, M., Huckinghaus, D., Clemens, T. and Teutsch, G., 2003. Simulation of the development of karst aquifers using a coupled continuum pipe flow model. *Water Resources Research*, 39(3): art. no.–1057.
- Liu, Z.H. and Dreybrodt, W., 1997. Dissolution kinetics of calcium carbonate minerals in H₂O-CO₂ solutions in turbulent flow: The role of the diffusion boundary layer and the slow reaction H₂O+CO₂ reversible arrow H⁺+HCO₃⁻. *Geochimica et cosmochimica acta*, 61(14): 2879–2889.
- Lowe, D.J., 1992. *The origin of limestone caverns: in inception horizon hypothesis.*, Manchester Metropolitan University.
- Lowe, D.J. and Gunn, J., 1997. Carbonate speleogenesis: an inception horizon hypothesis. *Acta Carsologica*, 22(2): 457–481.
- Menne, B., 1998. *Carbonatolyse und Biokonservierung als Mechanism der Verkarstung und Speläogenese*. Beiträge zur Hydrogeologie, 49.
- Milanović, P.T., 1981. *Karst Hydrogeology*. Water Resources Publications, Littleton.
- Milanović, P.T., 2000. *Geological Engineering in Karst*. Zebra Publishing, Belgrade, 347 pp.
- Morse, J.W. and Mackenzie, F.T., 1990. *Geochemistry of sedimentary carbonates*. Developments in sedimentology; 48. Elsevier, Amsterdam, New York, 707 pp.
- Motyka, I. and Wilk, Z., 1984. Hydraulic structure of karst-fissured triassic rocks in the vicinity of Olkusz (Polska). *Kras i Speleologia*, 14(5): 11–24.
- Palmer, A.N., 1988. Solutional enlargement of opening in the vicinity of hydraulic structures in karst regions, 2nd Conference on Environmental Problems in Karst Terranes and Their Solutions, Nashville, Tennessee. Assoc. of Groundwater Sci. and Eng.
- Palmer, A.N., 1991. Origin and morphology of limestone caves. *Geological Society of America Bulletin*, 103(1): 1–21.
- Plummer, L.N., Wigley, T.M.L. and Parkhurst, D.L., 1978. Kinetics of calcite dissolution In CO₂-water systems at 5 °C To 60 °C and 0.0 to 1.0 atm CO₂. *American journal of science*, 278(2): 179–216.
- Press, W.H., Teukolsky, S.A., Vettering, W.T. and Flannery, B.P., 2002. *Numerical recipes in C: the art of scientific computing*. Cambridge University Press, Cambridge Cambridgeshire; New York, xxvi, 994 pp.
- Rhoades, R. and Sinacori, M., 1941. The pattern of groundwater flow and solution. *American Journal of Science*, 49: 785–794.
- Romanov, D., 2003. *Evolution of Karst Aquifers in Natural and Man Made Environments: A Modeling Approach*. Ph.D. thesis, University of Bremen.
- Romanov, D., Gabrovšek, F. and Dreybrodt, W., 2003a. Dam sites in soluble rocks: a model of increasing leakage by dissolutional widening of fractures beneath a dam. *Engineering Geology*, 70(1–2): 17–35.



8. BIBLIOGRAPHY

- Romanov, D., Gabrovšek, F. and Dreybrodt, W., 2003b. The impact of hydrochemical boundary conditions on the evolution of limestone karst aquifers. *Journal of hydrology*, 276(1–4): 240–253.
- Romanov, D., Dreybrodt W. and Gabrovšek, F., 2004a. Interaction of fracture and conduit flow in the evolution of karst aquifers. In: J.B. Martin, C.M Wicks and I.D. Sasowsky (Editors), *Hydrogeology and Biology of Post-Paleozoic Carbonate Aquifers: Special publication 7. The Karst Waters Institute, Charles town, West Virginia*, pp. 38–44.
- Romanov D., Gabrovšek F. and Dreybrodt W., 2004b. Modeling the evolution of karst aquifers and speleogenesis. The step from 1-dimensional to 2-dimensional modeling domains. www.speleogenesis.info, ISSN 1814–294X.
- Siemers, J. and Dreybrodt, W., 1998. Early development of karst aquifers on percolation networks of fractures in limestone. *Water Resources Research*, 34(3): 409–419.
- Stauffer, D. and Aharony, A., 1992. *Introduction to percolation theory*. Taylor & Francis, London; Washington, DC, x, 181 pp.
- Stewart, D.E. and Leyk, Z., 1994. *Meschach: Matrix Computation sin C*. Proceedings of the Centre for Mathematics and its Applications, 32. Centre for Mathematics and its Applications, ANU, Canberra, 240 pp.
- Svensson, U. and Dreybrodt, W., 1992. Dissolution kinetics of natural calcite minerals in CO₂-water systems approaching calcite equilibrium. *Chemical Geology*, 100(1–2): 129–145.
- Swinnerton, A., 1932. Origin of limestone caverns. *Geological Society of America Bulletin*, 34: 662–693.
- Tsang, Y.W. and Tsang, C.F., 1989. Flow channeling in a single fracture as a two-dimensional strongly heterogeneous permeable medium. *Water Resources Research*, 25(9): 2076–2080.
- Uromeihy, A., 2000. The Lar Dam; an example of infrastructural development in a geologically active karstic region. *Journal of Asian Earth Sciences*, 18(1): 25–31.
- Weyl, P., 1958. The solution kinetics of calcite. *Journal of Geology*, 66: 163–176.
- White, W.B., 1977. Role of dissolution kinetics in the development of karst aquifers. In: J. Tolson and F. Doyle (Editors), *Karst hydrogeology*. UAH.
- White, W.B., 1988. *Geomorphology and hydrology of karst terrains*. Oxford University Press, New York, ix, 464 pp.
- White, W.B. and Longyear, J., 1992. Some limitations on speleogenetic speculation imposed by hydraulics of groundwater flow in limestone. *Nittany Grotto Newsletter*, 10: 155–167.
- Worthington, S., 1999. A comprehensive strategy for understanding flow in carbonate aquifers. In: A. Palmer, M. Palmer and I. Sasowsky (Editors), *Karst modeling: Special publication 5. The Karst Waters Institute, Charles town, West Virginia*, pp. 30–37.





SIMULATION OF KARST AQUIFER GENESIS USING A DOUBLE PERMEABILITY APPROACH – INVESTIGATIONS FOR CONFINED AND UNCONFINED SETTINGS

SEBASTIAN BAUER,
STEFFEN BIRK, RUDOLF LIEDL,
MARTIN SAUTER

Abstract

This chapter summarizes the model development performed at the University of Tübingen employing a hybrid, continuum-discrete approach. During the last decade, a karst genesis model simulating karstification was developed based on the fundamental assumption of a dualistic character of the karst flow system. A hybrid continuum-discrete pipe flow model (CAVE) is used for the modelling, which represents the slow fissured flow system by a continuum approach and the rapid conduit draining system by a pipe network. Dissolution of carbonate rocks is accounted for by the widening of the cylindrical pipes. Exchange between the two flow systems is allowed and can under certain circumstances influence the karstification process considerably, affecting both the position of the developing karst conduit as well as development time. In this chapter, examples from confined artesian settings and unconfined settings are presented which represent two basic settings for karst development. First, the influence of exchange flow is investigated studying the development of a single conduit embedded in a fissured system. Karstification for confined settings is studied for gypsum karst both for a simplified scenario using a single conduit as well as for a conduit network. For unconfined settings, the influence of an evolving epikarst is considered for a conduit network in carbonate rock. Finally, man enhanced karstification at a dam site is investigated demonstrating that solutionally enhanced leakage may cause severe water losses from reservoirs built on soluble rock.

1. INTRODUCTION

The permeability of karst aquifers increases during their exposure to circulating ground water undersaturated with respect to calcite. Pathways in the soluble rock are enlarged and karst conduits thus develop. The evolution of karst aquifers depends on a variety of processes as well as geologic and climatic boundary conditions. The most important of these are summarized schematically in Figure 1.



Karst aquifers exhibit a dual flow system (Király, 1998), consisting of a fissured or “diffuse” system, which represents the bulk mass of permeable limestone, and a conduit system representing the karst conduit network. Exchange between the two systems is controlled by differences in hydraulic head as well as the hydraulic conductivities and the geometric setting. Geological and climatic factors influencing the evolution of a karst aquifer are aquifer geometry, fracture density, lithology as well as water temperature, recharge rate and partial pressure of CO_2 . The climate parameters may vary with time. Karst aquifer evolution is also affected by landscape development, i.e. the relative topographic level of the river and the evolving relief (Figure 1).

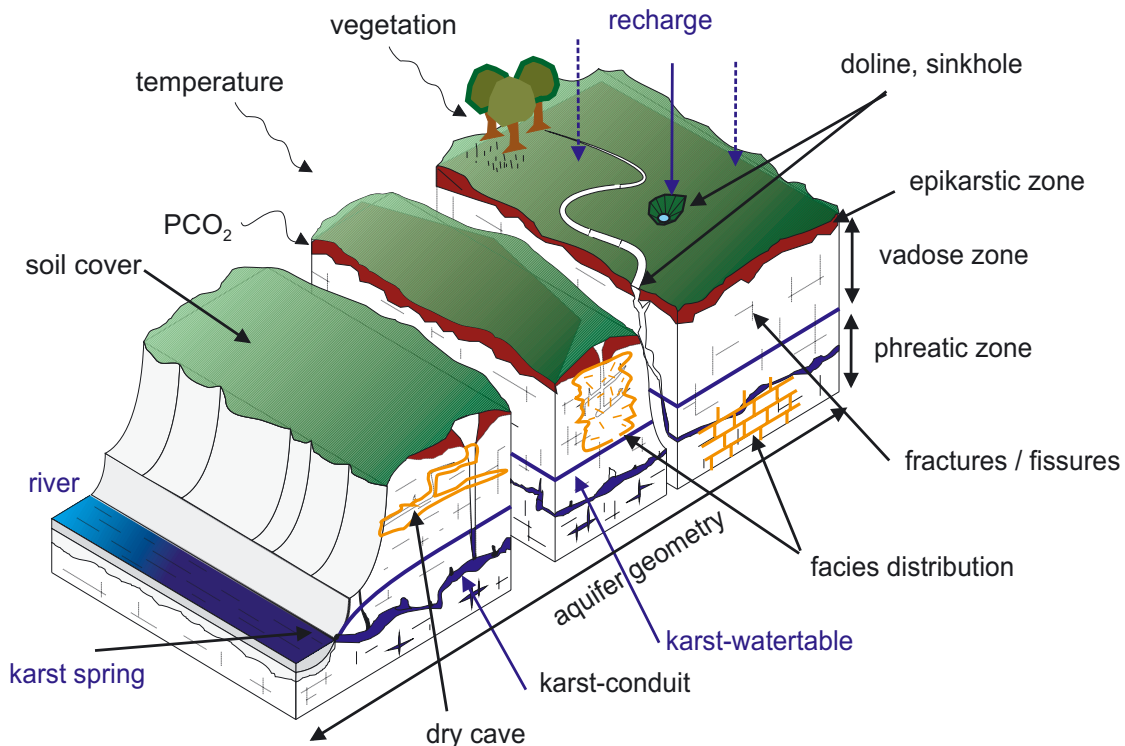


Figure 1: Major factors influencing the genesis of a karst aquifer (schematically): Geological conditions and climatic parameters.

The dual character of a karst flow system is widely recognized and stems from the existence of different types of porosities within a karst aquifer (Ford and Williams, 1989; Worthington *et al.*, 2000), which determine the type of flow prevailing in the aquifer (Ford, 1998). Schuster and White (1971) distinguished two major types of flow, which typically coexist in a karst aquifer. “Diffuse” flow prevails in the fissured system, which is characterized by a relatively low hydraulic conductivity and a high storage capacity and tends to behave as laminar flow in a porous medium. On the other hand, flow along the solutionally widened conduits focuses ground water flow paths and leads to turbulent flow conditions. The conduit system is characterized by a high hydraulic conductivity and a low storage capacity. This dualistic concept was later confirmed by Atkinson (1977),

Gunn (1985), Kiraly (1998) and White (1999) and is used in the work presented here (Figure 1). Worthington *et al.* (2000) use a triple porosity concept for the description of karst aquifers, i.e. the porosity of the porous rock matrix, the fissure porosity of the small fissures and the conduit porosity of the solutionally widened conduits. Following their classification, the fissured system used in this work comprises the matrix and fissured porosity, while the conduit porosity is simulated by the conduit system.

In the last decade, a number of numerical models have been developed to study karst aquifer genesis. This became possible after the quantification of calcite dissolution kinetics (Berner and Morse, 1974; Plummer *et al.*, 1978; Palmer, 1991). The most important ingredient of the models is the implementation of a higher order kinetics for calcite dissolution for waters close to equilibrium, which allows undersaturated water to penetrate deeply into the karst aquifer and still dissolve carbonate far from the infiltration point of meteoric water. This concept was first introduced by White (1977), who termed it the “kinetic trigger”, and has proven essential for the understanding of early karstification. Initially, models of a single phreatic parallel plate fracture or cylindrical conduit with simple boundary conditions were employed (Palmer, 1988, 1991; Dreybrodt, 1990, 1996). Subsequently, two dimensional models, capable of simulating the development of a conduit network, were developed by Lauritzen *et al.* (1992), Groves and Howard (1994a, 1994b), Howard and Groves (1995), Siemers and Dreybrodt (1998), Hanna and Rajaram (1998), Kaufmann and Braun (1999), Gabrovšek and Dreybrodt (2001), and most recently, Birk *et al.* (2003), Liedl *et al.* (2003), and Bauer *et al.* (2003). Some of these modelling efforts as well as much of the present knowledge on karst aquifer genesis is summarised in the speleogenesis book by Klimchouk *et al.* (2000).

Clemens *et al.* (1996) presented the first version of the CAVE model (Carbonate Aquifer Void Evolution). This was the first model to simulate the genesis of karst aquifers accounting for the dualistic behaviour of karst systems by a double permeability approach. The conduit flow system is represented by a network of cylindrical pipes, which are dissolutionally widened during the genesis simulation. The diffuse flow system or fissured system is represented by an equivalent porous medium and is coupled to the conduit system via linear exchange terms at the network intersections. An advanced version of the model was used by Bauer *et al.* (1999) to investigate leakage rates under dams in karst areas. They found, that leakage rates may be significantly enhanced, if exchange of water between the two flow systems is allowed for. Kaufmann and Braun (2000) coupled a pipe network to a continuum system and found that early karstification may be enhanced by the presence of a diffuse flow system. Gabrovšek and Dreybrodt (2001) demonstrated that the fissured system can in principle be represented by a dense network of small fissures and fractures. Romanov *et al.* (2002) found enhancement of karst development if dissolutional effects in the fissured system were considered. They could further demonstrate that dissolution in the fissured system is important only under very high hydraulic gradients.

This book chapter summarizes the development and applications of the karst genesis model CAVE by the karst group at the University of Tübingen (Clemens, 1998;



Hückinghaus, 1998; Birk, 2002; Bauer, 2002). After a mathematical model description of CAVE in section 2, this chapter introduces in section 3 the effects of exchange between the two flow systems by studying a single conduit embedded in a fissured system. Thus, the basic effects of exchange between the hydraulic systems are introduced, which are important for all further model applications presented here. Section 4 deals with karst genesis in confined settings using two scenarios from gypsum karst, the first with a single conduit, the second employing a conduit network. Section 5 presents karst genesis in an unconfined setting, where the epikarst and its evolution become important. Section 6, finally, studies karstification under a dam, i.e. under man made conditions.

2. MODEL FORMULATION

In order to model the characteristic flow patterns of karst aquifers, the dual structure of the flow system has to be considered (Figure 2). The model CAVE used in this work therefore is a double permeability model, simulating coupled flow in the fissured system and the conduit system. Transport of calcium ions, dissolution of calcite from the conduit walls and thus enlargement of the conduits is also considered.

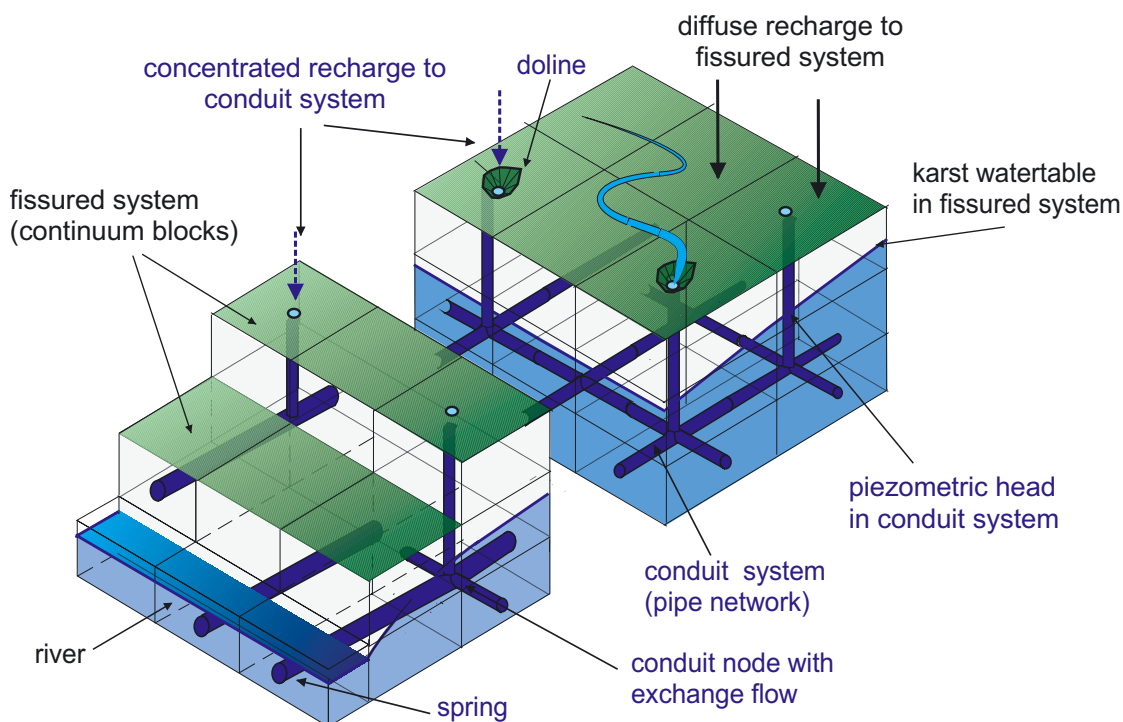


Figure 2: Schematic representation of the dualistic model concept of a karst aquifer. A typical spring catchment and its representation in the numerical model CAVE is depicted (compare Figure 1).



Ground water flow in the fissured system is described by a three dimensional continuum approach for heterogeneous and anisotropic flow (Bear, 1972):

$$\vec{\nabla} \left(K_F \vec{\nabla} h_F \right) + R_F - \Gamma_{ex} = S \frac{\partial h_F}{\partial t} \quad (1)$$

where K_F [$L T^{-1}$] is the tensor of hydraulic conductivity, h_F [L] is the piezometric head in the fissured system, R_F [T^{-1}] is recharge to the fissured system per unit volume, Γ_{ex} [T^{-1}] is exchange flow rate between the fissured and conduit system per unit volume, S [L^{-1}] is the specific storage coefficient of the fissured system and t [T] is time (Figure 3).

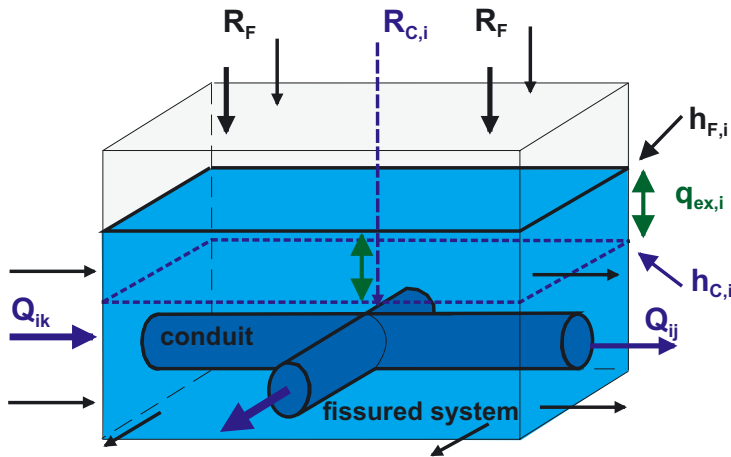


Figure 3: Hydraulics of CAVE represented for a control volume containing a conduit node embedded in a fissured system block. R_F and R_C are recharge to the fissured and conduit system, respectively, h_F and h_C are heads in the fissured and the conduit system, Q are the flow rates between adjacent nodes and q_{ex} is the exchange flow rate.

Flow in the conduit system, represented by cylindrical pipes intersecting at nodes, is governed by Kirchhoff's rule, stating that total inflow and total outflow balance at each node. For each node i therefore:

$$\sum_j Q_{ij} + R_{C,i} + q_{ex,i} = 0 \quad (2)$$

where Q_{ij} [$L^3 T^{-1}$] is the flow rate between node i and node j , $R_{C,i}$ [$L^3 T^{-1}$] is recharge to node i of the conduit system (used for the limited flow boundary condition) and $q_{ex,i}$ [$L^3 T^{-1}$] is the volumetric exchange rate between the conduit system and the fissured system at node i .

Q_{ij} is calculated according to the flow condition. In case of laminar flow, i.e. for Reynolds numbers less than 2300, the Hagen-Poiseuille formula is applied (White, 1988):

$$Q_{ij} = - \frac{a_{ij}^4 g \pi}{128 \nu} \frac{(h_{C,i} - h_{C,j})}{L_{ij}} \quad (3)$$

where g [$L T^{-2}$] is gravitational acceleration, L_{ij} [L] and a_{ij} [L] are the length and the diameter of the conduit between nodes i and j , ν [$L^2 T^{-1}$] is the kinematic viscosity of water and $h_{c,j} - h_{c,i}$ [L] is the head loss along the conduit.

For turbulent flow the Colebrook-White equation is used (Horlacher and Lüdecke, 1992):

$$Q_{ij} = -2Y \log \left(\frac{k_c}{3.71a_{ij}} + \frac{2.51\nu a_{ij}}{4Y} \right) \quad (4)$$

with k_c [L] the roughness of the conduit walls and

$$Y^2 = \frac{|h_{c,i} - h_{c,j}| g a_{ij}^5 \pi^2}{8L_{ij}} \quad (5)$$

Exchange of ground water between the fissured and the conduit system is modelled by a linear steady state exchange term (Barenblatt *et al.*, 1960), i.e. the flow rate is assumed to be proportional to the head difference between the flow systems and the exchange coefficient:

$$q_{ex,i} = \alpha_{ex,i} (h_{F,i} - h_{C,i}) \quad (6)$$

where α_{ex} [$L^2 T^{-1}$] is the exchange coefficient. α_{ex} is conceptually given by $\alpha A_F K_F$, where K_F [$L T^{-1}$] is the hydraulic conductivity of the fissured system, A_F [L^2] the exchange surface between the conduit and the fissured system, and α [L^{-1}] some factor, which depends on conduit geometry and might be interpreted as inverse fissure spacing. In this modelling approach, α_{ex} is the exchange flow model parameter and is independent of any other model parameter. Furthermore, the exchange coefficient is kept constant throughout each simulation. Integrating Γ_{ex} from equation 1 over the model domain equals the sum of all exchange flow rates $q_{ex,i}$, i.e.:

$$\Gamma_{ex} = \sum_i \delta(\vec{x} - \vec{x}_i) q_{ex,i} V^{-1} \quad (7)$$

where V [L^3] is the unit volume of the fissured system and \vec{x}_i is the location vector of node i .

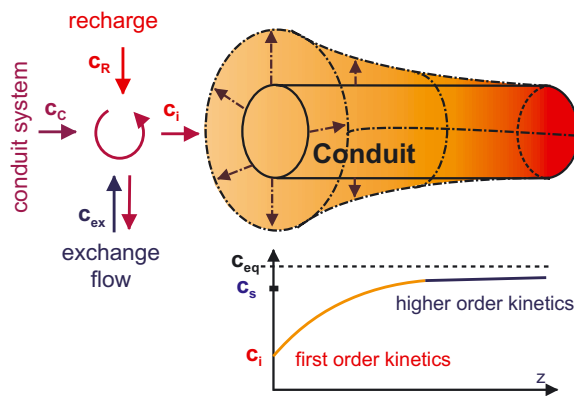


Figure 4: Chemistry of CAVE demonstrated at one node and pipe. Water derived from recharge, the upstream conduit system and exchange flow with the corresponding concentrations c_R , c_C and c_{ex} is mixed instantaneously and given to a conduit pipe with input concentration c_i . A possible concentration profile along the pipe is depicted as well, with c_s the switching concentration from first to higher order kinetics and c_{eq} the equilibrium concentration with respect to calcite.

Transport of calcium ions in the conduit system is described by the 1D advection equation, with an additional source term accounting for the increase in concentration due to calcium dissolution at the conduit walls (Figure 4):

$$\frac{\partial c}{\partial t} = -v \frac{\partial c}{\partial z} + \frac{A_c}{V_c} F(z, t) \quad (8)$$

where c [M L^{-3}] is the concentration of calcium, v [L T^{-1}] the flow velocity along a pipe, A_c/V_c [L^{-1}] is the (time dependent) surface to volume ratio of the conduit and F [$\text{M L}^{-2} \text{T}^{-1}$] is the dissolution rate of calcite per unit area. At the nodes of the conduit system additional inflow of calcium ions from the fissured system and from recharge is considered and instantaneous and complete mixing of all inflow concentrations is assumed.

Modelling of carbonate dissolution is based on experimental findings by Plummer *et al.* (1978), Palmer (1991), Buhmann and Dreybrodt (1985a, b), Svensson and Dreybrodt (1992), Dreybrodt *et al.* (1996), Liu and Dreybrodt (1997), and Eisenlohr *et al.* (1999). A summary and detailed discussion of the dissolution kinetics and rate limiting processes is provided by Dreybrodt (1998) and Dreybrodt and Eisenlohr (2000). They show that dissolution kinetics is fast if the calcium concentration is far from saturation with respect to calcite (first order kinetics) and slow if the concentration is close to saturation (higher order kinetics). The dissolution rate F is given by (Dreybrodt and Eisenlohr, 2000):

$$F(c) = \begin{cases} k_1(1 - c/c_{eq}) & , \quad c < c_s \\ k_n(1 - c/c_{eq})^n & , \quad c > c_s \end{cases} \quad (9)$$

where c_{eq} [M L^{-3}] is the calcium equilibrium concentration, n [-] is the reaction order, k_1 [$\text{M L}^{-2} \text{T}^{-1}$] is the rate constant for first order and k_n [$\text{M L}^{-2} \text{T}^{-1}$] for higher order dissolution. c_s [M L^{-3}] is the switching concentration, at which dissolution rates switch from lower to higher order kinetics. Different values of k_1 apply for laminar and turbulent flow conditions, accounting for the diffusion of species into the solution in the case of laminar flow. The amount of carbonate mass dissolved from the conduit walls is used to determine the increase of conduit diameter with time.

Over a period of three decades experimental investigation of gypsum dissolution (e.g., Liu and Nancollas, 1971; Barton and Wilde, 1971; Christofferson and Christofferson, 1976; James and Lupton, 1978; Lebedev and Lekhov, 1990; Opdyke *et al.*, 1997) did not find indications for higher order kinetics. Consequently, a first order rate law was assumed to be valid over the entire range of concentrations (e.g., Klimchouk, 2000a). Recently, however, Jeschke *et al.* (2001) provided evidence of a kinetic switch from first order to higher order kinetics at $c \approx 0.94 c_{eq}$, i.e., the dissolution of gypsum obeys the general rate law given by equation (9).

Flow in the fissured system is simulated by a central finite difference scheme using MODFLOW (McDonald and Harbaugh, 1988). Flow in the conduit system is solved utilizing an iterative Newton-Raphson method in order to deal with the non-linearities



occurring for turbulent flow conditions. Transport of calcium in the pipes is modelled by employing an upwind finite difference scheme with integrated reaction kinetics. The model supports a wide variety of boundary conditions, thus enabling a good approximation of natural situations.

3. INFLUENCE OF EXCHANGE FLOW ON EARLY KARSTIFICATION

In this section the influence of the existence of two hydraulic sub-systems, i.e. the conduit flow system and the fissured flow system, on early karstification is studied. The two flow systems interact via exchange flow processes, which may be directed either from the conduit to the fissured system or vice versa. By this process the two systems may act as sources or sinks for the other system, i.e. nearly saturated water from the conduit system may be exchanged to the fissured system and be replaced by more aggressive water. Thus, a strong impact of the exchange flow on the karstification process is found. This study is published more detailed in Bauer *et al.* (2003) and in an early version in Bauer *et al.* (2000).

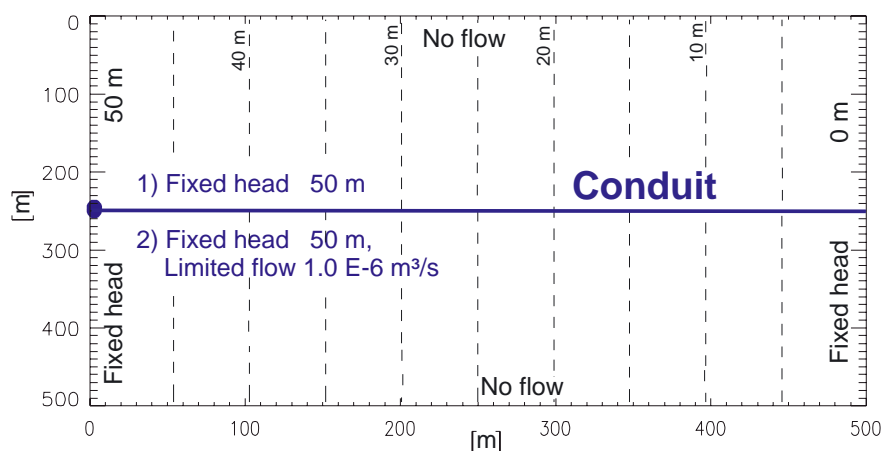


Figure 5: Plan view of the model scenario, depicting the single conduit embedded in the fissured system. Dashed lines are piezometric heads in the fissured system at the beginning of the simulation. The numbers at the upper boundary condition for the conduit correspond to the scenarios investigated, 1) designating a fixed head boundary condition, 2) a boundary condition switching from fixed head to fixed flow. From Bauer *et al.* (2003).

To study the effect of exchange flow between the conduit and the fissured system on the karstification of a carbonate rock aquifer, a simplified two dimensional scenario is used, as shown in Figure 5. A single conduit of 500 m length is placed within a fissured system of 500 m length and 500 m width. The conduit is subdivided into 50 pipes, each



10 m long, which are connected in series to form the conduit. The conduit represents a percolating pathway in the limestone, which can be enlarged by calcite dissolution. The initial diameter of the conduit is set to 2.5×10^{-4} m and a fixed head of 0 m at the outflow end of the conduit is used, representing the karst spring. Boundary conditions for the fissured system are a fixed head of 50 m at the upgradient end, of 0 m at the lower end and no flow at either side and the base. The hydraulic conductivity of the fissured system is 1.0×10^{-7} m s⁻¹, which is typical for the range given by Worthington *et al.* (2000), and the aquifer is assumed as confined. The temperature is set at 10 °C. Calcium equilibrium concentration is 2.0 mol m^{-3} , which corresponds to a partial pressure of CO₂ of about 0.01 and 0.045 atm for open-system and closed-system conditions, respectively. Water entering the conduit at the inflow end has a calcium concentration of 0 mol m^{-3} , while water entering the conduit from the fissured system shows equilibrium concentration. The first order kinetic rate constants for laminar and turbulent flow are $5.0 \times 10^{-7} \text{ mol m}^{-2} \text{ s}^{-1}$ and $1.0 \times 10^{-6} \text{ mol m}^{-2} \text{ s}^{-1}$, respectively. The kinetic constant for the higher, fourth order dissolution, active if calcium concentrations are above 0.9 of the equilibrium concentration, is $4.0 \times 10^{-4} \text{ mol m}^{-2} \text{ s}^{-1}$ for both laminar and turbulent flow. The kinetic parameters are taken from Dreybrodt and Eisenlohr (2000) and correspond to values used in recent karst genesis studies (e.g. Gabrovšek and Dreybrodt, 2001; Kaufmann and Braun, 2000; Romanov *et al.*, 2002). The setting described here represents a covered karst situation, i.e. carbonate rocks overlain by impermeable horizons, with no meteoric recharge to the aquifer. Water can enter the system only at the upgradient boundary. The lower fixed head boundary condition of the fissured system could possibly represent a river, a lake, or an alluvial aquifer, which has a higher hydraulic conductivity than the fissured system.

The temporal development of the conduit for the case of no exchange flow is shown in Figure 6. Conduit diameters are enlarged gradually at first, but almost uniformly along the conduit (Figure 6a, 20000 a). This is because fourth order kinetics is active along almost the whole conduit (relative concentration > 0.90), as shown in Figure 6c, 20000 a. Being controlled by the smallest diameters at the conduit outflow flow rates are low and constant along the entire conduit (Figure 6b). After 40000 a, conduit diameters have been widened to more than 0.001 m at the outflow end, and to more than 0.01 m at the inflow end (Figure 6a, 40000 a), due to the range of first order kinetics propagating into the conduit (Figure 6c, 40000 a). The distance across which first order kinetics prevails propagates now quickly along the conduit, and reaches the outflow end only 800 a later, i.e. after 40800 a. Turbulent flow becomes active, first at the outflow end of the conduit, then along the whole conduit length and the conduit is uniformly enlarged (Figure 6a, 41300 a) with first order turbulent kinetics (Figure 6c, 41300 a), resulting in a dramatic increase in flow rates (Figure 6b). The time until first order kinetics has propagated through the conduit and completely dominates further enlargement is termed the “breakthrough time” (Dreybrodt, 1990) and represents an important measure for early karstification. Breakthrough time in the case of no exchange flow is 40800 a for the parameters chosen here (Figure 6c, 40800 a).

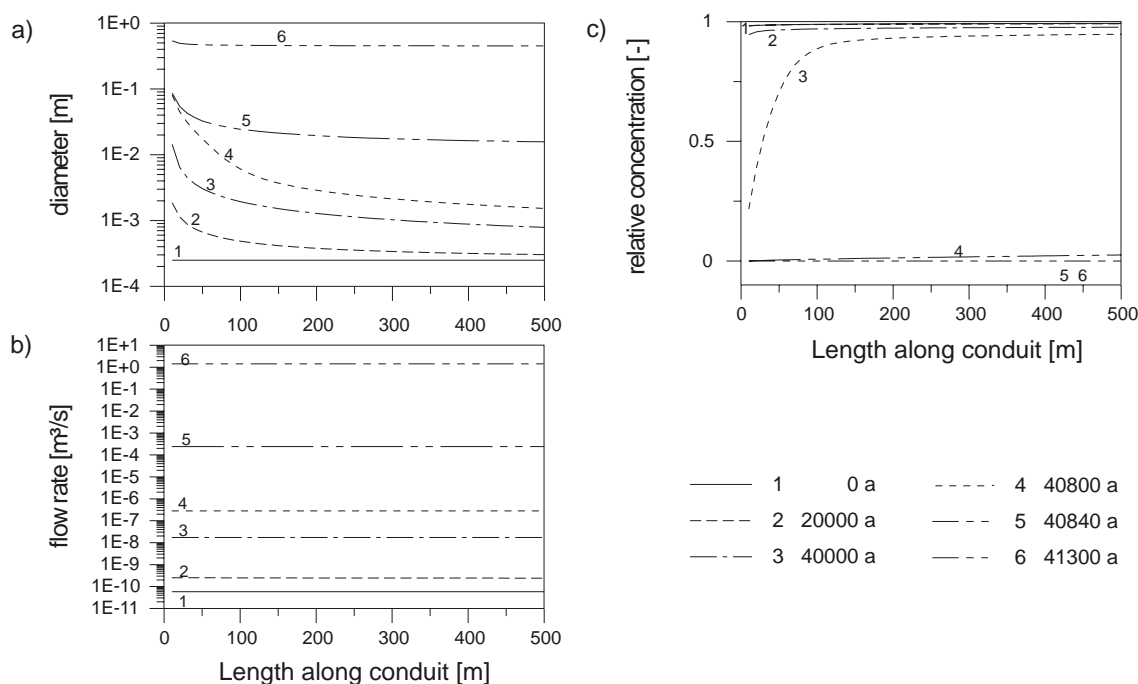


Figure 6: Temporal development of diameter, flow rate and relative concentration of the conduit for the case of no exchange flow. Direction of flow is from left to right. From Bauer *et al.* (2003).

Figure 7 shows the development of the conduit, if exchange flow is allowed for. An exchange coefficient of $\alpha_{ex} = 1.0 \times 10^{-7} \text{ m}^2 \text{ s}^{-1}$ is used in the simulations. Conduit development is much quicker than without exchange flow and breakthrough time is 392 a only. Before breakthrough, conduit diameters are widened nearly all along the conduit (Figure 7a, 390 a) as compared to the case of no exchange flow, where diameters were widened mainly at the conduit entrance (Figure 7a, 40000 a). Flow rates now differ along the conduit before breakthrough (Figure 7b, 390 a), as compared to the case of no exchange flow, where flow rates were constant along the conduit (Figure 7b, 40000 a). When the inflow end of the conduit has been somewhat enlarged, the hydraulic head in the conduit increases near the inflow end due to the higher hydraulic conductivity of the conduit. In contrast, the hydraulic heads of the fissured system remain unaffected due to the high storage capacity of the fissured system and correspond to curve 1 in Figure 7e all through the simulation. Therefore, the hydraulic head in the conduit just down-gradient of the inflow end is higher than in the fissured system (Figure 7e, 200 a or 350 a) and exchange flow is directed into the fissured system. As a result, water from the conduit system with a high calcium concentration and low aggressivity is directed into the fissured system and water with a low calcium concentration, i.e. more aggressive water, is resupplied to the conduit from the fixed head boundary up-gradient. Therefore, exchange flow provides an additional sink to water high in calcium and, as a result, acts as a mechanism enabling the deep penetration of aggressive water. This effect is shown in Figure 7c, 350 a, where first order dissolution (relative concentra-

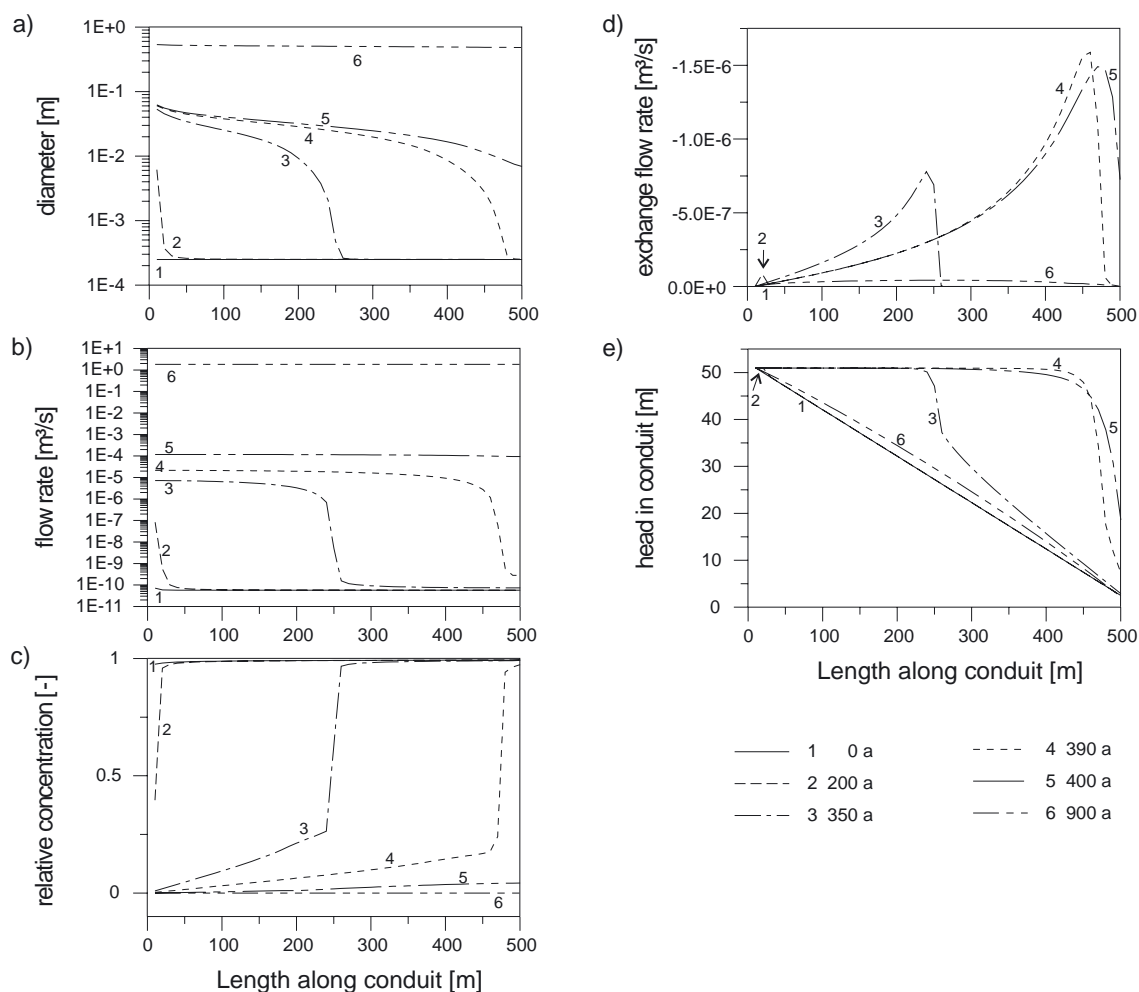


Figure 7: Temporal development of diameter, flow rate, relative concentration and exchange flow rate of the conduit in scenario 1, if exchange flow is accounted for. From Bauer *et al.* (2003).

tion < 0.9) has propagated to about half the conduit length. In the case of no exchange flow, relative concentrations smaller 0.9 are only found near the conduit inflow end (Figure 6c, 40000 a).

Without exchange flow, flow through the conduit is limited by the smallest diameter at the outflow end of the conduit (Figure 6b, 40000 a), while flow rates before breakthrough at the inflow end of the conduit are much higher than at the outflow end, if exchange flow is accounted for (Figure 7b, 350 a). The amount of water exchanged to the fissured system rises during the evolution of the conduit (Figure 7d). The region of high infiltration into the fissured system propagates down-gradient along the conduit until it reaches the outflow end of the conduit at breakthrough time (Figure 7d, 400 a). In this region conduit flow rates (Figure 7b, 390 a) and diameters (Figure 7a, 390 a) decrease along the conduit by orders of magnitude, while relative concentrations increase to more than 0.9 and kinetics switch from first to fourth order (Figure 7c, 390 a).



A parameter study conducted in Bauer *et al.* (2003) and not shown here in detail demonstrated that the evolution of the conduit for the boundary conditions applied is always enhanced, if exchange flow is accounted for. The reduction in breakthrough time depends on the values of the exchange coefficient and the hydraulic conductivity of the fissured system. Setting $\alpha_{ex} = K_F \times 1 \text{ m}$, the hydraulic conductivity of the fissured system is always limiting, not the exchange coefficient. Exchange flow is most efficient in reducing breakthrough times, if the exchange coefficient is chosen in such a way that the ratio of exchange flow to flow in the conduit is large and at the same time the ratio of exchange flow to flow in the fissured system is small. For an initial diameter of $2.5 \times 10^{-4} \text{ m}$ and $K_F = 1.0 \times 10^{-7} \text{ m s}^{-1}$ as used here, this is the case for $1.0 \times 10^{-12} \text{ m}^2 \text{ s}^{-1} < \alpha_{ex} < 1.0 \times 10^{-7} \text{ m}^2 \text{ s}^{-1}$.

Summarizing, this chapter demonstrates that if exchange flow is accounted for, karstification of small conduits with initial diameters in the order of 10^{-5} m to some 10^{-4} m may be faster by a factor of 100 as compared to the case without exchange flow. A positive feedback is active, as conduit growth leads to higher potentials in the conduit system and thus to higher exchange flow rates to the fissured system, which causes lower concentrations in the conduit and thus enhances further dissolutional growth. This finding is universal and valid for all early karstification, as due to the boundary conditions corresponding to early karstification exchange flow will always be directed into the fissured system. The representation of the fissured system in the model, e.g. by a fracture network of small fractures, as used by Romanov *et al.* (2002) or by an equivalent porous medium as used here (Bauer *et al.*, 1999; this work) has no effect on this basic finding. Romanov *et al.* (2002) could also show, that dissolution in the fissured system is negligible, if the openings of the fissures in the fissured system are smaller than the initial diameters of the conduit system and if the overall hydraulic gradient is smaller than about 1.0, which is always the case in our model runs. Together with the “kinetic trigger” (White, 1977) concept of higher order dissolution kinetics, this effect of exchange flow thus represents a most important ingredient for the understanding of early karstification. Exchange flow thus represents a powerful mechanism enhancing early karstification of limestone terrains.

4. KARST DEVELOPMENT IN CONFINED SETTINGS

According to Klimchouk (2000b) karst development “commonly – though not always – commences in a deep seated intrastratal setting”, i.e., under confined conditions in artesian basins. The concept of “transverse speleogenesis” introduced by Klimchouk (1997, 2000b) describes the mechanisms of cave development in this type of setting. Hydraulic heads increase with depth in artesian basins, the vertical hydraulic gradient being maximal in areas of topographical lows. Thus, flow is upward, preferentially discharging into valleys. These discharge areas are believed to be most favourable for conduit development, as upward flow of solutionally aggressive water from insoluble



aquifers causes an enlargement of conduits in the overlying soluble units. Consequently, the permeabilities of the soluble units increase with time, and the hydrogeological function of the soluble units changes from low permeable aquitards towards highly permeable karst aquifers.

The upper part of Figure 8 shows a conceptual model of an intrastatal setting with two confined aquifers consisting of insoluble materials, such as sandstone, separated by an initially less permeable soluble unit. The topographic height at the left hand side acts as a recharge area. Discharge is mainly to the right. In addition, a river cutting into the confining layer in the centre of the model domain drains the upper aquifer. This set up imposes a hydraulic head gradient between the aquifers and causes an upward directed flow from the lower to the upper aquifer.

The lower part of Figure 8 illustrates the translation of this conceptual setting into a numerical model. The model domain is a vertical slice with a length of 506 m and a total thickness of 70 m, subdivided into a soluble unit of 22 m and two insoluble aquifers of 24 m thickness. In the numerical model the slice is represented by a vertical layer of the continuum model. The slice is vertically discretized by 35 rows of 2 m width. Horizontally, it is subdivided into 95 columns. The width of the columns is set to 2 m in the

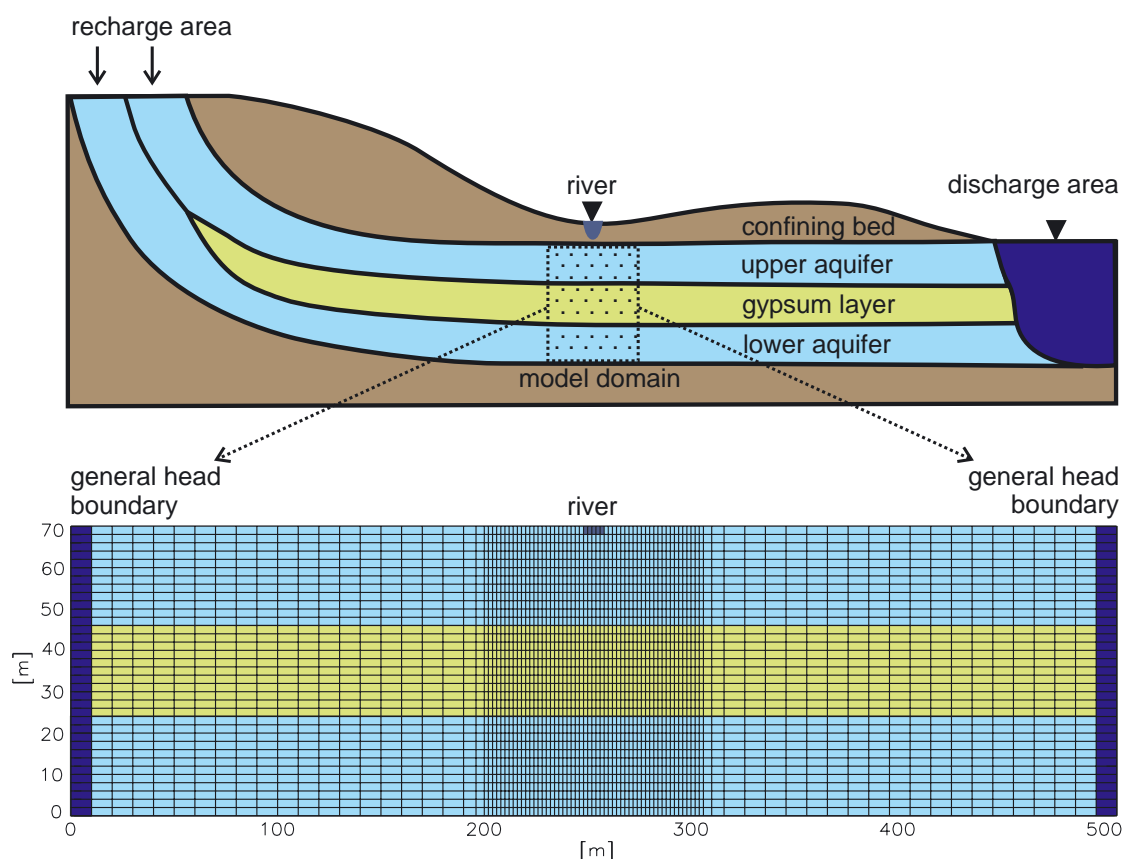


Figure 8: Conceptual model of an artesian setting and finite-difference grid of the corresponding numerical model. From Birk *et al.* (2003).



centre of the model domain and extended to 10 m toward the left and right boundaries. The transmissivity is set to $10^{-5} \text{ m}^2 \text{ s}^{-1}$ for the aquifers and $10^{-8} \text{ m}^2 \text{ s}^{-1}$ for the soluble unit. Thus, for a slice of 10 m width the hydraulic conductivities are 10^{-6} m s^{-1} for the aquifers and 10^{-9} m s^{-1} for the fissured system of the soluble unit. Head dependent flow boundaries (general head boundary and river boundary, see McDonald and Harbaugh, 1988) are used to quantify flow in or out of the model domain.

Both single conduit development and development of a conduit network are simulated in the conceptual setting defined above. As this type of setting frequently occurs in the gypsum karst of the Western Ukraine (Klimchouk, 2000c), the soluble unit in the model scenarios is understood as a gypsum layer. Following Klimchouk (2000a), gypsum dissolution is assumed to be entirely controlled by diffusion, thus obeying a first order rate law. A kinetic switch to a higher order rate law close to chemical equilibrium, as observed by Jeschke *et al.* (2001), has not been taken into account.

Single conduit development

Below the river a single conduit of 0.4 mm diameter intersects the gypsum layer (Figure 9). At four nodes, subdividing the conduit into three pipes, an exchange of water between the conduit and the fissured system is allowed. The value of the exchange coefficient at the nodes that couple the lower and upper aquifer to the conduit is set to a value that keeps the hydraulic resistance between the two nodes equal to the hydraulic resistance between two adjacent cells within the aquifers if the hydraulic resistance of the conduit is negligible. As it is generally believed that the exchange coefficient is proportional to the hydraulic conductivity of the fissured system (cf. section 2 of this chapter), the exchange coefficient is set three orders of magnitude smaller for the nodes in the gypsum layer. Since flow is directed upward, dissolved gypsum cannot be transported downward into the lower aquifer. Therefore, the conduit is supplied with aggressive water ($c = 0$) from the lower aquifer. Water flowing from the gypsum layer into the conduit, is assumed to be saturated with respect to gypsum ($c = c_{eq} = 15 \text{ mol m}^{-3}$).

The simulation results illustrate how conduit enlargement changes the flow field through time (Figures 9 and 10). At the early stage of conduit development the water flowing from the conduit into the upper aquifer is saturated with respect to gypsum. The uppermost pipe is not enlarged and restricts the discharge through the conduit. Hence, conduit enlargement is very slow and the hydraulic head gradient between the aquifers is maintained (Figure 9a). However, the conduit entry (i.e., pipe 1) is enlarged by inflow of highly undersaturated water from the lower aquifer. Therefore, the higher hydraulic head of the lower aquifer propagates upward with time along the conduit. This causes an increase of the hydraulic head difference between the conduit and the surrounding fissured system and thus a transfer of water from the conduit into the fissured system of the gypsum layer (Figure 9b). Hence, in the lower part (i.e., pipe 1 and pipe 2) of the conduit, flow rates increase (Figure 10) and outflow concentrations decrease. Aggressive





SIMULATION OF KARST AQUIFER GENESIS USING A DOUBLE PERMEABILITY APPROACH

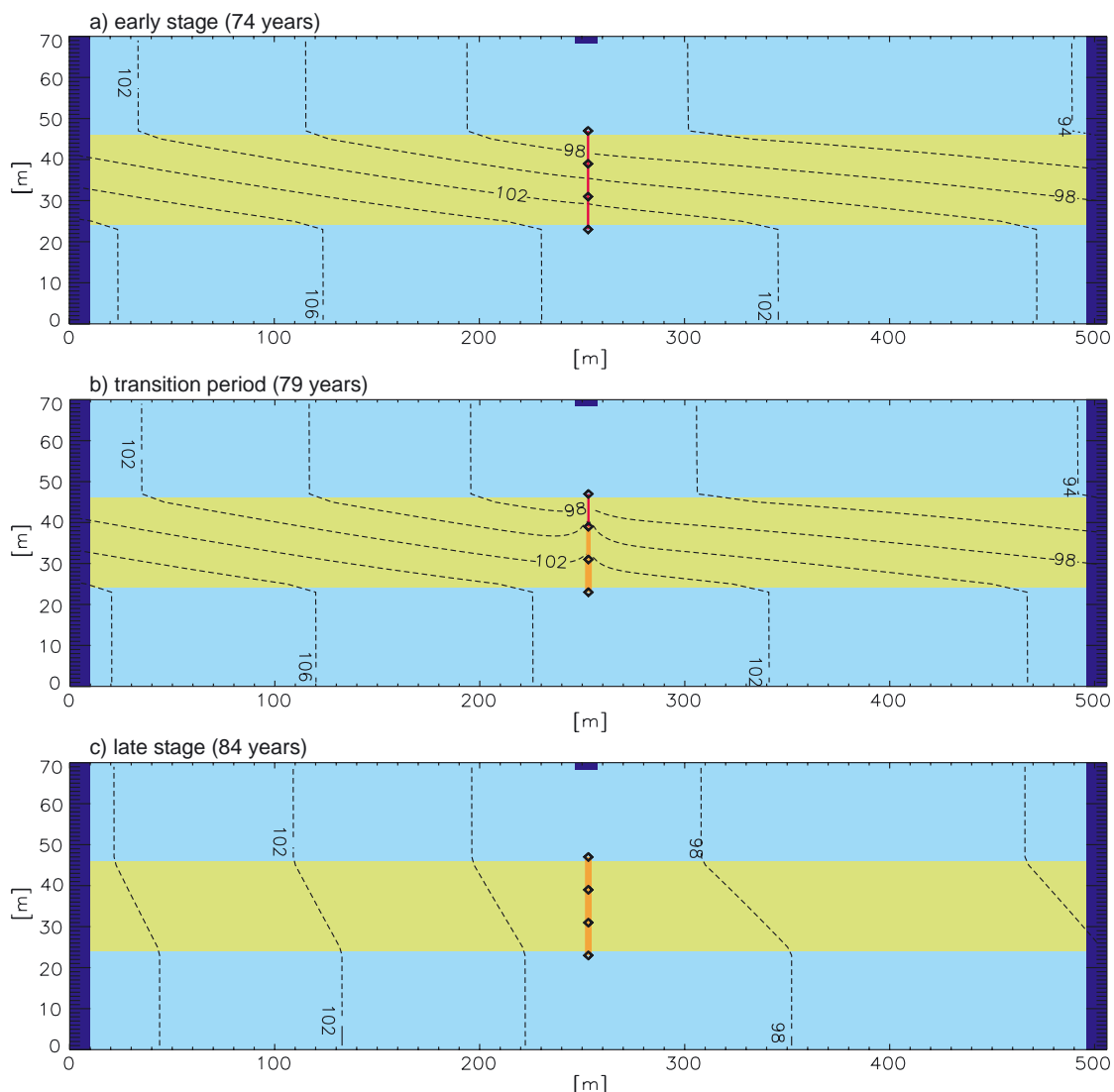


Figure 9: Different stages of conduit development. Dashed lines are hydraulic heads in the fissured system (in m). Pipe diameters of < 1 mm, < 10 mm, and < 100 mm are represented by solid lines of single, double, and triple thickness, respectively. Orange coloured pipes indicate that c/c_{eq} in the outflow is less than 0.9. From Birk *et al.* (2003).

water propagates further upward, and eventually water emerging at the outlet to the upper aquifer becomes undersaturated with respect to gypsum. Under these conditions, the mutual enhancement of discharge and solutional enlargement leads to a breakthrough. This breakthrough abruptly and strongly reduces the hydraulic head difference between lower and upper aquifer, as a highly permeable pathway is established between the two aquifers (Figure 9c). After breakthrough the hydraulic resistance of the conduit is smaller than that of the two aquifers. Discharge through the conduit is then controlled by the hydraulic boundary conditions and the transmissivity of the aquifers only and no longer by the conduit diameter as during the early stage of conduit development. Since





hydraulic boundary conditions are kept constant through time, the flow rate remains constant after breakthrough (Figure 10). Consequently, flow conditions do not switch to turbulent but stay laminar.

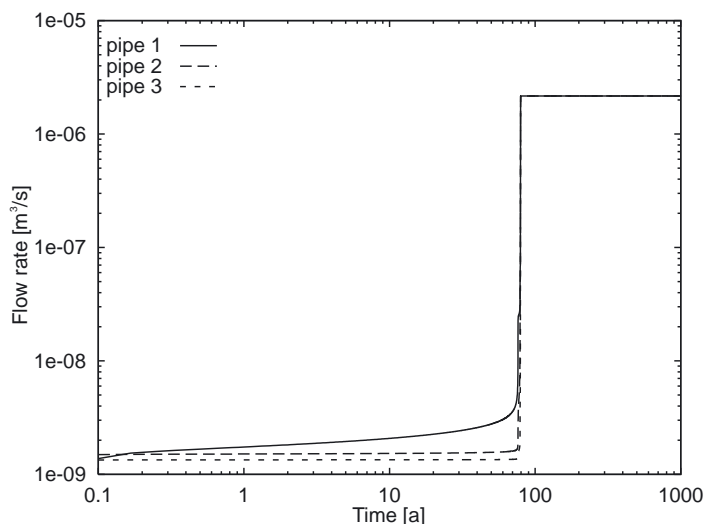


Figure 10: Flow rates in the pipes; “pipe 1” is at the bottom, “pipe 3” at the top of the gypsum layer, “pipe 2” is in between. From Birk *et al.* (2003).

The model scenario described above demonstrates that the hydraulic boundary conditions for the conduit system are time variant though boundary conditions for the overall system are constant in time. This is due to feedback of solutional conduit enlargement on the overall hydraulic system, which changes according to the decreasing hydraulic resistance of the conduit. The sequence of three pipes can be treated as an isolated conduit with a single outlet only at the beginning of the simulation and after breakthrough. In between, there is a time period during which conduit enlargement and subsequent head changes induce transient flow of conduit water into the fissured system at the nodes in the gypsum layer. The importance of this effect can be demonstrated by switching off the exchange flow at the conduit nodes within the gypsum layer. Under these conditions breakthrough does not occur for a simulation time of five million years.

Conduit network

In order to study the development of conduit networks in confined, intrastatal settings, a regular network, consisting of 63 pipes of 8 m length each, is linked to the continuum model. The boundary conditions for the pipe network are analogous to the above scenario. Flow from the upper or the lower aquifer into the pipe network is assumed to be without dissolved gypsum, flow from the fissured system of the gypsum layer into the pipe network is assumed to be saturated with respect to gypsum.

In a pipe network with constant initial diameters of 0.4 mm, a single conduit develops in vertical direction beneath the river (Figure 11), where the hydraulic gradient is steepest. As demonstrated for a single conduit (Figure 9), breakthrough strongly reduces the hydraulic head difference between lower and upper aquifer.



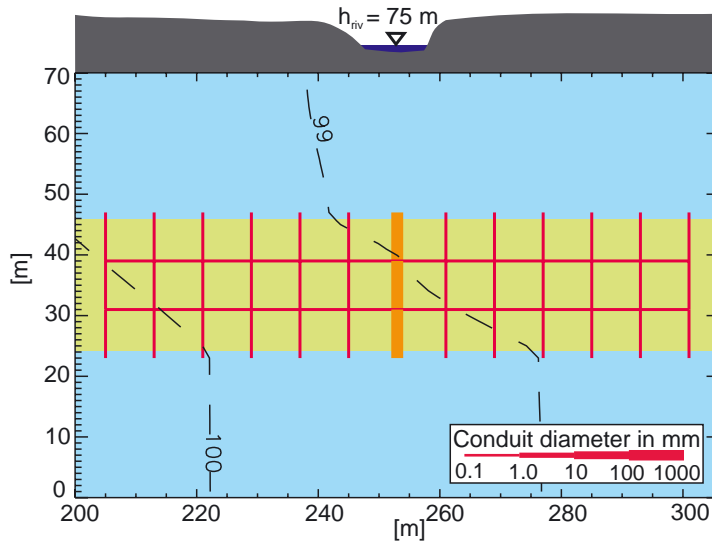


Figure 11: Conduit diameters and hydraulic heads (dashed lines) in the fissured system (in m) after 1000 a of solutional conduit development in a network with initial diameters of 0.4 mm. Orange coloured pipes indicate that c/c_{eq} in the outflow is less than 0.9. From Birk *et al.* (2003).

Hence, the hydraulic boundary conditions for the pipe network change at all entry and exit points almost simultaneously. Due to the considerably reduced hydraulic gradients, further conduit development is subsequently limited to the already enlarged conduit, whereas solutional widening of other pathways ceases after breakthrough. Thus, only a single vertical conduit is enlarged after a simulation period of 1000 a (Figure 11), although breakthrough occurred already after 100 a.

The simulation result demonstrates that horizontal pathways do not develop in a setting with predominant vertical hydraulic gradients if horizontal flow is not structurally preferred. Field observations from the Western Ukraine suggest that laterally extended fissure networks, which are poorly connected vertically, predetermine cave patterns (Klimchouk *et al.*, 1995; Klimchouk, 2000c). To account for such structural preferences, the initial diameters of the uppermost vertical pipes are reduced to 0.25 mm in the following simulation, while all other initial pipe diameters remain unchanged at 0.4 mm. Figure 12 shows the conduit system developed after 1000 a. In contrast to the scenario without structural preferences depicted in Figure 11, the smaller diameter of the uppermost vertical pipes inhibits the enlargement of a vertical pathway between the lower and the upper aquifer. Hence, the hydraulic head difference between the two aquifers is maintained. Beneath the horizon with the small diameter pipes, a horizontal pathway, which is connected to the lower aquifer by two vertical conduits, has been solutionally enlarged. As indicated by the colouration of the pipes, gypsum dissolution is still active in almost all sections of the solutionally enlarged conduit system (Figure 12). Only at the “dead end” on the right hand side of the horizontal conduit, the water is close to saturation with respect to gypsum. A hydraulic head increase caused by the incision of valleys may finally trigger breakthrough of a vertical pipe at the top of the gypsum, after which conduit development will cease everywhere apart from the pathways already established between the two aquifers (Birk *et al.*, 2003).

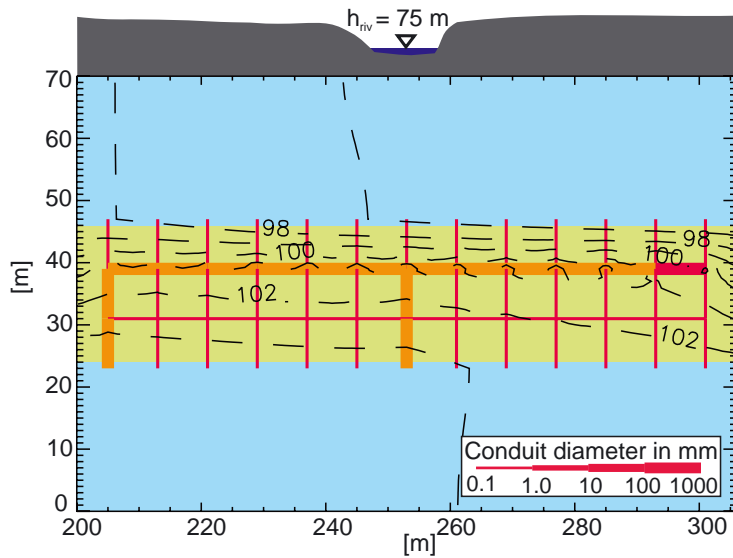


Figure 12: Conduit diameters and hydraulic heads (dashed lines) in the fissured system (in m) after 1000 a of solutional conduit development in a network where the initial diameters of the uppermost vertical pipes were 0.25 mm and 0.4 mm for all other pipes. Orange coloured pipes indicate that c/c_{eq} in the outflow is less than 0.9. From Birk *et al.* (2003).

5. KARST DEVELOPMENT IN UNCONFINED SETTINGS

In unconfined settings, as shown schematically in Figure 1, additional processes and karst features have to be considered for the simulation of karst aquifer evolution. Firstly, karst development in an unconfined setting is directly linked to the land surface and is therefore influenced by changes at the land surface, i.e. doline development, river incision as well as climatic changes. Thus recharge distribution to the underlying karst aquifer changes both spatially and with time as a result of changes in the above factors. These effects are transmitted to the main carbonate rock below by the epikarst, a perched aquifer system assumed to be located at the top of the unconfined carbonate rock just below the land surface. Secondly, in unconfined settings one has to consider dropping karst water tables, as karst conduits grow and transmit water more easily with time, but inflow is restricted by the recharge rate (Bauer *et al.*, 2002). Thus, in contrast to confined settings, not the hydraulic conductivity but the available recharge water is limiting flow through the karst aquifer in the later stages of development. This section presents the effects of a time variant recharge distribution due to epikarst development and an approach to physically model its hydraulic characteristics and geometry in space and time.

The term epikarst describes a horizon at the top of the vadose zone of a karst aquifer characterized by an enhanced storage capacity (Mangin, 1975). Later, Williams (1983, 1985) provided more experimental evidence for the existence of the epikarst, also referred to as subcutaneous zone. The epikarst may be visualized as a horizon of a few meters thickness with a high porosity and high permeability. The base of the epikarstic zone may be formed by a vertical decrease in fracture frequency and aperture, a capillary barrier in the narrowing fissures or by clay residues from the dissolution process blocking the fissures. A perched temporary water table defines the upper surface, which slopes towards areas of rapid vertical percolation (Williams, 1983). Thus lateral flow is



induced and water is focused into larger shafts leading to the phreatic water table. This also causes the development of dolines and surface depressions above areas of higher permeability. The epikarst includes most surface features of a karst system such as depressions, dolines and sinkholes. Furthermore, the epikarst transmits the prevailing climatic conditions to the karst aquifer. Williams (1983) therefore stresses, that with increasing age the permeability and the storage capacity of the epikarst increase. The epikarst strongly influences the distribution and the temporal distribution (delay) of recharge water (Williams, 1983; Palmer, 1991). Clemens *et al.* (1999) could numerically show the importance of an evolving epikarst on the developing karst system. In a recent study, Perrin *et al.* (2003) demonstrated by field investigations that the epikarst acts as the main storage element and distributes water into the different flow components, while the phreatic zone has only insignificant storage.

Distribution of recharge water to the karst aquifer has an important effect on the type of cave system evolving. White (1969) suggested, that maze caves develop, if recharge is spatially homogeneous, while concentrated recharge leads to dendritic cave systems. Palmer (1975) found, that 75 % of all maze caves developed beneath a sandstone layer, which prohibits concentrated recharge. Palmer (1991) emphasizes the role of the change in recharge conditions from what he terms hydraulic control, where discharge through the karst aquifer is limited by the capacity of the aquifer, to catchment control, where discharge is limited by the amount of recharge water available, during the evolution of a karst aquifer. The two conditions correspond to a fixed head boundary in the case of hydraulic control and a fixed or limited flow condition in the case of catchment control, the latter being typical for mature karst systems. Palmer (1991) further stresses that karst depressions form concurrently with caves, i.e. that the evolution of the subsurface conduit network and of surface features is directly linked. The same line of argument is followed by Klimchouk (1995; 2000d), who points out the connection between the epikarst and the evolution of major vertical shafts, some tens of meters deep. He provides experimental evidence and concludes that epikarst genesis, at least to a certain degree, reflects geologic structures of the type of bulk rock below.

The experimental findings and the genesis model of Williams (1983) introduced earlier were used to develop a conceptual model of the epikarst genesis. This conceptual model is also in accordance with the findings of Palmer (1975, 1991) and Klimchouk (1995, 2000d). It was designed to represent the physical processes of the epikarst evolution within a double permeability model like CAVE. The resulting concept is visualized in Figure 13, and is valid for the long term evolution of the epikarst, i.e. only temporal mean values are simulated.

During early karstification, dissolution is active mainly near the land surface, because here the infiltration water is most aggressive, but is quickly saturated further down due to slow seepage. A strongly weathered zone near the surface develops, which is connected hydraulically to the main karst body only by a few small fissures or cracks (Figure 13a). The karst water table is located near or at the surface. Since conductivities in the fissured system and diameters of the conduit system are both small, flow rates within the bulk



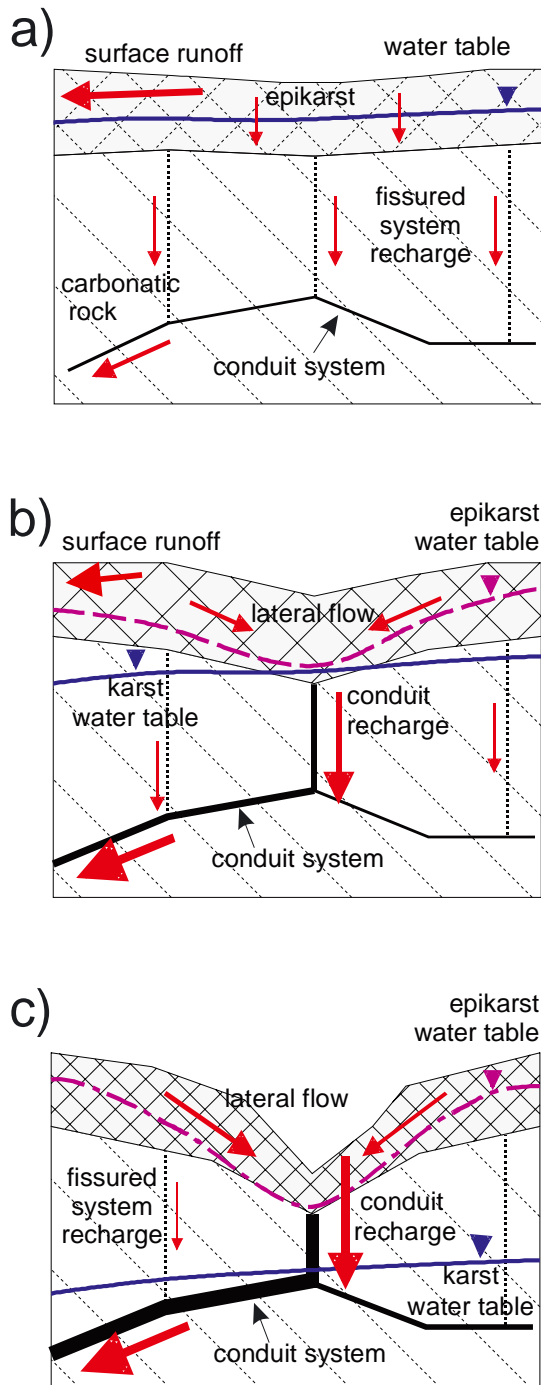


Figure 13: Conceptual model of the epikarst evolution. Depicted are **a)** an early, **b)** intermediate and **c)** well developed stage of the evolution. The epikarst is depicted shaded. Size and thickness of conduits and flow arrows correspond qualitatively to the magnitude of conduit size and flow rate, respectively.

rock in both systems are low and most of the precipitation becomes surface runoff. Water available for recharge to the karst aquifer consists of precipitation reduced by evapotranspiration and is termed total runoff here. As karstification progresses, the largest cracks and fissures are widened by dissolution. Substantial lateral flow now occurs within the weathered zone of the epikarst and infiltrating water is focused towards the enlarged fissures and cracks (Figure 13b). Thus their widening is preferentially enhanced by increasing flow rates, while the smaller cracks and fissures are widened only negligibly. Flow to the widening conduit system thus increases, while seepage to the fissured system stagnates at low values. The increased flow through the conduit system reduces surface runoff. Since conduits in the karst aquifer below are widened as well, the karst water table starts to drop. This process also leads to a selection of developing dolines because only rapidly growing dolines are capable of developing large catchment areas. The remaining shafts are deprived of recharge water and stagnate at low diameters. The recharge distribution to the underlying main karst aquifer is thus steered by a competition of initial dolines for catchment size and recharge water, synchronously to the dissolutional widening of pathways in the phreatic zone. Thus dolines can only develop considerable sizes if the recharge water is conveyed effectively to the system outlet (spring) via conduits in the phreatic zone. At a later, well developed stage, the karst ground water table and the temporary, perched epikarst water body are separated (Figure 13c). The larger cracks and fissures have grown enough

to allow rapid transmission of most infiltration water available. At the land surface, dolines have developed above the enlarged conduits and infiltrating water is diverted from the doline catchment areas to the conduit system. Thus surface flow has vanished, as most water is focused to the conduit system, and only a small amount percolates to the fissured system.

Throughout evolution, surface runoff decreases from a large proportion of the available total runoff to zero or small values, the fraction of water flowing through the conduit system increases from negligible amounts to nearly all available infiltration water while the amount percolating through the fissured system does not increase significantly. The karst water table falls from near the land surface to base level and surface land forms like dolines develop, which focus the infiltration water and enable lateral flow within the epikarst. The development has passed from hydraulic control during the early stages to catchment control in the mature stage. Since water entering the conduit system has passed the weathered epikarst zone and dissolved calcite there, calcium concentrations depend on the residence time in the epikarst and may vary from zero to values close to the equilibrium concentration.

The conceptual model as introduced above was set up by the numerical karst genesis model CAVE. Details of the implementation and the numerical approach can be found in Bauer *et al.* (submitted).

A small catchment zone is selected to investigate the effects of the epikarst and its development on the genesis of a karst aquifer (Figure 14a). The aquifer is simulated by a sequence of flat lying strata of outcropping carbonate rock. One major horizontal bedding plane is assumed. A river cuts into the rock and drains the aquifer which receives recharge water from precipitation. This setting is typical for many karst regions where limestone forms the outcrop at the land surface.

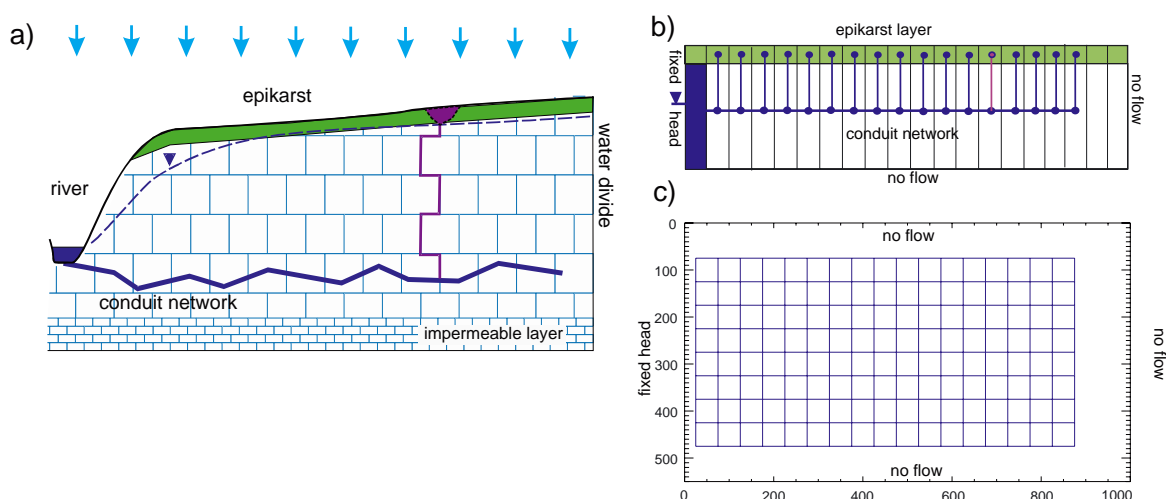


Figure 14: a) Conceptual model used for the simulations, b) cross section and c) top view of the initial and boundary conditions for the scenario considered. The regular grid in c) denotes the conduit network. Arrows in a) designate recharge.



The model used for the simulation is depicted in Figures 14b and 14c. The model domain is 1000 m long, 550 m wide and 40 m thick. The fissured system consists of two layers, each 20 m thick and is assumed as unconfined. A constant head boundary of 90 m is imposed along the lower side, representing the local drainage by a river. The conduit system is embedded in the lower layer of the fissured system and has 162 nodes arranged with an equal spacing of 50 m. It is directly connected to the local drainage, i.e. a fixed head boundary condition is imposed for the conduit nodes at the left hand side of the model domain. Above each node of the conduit network, an epikarst node and epikarst pipe are placed to simulate an initial doline (Figure 14b). Parameters used are 10^{-7} m s^{-1} for the hydraulic conductivity of the fissured system and $10^{-7} \text{ m}^2 \text{ s}^{-1}$ for the exchange coefficient. Initial heads in both systems are set at 110 m. Total runoff is assumed to be 10^{-8} m s^{-1} , which corresponds to a flow rate of $5.5 \times 10^{-3} \text{ m}^3 \text{ s}^{-1}$ for the total model area. A minimum of 5 % of the total runoff infiltrates into the fissured system. Temperature is set at $10 \text{ }^\circ\text{C}$. Calcium equilibrium concentration is 2 mol m^{-3} , the first order kinetic rate constants for laminar and turbulent flow are $4.0 \times 10^{-7} \text{ mol m}^{-2} \text{ s}^{-1}$ and $1.0 \times 10^{-6} \text{ mol m}^{-2} \text{ s}^{-1}$. If the calcium concentration is higher than the switching concentration, i.e. 0.9 of the equilibrium concentration, a slow fourth order kinetic rate constant of $4.0 \times 10^{-4} \text{ mol m}^{-2} \text{ s}^{-1}$ is used. The kinetic parameters are taken from Dreybrodt and Eisenlohr (2000) and correspond to values used in recent karst genesis studies. The infiltration concentration is set at 0.9 of the equilibrium concentration, while water originating from the fissured system has equilibrium concentration.

Temporal development of the karst aquifer is shown in Figure 15, where the heterogeneous initial conduit network is depicted as well. Karstification starts at the major spring near the river and propagates upgradient into the aquifer, following prominent conduits. Close to these enlarged conduits, hydraulic gradients in the conduit system are large and thus stimulate the development of the adjoining pipes. After 3000 a, conduits 600 m from the spring start to widen and the water table in the fissured system drops due to reduced recharge to the fissured system (Figure 15, 3000 a). After 9000 a, all prominent conduits and some of the smaller conduits directly linked to the dominant ones have widened, as well as the conduits near the river (Figure 15, 9000 a). Development of the epikarst is terminated after 12000 a (not shown in Figure 15) and recharge water distribution to the conduit network is constant with time after that. Epikarst nodes above areas of reduced widening receive only small quantities of recharge, limited by the small doline sizes, and thus karstification progresses only slowly. Main effects until the end of the simulation period are further widening of already enlarged conduits and development of some small conduits draining the areas of small recharge rates. Note that different pipe sizes in Figure 15 represent differences by one order of magnitude in the conduit diameters. At large distances from the river, piezometric heads are still high in the conduit system, because dissolutional widening is slow due to small flow rates and thus conduit diameters are still small.



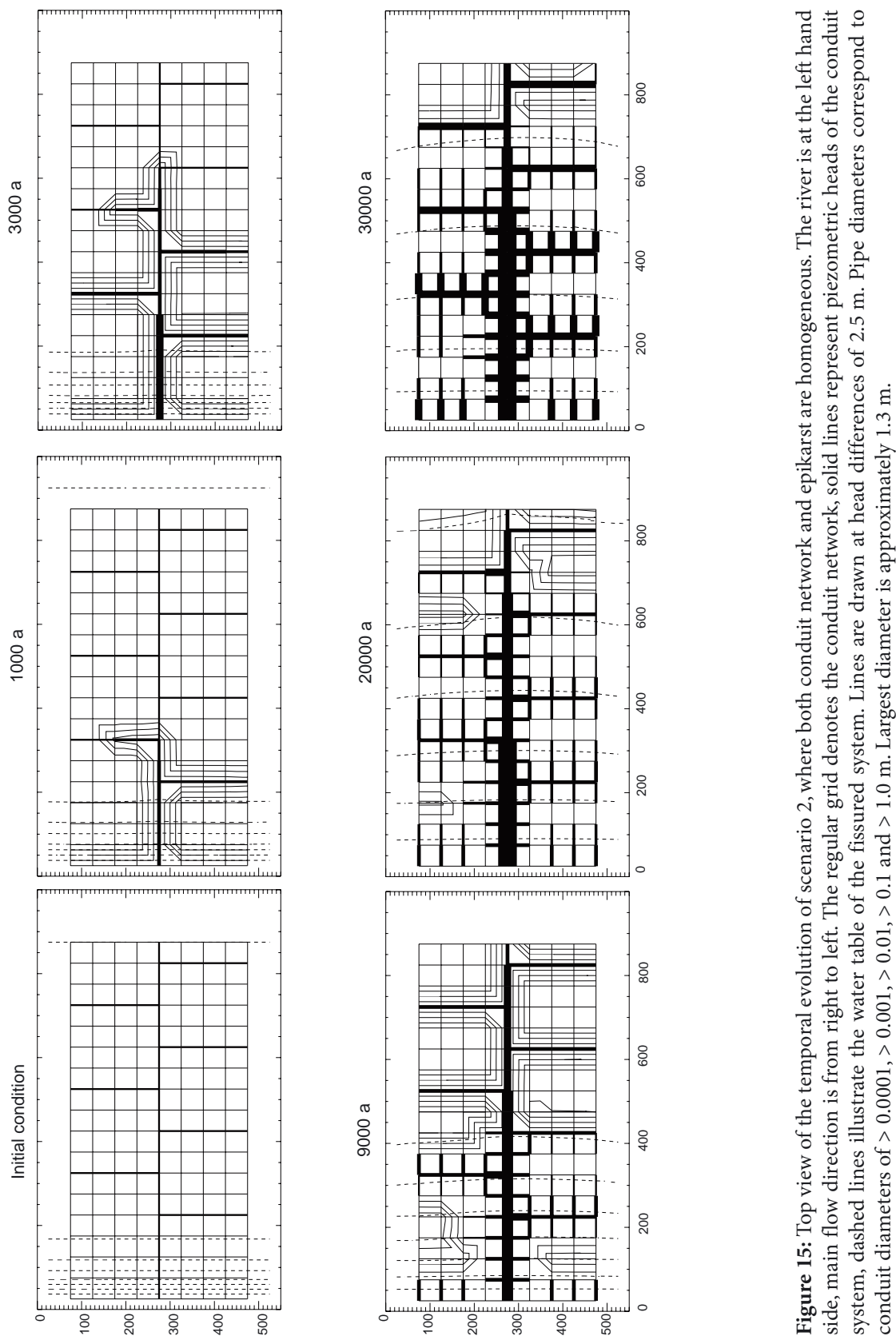


Figure 15: Top view of the temporal evolution of scenario 2, where both conduit network and epikarst are homogeneous. The river is at the left hand side, main flow direction is from right to left. The regular grid denotes the conduit network, solid lines represent piezometric heads of the conduit system, dashed lines illustrate the water table of the fissured system. Lines are drawn at head differences of 2.5 m. Pipe diameters correspond to conduit diameters of > 0.0001 , > 0.001 , > 0.01 , > 0.1 and > 1.0 m. Largest diameter is approximately 1.3 m.



The above model results are determined by the introduction of the epikarst module which allows the development of dolines and thus a process-oriented temporal and spatial distribution of recharge. Initially larger conduits induce more rapid growth of dolines attached to them by attracting more recharge water than the dolines in areas with small initial conduit diameters below. Thus a spatially heterogeneous distribution of recharge to the karst aquifer is induced which resembles the initial structure of the conduit network. A coupled evolution of the epikarst and the subsurface conduit system is achieved which is in accordance with field studies and the experimental findings cited above.

The time dependent recharge rates to the conduit system, as determined by the developing epikarst, also allow for a realistic representation of flow terms in the evolving aquifer. The temporal evolution of some characteristic parameters of the karst aquifer is shown in Figure 16 for demonstration purposes. At first, flow from the fissured system to the river (fissured system discharge) is larger than flow from the conduit connected to the spring (i.e. spring discharge). As the conduit network develops, spring discharge increases and flow from the fissured system to the river decreases, due to enhanced drainage of the fissured system by the conduit network. After termination of epikarst development at 12000 a, 97 % of the total outflow occurs at the conduit springs. About 40 % of the water volume recharged to the fissured system is drained by the conduit network, while 60 % is drained directly to the river. The maximum diameter observed for the pipe next to the largest spring, increases rapidly during the simulation. Likewise the rate of dissolved calcite volume, determined from the volume change of the conduit system, increases by orders of magnitude within the first 10000 a. After about 12000 a,

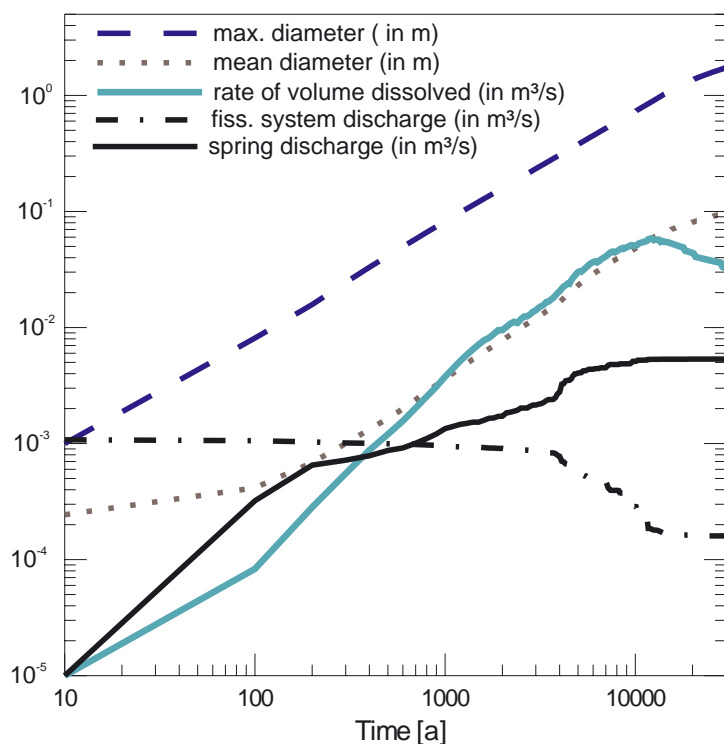


Figure 16: Temporal evolution of characteristic parameters of a karst system.





this removal rate slowly drops as more water enters the conduit system from the fissured system with high concentrations, thus lowering the dissolutional capacity of the water in the conduits. The temporal evolution of these characteristic parameters, especially spring discharge and diameters, emphasizes again the necessity of accounting for epikarst genesis in karst genesis modelling, because only then a realistic temporal development of important controlling factors can be obtained.

6. KARST DEVELOPMENT UNDER MAN MADE CONDITIONS

In many regions of the world, recharge to ground water is scarce or limited to only a few months of a year. Dams and reservoirs are means of ensuring more or less continuous water supply for the population over an extended period of time. Some of these dams are located in carbonate areas especially in the Mediterranean and the Middle East. High gradients and short flow paths along initial fissures and cracks under the dam support karstification and the dissolutional widening of conduits can be expected to lead to leakage and therefore to a considerable reduction in lifetime of the dam. This process has been analysed by Palmer (1988) and Dreybrodt (1992) for a single fracture. They both arrived at comparable results demonstrating that hydraulic structures may seriously be affected by dissolution of the underlying carbonate rock within a time span of 100 a.

A model dam was designed to examine the enhanced dissolutional widening of conduits under high gradients. The model consists of a 2 D cross-section of the carbonate aquifer below the dam, i.e. dissolution in the carbonate rock below the dam structure and the reservoir is considered. The cross-section represents a slice of 10 m thickness and contains one plane of solutionally enlargeable conduits. The conduit system thus represents a region of fractures every 10 meters. The bottom boundary represents a layer of different lithological composition, assumed to be much less permeable and not soluble, e.g. a clay layer. Different hydraulic scenarios are studied to investigate the effects of a grout curtain and a preferential flow path, and the model was designed accordingly.

Model dimensions, boundary conditions and geometry of the conduit network are shown in Figure 17. The model area is 500 m long, 10 m wide and 55 m deep. The reservoir is modelled by fixed head cells with a potential head of 40 m, downstream of the dam the potential is fixed at 0 m. The left, right and bottom side of the model domain are considered as no-flow boundaries. The hydraulic conductivity of the fissured system is set at 10^{-6} m s^{-1} , and the aquifer is considered to be confined. The exchange coefficient is set at $10^{-6} \text{ m}^2 \text{ s}^{-1}$. The dam base is 90 m long with a hydraulic conductivity of 10^{-8} m s^{-1} . The conduit system has equal spacing of 10 m between the nodes and initial diameters of $4.0 \times 10^{-4} \text{ m}$. The grout curtain is centrally located below the dam with the same conductivity as the dam itself. It reaches a depth of 30 m below the dam and is 10 m wide. A preferential flow path right below the dam is included and has a larger initial diameter of $1.0 \times 10^{-3} \text{ m}$. This preferential flow path is intercepted by the grout curtain in Scenario 4



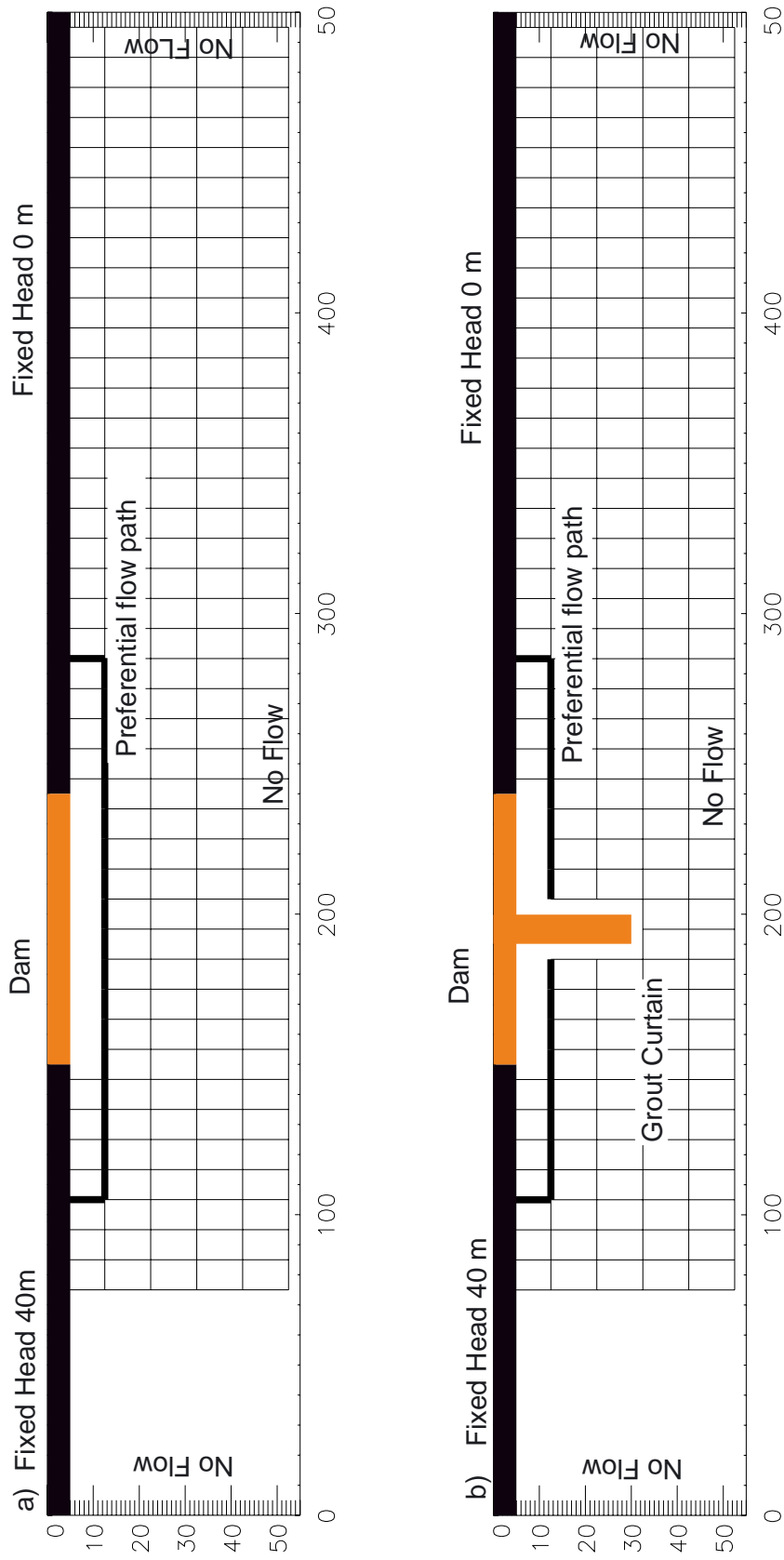


Figure 17: Model domain with geometry of the conduit network for (a) Scenarios 1 and 2, (b) Scenarios 3 and 4. The preferential flow path in Scenario 2 and 4 is depicted by fat lines. From Bauer *et al.* (1999).



(see Figure 17 b). Calcium equilibrium concentration is 1.0 mol m^{-3} , the fast first order kinetic rate constants for laminar flow and turbulent flow are $2.5 \times 10^{-7} \text{ mol m}^{-2} \text{ s}^{-1}$ and $5.0 \times 10^{-7} \text{ mol m}^{-2} \text{ s}^{-1}$, respectively. If the calcium concentration is near saturation (> 0.9 of the equilibrium concentration) with respect to calcite, slow fourth order kinetics is applied with only one constant for laminar and turbulent flow of $2.0 \times 10^{-6} \text{ mol m}^{-2} \text{ s}^{-1}$. The calcium concentration of water entering the conduit system from the reservoir is zero, the water entering the conduit system from the fissured system has equilibrium concentration.

The influence of a grout curtain and a preferential flow path on leakage flow from the reservoir is studied with four different scenarios:

1. Scenario 1 with neither preferential flow path nor grout curtain.
2. Scenario 2 with preferential flow path but no grout curtain.
3. Scenario 3 with no preferential flow path but a grout curtain.
4. Scenario 4 with both preferential flow path and grout curtain.

The preferential flow path and the grout curtain are shown in Figures. 17a and b. As a design criterion a critical leakage rate under the dam was calculated, above which the dam would theoretically lose more water than is supplied by recharge to its catchment area. A catchment area of 10 km^2 and a ground water recharge rate of 0.2 m/a are assumed for the calculation of a critical leakage rate of $0.06 \text{ m}^3 \text{ s}^{-1}$ ($230 \text{ m}^3 \text{ h}^{-1}$). The critical leakage rate is thus scaled to a catchment area of 10 km^2 and a dam width of 10 m , which enables comparison to dams with other dimensions. If the dam was 100 m wide with a catchment area of 50 km^2 , the critical leakage rate would be $0.03 \text{ m}^3 \text{ s}^{-1}$ ($115 \text{ m}^3 \text{ h}^{-1}$).

Figure 18 shows the development of the conduit system with time for Scenario 1 for 10, 30 and 73 a (a) and for Scenario 4 for 10, 20 and 50 a (b). Widening of the conduit system begins at the reservoir, from which aggressive water is entering the system. Conduits under high hydraulic gradients are enlarged first, because they display highest flow rates and thus the most aggressive water. Conduit diameters are decreasing with increasing flow length, as calcium concentrations increase due to dissolution, and slower kinetics become active. The flow path closest to the dam, which is most rapidly widened by dissolution changes from laminar to turbulent flow regime after 15 a. After 30 a the conduit system is widened more or less uniformly under the dam, even down to the impermeable base at 55 m depth. Most of the pipes are now turbulent and fast first order kinetics are active in most of the widened conduits. After 50 a the conduit system shows further enlargement and slowly extends further down-gradient. Most of the pipes have now diameters between 0.01 m and 0.05 m , and the conduits up-gradient of the dam have grown to just above 0.05 m diameter. After 73 a the leakage rate has risen to the critical leakage rate of $0.06 \text{ m}^3 \text{ s}^{-1}$, i.e. the catchment cannot supply enough recharge water to refill the reservoir. Similar patterns of dissolutional widening arise from the other scenarios (Bauer *et al.*, 1999), as is shown in Figure 18 (b) for Scenario 4. Here the development of conduits is also bound to the shortest hydraulic connection between the reservoir and the downstream hydraulic boundary.



SEBASTIAN BAUER, STEFFEN BIRK, RUDOLF LIEDL, MARTIN SAUTER

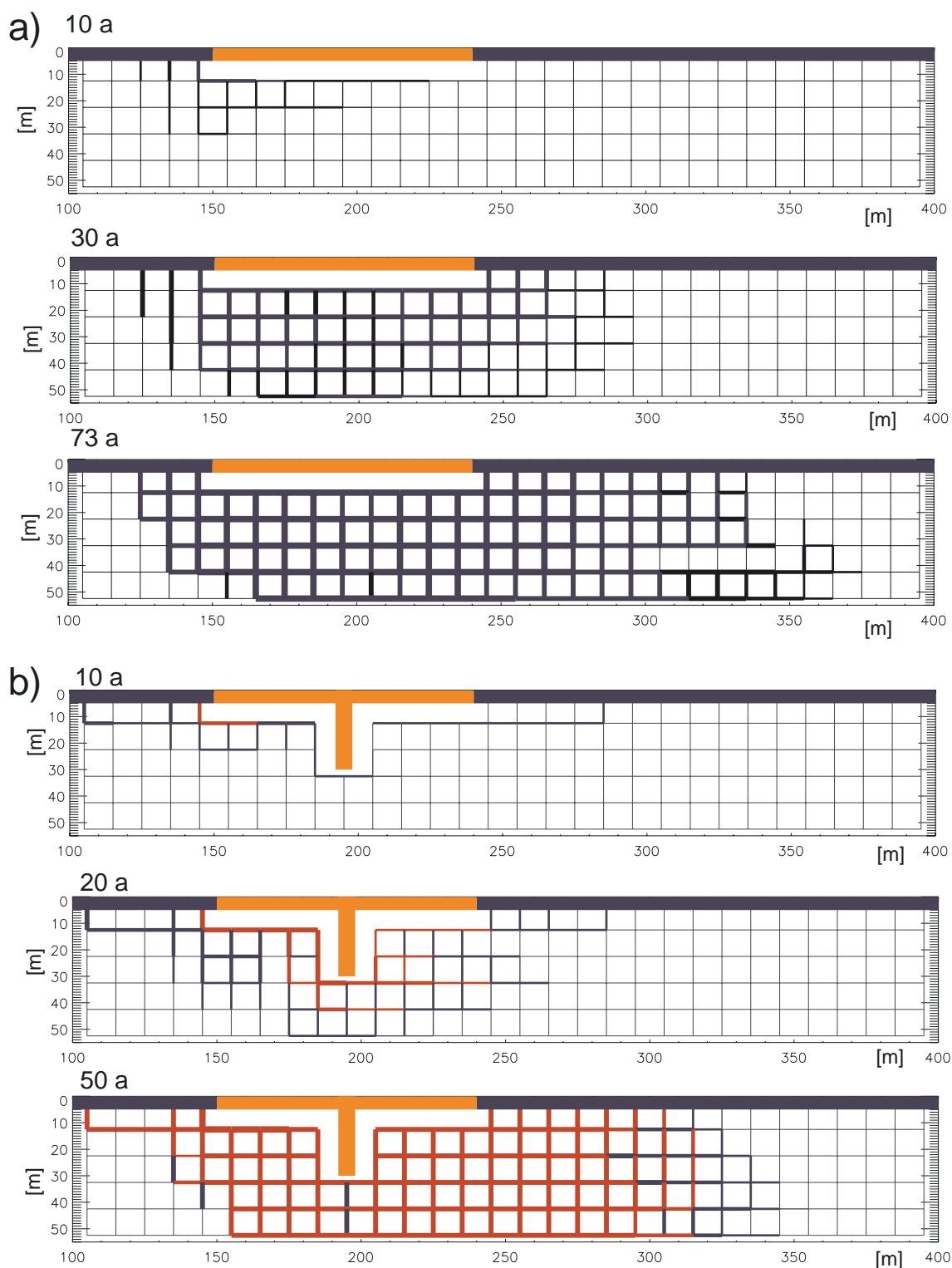


Figure 18: Model results for Scenario 1 (a) and Scenario 4 (b), depicting the conduit network after 10, 30, and 73 a (Scenario 1) and 10, 20 and 50 a (Scenario 4). The line thicknesses represent conduit diameters of > 0.0004 m, > 0.001 m, > 0.005 m, > 0.01 m and > 0.05 m, respectively. From Bauer et al. (1999).



Figure 19 shows leakage rates over time for the different scenarios considered. At the beginning of the simulation all leakage rates are approximately $10^{-4} \text{ m}^3 \text{ s}^{-1}$. Leakage rates for Scenarios 3 and 4 are a little lower, due to the presence of the grout curtain. During the early stages flow occurs mainly in the fissured system and flow through the conduit system is lower by approximately 4 orders of magnitude. Flow through the fissured system remains nearly constant throughout the simulation for all scenarios, since the hydraulic conductivity of the fissured system does not change. Leakage rates for Scenario 1 start to rise after 15 a. Breakthrough time of first order kinetics, defined as the time when the first pipe at the outlet at the lower head boundary shows a calcium concentration lower than 90 % of the equilibrium concentration, is 11 a. The first turbulent flow path from the reservoir to the outlet is established after 15 a. From then on the flow rate through the conduit system is comparable to the flow rate in the fissured system. It rapidly grows with increasing dissolutional widening of the conduits and eventually dominates the leakage rate. Due to the presence of an initial preferential flow path leakage rates rise first for Scenario 2 (Figure 17a). Breakthrough time is 2 a, the first turbulent flow path is established after 9 a and the critical leakage rate is reached after 72 a. Leakage rates of Scenario 3 are lowest compared to the other scenarios, due to the grout curtain. Breakthrough is achieved after 23 a, the first turbulent flow path after 28 a and the critical leakage rate after 82 a. Temporal development of the conduit network for Scenario 4 which includes both grout curtain and a preferential flow path is given in Figure 18 (b). The corresponding times in this case are 14, 21 and 78 a, respectively. Conduit diameters at the critical leakage rate vary between 0.06 m and 0.09 m for all scenarios.

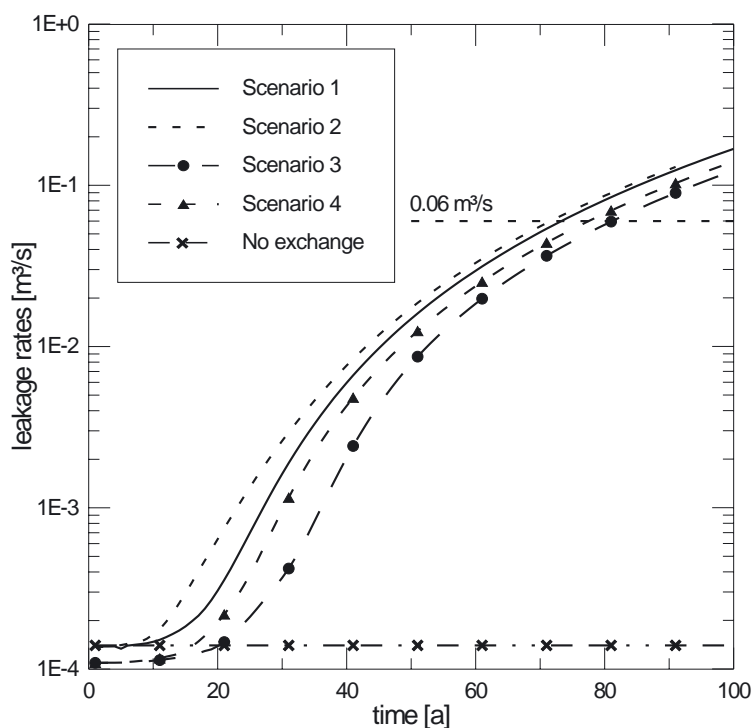


Figure 19: Development of leakage rates for the different scenarios with time. Also included is the leakage rate for a model with boundary conditions of Scenario 1, but no exchange between fissured and conduit system. From Bauer *et al.* (1999).



In the scenarios considered here, both grout curtain and initial preferential flow path have no significant effect on the development of the leakage rate with time (Figure 19). All scenarios reach the critical leakage rate within a time span of 10 a from 72 a onward. As expected from the boundary conditions, Scenario 2 with no grout curtain and an initial preferential flow path has highest leakage rates, while Scenario 3 without initial flow path but with grout curtain shows lowest leakage rates. The uniform widening of the conduit system eventually overrides differences which arise during the early stages of the conduit development. Although breakthrough time for Scenario 2 is only 2 a, compared to 14 a of Scenario 4, this initial difference in conduit conditions does not result in corresponding differences between leakage rates.

Figure 19 also shows the leakage rate for a model run with the boundary conditions of Scenario 1 but no exchange between fissured and conduit system. Almost no dissolutional widening is taking place, only the first few conduits directly beneath the reservoir are enlarged, and there is no breakthrough or turbulent flow. The reason is, that the special boundary conditions arising when modelling a dam lead to highly enhanced dissolution if exchange between fissured and conduit system is accounted for: from the beginning of the simulation, the hydraulic conductivity of the conduit network is higher than that of the fissured system. Therefore, down-gradient of the reservoir the hydraulic heads in the conduit system are higher than in the fissured system and exchange flow is directed into the fissured system. As a result, the conduit system loses water with high calcium concentration to the fissured system at each node below the reservoir. This amount of water flowing into the fissured system is resupplied to the conduit system from the fixed head reservoir with a calcium concentration of zero, i.e. by highly aggressive water. Therefore this exchange provides a sink for water high in calcium and acts as an additional source for aggressive water. This effect strongly enhances the development of the conduit system (compare section 3 of this chapter).

The model results presented here show that dissolution of small conduits under man made structures like a dam can have serious effects on the performance of the reservoir. The depth of 30 m of the grout curtain used in the simulations seems too small to effectively prohibit the strong increase of the leakage rate. The model results also suggest that small conduits with initial diameters of 4.0×10^{-4} m can be solutionally enlarged within tens of years and may cause serious water losses, if the effect of the fissured system is accounted for.

7. CONCLUSIONS

The double permeability model CAVE provides a flexible tool for simulating karstification within a large variety of hydrogeological settings. CAVE is based on a dualistic conceptualisation of karst systems which expresses itself by a hydraulic coupling of a continuum and a conduit network in order to account for the typical flow characteristics in karstic environments. With the usage of MODFLOW to represent the continuum, a





broad spectrum of hydrogeologically relevant boundary conditions like wells, rivers, evapotranspiration and others is made available and, moreover, domains experiencing conduit development may be integrated as parts of a regional scale model. In addition, a process based epikarst boundary condition and the water transfer mechanism between the continuum and the conduits were implemented to cover further essential features of karst hydraulics. Rock dissolution is simulated by experimentally verified relationships including the switch from first to higher order kinetics above a certain threshold concentration. With all this as background, CAVE can be applied to a large variety of hydrogeological settings of variable complexity. For instance, relatively simple set-ups can be studied to investigate the impact of individual processes on the development of a single conduit (e.g., exchange flow in section 3). Furthermore, more comprehensive settings typically encountered in karst development may be simulated by means of scenario based approaches related to fully natural (e.g. deep seated confined settings in section 4 and epikarst aquifer interaction in section 5) as well as partly anthropogenic environments (e.g., dam leakage in section 6).

ACKNOWLEDGEMENTS:

Part of this work was supported by the Deutsche Forschungsgemeinschaft (DFG) as part of the SFB 275, sub-project D3. We would also like to thank the EU for grants of the ROSES project (Risk of Subsidence due to Evaporite Solution, Contract number ENV4-CT97-0603).

REFERENCES

- Atkinson, T. C., Diffuse flow and conduit flow in limestone terrain in the Mendip Hills, Somerset (Great Britain), *Journal of Hydrology*, 35, 93–110, 1977.
- Barenblatt, G. I., Zheltov, I. P. and I. N. Kochina, Basic concepts in the theory of seepage of homogeneous liquids in fissured rocks, *Journal of Applied Mathematics and Mechanics*, 24, 1286–1303, 1960.
- Barton, A. F. M. and N. M. Wilde, Dissolution rates of polycrystalline samples of gypsum and orthorhombic forms of calcium sulphate by a rotating disc method, *Trans. Faraday Soc.*, 67, 3590–3597, 1971.
- Bauer, S. Simulation of the genesis of karst aquifers in carbonate rocks. Vol. 62 of *Tübinger Geowissenschaftliche Arbeiten, Reihe C*. Institut und Museum für Geologie und Paläontologie der Universität Tübingen, Tübingen, 2002.
- Bauer, S., S. Birk, R. Liedl, and M. Sauter, Solutionally enhanced leakage rates of dams in karst regions, In: Palmer, A.N., M.V. Palmer, and Sasowsky, I.D. (editors): *Karst Modelling, Karst Waters Institute Special Publication*, 5, 158–162, 1999.





- Bauer, S., R. Liedl, and M. Sauter, Modelling of karst development considering conduit-matrix exchange flow, *Calibration and Reliability in Groundwater Modelling: Coping with Uncertainty*, IAHS Publ., 265, 10–15, 2000.
- Bauer, S., Liedl, R. and M. Sauter, Modelling of karst genesis at the catchment scale – Influence of spatially variable hydraulic conductivity. *Acta Geologica Polonica* 52(1): 13–21, 2002.
- Bauer, S., R. Liedl, and M. Sauter, Modeling of karst aquifer genesis: Influence of exchange flow, *Water Resources Research*, 39(10), 1285, doi:10.1029/2003WR002218, 2003.
- Bauer, S., R. Liedl, and M. Sauter, Modeling the influence of epikarst evolution on karst aquifer genesis, submitted to *Water Resources Research*.
- Bear, J., *Dynamics of Fluids in Porous Media*, American Elsevier Publishing Company, New York, 1972.
- Berner, R. A. and J. W. Morse, Dissolution kinetics of calcium carbonate in seawater. IV. Theory of calcite dissolution, *American Journal of Science*, 274, 108–134, 1974.
- Birk, S., Characterisation of gypsum karst systems by simulating aquifer genesis and spring responses: Model development and application to gypsum karst. Vol. 60 of *Tübinger Geowissenschaftliche Arbeiten, Reihe C*. Institut und Museum für Geologie und Paläontologie der Universität Tübingen, Tübingen, 2002. Also available at: <http://w210.ub.uni-tuebingen.de/dbt/volltexte/2002/558>
- Birk, S., R. Liedl, M. Sauter, and G. Teutsch, Hydraulic boundary conditions as a controlling factor in karst genesis: A numerical modeling study on artesian conduit development in gypsum, *Water Resources Research*, 39(1), 1004, doi:10.1029/2002WR001308, 2003.
- Buhmann, D. and W. Dreybrodt, The kinetics of calcite dissolution and precipitation in geologically relevant situations of karst areas. 1. Open System, *Chemical Geology*, 48, 189–211, 1985a.
- Buhmann, D. and W. Dreybrodt, The kinetics of calcite dissolution and precipitation in geologically relevant situations of karst areas. 2. Closed System, *Chemical Geology*, 53, 109–124, 1985b.
- Clemens, T., Simulation der Entwicklung von Karstaquiferen. Dissertation am Institut und Museum für Geologie und Paläontologie der Universität Tübingen, Tübingen, 1998.
- Clemens, T., D. Hückinghaus, R. Liedl and M. Sauter. Simulation of the development of karst aquifers: role of the epikarst. *International Journal of Earth Sciences* 88, 157–162, 1999.
- Clemens, T., D. Hückinghaus, M. Sauter, R. Liedl, and G. Teutsch, A combined continuum and discrete network reactive transport model for the simulation of karst development, *Calibration and reliability in groundwater modeling – Proceedings of the ModelCARE 96 conference held at Golden, Colorado, September 1996*, IAHS Publ. no. 237, 309–318, 1996.
- Christofferson, J. and M. R. Christofferson, The kinetics of calcium sulphate dihydrate in water, *J. Crystal Growth*, 35, 79–88, 1976.
- Dreybrodt, W., The role of dissolution kinetics in the development of karst aquifers in limestone: a model simulation of karst evolution, *Journal of Geology*, 98, 639–655, 1990.
- Dreybrodt, W., Dynamics of karstification: a model applied to hydraulic structures in karst terranes. *Applied Hydrogeology*, 3, 20–32, 1992.



- Dreybrodt, W., Principles of early development of karst conduits under natural and man-made conditions revealed by mathematical analysis of numerical models, *Water Resources Research*, 32, 2923–2935, 1996.
- Dreybrodt, W., Limestone dissolution rates in karst environments. *Bulletin d'Hydrogéologie*, 16, 167–183, 1998.
- Dreybrodt W. and L. Eisenlohr, Limestone dissolution rates in karst environments. In: Klimchouk, A.B., D.C. Ford, A.N. Palmer and W. Dreybrodt, *Speleogenesis – Evolution of Karst Aquifers*, National Speleologic Society, Huntsville, 463–472, 2000.
- Dreybrodt, W., J. Lauckner, L. Zaihua, U. Svensson, and D. Buhmann, The kinetics of the reaction $\text{CO}_2 + \text{H}_2\text{O} \rightarrow \text{H}^+ + \text{HCO}_3^-$ as one of the rate limiting steps for the dissolution of calcite in the system $\text{H}_2\text{O} - \text{CO}_2 - \text{CaCO}_3$, *Geochimica et Cosmochimica Acta*, 60, 3375–3381, 1996.
- Eisenlohr L., K. Meteova, F. Gabrovšek, F. and W. Dreybrodt, The inhibiting action of intrinsic impurities in natural calcium carbonate minerals to their dissolution kinetics in aqueous $\text{H}_2\text{O}-\text{CO}_2$ solutions. *Geochimica et Cosmochimica Acta*, 63, 989–1002, 1999.
- Ford, D. C., Perspectives in karst hydrology and cavern genesis, *Bulletin d'Hydrogéologie*, 16, 9–29, 1998.
- Ford, D. C. and P. W. Williams, *Karst geomorphology and hydrology*, Unwin Hyman, London, 1989.
- Gabrovšek, F. and W. Dreybrodt, A model of the early evolution of karst aquifers in limestone in the dimensions of length and depth, *Journal of Hydrology*, 240, 206–224, 2001.
- Groves, C. G. and A. D. Howard, Minimum hydrochemical conditions allowing limestone cave development, *Water Resources Research*, 30, 607–615, 1994a.
- Groves, C. G. and A. D. Howard, Early development of karst systems: 1. Preferential flow path enlargement under laminar flow, *Water Resources Research*, 30, 2837–2846, 1994b.
- Gunn, J., A conceptual model for conduit flow dominated karst aquifers, *Proceedings International Symposium on Karst Water Resources, Ankara, Turkey*, 1–10, 1985.
- Hanna, R. B. and H. Rajaram, Influence of aperture variability on dissolutional growth of fissures in karst formations, *Water Resources Research*, 34, 2843–2853, 1998.
- Horlacher, H.-B. and H.-J. Lüdecke, *Strömungsberechnung für Rohrsysteme*, Expert Verlag, Eningen, 1992.
- Howard, A. D. and C. G. Groves, Early development of karst systems: 2. Turbulent flow, *Water Resources Research*, 31, 19–26, 1995.
- Hückinghaus, D., Simulation der Aquifergenese und des Wärmetransports in Karstaquiferen. Vol. 42 of *Tübinger Geowissenschaftliche Arbeiten, Reihe C*. Institut und Museum für Geologie und Paläontologie der Universität Tübingen, Tübingen, 1998.
- James, A. N. and A. R. R. Lupton, Gypsum and anhydrite in foundations of hydraulic structures, *Geotechnique*, 28, 249–272, 1978.
- Jeschke, A. A., K. Vosbeck and W. Dreybrodt, Surface controlled dissolution rates of gypsum in aqueous solutions exhibit nonlinear dissolution kinetics, *Geochimica et Cosmochimica Acta*, 65(1), 27–34, 2001.
- Kaufmann, G. and J. Braun, Karst aquifer evolution in fractured rocks, *Water Resources Research*, 35, 3233–3238, 1999.
- Kaufmann, G. and J. Braun, Karst aquifer evolution in fractured, porous rocks, *Water Resources Research*, 36, 1381–1391, 2000.



- Kiraly, L., Modeling karst aquifers by the combined discrete channel and continuum approach, *Bulletin d'Hydrogéologie*, 16, 77–98, 1998.
- Klimchouk, A. B., Karst morphogenesis in the epikarstic zone, *Cave and Karst Science*, 21(2), 45–50, 1995.
- Klimchouk, A. B., Artesian speleogenetic setting, *Proceedings of the 12th International Congress of Speleology, La Chaux-de-Fonds, Switzerland*, Volume 1, 157–160, 1997.
- Klimchouk, A. B., Dissolution and conversions of gypsum and anhydrite, In: Klimchouk, A. B., D. C. Ford, A. N. Palmer, and W. Dreybrodt, *Speleogenesis – Evolution of Karst Aquifers*, National Speleologic Society, Huntsville, 463–472, 2000a.
- Klimchouk, A. B., Speleogenesis under deep-seated and confined settings, In: Klimchouk, A. B., D. C. Ford, A. N. Palmer and W. Dreybrodt (eds.), *Speleogenesis – Evolution of Karst Aquifers*, National Geological Society, Huntsville, Alabama, 240–260, 2000b.
- Klimchouk, A. B., Speleogenesis of the great gypsum mazes in the Western Ukraine, In: Klimchouk, A. B., D. C. Ford, A. N. Palmer, and W. Dreybrodt (eds.), *Speleogenesis – Evolution of Karst Aquifers*, National Geological Society, Huntsville, Alabama, 261–273, 2000c.
- Klimchouk, A. B., The formation of the Epikarst and its Role in vadose speleogenesis, In: Klimchouk, A. B., D. C. Ford, A. N. Palmer and W. Dreybrodt, *Speleogenesis – Evolution of Karst Aquifers*, National Speleologic Society, Huntsville, 91–99, 2000d.
- Klimchouk, A. B., V. N. Andrejchouk and I. I. Turchinov, Structural prerequisites of speleogenesis in gypsum in the Western Ukraine, *Espeleotemas*, 5, 3–30, 1995.
- Lauritzen, S.-E., N. Odling, and J. Petersen, Modeling the evolution of channel networks in carbonate rocks, in Hudson, J. A. (ed.), *ISRM Symposium, Eurock '92*, 57–62, 1992.
- Lebedev, A. L. and A. V. Lekhov, Dissolution kinetics of natural gypsum in water at 5–25 °C, *Geochemistry International* 27, 85–94, 1990.
- Liedl, R., M. Sauter, D. Hückinghaus, T. Clemens and G. Teutsch, Simulation of the development of karst aquifers using a coupled continuum pipe flow model, *Water Resources Research*, 39(3), 1057, doi:10.1029/2001WR001206, 2003.
- Liu, S. T. and G. H. Nacollas, The kinetics of dissolution of calcium sulphate dihydrate, *J. Inorg. Nucl. Chem.*, 33: 2295–2311, 1971.
- Liu Z. and W. Dreybrodt, Dissolution kinetics of calcium carbonate minerals in H₂O-CO₂ solutions in turbulent flow: The role of the diffusion boundary layer and the slow reaction $\text{H}_2\text{O} + \text{CO}_2 \rightleftharpoons \text{H}^+ + \text{HCO}_3^-$, *Geochimica et Cosmochimica Acta*, 61, 2879–2889, 1997.
- Mangin, A., Contribution a l'étude hydrodynamique des aquifères karstiques. PhD thesis, Université de Dijon, Dijon, France, 1975.
- McDonald, M. G. and A. W. Harbaugh, A modular three-dimensional finite-difference groundwater model, *USGS Open-File Report*, 83–875, USGS, 1988.
- Opdyke, B. N., G. Gust, and J. R. Ledwell, Mass transfer from smooth alabaster surfaces in turbulent flow, *Geophysical Research Letters*, 14, 1131–1134, 1997.
- Palmer, A. N., The origin of maze caves. *The NSS Bulletin* 37: 56–76, 1975.
- Palmer, A. N., Solutional enlargement of openings in the vicinity of hydraulic structures in karst regions, *Proceedings of the 2nd Conference on Environmental Problems in Karst Terranes and Their Solutions*, Assoc. of Groundwater Sci. and Eng., Nashville, Tenn., Nov. 16–18, 1988.



- Palmer, A. N., Origin and morphology of limestone caves, *Geological Society of America Bulletin*, 103, 1–21, 1991.
- Perrin, J., P. Y. Jeannin and F. Zwahlen, Epikarst storage in a karst aquifer: a conceptual model based on isotopic data, Milandre test site, Switzerland, *Journal of Hydrology*, 279, 106–124, 2003.
- Plummer, L. N., T. M. L. Wigley and D. L. Parkhurst, The kinetics of calcite dissolution in CO₂ – water systems at 5 °C to 60 °C and 0.0 to 1.0 atm CO₂, *American Journal of Science*, 278, 179–216, 1978.
- Romanov, D., F. Gabrovšek, and W. Dreybrodt, Interaction of fracture and conduit flow in the evolution of karst aquifers, *Karst Waters Institute Special Publication*, 7, 38–43, 2002.
- Shuster, E.T. and W.B. White, Seasonal fluctuations in the chemistry of limestone springs: a possible means for characterizing carbonate aquifers, *Journal of Hydrology*, 14, 93–128, 1971.
- Siemers, J. and W. Dreybrodt, Early development of karst aquifers on percolation networks of fractures in limestone, *Water Resources Research*, 34, 409–419, 1998.
- Svensson U. and W. Dreybrodt, Dissolution kinetics of natural calcite minerals in CO₂-water systems approaching calcite equilibrium, *Chemical Geology*, 100, 129–145, 1992.
- White, W.B., Conceptual models for carbonate aquifers, *Ground Water*, 7(3), 15–21, 1969.
- White, W.B., Role of dissolution kinetics in the development of karst aquifers, *International Association of Hydrologists Memoirs*, 12, 503–517, 1977.
- White, W. B., *Geomorphology and hydrology of karst terrains*, Oxford University Press, New York, 1988.
- White, W.B., Conceptual models for karstic aquifers. In: Palmer, A.N., M.V. Palmer and I.D. Sasowsky, (editors): *Karst Modelling*, *Karst Waters Special Publication*, 5, 11–16, 1999.
- Williams, P.W., The role of the subcutaneous zone in karst hydrology, *Journal of Hydrology*, 61, 45–67, 1983.
- Williams, P.W., Subcutaneous hydrology and the development of doline and cockpit karst, *Zeitschrift für Geomorphologie*, 29, 463–482, 1985.
- Worthington, S.R.H., D. C. Ford and P.A. Beddows, Porosity and permeability enhancement in unconfined carbonate aquifers as a result of solution. In: Klimchouk, A. B., D. C. Ford, A. N. Palmer and W. Dreybrodt, *Speleogenesis – Evolution of Karst Aquifers*, National Speleologic Society, Huntsville, 463–472, 2000.

Address

*Sebastian Bauer, Steffen Birk, Rudolf Liedl, Martin Sauter**
 Center for Applied Geoscience, University of Tübingen,
 Sigwartstrasse 10, 72076 Tübingen, Germany
 phone: ++49 (0)7071 2973171; fax: ++49 (0)7071 5059
 E-mail: sebastian.bauer@uni-tuebingen.de
 * now at: Applied Geology,
 Geoscientific Centre of the University of Göttingen,
 Goldschmidtstrasse 3, 37077 Göttingen, Germany





STRUCTURE AND EVOLUTION OF KARST AQUIFERS: A FINITE-ELEMENT NUMERICAL MODELLING APPROACH

GEORG KAUFMANN

Abstract:

The evolution and flow in a karst aquifer is studied with numerical simulations, based on the KARST model (Karst AquifeR Simulation Tool). The aquifer consists of an interconnected network of fissures and a porous rock matrix. Flow through the aquifer is driven by both diffuse recharge from precipitation and localised sinking streams, and the aquifer drains towards a large karst resurgence representing the base level. Fissures are enlarged with time by chemical dissolution, enhancing the secondary porosity of the karst aquifer. The enlargement of fissures results in a dramatic increase of the aquifer conductivity over several orders of magnitude, and a change of flow pattern from an initially pore-controlled to a heterogeneous fracture-controlled aquifer. Several model scenarios are studied to elucidate the karst aquifer evolution under different parameter settings: (i) Structural control by large faults, (ii) recharge conditions along the karst surface, (iii) reaction kinetics of the aggressive water dissolving the rock. The evolution models are then complemented by event-type spring discharge modelling for the various numerical simulations, which can be used as a predictive tool for karst spring discharge and contaminant transport.

Key words: Karst, limestone

1. INTRODUCTION

Groundwater flow in a karst aquifer is an important subject, as rapid flow of water through highly permeable karst aquifers is prone to contamination. However, large-scale heterogeneities in the karst aquifer make it difficult to predict flow and transport in a karst catchment. While the primary conductivity of limestone is fairly low ($K \sim 10^{-8}$ m/s), fractures in the rock enlarged by chemical dissolution increase their conductivity by orders of magnitude ($K > 1-10$ m/s). The enlargement of initially small fractures into larger passages then forms a pattern of cave passages, which carry the majority of water flowing through the karst aquifer. The *short-term response* of a karst aquifer observed today is guided by the *long-term evolution* of secondary porosity within the karst aquifer. Hence we need to discuss both long-term evolution and short-term response to understand the complicated dynamics of a karst aquifer.



1.1 Aquifer geometry

Palmer (1991) has analysed several thousand of cave passage patterns and found that 57 percent of the total cave passages follow bedding planes and 42 percent are fracture-oriented. Only 1 percent of the total passages are related to intergranular porosity in the rock. In his classification, Palmer (1991) introduced four distinct patterns of cave passages: (i) *Branchwork caves* (65 percent of total passage length), resembling single passages joining larger passages downstream as tributaries and thus similar to surficial dendritic river patterns. (ii) *Network caves* (17 percent), with passage patterns of angular grids formed by dissolutional enlargement of most of the available fractures. (iii) *Anastomotic caves* (10 percent), with patterns of intersecting, curvilinear tubes, often superimposed on branchwork caves. (iv) *Ramiform and spongework caves* (8 percent), with random-like patterns of small cavities and larger, irregular rooms, mainly resulting from hydrothermally controlled dissolution and therefore not directly related to surface recharge. Examples for the first two cave passage patterns are shown in Figure 1.

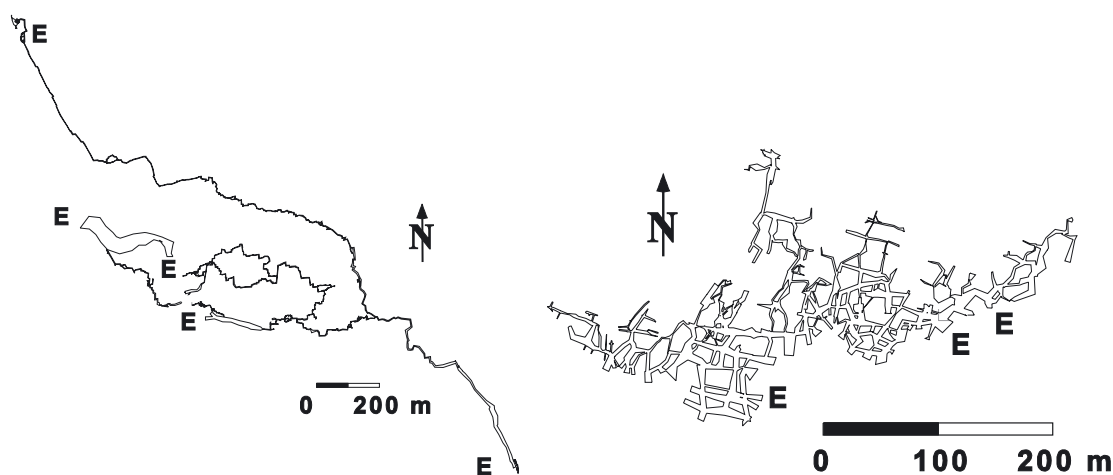


Figure 1: Left: Nandembo Cave System (7.5 km long), Matumbi Hills, Tanzania, as an example of a branchwork cave pattern. Right: Anjohiambovonomy (4.6 km long), Namoroka, Madagascar, as an example of a network cave pattern. Entrances are marked as E.

The *Nandembo Cave System* in the Matumbi Hills, Tanzania (Laumanns & Ruggieri, 1995), a 7.5 km long active river cave with three independent tributaries, is an example of a branchwork pattern. The system is recharged via sinking streams, and drains towards a single karst resurgence.

Anjohiambovonomy cave in Namoroka, Madagascar (Laumanns & Gebauer, 1993), a maze cave with a total length of 4.6 km, is a typical example of a network pattern. The cave is located in a karst outcrop, recharge is entirely diffusive over the entire surface, and water emerges in an overflow spring active only during the rainy season.

These widely different cave passage patterns pose the important question of identifying the characteristic processes responsible for the different evolution. We need to answer questions such as 'how important is the recharge condition', 'is the structural setting guiding the evolution', 'is water chemistry decisive in the long-term evolution'. Here, numerical simulations of long-term karst aquifer evolution both in terms of flow and geometry have been used intensely during recent years (e.g. Dreybrodt, 1990, Palmer, 1991, Groves & Howard, 1994a, 1994b, Howard & Groves 1995, Clemens *et al.*, 1996, 1997, Hanna & Rajaram, 1998, Siemers & Dreybrodt, 1998, Kaufmann & Braun, 1999, 2000, Gabrovšek & Dreybrodt, 2000, 2001, Romanov *et al.*, 2002, 2003, Kaufmann, 2002a, 2002b, 2003a, 2003b). Common to all of these numerical models is the change from an initially relatively homogeneous aquifer with small fractures, where flowrates are low and flow is diffuse, to a strongly heterogeneous aquifer with flow being fast and concentrated along enlarged fractures. Often, a preferential flowpath is established in the models, which guides recharge through cave passages towards a karst spring.

1.2 Aquifer response

The large variability in karst aquifer properties cannot be observed properly by field measurements, as typical methods such as injection, packer, and slug tests are more suitable to porous groundwater flow. Flow in the enlarged fracture system is, however, more difficult to estimate. Only in few cases it is possible to explore the enlarged fracture system directly. Hence, the prediction of flow and contamination needs to be studied by other means.

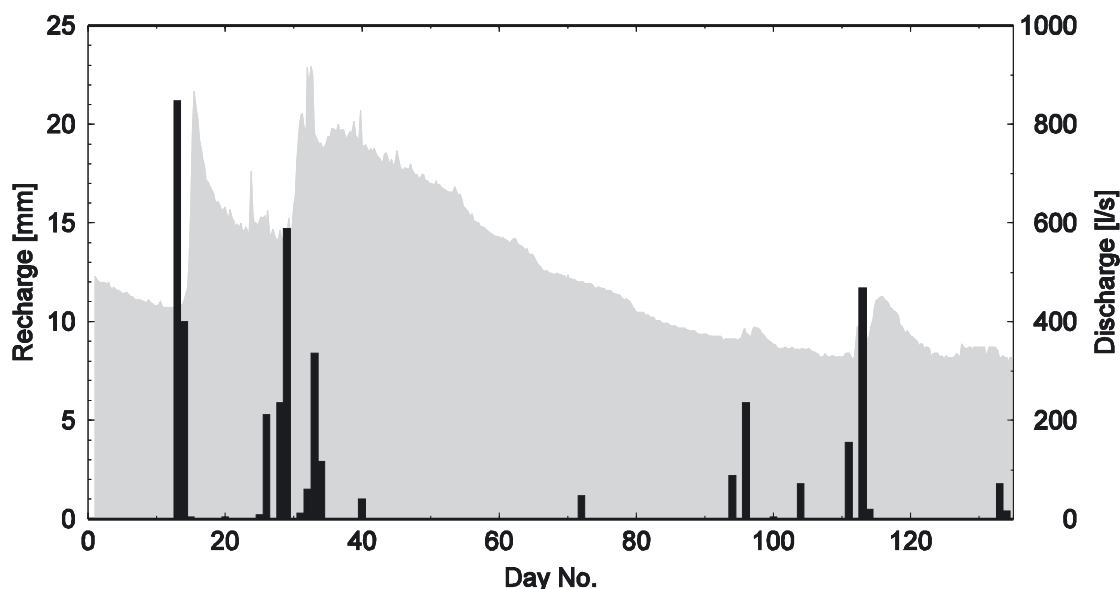


Figure 2: Recharge (bars) and discharge (line) measured at the Gallusquelle area, Swabian Alb, Germany, for the period 20.03.1989 to 31.07.1989. Data from Sauter, 1992.



A global observation of the response of a karst aquifer are hydrographs taken from large karst springs. These resurgences often collect water from the entire catchment area and show a rapid response to sudden recharge events, followed by an exponential decrease of discharge seen along the recession limb of the hydrograph. As an example, a four-month long hydrograph reading from the Gallusquelle in southwest Germany (Sauter, 1992) is shown in Figure 2. The large peaks after each rain event are attributed to the fast flow through the enlarged fractures of the karst aquifer, which have a low storage capacity. The recession limbs are controlled by slow flow through the finer fissures of the rock matrix, which has a high storage capacity. Analysis of karst spring hydrographs is a common tool to study the response of a karst aquifer to groundwater flow (e.g. Atkinson *et al.*, 1973, Sauter 1992, Grasso & Jeannin, 1998, Baedke & Krothe, 2001, Jeannin, 2001). However, the hydrograph analyses are often limited by a number of factors, e.g. the large catchment of karst aquifers, the strong heterogeneities in conductivity, and the scarcity of data (see Jeannin & Sauter, 1998, for a review).

Besides analysis of a measured spring discharge hydrograph, hydrograph time-series can be generated by numerical flow models, which describe a karst aquifer geometry in a simplified fashion. This numerical approach excludes per definition uncertainties in the hydraulic properties, and thus can be used to study the response of a karst aquifer to recharge events. For example, Eisenlohr *et al.* (1997a, b) have used the numerical model of transient groundwater flow described in Kiraly (1998), with flow driven by the rainfall time-series from the Areuse and Serrière catchments in the Swiss Jura. The finite-element model includes both low-flow, high-storage porous matrix, and high-flow, low-storage karst conduits into the approach. The resulting spring discharge was then analysed with an auto-correlation method, and it was shown that the recharge input (frequency and intensity of recharge events, infiltration, ...) strongly controls the correlation functions.

The numerical prediction of karst spring hydrographs also showed that an important input parameter for a quantitative hydrograph analysis is the karst aquifer geometry. Here, assumptions need to be made concerning the location and distribution of enlarged fractures, as well as hydraulic properties for both the highly permeable fractures and the low-permeability porous matrix. Often, these data are not available from field observations, and simplified models have to be used instead. While Eisenlohr *et al.* (1997a, b) have assigned a constant conductivity to karst conduits, which were placed in the numerical model domain in an 'ad-hoc' fashion, we discuss another possibility to access the karst aquifer properties: We make use of numerically generated long-term karst aquifer models and simulate short-term transient flow behaviour driven by a realistic recharge times series. Our aim is to test synthetic karst aquifer models, which are calculated as evolution models under the assumption of steady-state recharge, under transient event-based recharge conditions. We predict spring discharge time-series and show that a long-term numerical karst evolution model is capable of describing the flashy response typical to mature karst aquifers.

The outline of the following study is as follows: In section 2 we introduce the



basic theory of calcite dissolution chemistry, and the concept of flow and enlargement of a single fracture. We then embed the single fracture model into a larger karst aquifer model, consisting of fractures and bedrock matrix. In section 3, we discuss results for a small karst plateau consisting of flat-lying limestone and underlain by impermeable rocks. In the first part, the long-term evolution is studied under steady-state recharge conditions, and the effects of recharge, structure, and chemistry are discussed. In the second part, the evolved long-term evolution models are tested with a time-dependent recharge event to simulate the response of a karst resurgence at various stages of the long-term evolution.

2. THEORY

2.1 Dissolution kinetics of $\text{CaCO}_3\text{-CO}_2\text{-H}_2\text{O}$ system

In karst landscapes, soluble bedrock such as limestone or dolostone is dissolved by water enriched with carbon dioxide. On the surface, material is dissolved under conditions open to the atmosphere, and removed with the aqueous solution. This process, termed karst denudation, lowers the bedrock fairly uniformly, and a karst plateau will be lowered over time. Within the karst aquifer, material is removed from narrow fissures and bedding partings, in which water enriched by carbon dioxide circulates. The voids are enlarged over time, altering the permeability of the bedrock, and also changing the flow patterns through the aquifer. Depending on the situation within the aquifer, dissolution proceeds either under open-system conditions, where the solution is in contact with the atmosphere (soil, epikarst, vadose caves), or under closed-system conditions with solution completely filling the voids (phreatic caves, voids below the water-table), thus being decoupled from the atmosphere.

The dissolution process proceeds until the solution is in equilibrium with respect to calcite. The time needed to attain equilibrium is controlled by various rate-limiting reactions. Hence the need to understand both the equilibrium chemistry within the ternary system water (H_2O), carbon dioxide (CO_2), and calcite (CaCO_3), and the reaction kinetics controlling the speed of dissolution.

Equilibrium chemistry: For solutions, which are saturated with respect to calcite, an analytical expression for the calcium equilibrium concentration c_{eq} as a function of carbon-dioxide partial pressure p and temperature T can be derived (Dreybrodt, 1988):

$$c_{eq}^3 = \frac{K_1 K_C K_H}{4 K_2 \gamma_{\text{Ca}^{2+}} \gamma_{\text{HCO}_3^-}^2} p, \quad (1)$$

with K_1 , K_2 , K_C and K_H equilibrium constants for the fast reactions and $\gamma_{\text{Ca}^{2+}}$ and $\gamma_{\text{HCO}_3^-}$ activity coefficients for calcium and bicarbonate (see table 1). It is obvious that

the calcium equilibrium concentration depends non-linearly on the carbon-dioxide pressure, while the temperature dependence is hidden in the equilibrium constants K_i . The relation above is valid for the open system. For the closed system, the carbon dioxide partial pressure will reduce according to (Dreybrodt, 1988):

$$p = p_i - \frac{c_{eq}}{K_H \left(1 + \frac{1}{K_0}\right)}, \quad (2)$$

with p_i the initial carbon dioxide pressure and K_0 an equilibrium constant. Inserting (2) in (1) yields a cubic equation for the calcium equilibrium concentration, which needs to be solved to derive the calcium equilibrium concentration corresponding to an initial carbon dioxide pressure. From the simplified relation (1), several mechanisms can be discussed for calcite dissolution (Figure 3).

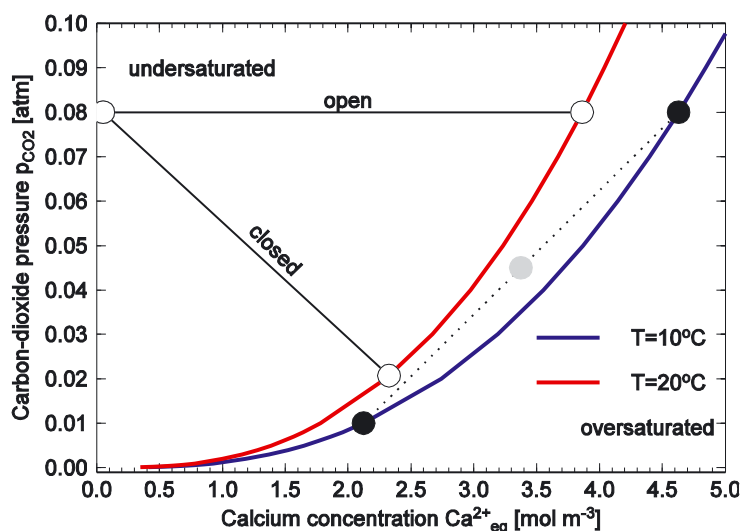


Figure 3: Calcium equilibrium concentration as a function of carbon dioxide pressure for the analytical expression (1) for two temperatures. Also shown are different pathways for solutions towards their equilibrium values. In the open system, dissolution proceeds along horizontal (dashed) lines, while in the closed system dissolution proceeds along sloping (solid) lines. Also shown is the effect of mixing two saturated solutions equally (black circles), resulting in a new undersaturated solution (gray circle), which again can dissolve calcium.

Normal corrosion: A solution undersaturated with calcium is located in the undersaturated field to the left of the equilibrium lines (white dots). Depending of the boundary conditions, dissolution proceeds either along the horizontal line, until the equilibrium is reached, thus maintaining the carbon dioxide pressure (open system). If the closed system condition holds, the carbon dioxide pressure decreases in the solution, and the calcium equilibrium line is reached at a lower value.

Temperature corrosion: The dissolution of calcite is temperature dependent, and a decrease in temperature results in an increase in dissolved calcium. Thus, a cooling of water either through daily variations in surface temperature or through thermal water

ascending in the rock can dissolve additional calcite. While the former process is limited to the first few meters in juvenile karst aquifers, thermal corrosion can be locally important in regions of hydrothermal water supply. Here, large temperature gradients are responsible for a significant amount of additional calcite dissolved. A temperature drop of 10 °C will result in around 0.5 mol/m³ additional calcium dissolved.

Pressure corrosion: The dissolution of carbon dioxide is also pressure dependent, an increase in atmospheric pressure will result in an increase of the dissolution rate. But flow in karst aquifers can be regarded as incompressible under normal conditions, thus pressure-induced corrosion due to the possible increase of partial carbon-dioxide pressure can be neglected in the solution. However, in air bubbles dragged under the surface in turbulent flow along the interface of the vadose and the phreatic zone air can be compressed, while carried down into greater depths (Bögli, 1978). In this case the partial carbon-dioxide pressure will increase and additional calcite can be dissolved, as it can be observed in Wirbelkanälen along the roof in cave passages initially developed in the shallow phreatic zone. Also, subterranean CO₂-sources from either biogenic or volcanic origin (e.g. Gabrovšek *et al.*, 2000) can increase the carbon-dioxide pressure.

Mixing corrosion: The mixing of two solutions saturated with respect to calcite, which, however, have different carbon dioxide concentrations, results in a solution, which again can dissolve calcite (black dots). This alternative form of corrosion, termed mixing corrosion (Bögli, 1971, 1978), is a result of the nonlinear relation between the calcium equilibrium concentration and the carbon dioxide pressure. As a consequence, water flowing in the karst aquifer through the network of small fissures and cracks all hydrologically connected will mix everywhere and thus results in additional corrosive power. As water with different partial carbon dioxide pressure is the normal case within a drainage area due to differences in surficial origin of the solution, in surface cover and soil on a scale of meters as well as daily variations of organic activity, mixing corrosion can be a significant process on a local scale, but the additional amount of dissolved calcium rarely exceeds 0.2 mol/m³. The mixing corrosion, though much less effective than the normal corrosion, will also occur in small fissures deep in the phreatic zone.

Reaction kinetics: A solution undersaturated with respect to calcite can dissolve limestone. The dissolution process is controlled by several rate-limiting reactions, which depend on parameters such as the thickness δ of the solution film, carbon-dioxide partial pressure p , and the degree of undersaturation. The rate-limiting reactions are: (i) the surface reaction along the limestone-solution interface, which has been determined experimentally by measuring dissolution rates of Iceland spar in large volumes of rigorously stirred, turbulent solutions (Plummer *et al.*, 1978). (ii) Conversion of carbon dioxide into carbonic acid and its dissociation products hydrogen and bicarbonate, (iii) diffusional mass transport of the dissolved species in the solution.

Dissolution experiments on natural limestone show a distinctive deviation from the linear relation predicted from theoretical models (Buhmann & Dreybrodt, 1985a, b) for calcium concentrations c close to the equilibrium concentration c_{eq} . Calcium fluxrates drop by several orders of magnitude, a mechanism termed “kinetic trigger” by White

(1977). This was first measured by Plummer *et al.* (1978), and subsequently verified for the open system (Svensson & Dreybrodt, 1992) and for the closed system (Eisenlohr *et al.*, 1999). The reason for the drop in fluxrates are impurities in the natural limestone, such as clay minerals. During dissolution, these impurities accumulate on the surface of the limestone and inhibit further dissolution. Hence, the experimental data on natural limestone can be described by a linear calcium fluxrate for large undersaturation, and a non-linear calcium fluxrate close to equilibrium:

$$F_{Ca^{2+}} = k_i \left(1 - \frac{c}{c_{eq}} \right)^{n_i}, \quad i = 1, 2, \quad (3)$$

Eq. (3) accounts for both the higher fluxrate (low-order kinetics) for $c < c_s$ and the several orders of magnitude lower fluxrate (high-order kinetics) for $c > c_s$. Here, c_s is the calcium threshold concentration, at which the fluxrate changes from low to high-order kinetics; it is generally between 60–90 percent of c_{eq} .

For low-order kinetics, the fluxrate can be approximated by a linear relation, and the rate coefficient k_1 based on the theoretical modelling of Buhmann & Dreybrodt (1985a, b) and the experimental results of Svensson & Dreybrodt (1992), Dreybrodt *et al.* (1996) and Eisenlohr *et al.* (1999) is

$$n_1 = 1, \quad k_1 = k_0 \left(1 + \frac{k_0 d(t)}{6Dc_{eq}} \right)^{-1}, \quad (4)$$

with the rate coefficient k_0 , and the diffusion coefficient D . When we assume $c_{eq} \sim 2 \text{ mol/m}^3$, we immediately see that $k_1 \sim k_0$ for $\delta < 0.1 \text{ mm}$. Thus, mass transport through diffusion only becomes important above a film thickness of 0.1 mm. Palmer (1991) has also derived rate coefficients k_1 from the experiments on calcite dissolution performed by Plummer *et al.* (1978). His coefficients depend on temperature T and CO_2 -pressure p , $k_1 = k_1(T, p)$, and the exponent is a function of CO_2 -pressure p , $n_1 = n_1(p)$, and varies between 1.5 and 2.2. Note that the coefficients k_1 tabulated in Palmer (1991) must be normalized by the atomic mass of calcite, m_r , to fit (3).

For high-order kinetics ($c > c_s$), a fourth-order power-law applies (Palmer, 1991, Eisenlohr *et al.*, 1999):

$$n_2 \cong 4, \quad k_2 = k_1 \left(1 - \frac{c_s}{c_{eq}} \right)^{(n_1 - n_2)}, \quad (5)$$

Note that k_2 is several orders of magnitude larger than k_1 , but the high-order fluxrate above the threshold remains much smaller than the low-order fluxrate valid for smaller calcium concentrations due to the power-law introduced by $n_2 = 4$ in (3).

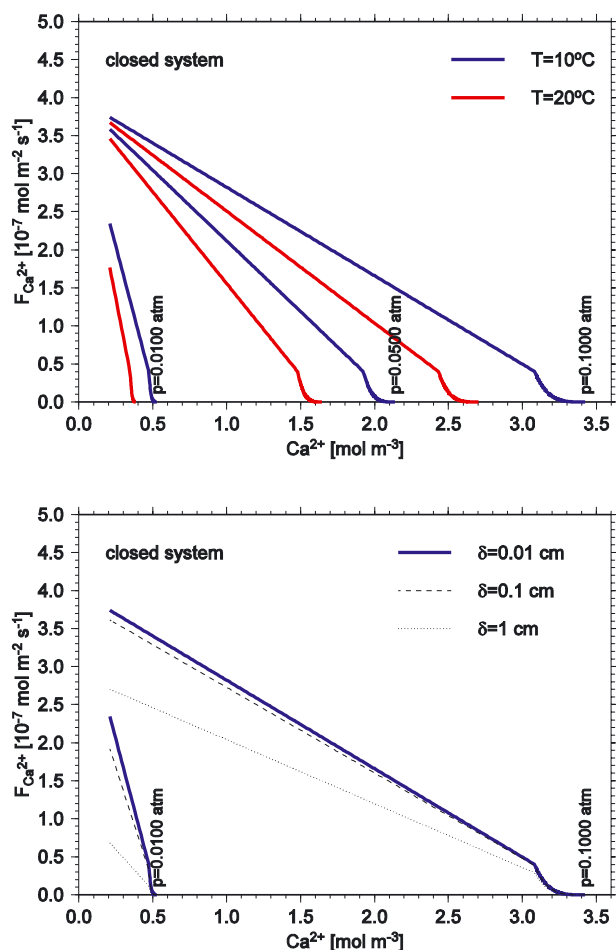


Figure 4: Low and high-order dissolution rates for a closed system. Top: Fluxrates as a function of temperature and carbon-dioxide partial pressure in the limit of very small film thickness. Bottom: Fluxrates as a function of film thickness for 10 °C and 0.1 atm.

Calcium fluxrates based on the non-linear approximation (3) and the rate coefficients given in (4) and (5) are shown in Figure 4a for various parameter settings. Several key aspects can be seen: Firstly, fluxrates depend strongly on the carbon dioxide pressure in the solution. The larger the carbon dioxide pressure the more calcite can be dissolved. Secondly, fluxrates are inversely proportional to temperature, which warmer solutions being able to dissolve less calcite. Thirdly, calcium fluxrates decrease linearly for calcium concentrations below 90 % of the equilibrium concentration. From then on, dissolution rates drop sharply and the 4th-order power law controls the fluxrates. This non-linear effect is important for the evolution of karst aquifers during their early phases, as the reduced fluxrates close to equilibrium increase the saturation length of solution penetrating into the aquifer significantly.

The effect of film thickness on the non-linear fluxrate approximation can be seen in the bottom panel of Figure 4b. For film thickness values below $\delta = 0.1 \text{ mm}$, fluxrates are controlled by surface dissolution rates and CO_2 -conversion, and diffusion is less important. For larger film thickness values above $\delta > 0.1 \text{ mm}$, the rate-limiting effect of diffusion becomes more pronounced, and dissolution rates drop with increasing film thickness.

2.2 Flow and evolution of single fracture

A first step in numerically modelling the evolution of a karst aquifer is the model of a single fracture, representing an initial channel in the rock, through which water enriched in carbon dioxide can flow. When the solution is undersaturated with respect to calcite, the fracture can be enlarged by chemical dissolution. Calcite will be removed from the fracture walls, and the solution subsequently becomes more and more saturated.

Several numerical models on single fracture growth have been published (e.g. Dreybrodt, 1990, Palmer, 1991, Groves & Howard, 1994a, Dreybrodt, 1996, Kaufmann & Braun, 1999, Dreybrodt & Gabrovšek, 2000, Palmer 2000). These models simulate the evolution of a single fracture as a simple analogue of flow along a fracture or a bedding plane, and the evolution of the fracture width is controlled by the dissolution rate. At the exit of the fracture, slow dissolution rates are responsible for the slow growth of the exit diameter, while the entrance of the fracture grows faster during this initial phase. As time proceeds, the solution at the exit becomes sufficiently undersaturated to increase the dissolution rate by several orders of magnitude, and a breakthrough is achieved. From then on, the entire fracture grows at a constant pace. Dreybrodt (1996) derived an analytical relation for this *breakthrough time* as a function of fracture geometry, hydrostatic pressure drop, and dissolution chemistry for a single fracture. In this relation, the breakthrough time is inversely proportional to the cube of the initial fracture width, thus the geometry of the pre-existing fractures largely controls the speed of the karstification process.

Geometry: We assume that flow in a limestone aquifer can be modelled using the concept of flow in fractured, porous rocks. Therefore, we regard the most probable flow path as given along the junctions of small fissures with bedding planes. We adopt a circular conduit model to simulate flow along the intersection (Figure 5). The conduit is characterised by its length l and its diameter d , the cross-sectional area is $A = \pi d^2/4$.

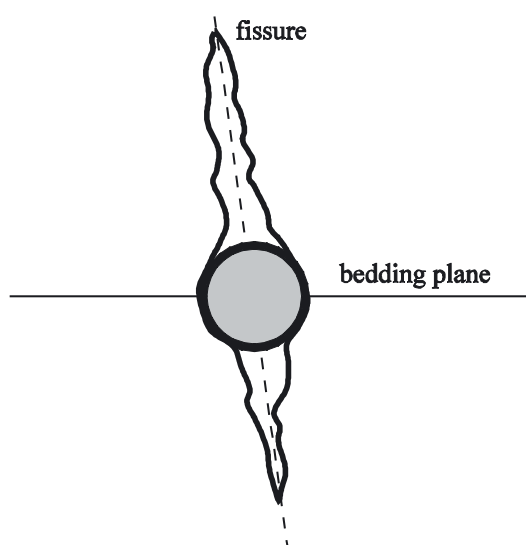


Figure 5: Geometrical model for the flow path along the intersection of a fissure and a bedding plane: circular conduit.

Flow: Flow in the conduit is modelled as fully developed, incompressible Poiseuille flow with no buoyancy forces (e.g. Turcotte & Schubert, 1982, pp. 237ff.). The flow is driven by the hydraulic pressure difference Δp across the conduit, which can also be expressed as *head loss* (in m), $\Delta h = \Delta p / \rho g + \Delta z$, with ρ the density of water, g the gravitational acceleration, and Δz the change in elevation between upstream and downstream ends of the conduit. Alternatively, we introduce the *hydraulic gradient*, $i = \Delta h / l$.

For a given head loss Δh , we calculate the *flow rate* Q (in m³/s) in the conduit. A general form relating head loss and flow rate is given by a power-law equation of the form

$$Q^n = K' \Delta h, \quad (6)$$

with K' a coefficient for the conduit geometry and flow properties, called diffusivity.

To distinguish between laminar and turbulent flow, the Reynolds number is used:

$$\text{Re} = \frac{ud(t)}{\eta}, \quad (7)$$

with $u = Q/A$ the Darcy-flow velocity (specific flowrate), t the time, $d(t)$ the time-dependent conduit diameter, and η the dynamic viscosity. For Reynolds numbers below a critical threshold, $\text{Re} < \text{Re}_c$, laminar flow occurs, and the laminar friction factor is derived:

$$f_l = \frac{64}{\text{Re}}, \quad \text{Re} < \text{Re}_c. \quad (8)$$

For Reynolds numbers above the critical threshold, turbulent flow occurs, and the turbulent friction factor needs to be derived from the maximum of

$$\begin{aligned} f_s &= 0.3164 \text{Re}^{-0.25}, \\ f_t^{-0.5} &= 1.14 - 2 \log \left(\frac{w}{d} + \frac{9.35}{\text{Re}} f_t^{-0.5} \right), \quad \text{Re} > \text{Re}_c, \\ f_r^{-0.5} &= 1.14 - 2 \log \left(\frac{w}{d} \right), \end{aligned} \quad (9)$$

with f_s smooth turbulence, f_r rough turbulence, and f_t the transition between smooth and rough turbulence, and the wall roughness, w . Usually, the critical Reynolds number is set to $\text{Re} \sim 2200$. Note that for rough turbulence, the friction factor becomes independent from Re . Note also that the friction factor for the transitional regime is given by an implicit equation, which has to be solved iteratively.

A comparison between friction factors depending on Re is shown in Figure 6. For small Re , the laminar friction factor is one order of magnitude larger than all turbulent friction factors. In the turbulent flow regime, the implicit equation for the transition between smooth and rough turbulence, f_t , can be approximated by f_s for small Re and large d , and by f_r for large Re .

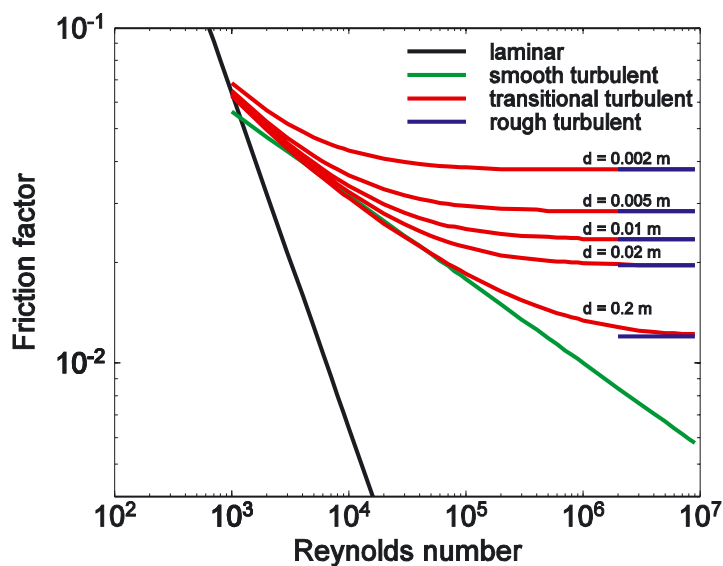


Figure 6: Friction factor as a function of Reynolds number, in the case of transitional and rough turbulence for different diameter d .

We first assume that flow is laminar. Then the linear Hagen-Poiseuille flow law applies, which reads (e.g. Beek & Muttzall, 1975)

$$n = 1, \quad K_l'(t) = \frac{g}{40\nu} \frac{d(t)^4}{l}. \quad (10)$$

Here, ν is the kinematic viscosity of water.

If turbulent flow is allowed, we apply the non-linear Darcy-Weissbach flow law. (e.g. Jeppson, 1976),

$$n = 2, \quad K_t'(t) = \frac{\pi^2 g}{8f} \frac{d(t)^5}{l}. \quad (11)$$

The Reynolds number (7) explicitly depends on the flow rate Q . Thus, a distinction between laminar and turbulent flow can only be made *a posteriori*. We start calculating a laminar flow rate, and then derive Re. For $Re > 2200$, flow is turbulent and has to be recalculated using a turbulent friction factor, which is taken as the maximum from (9). Note that for a given conduit the turbulent flow rate is smaller than the laminar flow rate, thus, turbulence is limiting the flow in a conduit.

Evolution: The fracture diameter $d(t)$ is a function of the initial diameter d_i and the calcium fluxrate $F_{Ca^{2+}}$ in the element:

$$d(t_i) = d(t_{i-1}) + \frac{F_{Ca^{2+}} m_r}{\rho} (t_i - t_{i-1}), \quad (12)$$

with m_r and ρ the atomic mass and the density of calcite, and t_{i-1} and t_i two subsequent time steps.

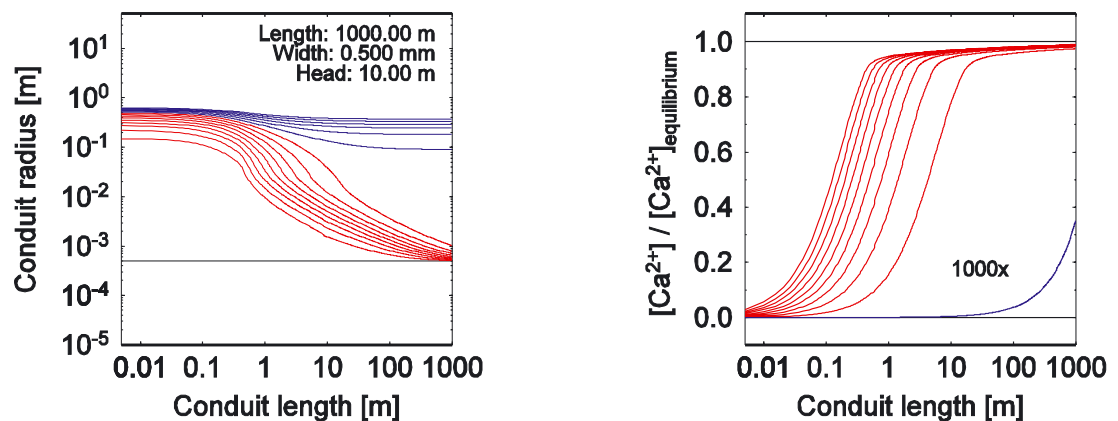


Figure 7: Left: Evolution of conduit radius. Flow is driven from left to right. The black line indicates the initial conduit width, red lines are enlarged conduit widths before, blue lines after low-order kinetics is established. Lines are plotted at time steps of 2000 years. Right: Profiles of calcium concentration in karst conduit for different times. The time step is 2000 years. Red lines indicate concentrations before, the blue line after low-order kinetics is established. Note that the blue line is scaled by a factor of 1000. Bottom right: Flow rate in a karst conduit. The red line represents an evolution, where only laminar flow is considered, for the blue line flow can switch into the turbulent flow regime, if the Reynolds number is large enough.

An example of the evolution of a circular conduit is shown in Figure 7. Here, the solution enters the conduit from the left side. As dissolution proceeds in the early phase, only the entrance section is sufficiently enlarged, the downstream section grows only slowly (red lines). This is a result of the slow high-order kinetics, as the Ca^{2+} -concentration quickly reaches levels close to saturation further downstream. Thus, sufficient dissolution only occurs within the entrance section. When enlargement proceeds, more highly undersaturated solution is carried further downstream, and the conduit finally grows at a relatively constant pace (blue lines).

The importance of high-order kinetics close to the saturation of the solution, c_{eq} , becomes obvious, when we discuss the Ca^{2+} -concentration along the conduit (Figure 7). At the onset of evolution, low-order kinetics in the entrance section results in solution close to saturation within a few centimetres. As a consequence, modelling only low-order kinetics would result in no significant conduit growth, and enlargement would be limited

to a few centimetres to meters from the entrance, depending on conduit geometry and film thickness. By taking high-order kinetics into account, when the solution is close to saturation, the Ca^{2+} -flux rate is reduced by several orders of magnitude, and now slightly undersaturated solution can be carried much farther downstream. Dissolution is now occurring several kilometres within a conduit. This mechanism, termed *kinetic trigger* by White (1977), is largely responsible for enlarging fracture in limestone during the early phase of karstification.

The flow rate at the exit of the conduit resembles the two-stage evolution. During the first stage, high-order kinetics controls the conduit growth, the flow rate increases slowly with time. When the more effective low-order kinetics is established within the entire conduit, the flow rate increases over several orders of magnitude within a very short time interval. This time interval is called *breakthrough time* by Dreybrodt (1990), it is a characteristic parameter for conduit growth and depends on the geometrical parameters conduit diameter d , length l , and head loss Δh , and the chemical parameters calcium equilibrium concentration c_{eq} , linear rate coefficient k_1 , and power-law exponent n :

$$T_B \sim (d)^{\frac{2n+1}{n-1}} (l)^{\frac{2n}{n-1}} (\Delta h)^{-\frac{n}{n-1}} (c_{eq})^{\frac{n}{n-1}} (k_1)^{\frac{1}{n-1}}. \quad (13)$$

Note that flow in the conduit also becomes turbulent, and neglecting turbulence would result in an overestimation of the flow rate.

2.3 Aquifer network

The concepts on limestone dissolution and flow through fractures developed in the previous sections are used to assemble a two-dimensional numerical model representing a karst aquifer, called KARST*. In the scenarios discussed, the aquifer is assumed to comprise a flat-lying layer of limestone, which is underlain by a layer of impermeable material such as sandstones or schists. Hence, all water entering the limestone layer must leave the model through its defined output.

Flow in a karst aquifer is modelled using the discrete fracture approach (Gureghian, 1975, Huyakorn *et al.*, 1983, Kaufmann & Braun, 2000), which incorporates fractures directly into the medium. The advantage of the discrete fracture approach is the combined modelling of matrix and fracture elements and the consistent modelling of flow in the matrix-fracture medium. Flow in the confined, fractured, porous karst aquifer is modelled by the transient continuity equation:

$$\frac{\partial}{\partial x} \left(bK \frac{\partial h}{\partial x} \right) + \frac{\partial}{\partial y} \left(bK \frac{\partial h}{\partial y} \right) = S \frac{\partial h}{\partial t} - q(t). \quad (14)$$

* Karst AquifeR Simulation Tool

Here, x and y are the northward and eastward coordinate directions, t is time, h is the hydraulic head in the model domain, K , and b are the conductivity and the aquifer thickness, S is aquifer storativity, and q is recharge at specified nodes. As $u = K \partial h / \partial x_i$ holds for the Darcy velocity, after some algebra we arrive at:

$$K_i = \frac{g}{10\pi v} d(t)^2, \tag{15}$$

$$K_i = \frac{2g}{f} d(t).$$

The transmissivity $T = bK$ controls the flow, hence for simplicity we choose a nominal aquifer thickness of $b = 1$ m. For a total of N nodes in the model domain, (14) represents a set of N equations for the N unknown heads h_i at nodes i . Equation (14) is solved with a Galerkin finite element method, with triangular elements for the porous matrix and linear elements for fractures and fissures (Figure 8).

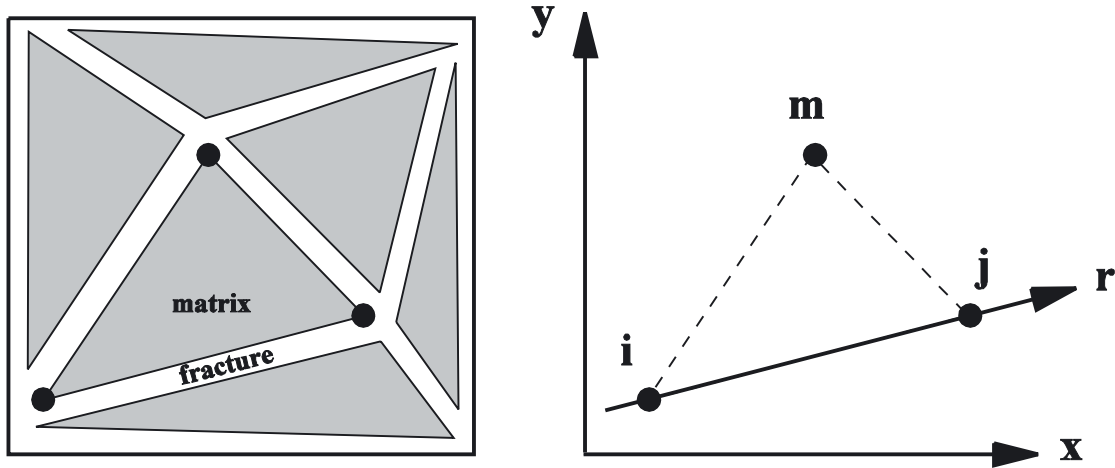


Figure 8: Conceptual model of fractured, porous aquifer (left) and geometrical realisation (right). Global x - y coordinate system for the porous matrix blocks with nodes i, j, k , and a local r coordinate system for a single fracture between nodes i and j are shown.

The conductivity K_m in the matrix representing micro-fissures in the rock remains constant throughout the evolution, while the conductivities in the fractures $K_c = K_c(t)$ increases with time due to the enlargement of the elements by chemical dissolution. Water entering the porous matrix can be aggressive ($c = 0 \text{ mol/m}^3$), water leaving the porous matrix is saturated ($c = c_{eq}$). At the intersections of fractures and fissures, instantaneous and complete mixing of incoming water is assumed.

3. RESULTS FOR FLAT-LYING STRATA

In this first part, we discuss the evolution of a karst aquifer embedded into flat-lying strata. The example chosen is a small limestone plateau of one square kilometre (1,000 m × 1,000 m), surrounded by insoluble bedrocks such as sandstones or schists (Figure 9). The limestone lies on top of an insoluble, impermeable layer, hence water circulating in the host rock cannot seep further down and can only leave the aquifer through a defined base level. The base level is in this case defined as a karst resurgence, located midway along the southern end of the limestone plateau.

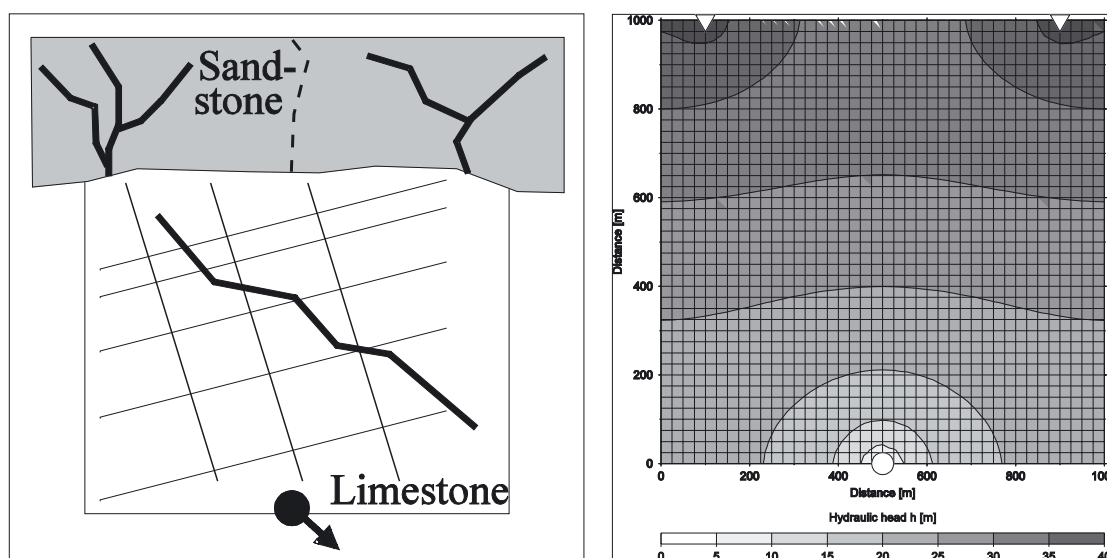


Figure 9: Left: Scenario for karst aquifer. Two independent streams drain the sandstone region and disappear into sinks along the top of the limestone domain. The water reappears in the large resurgence in the middle of the lower side. Additional recharge can arise from diffuse infiltration. The limestone region is fractured, with a dense net of fine fractures (thin lines), and possibly larger faults (thick line). Right: Realisation of the karst aquifer. The two sinks are marked as white triangles, the resurgence as white dot. Black lines indicate fractures, and the head distribution at the onset of karstification is shaded.

The limestone is horizontally bedded, and it is fractured, with an initial fissure width in the sub-millimetre range (0.2 mm). The fissures represent an interconnected system, through which water can circulate. Additionally, larger fractures can be present, which might be the result of the tectonic history of the limestone plateau (e.g. uplift, compression). The larger fractures, representing major faults in the plateau, have an initial width of 0.6 mm. In between the fissures and fractures, the bedrock matrix is present, also able to carry flow through the aquifer.

The subsurface flow through the karst aquifer is driven by a hydraulic pressure difference between input points and the karst resurgence. Water may enter the karst aquifer in two different ways: (i) A diffuse recharge seeping into the aquifer along the entire

plateau surface as a result of net precipitation (precipitation minus evapo-transpiration). This autogenic recharge is distributed evenly along the plateau surface. (ii) A discrete recharge along the boundaries between soluble limestone and insoluble sandstone through sinking streams. The two streams disappear through sinks along the northern edges of the karst plateau, and they originate from small catchments (catchment area around 0.5 km²) on the adjacent sandstone. Both streams might have different chemical compositions.

The numerical realisation is shown in the right panel of Figure 9: The model domain is discretised into a set of 41×41 nodal points, resulting in 3200 triangular matrix elements and around 5000 linear fracture elements. The average fracture density is 25 meter. Fractures can be irregularly distributed in the karst aquifer, thus simulating a preferential orientation due to tectonic forcing. All model boundaries are no-flow boundaries.

The two allogenic streams sink into the aquifer along the northern side (left and right), and the aquifer drains towards a resurgence located on the southern side (middle). The sinking streams are modelled as fixed inflow boundary conditions (9×10^5 mm/yr), the resurgence as fixed head boundary condition (0 m). Alternatively, the aquifer is recharged by a spatially constant precipitation, also modelled as fixed inflow boundary condition (300 mm/yr).

Flow in the aquifer is modelled both in the fractures connecting nodal points (linear bar elements), and in the smaller fissures simulated by the bedrock matrix (triangular elements). The fractures can be enlarged by chemical dissolution, but no dissolution takes place in the bedrock matrix. Here we argue that the residence time of seepage water in the matrix is long enough to fully saturate the water with respect to calcite. Hence, water originating from the matrix and flowing into the fissure system is fully saturated. The implementation of the flow and dissolution model is described in detail in Kaufmann & Braun (1999, 2000).

For all long-term evolution models, the transient storage of water in the aquifer is neglected ($S = 0$), and thus the steady-state equivalent of (14) is solved. Sink recharge and diffuse recharge are kept constant throughout the evolution, simulating an annually-averaged input. For the short-term spring response models, both sink recharge and precipitation vary with time on a daily basis, and consequently storage becomes important and the full transient continuity equation (14) is solved.

3.1 Long-term evolution

3.1.1 Distributed recharge

Our discussion starts with a hypothetical karst aquifer, which receives a temporarily and spatially constant diffuse recharge of 300 mm/yr over the entire plateau surface. However, no water is received from catchments outside the plateau. The seepage water infiltrating into the karst aquifer has a temperature of $T = 10$ °C and a partial carbon-dioxide pressure of $p = 0.05$ atm. We also assume that it has already dissolved calcite and set the input



concentration to $c_{in} = 0.9 c_{eq}$. This high input concentration keeps the dissolution in the non-linear regime described by (5), and thus the enlargement of fractures by chemical dissolution is slow.

Run d1: In the first run shown in Figure 10, fractures are oriented along the north-south and west-east directions, representing a checkerboard-type fracture network. At all fracture junctions, fractures meet at 90° -angles, which of course is unrealistic in nature. The first four panels (Figure 10a–d) are four time sequences of the evolution of secondary porosity in the karst aquifer. Shown are map-views of the plateau, with the karst resurgence marked by the dots. The hydraulic head distribution is contoured and shown as grey-scale.

At the beginning of the evolution (0 years), a smooth, regular hydraulic head distribution results, which increases from 0 m at the resurgence to around 25 m along the northern edge of the plateau. The steepest drop in hydraulic head occurs close to the resurgence. After 2,000 years, all fractures present have been widened to the millimetre scale (white lines), and some fractures close to the resurgence have reached a centimetre diameter, increasing their conductivity from the initially low value of $K_f \sim 10^{-2}$ m/s to around $K_f \sim 10^4$ m/s. The initially high hydraulic head distribution has collapsed, and hydraulic heads only increase from zero to two meters between resurgence and northern edge. Enlargement has started close to the resurgence, and then propagates backward from the resurgence into the aquifer, as it can be seen in the third time sequence (10,000 years). The reason for the headward propagation of enlargement is the availability of aggressive seepage everywhere in the karst aquifer through the evenly distributed recharge. As the initial fracture diameter is constant, breakthrough times (13) mainly depend on the length of the subsurface flow path, $T_B \sim l^{8/3}$. Hence, longer flow paths will significantly delay breakthrough, and the fractures close to the resurgence with their short flow paths have an advantage during the evolution. The run is terminated after 100,000 years of evolution. At this stage, a large dendritic cave passage pattern has evolved, with enlarged fractures draining the entire karst plateau subsurface. Enlarged passages generally converge towards the karst resurgence. Due to the rectangular geometry of the fracture distribution, the passage pattern exhibits a large degree of axial symmetry, with a symmetry axis running from the karst resurgence northwards. Within the northern half of the plateau, enlarged fractures up to the meter scale generally run along a north-south direction, which was the initial gradient of the hydraulic head early in the evolution. In the southern part of the plateau, enlarged fractures in the east-west direction redirect the flow towards the karst resurgence. However, a more direct path towards the resurgence is impossible, as there are no initial fractures, which could be enlarged. Thus the passage pattern looks very artificial.

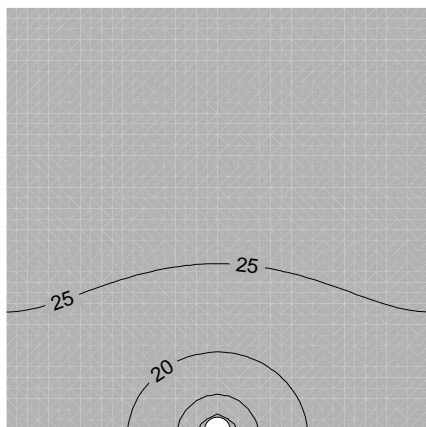
Figure 10: Run d1: Distributed recharge, regular fractures. (a)–(d): Four time slices of fracture-diameter evolution in the karst aquifer. Fractures are shown as lines, the fracture diameter is normalized relative to the initial fracture diameter, as indicated in the bar code. Black and red colours indicate laminar and turbulent flow. Also shown is the hydraulic head distribution (contour lines), and the location of the resurgence is marked with a triangle. (e)–(f): Evolution of integral parameters. →



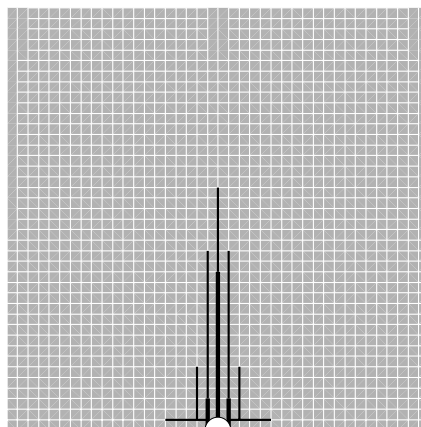


STRUCTURE AND EVOLUTION OF KARST AQUIFERS: A FINITE-ELEMENT NUMERICAL MODELLING APPROACH

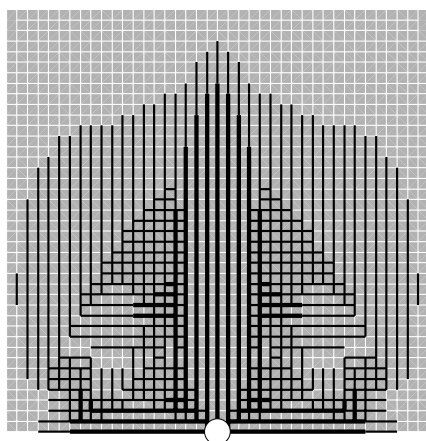
Time = 000000 years a



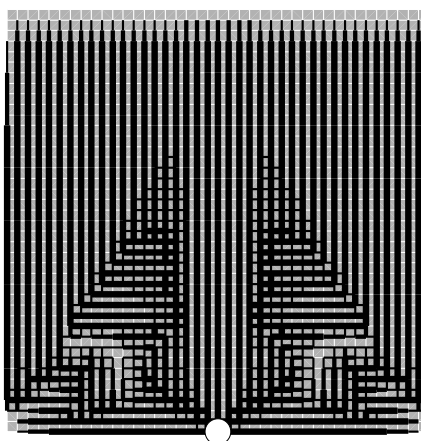
Time = 002000 years b



Time = 010000 years c



Time = 100000 years d

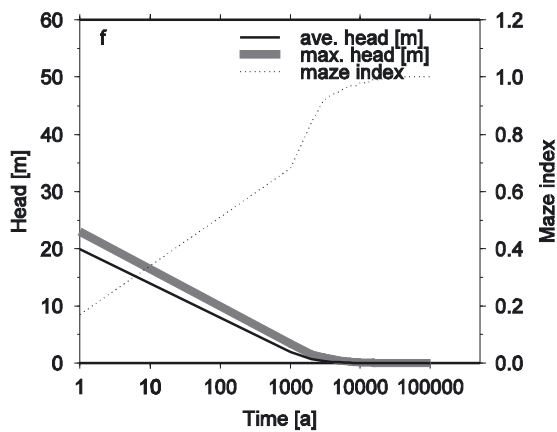
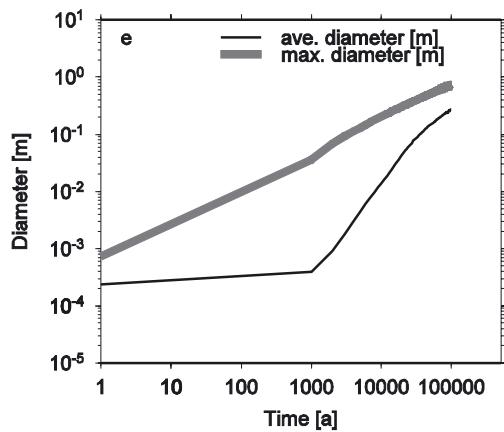
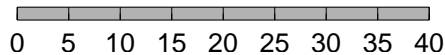


Fracture diameter d / d_{ini}



run41x41_flatd1

Hydraulic head h [m]



Transition from the early, porous-controlled flow to a more mature, fracture-controlled flow can be discussed with the help of some integral parameters of the karst evolution. Therefore, in Figure 10e, we compare the temporal evolution of two fracture diameter quantities: The *maximum diameter* indicates the largest fracture at a specific time in the karst plateau, while the *average diameter* is the mean value of all fracture diameters. Note that times are plotted on a logarithmic scale, hence both quantities already differ for $t = 1$ year. During the first 1,000 years of evolution, the maximum diameter increases from its initial value of 0.2 mm to around 3 cm, while the average diameter increases slowly. This behaviour reflects the selective enlargement close to the karst resurgence, while most of the fractures further away from the resurgence still remain small. Shortly after 1,000 years of evolution, the average diameter suddenly increases and catches up with the maximum diameter. The transition point around 1,000 years marks something similar to the breakthrough time defined earlier. However, we need to keep in mind that breakthrough times have been defined for a karst system with flow driven by fixed-head conditions, while our models are driven by fixed-recharge conditions, which are more likely to represent a catchment-controlled situation. Hence, it seems more appropriate to define the transition as change from porous-controlled to fracture-controlled flow, representing the degree of karstification.

In Figure 10f, two integral parameters of the hydraulic head distribution are plotted, the *maximum head* within the karst aquifer, and the *average head* as the mean of the entire hydraulic head distribution. Both parameters confirm the transition discussed above: The drop from initially high values around 25 m to almost zero over the evolution time of 1,000 years. From then on, they remain low. The kink in both curves indicates the transitional period, before 1,000 years a more or less continuous water table is present and thus flow is more pore-controlled, while after 1,000 years the entire karst plateau is drained through the enlarged fracture system, a more mature fracture-controlled karst aquifer has evolved. The last integral parameter also shown in Figure 10f is the *maze index*. The maze index is a ratio of the total length of all fractures in the karst aquifer, l_{total} , and the length of all fractures, which are enlarged to at least $1.1 \times d_{ini}$, $l_{enlarged}$. Thus,

$$M = \frac{l_{enlarged}}{l_{total}}. \tag{16}$$

Initially, the maze index is $M = 0$, and then it increases to a possible maximum of one, if all fractures are enlarged. Thus, the maze index can be used as an indicator of the degree of enlargement in the system. In the figure, the maze index linearly increases to $M = 0.6$ at 1,000 years of evolution, then over the transitional period a larger increase occurs, and finally the maze index reaches its saturation limit $M \sim 1$, indicating that all fractures are enlarged at least by 10 % in this run.

Now we have established a reference run, and we proceed investigating the effects of *structure* on the karst aquifer evolution. Structure in our case is defined as a more natural distribution of initial fractures, with some random orientation, and the possible

presence of larger faults due to tectonic forces such as compression or uplift, but also the presence of insoluble parts within the limestone plateau, e.g. sandstone lenses.

Run d2: In this second run shown in Figure 11, we have used the same initial fracture distribution as before, but now the orientation of each fracture is perturbed by some random value. The resulting initial fracture distribution represents two main fracture systems, one north-south oriented, the other east-west oriented, but the irregular positions resemble the fractal character of a natural distribution better.

For the evolution of fracture diameters shown in Figure 11a–d the same time steps as before are chosen. At the initiation (0 years), the large-scale features of the hydraulic head distribution are essentially similar to that of run d1. Only on a smaller scale the influence of the irregular fracture distribution can be seen, as the pressure isolines are no longer smooth, but wiggle slightly. After 2,000 years of evolution, several fractures close to the karst resurgence have been enlarged to the ten centimetre-scale, and propagate into the karst aquifer. The symmetry of run d1 has been broken, as the irregular fracture distribution now allows for more direct flow paths to evolve. Now a closer correlation between pressure isolines and enlarged fractures can be seen, as fractures perpendicular to the pressure isolines experience the largest head differences and thus are most likely to be enlarged. After 10,000 years of evolution, a typical dendritic cave passage pattern has evolved, and several branches of enlarged fractures radiate away from the karst resurgence. After 100,000 years the run has been terminated, and the resulting passage pattern now drains the entire karst plateau.

The integral parameters maximum und average diameter, maximum and average head, and maze index shown in Figure 11e and f are very similar to the ones discussed for run d1: A distinct change in slope around 1,000 years, which again is the time the karst aquifer changes from more pore-controlled to more fracture-controlled flow. Thus we can conclude that a structural change in the distribution of fractures will affect the cave passage pattern evolving, but the hydraulic behaviour of the karst aquifer is essentially the same for both runs.

Run d4: In this third run shown in Figure 12, the irregular fracture distribution with fractures in north-south and east-west directions is kept, but additionally a larger fault is present in the karst plateau. This fault, which has an initial diameter of 0.6 mm, only three times larger than the other fractures, can be seen in Figure 12a: It runs midway through the karst aquifer from east to west. The position of the fault is almost parallel to the initial pressure isolines, thus almost no flow will initially be redirected through the fault. Consequently, the hydraulic head distribution remains similar to that of runs d1 and d2. However, the fault as additional structural element exerts its influence on the evolution of secondary porosity, as it can be seen for the 2,000 year evolution time step. Here, a set of enlarged fractures radiates away from the karst resurgence, as in the previous run, but the fault has also been enlarged. After 10,000 years of evolution, the effect of the fault becomes more pronounced. While the southern part of the karst aquifer has evolved as before, with a radial pattern of enlarged passages, the fault acts as a local base level, which collects flow from the northern part of the aquifer. Here, passages evolve in a north-south

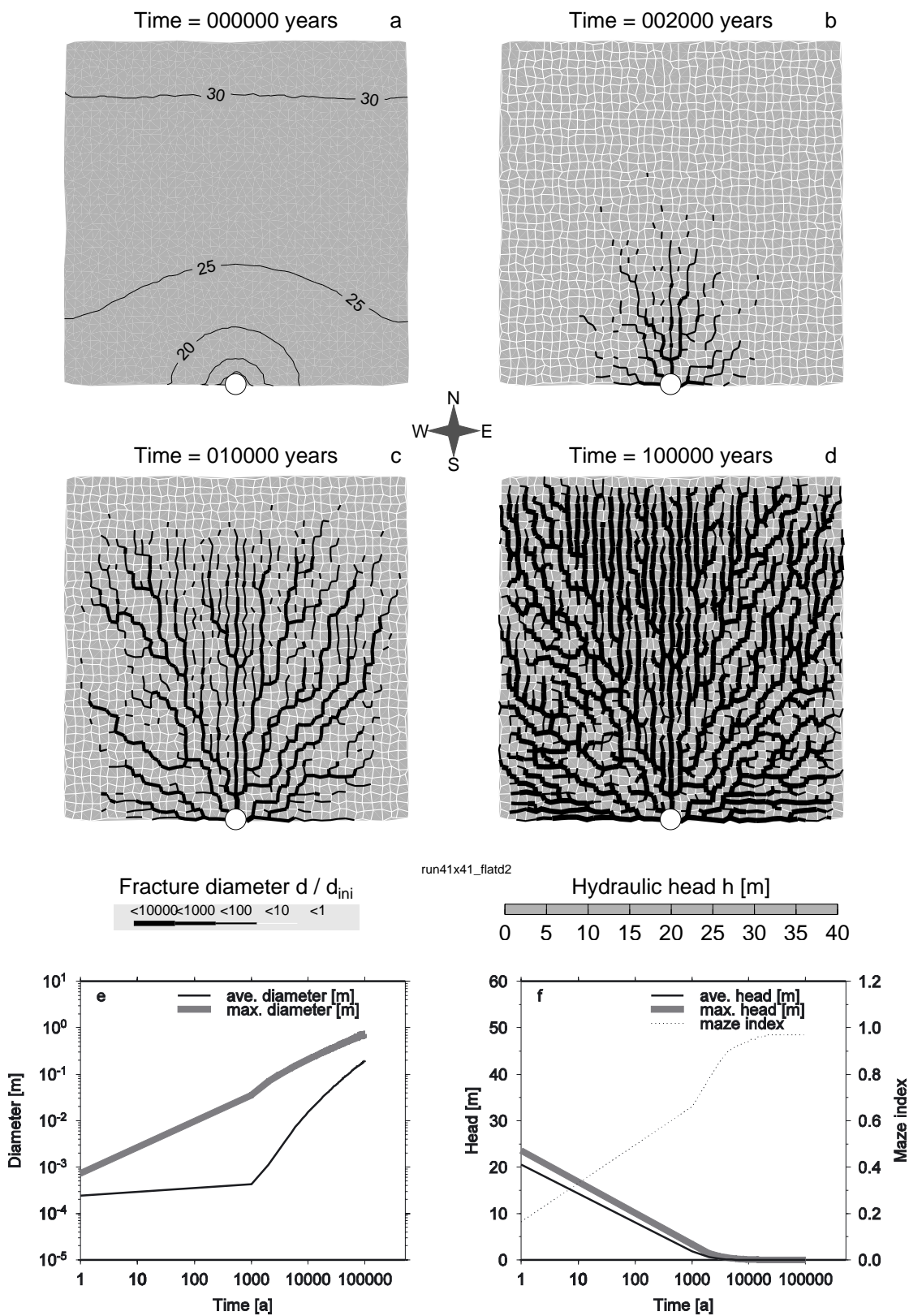


Figure 11: Run d2: Distributed recharge, irregular fractures.

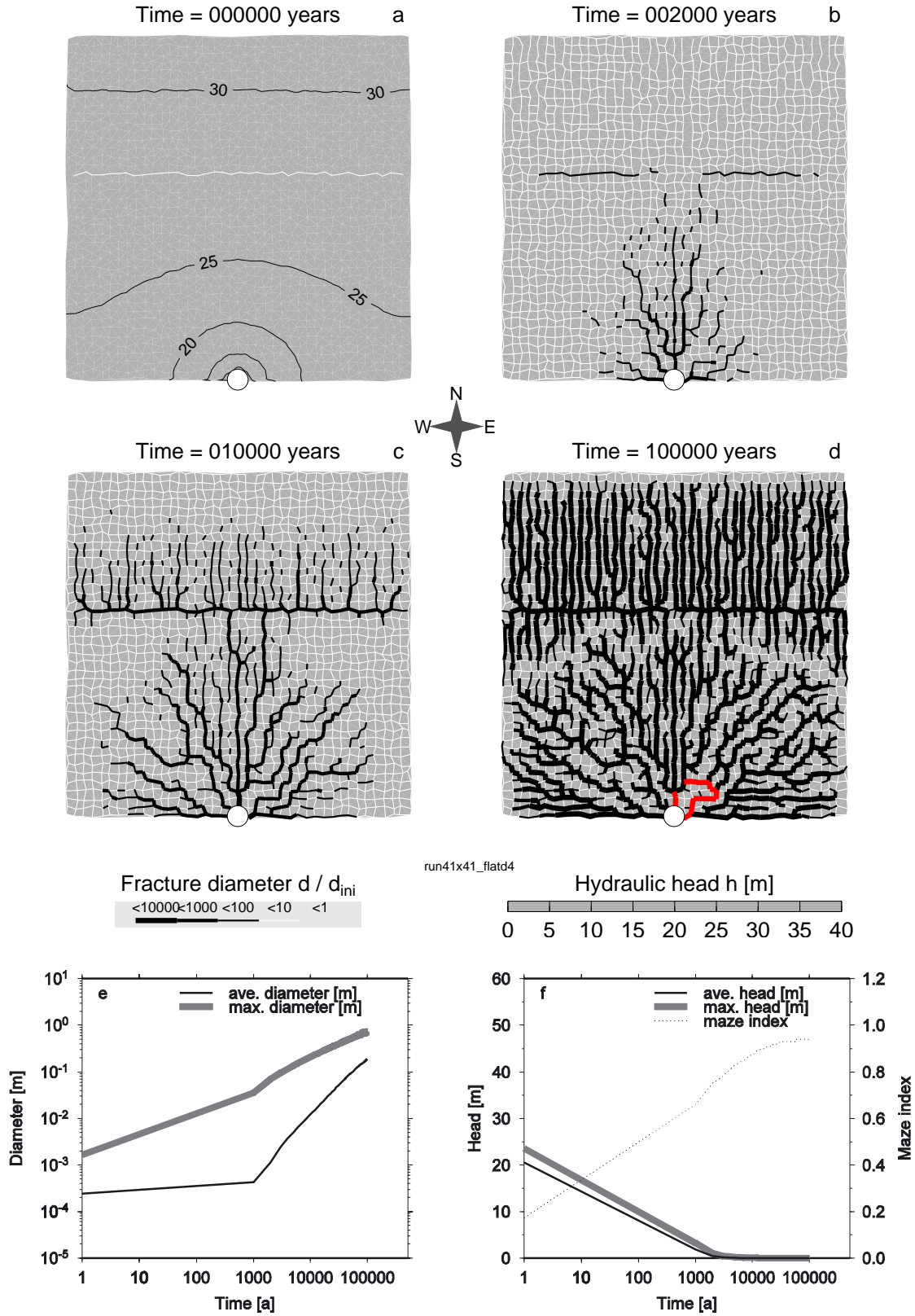


Figure 12: Run d4: Distributed recharge, irregular fractures, and prominent fault.



orientation, draining that part of the plateau towards the fault. The fault then carries that water towards the central part of the aquifer, where fracture systems originating from the karst resurgence have propagated upstream and provide a localised sink for the fault. After 100,000 years of evolution the different cave passage pattern is evident: North-south trending fractures drain the northern parts towards the fault, which then collects the flow and discharges into the southern part via the radially grown enlarged fractures here. The convergence of flow towards the resurgence results in several branches, which experience turbulent flow, as it can be seen by the different shading of the enlarged fractures.

Yet, even the fault resulting in a reorganised cave passage pattern distinctively different to that of runs d1 and d2, the integral parameters maximum und average diameter, maximum and average head, and maze index shown in Figure 12e and f are very similar to the ones discussed before. Hence, the different passage patterns present do not affect the more integral response of the karst aquifer.

Run d5: We conclude the section for distributed recharge with a fourth run shown in Figure 13. Here, the irregular fracture distribution with fractures in north-south and east-west directions is amended by a third set of fractures, following a northwest-southeast trend. In addition, we have incorporated a fault of 0.6 mm initial diameter also running from northwest to southeast, as it can be seen in Figure 13a. Note that the fault bypassed the karst resurgence, hence no prominent initial flowpath towards the resurgence is present. Finally, the upper northwest corner of the karst plateau is modelled as a sandstone region, with no fractures present. Thus, in this region no secondary porosity can evolve.

The hydraulic head distribution reflects the structural changes of this run: Heads are higher in the sandstone region (almost 35 m in the northwest corner), and the pressure isolines in the limestone region follow the northwest-southeast direction, as the karst aquifer now has a pronounced anisotropy in initial permeability due to the additional northwest-southeast fractures and the fault. 2,000 years into the evolution, the fault has been enlarged to the ten centimetre-scale from its north-western end towards the southeast. However, the final end of the fault, which bypasses the resurgence, is less enlarged. Instead, a normal fracture connects the fault to the karst resurgence. Clearly, the fault again acts as local catchment, and the connection is established on the shortest possible flowpath between fault and resurgence. Note that while the head distribution within the limestone region has already collapsed, the heads within the sandstone region remain high. After 10,000 years, a large cave passage drains the plateau, mainly following the fault and running northwest-southeast, then sharply turning close to the karst resurgence. Thus, the more direct passage pattern evolved in run d2, with the radial pattern around the resurgence, has been replaced by a more tortuous path using the fault. Again, the fault as a local catchment redirects fracture growth, and cave passages in the upper part of the plateau grow perpendicularly towards the fault. After 100,000 years of evolution, two large catchments can be distinguished: The larger one with the fault as central drainage, and a smaller one in the lower south-western corner, where normal fractures have been enlarged as in the runs before.



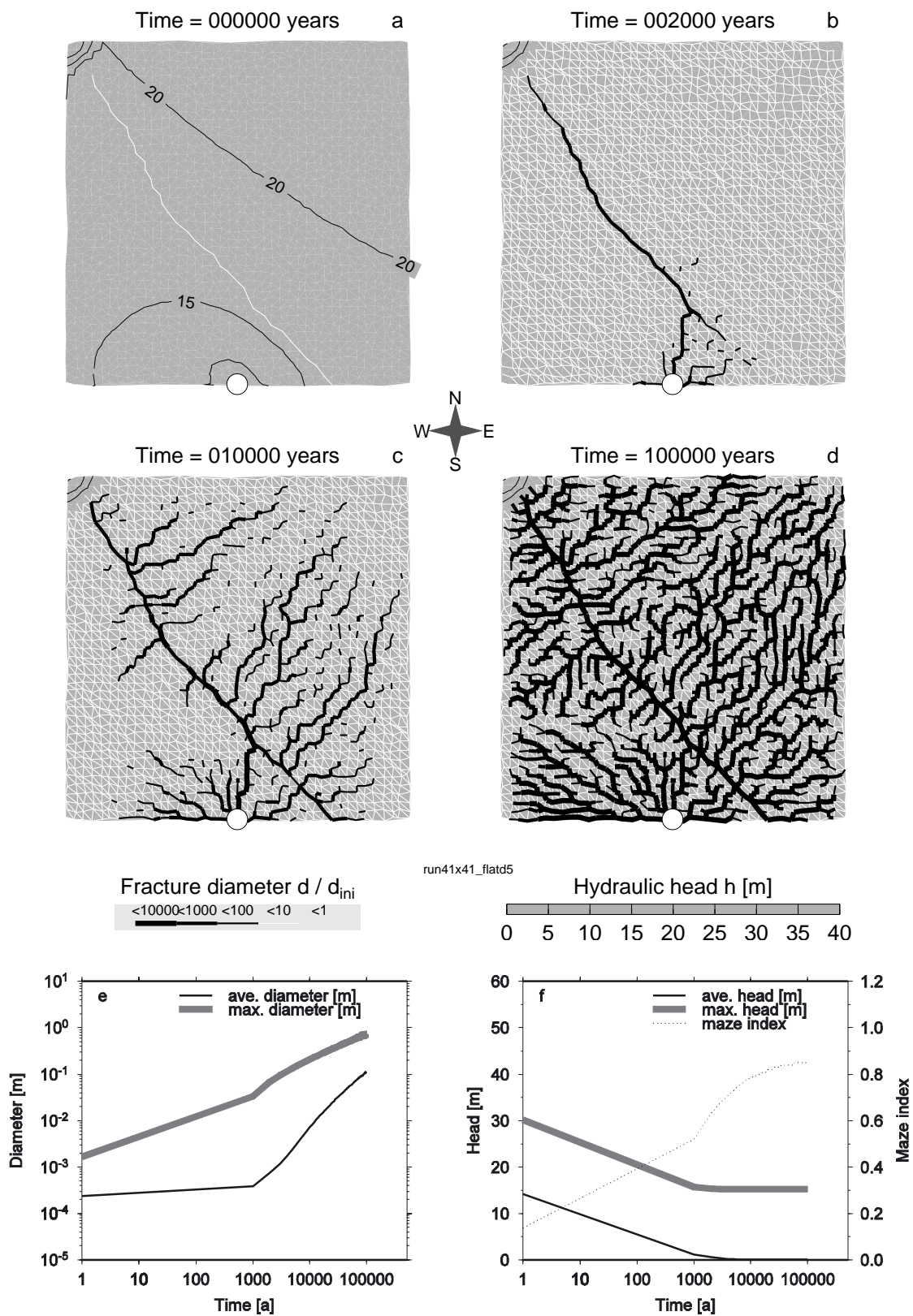


Figure 13: Run d5: Distributed recharge, irregular fractures, prominent fault, and sandstone domain.

The integral parameters maximum and average diameter shown in Figure 13e have evolved similarly as in the previous runs, with the distinct change around the transition from pore-controlled to fracture-controlled flow. The maximum head in Figure 13f drops quickly from 35 m to 15 m over the 1,000 year period, and then remains at the 15 m level, indicating the influence of the sandstone region, which through its high hydraulic heads enhances flow and thus accelerates the evolution. The initial average head is around 5 m lower, when compared to the previous runs, as the karst plateau has more fractures and thus is more permeable from the beginning. The evolution of the two drainage areas discussed above results in a small region within the karst plateau, in which fracture enlargement is inhibited (around the drainage divide). As a consequence, the maze index increases as before, but reaches a saturation limit around $M \sim 0.8$.

3.1.2 Recharge through sinks

In this next section, we discuss a different recharge condition for the karst plateau. Instead of a distributed recharge, we now model a discrete input into two sinks, located at the north-western and north-eastern corners of the plateau. Both streams have a catchment of 0.5 km², which receives 300 mm/yr annual precipitation, and the bedrock is insoluble. Water entering the karst aquifer is aggressive, $T = 10$ °C cold and the partial carbon-dioxide pressure in both streams is set to $p = 0.05$ atm. We also assume that the input concentration with respect to calcite is $c_{in} = 0.9c_{eq}$. For the evolution models, the sink input is both spatially and temporarily constant, representing annually-averaged values. The karst plateau itself is covered by a thin layer of impermeable material, thus no seepage within the plateau is present.

Run s1: The first run of this section is shown in Figure 14a–d. Here, we start again with the unlikely distribution of two rectangular fracture directions in north-south and east-west directions, which form a perfectly regular, checkerboard-style fracture network. Sinks are located in both upper corners of the karst plateau, while the karst resurgence is located midway along the southern margin. The initial hydraulic head distribution (0 years) reveals a perfectly symmetric pattern, with heads close to 45 m at the sinks, dropping to 0 m at the karst resurgence. Pressure isolines are concentric in vicinity of the sinks, become almost east-west trending in the central part of the plateau, then again concentric closer to the resurgence.

After 10,000 years of evolution, two sets of enlarged fractures have started growing from the sinks, following the steepest gradient of the hydraulic head distribution. A fringe of enlarged fractures radiates away from both sinking streams, with the largest fractures reaching the meter-scale close to the sinks. The head distribution has not dropped significantly, only locally around both sinks a drop can be observed. 50,000 years into the evolution, the two fringes of enlarged fractures extend all the way down to the karst resurgence. From each sink, two prominent fractures grow, one evolving south, and one evolving east resp. west. Due to the regularity of the fracture network, no direct growth

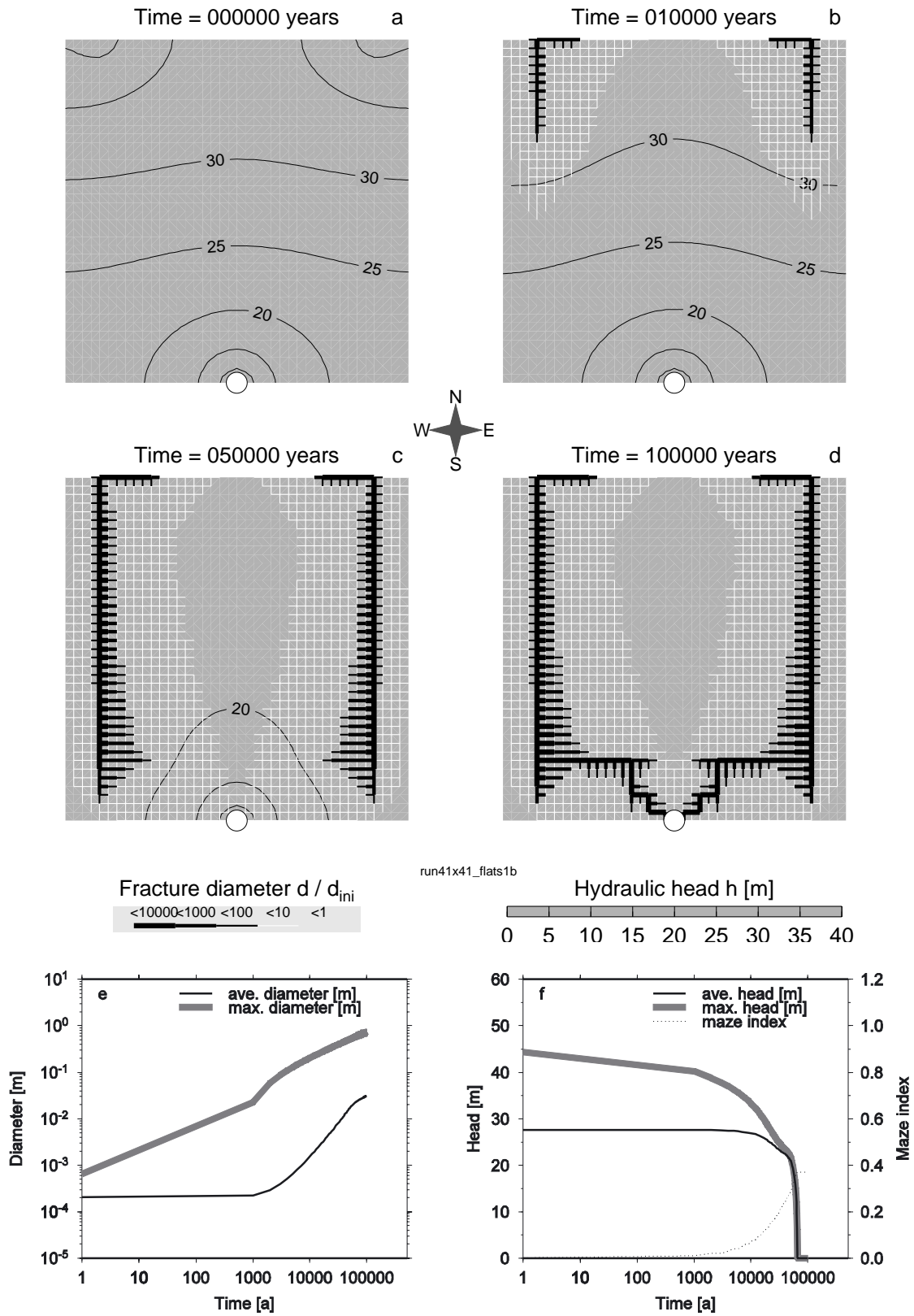


Figure 14: Run s1: Sink recharge, regular fractures.

towards the resurgence is possible. Still, the hydraulic heads remain high in the karst aquifer. The high hydraulic heads are a consequence of the grow pattern in this recharge situation: Water undersaturated with respect to calcite is only injected at both sinks, and on its way down it dissolves the bedrock and quickly becomes saturated. Analogous to the single conduit case, only the section close to the input points (the sinks) are significantly enlarged. Further downstream, enlargement of fractures is very slow and many competing fractures evolve at a similar pace, resulting in the large fringes. After 100,000 years of evolution, enlargement has proceeded further, and two continuous flowpaths between sinks and resurgence have been established. The two fracture systems resemble two independent drainage systems. The hydraulic head distribution has collapsed, as now the entire flow is carried through the enlarged fracture system. The late breakthrough of the fracture systems has occurred simultaneously in both branches, a consequence of the symmetry of the fracture network.

The integral parameters maximum diameter and average diameter are shown in Figure 14e. The maximum diameter increases about one order of magnitude during the first 1,000 years, then levels off and reaches a value around 1 m after 100,000 years. The average diameter, however, remains almost constant during the first 1,000 years, reflecting the selective local enlargement around the two sinks. Later on, this parameter increases quickly, as the fringe of enlarged fractures propagates downstream towards the karst resurgence. The maximum and average head shown in Figure 14f clearly reveal the distinctively different evolution of the sink recharge model, compared to the distributed recharge models of the last section. The maximum head drops slowly from 45 m to 30 m over a period of 10,000 years, and drops to zero just before the end of the run at 100,000 years. The average head remains constant for about 10,000 years, revealing the local drop in heads close to the sinks. In the majority of the karst aquifer, hydraulic heads remain high during that early phase. The maze index starts growing just 1,000 years into the evolution. It reaches a value around $M \sim 0.4$ at the end of the run, indicating the selective enlargement of fractures in this model.

Run s2: The second run is shown in Figure 15a–d. Here, the orientation of fractures has been perturbed by a random value, resulting in an irregular fracture network. The pattern of the initial hydraulic head distribution (0 years) is almost identical to that of the previous run s1, only the wiggling pressure isolines indicate the irregularity of the fracture network. After 10,000 years of evolution, two independent systems of enlarged fractures have started growing from the sinks towards the karst resurgence. Due to the irregular fracture distribution, the pattern of enlarged fractures originating from the two sinks already shows marked differences. Hydraulic heads remain high, as the southern part of the karst aquifer is still controlled by pore-controlled flow and thus is the bottleneck for flow resistance. After 50,000 years, both fringes of enlarged fractures have reached the karst resurgence. Hydraulic heads have dropped, and significant gradients remain only present close to the resurgence. Most of the karst aquifer, however, is already efficiently drained through the enlarged fractures and thus characterised by an almost constant hydraulic head. From both sinks, two larger fracture-systems have evolved,



STRUCTURE AND EVOLUTION OF KARST AQUIFERS: A FINITE-ELEMENT NUMERICAL MODELLING APPROACH

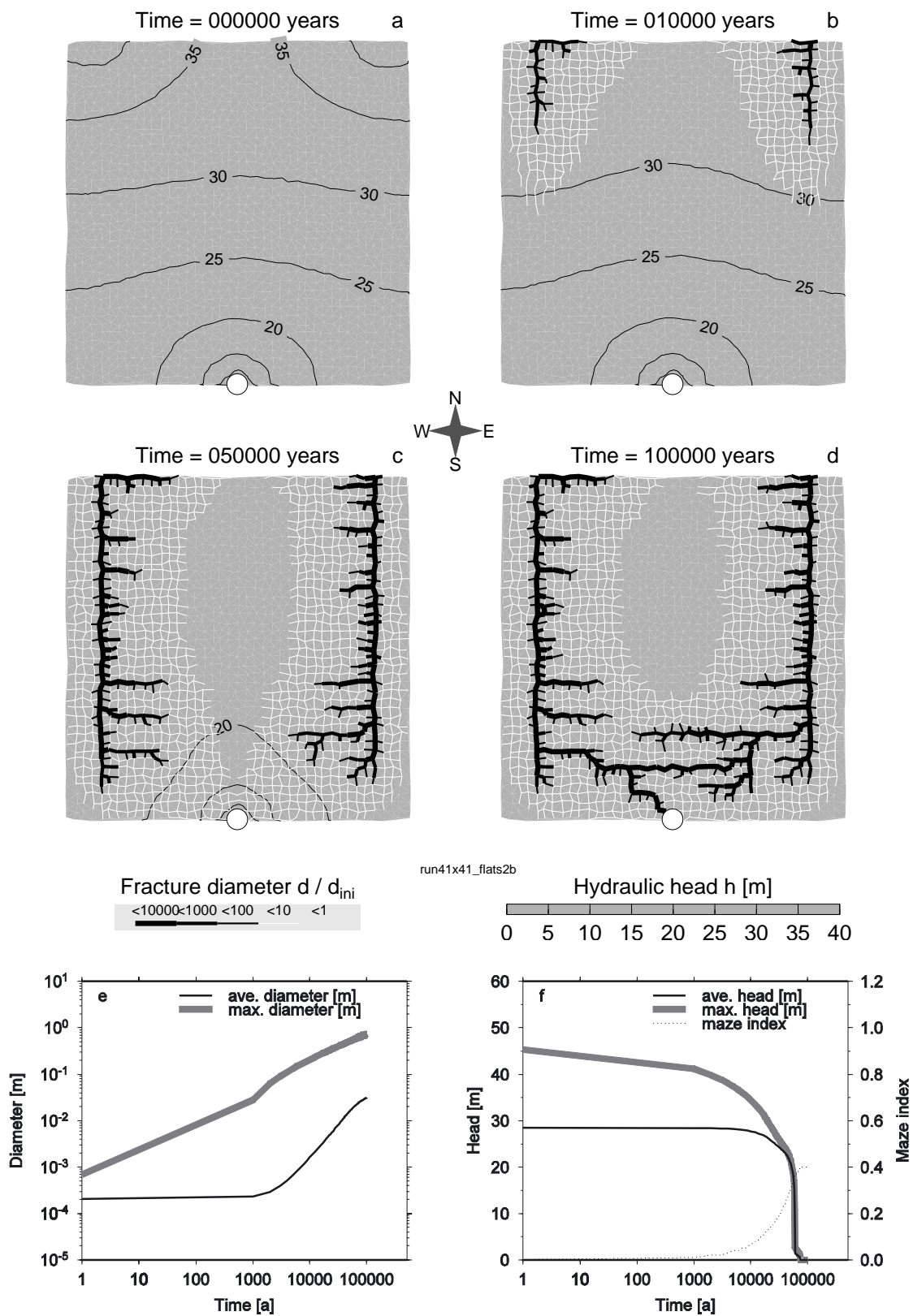


Figure 15: Run s2: Sink recharge, irregular fractures.



enlarged to the meter scale. Both of these fracture systems have developed competing branches, with most of them losing out to competition of flow. After 100,000 years of evolution, the effect of the irregular fracture network becomes apparent: Instead of two independent drainage systems as in the run s1 before, the western branch was the first one to break through to the karst resurgence. The eastern branch was at that time evolving towards the resurgence, too, but the breakthrough of the western branch caused a reorganisation of the eastern branch: Instead of continuing to grow directly towards the resurgence, it was hydraulically easier to connect to the western branch and use the already existing drainage system. Hence, the lower reaches of the drainage system are no longer independent.

The integral parameters maximum diameter, average diameter, maximum head, average head, and maze index are shown in Figure 15e–f. Despite the different passage pattern evolving, when compared to run s1, the integral response is almost identical to the previous runs: A late drop in heads, as breakthrough occurs fairly late in these models, and a low final maze index, representing the selective enlargement of fractures.

Run s3: The third run is shown in Figure 16a–d. Here, the irregular fracture distributions characterised by north-south and east-west directions are complemented by a third fracture set heading from north-west to south-east. This third fracture set increases the primary porosity of the karst aquifer, and is responsible for a pronounced anisotropy in flow resistance from the onset of evolution on. The hydraulic head distribution at the onset (0 years) mirrors the anisotropy well. Both sinks are still maxima for heads, though with lower values around 40 m due to the increased conductivity. However, pressure isolines in the karst aquifer are no longer east-west oriented, but dip slightly towards the south-east. 10,000 years into the evolution, two fringes of enlarged fractures have evolved around the sinks. While the form of the eastern fringe is comparable to the previous two runs, the western fringe is elongated in the southern direction, and has already gained a hydrological advantage in reaching the karst resurgence. This becomes more obvious after 50,000 years of evolution. The western fringe has reached the resurgence, and a large fracture zone, widened to the ten-centimetre scale, has almost reached the karst resurgence. The evolution of the eastern fringe is completely different: Several competing branches evolve, one set growing southward and trying to establish a direct flowpath to the karst resurgence, the other set growing westward towards the flowpath of the other sink. Hence, we have a strong competition in this case between direct flowpath and an alternative route through existing enlarged fractures. In the case chosen here, the second alternative has won, as it can be seen after 100,000 years of evolution. The sinking water from the eastern sink now flows through an enlarged fracture towards the west, then draining through the fracture network established by the western sink. Instead of two independent drainage systems, the water from the eastern sink now follows a very tortuous path towards the resurgence. Large parts are already experiencing turbulent flow conditions, as it can be seen by the different shading of the fractures.

The integral parameters maximum diameter, average diameter, maximum head, average head, and maze index are shown in Figure 16e–f. Again, no significant change

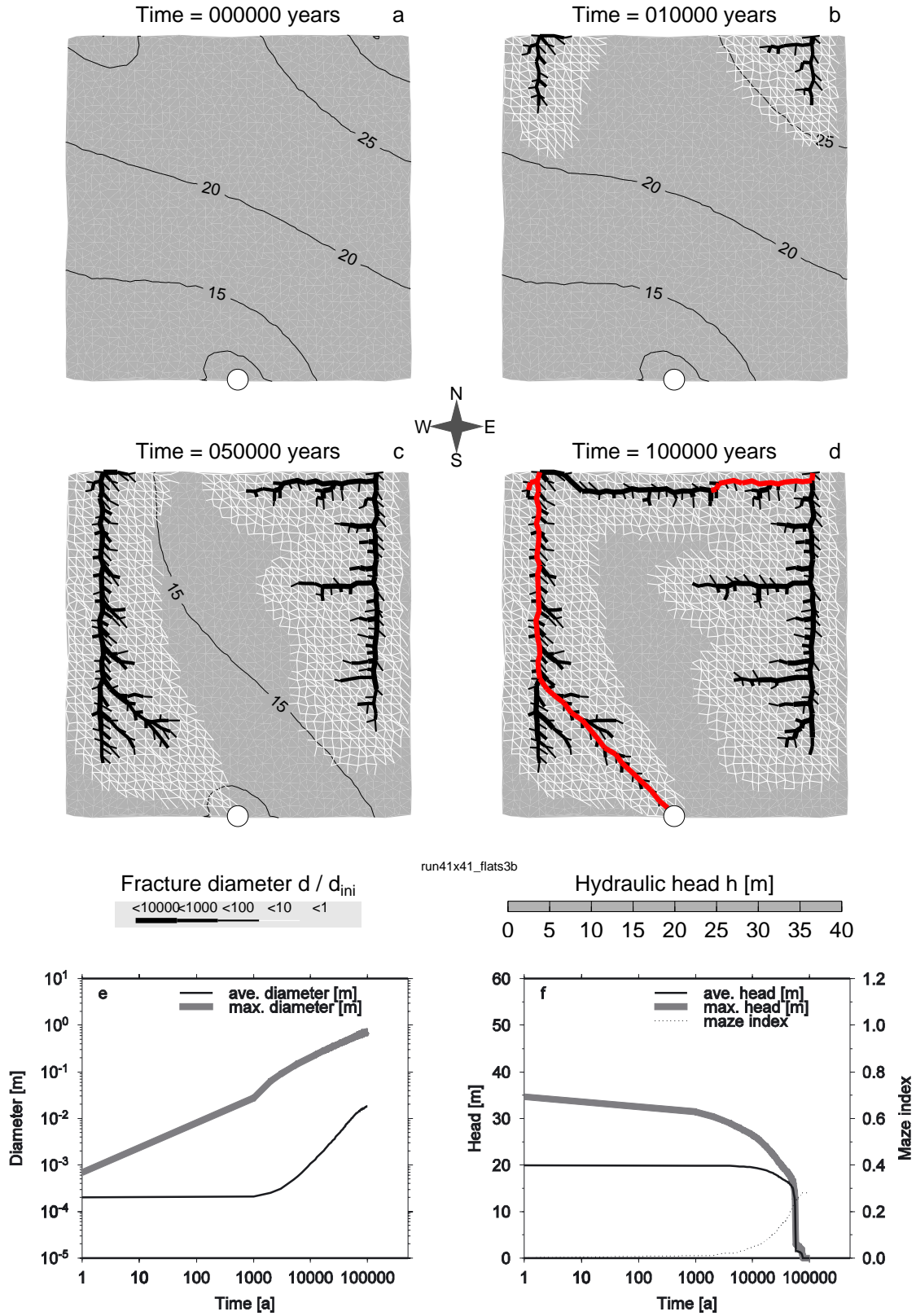


Figure 16: Run s3: Sink recharge, irregular fractures, and additional NW-SE fractures.

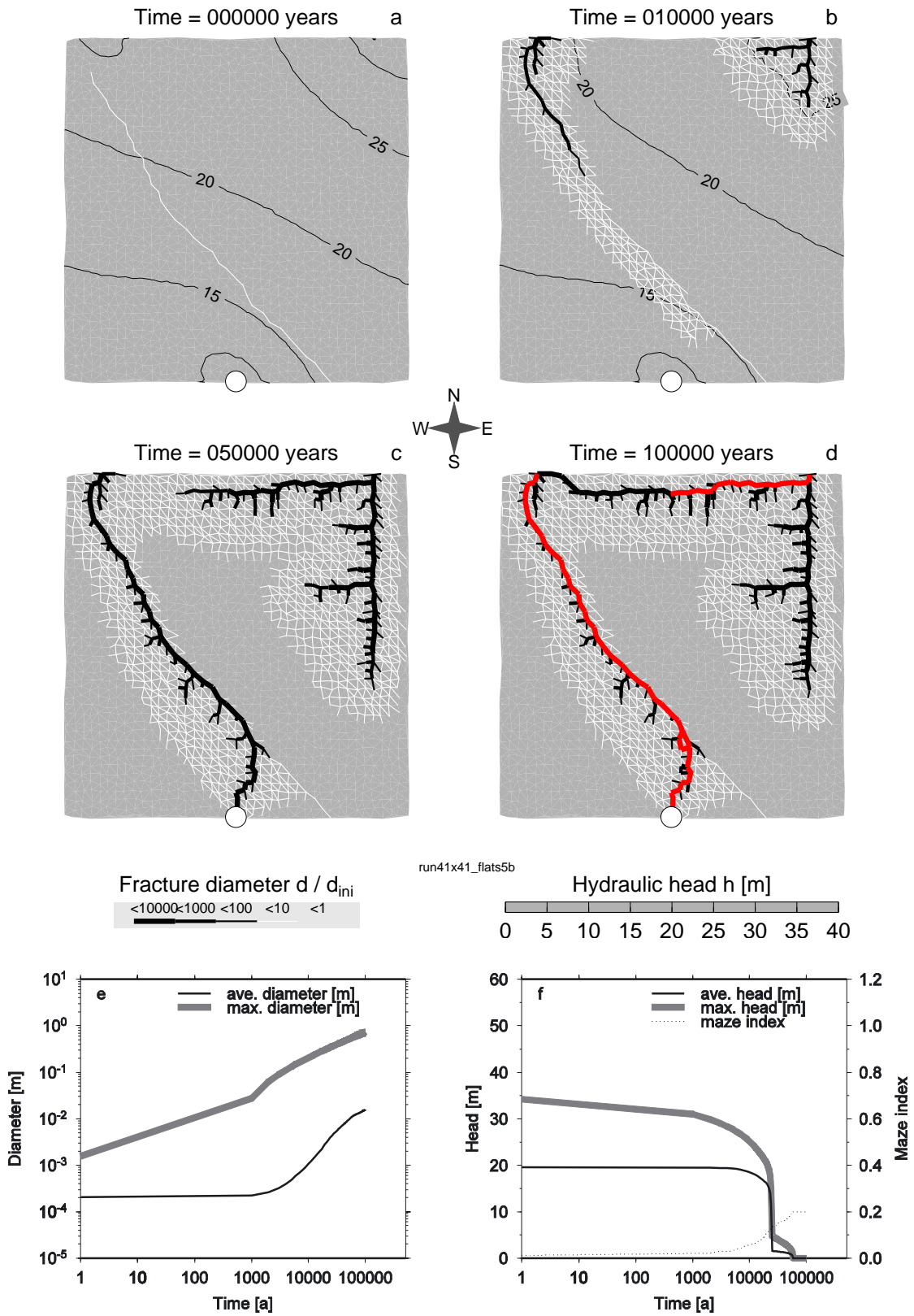


Figure 17: Run s5: Sink recharge, irregular fractures, and prominent fault.

is visible for the diameter evolution, but both maximum and average heads are lower by about 8 m, when compared to the previous runs s1 and s2. The final maze index is with $M \sim 0.3$ lower than in the previous cases, a consequence of the different evolution of the eastern sink.

Run s5: The last run of this section is shown in Figure 17a–d. In addition to the three fracture directions used in the last run s3, north-south, east-west, and northwest-southeast, we have included a fault with an initial diameter of 0.6 mm. The fault is also running from northwest to southeast, as it can be seen in Figure 17a, and it bypasses the karst resurgence. The hydraulic head distribution at the onset of karstification (0 years) is very similar to that of the last run s3, despite the larger fault. The reason for the similarity is the orientation of the fault, which roughly dips in the same direction as the pressure isolines. After 10,000 years of evolution, we identify the two fringes of enlarged fractures radiating out from the sinks, with the western fringe more elongated due to the anisotropy in conductivity. In addition, a fringe of enlarged fractures has propagated into the karst aquifer along the fault. This enlarged fringe around the fault provides a competitive advantage for the western sink, as it can be seen after 50,000 years of evolution. Instead of continuing to grow along its southern fracture system, it uses the fault as an easier route and a flowpath between western sink and karst resurgence is established via the fault. The eastern sink during its evolution tries to establish two different flowpaths, one southward, and the other one heading towards the fault. The latter flowpath is winning, as it can be seen after 100,000 years of evolution. The final drainage pattern in this run are two independent passages originating from the two sinks, which merge in vicinity of the fault to continue as one single drainage path towards the karst resurgence. Again, the concentration of flow into one fracture system initiates turbulent flow in the downstream end of the drainage system.

As the passage pattern resulting from this run is not too different from the previous run s3, the integral parameters shown in Figure 17e–f are essentially telling the same story: A late drop in heads due to the slow initial growth of fractures, until a continuous flowpath from sinks to resurgence is established. Then heads drop rapidly, as the transition from pore-controlled to fracture-controlled flow has occurred. With $M \sim 0.2$ the final maze index again reflects the very selective enlargement of fractures within the karst plateau.

3.1.3 Recharge through sinks including mixing corrosion

So far we have discussed the effects of recharge (distributed versus discrete recharge) and structure (regular versus irregular fractures, faults) on the long-term evolution of a karst plateau. In this section, we add another decisive effect, chemistry. The setting is similar to that of the last section, a capped karst plateau, thus no recharge through its surface is possible. Two streams with catchments of 0.5 km² collect water from sandstone regions, and the resulting two streams disappear into sinks along the upper western and eastern tips of the karst plateau. The water is assumed to be $T = 10$ °C cold, but now we allow for different carbon-dioxide concentrations. This situation can be compared to one

sandstone catchment with sparse vegetation and consequently low concentration of CO_2 in the stream ($p = 0.01$ atm), and the other catchment dominated by thick, fertile soil and thus a runoff significantly enriched in CO_2 ($p = 0.1$ atm). The different carbon-dioxide concentrations provide an alternative dissolution mechanism, the mixing-corrosion effect, which we have introduced before.

Run sm7: The first run of this section is shown in Figure 18a–d. It resembles a karst plateau with initial fractures in north-south and east-west direction, irregularly distributed, as in run s2. Thus, the initial hydraulic head distribution (0 years) is the same as in run s2, with 45 m high heads around the two sinking streams, dropping to 0 m close to the karst resurgence.

The water entering the karst aquifer via the western (left) sink has a low CO_2 -partial pressure of $p = 0.01$ atm, and the water disappearing into the eastern (right) sink a higher value of $p = 0.1$ atm. Therefore, after 10,000 years of evolution, a situation distinctively different from run s2 can be observed: From the eastern sink a fringe of enlarged fractures evolves, radiating away towards the karst resurgence. From the western sink another fringe of enlarged fractures develop, but this fringe evolves much slower due to the lower carbon-dioxide concentration of the seepage water. Thus the eastern sink has a competitive advantage due to its larger potential to dissolve bedrock. Additionally, a fringe of enlarged fractures appears deep within the karst aquifer, evolving in a north-south direction. This third area of significant enlargement is a result of the mixing of the two seepage waters: While the seepage from both sinks will quickly be saturated with respect to calcite and thus no longer able to dissolve bedrock, the mixing of the two saturated contributions deep within the aquifer will result in a solution, which is again aggressive due to the different carbon-dioxide concentrations (see Figure 3). The influence of mixing corrosion becomes more clear after 20,000 years of evolution. While the fracture system originating from the western sink is retarded in its growth, the enlarged fractures from the eastern sink have almost established a connection to the fracture system in the central part of the karst aquifer. The hydraulic head distribution reflects the two-fold evolution: In the western section heads are still higher, as no continuous flowpath has evolved yet. The entire eastern section, however, has an almost constant hydraulic head, as here drainage is efficiently carried through the enlarged fractures towards the karst resurgence. At the end of the run at 100,000 years, a large drainage system connects the eastern sink to the resurgence, but not along the most direct way. Instead, flow is channelled through the enlarged fractures in the central part of the aquifer, which are a result of the mixing-corrosion effect. The water disappearing into the western sink flows eastward to directly drain into the enlarged fault.

The integral parameters for this run are shown in Figure 18e–f. Both the maximum and the average diameter are evolving in a similar way as for run s2, with an almost constant average diameter during the first 1,000 years indicating slow initial enlargement. Both the maximum and the average heads drop slowly during that early phase, but from 1,000 years on they drop more rapidly. However, even very close to the end of the evolution at 100,000 years, the final maximum head is still around 10 m, a consequence of the delayed evolution of the western drainage area.

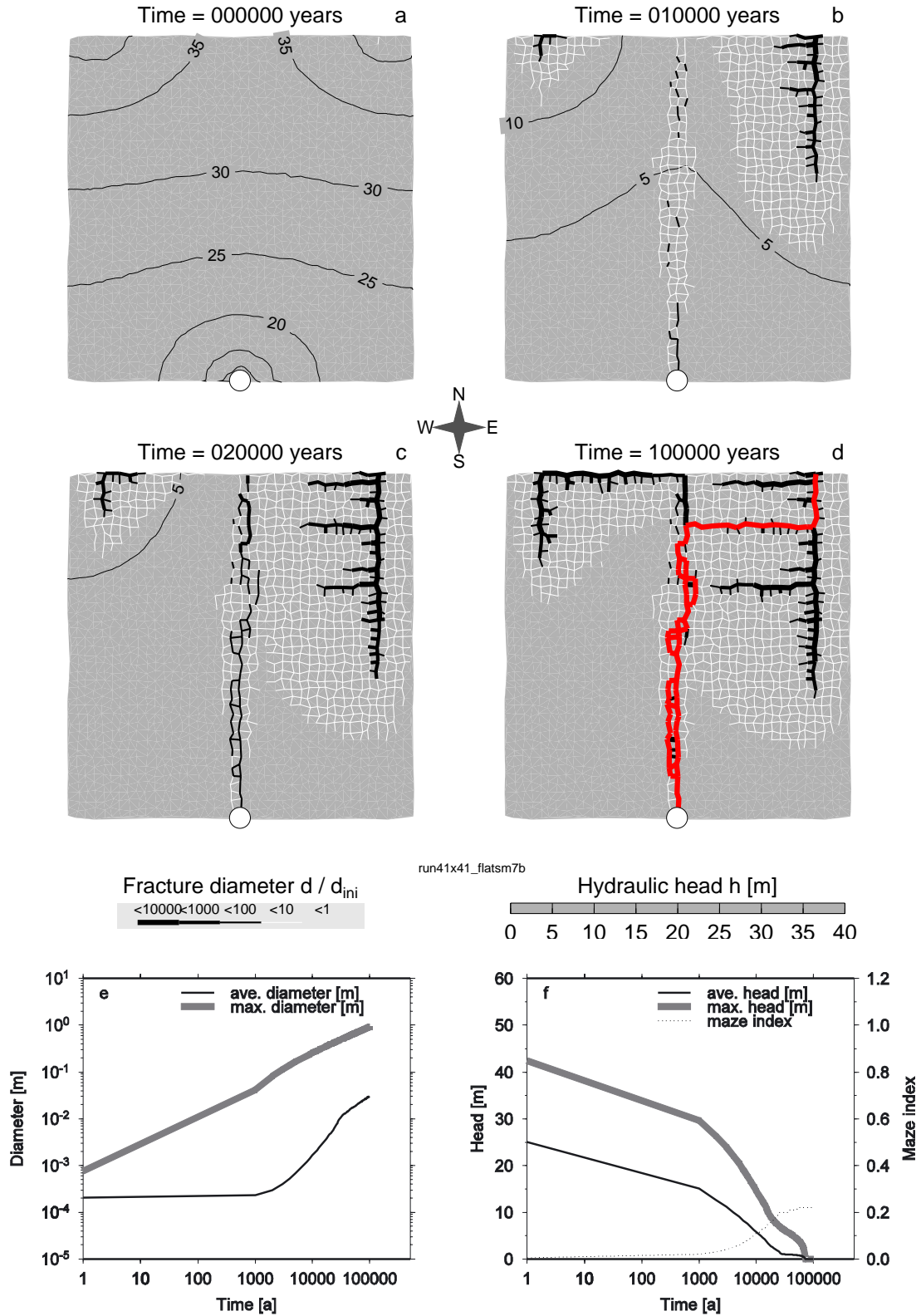


Figure 18: Run sm7: Sink recharge, irregular fractures, undersaturated input, and different CO_2 -concentrations.

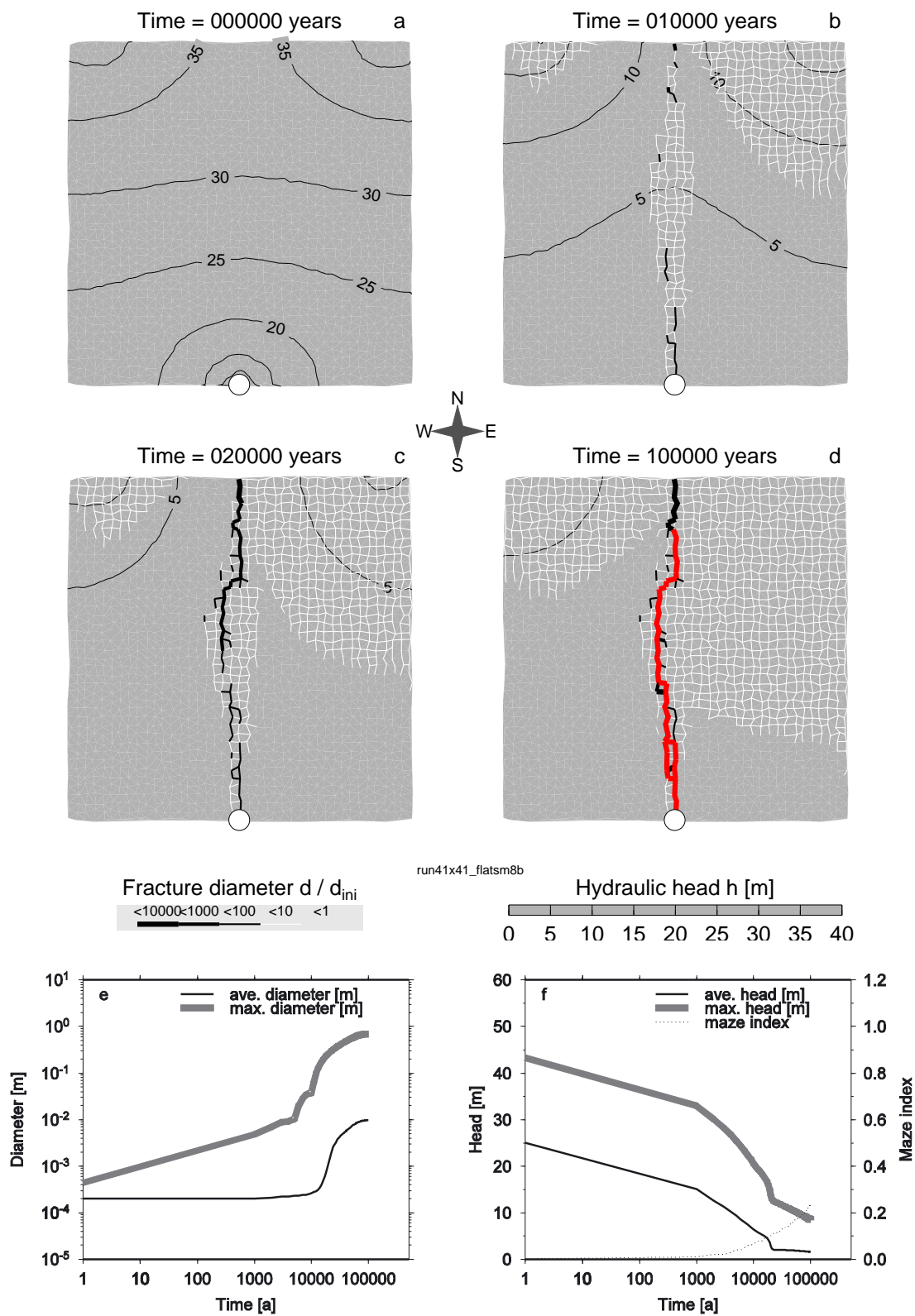


Figure 19: Run sm8: Sink recharge, irregular fractures, saturated input, and different CO₂-concentrations.

Run sm8: The second run of this section is shown in Figure 19a–d. This run provides more insight into the effect of mixing corrosion, as both sinking streams in this case are almost saturated with respect to calcite ($c_{in} = 0.99c_{eq}$), thus not able to dissolve significant amounts of limestone. The fracture geometry is as before, two sets of irregular fractures, one in north-south direction, the other in east-west direction. The initial hydraulic head distribution (0 years) is as before. After 10,000 years of evolution, fracture enlargement is visible close to both sinks and in the central section of the karst aquifer. However, enlargement is very slow, with fracture diameters still restricted to the millimetre-scale. After 20,000 years of evolution, the fringes originating from the two sinks have expanded, but still fracture diameters are small there. But the mixing of the almost saturated seepage waters occurring in the central part has resulted in aggressive solution enlarging a central drainage channel, heading from north to south towards the karst resurgence. This central drainage channel evolves further due to the mixing effect and the focussing of flow. At the end of the run after 100,000 years, a large single fracture system with diameters in the meter range has evolved. However, the upstream portions are drained through a dense network of small fractures, only enlarged to the millimetre scale.

This distinctively different passage pattern is reflected in the integral parameters shown in Figure 19e–f: Both the maximum and the average diameters evolve very slowly during the first 10,000 years. Then, the maximum diameter quickly rises and reaches meter-scale values present in the central channel. The maximum head drops slowly during the initial 1,000 year phase, then faster, but the final value is still above 10 m, reflecting the more pore-controlled flow through the dense fringe of marginally enlarged fractures close to the two sinks. The maze index also evolves slowly, with enlarged fractures appearing just close to 10,000 years. The final value of $M \sim 0.2$ indicates the restriction of enlarged fracture to the central channel.

Run sm10: The last run of this section is shown in Figure 20a–d. Here, we combine mixing corrosion and faults in one model. Three sets of fractures are present, one north-south oriented, one east-west oriented, and one northwest-southeast oriented. A large fault with an initial diameter of 0.6 mm strikes in the northwest-southeast direction. The stream sinking in the north-western corner has a low carbon-dioxide concentration ($p = 0.01$ atm), the stream sinking in the north-eastern corner a higher value ($p = 0.1$ atm). Both streams are saturated with respect to calcite. The initial hydraulic head distribution is skewed, with 40 m high values close to the sinks, dropping to 0 m at the karst resurgence. Pressure isolines are northwest-southeast oriented due to the anisotropy in conductivity. Again, the fault bypasses the resurgence. After 10,000 years of evolution, fringes of enlarged fractures have evolved around the two sinks, with the one around the western sink much smaller in size due to the low CO_2 -concentration. However, an interesting effect occurs deeper within the karst aquifer, where the seepage water from both sinking streams mix. As the fault provides a path favourable to flow due to its higher conductivity from the onset of karstification on, the mixing zone is now oriented around the fault in northwest-south-eastern direction. As it can be seen

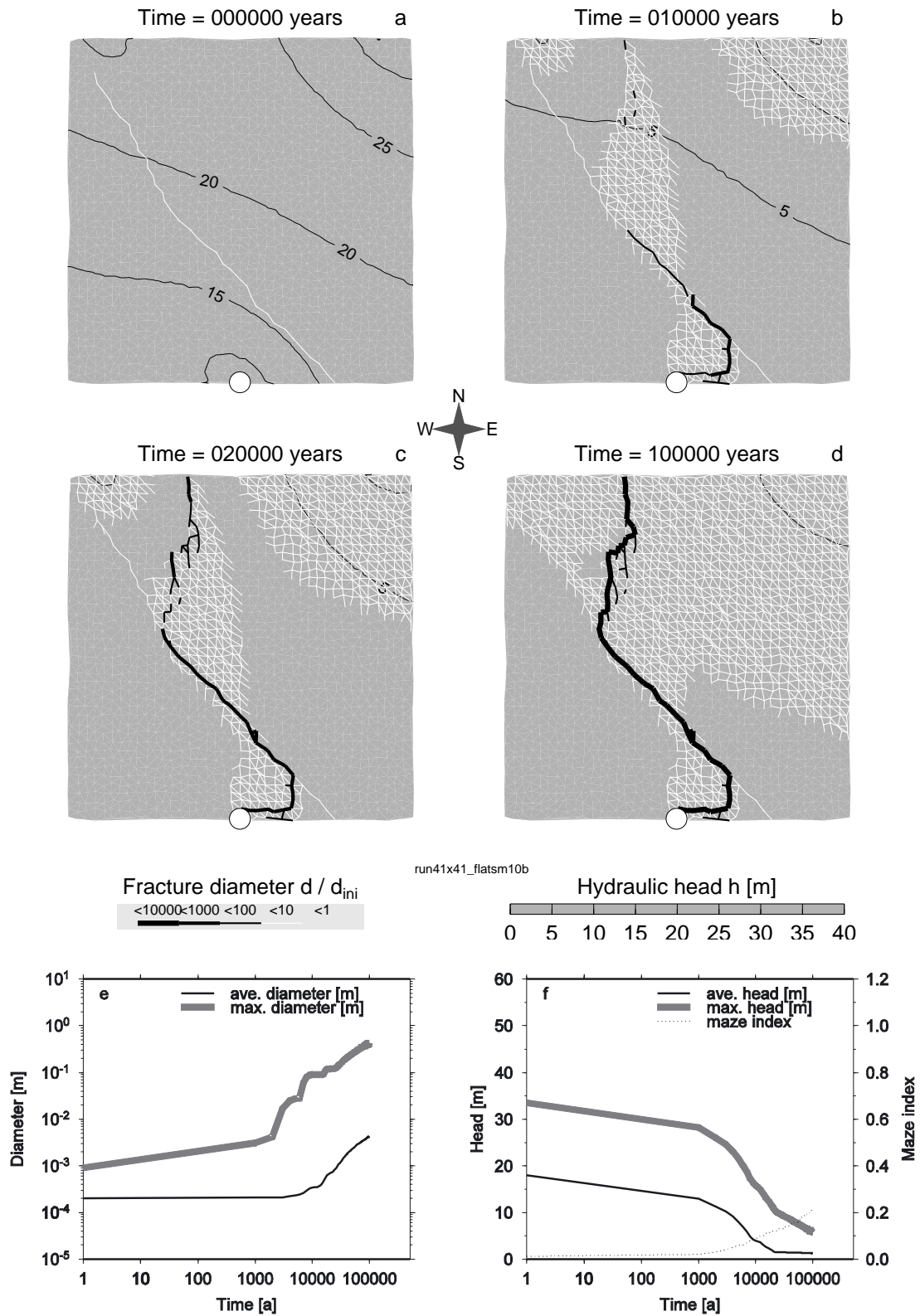


Figure 20: Run sm10: Sink recharge, irregular fractures, additional prominent fault, saturated input, and different CO₂-concentrations.

after 20,000 years of evolution, an enlarged fracture system has evolved deep within the karst aquifer, which is a result of mixing corrosion, but its position has been controlled by the fault. After 100,000 years of evolution, both sinking streams drain through a fringe of slightly enlarged fractures towards the significantly enlarged fault, which then drains large parts of the aquifer towards the karst resurgence. As the fault bypasses the resurgence, the drainage close to the resurgence follows an indirect, twisted path.

Again, the integral parameters shown in Figure 20e–f depict a similar evolution as before.

3.1.4 Summary of long-term evolution models

We have discussed three key parameters controlling long-term evolution of a karst aquifer:

(i) *Structural control by large faults*: The evolution of the karst aquifer is guided by the hydraulic pressure distribution in the system, which is changing with time. In general, the most likely fissures to be enlarged are the ones oriented perpendicular to the pressure isolines, following the steepest pressure gradient. In an ideal karst aquifer with fractures present in every direction, the most direct flow path will be enlarged. If the tectonic setting does not provide enough fissures in the direction of the largest pressure gradient, the evolving fracture system becomes more tortuous. The presence of larger faults induced by tectonic forces provides an alternative flow path, which guides water away from the most direct path. Hence, the structural setting of the limestone plateau at the onset of karstification is responsible for the type of cave-passage pattern evolving.

(ii) *Recharge conditions along the karst surface*: The type of recharge mainly controls the temporal evolution of secondary porosity. If the karst plateau is recharged by precipitation, which infiltrates everywhere over the karst surface, fracture enlargement starts close to the base level, and then propagates upstream into the karst aquifer. This type of evolution is directly controlled by the breakthrough time, as aggressive recharge is injected everywhere and the shortest distances are evolving first. If the karst plateau is recharged only by sinking streams, the fracture enlargement starts at the sinks and propagates downstream towards the resurgence. As aggressive solution is only replenished at the sinks, the infiltrating water quickly becomes saturated and thus enlargement is delayed. In this case the bottleneck are the small fractures close to the base level, which are enlarged very slowly in the early phase.

(iii) *Reaction kinetics of the aggressive water dissolving the rock*: If the infiltrating water, e.g. two sinking streams, are chemically different (different carbon-dioxide concentrations, different temperatures), the mixing of water in the aquifer can result in the evolution of secondary porosity deep within the aquifer. The mixing zone acts in a similar way as a prominent fault, it enlarges faster and provides alternative, more tortuous flow paths.

3.2 Short-term spring response

In this section, we use the long-term karst aquifer evolution models developed in the last section, but now flow is driven by a time-dependent recharge, simulating the karst aquifer hydraulics for a short-term recharge event. The recharge data are taken from the Gallusquelle catchment in southwest Germany (Sauter, 1992). The Gallusquelle is located in the Swabian Alb, a tilted plateau landscape reaching heights between 700 and 900 m asl. Along the northern portion, the plateau emerges as a steep escarpment, and the plateau then gently drops towards the south, where the Danube river is the base level. The plateau consists of bedded, massive and marly carbonate limestone of Upper Jurassic origin, with thickness ranging between 200 and 500 m.

The Gallusquelle catchment is located in a deep-karst setting, and the catchment area is around 45 km². Recharge by precipitation is dominant, and the total discharge of the spring is almost equal to the total recharge. Hence, no significant surface runoff occurs. The response of the Gallusquelle spring to a typical series of recharge events is shown in Figure 2. Discharge peaks 2–3 days after a recharge event, and the flashy response is characteristic to a karst aquifer. However, the long recession limb indicates that the karst aquifer is not mature, with flow occurring mainly through smaller fissures of the limestone.

Sauter (1992) has analysed spring flow, variation in groundwater levels, borehole hydraulic tests, and water chemistry fluctuations of the Gallusquelle hydrological data, and thus was able to estimate hydrological parameters for the area: For the high-storage, low-flow porous matrix he derived values of $K_m \sim (1-10) \times 10^{-4}$ m/s and $S_m \sim 0.01-0.02$, and for the low-storage, fast-flow conduit system $K_f \sim 2-10$ m/s and $S_f \sim (1-3) \times 10^{-4}$. Assuming a circular geometry and laminar flow in the fractures, the fracture conductivities correspond to fracture diameters in the range 2–6 mm. Our estimates of K_m , S_m , and S_f are guided by these values (table 1). We solve (14) for various matrix conductivities and storativities, both for a homogeneous fracture distribution and the fracture distributions resulting from the long-term evolution models. The transient continuity equation is solved with daily time steps, and the model evaluation is initiated with a steady-state solution driven by an annual recharge of 300 mm/yr. This initial condition mimics a normally wet year for the karst aquifer and provides a base-flow component.

3.2.1 Homogeneous karst aquifer

In this first set of model runs, we assume a karst aquifer geometry with constant parameters for both the porous matrix and the fracture system. These runs establish the general behaviour of our simple model, and by varying the principal parameter matrix conductivity K_m , matrix storage S_m , and fracture diameter d_f , the sensitivity of the numerical karst aquifer can be discussed. Recharge in these cases is diffusive, infiltrating the karst aquifer through the entire plateau surface as time-dependent inflow. Again, the

models drain towards a single outlet, a karst resurgence in the middle of the southern boundary modelled as fixed head.

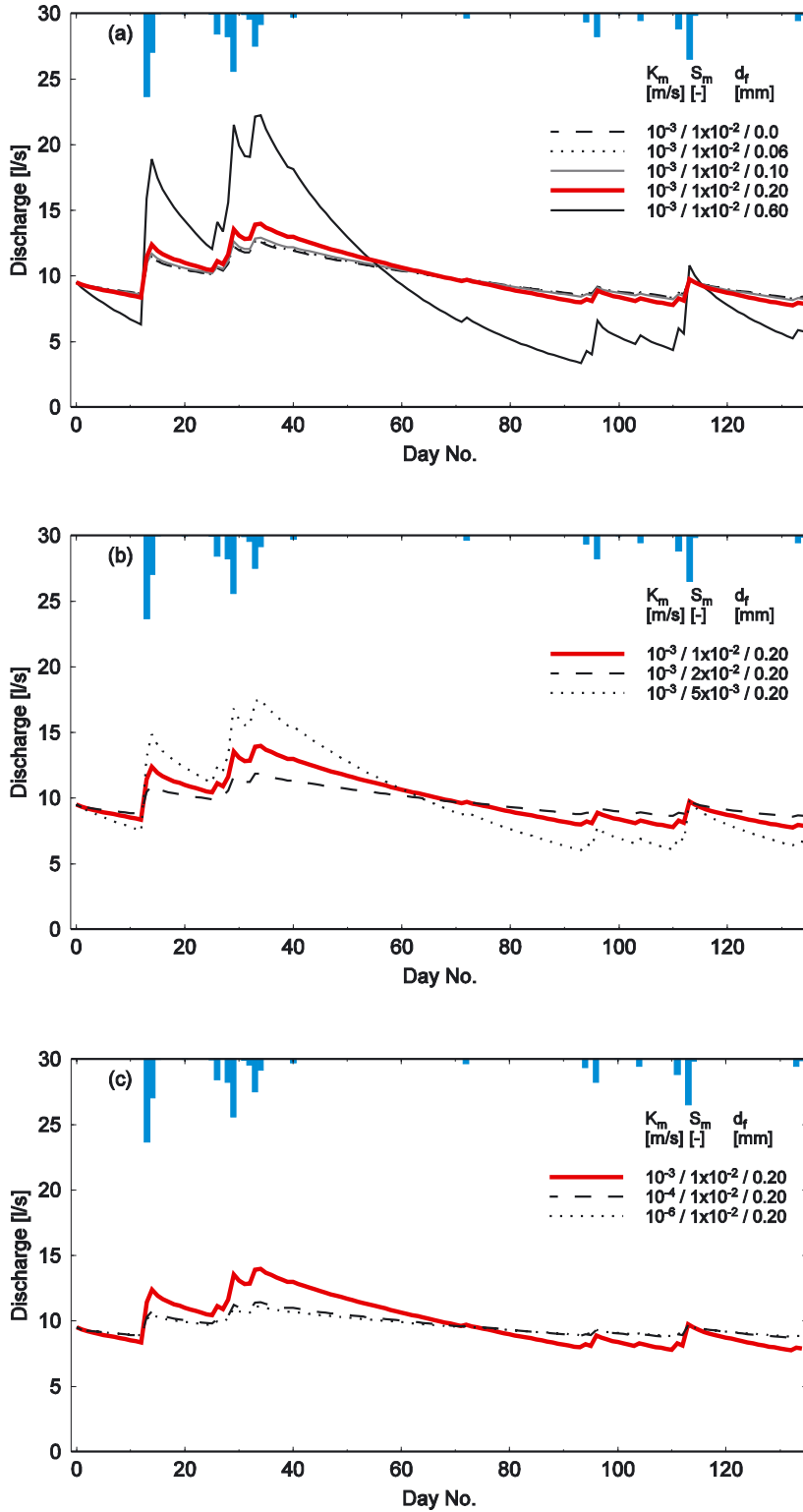


Figure 21: Modelled discharge for homogeneous karst aquifer models. Shown are the spring discharge time series as lines, and the recharge events as bars on top. For further discussion see text.

In Figure 21a, discharge time series are shown for five models, which all have in common a high matrix conductivity of $K_m = 10^{-3}$ m/s, and a matrix storativity of $S_m = 0.01$. The diameter of the fractures varies from $d_i = 0$ to 0.6 mm. Hence, fracture conductivity ranges between zero and 10^{-1} m/s. The pure matrix model ($d_i = 0$) results in the longest recession limb, as in this model water must percolate through the porous matrix and thus storage will take place within the entire model domain. If small fractures ($d_i = 0.06/0.10$ mm, $K_f \sim 10^{-3}$ m/s) are present, the recession limb is slightly reduced, as now parts of the water are able to bypass the porous matrix through the small fractures, which have a very low storage and thus pass the incoming water down immediately. Increasing the fracture width ($d_i = 0.2$ mm, $K_f \sim 10^{-2}$ m/s) will reduce the recession limb further, as in these model the fractures provide an efficient drainage path, which is continuous through the entire aquifer. For ($d_i = 0.6$ mm, $K_f \sim 10^{-1}$ m/s), the hydrograph response becomes much more flashy, an indication of a more effective karst aquifer system with efficient drainage of the fast-flow component through fractures.

We now fix the fracture diameter to $d_i = 0.2$ mm, a value commonly assigned in numerical karst aquifer evolution models for the initial stage. Keeping the matrix conductivity high with $K_m = 10^{-3}$ m/s, we now vary the matrix storage from $S_m = 0.005$ to 0.02 (Figure 21b). A pronounced effect can be observed for the recession limb: Decreasing the matrix storativity to lower values significantly reduces the recession limb, as water is stored less effectively in the system. Conversely, increasing matrix storativity results in a discharge for typical for porous aquifers, as the retention of the water is very effective.

In the last panel (Figure 21c), we keep matrix storage ($S_m = 0.01$) and fracture diameter ($d_i = 0.2$ mm) fixed, and vary the matrix conductivity from $K_m = 10^{-6}$ to 10^{-3} m/s. Hence, we reduce the efficiency of the porous matrix further, as it can be seen in the longer recession limbs for low-conductivity matrix models.

3.2.2 Heterogeneous karst aquifer

Now we apply the time-dependent recharge from the Gallusquelle catchment to different karst aquifer evolution models from the last section. We start with two models obtained by the diffuse recharge condition, runs d2 and d5. For both of these runs, we choose four time slices representative for different stages of the evolution, and we distribute the time-dependent recharge over the entire plateau surface.

Run d2: In Figure 22, the fracture distributions for the four chosen time slices are shown on top.

The corresponding discharge curves as a function of time are shown below. At the initiation of the karst evolution (0 yrs), the hydrograph response (thick red line) is identical to the homogeneous karst aquifer case with $d_i = 0.2$ mm (Figure 21c, dotted line). A moderate recession limb resulting from the combination of permeable matrix ($K_m = 10^{-6}$ m/s in this case) and small fractures ($d_i = 0.2$ mm). Then fractures start evolving

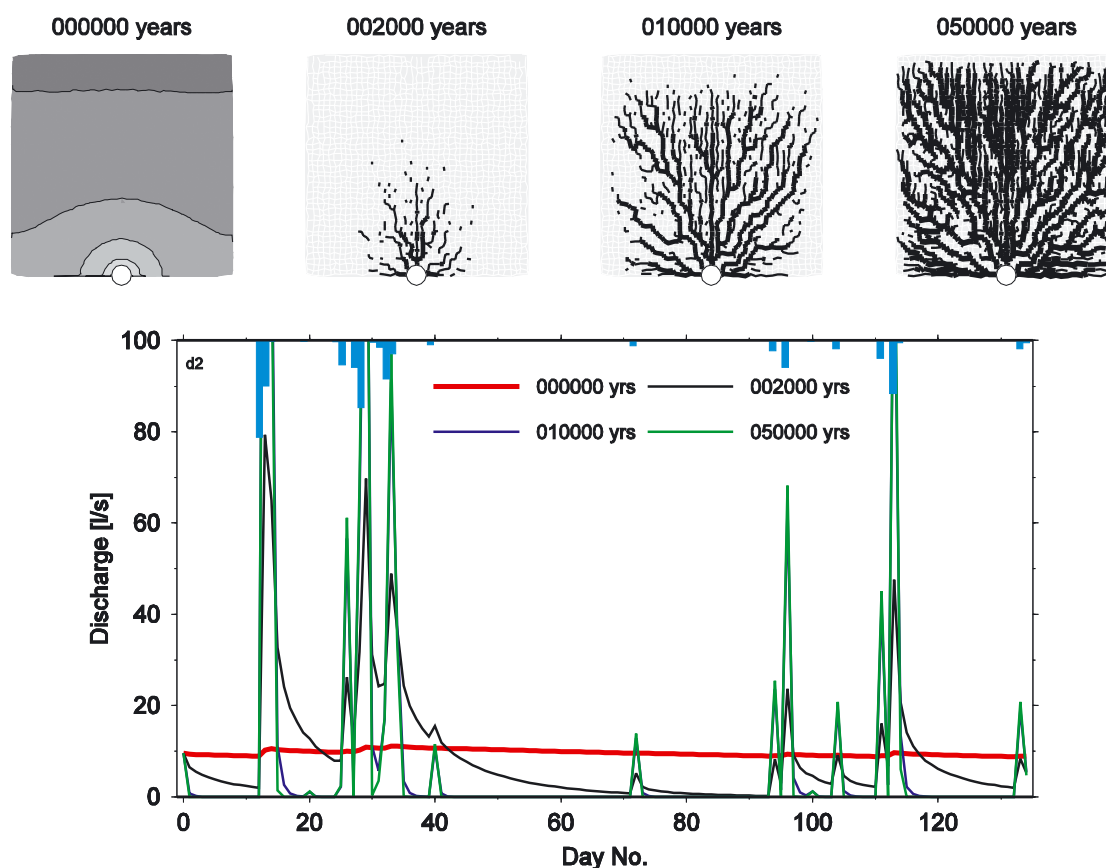


Figure 22: Run d2: Distributed recharge, irregular fractures. Top: Fracture-diameter evolution for four chosen time slices. Bottom: Discharge through karst resurgence as a function of time for the four chosen time slices. Shown are the discharge time series as lines, and the recharge events as bars on top.

around the karst resurgence, and 2,000 years into the evolution, the southern part of the karst plateau is efficiently drained through the enlarged fractures, while in the northern part flow is still slow and pore-controlled. The discharge series (black line) reflects this bimodal behaviour, small peaks from the rapid transmission of water through the enlarged fractures, followed by a long recession limb from the slow drainage of the northern part. After 10,000 years, the fractures within the entire karst plateau are enlarged, and drainage is fast and effective (blue line). Discharge is characterised by large peaks and a very short recession limb. Hence, within 10,000 years, flow through the evolving karst aquifer has changed significantly. Even further into the evolution (50,000 years), the transmission of flow is almost instantaneous, as every part of the karst plateau is directly drained through enlarged fissures. Following Hobbs & Smart (1986), the evolution can be classified as follows: Early discharge is characterised by high storage in the matrix and flow transmission controlled by both diffuse flow through the porous matrix and concentrated flow through the small initial fractures. Later, discharge is almost entirely concentrated to the enlarged fissures, and storage is insignificant.

Run d5: In Figure 23, the long-term evolution model with a prominent fault has been used. In this model the evolved cave passage pattern is remarkably different from the previous run, but the discharge response shown is almost identical. Thus, even for significantly different cave passage patterns, the response of the karst resurgence gives no clue about the fracture distribution.

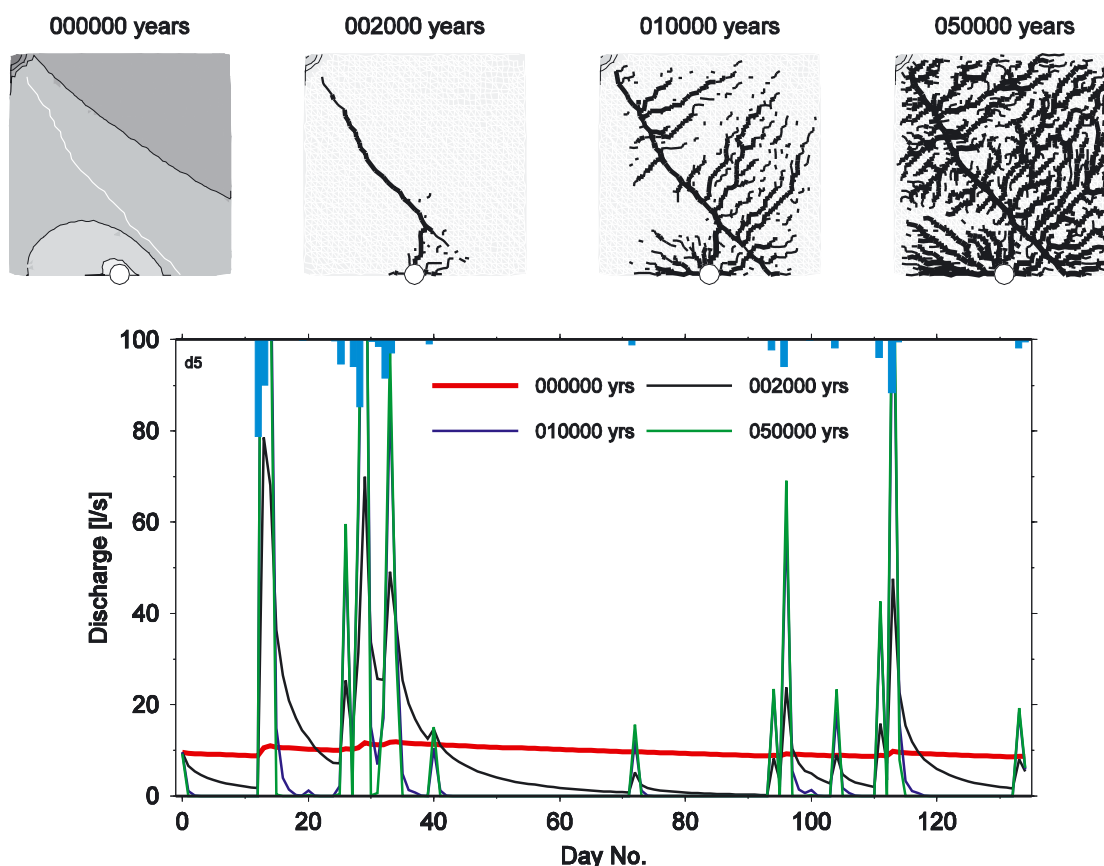


Figure 23: Run d5: Distributed recharge, irregular fractures, prominent fault, and sandstone domain.

The next two models, runs s2 and s5, are taken from the sink recharge runs. In this case, the time-dependent recharge series is injected into the two sinks only, and scaled to a catchment size of 0.5 km² for each sink. As we have already emphasised, this models evolve much slower, when compared to the distributed recharge runs.

Run s2: In Figure 24, the fracture distributions for the four chosen time slices are displayed. They result from a karst plateau with irregular fracture distribution, but no prominent faults. Early in the evolution of this run (0 years to 10,000 years, red and black lines), the discharge time series depict a very smooth curve, with almost no variation through time. Drainage in this early phase is entirely controlled by the rock matrix close to the karst resurgence. The enlarged fractures close to the sinks at 10,000 years have no pronounced effect on the discharge.

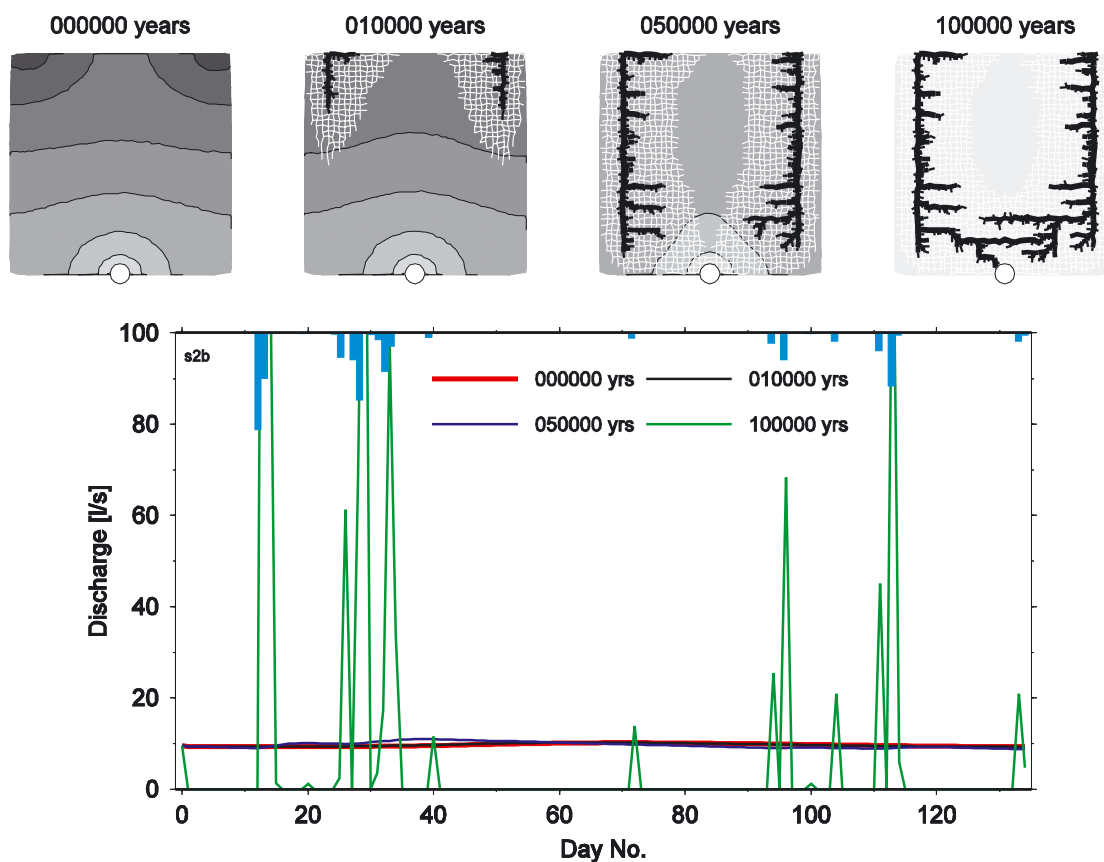


Figure 24: Run s2: Sink recharge, irregular fractures.

After 50,000 years of evolution, fractures enlarged to the millimetre-scale connect sinks and karst resurgence, but they are still too small to carry enough flow (blue line). The discharge characteristics have changed dramatically, when we consider the end of evolution at 100,000 years (green line). Now two independent cave passages drain the sinks, as two large fracture systems connect sinks and resurgence. Flow is carried efficiently through the fractures, and discharge is very flashy, with large peaks and very small recession limbs.

Run s5: In Figure 25, the irregular fracture distribution is complemented by a prominent fault, as it can be seen in the four time slices. Again, the early phase of the evolution results in a smooth discharge curve, as it can be seen for the times 0 years and 10,000 years. In both cases there is no continuous enlarged fracture system between sinks and resurgence, and the rock matrix close to the resurgence is the bottle neck, delaying flow. An interesting transitional period is captured at 50,000 years. Here, the prominent fault provides a direct connection between western sink and resurgence, thus a fast flow component without significant storage.

Fractures from the eastern sink, however, have not managed to break through. Hence, water from the eastern sink needs to percolate through a zone, where the rock

matrix still dominates, and thus provides a slow, high-storage flow component. This dual behaviour is obvious in the discharge series (blue line). Flashy peaks from the fast water of the eastern sink, but still a significant recession limb from the slow-flowing water from the eastern sink. After 100,000 years, the eastern sink is also drained by a continuous fracture system, hence discharge (green line) now is characterised by flood peaks, and no significant recession limb any more.

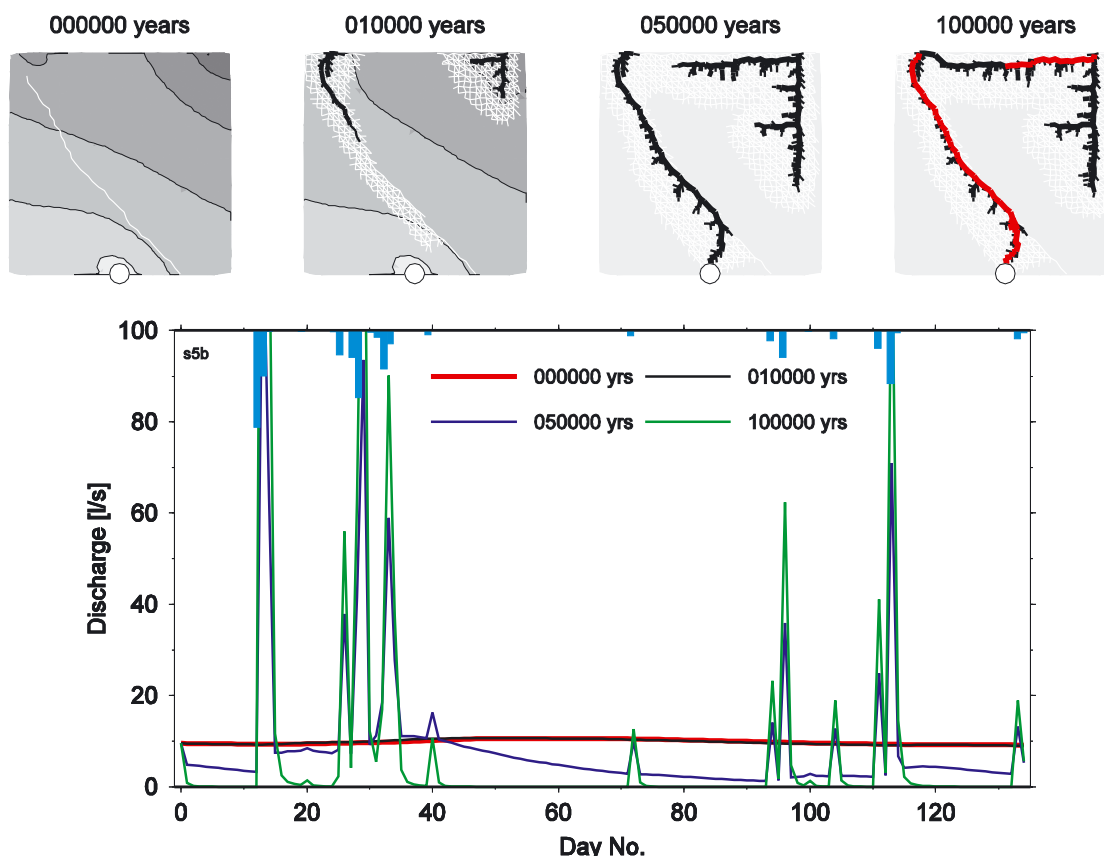


Figure 25: Run s5: Sink recharge, irregular fractures, and prominent fault.

Run sm10: The last example considers long-term evolution model sm10, which is recharged by two sinking streams saturated with respect to calcite, but with different carbon-dioxide concentrations. Fractures are irregularly distributed, and a prominent fault is present.

The four time slices shown in Figure 26 reveal the single drainage system connected to the karst resurgence, but no large fractures between sinks and the drainage channel. The discharge series in this case are revealing flow characteristics from the different regions in the karst plateau. While initially (0 years, red line) the system responds as an entirely pore-controlled aquifer, the enlarging main conduit imprints its fast-flow

component from 10,000 years on. First a reduction in recession limb (black line), and from 50,000 years on (blue and green lines) a marked peak, which, however, is not as flashy as in the previous cases. This is a result of the narrow fringe of fractures between the sinks and the large conduits, as each recharge event first needs to pass this region, transmitting water slowly. Once the water reaches the enlarged conduit, it rapidly flows towards the resurgence.

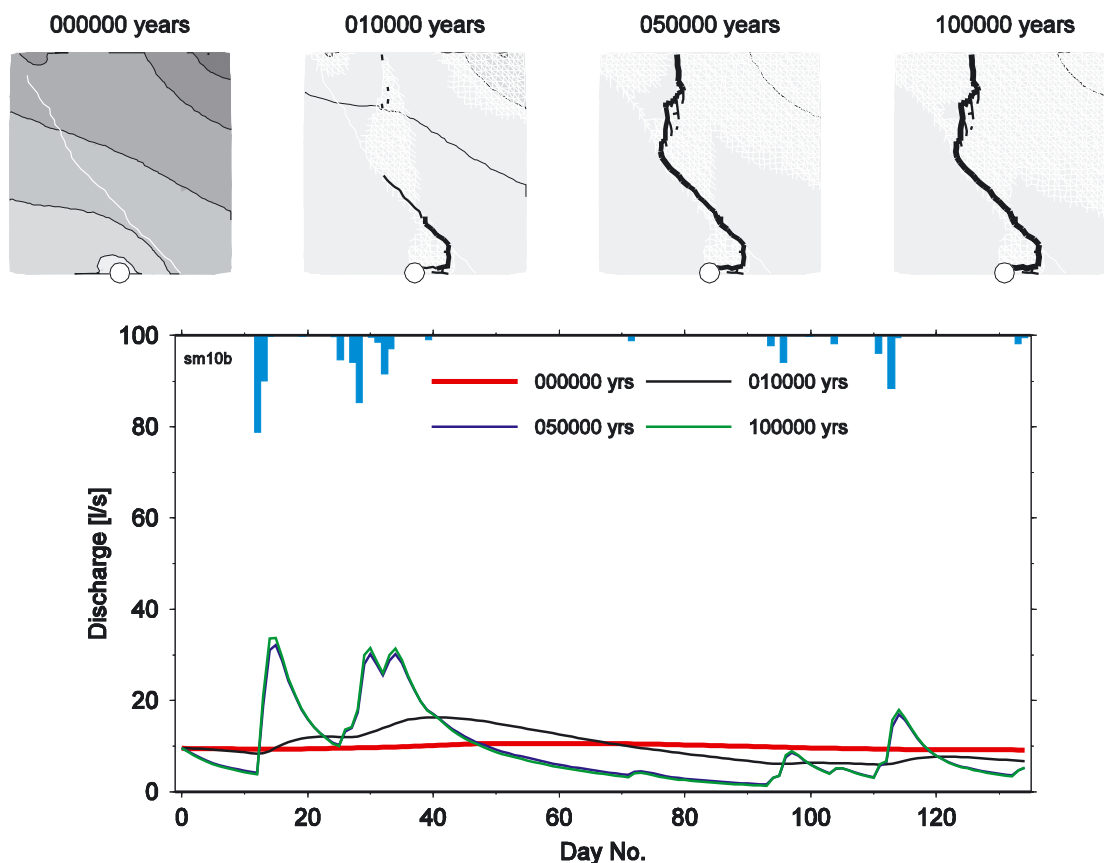


Figure 26: Run sm10: Sink recharge, irregular fractures, additional prominent fault, saturated input, and different CO₂-concentrations.

3.2.3 Summary of short-term spring response models

The short-term spring response modelling has shown that the long-term karst aquifer evolution is characterised by distinct phases of the short-term hydrograph response. Several key aspects can be observed:

(i) Spring discharge during the early evolution is controlled by the slow-flow, high-storage regime both in the porous matrix and the not yet enlarged primary fissures. Thus the initial conditions of our long-term evolution models depicts a juvenile karst aquifer.



GEORG KAUFMANN

(ii) After a characteristic time, depending on the type of recharge, the spring response becomes very flashy, as the fast-flow, low-storage fracture system entirely controls the transmission of water. The change from smooth to flashy spring responses occurs early, if recharge is assumed to originate from precipitation over the entire model domain, but late, if only sinking streams provide water to the aquifer.

(iii) The structural control of larger faults, which was responsible for different cave passage patterns during the long-term evolution, leaves no significant fingerprint on the spring discharge, as long as the entire region is drained by enlarged fractures. This confirms our earlier statement that a spring discharge time series reflects rather global, integral parameters of a karst aquifer.

(iv) If the karst aquifer has only been enlarged by mixing corrosion, the recession limb of the hydrograph time series remains prominent, as in this case parts of the aquifer (in our case close to the sinks) remain controlled by the low-flow, high-storage regime.

ACKNOWLEDGEMENTS

I would like to thank Wolfgang Dreybrodt, Franci Gabrovček, and Dushko Romanov for the possibility to contribute to the karst modelling book. The figures in this paper are drawn using the GMT graphics package (Wessel & Smith, 1991, 1998).



REFERENCES

- Atkinson, T. C., Smith, D. I., Lavis, J. J., and Whitaker, R. J. (1973). Experiments in tracing underground waters in limestones. *J. Hydrol.*, 323–349.
- Baedke, S. J. and Krothe, N. C. (2001). Derivation of effective hydraulic parameters of a karst aquifer from discharge hydrograph analysis. *Water Resour. Res.*, **Vol. 37, No. 01.**, p. 13 (2000WR900247).
- Beek, W. J. and Mutzall, K. M. K. (1975). *Transport Phenomena*. John Wiley, London.
- Bögli, A. (1971). Corrosion by mixing of karst waters. *Trans. Cave Res. Group G.B.*, (2), 109–114.
- Bögli, A. (1978). *Karsthydrographie und physische Speläologie*. Springer, Berlin, Heidelberg, New York.
- Buhmann, D. and Dreybrodt, W. (1985a). The kinetics of calcite dissolution and precipitation in geologically relevant situations of karst areas. 1. Open system. *Chem. Geol.*, 189–211.
- Buhmann, D. and Dreybrodt, W. (1985b). The kinetics of calcite dissolution and precipitation in geologically relevant situations of karst areas. 2. Closed system. *Chem. Geol.*, 109–124.
- Clemens, T., Hückinghaus, D., Sauter, M., Liedl, R., and Teutsch, G. (1996). A combined continuum and discrete network reactive transport model for the simulation of karst development. In *Calibration and Reliability in Groundwater Modelling, IAHS Publ.*, volume 237, pages 309–318. Proceedings of the ModelCARE 96 Conf.
- Clemens, T., Hückinghaus, D., Sauter, M., Liedl, R., and Teutsch, G. (1997). Modelling the genesis of karst aquifer systems using a coupled reactive network model. In *Hard Rock Hydrosciences, IAHS Publ.*, volume 241, pages 3–10. Proceedings of Rabat Sym. S2.
- Dreybrodt, W. (1988). *Processes in Karst Systems*. Springer, Berlin.
- Dreybrodt, W. (1990). The role of dissolution kinetics in the development of karst aquifers in limestone: a model simulation of karst evolution. *J. Geol.*, (5), 639–655.
- Dreybrodt, W. (1996). Principles of early development of karst conduits under natural and man-made conditions revealed by mathematical analysis of numerical models. *Water Resour. Res.*, (9), 2923–2935.
- Dreybrodt, W. and Gabrovšek, F. (2000). Dynamics of the evolution of single karst conduits. In A. B. Klimchouk, D. C. Ford, A. N. Palmer, and W. Dreybrodt, editors, *Speleogenesis: Evolution of Karst Aquifers*, pages 184–193. National Speleological Society, New York.
- Dreybrodt, W., Laukner, J., Zaihua, L., Svensson, U., and Buhmann, D. (1996). The kinetics of the reaction $\text{CO}_2 + \text{H}_2\text{O} \rightarrow \text{H}^+ + \text{HCO}_3^-$ as one of the rate limiting steps for the dissolution of calcite in the system $\text{H}_2\text{O} - \text{CO}_2 - \text{CaCO}_3$. *Geochem. Cosmochem. Acta*, (18), 3375–3381.
- Eisenlohr, L., Király, L., Bouzelboudjen, M., and Rossier, Y. (1997a). Numerical simulation as a tool for checking the interpretation of karst spring hydrographs. *J. Hydrol.*, 306–315.
- Eisenlohr, L., Bouzelboudjen, M., Király, L., and Rossier, Y. (1997b). Numerical versus statistical modelling of natural response of a karst hydrogeological system. *J. Hydrol.*, 244–262.

- Eisenlohr, L., Meteva, K., Gabrovšek, F., and Dreybrodt, W. (1999). The inhibiting action of intrinsic impurities in natural calcium carbonate minerals to their dissolution kinetics in aqueous H₂O-CO₂ solutions. *Geochem. Cosmochem. Acta*, (6), 989–1001.
- Gabrovšek, F. and Dreybrodt, W. (2000). The role of mixing corrosion in calcite aggressive H₂O-CO₂-CaCO₃ solutions in the early evolution of karst aquifers in limestone. *Water Resour. Res.*, 1179–1188.
- Gabrovšek, F. and Dreybrodt, W. (2001). A comprehensive model of the early evolution of karst aquifers in limestone in the dimensions of length and depth. *J. Hydrology*, (3–4), 206–224.
- Gabrovšek, F., Menne, B., and Dreybrodt, W. (2000). A model of early evolution of karst conduits affected by subterranean CO₂ sources. *Environ. Geol.*, (6), 531–543.
- Grasso, D. A. and Jeannin, P.-Y. (1998). Statistical approach to the impact of climatic variations on karst spring chemical response. *Bull. d'Hydrogeol.*, 59–74.
- Groves, C. G. and Howard, A. D. (1994a). Minimum hydrochemical conditions allowing limestone cave development. *Water Resour. Res.*, (3), 607–615.
- Groves, C. G. and Howard, A. D. (1994b). Early development of karst systems 1. Preferential flow path enlargement under laminar flow. *Water Resour. Res.*, (10), 2837–2846.
- Gureghian, A. B. (1975). A study by the finite element method of the influence of fractures in confined aquifers. *Soc. Pet. Eng. J.*, 181–191.
- Hanna, B. R. and Rajaram, H. (1998). Influence of aperture variability on dissolutional growth of fissures in karst formations. *Water Resour. Res.*, 2843–2853.
- Hobbs, S. L. and Smart, P. L. (1986). Characterisation of carbonate aquifers: a conceptual base. In *Proceedings of the 9th Int. Congress of Speleology*, pages ?–?, Barcelona. UIS.
- Howard, A. D. and Groves, C. G. (1995). Early development of karst systems 2. Turbulent flow. *Water Resour. Res.*, (1), 19–26.
- Huyakorn, P. S., Lester, B. H., and Mercer, J. W. (1983). Finite element techniques for modeling groundwater flow in fractured aquifers. *Water Resour. Res.*, (4), 1019–1035.
- Jeannin, P.-Y. (2001). Modeling flow in phreatic and epiphreatic karst conduits in the Hölloch cave (Muotatal, Switzerland), (2), 191–200.
- Jeannin, P.-Y. and Sauter, M. (1998). Analysis of karst hydrodynamic behaviour using global approaches: a review. *Bull. d'Hydrogeol.*, 31–48.
- Jeppson, R. W. (1976). *Analysis of flow in pipe networks*. Ann Arbor Sci. Pub., Ann Arbor.
- Kaufmann, G. (2002a). Karst aquifer evolution in a changing watertable environment. *Water Resources Res.*, (6), 10.1029/2001WR000256, 26–1–26–9.
- Kaufmann, G. (2002b). Karst conduit evolution. In F. Gabrovšek, editor, *Evolution of Karst: From Prekarst to Cessation*, pages 327–338, Postojna-Ljubljana. Carsologica, ZRC SAZU.
- Kaufmann, G. (2003a). Numerical models for mixing corrosion in natural and artificial karst environments. *Water Resour. Res.*, (6), SBH9–1–SBH9–12.
- Kaufmann, G. (2003b). A model comparison of karst aquifer evolution for different matrix-flow formulations. *J. Hydrol.*, (1–4), 281–289.
- Kaufmann, G. and Braun, J. (1999). Karst aquifer evolution in fractured rocks. *Water Resources Res.*, (11), 3223–3238.
- Kaufmann, G. and Braun, J. (2000). Karst aquifer evolution in fractured, porous rocks. *Water Resources Res.*, (6), 1381–1392.

- Kiraly, L. (1998). Modelling karst aquifers by the combined discrete channel and continuum approach. *Bull. d'Hydrogeol.*, 77–984.
- Laumanns, M. and Gebauer, H. D. (1993). Namoroka 1992. Expedition to the karst of Namoroka and Narinda, Madagascar. *Int. Cav.*, 30–36.
- Laumanns, M. and Ruggieri, R. (1995). The latest investigations of the caves of the Matumbi Hills. *Int. Cav.*, 3–11.
- Palmer, A. N. (1991). Origin and morphology of limestone caves. *Geol. Soc. Am. Bull.*, 1–21.
- Palmer, A. N. (2000). Digital modeling of individual solution conduits. In A. B. Klimchouk, D. C. Ford, A. N. Palmer, and W. Dreybrodt, editors, *Speleogenesis: Evolution of Karst Aquifers*, pages 194–200. National Speleological Society, New York.
- Plummer, L. N. and Busenberg, E. (1982). The solubilities of calcite, aragonite and vaterite in CO_2 - H_2O solutions between 0 and 90 °C, and an evaluation of the aqueous model of the system CaCO_3 - CO_2 - H_2O . *Geochim. Cosmochim. Acta*, 1011–1040.
- Plummer, L. N., Wigley, T. M. L., and Parkhurst, D. L. (1978). The kinetics of calcite dissolution in CO_2 -water systems at 5 °C to 60 °C and 0.0 to 1.0 atm CO_2 . *Am. J. Sci.*, 179–216.
- Robinson, R. A. and Stokes, R. H. (1955). *Electrolyte solutions*. Butterworths Sci. Publ., London.
- Romanov, D., Dreybrodt, W., and Gabrovšek, F. (2002). Interaction of fracture and conduit flow in the evolution of karst aquifers. In J. B. Martin, C. Wicks, and I. D. Sasowsky, editors, *Proceedings of the Symposium on Karst Aquifers: Florida and Related Environments*, pages 1–6. Karst Water Institute, Charles Town, West Virginia, KWI Special publ. 7.
- Romanov, D., Gabrovšek, F., and Dreybrodt, W. (2003). The impact of hydrochemical boundary conditions on the evolution of limestone karst aquifers. *J. Hydrol.*, (1–4), 240–253.
- Sauter, M. (1992). *Quantification and forecasting of regional groundwater flow and transport in a karst aquifer (Gallusquelle, Malm, SW. Germany)*. Tübinger Geowiss. Arb., TGA C13, Tübingen.
- Siemers, J. and Dreybrodt, W. (1998). Early development of karst aquifers on percolation networks of fractures in limestone. *Water Resour. Res.*, (3), 409–419.
- Svensson, U. and Dreybrodt, W. (1992). Dissolution kinetics of natural calcite minerals in CO_2 -water systems approaching calcite equilibrium. *Chem. Geol.*, 129–145.
- Truesdell, A. H. and Jones, B. F. (1974). WATEQ, a computer program for calculating chemical equilibria of natural waters. *U.S. Geol. Surv. J. Res.*, (2), 233–248.
- Turcotte, D. L. and Schubert, G. (1982). *Geodynamics*. John Wiley and Sons, New York.
- Wessel, P. and Smith, W. H. F. (1991). Free software helps map and display data. *EOS*, 441–446.
- Wessel, P. and Smith, W. H. F. (1998). New, improved version of generic mapping tools released. *EOS*, 579.
- White, W. B. (1977). The role of solution kinetics in the development of karst aquifers. *Mem. Int. Assoc. Hydrogeol.*, 503–517.

Table 1: Reference model parameters.

Parameter	Description	Unit	Value
Equilibrium Chemistry			
T_c	Temperature	°C	10
T	Temperature	°C	$273.16+T_c$
P	Carbon-dioxide pressure	atm	0.001–0.1
I	Ion activity	mol/l	3c
A	Debye-Hückel coefficient	–	$0.4883+8.074 \times 10^{-4} T_c$
B	Debye-Hückel coefficient	–	$0.3241+1.600 \times 10^{-4} T_c$
$\log \gamma_{Ca^{2+}}$	Activity coefficient	–	$-4A\sqrt{I}/(1+5.0 \times 10^{-8} B\sqrt{I})$
$\log \gamma_{HCO_3^-}$	Activity coefficient	–	$-1A\sqrt{I}/(1+5.4 \times 10^{-8} B\sqrt{I})$
$\log K_0$	Equilibrium coefficient	–	see Plummer & Busenberg (1982)
$\log K_1$	Equilibrium coefficient	mol/l	see Plummer & Busenberg (1982)
$\log K_2$	Equilibrium coefficient	mol/l	see Plummer & Busenberg (1982)
$\log K_5$	Equilibrium coefficient	mol/l	see Plummer & Busenberg (1982)
$\log K_C$	Equilibrium coefficient	mol ² /l ²	see Plummer & Busenberg (1982)
$\log K_H$	Equilibrium coefficient	mol/l/atm	see Plummer & Busenberg (1982)
Fluxrates			
n_1	Linear exponent	–	1
n_2	Non-linear exponent	–	4
k_0	Dissolution-rate constant	mol/m ² /s	4×10^{-7}
D	Diffusion constant	m ² /s	10^{-9}
c_i	Initial calcium concentration	mol/m ³	0–2
c_s	Threshold calcium concentration	mol/m ³	$0.9 c_{eq}$
c_{eq}	Equilibrium calcium concentration	mol/m ³	Eq. (1)
Conductivities			
d_i	Initial fracture diameter	mm	0.2
d_f	Initial fault diameter	mm	0.6
K_m	Matrix conductivity	m/s	1×10^{-6}
K_f	Fracture conductivity	m/s	Eq. (15)
S_m	Matrix storativity	–	0.005–0.02
S_f	Fracture storativity	–	0.0001
g	Gravitational acceleration	m/s ²	9.81
ρ	Density of calcite	kg/m ³	2700
m_r	Molecular weight of calcite	kg/mol	0.10009
ν	Kinematic viscosity of water	m ² /s	1.14×10^{-6}
Grid			
$sidex$	Model x-dimension	m	1000
$sidey$	Model y-dimension	m	1000
nx	Model x grid points	–	41
ny	Model y grid points	–	41
T	Time step	yr	1

Table 2: Run parameter.

Run no.	fractures					recharge				sinks	
	x	y	d	f	s	q	c_{in}	p	q	c_{in}	p
d1	X	X	–	–	–	300	0.90	0.05	–	–	–
d2	x	x	–	–	–	300	0.90	0.05	–	–	–
d3	x	x	x	–	–	300	0.90	0.05	–	–	–
d4	x	x	–	x	–	300	0.90	0.05	–	–	–
d5	x	x	x	x	x	300	0.90	0.05	–	–	–
s1	X	X	–	–	–	–	–	–	9×10^5	0.90	0.05
s2	x	x	–	–	–	–	–	–	9×10^5	0.90	0.05
s3	x	x	x	–	–	–	–	–	9×10^5	0.90	0.05
s4	x	X	–	x	–	–	–	–	9×10^5	0.90	0.05
s5	x	x	x	x	–	–	–	–	9×10^5	0.90	0.05
sm7	x	x	–	–	–	–	–	–	9×10^5	0.90	0.1/0.01
sm8	x	x	–	–	–	–	–	–	9×10^5	0.99	0.1/0.01
sm9	x	x	x	x	–	–	–	–	9×10^5	0.90	0.1/0.01
sm10	x	x	x	x	–	–	–	–	9×10^5	0.99	0.1/0.01
X	regular fracture in x-direction										
Y	regular fracture in y-direction										
x	irregular fracture in x-direction										
y	irregular fracture in y-direction										
d	fracture in dip-direction										
f	fault										
s	sandstone										
r	random initial width										
q [mm/yr]	Recharge rate										
c_{in} [-]	normalized initial calcium concentration										
p [atm]	CO_2 partial pressure										

*Address**Georg Kaufmann**Institute of Geophysics, University of Göttingen,**Herzberger Landstrasse 180, 37075 Göttingen, Germany.**E-mail: gkaufman@uni-geophys.gwdg.de*



The companion CD-ROM contains:

- **Animations** of selected scenarios presented as **PowerPoint Shows (PPS)**
- **JPG** files of all figures for fast screen preview
- **PDF** vector files of all figures for a detailed view

Instructions for use:

The file numbers of **PDF** and **JPEG** files correspond to the figure numbers in the book. To see the PDF or JPEG files, open them by your preferred viewer/reader.

To watch animations, open the file **Animations.pps**, which is in the root directory of the CD. Within this file, you can navigate through the chapters and select animations. The number of the animation corresponds to the number of the figure in the book. Navigate through the selected animation with the mouse wheel or use arrow keys on your computer. To exit animation and to return to the main selection file, click **Exit Navigation** or press **ESC** key. If you do not have Microsoft Powerpoint installed on your computer, you can obtain a free Microsoft Powerpoint viewer from the Microsoft web page.



This book draws together the major recent advances in the modeling of karst systems. Based on the dissolution kinetics of limestone, and flow and transport processes in its fractures, it presents a hierarchy of cave genetic situations that range from the enlargement of a single fracture to the evolution of cavernous drainage patterns in confined and unconfined karst aquifers. These results are also applied to the evolution of leakage below dam sites in karst. The book offers a wealth of informations that help to understand the development of cave systems. It addresses geologists, hydrologists, geomorphologists, and geographers. It is also of interest to all scientists and engineers who have responsibilities for groundwater exploration and management in karst terrains.

7.940 SIT 33,20 EUR

ISBN 961-6500-91-0



ZALOŽBA
Z R C

ZALOŽBA ZRC • ZRC PUBLISHING

www.zrc-sazu.si/zalozba